Forschungszentrum Jülich
in der Helmholtz-Gemeinschaft



First Cairo Conference on Plasma Physics & Applications

edited by
H.-J. Kunze, T. El-Khalafawy, H. Hegazy

International Cooperation
Bilateral Seminars

Vol. 34

Schriften des Forschungszentrums Jülich
Bilateral Seminars of the International Bureau Vol. 34

Forschungszentrum Jülich GmbH
Bilateral Seminars of the International Bureau

First Cairo Conference on

Plasma Physics & Applications: CCPPA 2003

Cairo 11 – 15 October 2003

edited by
H.-J. Kunze, T. El-Khalafawy, H. Hegazy

Schriften des Forschungszentrums Jülich
Bilateral Seminars of the International Bureau Vol. 34

ISSN 1433-5581 ISBN 3-89336-374-2

Bibliographic information published by Die Deutsche Bibliothek.
Die Deutsche Bibliothek lists this publication in the Deutsche Nationalbibliografie; detailed bibliographic data are available in the Internet at <http://dnb.ddb.de>.

Publisher and Distributor: Forschungszentrum Jülich GmbH
Central Library
52425 Jülich
Germany
Phone +49 (0) 2461 61 - 5368 · Fax +49 (0) 2461 61 - 6103
e-mail: zb-publikation@fz-juelich.de
Internet: http://www.fz-juelich.de/zb

Coverdesign: Grafische Betriebe, Forschungszentrum Jülich GmbH

Printer: Grafische Betriebe, Forschungszentrum Jülich GmbH

© Forschungszentrum Jülich 2004

Schriften des Forschungszentrums Jülich
Bilateral Seminars of the International Bureau Vol. 34

ISSN 1433-5581
ISBN 3-89336-374-2

Neither this book nor any part may be reproduced or transmitted in any form or by any means, electronic or mechanical, including photocopying, microfilming, and recording, or by any information storage and retrieval system, without permission in writing from the publisher.

Proceedings of the

First Cairo Conference on Plasma Physics & Applications
CCPPA2003

Cairo, Egypt, 11-15 October 2003
Tibarose Hotel

Organized by

Plasma Physics Department, N.R.C.,
Egyptian Atomic Energy Authority

under the Auspices of
His Excellency

Dr. Eng. Hassan Younes
Minister of Electricity & Energy
Conference Honorary Chairman

Prof. Dr. Aly I. M. Aly
President Egyptian Atomic Energy Authority, Egypt

Honorary Directors
Prof. Dr. E. Hintz Prof. M. M. Masoud

Executive Scientific Board
Prof. T. El-Khalafawy Prof. Sh. Khalil Dr. H. Hegazy

Chairpersons
Prof. H. Soliman Prof. Y. A. Sayed

Co Chairman
Dr. B. F. Mohamed

Scientific Secretary
Dr. A. Mahdy Dr. T. Allam Dr. A. Elsisi

Local Organizing Committee
Plasma Physics Department Staff, N.R.C. Atomic Energy Authority

Sponsors
Egyptian Energy Authority (EAEA)
The Abdus Salam International Center for Theoretical Physics (ICTP), Trieste, Italy
Asian African Association for Plasma Training (AAAPT)
International Bureau of the Federal Ministry of Education and Research (BMBF), Germany

Preface

The 1st Cairo Conference on Plasma Physics & Applications 2003 (CCPPA2003) was organized by the Plasma Physics Department, Nuclear Research Centre, of the Egyptian Atomic Energy Authority. The Conference was a continuation of a series of activities started in 1987 with the First Workshop on Plasma Physics and Laser Technology in cooperation with the Institute for Plasma Physics at Jülich, Germany, under the umbrella of the Egyptian-German Bilateral Agreement. These activities comprised in total four workshops in the years 1987, 1990, 1993, 1996, a one-day seminar in 1991 and a training course in 1992 for Asian–African countries under the auspices of the Asian-African Association for Plasma Training (AAAPT).

CCPPA2003 was sponsored by the Egyptian Atomic Energy Authority (EAEA), the Abdus Salam International Centre for Theoretical Physics (ICTP), and the Asian African Association for Plasma Training (AAAPT).

The conference was held from 11 to 15 October 2003 in the Tibarose Hotel, Nasr City, Cairo, Egypt. The aim of the conference was to provide a suitable scientific forum for plasma physicists from developing countries. Besides, participants had the chance to interact with international scientists and to learn about advanced topics and newly emerging research directions. The conference proceedings contain about 13 invited lectures given by researchers eminent in their fields.

Participants from 25 countries participated and presented their contributions during the conference days. All contributions were followed by informal discussions which brought additional information to the understanding of the most recent results. These contributions were refereed. After inclusion of the suggestions and the comments of the referees, 63 contributions were accepted for publications in these proceedings. The contributions cover a wide area in plasma physics & applications: tokamaks, plasma diagnostics, small plasma devices, plasma applications, laser plasma interaction, laser applications, and plasma theory.

We must thank

Prof. J. Badziak (Poland)
Prof. W. Demtröder (Germany)
Prof. A. El-Nadi (Egypt)
Dr. K.H. Finken (Germany)
Prof. Sh. M. Khalil (Egypt)
Prof. S. Lee (Malaysia)
Prof. M. Shoucri (Canada)
Prof. H. Soliman (Egypt)
Prof. J. Stöckel (Czech Republic)
Prof. G. Van Oost (Belgium)

for their time given to referee the conference contributions.

We are indebted to Prof. Aly Islam M. Aly for his strong support and commitment to the organization of the conference. Thanks for the helpful support of the International Bureau Jülich, Germany, which is very much appreciated and is gratefully acknowledged.

Last but not least many thanks to the hosts for their skill and effort in the conference organization and the great hospitability to make the stay of the participants so pleasant.

The Editors

H.-J. Kunze
T. El-Khalafawy
H. Hegazy

CONTENTS

III Preface

INVITED TALKS

1 Edge Plasma Physics and Relevant Diagnostics on the CASTOR Tokamak
J. Stöckel

7 Turbulent Transport Reduction by ExB Velocity Shear during Edge Plasma Biasing in Tokamaks
G. Van Oost

13 First Experience with the Dynamic Ergodic Divertor on TEXTOR
K.H. Finken

19 The Theta – Pinch - A Versatile Tool for the Generation and Study of High Temperature Plasmas
E. Hintz

27 Characterising the Plasma Focus Pinch and Speed Enhancing the Neutron Yield
S. Lee

34 Research on Pinch Devices of Tens of kA to MA
L. Soto

40 Nano-Sized Material Preparation in Ultrathin Film Form Using Dense Plasma Focus
M.P. Srivastava

46 X-Ray Lasing in Ablative Capillary Discharge
H.-J. Kunze

52 Applications of Laser-Spectroscopy in Plasma Physics and in Analytics
W. Demtröder

58 Influence of Optical Feedback on the Dynamics on a Semiconductor Laser Having a Short External-Cavity
A.M. El-Nadi

64 Large Plasma Set-up for Modeling Space Phenomena and Technological Applications
A.V. Kostrov

68 Plantary Electromagnetic Waves in the ionospheric E-layer
T.D. Kaladze

75 Nonrelativistic Plasma Electronics
I.N. Onishchenko

TOKAMAK

81 Measurement of Electron Temperature Fluctuations with Tunnel Probe in the CASTOR Tokamak
J.P. Gunn, J. Stöckel, T. Van Rompuy, J. Adámek, P. Balan, O. Bařina, P. De Beule, I. Ďuran, R. Hrach, M. Hron, R. Pánek, R. Schrittwieser, G. Van Oost, M. Vicher, and F. Žáček

85 EGYPTOR Tokamak: Modification of the Original Design Using Permanent Compensation Coils and First Results of the Breakdown Discharge
A.B. El Sisi and H. Hegazy

90 Study of the Formation of a Charge Separation and Electric Field at a Plasma Edge using Eulerian Vlasov Codes
M. Shoucri, H. Gerhauser, and K.-H. Finken

94 Modelling of Rotating Plasma States and their Stability Under the Influence of Helical Perturbations in TEXTOR and JET
A.Nicolai, U. Daybelge, and C. Yarim

98 Plasma Separatrix in Toroidal Pinch
S.A. Shalaby, A.B. Beshara, A.B. El-Bialy, and M.M. Masoud

102 Energy Confinement Analysis on the Libtor Tokamak
A.M. Alabyad, B.M. Esmail, and R M. Al-Habashi

PLASMA DIAGNOSTICS

106 Laser Scattering for Plasma Diagnostics in Gas Liner Pinch
H. Hegazy, S. Seidel, Th. Wrubel, and H.-J. Kunze

110 Comparison of Low Density Plasma Property Measurements in a Magnetic Multipole Source by Langmuir Probe and Laser Thomson Scattering Techniques
Ahmed A. I. Khalil, S. Maurmann and H.-J. Kunze

114 Observation of Non Thermal N_2 Second Positive Emission in Quasi Thermal Air Plasma
S. Saloum, A.M. Gomes and J.P. Sarrette

118 Temperature Distribution Induced by Electron Beam in a Closed Cavity
A.G. Molhem and S.Sh. Soulayman

122 Electron Temperature in Ar Glow Discharge
A.A. Garamoon, F.F. Elakshar, E.F. Kotp, and A. Samir

126 A Practical Mthod Using Labview for Measurements of the Electron Temperature in a Helium Glow Discharge by Optical Emission Spectroscopy
Eynas Amer, I.Z. Ismail, M. El Shaer

130 Measurement of the Formative Time Lag of Argon Using Magnesium Electrode
E.F. Kotp, A.H. Saudy, F.F. Elakshar, A.M. Bakry and A.A. Garamoon

134 VUV Spectrum and Plasma Dynamics in a Small and Fast Capillary Discharge Operating in Argon. Observation of the ArIX 46.9 nm Line
Leopoldo Soto, Andrey Nazarenko, Cristian Pavez, and Patricio Silva

138 Proportional Counter of ^{3}He Adapted to Measure Neutron Pulses of Low Total Yield in Pinch Devices
José Moreno, Lipo Birstein, Roberto Mayer, Patricio Silva, and Leopoldo Soto

142 Density Diagnostics of Hot Plasmas Using Intensity Ratios of Emission Lines from Be-Like Fe^{22+} Ions
S.W. Rachedi and M.K. Inal

146 Polarization Spectroscopy of Anisotropic Hot Plasma
Z. Bedrane and M.K. Inal

150 Polarization of the Line x Emitted by Nb^{39+} Ions From Anisotropic Hot Plasmas
R. Bensaïd and M.K. Inal

SMALL PLASMA DEVICES

154 Route to Soft X-ray Laser Pumped by Gas-Filled-Capillary Discharge
K. Koláček, J. Schmidt, V. Boháček, V. Prukner, M. Řipa, O. Frolov, J. Štraus, and P. Vrba

158 Spectroscopic Measurement of Radiation Generated by Discharge in Alumina Capillary
J. Schmidt , K. Koláček, V. Boháček, M. Řipa, V. Prukner, O. Frolov, and J. Štraus

162 Ramp Discharge in Z-Pinch
W.H. Gaber, A.B. Beshara, A.B. El-Bialy and M.M. Masoud

166 Magnetic Forces Distribution in a 4.4 kJ Plasma Focus Device
G.M. El-Kashef and H.M. Soliman

170 Operation of a Plasma Focus Device with Energy of 2.8 kJ in Various Gases
Sh.H. Al-Hawat and O. Othman

174 Magnetic Field and Plasma Sheath Velocity Profiles in a 2 kJ Plasma Coaxial Accelerator
M.M. Masoud, H.M. Soliman, A.B. El-Bialy, and F.A. Ebrahim

178 Investigation of Plasma Current Sheath Dynamics in a Plasma Focus Discharge
T.Y. Allam, G.M. El-Kashef, and H.M. Soliman

182 Effect of Applied Magnetic Field Variation on Microwave Radiation from Coaxial Discharges
T.Y. Allam

186 Design Aspects of an Ion Injector
N.I. Bassal, M.S. Ragheb, and S.G. Zakhary

191 Phase Space Measurements at Non-Accessible Point on the Beam Path of an Accelerator Facility
A. Hassan

PLASMA APPLICATIONS

195 Application of Dense Plasma Focus Device for Thin Film Deposition and Modification
R.S. Rawat, R.S. Joseph, W.L. Clarissa, L.Y. Soh, P. Arun, A.G. Videshwar, W.M. Chew, V. Aggarwal, P. Lee, and S. Lee

199 Tailoring of Materials by Atomic Oxygen from ECR Plasma Source
Munzer Naddaf and S.V. Bhoraskar

203 Deposition of Different Thin Films Using Dense Plasma Focus
U.M. Rashed, A.H. Saudy, W. Sharkawy, and M.A. Eissa

207 Carbonitriding of ASS by ICRF Discharge
M.A. Eissa, A.M. Nossair, F.F. Alakshar, F.M. El-Hossary, and A.M. El-Halafawy

211 Characteristics of Plasma Etching Associated with a Multihollow Cathode Glow Discharge
Ahmad R. Galaly, M. Atta Khedr, F.F. El-Akshar, and Y. Badr

215 Surface Treatment of Polymer Material Using Argon Glow Discharge
M.A. Hassouba, N.I. Hendawy, and F.F. Elakshar

219 Improvement of Stainless Steel Properties with Titanium Oxides Deposited by Pulsed Ion Implantation Using DPF
S.A. El-Badry, Z. Abdel Hamid, U.M. Rashed, and A.H. Saudy

223 Dc Plasma Ion Implantation in an Inductively Coupled RF Plasma
C. Silawatshananai, N. Matan, C. Pakpum, N. Pussadee, P. Srisantitam, S. Davynov, and T. Vilaithong

227 Ion Implantation on Nickel Targets by Means of Repetitive Plasma Focus Device
S. Vitulli, M.L. Apicella, L. Rapezzi, and M. Samuelli

LASER PLASMA INTERACTION

232 Fast Ions From Picosecond Laser-Plasma Interaction
J. Badziak, H. Hora, S. Jabłoński, J. Krása, L. Láska, P. Parys, K. Rohlena, and J. Wołowski

236 Detection and Evaluation of Uranium in Different Minerals by Gamma Spectrometry and Laser Induced Breakdown Spectroscopy
F.M. Sergani, M.A. Khder, Sayed A. El Mongy, and M.A. Harith

240 Quantitative Elemental Analysis of Agricultural Drainage Water Using Laser Induced Breakdown Spectroscopy
M. Soliman, W. Tawfik, and M.A. Harith

LASER APPLICATIONS

244 A Comparative Study of Nd-Yag and Excimer Lasers Induced Plasma Evolution
S. Abdelli-Messaci, T. Kerdja, S.M. Aberkane, and S. Malek

247 Modelling of Vapour Expansion in Deep Penetration Laser Welding
E.H. Amara, R. Fabbro, and A. Bendib

251 Experimental and Theoretical Investigations of Craters Formation in Solid Targets Under the Action of Powerful Laser Pulse
T. Pisarczyk, S. Gus'kov, Ya. Doskach, A. Kasperczuk, S. Borodziuk, M. Kalal, E. Krousky, J. Limpouch, K. Masek, P. Pisarczyk, K. Rohlena, V. Rozanov, J. Ullschmied

255 Relativistic Electron Motion in Plasma During the Interaction of a Short Intense Laser Pulse
R. Ondarza and F Gómez

259 Studies of Tungsten Laser-Produced Ion Stream Expanding in Magnetic and Electric Fields.
J. Wołowski, J. Badziak, P. Parys, and E. Woryna

263 Design and Construction of a Copper Halide CuBr Laser
K. Bourai, D. Louhibi, S. Messaoud, F. Siserir, A. Noukaz, and Y. Hammoum

267 Volatilization of Tracheal Tumors by CO_2 Laser
S. Bouzid, T. Benguedouar, A. Bouzid, and Z. Daouadi

PLASMA THEORY

271 Linear Landau Damping in Strongly Relativistic Quark Gluon Plasma
G. Murtaza, N.A.D. Khattak, and H.A. Shah

275 Dust Acoustic Waves in a Warm Dusty Plasma with Trapped Electrons
W.F. El-Taibany, and S.K. El-Labany

279 MHD Plasma: Spherical Region Model- Analytical and Numerical Investigation
Ali I Mussa

283 Field Stability by the Electron Beam in a Warm Magnetized Plasma-Filled Waveguide
Sh.M. Khalil, Y.A. Sayed, Kh.H. El-Shorbagy, and A.T. El-Gendy

287 On the Theory of Stochastic Dynamics of Magnetically Confined Plasma
R.N. El-Sharif and N.S. El-Atoy

292 Axisymmetric Mode Analysis for Plasma in Toroidal Devices
Bahaa F. Mohamed

296 Propagation of Solitary Ion Acoustic Waves in a Weakly Relativistic Warm Plasma: Isothermal Case
S.A. Elwakil, G. Rowlands, S.K.El-Labany, A.M. El-hanbaly, and E.K. El-shewy

300 Higher-Order Solution of an Ion Acoustic Solitary Waves in a Warm Ion Plasma: Non Isothermal Case
E.K. El-shewy

304 Description of an Experimental Tripolar Vortex
J. Vranješ, A. Okamoto, S. Yoshimura, S. Poedts, M. Kono, and M.K. Tanaka

307 Nonlinear Wave Interaction in Selfgravitating Fluid
J. Vranješ, S. Poedts, and M. Kono

311 Dust Charge Fluctuations in a Magnetized Dusty Plasma
M. Salimullah, I. Sandberg, and P.K. Shukla

315 PIC-Monte Carlo Simulation of Electronic Avalanches Leading to the Formation of Discharges
H. Ghalila, M. Chrigui, and Z Ben Lakhdar

319 Dielectric Permittivity of Dusty Plasma with Account of Dipole Moments of Granules
V.N. Mal'nev and Eu.V. Martysh

323 *Magnetic Susceptibility of Complex Plasma with Ferromagnetic Granules*
V.N. Mal'nev and Eu.V. Martysh

MISCELLANEOUS

327 FTIR Spectroscopic Study of the Low-Temperature Dependent Structural Changes in Isotactic Polypropylene
Rasha M. Khafagy and Y.A. Badr

331 Computer Controlled Atom-Trapping Atomic Absorption Spectrophotometer with Water Cooled Stainless Steel Collector Tubes
A.N. Abdel Rahman, A.M. Abdel-Daiem, and M.A. Ebraheim

335 **LIST OF PARTICIPANTS**

Invited Talks

Edge Plasma Physics and Relevant Diagnostics on the CASTOR Tokamak

J. Stöckel[1], P. Devynck[2], J. Gunn[2], E. Martines[3], G. Bonhomme[4], G. Van Oost[5], M. Hron[1], I. Duran[1], R. Pánek[1], P. Stejskal[1], J. Adamek[1]

[1]*Institute of Plasma Physics, Association Euratom/IPP.CR, AS CR, Prague, Czech Republic*
[2]*Association Euratom/CEA sur la fusion controlèe, Saint Paul Lez Durance, France*
[3]*Consorzio RFX, Associazione Euratom/ENEA sulla Fusione, Padova, Italy*
[4]*LPMI, UMR 7040 du CNRS, Université Henri Poincaré, Vandoeuvre-lès-Nancy, France*
[5]*Department of Applied Physics, Ghent University, Gent, Belgium*

ABSTRACT

We describe results of two sets of measurements performed with a full poloidal array of Langmuir probes located in the scrape-off layer (SOL) of the CASTOR tokamak. At first, a biased electrode is inserted into the SOL. The resulting poloidally localized electric field structures are identified by means of the ring of probes and a consequent modification of the convective transport is demonstrated. In the second experiment, the turbulent fluctuations are measured in standard ohmic discharges. The analysis of the probe signals reveals a spatially periodic mode with the poloidal mode number equal to the edge safety factor q, which propagates poloidally in the direction of the E_rxB drift. This observation is interpreted as a signature of a single turbulent structure, which snakes around the torus several times following the local helicity of the magnetic field.

Keywords: tokamak, edge plasma, probe diagnostics, biasing

INTRODUCTION

It is widely recognized that the Langmiur probes are a primary tool for studying edge plasma physics in tokamaks because of their temporal and spatial resolution. Single probes are used to measure the local plasma parameters. In large-scale tokamaks with a long pulse length, the probe's tip is fixed to a reciprocating head to avoid its overheating followed by destruction. One such excursion of the probe head inside and outside the plasma takes typically ~ 200 ms. During this time interval, the radial profiles of the plasma density, electron temperature and floating potential can be determined from the IV characteristics of the probe several times during a discharge.

In small-scale experiments, however, the overheating is avoided automatically because the pulse length is relatively short, typically of the order of several tens of milliseconds. Therefore, the Langmuir probe can survive at a fixed position during the whole discharge. The radial profiles are measured by changing the probe position on a shot-to-shot basis. However, this approach requires sufficiently reproducible discharges and measurements become slightly cumbersome. The above-mentioned complication can be partially overcome by using a row of tips oriented either in the radial or poloidal direction. Such probe arrays appeared to be extremely useful for the analysis of plasma fluctuations. For this purpose, a temporal resolution ~1μs is required and the spatial resolution must be in the range of 2-3 mm.

Pioneering experiments with the probe arrays were performed by Zweben[(1)] in the 80s. These measurements have identified turbulent structures with a typical lifetime 5-40 μs and a poloidal and radial correlation length of ~ 1 cm. Systematic measurements of the edge turbulence by probe arrays in large scale experiments were carried out in the ASDEX tokamak[(2)] and the W7-AS stellarator[(3)]. There, an array of 16 tips, oriented in the poloidal direction, was fixed to a reciprocating head. In spite of a spatially limited picture, the poloidal periodicity of the turbulent events in the SOL (with a typical poloidal wavelength of about 5-15 cm) has been also observed. Comparable measurements performed in the CASTOR tokamak[(4)] with a similar array have demonstrated that the SOL turbulence in small tokamaks is basically of the same nature as in larger machines. Later on, a two-dimensional array of 64 tips (8x8 tips) was used on CASTOR to analyze the properties of the edge turbulence

simultaneously in the poloidal and radial direction. Coherent structures were identified in these experiments[5].

The probe arrays oriented in the radial direction (so called rake probes) play a decisive role in experiments with biasing of a material object (electrodes, limiter) localized in the edge plasma. They measure the radial profile of electric field, which generates sheared poloidal flows. The consequent edge turbulence reduction leads to the formation of a transport barrier within the last closed magnetic surface (separatrix), as reviewed in (6).

This contribution is devoted to two examples of use of a recently developed probe array consisting of 124 Langmuir probes uniformly distributed along the poloidal circumference of the plasma column on the CASTOR tokamak. Details of the experimental arrangement are described in Sec. 2. The first example (Sec. 3) demonstrates modification of the particle transport at the plasma edge by inserting a biased electrode into the SOL. The second example (Sec. 4) shows results of measurements of the plasma fluctuations with a high spatial and temporal resolution, which reveal useful information on the structure of the SOL turbulence in tokamaks.

ARRANGMENT OF THE EXPERIMENT

The experiments have been carried out on the CASTOR tokamak, which is a small size torus with a major radius of 0.4 m and a minor radius of 0.1 m, operational in the Institute of Plasma Physics, Prague. The toroidal magnetic field is 1.3 T and the plasma current is varied between 5-12 kA. The line averaged density is $n_e=10^{19}$ m^{-3}. In the present experiment, a poloidal limiter with the radius a = 58 mm is inserted into the vacuum vessel and equipped with 124 Langmuir probes, uniformly distributed along its circumference, as apparent from the photo shown in Fig. 1 (left panel). The individual tips are 2.5 mm long and spaced poloidally by ~3 mm.

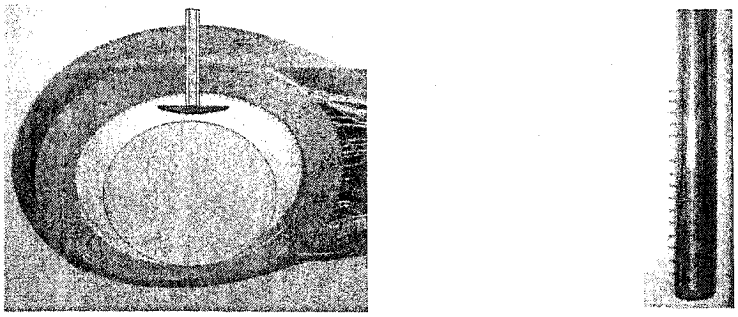


Fig 1. *Probe arrays for spatially resolved measurements. Left picture - the poloidal limiter equipped with 124 Langmuir probes. The respective position of the limiter and the plasma column and location of the biasing electrode are shown schematically; Right picture - the rake probe.*

In addition, the rake probe, seen also in Fig. 1 (right panel), is used to measure radial profiles of the edge plasma parameters in a single shot. The probe head is composed of 16 tips spaced radially by 2.5 mm and inserted into the edge plasma from the top of the torus 180° toroidally away from the poloidal limiter. The tips of both probe arrays can measure either the floating potential or the ion saturation current. Gradients of floating potential are indicative of electric fields, and the ion saturation current gives an estimate of the plasma density. The signals are digitized with a 1 MHz sampling rate, 64 synchronized data acquisition channels are available.

Simultaneous measurements with the radial and poloidal probe arrays allow to deduce positioning of the plasma column within the vacuum vessel. The final result is schematically shown in the left panel of Fig. 1, from which the respective position of the separatrix (the last closed magnetic flux surface) and the poloidal limiter is evident. As can be seen, the plasma column is displaced in the downward direction, and its radius is consequently less then the radius of the limiter. It is evident that the plasma outside the separatrix is divided into two regions, according to the parallel connection length L to a material surface, which is represented by the poloidal limiter:

- *Limiter shadow* is the region between the chamber wall and the leading edge of the poloidal limiter (58 mm < r < 100 mm). The corresponding connection length is about one toroidal circumference, L~ 2πR.
- *Scrape-off layer* (SOL) with a much longer connection length is formed at the upper part of the plasma column because of the vertical shift of the plasma. The connection length L~ q2πR is proportional to the local safety factor q (typically q = 6-9 in CASTOR). The radial extent of the SOL is largest at the top of the torus (typically 10-20 mm) and depends on the plasma displacement. This SOL has a magnetic configuration similar to that of a tokamak equipped with divertor or toroidal limiter.

Measurements are performed either in standard ohmic discharges or in regimes with edge plasma biasing. In the latter case, a mushroom-shaped graphite electrode is immersed into the edge plasma from the top of the torus (see Fig. 1). Its total collecting area is of about ~ 15 cm^2. The electrode is biased with respect to the tokamak vessel by applying a positive pulsed voltage (V_b = 100-200 V I_b = 20-40 A) during the flat-top phase of the discharge.

FIRST EXAMPLE – FORMATION OF CONVECTIVE CELLS IN THE SOL

A rather complex picture is observed, when the biasing is inserted into the SOL, as documented in Fig. 2, where the poloidal distribution of the mean floating potential in ohmic and biasing phase of a discharge is compared.

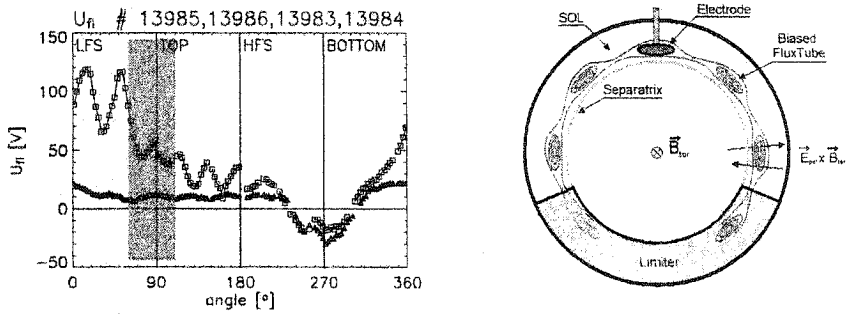


Fig 2. Left - *Poloidal distribution of the mean floating potential U_{fl} along the ring in ohmic (triangles) and biasing (squares) phase, as measured in four reproducible discharges. The poloidal position of the biasing electrode is marked by the bar. The biasing voltage is +150 V.* Right - *Projection of the biased flux tube originating at the electrode to a poloidal plane is shown schematically for q_{edge} ~ 8. Some equipotential surfaces are shown.*

It is seen that the whole upper part of the plasma column is biased with respect to the ohmic level. Moreover, a strong poloidal modulation of the floating potential is observed in the range of poloidal angles θ = 0°-200°. The peaks are interpreted as a signature of a biased flux tube, which originates at the electrode and extends along the helical magnetic field line. The electrode current flows predominantly parallel to the magnetic field in the upstream and downstream direction and terminates on the electron and ion side of the bottom part of the poloidal limiter.

The projection of this biased tube on a poloidal plane is schematically depicted in Fig. 2. It is seen from the figure that the resulting perpendicular electric field is two-dimensional, having not only a radial, but also a poloidal component E_{pol}. Its amplitude and even the sign change with the poloidal angle. A possible consequence of this is the occurrence of a convective motion of the SOL plasma because of the $E_{pol}\times B_t$ drift directed either inward or outward according the sign of the E_{pol}. In order to detect this effect, the tips of the poloidal ring have been used to measure either the floating potential or the ion saturation current in two subsequent discharges. A detailed distribution of these two quantities along one quarter of the poloidal ring is shown in Fig. 3.

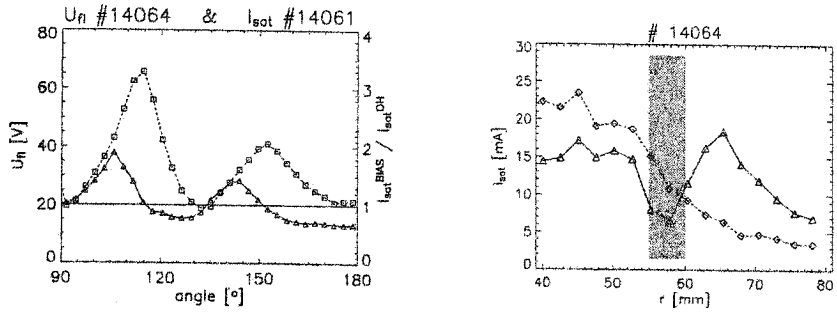


Fig. 3.
Left - Poloidal distribution of the floating potential (squares) and of the ion saturation current (triangles) along one quarter of the poloidal ring (High field side – top). The ion saturation current is normalized to its ohmic value. Right- Radial profile of the ion saturation current in the ohmic (diamonds) and biasing (triangles) phase of the discharge. The gray bar marks the electrode position.

It is seen from the figure that the poloidal distribution of the ion saturation current (proportional to the plasma density) is indeed modulated by biasing with the same periodicity as the potential distribution, but is shifted poloidally. The ion saturation current (plasma density) increases at one side of the potential hills, while it is reduced below the ohmic level on the other side, i.e at the angles where the poloidal electric field is maximum or minimum. The right panel in Fig. 3 demonstrates a strong modification of the radial plasma density profile.

These measurements demonstrate a strong impact of the poloidal electric field on the particle transport in the plasma edge. A similar effect was recently obtained in the JFT-2M[7] and MAST [8,9] tokamaks, where the divertor plates are biased and broadening of the SOL profiles has been achieved. It is assumed that this is because of the formation of a toroidally elongated flux tube of potential - convective cells, associated with the biased plate. The experiments on CASTOR described above employ the exceptional spatial resolution of the new poloidal probe array of 124 Langmuir probe to investigate properties of such convective cells in detail.

SECOND EXAMPLE – FLUCTUATION MEASUREMENTS

The second example of using the poloidal probe array is devoted to the analysis of plasma fluctuations in the SOL. In this particular case, the floating potential U_{fl} is recorded simultaneously by 32 tips uniformly distributed around the plasma column. Consequently, the spatial resolution in the poloidal direction is ~11 mm. The signals of individual tips, recorded by the sampling rate 1 μs, consist of the time-averaged and fluctuating parts $U_{fl} = \langle U_{fl} \rangle_T + \delta U_{fl}$. Figure 4 shows the spatial-temporal plot of the fluctuating part δU_{fl} during a part of the ohmic discharge. The red (or blue) patterns emphasize the poloidal position/time instant where the floating potential is higher (or lower) than its mean value. The most interesting feature, which can be drawn from the plot are quite regular red/blue belts, which are apparent in the range of poloidal angles 0-200°, i.e. at the top of the torus, where the probe tips are located in the SOL (see again the displacement shown in Fig. 1). One such pattern is marked by the yellow line.

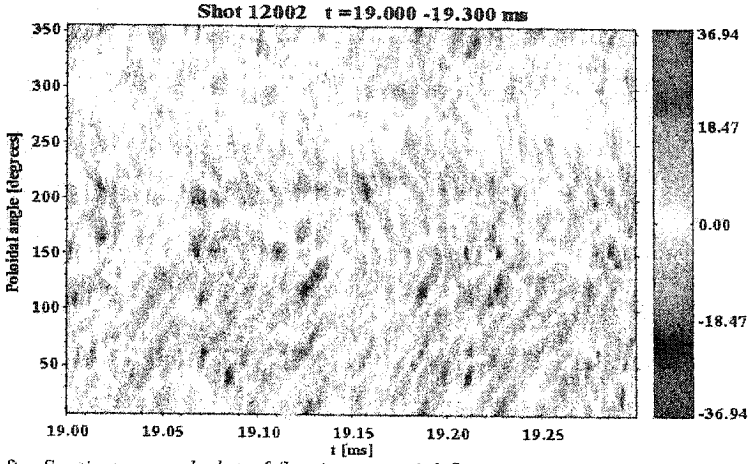


Fig. 4: Left - *Spatio-temporal plot of floating potential fluctuations measured by the poloidal array during the quasistationary phase of a discharge.*

A detailed statistical analysis was performed on the data from probes from the upper half of the torus, which are located in the SOL roughly at the same magnetic surface. The belts have significantly different character in the range of poloidal angles 200 ° - 300°. The following explanation of the plot is offered:

- The patterns are a signature of turbulent features existing in the SOL.
- The turbulent features propagate poloidally. The poloidal velocity, deduced from the inclination of the patterns is typically 1 km/s. This is consistent with the value of the local ExB drift deduced from the rake probe data.
- The turbulent features appear to be poloidally periodical. For example, 3-4 belts can be observed simultaneously in this range of poloidal angles at the time t = 120 μs, which implies the poloidal mode number m= 6-8. Additional measurements[10] have shown that the poloidal mode number m is equal to the edge safety factor q(a) and the toroidal mode number is n=1.
- Correlation measurements using a probe located toroidally away of the ring proved that the patterns correspond to turbulent structures of potential elongated along the magnetic field lines.
- Some observed temporal periodicity is a result of poloidal propagation. Frequency spectra of individual signals are broad and peaked around ~20-60 kHz.

All these experimental observations can be simply interpreted, just assuming that only a **single dipole turbulent structure** is formed in the SOL, where the magnetic connection length is long enough because of the downward displacement of the plasma column. Such turbulent structure snakes several times around the torus and ends up at the electron and ion side of the poloidal limiter. Figure 5 shows a dipole turbulent structure schematically plotted on the unfolded magnetic surface, which is associated with the upper part of the poloidal probe array.

The formation of the dipole structure can be explained by the flute-like instability model in the SOL described in the ref. (11), which predicts fluctuating parallel currents flowing in the SOL to the surface of the limiter (divertor plates). These currents charge flux tubes connected to the limiter at different potentials [4]. Such a model has been adopted by M. Endler et al [6] to describe the SOL turbulence in the ASDEX tokamak where individual fluctuation events with a bipolar structure and propagating poloidally have been observed.

Finally, it must be noted that the m=q mode discussed above is superimposed to a broadband turbulence. Moreover, features with a significantly lower mode number (m = 0 or 1) are also observed under some discharge conditions.

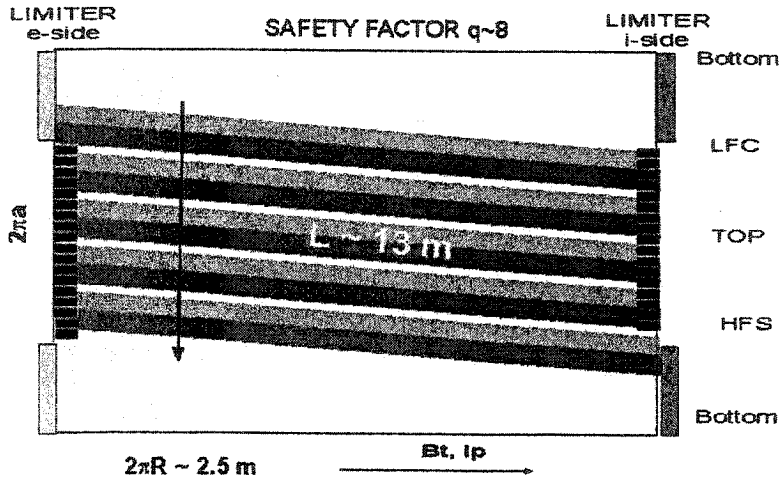


Fig. 5: *Unfolded magnetic surface in the SOL of the CASTOR tokamak for the edge safety factor q~8. The red/blue colors denote regions of the magnetic surface with a higher/lower potential then its time-average value. The dipole structure of a length ~13 m, which follows helical magnetic field lines from one to the other side of the poloidal limiter, is depicted. The poloidal mode number is m=q. It propagates poloidally because of $E_r x B_T$ drift. The lifetime of the structure is probably determined by duration of its contact with the limiter surface. When the contact is lost, the structure dies, but a new structure is formed.*

CONCLUSIONS

It is evident that full understanding of the edge plasma physics in tokamaks requires experimental information with a high spatial and temporal resolution. A good representative of the diagnostic, providing such kind of experimental data are the arrays of Langmuir probes, which are relatively non-expensive and easy to build. Major investments are a multichannel and fast data acquisition system and sophisticated software for data processing.

We try to demonstrate in this contribution that the probe arrays can be efficiently employed in small tokamaks because of their flexibility. The most important point is to find whether the obtained results do not reflect only particular features of the given experiment, but that they are relevant also for large-scale devices.

ACKNOWLEDGEMENT

This work has been carried out with the support of the projects 202/03/0786 and 202/03/P062 (Grant Agency of the Czech Republic) and No. 2001-2056 (INTAS).

REFERENCES

(1) S.J. Zweben et al, *Nucl. Fusion*, **25**, 1985, 543.
(2) M. Endler et al, *Nucl. Fusion, 35, 1995, 11.*
(3) J. Bleuel et al, *New Journal of Physics* **4**, *2002, 38.1-38.38.*
(4) J. Stöckel et al, Plasma Phys. Contr. Fusion, **41**, 1999, A577.
(5) E. Martines, M. Hron and J. Stöckel, *Plasma Phys. Control. Fusion* **44**, *2002, 351.*
(6) G. Van Oost et al, *Plasma Phys. Contr. Fusion*, **45**, 2003, 621-623.
(7) J. Hara et al: *Journal of Nuclear Materials* **241-243**, 1997, 338.
(8) D.D. Ryutov, P Helander, RH Cohen, *Plasma Phys. Contr. Fusion*, **43**, 2001, 1399
(9) G.F. Counsell et al: in *Proc. of 30th EPS Conf. on Contr. Fusion Plasma Phys.*, St Petersburg, July 2003, P-3.202.
(10) M. Hron, E. Martines et al, In Proc. of 29th EPS Conference on Plasma Physics and Controlled Fusion, Montreux, June 2002, ECA, Vol. 26B, P-5-043.
(11) A.V. Nedospasov, *Sov. J. Plasma Phys.* **15**, *1989*, 659.

Turbulent Transport Reduction by ExB Velocity Shear during Edge Plasma Biasing in Tokamaks

G Van Oost[1], J Adámek[2], V Antoni[3], P Balan[4], J A Boedo[5], P Devynck[6], I Ďuran[2], L Eliseev[8], JP Gunn[6], M Hron[2], C Ionita[4], S Jachmich[7], GS Kirnev[8], E Martines[3], A Melnikov[8], P Peleman[1], R Schrittwieser[4], C Silva[9], J Stöckel[2], M Tendler[10], C Varandas[9], M Van Schoor[7], V Vershkov[8], R R Weynants[7]

[1]Department of Applied Physics, Ghent University, Ghent, Belgium
[2]Institute of Plasma Physics, Association EURATOM/IPP.CR, Prague, Czech Republic
[3]Consorzio RFX, Associazione EURATOM-ENEA sulla Fusione, Padova, Italy
[4]Department of Ion Physics, University of Innsbruck, Innsbruck, Austria
[5] Department of Mechanical and Aerospace Engineering, University of California, San Diego, La Jolla, California, United States of America
[6]Association EURATOM/CEA sur la fusion contrôlée, Saint Paul Lez Durance, France
[7]Laboratoire de Physique des Plasmas-Laboratorium voor Plasmafysica, Association 'Euratom-Belgian state', Ecole Royale Militaire- Koninklijke Militaire School, B-1000 Brussels, Belgium, Partner in the Trilateral Euregio Cluster
[8]RRC Kurchatov Institute, Moscow, Russian Federation
[9]Centro de Fusão Nuclear – Association EURATOM/IST, Instituto Superior Técnico, Lisboa, Portugal
[10]Alfvén Laboratory, Royal Institute of Technology, Stockholm, Sweden
g.vanoost@fz-juelich.de

ABSTRACT

Experiments in the tokamaks TEXTOR, CASTOR, T-10 and ISTTOK have provided new and complementary evidence on the physics of the universal mechanism of ExB velocity shear stabilization of turbulence, concomitant transport barrier formation and radial conductivity by using various edge biasing techniques.

Keywords: ***Tokamaks, edge plasma, electric biasing, electrostatic turbulence, plasma confinement***

INTRODUCTION

The understanding and reduction of turbulent transport in magnetic confinement devices is not only an academic task, but also a matter of practical interest, since high confinement is chosen as the regime for ITER and possible future reactors since it reduces size and cost.

An extensive review on the physical mechanisms determining the radial electric field in a toroidal plasma has been published by Ida[(1)]. He describes amongst others the effect of variations in the radial electric field and shear in the bulk rotation velocity on the improvement of transport properties. Since the pioneering work on the tokamak CCT[(2)], many papers have been devoted to the effect of electric field biasing in specific machines (see e.g. reviews 3,4,5), which in general leads to a strongly varying radial electric field as a function of radius and a resulting sheared E×B flow, giving rise to improved confinement properties. Due to space limitation, an historical overview of edge biasing work will not be given here, and the collection of material is limited. This paper attempts at bridging the gap between the early and the new, more detailed understanding.

The importance of radial electric fields for plasma transport was in the past repeatedly established. Since the discovery of the transition from a low confinement mode (L-mode) to a high confinement mode (H-mode) in 1982[6], a flurry of activity started with the experimental and theoretical recognition of a link between E_r and the formation of edge and internal transport barriers in toroidal plasmas. The importance of radial electric field shear in the L-H transition was suggested for the first time in ref. (7,8). The (spontaneous) H-mode has been obtained in a variety of tokamaks mainly with elongated plasma cross section and divertor, and recently also in the limiter tokamak T-10 with ECRH as the only auxiliary heating. An (induced) H-mode can also be triggered externally by imposing an electric field and the resulting ExB rotation in tokamaks like TEXTOR, CASTOR, T-10 and ISSTOK, as well as in reversed field pinches like RFX. These electrode biasing experiments have contributed significantly to the understanding of the H-mode phenomenon and of the effects of E_r on plasma transport.

The L-H transition is accompanied by a reduction of turbulent transport, confirming the paradigm that microturbulence is responsible for a considerable part of energy and particle losses. The shearing of turbulent eddies by differential ExB flow velocity has been proposed as a universal mechanism to stabilize turbulence in plasmas[9], an hypothesis supported by early work on the tokamak TEXT[10], and has been observed with different magnetic configurations. The ExB velocity shear can suppress turbulence due to linear stabilization of turbulent modes, and in particular nonlinearly by decorrelation of turbulent vortices, thereby reducing transport by acting on both the amplitude of the fluctuations and the phase between them[11]. The shearing rate, ω_{ExB}, must be comparable to $\Delta\omega_D$, the nonlinear turbulence decorrelation rate in the absence of shear.

This paper reports on recent results of a coordinated study of radial electric fields (E_r) and their role in the establishment of edge transport barriers and improved confinement in the circular limiter tokamaks TEXTOR in Jülich, CASTOR in Prague, and T-10 in Moscow, where E_r is externally applied to the plasma in a controlled way using a biased electrode. Edge biasing is the controlled creation of radial electric fields by driving a current through the edge plasma inside the last closed flux surface (LCFS). In the circular limiter tokamak ISSTOK in Lisbon Er is externally applied by DC or AC electrode or limiter biasing.

TEXTOR: SCALING OF TURBULENCE WITH SHEAR, AND CAUSALITY BETWEEN ExB SHEAR AND TRANSPORT BARRIER FORMATION

Since the early nineties pioneering research has been conducted on TEXTOR in the domain of edge radial electric fields using electrode biasing[13-21]. The biasing experiments on TEXTOR (R=1.75 m, a=0.46 m) with the well diagnosed plasma edge using probes to measure all relevant quantities such as electric field, parallel and perpendicular plasma flow, fluctuation and turbulent particle flux, have given the first proof for transport suppression due to sheared ExB flows. Quantitative analysis has shown that the diffusion coefficient decreases at the shearing rate predicted by theory. These findings are in good agreement with measurements of the fluctuating quantities, which contribute to the turbulent transport. Changes in the cross-phase are essential for substantial quenching of turbulence. A 1D fluid model, in which parallel viscosity and neutral friction were already identified as important components to explain the very important and localised electric fields has been developed. Recent work has focused on the convection and shear viscosity, introduced by anomalous radial flows, and their subsequent reduction by the quenching of the turbulence. It has been shown that without the quenching of the turbulence, it is impossible to explain the magnitude and the shape of the measured electric field. The destruction of parallel viscosity by strong poloidal plasma rotation has been identified to cause a bifurcation in the electric field. Rapid changes in the polarisation driving current have been used as a diagnostic tool to study the causality between rotational shear and confinement improvement. The flow shear is clearly leading the transport changes and as a result, a hysteresis between the imposed shearing rate and the particle diffusion coefficient arises.

The scaling of plasma turbulence suppression with velocity shear has been established, revealing the cross-phase as a key element. To important results should be noted: Firstly, that the scaling of the cross-phase term is as strong as that of the turbulence amplitudes, revealing the cross-phase as a key element in the suppression of turbulent transport. Secondly that there is a difference in the scaling of the cross-phase between the positive and negative shear regions, an effect not included in the theories[22-24], which are phase-sign blind and therefore these results[25,26] should be considered closely by theoreticians. First measurements of the suppression of electron temperature fluctuations in a strongly sheared velocity field have been made[27]. Reduction in poloidal electric field, temperature, and density fluctuations across the shear layer lead to a reduction of the anomalous conducted and convected heat fluxes resulting in an energy transport barrier that is measured directly.

CASTOR: ExB FLOW MEASUREMENTS AND STRUCTURE OF EDGE TURBULENCE

CASTOR (R=0.4 m, a=60 or 85 mm) . The impact of sheared electric fields on the structure of edge fluctuations and plasma flows is investigated on the CASTOR tokamak with a non-intrusive biasing scheme, whereby a mushroom-like electrode (made of carbon) is located in the scrape-off layer (SOL), but its top is just touching the separatrix (see Fig. 1). In such scheme, called "separatrix biasing", the potential is affected only in a relatively narrow region near the separatrix and the radial electric field is amplified at both sides of the electrode, because, in contrast to the standard biasing arrangement, the bulk plasma remains unbiased[28].

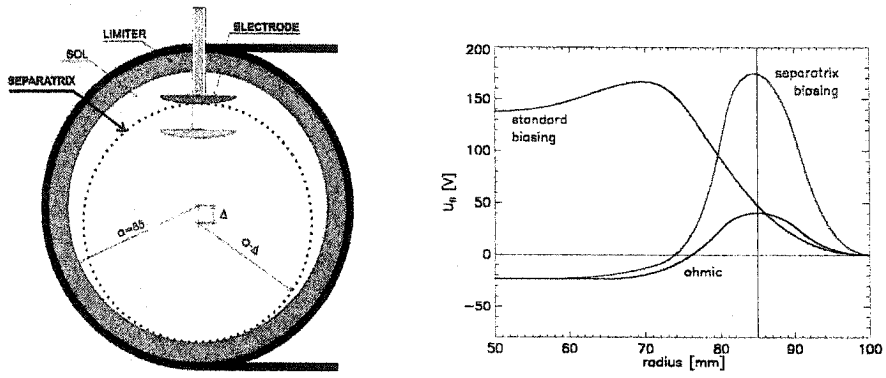


Fig. 1 Left: Poloidal cross section of the CASTOR tokamak, schematically showing the respective position of plasma column and biasing electrode at the "standard" and at the "separatrix biasing" arrangements. Right: Comparison of radial profiles of floating potential inohmic and biasing cases (schematically). Here, the separatrix is at 85 mm. Position of the electrode at standard biasing scheme is 70 mm.

This experiment has been predicted theoretically[12]; in order to trigger an L-H transition, the model requires a value of the electric field larger than that given by neoclassical theory. At the separatrix the electric field within the SOL is governed by a contact with plates. This has to match the self-generated electric field on closed field lines governed by plasma flows and magnetic field geometry. Therefore, the peripheral plasma plays the crucial role in controlling the global confinement and affecting plasma profiles and local transport diffusivities[29].

The impact of sheared ExB flow on edge turbulent structures has been measured directly using an optimized Gundestrup probe, a comprehensive set of electrostatic probe arrays as well as emissive probes which provide direct plasma potential fluctuation measurements[30-34]. The Gundestrup probe provides the simultaneous measurement of toroidal and poloidal flows, and of electrostatic turbulence, and has demonstrated the correlation between sheared ExB flow and reduction of turbulence[35-39]. Very recently, a novel concept has been suggested to measure the electron temperature fluctuations and a prototype of the so-called tunnel probe has been successfully tested on CASTOR. Measurements with a full poloidal array[40] with 32 electrodes plus Langmuir probes have revealed quasi-coherent electrostatic waves in the SOL with a dominant poloidal mode number[6] equal to the edge safety factor. At DC biasing with an electrode located near the separatrix, the edge turbulence is modified by a sheared radial electric field, which is imposed to this region. The poloidal velocity of turbulent structures strongly increases and the poloidal mode number is reduced significantly down to 1-2.
The plasma potential and its fluctuations were measured by electron emissive probes in the edge plasma region of two fusion experiments: the ISTTOK (see below) and the CASTOR tokamaks[41,42]. Into ISTTOK, three emissive probes were inserted outside the LCFS on different minor radii. In CASTOR, two poloidally separated emissive probes and two cold cylindrical probes, mounted on the same shaft, were used, which could be radially shifted outside and inside the LCFS. The advantage of a sufficiently emissive probe is that in principle the plasma potential and its fluctuations can be measured directly, without being affected by electron temperature fluctuations or drifting electrons.

T-10: ELECTRODE BIASING IN REGIMES WITH ECR PLASMA HEATING

The H-mode was achieved by inserting the positively biased electrode into the plasma edge inside the limiter in the T-10 tokamak (R=1.5 m, a=0.3 m) in regimes with electron-cyclotron resonant heating[43,44]. The H-mode is characterised by a decrease of D_α emission intensity, a rise of line-average plasma density and an increase of energy confinement time. The increase of core electron and ion temperatures during the electrode biasing implies the formation of the thermal barrier in addition to the barrier for particles.
The Heavy Ion Beam Probe (HIBP) diagnostic was used to directly measure the local values of the plasma potential in the core and edge plasmas[45,46]. It is located at a toroidal angle of $\varphi=180^0$ from the electrode. To obtain the radial potential profile the HIBP was used in the scanning mode. Scanning along the detector line allows to get a set of profiles in a single shot. The scanning was realized by periodical variation of the injection angle. The sampling frequency and bandwidth of the acquisition system allow the observation of slow oscillations.

The first biasing experiments performed on the T-10 tokamak have shown that positive voltage applied to an electrode results in an increase of core electron and ion temperatures and in of energy confinement time in regimes with ECR auxiliary heating, in contrast to the ohmic regime. Hence, edge biasing is clearly improving the global performance of ECR heated discharges. Reflectometry shows the existence of a narrow plasma layer where strong changes of turbulence levels occur. A heavy ion beam probe diagnostic has been used to directly measure the local values of the plasma potential in the vicinity of the electrode radius, outside as well as inside, showing two regions with strong radial electric field and a strong reduction of plasma potential and density fluctuations in the vicinity of the electrode radius, outside as well as inside. To explain the different plasma behaviour in OH and ECRH regimes it is planned to carry out the measurements of profiles of radial electric field, toroidal and poloidal plasma rotation velocity in the plasma periphery between the electrode and limiter.

ISTTOK: COMPARISON OF ALTERNATING ELECTRODE AND LIMITER BIASING

In the ISTTOK tokamak (R=0.46m, a=85 mm) electrode (EB) and limiter biasing (LB)[47,48,50] have been performed. LB has the advantage of using existing plasma facing components in the device contrary to electrode bias where an object must be inserted into the plasma, which is not compatible with plasma

operation in large devices. However, the modifications in E_r for limiter biasing are, in general, limited to the SOL[49].

Electrode biasing is found to be more efficient in modifying Er and confinement. The best confinement improvement is obtained with positive electrode biasing, showing a good correlation between confinement changes and ExB shear. Negative (positive) limiter biasing leads to improved (deteriorated) confinement and better (worse) stability of the plasma column. Coordinated emissive probe direct measurements of the plasma potential and its fluctuations are planned on ISTTOK and CASTOR.

ACKNOWLEDGMENT

This work is partially supported by INTAS Project 01-2056

REFERENCES

(1) Ida K 1998 *Plasma Phys. Contr. Fusion* **40** 1429.
(2) Taylor R J *et al* 1989 *Phys.Rev.Lett.* **63** 2365
(3) Weynants R R and Van Oost G 1993 *Plasma Phys. Contr. Fusion* **35** B177
(4) Weynants R R 2001 *Journ. of Plasma Fusion Res. Series* **4**
(5) Van Oost G et al 2001 *Czech. J. of Phys.* **51** 957.
(6) Wagner F *et al* 1982 *Phys.Rev.Lett.* **49** 1408
(7) Groebner R J *et al* 1990 *Phys.Rev.Lett.* ***64*** 3015
(8) Ida K *et al* 1990 *Phys.Rev.Lett.* **65** 1364
(9) Biglari H, Diamond P H, Terry P W 1990 *Phys. FluidsB* **2** 1
(10) Ritz C P *et al* 1990 *Phys.Rev.Lett* **65** 2563
(11) Ware A S, Terry P W, Carreras B A and Diamond P H 1998 *Phys. Plasmas* **5** 173
(12) Rozhansky V, Tendler and Voskoboinikov M S 1996 *Plasma Phys. Contr. Fusion* **38**, 1327
(13) Weynants R R, Van Oost G *et al* 1992 *Nucl. Fusion* **32** 837
(14) Jachmich S *et al* 1998 *Plasma Phys. Contr. Fusion* **40** 1105, and Cornelis J *et al* 1994 *Nucl Fusion* **34** 171
(15) Jachmich S, Van Oost G, Weynants R R and Boedo J A *Czech. J. of Phys.* **48** 32
(16) Van Goubergen H *et al* 1999 *Plasma Phys. Contr. Fusion* **41** L17
(17) Boedo J A, Gray D, Luong P, Conn R W *et al* 1999 *Rev. Sci. Inst* **70** 2997.
(18) Jachmich S, Van Schoor M and Weynants R R, in Proc. of 29th EPS Conference on Plasma Phys and Contr Fusion, Montreux, 2002, ECA Vol **26B**, O-1.01, to be published in Plasma Phys. Contr. Fus.
(19) Weynants R R, Jachmich S and Van Oost G 1998 *Plasma Phys. Contr. Fusion* **40** 635
(20) Jachmich S and Weynants R R 1999 *Czech. J. of Phys*; **49** 191
(21) Jachmich S *et al 2000 Plasma Phys. Contr. Fusion* **42** A147
(22) Staebler G *et al* 1994 *Phys. Plasmas* **1** 909
(23) Shaing K C *et al* 1990 *Phys. FluidsB* **2** 1492
(24) Zhang Y Z and Mahajan S M 1992 *Phys. FluidsB* **4** 1385
(25) Boedo J A *et al* 2000 *Nucl. Fusion* **40** 1397
(26) Boedo J A *et al* 2002 *Nucl. Fusion* **42** 117
(27) Boedo J A *et al* 2000 *Phys.Rev.Lett* **84** 2630
(28) Van Oost G, Stöckel J, Hron M, Devynck P, Dyabilin K, Gunn JP, Horacek J, Martines E, Tendler M. 2001 *Journal of Plasma Fusion Res. Series* **4** 29-35
(29) Tendler M, Van Oost G and Stöckel J 2002 *Comments on Modern Physics* **2** C203
(30) Petrzilka J and Stöckel J 1998 *Contrib. Plasma Physics* **38** 74-79

(31) Blauel J, Endler M, Niedermayer H, Schubert M, Thomsen H 2002 *New Journal of Physics* **4** 38.1-38.38
(32) Stöckel J *et al* 1999 *Plasma Phys Contr Fusion* **41** A577-A585 Suppl. 3A
(33) Martines E, Hron M and Stöckel J 2002 *Plasma Phys Contr Fusion* **44** 351-359
(34) Martines E *et al* 2002 *Czech J Phys* **52** Suppl D, D13-D24
(35) Gunn J P *et al* 2001 *Phys Plasmas* **8** 1995.
(36) Dyabilin K, Hron M, Stöckel J and Zacek F 2002, *Contrib. Plasma Physics* 99
(37) Gunn J P 2001 *Phys Plasmas* ***8*** 1040
(38) Gunn J P *et al* 2002 *Czech J Phys* **52** 1107 and Gunn J P.*et al*, to be published in Proc. of 19th IAEA Fusion Energy Conference, Lyon, 2002 (paper EX/P1-06)
(39) Gunn J P *et al*, 2001 *Czech J Phys* **51** 1001-1010
(40) Hron M, Martines E, Devynck P, Bonhomme G, Gravier E, Adamek J, Deveil F, Voitsekhovitch I, Stockel J, Azeoural A, Duran I, Van Oost G, Zacek F, in Proc. of 29th EPS Conference on Plasma Phys and Contr Fusion, Montreux, 2002, ECA Vol **26B**, P-5.043
(41) Schrittwieser R *et al* 2002 *Plasma Phys Contr Fusion* **44** 567
(42) Balan P *et al* 2003 *Rev. Sci. Inst* **74**, Nr. 3, in print
(43) Kislov D A *et al* 2001 *Nucl. Fusion* **41** 1473
(44) Kirnev G S *et al* 2001 *Czech J. Phys.***51**1011Kislov D A *et al* 2001 *Nucl. Fusion* **41** 1473
(45) Melnikov A *et al* 2000 *J. Plasma Fusion Res. Series* **3** 917
(46) Melnikov A., Eliseev L., Perfilov S., Mavrin V., Lysenko S., Razumova K., Dnestrovskij Yu., Krupnik L., in Proc. of 29th EPS Conference on Plasma Phys and Contr Fusion, Montreux, 2002, ECA Vol **26B**, P-1.115
(47) Cabral J A C *et al* 1998 *Plasma Phys Contr Fusion* **40** 1011
(48) Cabral J A C *et al* in Proc. of 28th EPS Conference on Plasma Phys and Contr Fusion, Funchal, 2002, ECA Vol.25A,605
(49) Doerner R P *et al* 1994 *Nucl. Fusion* **34** 975
(50) Silva C *et al* 2003 *Plasma Phys Contr Fusion* **45** , in print

First Experience with the Dynamic Ergodic Divertor on TEXTOR

K.H. Finken, S.S. Abdullaev, M. Jakubowski, M. Kobayshi, M. Lehnen, G. Matsunaga, A. Pospieszczyk, B. Schweer, G. Sergienko, R. Wolf

Institut für Plasmaphysik, Forschungszentrum Jülich GmbH, EURATOM Association, Partner in the Trilateral Euregio Cluster, D-52425 Jülich, Germany
k.h.finken@fz-juelich.de

Abstract:
The Dynamic Ergodic Divertor, DED, is a new experiment on the TEXTOR tokamak in Juelich. The DED consists of a set of coils with DC or AC (4 phases) electrical currents flowing parallel to the magnetic field lines. This causes a braiding of the magnetic flux tubes which is called ergodization. The strongly deflected field lines at the plasma edge form the laminar zone. The dynamic operation of the DED (AC current operation) should distribute the heat load to a large surface area and possibly induce a rotation of the plasma. First results are discussed.

Key words: Ergodization, edge plasma, laminar zone, 3D-modelling

Introduction

The formation of an ergodic layer can be an interesting means of destroying the good confinement properties of closed flux surfaces at special locations. Such a location of interest is the boundary of the plasma: The power – with the exception of the radiated fraction - leaves the plasma by cross field diffusion and the heat is conducted and particles are convected along the magnetic fields of a relatively thin boundary layer to the target plate. In order to spread the heat to a larger area, the Dynamic Ergodic Divertor (DED) (1) has been developed. The DED creates an ergodic boundary layer of the plasma and thus allows for wider power deposition pattern, for an improved screening of impurities, and for an enhanced particle removal by the pump limiter ALT-II. The expression "dynamic" refers to a rotating perturbation magnetic field imposed by the DED coils. For the rotation, different frequencies are foreseen: At a few Hertz, the heating pattern of the divertor strike zone is smeared out over the large area of the divertor target plate; at frequencies up to 10 kHz, locked modes can be unlocked, or a differential rotation in the plasma edge can be imposed with hopefully favorable effects on confinement. It is estimated that the rotating DED current generates a torque at the plasma edge.

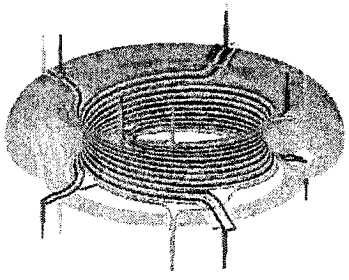


Fig. 1: *Schematic drawing of the DED*

The experimental set-up

The Dynamic Ergodic Divertor, as shown in Fig. 1, is a new conceptual approach which recently has been installed in TEXTOR. The main component of the DED is a set of magnetic perturbation coils whose purpose is to ergodize the magnetic field structure in the plasma edge region; these coils are located inside the vacuum vessel at the high field side of the torus. The set consists of 16 individual coils (4

quadruples) plus two compensation coils. The individual perturbation coils follow the direction of the equilibrium magnetic field of the plasma edge helically once around the torus. The maximum coil currents amounts to 15 kA.
The main perturbation modes (m=10...14, n=4) are centered at m/n = 12/4; this mode structure has been selected because it creates only small local perturbations (magnetic islands) and avoids undesired disturbances in the plasma core. The DED has the unique feature that the perturbation field is not static as in most other devices but that it has the option of rotation. This is achieved by supplying the DED coils with a 4 phase AC current similar as it is done for an induction motor. To our knowledge only the tokamak CSTN (2) at Nagoya University has similar features and - at low perturbation current levels - also the TEXT (3) tokamak. The DED can be operated DC, around 50 Hz or at 7 frequencies in the band from 1 kHz to 10 kHz.

The ergodic layer

The perturbation coils impose structures with different properties in the plasma boundary: The interior closed flux surfaces, $q(r) \leq 2$, remain nearly undisturbed and form for at least well structured KAM (4)-surfaces. Further towards the boundary, islands develop and start to grow; finally, different islands overlap and form an ergodic sea (5,6,7) such that the magnetic surfaces are destroyed. The very outermost magnetic field lines intersect the divertor target plate. These field lines form the so called laminar zone (8); here the transport changes character from diffusive to convective with plasma streaming to the plasma facing components as in the conventional scrape-off layer.

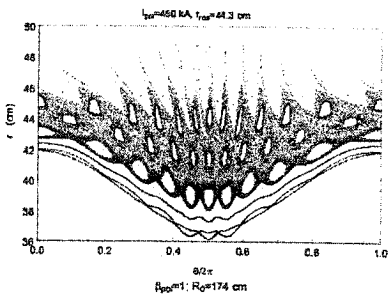


Fig 2: Poincaré plot showing the ergodization of the magnetic field lines. The area with the "many dots" represents the proper ergodic zone while the area with the "few dots" (above the ergodic zone) is the laminar zone. The horizontal axis is the poloidal angle and the vertical one the radius.

Field line tracing and field line mapping (9,10) are basic techniques for investigating the ergodic structure. These techniques provide a picture of the areas with intact magnetic surfaces, of island structures and of ergodized regions. The resonant radius can be adjusted via the plasma current; in this way the ergodic zone can be shifted radially in the range $0.9 \leq r/a \leq 1$ keeping the Chirikov parameter above one. Individual adjustment of the coil currents allows the superposition (11) of different base modes. In order to minimise the interaction with the core plasma, high m/n (e. g. m/n = 12/4) are preferred; for the given coil arrangement, Fourier mode numbers $m \leq 8$ can be neglected. This choice creates many small islands instead of a few islands with large poloidal extent.

Fig. 2 shows an example of Poincaré plots at full perturbation current. The details of the ergodization depend on the plasma current, respectively on the inclination of the local magnetic field which is given by the safety factor q(r). With increasing plasma current, the resonant surfaces ($2.25 \leq q_{res} \leq 3.75$) move towards the outside, closer to the DED coils. Highest ergodization levels with Chirikov parameters up to 6 are expected for plasma currents around 600 kA. The results of the field line mapping seem at a first glance to be in conflict with this expectation: the radially widest ergodic zone is found at the relatively low plasma current of 480 kA which is shown in the figure. At higher values of I_p, the properly ergodic zone shrinks to a small band surrounded by the laminar zone which is discussed below. The outer zone

of the figure is nearly empty of Poincaré intersection points and appears white. The absence of the intersection points is a consequence of stopping the field line tracing after an intersection with a wall element. The reason for this stopping is that particles following field lines would be neutralised and can leave their field line. The "white" area contains field lines with a short connection length. This area of short connection length is called the "laminar zone" (12,13). Because of its short connection lengths, the laminar zone is related to the scrape-off layer properties. The attempt to increase the ergodic zone by increasing the resonant perturbation at the edge evidently leads more to an increase of the laminar layer than to a widening of the ergodic zone.

The Laminar Zone

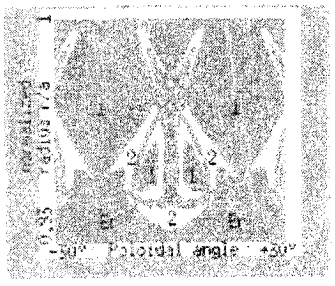


Fig. 3: Example of a laminar plot. The horizontal axis represents the poloidal angle while the vertical one shows the radius. The magnetic field lines of different connection length are plotted in different gray tones and marked with "1","2" and "Er" for 1&2 pol. turns resp. ergodic zone.

Properties of the laminar zone are best represented in a poloidal cut of the plasma edge at the HFS or LFS where areas are ordered according to the connection lengths of the magnetic field lines between two intersections with the walls. Fig. 3 shows an example of such a laminar plot.

The magnetic field lines of different connection length are plotted in gray tones; additionally, the areas with a connection length of 1 poloidal turn is marked with a "1", that of two with the "2" and the ergodic zone with "Er".

For the case of a strong laminar zone, the areas of short connection length (one poloidal turn) is relatively large, followed by successively smaller areas of two and three poloidal turn areas. The structure of the laminar zone are simple as compared to the one of the ergodic zone, which has fractal properties. The channel of field lines connecting the inner ergodic zone with the wall is small (so called fingers), for some conditions even smaller than the Larmor radius. In our picture, the area with field lines of short connection length region will be most responsible for the final step of the transport of energy and particles to the wall. In this sense the laminar zone is similar to the scrape-off layer of a divertor tokamak.

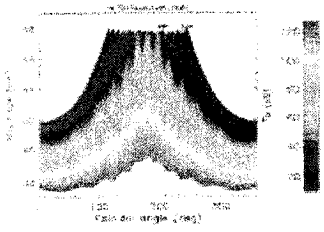


Fig.4: Te profile according to the 3D transport modeling.

Application of the EMC3-EIRENE Modeling to the DED configuration

In order to obtain quantitative predictions of the plasma in the boundary zone, a 3D modeling has been started. The inner radial boundary is at the flux surface just inside the m = 11 islands, where the flux boundary condition was imposed, while the outer radial boundary is a few centimeter outside of the divertor edge, where the decay lengths are specified as the boundary condition. At the divertor surface, the Bohm condition was imposed, accelerating the plasma up to the sound speed, and the recycling flux

proportional to the particle deposition pattern was taken into account by the EIRENE neutral particle Monte Carlo code.

Figure 4 shows the resulting T_e profiles. It is found that the Te-pattern clearly matches the long connection flux tubes region, indicating that the flux tubes provide the loss channel of the plasma. The averaged value of the Mach number is maximum in the area of the flux tubes with short connection length. A rather high density is found in front of the divertor due to the recycling, as well as the strong poloidal modulation for both profiles. The ionization profile was found to have a strong correlation with the particle deposition pattern, affecting the density profile

The energy deposition pattern onto the divertor is shown in Fig.5. Almost the same pattern is obtained as for the particle deposition. The energy is deposited in-between the DED coil structure, where the radial component of the perturbation field is strongest. 80% of the energy flux is brought by the 1 turn flux tubes to the divertor, although the hot plasma comes along the long flux tubes (> 180 m). This means that the 1 turn flux tubes act as a strong sink of the energy to the divertor plate. For the given structure of the laminar zone and for the assumed transport coefficients, one expects a rather frequent heat exchange between flux tubes during the travel along field lines of several tens meters up to the divertor. Additionally, the perpendicular convection might help to give the energy flux to the 1 turn flux tubes.



Fig.5: The energy deposition pattern onto the divertor.

Dynamic aspects

The high frequency aspect of the DED-field has been analysed in cylindrical approximation (14). It has been shown that the „low frequency" (relative to the ion cyclotron frequency) electromagnetic wave of the DED effectively propagates in the area between coils and resonance layer as the compressional Alfvén wave (fast wave) (15). At the resonance layer of the plasma different approximations is described either by a resistive annulus or by tearing modes. The interaction of the external rotating field with the current driven in the shielding layer results in the transfer of angular momentum between DED-coil and plasma (14). The maximum poloidal torque applied to the plasma amounts to about 100 Nm; this maximum occurs at a frequency which seems to depend mainly on the width of the current layer. In detail it depends on the assumed plasma temperature, on the applied frequency and on the assumed island or ergodization width. The toroidal projection of the applied force has about the same value as the one imposed by tangential NBI.

First Measurements

Previous calculations (16) suggest that the strongest action of the DED can be expected for a) maximum DED currents, b) for a plasma shifted to the HFS, c) for plasma with a low value of the safety factor q(a), d) for a low value of B_t and e) for plasma with low β_{pol}. For machine safety reasons, the initial values of the DED current are limited to 1/3 of the nominal amplitude for low frequency operation and to 1/2 in the high frequency band above 1 kHz. In this series of discharges, the plasma was shifted by 3 cm to 4 cm towards the DED, i.e. towards the HFS.

Typical pictures of the particle (H_α) and power deposition pattern with active DED is shown in Fig. 6. The left most picture is a toroidal view with a CCD camera in the visible spectral range, the middle one a view on the divertor target plates (again CCD camera) and the right one is taken by an IR cam-

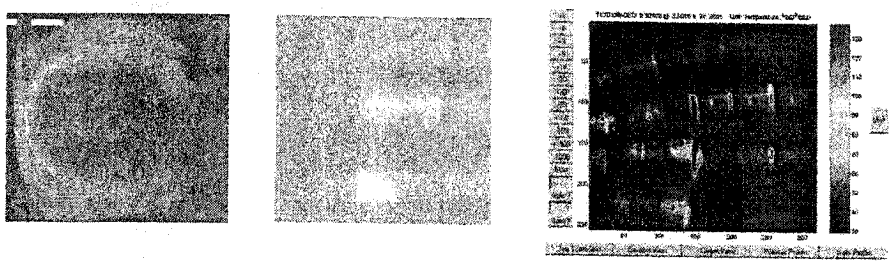


Fig. 6: *Pattern induced by the action of the DED. Left: Toroidal view, middle: perpendicular view of a color CCD camera into TEXTOR, right picture: View by an IR camera. The stripes in front of the DED coils are a prominent feature of the DED operation.*

era. The superposition of the equilibrium field of the plasma and the externally applied near field of the DED generates a characteristic stripe pattern in front of the DED coils. At a low ergodization level, one expects four rather broad stripes as shown in Fig. 7. These data are obtained by a 3-D plasma transport modeling of the DED (17). As one can easily see, the measured width of the stripes and their shape agree very well with the results from the modeling.

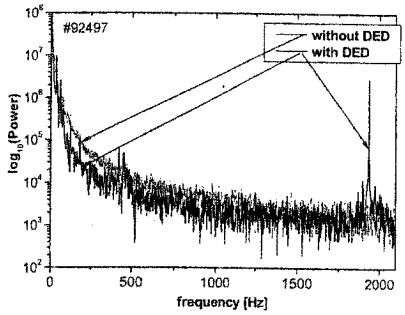


Fig. 7: Spectrum of the heat deposition for discharges with and without DED.

The static operation has shown that – as expected – the heat flux is deposited along stripes in front of the DED coils. The dynamic operation of the DED has been foreseen to smear out the inhomogeneous heat flux to a large surface. A rough inspection by thermography confirms that this assumption is correct. The temperature development of a point of the divertor target surface has been recorded and a Fourier analysis of this temperature yields the spectrum shown in Fig. 7. Both curves represent spectra for the case of NBI heating; the ones with and without rotating DED-field are marked by arrows. As expected, the DEDcurve shows a pronounced peak at the DED frequency. The low frequency part of the curve without DED is larger than the one with the rotating perturbation field; this agrees with the expectation that the rotating DED field smears out the temperature oscillations.

8. Conclusions

Considerable progress has been made in recent years in the understanding of the *static* ergodic divertor (12), both theoretically and experimentally. It has been understood that the ergodic zone with very long magnetic field lines – which show (sub-) diffusive properties in a finite volume – and the laminar zone with open field lines are important, and that both regions have different and partially complementary properties. For analysing the ergodic zone and the transport in that region, powerful mapping methods have been developed.

The understanding of a *rotating* perturbation magnetic field on the other hand is very new ground and this contribution is one of the first steps into the field. A first basic question concerns the physics of the reconnection of the magnetic field in an ergodized layer and what assumption to make about the thickness of the induced shielding current layer there. An earlier model of the shielding current is extended and new results are presented for the torque exerted by the external field on the plasma.

First measurements performed so far show good agreement between modeling and experimental data. A prominent feature is the strip pattern in front of the DED coils. For the full DED current, the stripes should split up and get narrower. The smearing of this heat pattern will be an important aim of the DED research. For obtaining a substantial force transfer from the rotating DED field, the full DED current will be required and it would be preferential to operate at a lower mode such as m/n = 6/2 or 1/3.

References

(1) Special Issue: Dynamic Ergodic Divertor, *Fusion Engineering and Design*, **37** (1997) 335-450
(2) Kobayashi, M., Tuda, T., Tashiro, K., et al, Nucl. Fusion, **40** (2000) 181
(3) Foster, M.S., McCool, S.C., Wooton A.J., Nucl. Fusion, **35** (1995) 329
(4) Lichtenberg, J.A., Lieberman, M.A., „Regular and stochastic motion" in *Applied Mathematical Sciences,* 38, Springer, New York, 1983
(5) Evans, T.E., et al., *J. Nucl. Mater.*, **145-147** (1987) 812
(6) Grosman, A., et al., *J. Nucl. Mater.*, **196-198** (1992) 59
(7) Takamura, S., et al., *Phys. Fluids*, **30** (1987) 144
(8) Eich, Th., Reiser, D., Finken, K.H., *Nucl. Fusion*, **40** (2000) 1757
(9) Abdullaev, S.S., Finken, K.H., Kaleck, A., and Spatschek, K.H., *Phys. Plasmas*, **5** (1998) 196
(10) Abdullaev, S.S., Finken, K.H., Spatschek, K.H., *Physics of Plasmas*, **6** (1999) 153
(11) Finken, K.H., Abdullaev, S.S, Kaleck, A., Wolf, G.H., *Nucl. Fusion*, **39** (1999) 637
(12) Ghendrih, P., Grosman, A., Capes, H., *Plasma Phys. Contr. Fusion*, **38** (1996) 1653
(13) Finken, K.H., Eich, T., Kaleck, A., *Nucl. Fusion*, **38** (1998) 515
(14) Finken, K.H., *Nucl. Fusion*, **30** (1999) 707
(15) Faulconer, D.W., Koch, R., *Fusion Engineering and Design*, **37** (1997) 399
(16) Finken, K.H., Abdullaev, S.S, Kaleck, A., Wolf, G.H., *Nucl. Fusion*, **39** (1999) 637
(17) Kobayashi, M., Fang, Y., Sadei F., et al., EPS 2003, St. Petersburg (to be published).

The Theta-Pinch -- A Versatile Tool for the Generation and Study of High Temperature Plasmas

E. Hintz
Institut fuer Plasmaphysik, Forschungszentrum-Juelich GmbH, Germany
E.Hintz@t-online.de

ABSTRACT

The more general technical and physical features of theta-pinches are described. Special field of their application are high-ß plasmas. Two examples are analysed and studied in more detail: a high density plasma near thermal equilibrium and a low density plasma far from equilibrium. The latter is of special interest for future investigations. Possibilities of field-reversed configurations are pointed out.

Key words: Hydrogen Plasma, Fast Magnetic Compression, Current Sheath, Collisionless Dissipation

INTRODUCTION

The main intention of this contribution is to recall the good suitability of the theta-pinch technique for the study of high temperature plasmas, in particular, of high-ß plasmas. After some introductory remarks on the more general characteristics of theta-pinches [1],[2], we present two experimental situations in more detail. The first one, where a hydrogen plasma with temperatures of a few hundred eV and conditions close to thermal equilibrium is studied, has been investigated in great detail and seems to be rather well understood [3]. Theoretical expectations have been confirmed. It has served, so to speak, as a very reasonable introduction to high temperature plasma physics. This is especially true with respect to the elementary diagnostics. The second one deals mainly with plasmas far from thermal equilibrium and is technologically much more demanding. It has been possible to achieve interesting results on important questions [4], arising for almost collisionfree plasmas, e.g. on relaxation and dissipation processes. We hope, that we will be able to show, that in this wide field of plasma physics there are many interesting questions left open and are awaiting to be studied.

The plasma initial conditions for this type of experiment and for the second one to be discussed later are summarized in the following table.

Plasma initial conditions

Plasma parameters	**Near thermal equilibrium**	**Far from thermal equlibrium**
Density	10^{16} cm^{-3}	10^{13} cm^{-3}
Temperature	2 eV	5 eV
$ß = 8\pi\ nkT/B_{ext}^2$	1	1
Compression time t_c	$2\ 10^{-7}$ s	$4\ 10^{-7}$ s
Collision time τ_{ii}	$3\ 10^{-10}$ s	1 µs
Mean free path λ_{ii}	$7\ 10^{-4}$ cm	5 cm
Sheath width c/ω_{pi}	0.3 cm	10 cm

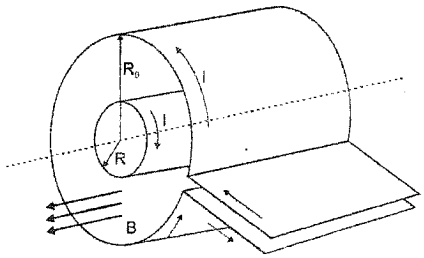
The special case of field-reversed configurations (FRC's) can be dealt with only briefly because of lack of time. The main purpose of this section is to point out the basic aspects of this scheme and turn your attention to it.

GENERAL TECHNICAL AND PHYSICAL FEATURES OF THETA-PINCHES

The principles of a theta-pinch experiment are as follows (Fig. 1). In a straight cylindrical quartz tube is a well conducting, fully ionized gas, e.g. hydrogen, on which a magnetic field B_i eventually is superimposed .The discharge tube is surrounded by a single turn coil, which is connected by way of a switch to a low-inductance capacitor bank. The discharge of the bank generates a magnetic field in the coil and simultaneously causes a current density **j** in the boundary zone of the plasma. Consequently a magnetic pressure gradient **j**×**B** acts on the plasma (B_{ext} is the axial magnetic field). As soon as the external magnetic pressure becomes greater than the sum of the kinetic pressure of the plasma n_0kT_0 (n_0 = initial particle density of the plasma; T_0 = initial temperature of the plasma) and the pressure of the internal magnetic field $B_i^2/8\pi$, the plasma is accelerated towards the axis of the cylinder.

In general, the experimental arrangement is dimensioned such that the time after which $B_{ext}{}^2/8\pi >> n_0\, k\, T_0$, is reached is small compared to the time a_0/v_S (a_0 = initial radius of the plasma; v_S = velocity of a pressure perturbation) which a pressure perturbation needs to move towards the axis. As a consequence a cylindrical hydromagnetic shock wave is generated, which causes an irreversible temperature rise of the plasma behind the shock front. The plasma behind the shock front is acted upon by the magnetic piston, and the plasma cylinder as a whole is thus compressed with supersonic speed. When the shock front arrives at the axis it is reflected and the radial plasma flow is brought to rest. The flow energy is entirely converted into thermal energy. When the reflected shock hits the magnetic piston, the plasma expands until it is in equilibrium with the external magnetic pressure again.

Fig.1 Theta-pinch configuration



We are interested to calculate the plasma conditions of this state from those of the pre-shock, i.e. from the initial state. For this purpose we start from the so-called shock relations. They are identical with those for an ideal gas with a constant ratio of specific heats. For simplicity we consider only the case of strong shocks, i.e. with the Mach-number $M= u_1/c_{S1}>>1$. Then we obtain

$$\eta= n_2/n_1 = \frac{(\gamma+1)}{(\gamma-1)} = f+1$$

$$p_2/p_1 =[\, 2\gamma /(\gamma+1)]\, M^2\,;$$

$$T_2 /T_1 =[(\gamma-1)/(\gamma+1)]\, p_2/p_1$$

In the laboratory system (shockwave moving with u_1) the following relation holds for the piston velocity

$$m_i\, u_p^{\,2}/2 = (f/2)\, kT_2\,;$$

furthermore $B_p^2/8\pi = p_2 = n_2kT_2$.

If we denote the plasma state behind the reflected shock with the subscipt 3, we can write down the equations connecting state 3 and 2; in the strong shock limit:

$$n_3/n_2 = \gamma /(\gamma -1) = (f + 2))/2\,;$$
$$p_3/p_2 = (3\gamma - 1)/(\gamma - 1) = f + 3;$$
$$T_3 = [(f+3)/(f+2)]\, T_2\,.$$

The magnetic field pulse for the fast magnetic compression of the plasma will be generated by the sudden discharge of a low-inductance capacitor bank through the compression coil. The discharge is initiated by closing a switch. After a transient phase, after which the radius of the piston a_P will still be of the order a_0, the voltage at the coil is given by

$U_C = I\, dL_C/dt$;

using $U = 2R_p\, \pi\, E_p$

and $L_c = 1.25\ 10^{-7}\, \pi\, (a_0^2 - a_P^2) / l$

one obtains $E_P = u_P\, B_P$

These equations allow us to derive the following important scaling relations:

$$T_2(K = 1.86\ 10^{10}\ U_0\,(V)/\sqrt{N}\,(cm^{-1}) \quad \text{and} \quad T_3(K) = 4.5\ 10^{10}\ U_0\,(V)/\sqrt{N}\,(cm^{-1})$$

The main objectives of the first experiment were:

- generation of a hydrogen plasma of 200 – 300 eV
- collsion-dominated, i.e. $\lambda_{ii} << a_0$;
- mainly for the study of the shock wave phase of an eventual larger experiment.
- with modest technical expenditure.

These requirements led to the followinh experimental parameters:

Coil radius	2 cm
Coil length	12 cm
Initial density	10^{16} cm^{-3}
U_0	$\approx$ 20 kV .

With the stated dimensions the compression coil had an inductance of about 10 nH. This required a very low inductance of $L_B \approx 1$ nH of the capacitor bank, which could only be achieved by switching many capacitors in parallel, together with the accompanying spark gaps as switches [5]. For shock heating the plasma the penetration of the the magnetic field during the build-up phase had to be avoided, i.e., a well conducting nearly fully ionized plasma was needed before shock compression. This was to be prepared by a preheating discharge, which, if possible, should produce no impurities. For this purpose we decided to use an electrodeless ring discharge [6], which was driven by a small capacitor bank coupled to the compression coil via the collector plate. In order to guarantee an immediate breakdown, a high-frequency transmitter was coupled to the discharge tube, and a discharge was started ahead of the main discharge. By means of an additionnal capacitor bank, connected to the collector plate, an initial magnetic field of the desired magnitude could be provided. With this procedure it turned out that the generation of highly reproducible well-defined plasmas was possible. Impurity concentrations were below 0.1%.

For the first theta-pinch experiments mainly the following diagnostic methods have been used: Magnetic probes, time-resolved photographic measurements by means of a streak camera, refractivity measurements with the help of microwaves, and plasma spectroscopy. Here we shall refrain from a more detailed discussion.

FAST MAGNETIC COMPRESSION OF A PLASMA NEAR THERMAL EQUILIBRIUM

In Fig. 2 we show a streak photo of plasma compression, taken side-on, and the internal magnetic field on the axis of the coil as function of time, with $N_0 = 1.8\ 10^{17}$ cm^{-1} and $B_0 = 900$ G. The radial oscillations of the plasma cylinder after the first maximum compression, as seen in Fig. 2, can be easily understood. During the compression of the plasma cylinder the internal magnetic field increases according to $B_{int}(t) = B_{int}(t=0) \times a^2(t=0)/a^2\,(t)$. At some point in time equilibrium is reached between the external magnetic pressure and the magnetized plasma. Due to the directed kinetic energy of the particles, the plasma cylinder oscillates beyond this state of equilibrium and is then expanded again by the internal pressure. If attenuation is weak, the oscillations are repeated. From more detailed measurements of B(r) and n(r) at different times we may conclude, that the magnetic flux is conserved during the fast compression and that all plasma particles are captured by the magnetic field. We are

very interested in, what temperature has been reached by the fast plasma compression. This we can learn from Fig. 3:

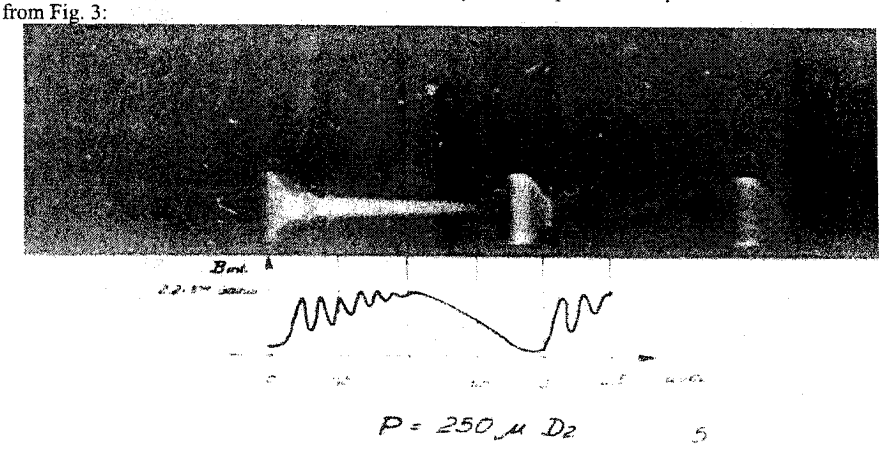
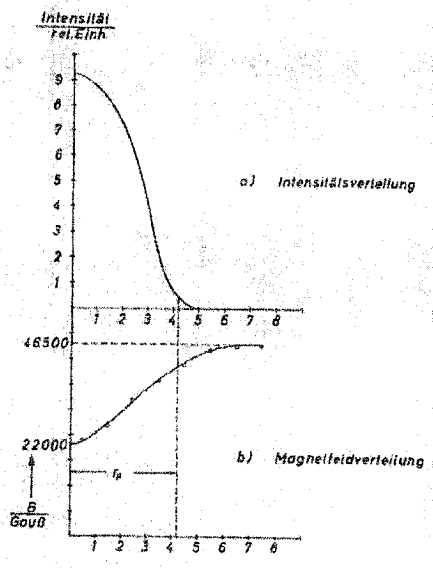


Figure 2. Streak photo of plasma compression and B_{int} as function of time

Figure 3. Radial distribution of magnetic field (b) and of light intensity (a), in relative units



It has been shown, that the impurities in the plasma are negligible [7]. We may assume therefore for the intensity of the radiation emitted by the plasma, that

$$I = n_e^2 \, T_e^{-1/2} .$$

The dependence of the intensity on the temperature is only slight and may be neglected in the interpretation of the intensity distribution as a first approximation.
The line density N is known if we make use of the relation

$$\tau = \frac{2\pi}{B_{ext}} (m_i \, N)^{1/2}$$

and determine τ e.g. from Fig. 2. Now the relation

$$N = \int_0^{a_p} n(r)dr$$

can be utilized in order to normalize the distribution and to determine the maximum density $n_{max} = 4.7 \times 10^{17}$ cm^{-3}.

The measurement of radial distributions is persistent only, if rotational symmetry exists. In order to test this assumption, the plasma was photographed under axial observation at an exposure time of 1×10^{-7} s at the instant of maximum compression. A Kerr cell was used as fast shutter. Figure 4 shows such a photograph.

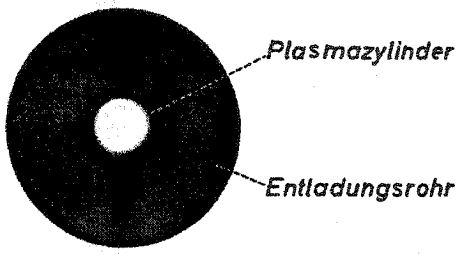


Figure 4: Photograph of the plasma cylinder at maximum compression

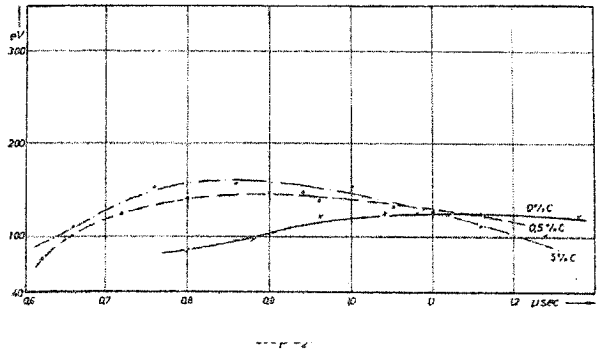
The deviations from rotational symmetry of the plasma cylinder are very minor. The axes of discharge tube and of plasma cylinder coincide.

From the magnetic field distribution we derive $\beta_{max} = 0.8$ in the vicinity of the axis; for the particle density on the axis we obtained $n_{max} = 4{,}5\ 10^{17}\ cm^{-3}$. Now we can calculate the mean energy:

$$k\,(T_e + T_i) = 1.2\ 10^2\ eV.$$

From the equation utilized for the calculation of the dimensions follows $k(T_e + T_i) = 1.3\ 10^2$ eV.

One may assume, that initially the energy will be predominantly with the ions. To investigate this question we have measured the electron temperature independently. T_e was determined from the ratio of soft x-ray intensities transmitted through Be and Al foils assuming a Maxwellian distribution of electron velocities. T_e as a function of time measured side-on by this foil method is shown in Fig. 5.



At 0 % carbon impurity the plasma reaches $T_e = 100$ eV after about 0.8 μs, the lowest T_e measurable with the existing method. Then it rises rapidly even after peak magnetic field. T_e shows an unexpected increase near the peak magnetic field. This may be caused by end effects, energy transfer from ions to electrons or by magnetic field diffusion.

Figure 5. $T_e(t)$ for increasing concentrations of carbon in 250 μ D_2

STUDIES OF A HIGH-ß, LOW-DENSITY PLASMA FAR FROM THERMAL EQUILIBRIUM

Our experience with straight theta-pinches gave rise to the hope that the fast magnetic compression of a highly ionized afterglow plasma might be one way to produce a plasma with thermonuclear temperatures. From the scaling law of plasma heating by fast magnetic compression we inferred that we had to work at high voltage and low density. On the basis of existing low-inductance commercial capacitors and by using a new technique of voltage doubling we planned to provide a voltage of 120 kV at the compression coil. From detailed studies of plasma preheating we learned that it would be possible to generate an almost fully ionized hydrogen plasma at a density of 5×10^{12} cm^{-3} for fast compression. These were the design parameters of the low-density high-voltage theta-pinch at the IPP.
Main objectives were:
Thermonuclear temperature,
Volume compression ratio of about 10
Study of relaxation phenomena
Investigation of the current sheath.
The electrical circuit of the 120 kV experiment is shown in Fig. 6

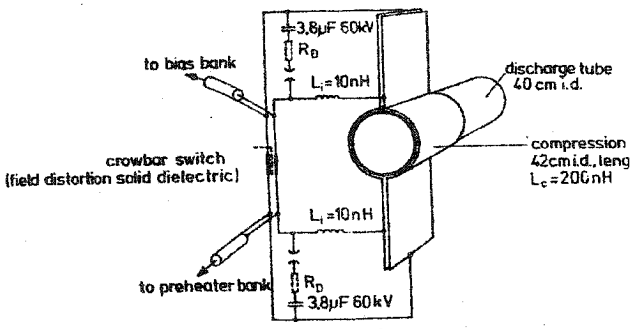


Figure 6. 120 kV theta-pinch experiment (4)

In addition to the diagnostic methods already described, Thomson scattering of laser light was applied for the determination of electron density and electron temperature. Electric fields in the plasma, interpreted as turbulent fields, have been determined by the ratio of forbidden to allowed line intensity of two neutral He lines ($\lambda = 4472$ Å; $\lambda = 4922$ Å:) using the equation given by Baranger and Mozer[8]. Mean ion energies were determined by measuring the neutron yields and, in addition, by using the pressure balance equation. Results are shown in Fig. 7.

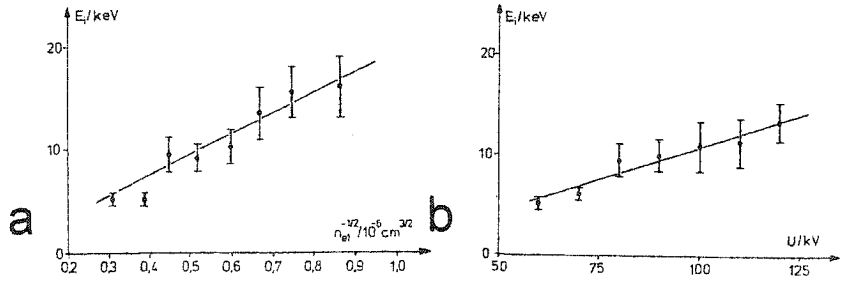


Figure 7. Mean ion energy as a function of intial density (a), and as function of voltage (b)

In order to determine the development of the radial plasma flow, the time history of the electron density pulse generated by the piston has been measured.-Figure 8 shows an example at a_P = 8cm. The velocity of the first two peaks is about twice the piston velocity. The third peak coincides with the piston and its velocity is about equal to that of the sheath, as measured by magnetic probes. Most of the initial plasma is trapped by the piston. We may conclude,that the first two density pulses are generated by the magnetic piston at the beginning of the implosion by elastic reflection of particles. After a short time the reflection properties of the piston change, probably because of the development of micro-instabilities in the current sheath. As a result of the turbulence, the plasma encountered by the piston is trapped and electrons as well as ions are heated.

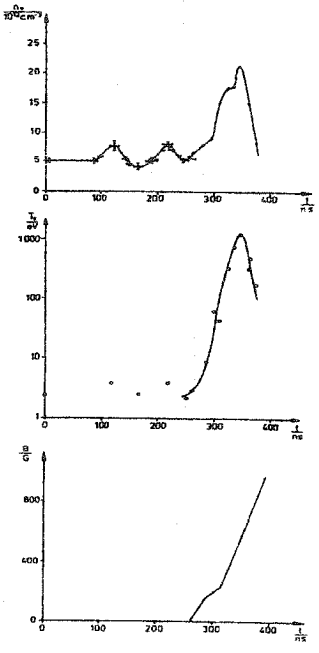


Figure 8. $n_e(t)$, $T_e(t)$ and B(t) for a_P = 8 cm

These results are confirmed by spectroscopic measurements. - Obviously the sheath properties in low density theta-pinches are of great interest and importance. We therefore have made an effort to obtain a description of the plasma state for this situation as complete as possible (n_e, v_d, T_e, $f(v_i)$ and $W = \langle E^2 \rangle / 8\pi nkT$). Unfortunately space is not sufficient to show detailed results of these measurements.

Suffice it to summarize the results of these investigations:
The plasma state in the current sheath is determined by ion sound turbulenece, driven by currents perpendicular to the magnetic field. The measured properties of the turbulent plasma are in good agreement with predictions by theory and by numerical simulations.

Let us return briefly to the state of the plasma near the axis.

When the magnetic piston passes R=8 cm, 80% of the total kinetic energy of the particles is stored in the flow energy of the ions. Upon reflection at the axis most of the ion flow energy is converted into random energy perpendicular to the magnetic field. At 800 ns the ion velocity distribution has almost approached a Gaussian. The mean ion energy derived from end-on measurements is smaller by a factor of 4. T_e near the axis approaches 30eV and is determined by the balance between energy transfer from the ions and heat conduction losses to the ends.

REMARKS ON FIELD-REVERSED CONFIGURATIONS (FRC's)

We have also done some investigation on low-ß plasmas. Here we shall deal only with one special case, when an initial magnetic field of –2500 G is superimposed on the preheated plasma. The minus sign here means that the direction of the initial magnetic field is antiparallel to the compression field.

Let us consider the conditions immediately after the compression field is switched on. The magnetic field between plasma boundary and the wall will, for a short time, become zero. As a consequence the pressure of the internal magnetic field will drive the plasma towards the wall. Then the pressure of the reversed field will be built up again. It soon will exceed that of the internal field and then compression starts again. At some point we may stop the further increase of B_{ext}. The most interesting development will happen at the ends of the compression coil. The magnetic field lines close and a configuration with closed magnetic field lines, i.e. a toroidal system , will develop (Fig. 9).

Densities and temperatures achieved in theta-pinches with trapped reverse field seem to be similar to those in standard theta-pinches. Impurity concentrations are somewhat higher. Concerning the main loss mechanism in theta-pinches, our experience was. that the comparatively high concentration of

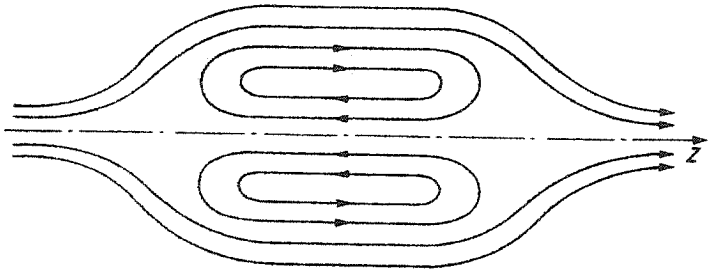


Figure 9. Field-reversed configuration of a theta-pinch

neutral hydrogen (e.g. 50%) leads to correspondingly high losses due to charge exchange.This should also be the case for FRC's. We have found no way to avoid these losses.

However, there have been successful attempts to transfer FRC's into different vacuum chambers [9]. This way it might be possible to get rid of the neutral particle background. The possibility to transfer large numbers of hot ions by means of FRC's (e.g. into tokamaks) could raise new interest in research on this type of theta-pinches.

REFERENCES

(1) "Plasma Physics and Controlled Nuclear Fusion";1962, Supplement Part 2, IAEA Vienna. (1962).
(2) P. Bogen and E. Hintz; "Shock Induced Plasmas" in "Gaseous Electronics", M.N. Hirsch and H.J. Oskam, eds., Academic Press (1978).
(3) E. Hintz; Plasma Physics and Contr. Nucl. Fusion Res., Suppl. Part 2, IAEA Vienna; 601 (1962).
(4) P. Bogen, et al.; Plasma Phys. Contr. Nucl. Fusion Res.; 3, 349 (1975).
(5) H. Beerwald and E. Hintz; 1960, Proc. 4 th Int. Conf. Ion. Phen. Gases, Uppsala, North-Holland Publ., Amsterdam; 2, 468 (1960).
(6) H. Beerwald, P. Bogen, T. El-Khalafawi, H. Fay, E. Hintz, and H. Kever; Nucl. Fusion Suppl., IAEA Vienna; Part 2, 595 (1962).
(7) P. Bogen, E. Hintz, J. Schlüter; Phys. Fluids; 7, (1964).
(8) M. Baranger, B. Mozer; Phys. Rev.; 123, 25 (1961).
(9) A.G. Es'kov, et al.; Plasma Phys. and Contr. Nucl. Fusion 1976, IAEA Vienna; 2, 187 (1976).

Characterising the Plasma Focus Pinch and Speed Enhancing the Neutron Yield

S. Lee
International Centre for Dense Magnetised Plasmas, Warsaw, Poland, and
Plasma Radiation Lab, NIE, Nanyang Technological University, Singapore
leesing@optusnet.com.au

ABSTRACT

From dimensional considerations and also experiments the compressed radius, pinch length and 'lifetime' of the plasma focus pinch are each proportional to the anode radius 'a'. Further an analysis of a range of plasma focus machines shows that the speed parameter $(I/a)/\rho^{1/2}$, where I is the driving current and ρ is the ambient density, has practically the same value (90 kA m^{-1} per $torr^{1/2}$ in deuterium, variation of less than 10%) over the whole range of small to big machines. This indicates that the speed v and energy density (hence plasma temperature T) have practically the same values over the range of machines. This gives us the well-known $Y \sim I^4$ neutron yield law that is observed. This observed law is due to the fixed speed operation over the whole range of these machines. If the value of (I/a) is allowed to increase, speed will increase with (I/a) and yield scaling will change to $Y_{th} \sim I^4(I/a)^4$ or I^4v^4 giving rise to the concept of speed enhancement of the neutron yield.

Key Words: ***Plasma focus scaling, Neutron yield enhancement, Plasma Focus computation***

I. THE SPEED PARAMTER S: $(I_p/a)\rho^{-1/2}$

Using a snowplow model for the axial phase and a slug model for the radial phase (Fig.1), simply by normalizing equations, characteristic axial and radial transit times for the plasma shock are[1-4]:

$$t_a = \left[\frac{4\pi^2 (c-1)}{\mu \ln c}\right]^{1/2} \frac{z_o \rho^{1/2}}{(I/a)} \tag{1}$$

$$t_r = \left[\frac{16\pi^{2}}{\mu(\gamma+1)}\right]^{1/2} \frac{a\rho^{1/2}}{(I/a)} \tag{2}$$

where $c = b/a$, b is the outer radius of the coaxial electrodes, a is inner radius, μ is permeability, z_0 is length of inner electrode, I is characteristic current, ρ is ambient density and γ is the specific heat ratio.

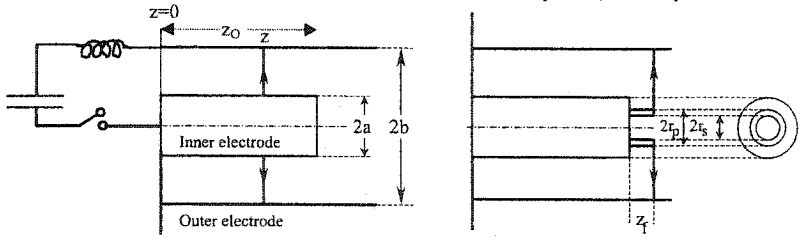


Fig. 1. Schematic of the dynamics of the plasma focus for the 1-D computational model: (a) axial phase - snowplow model; (b) radial phase - slug model

From these we write the characteristic speeds for the axial and radial shock, respectively as [5]:

$$c_a = \frac{z_o}{t_a} = \frac{(I/a)}{\rho^{1/2}}\left[\frac{\mu \ln c}{4\pi^2 (c-1)}\right]^{1/2} = \frac{(I/a)}{\rho^{1/2}} g_a \tag{3}$$

$$c_r = \frac{a}{t_r} = \frac{(I/a)}{\rho^{1/2}}\left[\frac{\mu(\gamma+1)}{16\pi^2}\right]^{1/2} = \frac{(I/a)}{\rho^{1/2}} g_r \tag{4}$$

where g_a and g_r are effective geometrical constants governing the axial and radial phases, respectively; g_r is a constant and g_a varies by less than 10% from a mean value of 0.52 over the range of c = 1.5 to 2. Hence c_a and c_r and the operational speeds in the axial and radial phases depend only on the speed parameter S: $(I_p/a)\rho^{-1/2}$, where I_p is the peak current entering the focus tube.

II. SCALING: FOCUS PINCH LENGTH, RADIUS, AND LIFETIME, EACH DEPENDENT ON ANODE RADIUS 'a'

A radial collapse model which has proven useful for comparison with experimental work is as shown in Fig. 1b. Essentially a zero length pinch starts at $r = a$ and elongates as it pinches inwards. The collapsing magnetic piston at position r_p pushes ahead of it a radially converging structure at position r_s. Using this model and having shown that the characteristic speed of radial transit is the same over the range of devices, it follows that the compression time $t = t_{comp}$ (see Fig. 2) depends on the radius a of the anode. As the shock converges on the axis we may define the position of the piston at this time as r_c. After the shock hits the axis a reflected shock propagates outward. In the meantime the piston (see Fig. 2) continues inwards until it is hit by the reflected shock at which point the radially inward motion of the piston is reversed at position $r_p = r_{min}$. Experimentally it is observed that the plasma column usually pinches a second time sometimes to an even smaller radius before finally exploding outward. This ends the pinch phase and defines the quantity t_{pf} as shown in Fig. 2.

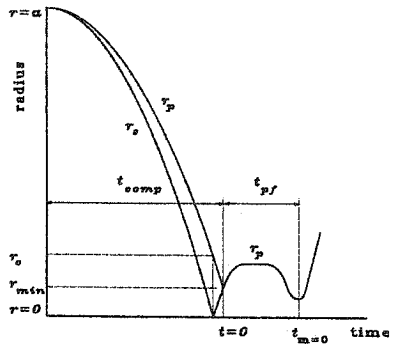


Fig. 2: Schematic of the radial collapse

A numerical computation of this model [1-4,7] shows that both r_c and r_{min} are proportional to anode radius 'a'.The ending of the pinch phase is observed to be caused by instabilities. Thus we may relate the period t_{pf} to the transit time of small disturbances across the compressed plasma column. The speed of these small disturbances is practically a constant over the range of devices because of the near constancy of plasma temperature, density and magnetic flux. Thus in such a scenario t_{pf} also depends on the radius a. We have carried out a numerical computation with end-point fixed by an energy-balance consistent method [8,9] and found the following for the deuterium focus and the neon focus:

		Deuterium	Neon (for SXR)
minimum radius	r_{min}	0.12a	0.04a
maximum length	z	0.8a	0.8a
radial shock transit	t_{comp}	$5x10^{-6}a$	$4x10^{-6}a$
pinch lifetime	t_f	$2x10^{-6}a$	$1x10^{-6}a$

where, for the times in sec, the value of anode radius, a, is in m.

Similar results are applicable to the gross pinch of the plasma focus in other gases such as Argon, Neon and Xenon. Generally for these other gases $r_{min} < 0.1a$. The difference in the computation involves the value of γ. Scaling these parameters of the focus to the anode radius a is extremely useful for understanding and for applications. We have carried out exhaustive series of experiments [7,10], using TEA nitrogen laser nanosecond shadowgraphy (see Fig. 3), which confirm these theoretical results. Agreement is also observed with more recent detailed computations [1].

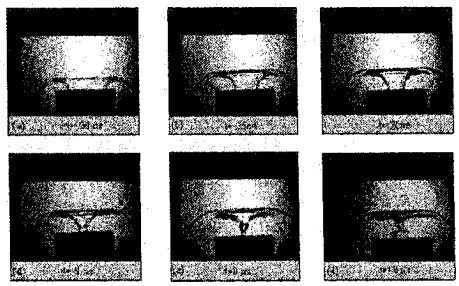


Fig. 3. Sequence of compression in UNU/ICTP PFF at 4.0 mbar deuterium[20]

III. DRIVE PARAMETER S IS CONSTANT OVER RANGE Of MACHINES

We next return to discuss the drive parameter S: $(I_p/a)\rho^{-1/2}$. We had surveyed [5] the drive parameter for a range of machines, from large to small, as compiled in Table 1.

Device/(Author reference)	V (kV)	W (kJ)	p (torr D_2)	I_p (kA)	a (cm)	$I_p/a/p^{1/2}$ (kA/cm/[torr D_2]$^{1/2}$)
DPF-78 [24]	60	28	5	550	2.5	98.4
SPEED 2 [25]	183	70	4	1000	6	83.3
PF-360 [18]	21	60	3	750	5	86.6
Mather [19]	17.3	13.5	6.5	537	2.5	84.3
UMPF [20]	14	6	6.5	300	1.25	94.1
UNU/ICTP-PFF [23]	14	2.9	3.5	172	0.95	96.8
Bernstein [21]		27	8	820	3.9	74.3
POSEIDON [22]	60	280	3.8	1200	6.55	94.0

Table 1. Actual-shot data of some neutron-optimized Mather-type plasma focus devices and their calculated drive parameter. The mean value and the corresponding standard deviation of the drive parameter are 89.0 and 7.7 kA/cm/(torr D_2)$^{1/2}$, respectively.

In this compilation care is taken that the data represent actual neutron-optimized shots as published. Actual-shot data need to be distinguished from machine data which may give maximum current capability of a machine or design current which, when combined with the pressure of an actual shot, may give a misleading drive parameter since the actual shot is usually carried out not at the maximum or designed current. Thus much published data of machines could not be used in this compilation because of uncertainty over actual shot data. In Table 1 the value of the peak current I_p flowing into the focus tube is used as this value is more usually quoted than the plasma current and thus using the peak current more actual shot data points are available.

Table 1 shows that the drive parameter S for a range of neutron-optimized plasma focus devices is 89±8 kA/cm per $(\text{torr})^{½}$ of deuterium. The standard deviation of less than 10% is quite remarkable since the machines in the compilation range from 3 to 280 kJ and include early machines of Mather and Bernstein, advanced machines such as SPEED 2 and small training machines.

Any modeling based on electromagnetic drive such as we have shown in Section I will show that the drive parameter S determines the speed in both the axial and radial phases [2,3]. Having the same value of drive parameter S indicates that the range of machines surveyed all operate with the same axial and radial speeds. This is not contradictory to the oft-reported speeds of almost 10 cm/μs for the axial phase just before the radial phase and a radial speed of about 25 cm/μs when the imploding shock is nearing the axis. Since the energetics of the plasma focus is determined by the shock speed up to the time the radial shock goes on axis, constancy of the drive parameter gives a strong indication that the temperature is also the same over the range of plasma focus surveyed. The density also varies remarkably little, a range of 2, considering the large range of energies encompassed in the survey. Thus the plasma energy density of the machines has also relatively small variation. The mechanisms for radiation of energy and particles depend ultimately on the energy density and/or the temperature. The small variations observed in these quantities over the large range of machines whilst on the one hand is an advantage for comparing experiments may perhaps on the other hand act as a severe limitation.

IV. SCALING OF YIELD

To a thermalised plasma we can generally assign density n and temperature T. If the particles of density n interact among themselves with a cross section C(T), generally dependent on T, we may write down a general radiation yield, Y, relationship as follows:

$$Y \sim n^2 \text{ (volume) (lifetime) } C \tag{5}$$

For the plasma focus, given the dimensional and temporal dependence as discussed in Section II we have:

$$Y \sim n^2 a^4 C \tag{6}$$

Constant S operation

Given the observed constancy in S we have:

$$I \sim a\rho^{½} \tag{7}$$

Hence applying Eq.(7) to Eq. (6) with $n \sim \rho$ and noting that since T=constant over the range of devices, the cross section C is also constant and we have [9]:

$$Y \sim I^4 \tag{8}$$

This yield law really applies to the thermonuclear neutron yield. Experimentally for a small neutron-optimised plasma focus it has been shown [11] that the thermonuclear component of the neutron yield is only 15%, the other 85% being ascribed to beam-target mechanisms. Nevertheless, we note that these yield proportions are occurring at a plasma ion temperature of about 1 keV and a beam energy of about 50 keV.

V. SPEED-ENHANCEMENT OF NEUTRON YIELD

We now discuss the concept of speed enhancement [12,6]. If the driver parameter S is increased, the drive energy density increases, the speed increases and we may expect the focus pinch ion temperature also to increase. This leads to a dramatic increase in neutron yield since in the range of 1 – 10 keV, the neutron fusion cross-section is a rapid function of T with $C \sim T^n$, n being greater than 4. We note $T \sim v^2$ where v is the driven plasma shock speed. If we keep 'a' constant as the drive current is increased, we increase the drive parameter S. This will give us a thermonuclear yield component better than

$$Y \sim I^8 \tag{9}$$

Increase in speed will also increase the energy of the beam component. The beam component will however not have a significant increase since above 50 keV the cross section C barely increases with T. This means that as operational speed is increased, the plasma focus neutron yield becomes more thermonuclear.

Operating the focus at higher velocities, hence higher temperatures, the thermonuclear component Y_{th} of the total neutron production is enhanced. A more general analysis shows that

$$Y_{th} \sim I^4 v_{axial}^4 \tag{10}$$

and the beam-target component of the neutron yield

$$Y_{b\text{-}t} \sim I^{4.5} v_{axial}^{-1.5}. \tag{11}$$

The total neutron yield is $Y_n = Y_{th} + Y_{b\text{-}t}$. If the experiments do not limit the speed of operation, then Y_{th} will increase above the I^4 scaling whilst $Y_{b\text{-}t}$ will have a scaling law poorer than $I^{4.5}$. In the limit keeping the anode radius constant whilst increasing the current,

$$Y_{th} \sim I^8 \text{ and } Y_{b\text{-}t} \sim I^3 \tag{12}$$

VI. EXPERIMENTAL CONSIDERATIONS

However, it is not a simple matter to increase the drive speed. Experiments in deuterium have shown that if the peak axial speed is pushed above 10 cm/μs, plasma focus quality simply deteriorates. A force-field flow-field separation mechanism [13] has been proposed to account for the deterioration of the focus quality. At speeds above 5 cm/μs the specific heat ratio γ of the heated deuterium plasma [16] rises rapidly towards 5/3. The shock layer thickness is extremely sensitive to γ, and thickens above these speeds. Moreover above these speeds the Magnetic Reynolds Number (MRN) is in a crucial transition above 1. The transition from low MRN to high MRN with increasing speed is extremely rapid as, in this ionizing regime, the MRN is proportional [17] to (speed)^4. Thus as the speed increases from a crucial 5cm/μs, say, to 10 cm/μs, the MRN would have transitioned from a value of 1 (poor electromagnetic coupling) to 16 (good electromagnetic coupling). This latter case provides a separation between the force field and the mass field it is driving; a separation which increases with distance traveled at speeds in the region of 10 cm/μs and above. Whilst such a separation is conducive to energy transfer, at the end of the axial phase, as the mass-force system expands from the axial to the radial phase, the force field is left behind and is still pushing axially whilst the radial shock is already imploding inwards. As this separation increases the quality of the radial focus pinch deteriorates. There are indications of such a mass field-force field separation at the higher speeds from schlieren photographs (see Fig. 4).

Stepped Anode for Speed Enhancement whilst minimizing Separation

An experiment[7] was carried out to achieve this speed increase yet overcome the separation effect by keeping the 'speed-enhanced' region short. A stepped-anode, Fig 5, was used consisting of a 'normal' radius section designed with the normal S value, followed by a short 'speed-enhanced' section for which the S value was increased by a reduction of 'a'. By this means speeds up to 15cm/μs were

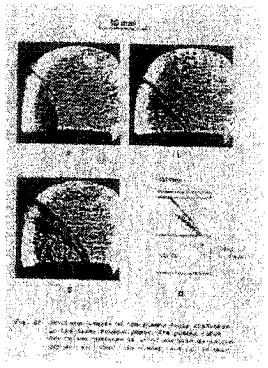


Fig.4. Schlieren pictures showing current sheet from shock front, indicating increasing force field - mass field separation at increasing speeds

achieved with reasonably consistent focussing. Neutron-yield enhancement [7,14] was indicated (see Fig.6). SXR yield in DEUTERIUM was also speed-enhanced [15]

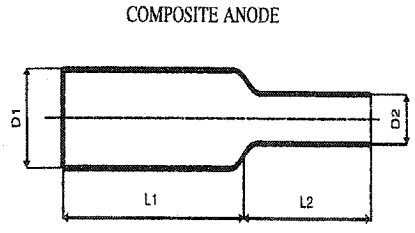


Fig. 5. Stepped anode

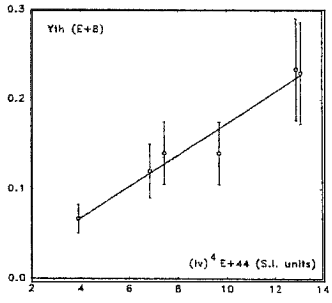


Fig. 6. Non-beam component of neutron yield as function of $(Iv)^4$, speed-enhanced UNU/ICTP PFF, operated at 14 kV, 4.5 mb deuterium

Argon in Axial Phase Collapsing onto Deuterium in Radial Phase

Another method would be to use argon or krypton in the axial phase collapsing onto a deuterium gas (e.g. jetting out of a hollow anode). Even at speeds of 15 or 20 cm/μs the argon or krypton will not be fully ionized, hence the axial shock will have a specific heat ratio γ close to 1, with the piston moving almost together with the shock, thus reducing the mass field-force field separation. In this manner could be obtained much higher focus collapse speed in deuterium, with attendant speed-enhanced neutron yield.

REFERENCES

(1) S. Lee; "Plasma Focus (Radiative) Computation Model and Code"; http://sci.nie.edu.sg/ckplee; e-published by CKP Lee, NTU/NIE-first published June 2000.

(2) S. Lee et al.; "Technology of the Plasma Focus" in *Laser and Plasma Technology*, Ed. by S. Lee et al., World Sci Pub Co, Singapore (1985) p387-420.

(3) S. Lee; "Plasma Focus Model Yielding Trajectory and Structure" in *Radiation in Plasmas,* Eds. B. McNamara, World Sci Pub Co (1984) 978-987.

(4) S. Lee; "Technology of a small plasma focus-incorporating some experience with UNU/ICTP PFF" in *Small Plasma Physics Experiments II*, Eds. S. Lee and P. H. Sakanaka, World Sci Pub Co (1989) p113-169

(5) S. Lee and A. Serban; IEEE Trans Plasma Sci.; 1101 (1996).

(6) S. Lee and A. Serban; "Speed–enhanced Neutron Yield in Plasma Focus", Int. Conf. Plasma Phys, Foz do Iguassu, Brazil, Oct. 1994, Conf. Proc. Vol 1, p181-184.

(7) A. Serban; "Anode Geometry and Focus Characteristics" PhD thesis, NTU (1995).

(8) S. Lee; J. Phys. D: Appl. Phys.; 16, 2463 (1983).

(9) S. Lee; Laser & Particle Beams; 6, 597 (1988).

(10) M. H. Liu; "Soft X-rays from Compact Plasma Focus", PhD thesis, NTU (1997)

(11) S. P. Moo, C. K. Chakrabarty, and S. Lee; IEEE Trans Plasma Sci.; 19, 515 (1991).

(12) S. Lee; The sharing of fusion-related technology among developing countries. Invited paper. Energy Independence Conf., August 1987; Rio de Janeiro, Brazil; also appeared in revised version in Majalah Fizik. Proc. Fusion Energy and Plasma Physics, World Scientific (Ed.: P. H. Sakanaka). (1988). 754-781.

(13) S. Lee; Technology of a Small Plasma Focus in "Small Plasma Experiments II" Eds. S. Lee and P. H. Sakanaka, World Scientific Publishing Co (1990).

(14) A. Serban and S. Lee; J. Plasma Phys.; 60, 3 (1998).

(15) A. Serban and S. Lee; Plasma Sources Sci. Technol.; 16, 25 (1997.

(16) S. H. Saw, S. Lee and C. S. Wong; J. Fizik Malaysia; 9, 93 (1988).

(17) S. Lee, S. H. Saw, A.A. Elfetouri, A. M. Shengher, E. O. Shumaki and N. A. Hassan; J. Fizik Malaysia; 12, 25 (1991).

(18) S. Czekaj, A. Kasperczuk, R. Miklaszewski, M. Paduch, T. Pisarczyk, and Z. Wereszczynski; Plasma Phys. Contr. Fusion; 31, 587 (1989).

(19) J. W. Mather, P. J. Bottoms; Phys. Fluids; 11, 611 (1968).

(20) K. H. Kwek, T.Y. Tou, and S. Lee; IEEE Trans. Plasma Sci.; 18, 826 (1990).

(21) M. J. Bernstein and G. G. Comisar; Phys. Fluids; 15, 700 (1972).

(22) U. Jager; "Uber die Reaktionsmechanismen im Plasmafokus - Untersuchen an beschleunigten Deuteronen und Reaktionsprotonen", Univ. Stuttgart, Report IPF-86-1, (1986).

(23) S. Lee, T.Y. Tou, S.P. Moo, M.A. Eissa, A.V. Golap, K.H. Kwek, S. Mulyodrono, A.J. Smith, Suryadi, W. Usada, and M. Zakaullah; Am. J. Phys.; 56, 62 (1988).

(24) H. Schmidt; "Generation, Physics and Applications of Superdense Hot-Z-Pinch Plasmas", Rep. on activities, March '92 - Feb. '93, Univ. Stuttgart, Germany (Contr. SCI CT91-0728 (TSTS)).

(25) G. Decker, W. Kies, M. Malzig, C. van Calker, and G. Ziethen; Nucl. Instrum. Meth. Phys. Res.; A249, 477 (1986).

Research on pinch devices of tens of kA to MA

Leopoldo Soto[1], Patricio Silva[1], José Moreno[1], Gustavo Silvester[1], Marcelo Zambra[1], Cristian Pavez[2], Renato Saavedra[2], Horacio Bruzzone[3, 4], Mario Barbaglia[3], Roberto Mayer[3, 5], Yurii Sidelnikov[7], Walter Kies[7]

1 Comisión Chilena de Energía Nuclear, Casilla 188-D, Santiago, Chile
2 Universidad de Concepción, Chile
3 PLADEMA, Argentina
4 Universidad de Mar del Plata and CONICET, Argentina
5 Instituto Balseiro, Bariloche, CNEA and CONICET, Argentina
6 Institute of Spectroscopy, RAS, Troitsk, Moscow Region, Russia
7 Heinrich-Heine-Universität, Düsseldorf, Germany
lsoto@cchen.cl

ABSTRACT

At present the Plasma Physics and Plasma Technology Group of the Comisión Chilena de Energia Nuclear (CCHEN) has the experimental facilities in order to study dense transient discharges in a wide range of energy and current, namely: I) energy from tens of joules to hundred of kilojoules, II) current from tens of kiloamperes to some mega-amperes. Also several diagnostics have been implemented. An overview of the work being carried out on dense pinch discharges at the Comisión Chilena de Energía Nuclear is presented.

Keywords: z-pinch, plasma focus, neutron and x-ray nanoflashes, plasma diagnostics

INTRODUCTION

At present the Plasma Physics and Plasma Technology Group of the Comisión Chilena de Energia Nuclear (CCHEN) has the experimental facilities in order to study dense transient discharges in a wide range of energy and current keeping the same time scale. These plasmas can produce high energy density conditions, instability phenomena, plasma jets, X-ray and neutron emission. Many of the observed phenomena in pinch plasmas are not completely understood. The program research includes: a) mechanism of X-ray emission (thermal vs. beam bremsstrahlung, population inversion in soft X-ray to VUV region, mechanism of neutron emission (thermonuclear vs. beam-target), charged particles beams emission; b) development of diagnostics; and c) development of optimized apparatus for flash sources of neutrons and x-rays (nanoflashes) and possible applications.

The devices at CCHEN are: a small and fast capillary discharge (1-2 nF, 5 kA, <1J, 5 ns time to peak current, dI/dt ~10^{12} A/s); two very small plasma focus devices, PF-50J (160 nF, 25 kV, 50 kA, 50 J, 150 ns time to peak current, dI/dt~$3x10^{11}$ A/s) and PF-400J (880 nF, 25 kV, 120 kA, 400 J, 300 ns time to peak current, dI/dt~$4x10^{11}$ A/s); a small plasma focus SPEED4 (1.25 μF, 70 kV, 450 kA, 3 kJ, 400 ns time to peak current, dI/ dt~10^{12} A/s); and the pulse power generator SPEED2, a medium energy and large current device (4.1 μF, 300 kV, 4 MA, 187 kJ, 400 ns time to peak current, dI/dt~10^{13} A/s). The SPEED2 arrived at the CCHEN in May 2001 from Düsseldorf University, Germany, and it is in operation since January 2002, being the most powerful and energetic device for dense transient plasma in the Southern Hemisphere.

Several diagnostics have been implemented: voltage, total current and current derivative monitors; plasma images with an intensified CCD camera gated at 5 ns exposure time; silver activation counter and ^{3}He detectors for neutron yield measurements; plastic scintillator with photomultiplier for X-ray and neutron detection with temporal resolution; VUV and soft X-ray spectroscopy; and pulsed optical refractive diagnostics using a pulsed Nd-YAG laser.

In this article we present results related to design and construction of very small plasma foci (PF-50J and PF-400J); development of diagnostics and instrumentation (plasma dynamics observations and low fluence neutron detection); plasma dynamics and neutron emission from PF-50J and PF-400J; and preliminary results in SPEED2 operated in plasma focus mode.

COMPACT AND FAST PLASMA FOCI PF-50J AND PF-400J

As first stage of a program to design a repetitive pulsed radiation generator for industrial applications we constructed two very small plasma focus operating at an energy level of the order of a) tens of joules (PF-50J, 160 nF capacitor bank, 20-35 kV, 32-100 J, ~150 ns time to peak current)[8-10] and b) hundred of joules (PF-400J, 880 nF, 20-35 kV, 176-539 J, ~300 ns time to peak current)[11].

Criteria design. The compact and fast plasma foci devices constructed by CCHEN, PF-400J and PF-50J, consists of capacitors banks that discharge over coaxial electrodes through spark-gaps. The capacitor bank consists in four capacitors connected in parallel. Four capacitors of 220 nF-20 nH in PF-400J case and 40 nF-20 nH in PF-50J case. The devices operate with charging voltages of 20 to 35 kV. In order to obtain low inductance the capacitors were connected in a compact layout. Short and coaxial spark-gaps were designed for the same purpose. The measured total external inductance is 38 nH. The total impedance of the generator is of the order of 0.2 Ω for the PF-400J and 0.5 Ω for the PF-50J. To determine the size of the electrodes the design relations suggested by S. Lee[4] and a theoretical model of plasma focus for neutron production[12] were applied. It is known that the pinch phase in a plasma focus is highly dependent of the current sheath formation over the insulator. Unfortunately, there are still not validated theoretical models to determine the dimensions of the insulator. Therefore, several tests with different insulator length and diameter, scanning pressure range from 1 to 12 mbar, were necessary to determine the size of the insulator in order to obtain a homogeneous initial sheath. The current sheath was studied with an image converter camera with 5ns exposure time. The final electrodes for the PF-400J consist of a 28 mm long, 12 mm diameter cooper tube anode, and an outer cathode of eight 5mm diameter cooper rods uniformly spaced on a 31mm diameter. The anode and cathode were separated by an alumina tube of 21 mm length. In the case of the PF-50J after some improvements from the original design[9,10], the electrodes configuration consists of a 29 mm long, 6 mm diameter cooper tube anode, and an outer cathode of eight, 5 mm diameter cooper rods uniformly spaced on a diameter of 27 mm. Anode and cathode were separated by an alumina tube of 24 mm length. Such configurations resulted from the short first quarter period of the discharge current (200-300 ns, due to the small bank capacity), which require a short effective anode (6-7 mm). The size of these devices is of the order of 25 cm x 25 cm x 50 cm. The design calculations indicate that neutrons yields of $10^4 - 10^5$ neutrons per shot are expected with discharges in deuterium in the PF-50J and $5x10^5 - 5x10^6$ neutrons per shot in the PF-400J.

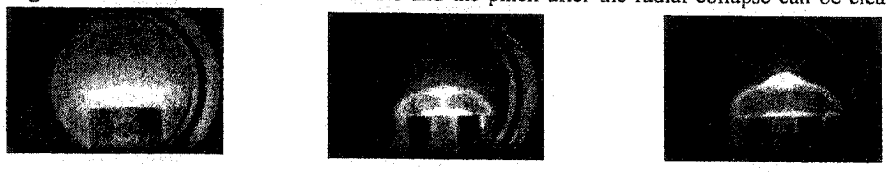
Electrical diagnostics. Voltage, total current and current derivative are measured with usual monitors, a fast resistive divider, and a Rogowsky coil. The voltage monitor was located close to the plasma load. The Rogowsky coil monitored the current derivative signal in the capacitor bank.

Images from the visible plasma light. An intensified CCD camera (ICCD) gated at 5 ns exposure time, and synchronized with the discharge has been used in order to obtain side view images of the visible light emitted from the plasma[10]. For imaging the plasma over the microchannel plate in the ICCD camera, a regular bi-convex lens with a focal length of 12.5 cm and 5 cm of diameter was used. In order to increase the field depth a mask with an open circle of 1 cm diameter was attached to the lens, so an optical number F=1/12.5 was obtained. A magnification m=0.2 was used. The resolution of the camera for magnification m=1 is 23 μm, thus for m=0.2 a resolution of 95 μm (~0.1 mm) is achieved.

Neutron detection. A silver activation counter, calibrated with an Am-Be source, placed at 30cm in the side-on direction was used to record the integrated neutron signal for total yield over $5x10^5$ neutrons per shot (PF-400J). For total neutron yield lower $5x10^5$ neutrons per shot (PF-50J) a system

based ^{3}He detector was developed[13]. Also plastic scintillator with photomultiplier for X-ray and neutron detection with temporal resolution have been implemented.

Results. In order to study the plasma motion images in the visible region were obtained with a 5 ns gated ICCD camera for different times of the discharge and for different Hydrogen pressures. A sequence of the plasma images of the PF50 is presented in Fig. 1. The umbrella-like current sheath running over the end of the coaxial electrodes and the pinch after the radial collapse can be clearly



37ns 222ns 309ns

Figure 1. Sequence of the plasma images obtained with a ICCD camera gated at 5ns of exposure time from different discharges in hydrogen at 0.47 mbar in the PF-50J[10].

observed in the photographs. Radial collapses of the order of 10^5m/s were observed[10]. The first frame (37ns) suggests that there is not a good current sheath formation over the insulator. Several tests and improvements were necessaries to determinate the dimensions of the insulator (see section "Criteria design").

After some improvement from the original design, neutron emission studies were performed in discharges in deuterium at different pressures, 5 to 12 mbar, with a charging voltage of 30±2 kV in the PF-400J and 29±2 kV in the PF-50J (~400 J and ~70 J stored in the capacitor bank respectively). Electrical traces for a shot in deuterium at some mbar pressure is shown in Fig. 2 where 127±6 kA and 60±3 kA peak current is obtained for the PF-400J and PF-50J. The typical dip in the signal of the current derivative associated with the formation of a pinched plasma column on the axis was observed. From the current derivative signals the implosion time (pinch time, measured at the moment for the minimum in dI/dt) versus filling pressure was obtained. The maximum compression of the plasma occurs close to the peak current for a pressure close to 7mbar in the PF-400J and close to 6mbar in the PF-50J.). Also signals with scintillator with photomultiplier (FM1 and FM2) are shown for the PF-400J. The distance ΔL, between FM1 and FM2 was ΔL =1.5 m and the time of flight for the neutrons was ~65ns, thus an energy of the order of ~2.77MeV is estimated for the neutrons.

The neutron yield as a function of the filling gas pressure is shown in Fig. 3. Each point is the average of ten shots and the error bars are the standard deviations. The maximum measured neutron yield was $(1.06\pm0.13)\times10^6$ neutrons per shot at 9 mbar in the PF-400J and $(2\pm1)\times10^4$ neutrons per shot close to 6 mbar in the PF-50J (previously[19] we report $(7.5\pm1)\times10^4$ for this case, but it was wrong, a detailed data analysis of the ^{3}He calibration showed a lower yield). These maximum neutron yield occurs for discharges with pinch close but after the current peak. The maximum observed yield agrees roughly with the empirical scaling laws available in the literature for drivers with energy in the range 1 to 100kJ[14], $Y=10^7 E^2$ and $Y=I^{3.3}$ (the storage energy in the driver E in kJ and the current pinch I in kA). It is probably that the electrodes and insulators size could be optimized in order to increase the neutron emission.

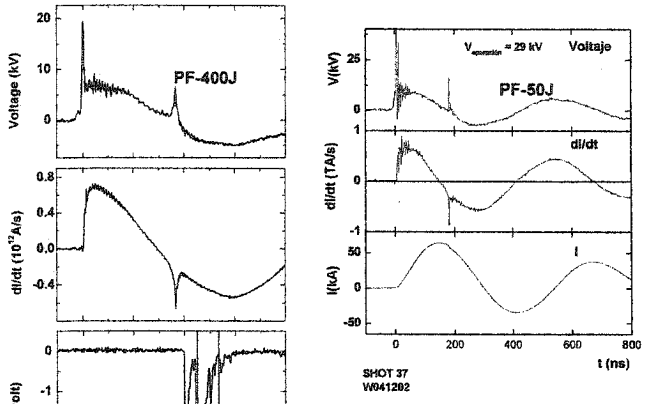


Figure 2. Electrical traces for a shot in deuterium at some mbar pressure. Peak currents of 127±6 kA and 60±3 kA were obtained for the PF-400J (8.7mbar) and PF-50J (7mbar). Also signals with scintillator with photomultiplier (FM1 and FM2) are shown for the PF-400J. The distance ΔL, between FM1 and FM2 was ΔL= 1.5 m and the time of flight for the neutrons was ~65 ns, thus ~2.77 MeV for the energy of the neutrons.

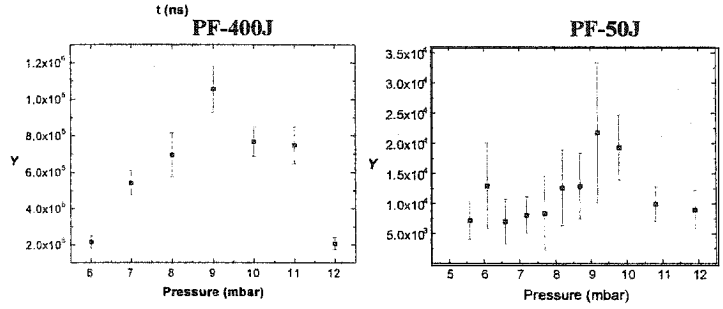


Figure 3. Neutron yield as a function of the filling gas pressure for the PF-400J (operated at ~400J) and PF-50J (operated at ~70J) .

SPEED2 AND SPEED4 GENERATORS

Recently, the pulse power generator SPEED 2, a medium energy and large current device (4.1μF equivalent Marx generator capacity, 300 kV, 4 MA, 187 kJ, 400 ns rise time, dI/dt~10^{13} A/s)[2], is in operation at CCHEN. The SPEED 2 arrived at the CCHEN in May 2001 from Düsseldorf University, Germany, and it is in operation since January 2002, being the most powerful and energetic device for dense transient plasma in the Southern Hemisphere. Moreover, SPEED 2 is the unique dense plasma transient experiment operating at currents of Mega-amperes in Chile. Simultaneously an intermediate device has been constructed (1.25 μF equivalent Marx generator capacity, 100 kV, 700 kA, 400 ns rise time, dI/ dt~10^{12} A/s) and currently is being set up in operation.

Experiments in different Z-pinch configurations, at current of hundred of kiloamperes to mega-amperes, using the SPEED 2 generator will be carried out. A device designed 15 years ago will

be used for the research of scientific topics relevant today and for the research and development of new ideas.

Most of the previous works developed in SPEED 2 at Düsseldorf were done in a plasma focus configuration. The Chilean operation has begun implementing and developing diagnostics in a conventional plasma focus configuration. Then, after getting the experimental expertise with SPEED 2, new experiments in a quasi-static Z-pinch[15-18], gas puffed plasma focus, and wires array will be developed to extend the device capabilities. Also SPEED2 and SPEED4 will be used in the development of applications of radiation pulses from hot, dense plasmas, including X-ray and neutron radiography, detection of substances, micro-radiography for applications to microelectronic lithography and diagnostics of nanostructures. Plasma foci on SPEED 2 are an intense pulsed source of neutrons (10^{11}-10^{12} neutrons per pulse) and X-rays. Plasma focus in SPEED 4 with heavy gases will be used as an intense source of soft X-rays. The applications will be developed using the above generators in order to determine the radiation threshold for the various types of applications (radiography, neutrography, substances detection). This information will be used to design smaller devices suited for applications.

Preliminary results in SPEED2. The Chilean operation of the SPEED2 device has begun implementing and developing diagnostics in a conventional plasma focus configuration. Discharges in plasma focus mode have been performed at +/-30 kV charging voltage in a three step +/- Marx generator (i.e. 180 kV, 100 kJ). A peak current greater than 2 MA was achieved. Figure 4 shows the corresponding electrical traces. Fig. 1 a) corresponds to a discharge at 5.9 mbar deuterium, where the load is practically the inductance of the central collector and electrodes (~5nH). Figure 1 b) corresponds to 2.5mbar, where the pinch phenomenon is clearly observed in the peak voltage and in the dip of the dI/dt.

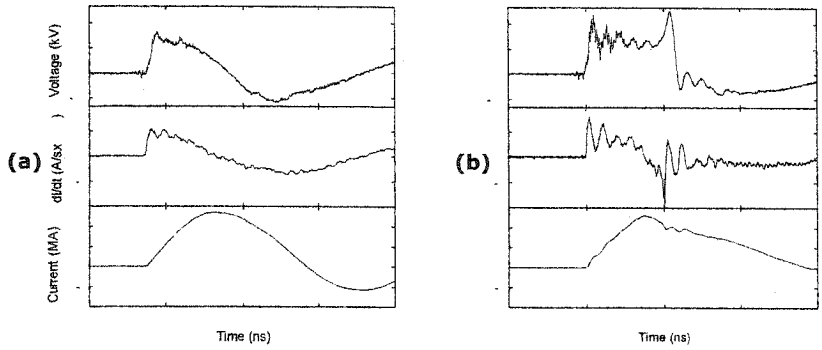


Figure 4. Electrical signals in SPEED 2 generator operating in Chile at CCHEN. Discharges in plasma focus mode have been performed (+/-30kV charging voltage in a three step +/- Marx generator, i.e. 180 kV, 100 kJ). A peak current greater than 2MA is achieved. a) 5.9 mbar D_2, b) 2.5 mbar D_2, at this pressure the pinch phenomena is clearly observed in the peak voltage and in the dip of the dI/dt.

Preliminary results obtained with silver activation counters show a neutron yiled of the order of 10^{10}-10^{11} neutrons per shot. Time resolution neutron detection are now being implemented. The future diagnostics program considers time integrated and time resolution X-ray images, PIN diode and plastic scintillator with photomultiplier, X-ray spectroscopy, as well as pulsed interferometry.

DISCUSSIONS AND CONCLUSIONS

The experimental facilities and diagnostics capabilities achieved by the Plasma Physics and Plasma Technology group at CCHEN opens a wide spectrum of possibilities of new research in basic plasma physics an applications. These facilities (PF-50J, PF-400J, SPEED4, SPEED2) compliment each

other enabling the study of various types of pinch plasmas (X pinches, plasma foci and wire arrays) over a wide range of parameters; currents from tens of kilo-amps to Mega-amps, with energies from tens of joules to hundreds of kilojoules, keeping the same timescale (hundreds of nanoseconds). This unique will allow the study of physical phenomena (e.g., the formation of jets or the emission of neutrons and x-ray) on different load configurations. Theoretical modeling can be tested against a variety of experiments. This would help in revealing more of the physics behind the phenomena. On the other hand, the achievement of designing and constructing a miniature pulsed neutron generator (miniature plasma focus, operating only at tens of joules), opens the possibility to extend the experimental and theoretical studies in dense-transient plasmas to the unexplored region of very low energy. A miniature plasma focus with an energy <1 J is currently being tested. This a special opportunity to develop X-ray and neutron "nanoflashes" for applications, with many potential uses in other sciences, as well as in industry, mining, agriculture and medicine.

ACKNOWLEDGEMENTS

This work has been funded by CCHEN (grants 562 and 573), by a Presidential Chair in Sciences awarded to L. Soto by the Chilean Government, and by the FONDECYT grant 1030062 and IAEA. This work is part of the Bilateral Agreement: Comisión Chilena de Energía Nuclear, (CCHEN, Chile) - Comisión Nacional de Energía Atómica (CNEA, Argentina).

REFERENCES

(1) P. Silva and M. Favre, Journal of Physics D: Applied Physics 35, 2543 (2002).
(2) G. Decker, W. Kies, M. Mälzig, C. Van Valker and G. Ziethen, Nucl. Instrum. and Methods, **A249**, 477 (1986).
(3) M. Scholz, L. Karpinski, M. Paduch, K. Tomaszewsky, R. Miklaszewsky, and A. Szydlowski, Nukleonika **46**, 35 (2001).
(4) S. Lee, T. V. Tou, S. P. Moo, M. A. Eissa, A. V. Golap, K. H. Kewk, S. Mulyodrone, A. J. Smith, Suryad, W. Usada, and M. Zakaullah, Amer. J. Phys. **56**, 62 (1988).
(5) M. Zakaullah, K. Alamgir, M. Shafiq, S. M. Hassan, M. Sharif, S. Hussain, and A. Waheed, Plasma Sources Sci. and Technol. **11**, 377 (2002).
(6) A. V. Dubrovsky, V. A. Gribkov, Yu. P. Ivanov, P. Lee, S. Lee, M. Lieu, V. A. Samarain, Nukleonika 46 S1, S107 (2001).
(7) V. A. Gribkov (private communication).
(8) L. Soto, A. Esaulov, J. Moreno, P. Silva, G. Sylvester, M. Zambra, A. Nazarenko, and A. Clausse, Physics of Plasma **8**, 2572 (2001).
(9) P. Silva, L. Soto, J. Moreno, G. Sylvester, M. Zambra, L. Altamirano, H. Bruzzone, A. Clausse, and C. Moreno, Rev. Sci. Instrum. **73**, 2583 (2002).
(10) J. Moreno, P. Silva and L. Soto, Plasma Sources Sci. and Technol. **12**, 39 (2003).
(11) P. Silva, J. Moreno, L. Soto, L. Birstein, R. Mayer, and W. Kies, App. Phys. Lett. **83**, 3269 (2003).
(12) C. Moreno, H. Bruzzone, J. Martinez and A. Clausse, IEEE Trans. Plasma Sci. **28**, 1735 (2000).
(13) J. Moreno, L. Birstein, R. Mayer, P. Silva, and L. Soto, "Measurement of low yield neutron pulses using a proportional counter of ^{3}He", submitted for publication.
(14) S. Lee, *Laser and Plasma Technology*, edited by S. Lee, B. C. Tan, C. S. Wong, and A. C. Chew (World Scientific, Singapore, 1985).
(15) L. Soto, H. Chuaqui, M. Favre, and E. Wyndham, Phys. Rev. Lett. **72**, 2891 (1994).
(16) L. Soto, H. Chuaqui, M. Favre, R. Saavedra, E. Wyndham, M. Skowronek, P. Romeas, R. Aliaga-Rossel and I. Mitchell, IEEE. Trans. Plasma Science **26**, 1179 (1998).
(17) A. Esaulov, P. Sasorov, L. Soto, and M. Zambra, Physics of Plasma **8**, 1395 (2001).
(18) L. Soto and A. Clausse, Physica Scripta **67**, 77 (2003).
(19) L. Soto et al. "Research on pinches of tens of joules to hundred of kilojoules", 15th IAEA Technical Committee Meeting Using Small Devices (Vienna, May 2003).

Nano-sized Material Preparation In Ultrathin Film Form Using Dense Plasma Focus

M. P. Srivastava
Department of Physics and Astrophysics, University of Delhi, Delhi, Delhi-110007, INDIA
mps@himalaya.du.ac.in

ABSTRACT

In this invited talk, the importance of nanoparticles and nanosized grains has been highlighted. The DPF device has been suitably modified for the preparation of nanoparticles , nanosized ultrathin films or ultrathin films with nanosized grains. Grain size for ultrathin film making use of X-ray diffraction spectra (XRD), scanning electron microscope (SEM) data and transmission electron microscope (TEM) data, have been given for some materials.

Keywords: Nanosized Grains, Dense Plasma Focus, Energetic high fluence ions

INTRODUCTION

Nanoparticles called quantum dots, ultra thin films with thickness in tens of nm and nano-sized grains in a polycrystalline ultra thin films can possess properties that are entirely different from their parent materials. Nanoparticles and nano-sized grains are generally used to indicate particles with dimensions less than 100nm. For comparison, human hair is about 50,000 nm in diameter while a smoke particle is about 1000 nm in diameter. Methods are being developed to selectively control the electrical, optical, chemical, mechanical and magnetic properties of nanoparticles and nano-grains by engineering the size, morphology and composition of these particles. Nanoparticles and nano-sized grains offer radical breakthroughs in areas such as materials and manufacturing, electronics, medicine and health care, environment and energy, chemical and pharmaceutical, biotechnology and agriculture, computation and information technology.

Nanoparticles and nano-sized grains can make metals stronger and harder, give ceramics enhanced ductility and formability, enable a normally insulating materials to conduct heat or electricity and make protective coatings transparent. Carbon nanotubes which were thought to be sheet of graphite turned in a tube (diameter ~1 nm and length 1~ μm) with different helicity were theoretically predicted by a group[1] at Naval Research Laboratory to possess the charge carrier density similar to metals. Experimentally carbon nanotubes were discovered by Suimo Iijima[2] in 1991 while analysing fullerenes soots produced in an arc discharge through scanning electron microscopy. Carbon nanotubes have unusual mechanical and electrical properties. For example carbon nanotubes have light weight, record high elastic modulus with very strong and flexible fibres that has the ability to buckle in a reversible manner. Carbon nanotubes can be semi-conducting or metallic electrical properties depending on their diameter and chirality and it is found that a slight change in the winding of hexagon along the tube can change from metal to semiconductor. Since then the nanoparticles having different properties such as conducting , semi-conducting, insulating, magnetic, non-magnetic have been attempted both from the point of view of miniaturization for low power consuming devices as well as for making devices which possess properties entirely different from their bulk materials. Most of the methods adopted are either plasma based or chemical. Chemical methods are usually adopted for nano-sized grains whereas plasma methods are adopted for making nanoparticles or nano-sized grain in the thin films on different substrates.

In this invited talk, I would like to discuss the manner in which the nanoparticles and nano-sized grains along with thin films can be formed making use of the Dense Plasma Focus device. We make use of different materials in the bulk form and shape them in the form of discs to fix them at the top of hollow anode. The material of the disc is ablated by high

temperature high-density plasma creating the ions, which are accelerated upward and get deposited on the substrate. The dimension of the nano-grains or nanoparticles is measured with the help of X-ray diffraction spectra (XRD), scanning electron microscopy (SEM) and/or transmission electron microscopy (TEM). The electric, optical, magnetic properties of the nanosized grains are studied subsequently depending on the type of material used.

EXPERIMENTAL SET UP AND MATERIAL PREPARATION

The DPF is simply a coaxial gun accelerator consisting of two coaxial electrodes separated by an insulator sleeve. The DPF device in different laboratories all over the world is either of Fillipov type[3] or Mather type[4]. We will discuss the Mather type DPF since a Mather type DPF having energy of 3.3 kJ is being operated at Plasma Research laboratory, Delhi University. The focus is being energized by a single 30 μF 15 kV fast discharging energy storage capacitor. The schematic of DPF device showing various subsystems with suitable modifications for the preparation of nanoparticles or nanosized grains on ultra thin films is as shown in Figure 1. The subsystems of DPF are (i) focus chamber consisting of coaxial assembly of electrodes with one hollow anode surrounded by six symmetrically placed cathode rods around it, (ii) high voltage power supply to charge the capacitor, (iii) the spark gap as a fast switching device for discharging the capacitor through the electrode assembly inside the focus chamber, (iv) the triggering electronics to activate the spark gap switches and (v) focus diagnostics and data acquisition system. For the deposition of nano-particles or for preparation of nano-sized grains, the anode is slightly modified in a manner so that a disc of that material having diameter 15mm and thickness about 5 mm can be fixed at the top of the anode. The substrate is inserted from the top of the focus chamber. A cylindrical brass rod which has a substrate holder attached to one end is inserted from the top of plasma focus chamber. The brass rod can be moved up and down along the anode axis so that the substrate can be adjusted at different heights from the top of the anode.

The focus chamber is evacuated by a rotary pump and then filled by an inert gas such as argon with pressure generally in the range of 50 to 150 Pa. The capacitor is charged by high voltage power supply and then allowed to discharge through a spark gap arrangement so as to transfer the energy from capacitor to focus chamber. The gas breakdown occurs initially across the surface of the insulator separating the anode and the cathode. The insulating sleeve made normally of glass at the bottom of the chamber gives rise to axial filamentary currents which along with azimuthal magnetic field produced by the current flowing in the copper anode gives rise to Lorentz force in the radially outward direction towards cathode rods like an inverse pinch. At this stage radial component of current density along with azimuthal magnetic field gives rise to Lorentz force in the axial direction. The current sheath due to this force is accelerated axially up the plasma chamber. The current sheath when reaches the top of the anode experiences Lorentz force radially inwards which causes the radial collapse inward of the plasma sheath giving rise to thin column of extremely hot and dense plasma. The plasma temperature is in the range of 1-2 keV and plasma density is about 10^{26} m^{-3} . The hot temperature plasma ablates the material from the disc whose nanoparticles or nano-sized grains on ultra-thin film is to be prepared. The argon ions along with the ions of the material of disc are accelerated upwards in a fountain like structure due to m = 0 instability and the electrons are accelerated to reach the bottom of the anode. The energetic high fluence argon ions reach first the substrate and create pitholes in the substrate which gives good adhesion to the nanoparticles or the ultra thin film with nano-sized grains. The thickness of the film deposited on the substrate, depending on the distance of the substrate from the top of anode is in the range of 40 nm to 70 nm in a single shot. The thickness of the film can be increased by either keeping the substrate closer to top of anode (> 2.0 cm) or by multiple shots. The substrate is always kept at a distance greater than anode radius so that the focus formation is not disturbed by the presence of substrate. By suitably adjusting various parameters in the DPF device, it is possible to get nano-sized grains.

If we want to prepare the nanoparticles or ultrathin films with nano-sized grains of metals or semiconducting, magnetic insulating material which exists in solid form, then we

cut the discs having the diameter of about 15 mm and thickness of about 5 mm. However, if we have the material in powder form or we have to make the nano-sized grains of more than one element in a fixed ratio such as lead zirconate titanate (PZT) then we have to adopt a little complicated procedure. For example PZT disc is made by solid state reaction[5]. The materials initially taken are the oxides of zirconium, titanium and lead in the percentage ratio 53 mol; 47 mol; 110 mol respectively. During the deposition of nano-sized films there is a lead loss and therefore lead is taken in exess by about 10 %. The powder of three oxides are mixed, grinded to a fine powder and pressed into a discs of 15 mm diameter and 5 mm thickness. These discs are preheated in a furnace at 850 °C for 3 hours. These discs are grinded to a fine powder and again pressed into discs. These discs are sintered at 950 °C for two hours.

RESULTS AND DISCUSSION

The films of several materials having thickness in nano-size (<100 nm) have been made. If we deposit the material on different substrate by ablating from the disc placed at the top of the anode; it is possible to get 40 nm to 70nm ultrathin film with a single shot of DPF. If the material so deposited is in the amorphous form, it is not possible to get the peaks in XRD spectra and also the SEM of such films do not give any information about the grain size as no grains are formed. For such ultrathin films, it may however be possible to study their electrical, optical, magnetic properties. If on the other hand the film deposited on the substrate is polycrystalline, it is possible to get peaks in the XRD spectra corresponding to the polycrystalline material. It is also possible to estimate the average grain size on the ultrathin film. The SEM micrographs can also give us the average grain size on the films and also the shape of the grains. We will give here some typical results.

If a graphite disc is kept at the top of the anode, the film formed on quartz substrate is found to possess diamond like carbon (DLC) properties[6] which is also known as amorphous diamond. The thickness of the film is found to be 45 nm with a single DPF shot. The laser Raman spectroscopy indicates greater fraction of sp^3 bonded carbon. Both the XRD spectra and SEM studies have shown that nano-sized ultrathin film is amorphous. The electrical resistivity is found to be of the order of 10 MΩ cm.

The PZT discs formed by the method explained earlier are fixed at the top of the anode. The films has been prepared with different number of DPF shots[7] on glass substrate. The average grain size for the PZT films have been estimated from XRD data making use of Scherrer's equation. The XRD spectra show the peaks corresponding to perovskite phase of PZT. There is wide distribution of grain sizes and XRD signals is weighted for the grain volume heavily favouring larger grains. The EDX spectrum and the TEM micrograph are shown in figure 2 and 3 respectively for 10 DPF shots. The grain size is of the order of 0.5 nm arranged in a regular pattern. The shape of the grains is both rectangular and columnar.

For obtaining nano-grains of Germanium[8], Germanium disc is fixed at the top of anode. The films have been formed on glass and silicon substrate with different DPF shots. The XRD spectra of the film with different DPF shots have been obtained. The peaks in the XRD spectra show the formation of crystalline Germanium. The average grain sizes of Germanium using Scherrer's equation are found to be 29.3 nm and 27.6 nm corresponding to two peaks at $2\theta = 27.25°$ and $2\theta = 45.31°$ respectively for the films with 5 DPF shots. The grain sizes for the films deposited on glass with 25 DPF shots are 24.9 nm and 26.9 nm for $2\theta=27.22°$ and $45.30°$ respectively. Both current-voltage and capacitance-voltage characteristics of nano-sized Germanium is also investigated.

REFERENCES

(1) J.W. Mintmire, B.I. Dunlap, C.T. White, Phys. Rev. Letters, 68, 631 (1992).
(2) S. Iijima, Nature 354, 56 (1991).
(3) N.V. Filopov *et.al.*, Nuclear Fusion Supplement 2, 577 (1962).
(4) J.W. Mather, Physics Fluids 7, 528 (1964).
(5) X. Liu, Z.G. Liu, Y. Yin and M. Liu, J. Phys. Condensed Matter 12, 9189 (2000).
(6) M.P. Srivastava, Savita Roy and Chhaya R.Kant; Diamond like Carbon films using Dense Plasma Focus Device, Pat/ 3.16.19/ 98060/ 98.
(7) R. Gupta, M. P. Srivastava, V. R. Balakrishnan, R. Kodamma and M. C. Peterson Communicated to Journal of Physics D, Applied Physics (2003).
(8) R. Gupta, M. P. Srivastava, N. Bilasini Devi and V. R. Balakrishnan Communicated to Journal of Applied Physics (2003).

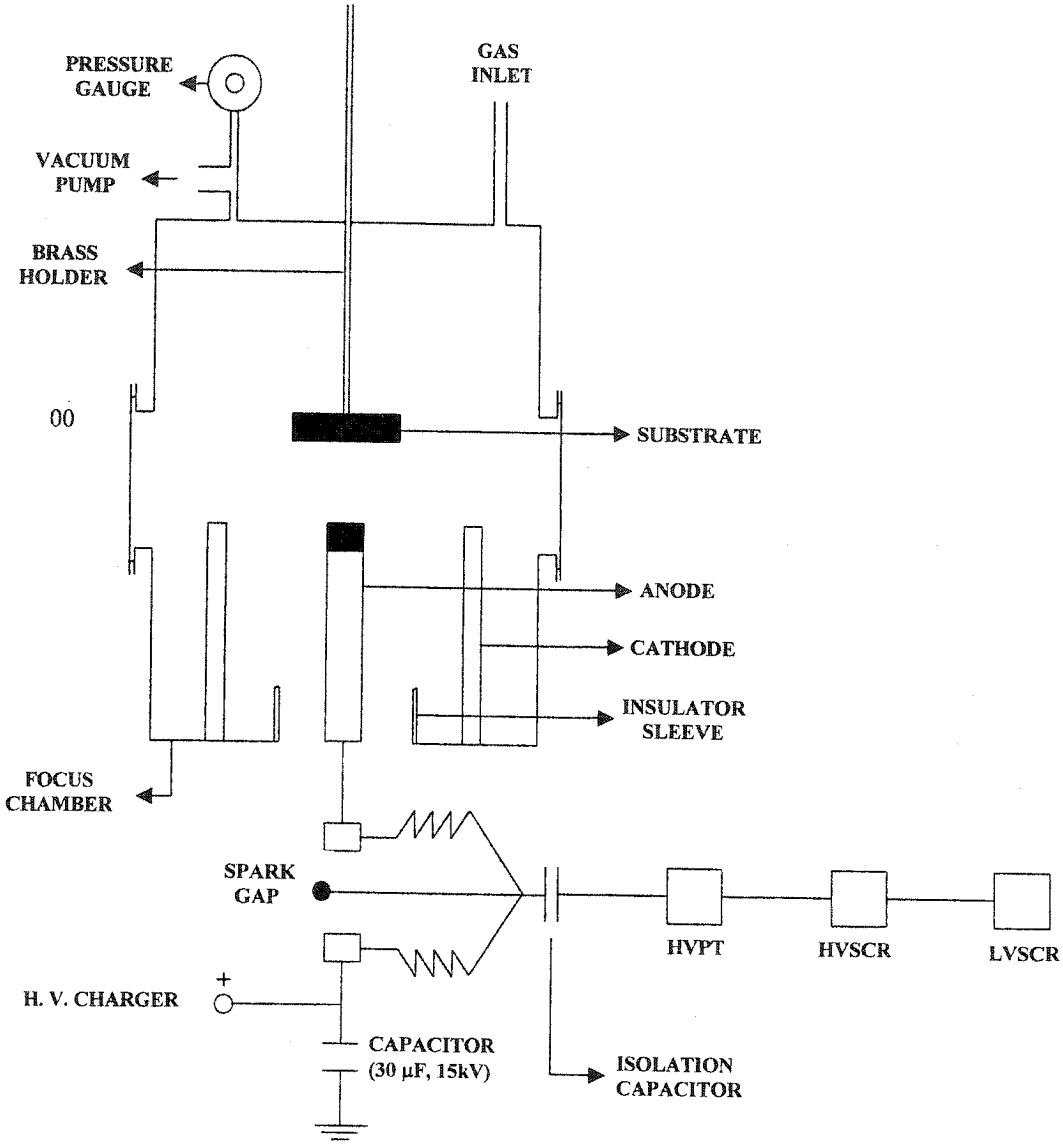


Fig. 1. Schematic of Dense Plasma Focus Device

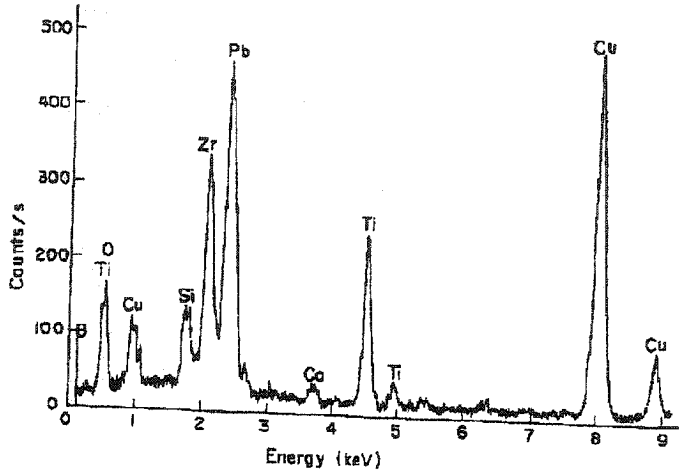


Fig. 2. EDX spectra of PZT film

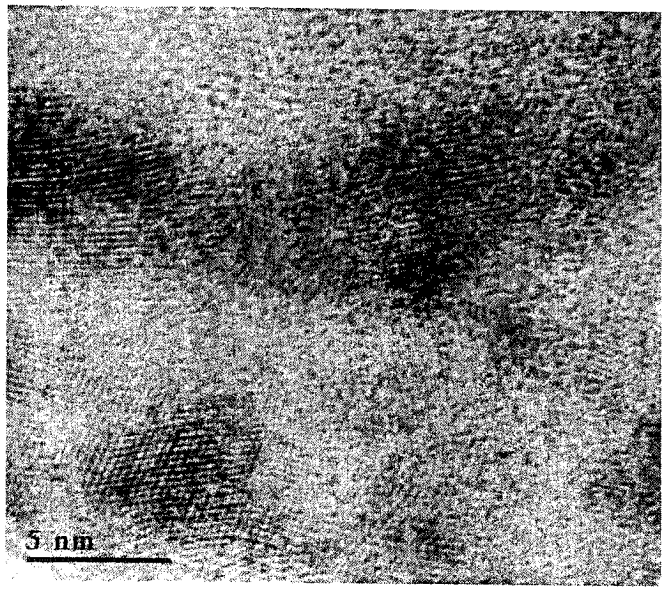


Fig. 3. TEM micrograph of PZT film

X-Ray Lasing in Ablative Capillary Discharges

H.-J. Kunze, S.S. Ellwi* and Ž. Andreić**
Institut für Experimentalphysik V, Ruhr-Universität, 44780 Bochum – Germany
Hans-Joachim.Kunze@ruhr-uni-bochum.de

ABSTRACT

Lasing in the soft x-ray region at 18.2 nm is observed on the Balmer-alpha line of CVI ions in ablative capillary discharges made of polyacetal. Population inversion is by charge exchange collisions between CIII ions and fast fully stripped carbon ions, which are produced in the neck regions of an m=0 instability and penetrate into the weakly ionized plasma outside the necks. Exponential growth of the lasing spike with length of the discharge column and a strong increase when employing a multilayer mirror prove lasing and give a life time of the population inversion of 400 ps. The instability can be induced by a waved structure of the inner wall of the capillary as well as by a waved return conductor.

Key Words: ***X-Ray Lasers, Capillary Discharges***

INTRODUCTION

After lasing in the soft x-ray region had been demonstrated in 1985 by groups in Livermore and Princeton [1-2], research activities were stepped up in many laboratories and lead to significant progress in several directions. Plasmas showing population inversion sufficient for lasing were usually produced by powerful line-focused laser beams hitting targets of suitable materials. The main schemes to achieve population inversion were collisional excitation of Ne-like and Ni-like ions as well as three-body recombination to H-like and Li-like ionization stages. Due to the lack of cavities at the short wavelengths, amplification was usually by single pass through the plasma column, although double pass was possible in some cases. Accounts of the impressive progress are found, for example, in the proceedings of biannual conferences on x-ray lasers, the last one in 2002 in Aspen, Colorado [3], and in a recent review by Daido [4].

Soon it was recognized that small "table-top" systems were highly desirable for most applications since potential users were deterred to come to the large laser facilities with low shot frequencies. Research was most successful along two lines:

(a) Improvement of the collisional excitation scheme by using two subsequent laser pulses for production of the plasma with the desired ions followed by heating to optimum excitation conditions, improved modeling based on better and new atomic data, and employing more suitable pump lasers.

(b) Using discharge plasmas as active medium.

Although lasing was demonstrated in several linear discharge arrangements, small diameter systems (known as capillary discharges) advanced best. Rocca and his group at Colorado State University built a fast high-voltage driver for such a discharge with an inner diameter of 4 mm, which after preionization of the argon gas filling produced a high-temperature plasma column of about 200 μm in diameter, and by the electron collisional excitation scheme obtained strong lasing at 46.9 nm on the J=0 to J=1 transition of the 3p-3s multiplet of Ne-like ArIX [5]. They demonstrated saturated amplification later [6], and finally applied the laser to interferometry of dense plasmas [7].

Another approach was to use capillaries of diameter 1 mm and smaller in vacuum and to start the discharge by a sliding spark along the inner wall: material is ablated from the wall and supplies the discharge plasma. Shin et al.[8] observed increased emission of the Balmer-α line of CVI ions at 18.22 nm in a capillary made of polyethylene and interpreted this as lasing due to population inversion by three-body recombination after rapid cooling. A theoretical explanation, however, was difficult.

At Bochum a different scheme was pursued: in ablative capillaries made of polyacetal an m=0 instability produces hot plasma of completely fully ionized carbon atoms in the necks of the instability which stream into the cold plasma outside the necks. Highly selective charge exchange collisions efficiently result in population inversion, and lasing takes place on the Balmer-α line of CVI.

EXPERIMENTAL SETUP

The discharge arrangement is a classical low-inductance setup consisting of 5 capacitors of 20 nF each connected directly to the capillary mount in the shape of a star, the capillary being made of polyacetal (CH_2O_n). The two electrodes at the ends of the capillary are made of tungsten and have an axial bore. Triggering is by a separate high voltage pulse to a third electrode. The incoherent emission of such fast discharges had been studied already some time ago by Bogen et al.[9]. Polyacetal was now selected because of low debris ejected from the discharge channel. Figure 1 shows a schematic.

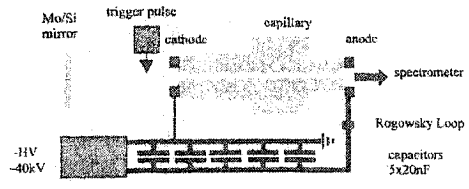


Figure 1. Schematic of the capillary discharge

The lengths of the capillaries were from 15 to 50 mm, and the inner diameters varied from 0.4 to 1.2 mm. The period of the discharge cycle depends on the capillary length and on damping and is around 250 ns for a 4 cm capillary. The current derivative dI/dt is recorded by a shielded Rogowski loop. Time resolved spectra are obtained with a 1 m grazing incidence spectrometer combined with a NE111 plastic scintillator with a quenching agent for fast response (exit slit of 200 μm) linked to a photomultiplier by fiber optics. Recording is by a fast digital oscilloscope (2 Gs/s, 500 MHz analogue bandwidth). The emitting plasma column is also studied end-on in the vuv spectral region employing a pinhole camera, the pinhole being of square shape 100×100 μm. It is covered with an aluminum filter 0.2 μm thick. The images are recorded with a combination of a microchannel plate (MCP) and a CCD camera at a magnification of 2.4. The gating time is typically 5 ns. Depending on the capillary length discharge voltages are between 6 and 18 kV.

RESULTS AND DISCUSSION

A typical time history of the current through a capillary of 50 mm length and 0.7 mm diameter with straight inner wall and of the emission of the Balmer-α line of CVI at 18.22 nm are shown on

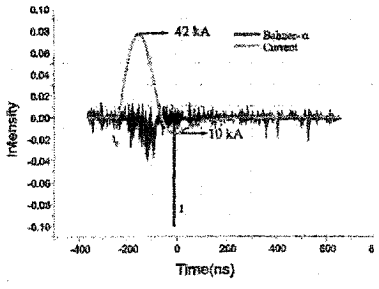


Figure 2. Current I and time history of the Balmer-α line of CVI at 18.22 nm

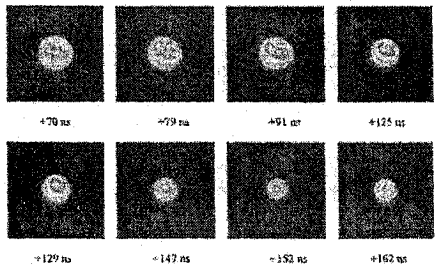


Figure 3. Pinhole images of the plasma column at different times of the discharge

Fig. 2. At the maximum of the second half-cycle the emission shows a short spike of duration of 1 ns or shorter, which does not show up on other close-by lines of CV, OV and OVI ions. It is interpreted as lasing [10], and this will be analyzed in the following. Other materials have been used, too, even other brands of polyacetal; however, it was found that only discharges through capillaries of one brand develope this spike. The initial sliding spark and the discharge during the first half-cycle must ablate the right amount of material from the wall to provide the right plasma for the second half-cycle! Figure 3, which shows pinhole images of a 3 cm capillary, reveals that at the time of the second current maximum (here at 156 ns) the plasma has to be compressed and well detached from the wall. With other non-lasing brands of polyacetal this is not achieved, in most cases damping is so severe that even no second half-cycle appears.

A series of investigations lead to a model which now explains the mechanisms and processes resulting in population inversion; they also confirm that charge exchange between carbon ions and bare carbon nuclei can be an efficient population mechanism. It was observed [11]:

- The intensity of the spike always occurs at the time of the second current maximum, the jitter being a few ns.
- The divergence of the line decreases with capillary length L; it is about 1 mrad for a length L=5 cm.
- The narrower the capillary, the better is spiking.
- The adjacent CV, OV and OVI lines do not show this effect.
- A mirror of 12% reflectivity behind the capillary increases the spike by factors between 1.5 and 1.7.
- The spike increases with capillary length; this occurs linearly and not exponentially as lasing would demand.
- Cutting the capillary lengthwise after use shows the imprint of an m=0 instability, and small perturbations on the dI/dt signal at the time of second current maximum suggest that the instability also occurs at that time.

Our model now is as follows:

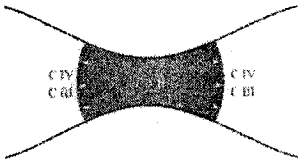


Figure 4. Hot plasma in the necks of the m=0 instability

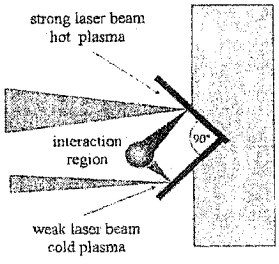


Figure 5. Arrangement for colliding laser produced plasmas

At the time of the second current maximum a m=0 instability produces hot plasma in the necks of the instability. The instability can indeed grow since the plasma is well detached from the wall (Fig. 3) and the Lunquist number is above the critical Lunquist number for stability, if not too much material is ablated from the wall [12]. The instability grows in about 1 ns and bare C^{6+} ions stream from the necks into the cold plasma outside the necks as illustrated in Fig. 4. There charge exchange collisions with low temperature carbon ions such as C^{2+} lead to a highly efficient population of the n=3 levels of C^{5+}.

$$C^{6+} + C^{2+}(2s^2) \Rightarrow C^{5+}(n=3) + C^{3+}$$
$$C^{6+} + C^{2+}(2s2p) \Rightarrow C^{5+}(n=3) + C^{3+}$$

At the low energy range these recombination processes are highly selective into the n=3 level; they have large cross sections and result in population inversion in a chain of inversion layers along the axis of the capillary.

Although theoretical calculations predicted large cross sections (10^{-15} cm^2) an experimental proof was desirable. This was done with colliding laser-produced plasmas according to the arrangement shown in Fig. 5 [13-14]. The beam from a ruby laser was split by a wedge into two beams of 1 and 5.6 Joule energy, and both were focused onto target slabs of glass-like carbon mounted at 90° to each other. The hot and cold carbon plasmas produced were interpene-

trating, and both as well as the interaction region were studied spectroscopically employing a flat-field grazing incidence spectrograph equipped with microchannel plate MCP and CCD detector.

The evidence of enhanced population of the upper level of the Balmer-α line of CVI at 18.22 nm in the interaction region was unambiguous, and the results of cross section calculations and of a collisonal radiative model fitted well to the experimental observations.

It was also possible to explain the linear increase of the lasing spike with the length L of the capillary: the marks on the inner wall of the capillary revealed that the wavelength of the instability also increased with increasing length L and thus the number of inversion layers per unit length did effectively decrease. We obtained

$ka_0 \approx 2.4$ for L = 1 cm $ka_0 \approx 0.8$ for L = 3 cm
$ka_0 \approx 1.6$ for L = 2 cm $ka_0 \approx 1.2$ for L = 5 cm,

where k is the wavenumber of the instability and $2a_0$ is the inner diameter of the capillary. The values are in the range of fastest growth rates of the instability.

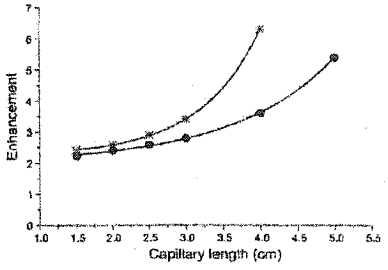


Figure 6. Enhancement of the Balmer-α line of CVI as function of capillary length L for waved capillaries with * 0.8 mm and • 1.0 mm inner diameter

The above observations stimulated attempts to manipulate the wavelength of the instability. This was done by imprinting a waved structure onto the inner wall of the capillary. Figure 6 shows the enhancement of the lasing spike (intensity of spike normalized to the maximum intensity of the first half-cycle) versus the length of the capillary. Now lasing indeed increases exponentially with the length L of the capillary revealing that the instability is induced with the respective imprinted wavelength. Two cases are shown: one capillary with a diameter of 0.8 mm and a neck to neck separation of 0.8 mm (*), and one capillary 1.0 mm in diameter and a neck to neck separation of 1.0 mm (•). Both correspond to ka_0-values of 1.6. Fitting the Linford formula [15] to the results of the 0.8 mm capillary with the neck distance of 0.8 mm gives a gain length product of GL ≈ 4.5. It is evident that capillaries with shorter neck to neck distance and hence with more discs having inverted population on the n=3 levels of CVI result in better lasing.

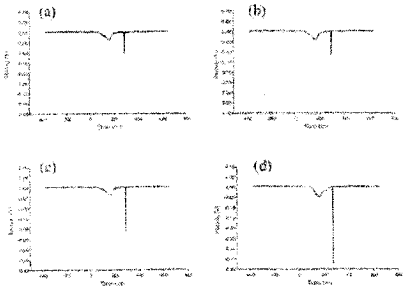


Figure 7. Emission of the Balmer-α line (a) without mirror, with mirrors positioned (b) at d = 70 mm, (c) at d 0 50 mm, (d) d = 30 mm.

Double-pass experiments employing mirrors provide unambiguous proof of lasing, when a small fraction of the laser beam is reflected back into the active medium and amplification is observed. Although this had been demonstrated already earlier [11], a recent systematic study [16] gave even further insight. A plane multilayer mirror having a reflectivity of about R ≈ 30% at 18.22 nm was positioned and aligned at several distances d from one end of a waved capillary of a length L = 30 mm. The reflected beam can be considered thus as a probe beam of the lasing medium. It is important to state that the mirror is to be rotated after every few shots as it is destroyed locally by the laser beam. Figure 7 shows the results. In the analysis geometrical losses of

the reflected beam due to its finite divergence have to be taken into account. These losses can be included as reduction of the mirror reflectivity which thus becomes effectively a function of the mirror distance:

$$R_{eff}(d) = R\left[\frac{1}{1+2d/L}\right]^2 .$$

For a mirror position d = 30 mm the effective reflectivity thus reduces from 30% to 3.3%, for example, and still gives a laser pulse intensity 3.5 times that of the primary beam without mirror.

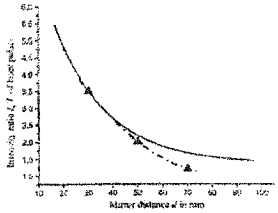


Figure 8 Experimental ratios (I_R/I_0) of the laser pulses (▲) and theoretical dependence (full line), from (16).

Amplified reflected laser pulse and primary pulse I_0 simply add and in case of constant population inversion during the duration of the pulse we may write

$$I_R = I_0 + I_0\, R_{eff}\, \exp(GL) .$$

In Fig. 8 the experimental ratios I_R/I_0 are plotted as well as the theoretical ratio fitted to the experimental one for d = 30 mm. The results indicate significant deviation starting around d = 60 ± 10 mm which corresponds to a mean transit time of the laser pulse of 400 ± 70 ps. We conclude that after this time the population inversion produced by charge exchange disappears in the layers. This agrees with the time of interpenetrating laser-produced plasmas. We also obtain a GL-value of 4.3 for the 30 mm long capillary.

Since it is difficult to produce small-diameter capillaries of larger length, attempts were finally started to induce the m = 0 instability in a straight capillary by having a waved structure on the inner surface of the return conductor. The capillary lengths chosen were L = 25 mm and L = 40 mm; the waved section was 15 and 30 mm, respectively. Best results were obtained with a wavelength of 1.1 mm on the return conductor. Figure 9 shows, as example, current and the time history of the emission of the Balmer-α line of CVI at 18.22 nm for a 0.8 mm diameter and 40 mm long capillary. The lasing spike at around the time of the second current maximum is again clearly identified. In general, however, it was observed that in the case of the short capillary good lasing occurs once out of three discharges. For the longer capillary good lasing is less frequent, it is about one discharge out of five. This is certainly connected with the necessity that the necks of the instability have to develop

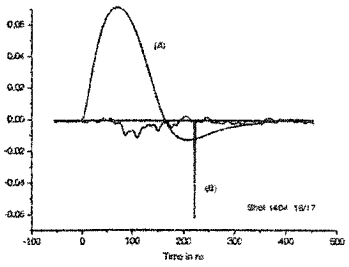


Figure 9: Current (A) and H-α Line of CVI (B) for a capillary 0.8 mm in diameter and 40 mm long with waved return conductor.

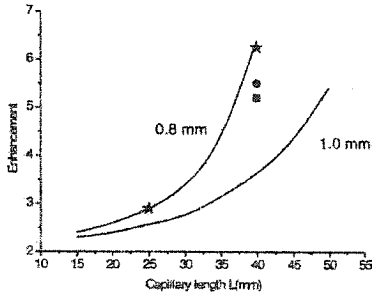


Figure 10. Balmer-α spike with waved return conductor for capillaries 0.8 mm (★) and 1.0 mm (●) in diameter at second current maximum, and for the 0.8 mm capillary during first half cycle (■).

along the axis at exactly the same time. Furthermore, the time of occurrence of the laser spike varies stronger, it is now even quite often in the first half cycle before current zero.

Figure 10 shows the obtained average intensity of the lasing spike normalized to the maximum of the emission of the first half cycle for capillaries of diameter 0.8 mm (⋆) and 1.0 mm (●). For comparison the results of Fig. 6 obtained with the waved capillaries are also shown as full lines. The values quoted are averages of good lasing when the normalized spike intensity was larger than 4. The rms scatter is less than 10%. The agreement with the previously studied internally waved capillaries is very good for the 0.8 mm capillaries, the new data points (⋆) are on the graph of the previous results. For 1.0 mm capillaries lasing is better than previously indicating that the neck regions are probably produced more likely at the same time. Lasing spikes (■) towards the end of the first half cycle had not been seen previously with the waved capillaries.

REFERENCES

*Present address: Powerlase Ltd., Crawley, RH10 9RA, UK
**Present address: Faculty of Mining, Geology and Petrol. Eng., University of Zagreb, Zagreb, Croatia

(1) D.L. Matthews, P.L. Hagelstein, M.D. Rosen, M.J. Eckart, N.M. Ceglio, A.U. Hazi, H. Medecki, B.J. MacGowan, J.E. Trebes, B.L. Whitten, E.M. Campbell, C.W. Hatcher, A.M. Hawryluk, R.L. Kauffmann, L.D. Pleasance, G. Rambach, J. Scofield, H. Stone and T.A. Weaver; Phys. Rev. Lett.; 54, 110 (1985).
(2) S. Suckewer, C.H. Skinner, H. Milchberg, C. Keanne and D. Voorhees; Phys. Rev. Lett.; 55, 1753 (1985).
(3) J.J. Rocca, J.D. Dunn, S. Suckewer; "X-Ray Lasers 2002: 8th International Conference on X-Ray Lasers", AIP Conf. Proc. 641.
(4) H. Daido; Rep. Prog. Phys.; 65, 1513 (2002).
(5) J.J. Rocca, V. Shlyapsev, F.G. Tomasel, O.D. Cortazar, D. Hartshorn and J.L.A. Chilla; Phys. Rev. Lett.; 73, 2192 (1994).
(6) J.J. Rocca, D.P. Clark, J.L.A. Chilla, and V.N. Shlyapsev; Phys. Rev. Lett.; 77, 1476 (1996).
(7) C.H. Moreno, M.C. Marconi, K. Kanizay, J.J. Rocca, Yu.A. Uspenskii, A.V. Vinogradov, Yu.A. Pershin; Phys. Rev. E; 60, 911 (1999).
(8) H.J. Shin, D.E. Kim, and T.N. Lee; Phys. Rev. E; 50, 1376 (1994).
(9) P. Bogen, H. Conrads, G. Gatti, and W. Kohlhaas; J. Opt. Soc. Am.; 58, 203 (1968).
(10) C. Steden and H.-J. Kunze; Phys. Lett. A; 151, 534 (1990).
(11) H.-J. Kunze, K.N. Koshelev, C. Steden, D. Uskov, H.T. Wieschebrink; Phys. Lett. A; 193, 183 (1994).
(12) S. Ellwi, S. Ferri, L. Juschkin, H.-J. Kunze, Z. Andreic, K. Koshelev; Nukleonika; 46, 1 (2001).
(13) F. Ruhl, L. Aschke, H.-J. Kunze; Phys. Lett. A; 225, 107 (1997).
(14) L. Aschke, Yu.V. Ralchenko, E.A. Solov'ev and H.-J. Kunze; J. Phys. IV France; 11, Pr2-547 (2001).
(15) S.S. Ellwi, L. Juschkin, S. Ferri, H.-J. Kunze, K.N. Koshelev and E. Louis; J. Phys. D: Appl. Phys.; 34, 336 (2001).
(16) S.S.Ellwi, Z. Andreic, S. Pleslic, H.-J. Kunze, Phys. Lett. A; 292, 125 (2001).

Applications of Laser-Spectroscopy in Plasma Physics and in Analytics

A. Baig, F. Bylicki, Th. Platz, H. Wenz and W. Demtröder
Department of Physics, University of Kaiserslautern
D67663 Kaiserslautern

INTRODUCTION

The application of narrow-band tunable lasers to spectroscopic problems has several advantages. Firstly profiles of absorption lines can be measured with high accuracy. This gives information on the different broadening mechanisms, such as Doppler-broadening or pressure broadening, and allows one to determine for example gas temperatures and densities of the absorbing species. Doppler-free techniques, such as saturation spectroscopy or polarisation spectroscopy, eliminates the Doppler-width and can therefore measure Stark-broadening and broadening by neutral particles in a plasmas more accurately than conventional methods. Several examples shall illustrate the different techniques.

Secondly, measurements of population densities in specific levels of atoms, molecules or ions can be performed with high sensitivity by different modulated absorption techniques, by laser induced fluorescence or by ionization spectroscopy. Due to the high collimation of the laser beam and spatial filtering of the observation region, local variations of densities of species in selected states can be monitored. Recently even Doppler-free two photon polarisation spectroscopy has been performed for the quantitative determination of atomic hydrogen densities in the 1S and 2S states in a plasma[1]. Electronic recombination often populates high lying Rydberg levels.This process in the photosphere of our sun is the main source for its visible radiation. The inverse process is auto-ionization of Rydberg states. This autoinization has been studied in detail for molecular Rydberg states in our laboratories and some results about the different line profiles will be presented[2].

The high Rydberg levels with large principal quantum number n are very sensitive probes for small electric fields because their polarisability scales as n^7! In Fig.1 the Stark splittings of Rydberg levels with n = 50 in the Li_2 molecule in very small electric fields are shown. The level pattern can become very complex, because the electric field mixes Rydberg levels with different angular momentum quantum numbers l and a mixture of linear and quadratic Stark-effect further complicates the structure and the field dependence of the Stark components. Nevertheless measurements of such Stark splittings in molecular plasmas opens the possibility of accurate local measurements of electric fields in plasmas.

In recent years several sensitive detection techniques of laser spectroscopy have been developed, which allow measurements of very small absorptions, i.e very small concentrations of atomic or molecular species.They are applicable to gaseous samples and also to plasma spectroscopy. One example is the above mentioned modulated absorption spectroscopy, which allows measurements of absorption coefficients down to $\alpha = 10^{-10}cm^{-1}$. The experimental setup and the application to overtone spectra of ozone, water molecules and other molecules relevant for our atmosphere are demonstrated later on[3].

A particularly interesting technique for the detection of long living excited molecular states is opto-thermal spectroscopy with cooled bolometers[4]. The beauty of this techniques was illustrated by measurements of overtone spectra of ethylen and chloroform, molecules that are relevant for biological and medical applications.

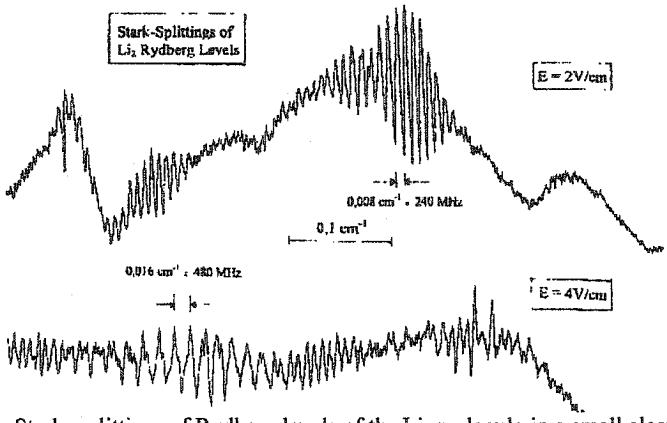


Fig.1: Stark- splittings of Rydberg levels of the Li_2 molecule in a small electric field

LASER SPECTROSCOPY OF PLASMAS

Contrary to many other techniques for the measurement of local plasma parameters, spectroscopic methods are noninvasive, i.e they do not change the plasma conditions, except for the small change of population densities by absorption of laser photons. The first applications of laser spectroscopy to plasma physics were investigations of low pressure gas discharges forming the active medium of gas lasers. Here measurements of laser induced fluorescence, emitted to the side of the discharge tube, gave information on the relative populations of relevant levels in neutral neon in low current helium/neon discharges (He-Ne-Laser) or in Ar^+-Ions in high current argon discharges. In particular the population and deactivation processes induced by electron collisions were investigated in detail. This could be achieved by monitoring the change of the intensity from levels populated by the laser. Using calibration techniques for known level populations even quantitative measurements of population densities could be performed.

Another well suited method for the study of plasma parameters is optogalvanic spectroscopy, where the change ΔI of the discharge current I at constant voltage is measured when the laser is tuned to a transition between levels of neutral or ionized species in the discharge. The magnitude and the sign of ΔI gives information on the different ionization probabilities of the levels involved in the laser-induced transition. This technique can be also applied to low pressure molecular plasmas which often show a high reactivity and can be used for surface processing.
More information can be extracted by Doppler-free techniques, such as saturation spectroscopy or by the more sensitive polarisation spectroscopy[4,5]. Here line profiles can be determined with high accuracy, giving information on temperature and pressure in plasmas and on their local variation.
One example is the polarization spectroscopy in a helium discharge, where a circularly polarized pump laser orientates the atoms in a definite level and a probe laser probes the corresponding transition. Since the two laser beams travel in opposite ± z-directions through the plasma tube, only those molecules contribute to the Doppler-free signal, which can absorb both laser beams. Generally these are molecules with a velocity component $v_z = 0$. However, it can happen, that molecules with $v_z \neq 0$ can absorb pump and probe beam simultaneously on two different transitions, sharing a common level. This gives rise to so called „cross-over" signals, which are useful for the assignment of the transitions. In Fig. 2 Doppler-free signals and their cross-overs are shown, which correspond to finestructure components of the transition $3^3D \longleftrightarrow 2^3P$ in He.

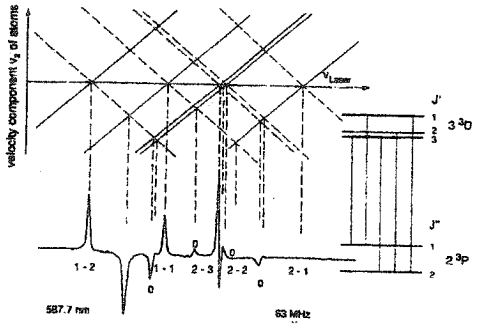


Fig.2: Doppler-free polarisation spectroscopy of the transition $^3P \longleftrightarrow {}^3S$ in a helium discharge

SENSITIVE ABSORPTION TECHNIQUE

If a light beam with intensity I_0 passes through a sample of absorbing molecules, the transmitted intensity is for small absorptions

$$I_t = I_0 e^{-\alpha L} \approx I_0(1-\alpha L) \tag{1}$$

where $\alpha = \sigma \cdot N_i$ is the absorption coefficient , which depends on the absoption cross section per molecule σ and the number density N_i of absorbing molecules in level $|i>$. The total absorption after a pathlength L is then

$$(I_0 - I_t) = I_0 \cdot \alpha \cdot L = \sigma \cdot N_i \cdot L \tag{2}$$

The minimum detectable number of molecules N_i^{min} depends on the achievable signal-to-noise ratio S/noise, because the measured signal $S \propto (I_0 - I_t)$ must be at least as large as the noise N. This gives for the minimum number density of molecules in the absorbing level $|i>$ in a gas , when the absorbing pathlength is L

$$N_i^{min} \geq \text{noise}/(\sigma \cdot L \cdot I_0) \tag{3}$$

and illustrates, that N_i^{min} depends on the absorption cross section σ, on the realized absorption pathlength L and on the incident intensity I_0.
The different techniques for sensitive absorption spectroscopy mainly aim on minimizing S/N and maximizing the absorption pathlength L by using multipass cells with highly reflecting focussing mirrors allowing up to hundred passes through the cell.
The main noise source comes from intensity fluctuations of the laser intensity. In this case the noise is proportional to I_0 and S/noise becomes independent on I_0. Therefore one has either to minimize these intensity fluctuations by stabilizing the laser intensity or to choose a detection techniques that is insensitive to them.

The absorption cross section depends on the molecular species and on the transition chosen for detecting the molecules. Most absorption methods use the fundamental vibrational transitions in the mid infrared region. Since the vibrational frequencies of these transitions are characteristic for any molecular species, this spectral range is called the fingerprint region for molecular detection. The absorption cross sections are fairly large, but reliable and easy to handle tunable laser sources for high resolution spectroscopy in this region had been lacking until recently when cw optical parametric oscillators or difference frequency laser spectrometers were developed.

Overtone transitions have much smaller absorption coefficients but since their wavelengths range from the near infrared into the visible region, widely tunable cw semiconductor lasers are here available, which can be modified into single mode lasers by using external cavity devices. Furthermore the detectors,such as photodiodes, avalanche diodes or photomultipliers are more sensitive in this range. Therefore the disadvantage of smaller absorption cross sections might be outweighed by the better experimental conditions.
In the following experimental techniques for sensitive overtone absorption spectroscopy will be discussed:
The experimental setup is shown in Fig. 2. The widely tunable cw single mode Al/Ga/As diode laser has an antireflection coating on one endface of the diode and is operated in an external cavity of the Littman type[6], consisting of a grazing incidence optical grating and a highly reflecting flat mirror. The mirror can be tilted by a piezo device around an axis, located at the intersection of the grating and the mirror planes. In this case the two conditions for the grating equation

$$d(\sin\alpha+\sin\beta) = \lambda$$

where d is the separation of the grating grooves, and for the cavity length

$$L_c = m\cdot\lambda/2$$

can be simultaneously fulfilled over a wide tuning range of the laser wavelength λ. In our setup the continuous tuning range without mode hops is about 400GHz, allowing the spectroscopy of a whole molecular band.

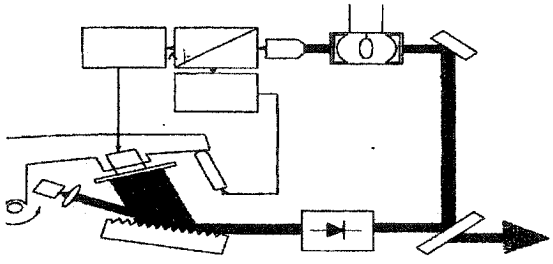


Fig.3 :Widely tunable single mode diode laser with external Littman-cavity

If the laserwavelength is modulated, the derivative of absorption lines is monitored and the noise, due to intensity fluctuations of the laser is greatly reduced. A further noise reduction can be achieved by a difference technique. The laser beam is split into two parts: One is passing through the absorption cell, the other serves as reference beam. A special detector consisting of two matched diodes on one chip measures the intensities of both beams and forms the difference divided by the reference intensity.

The techniques has been applied to the spectroscopy of high lying vibrational-rotational levels of ozone O_3 in its electronic groundstate, closely below the dissociation limit. This molecule plays an important role in the high atmosphere of the earth., because it absorbs the ultraviolet part of the sunlight below 320nm. The sunlight excites the O_3 molecules into high vibrational levels which can be readily dissociated by collisions with other molecules in the atmosphere, resulting in a destruction of ozone.. Therefore studies of the lifetimes and the deactivation cross sections of these states are essential for a quantitative understanding of these processes.
For calibration purposes lines of a reference molecule C_2H_2 and frequency markers of two Fabry-Perot etalons were simultaneously recorded. This allows an accuracy in the determination of the line positions of $0.01 cm^{-1}$. This high accuray is needed in order to guarantee an unambigouos identification and assignment of the individual lines in the dense spectrum.

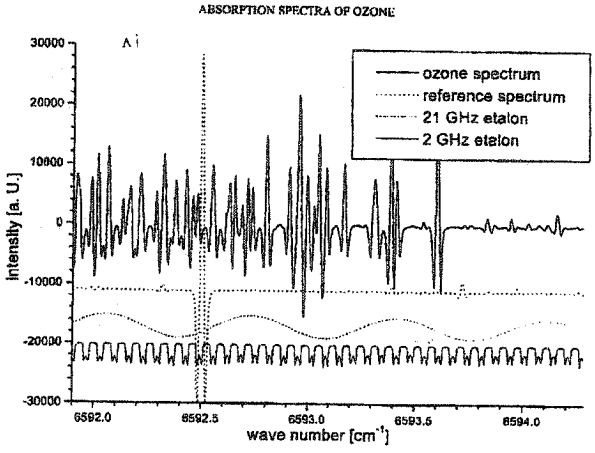


Fig.4: Small section of the overtone spectrum of O_3

OPTOTHERMAL SPECTRSOPCOPY

This technique is not directly relevant for plasma spectroscopy, since it needs a molecular beam, but it can be applied to many sectroscopic problems related to chemistry and biology. It belongs to one of the very sensitive detection techniques for small absorptions. Molcules in a beam are excited into long living high vibrational levels by absorption of laser photons. After their excitation they impinge on a cold (1.5K) bolometer where they are adsorbed and transfer their excitation energy into heat, which increases the temperature of the semiconductor bolometer by a very small amount. This temperature increase decreases the electric resistance which can be monitored by sending a small electric current through the semiconductor.
The lower limit of the detection sensitivity is about 10^{-14}W!!

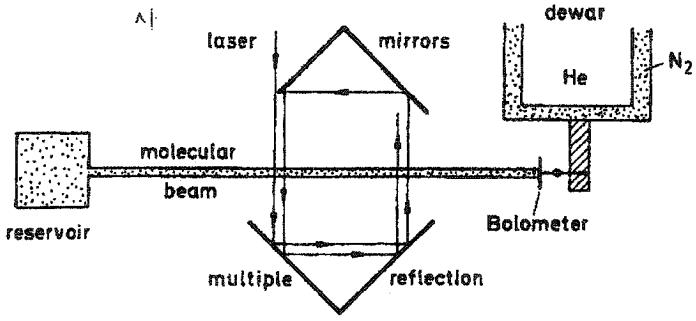


Fig.5: Molecular beam , laser excitation and bolometer for optothermal spectroscopy

In our labs the optothermal spectroscopy has been applied to overtone spectroscopy of ethylene, a molecule which is important for plant physiology[7]. For instance, it is used to ripen green babanas by exposing them to an ethylene atmosphere. Furthermore, if plants are under stress, they emit ethylene. The biological status of plants can be therefore monitored by measuring the amount of emitted ethylene. Since the overtone spectrum of ethylene is very dense, Doppler-free techniques have to be

used for quantitative information of the structure of excited ethylene. In fig. 4 a comparison is given between the smae spectral region measured by Fourier-spectroscopy, by Doppler-limited opto-acoustic spectroscopy and by Doppler-free optothermal spectroscopy. It shows, that many spectral features are completely masked in Doppler-limited spectroscopy, which can be clearly separated by Doppler-free optothermal spectroscopy.

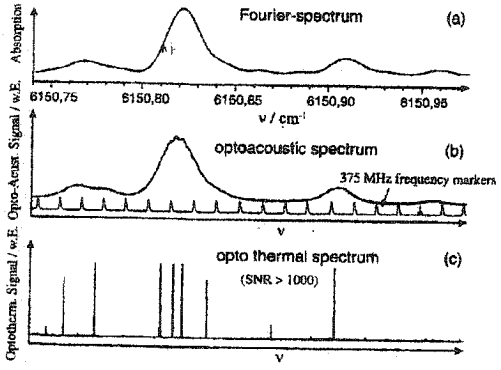


Fig.6:Section of the ethylen spectrum measured with Fourier-, optoacoustic, and optothermal spectroscopy [8].

REFERENCES

(1) K. Grützmacher, M.I.de la Rosa, A.B.Gonzales, M.Steiger and A.Steiger; Appl. Phys. B in print (2003)
(2) M.A. Baig, F. Bylicki, M. Keil, J. Zhu and W. Demtröder; Spectral Line Shapes Vol 11, ed. by J. Seidel (Am. Institut of Pysics, New York 2001)
(3) H. Wenz, W. Demtröder, J.M. Flaud; Mol. Spectros. 209, 267 (2001)
(4) W. Demtröder, Laser Spectroscopy. 3.ed. (Springer, Heidelberg 2002)
(5) Th. Platz, W. Demtröder; Chem. Phys. Lett. 294, 397 (1998)
(6) Ch. Hertzler, H.J. Foth, Chem.Phys. Lett. 166, 551 (1990)
(7) H. Wenz, PhD Thesis, Universität Kaiserslautern (2001)
(8) Th. Platz, PhD Thesis, University of Kaiserslautern (1999)

Influence of Optical Feedback on the Dynamics on a Semiconductor Laser Having a Short External-Cavity

A.M. El-Nadi* and J.M. ElAzab
National Institute of Laser Enhanced Sciences, Cairo University, Giza, Egypt
** and Faculty of Engineering, Cairo University.*
aelnadi@hotmail.com

In this work we have used a fourth order Runge-Kutta algorithm to model the time-dependent behavior of an extended cavity semiconductor laser diode (ECLD) in the short cavity limit. The effect of increased feedback level on the wave field, carrier density, oscillation spectra and number of excited external-cavity modes (ECM) is presented.

Key words: ***Semiconductor lasers, Chaos, Short External-Cavity, Regular Pulse Packages.***

INTRODUCTION

The study of the various operation regimes of ECLD has been an active area of research during the last two decades[1-4]. The importance of such studies originated from the high sensitivity of the optical output to the electric field fed back from the external cavity. This can have detrimental effects in many situations including optical communications. It was also suggested that the chaotic output obtainable under certain conditions offers possible means for signal encoding[5]. While various regimes of operation have been already investigated, the output variation during a sizable variation of one parameter is of great interest since the transition between different regimes can thus be accounted for, particularly when approaching chaotic regimes. Limiting our present study the short cavity case, we will study the influence of the variation of feedback level on the different laser output properties.

RATE EQUATIONS

The behavior of semiconductor laser diode with external feedback (Fig.1) can be described by the Lang-Kobayashi system of nonlinear first order equations[1]. Let us write the output electric field in the form $\mathcal{E}(t) = E(t)\exp[\,j(\omega_0 t+\Phi(t))\,]$ where $E(t)$ is the amplitude, ω_0 is the angular frequency of the solitary laser and the $\Phi(t)$ is the phase, so that the LK equations may be written as

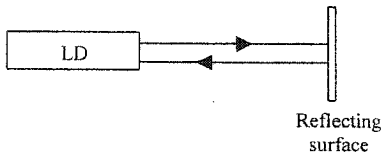


Fig1: A schematic diagram of the laser diode with an external cavity.

$$\frac{dE(t)}{dt} = \frac{1}{2}\left[G_N(N-N_0) - \frac{1}{\tau_p}\right]E(t) + \frac{k}{\tau_{in}}E(t-\tau)\cos\left[\Phi(t)-\Phi(t-\tau)+\omega_0\tau\right], \qquad [1]$$

$$\frac{dN(t)}{dt} = J - \frac{N(t)}{\tau_s} + G_N(N - N_0)|E(t)|^2, \qquad [3]$$

where

G_N: the modal gain [$8.4*10^4$ m^{-3}/s]

N_0: the transparency carrier density [$1.6*10^8$ m^{-3}]

τ_p : the photon lifetime [3 ps],

τ_{in}: the internal cavity round trip time [8 ps],

ω_0: the angular frequency of solitary laser diode [λ=693 nm],

α: the line width enhancement factor[5]

τ_s : the carrier lifetime [0.6 ns],

J: the injection current density,

k: the feedback level and

τ: the round trip time of the external cavity.

As mentioned above, we will consider here the case of a short external cavity (τ =0.2ns) at low injection current (J=1.08 J_{th}). But first we will describe the behavior of a solitary laser diode (k=0) and solving the rate equations using a fourth order Runge-Kutta algorithm. We notice here that we have normalized the amplitude of the electric field and the carrier density to their values in the case of solitary laser, E_{sol} and N_{th} respectively. The characteristics of the solitary laser diode are shown in Fig.2. Figs.2(a-c) show the temporal behavior of the normalized amplitude $E_N(t)$ and phase $\Phi(t)$ of the electric field and the normalized carrier density $N_N(t)$. The electric field decays during the transient part and reaches a dc steady-state resulting in a point in the phase portrait N_N-E_N (Fig.2d). The frequency of relaxation oscillation may be calculated from Fig.2a ($f_{RO} \approx$ 2GHz).

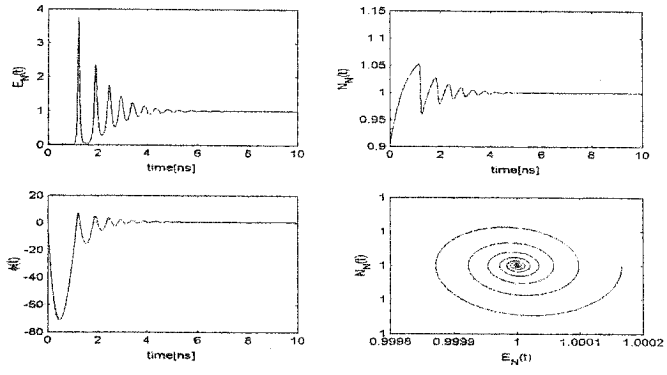


Fig.2: The temporal behavior of a solitary laser diode. (a) The output field amplitude. (b) The carrier density. (c) The output phase. (d) The phase-portrait.

ROUTE TO CHAOS

In this section, we will study the short ECLD behavior with different feedback levels. Starting with very weak feedback (k=0.01), the laser output amplitude oscillates sinusoidally as shown in the first column of Fig.3. Fig.3 shows the temporal behavior of the normalized amplitude $E_N(t)$ and the phase $\Phi(t)$ of the electric field, the normalized carrier density $N_N(t)$ and the phase portrait N_N-E_N. It may be seen that the phase portrait turns to a limit cycle corresponding to the output oscillation. If we observe the corresponding spectrum of $E(t)$, $S_f[E(t)]$, the frequency of oscillation is found to be 2.3GHz which is close to the relaxation oscillation frequency f_{RO}. While the spectrum of cos $[\Phi(t)]$,

$S_f[\cos\Phi]$, gives an indication of a shift in the operating frequency from that of the solitary laser diode by 0.8GHz. The slope of the phase of the electric field indicates the direction of the shift, i.e. the operating frequency decreases in this case.

Increasing the feedback level k to 0.02 (2nd column in Fig.3), we notice the appearance of the nonlinear higher harmonics in addition to a subharmonic which can be seen in the spectrum $Sf[E(t)]$ (2nd column in Fig.4), $f_{1/2}$=1.12GHz, while the fundamental frequency becomes 2.25GHz. In this case, the limit cycle changes into a period-2 figure as shown in the phase portrait. With more increase in k, a new subharmonic is generated as shown in the 3rd column of Figs.3 and 4, and the phase portrait turns to period-4. Unfortunately, the spectrum shown in Fig.4 does not show the new subharmonic ($f_{1/4}$=0.52GHz), as it is still weak, but it can be easily detected from the repetition of the pattern in Fig.3

As the feedback level is slightly increased to k=0.023, quasiperiodic output sets in, marked by the spectrum becoming continuous and wider as shown in the 1st column of Fig.5. Then, the quasiperiodic output develops into chaos for higher feedback (2nd column in Fig.5) and the spectrum $S_f[E(t)]$ becomes wider. A characteristic phenomenon develops for higher k= 0.2, as may be seen in the 3rd column. Regular pulse packages (RPP) appear in the output and the spectrum shows two frequency groups. The lower group indicates the envelope frequency while the higher one shows the cavity modes. This will be discussed in detail in next section.

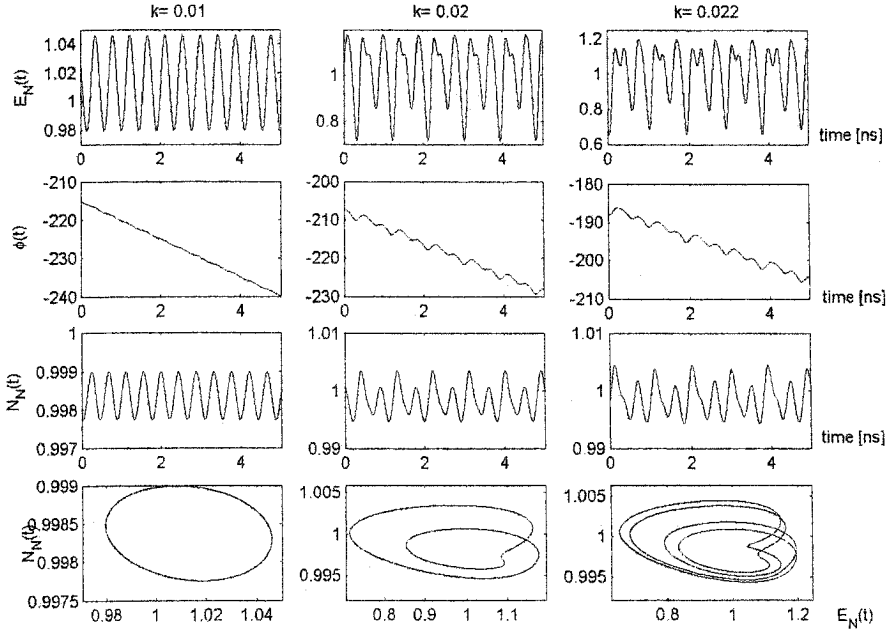


Fig.3: The temporal behavior and the phase portrait of the output of an ECLD with different feedback levels (k= 0.01, 0.02 and 0.022)

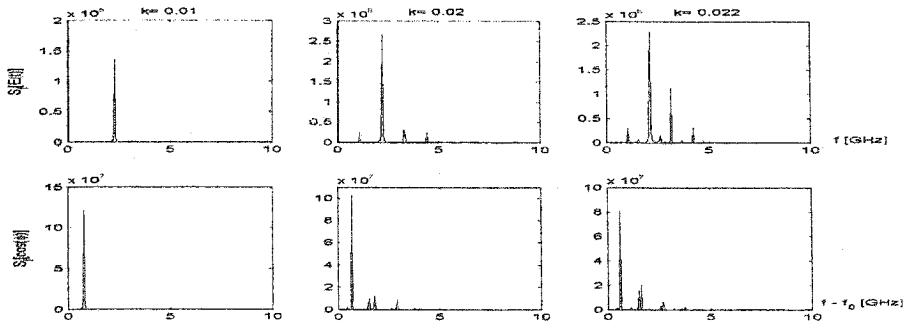


Fig.4: The corresponding spectra of the amplitude of the electric field: Sf[$E(t)$] and cosΦ: Sf[cosΦ] for each case in Fig.3.

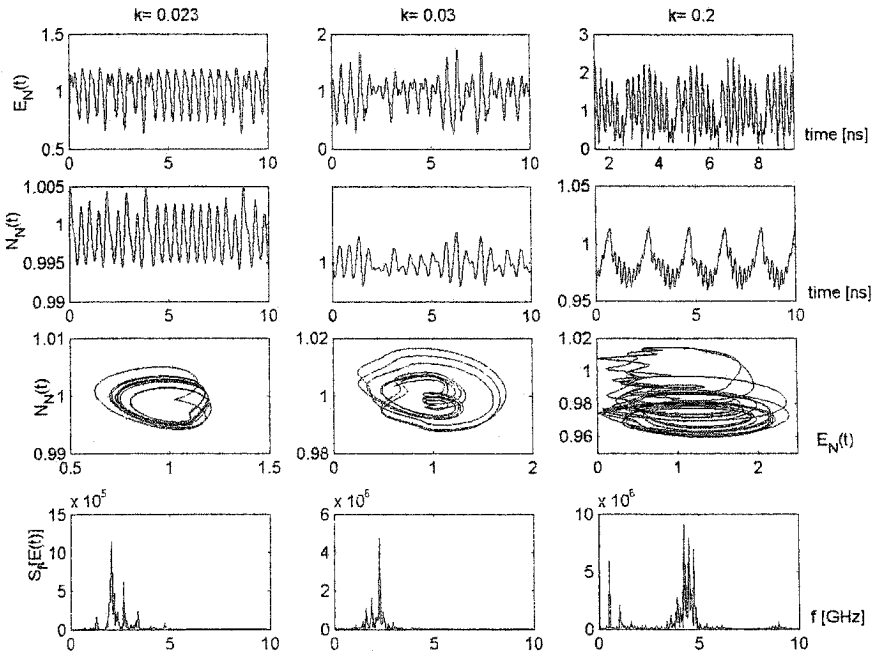


Fig.5: The temporal behavior, phase portrait and spectrum of the output of an ECLD with different feedback levels (k= 0.023, 0.03 and 0.2)

REGULAR PULSE PACKAGES

At high feedback values, the laser output shows a periodic emission of regular pulse packages (RPP) separated by short intervals of very low amplitudes[3]. Each pulse package consists of a train of regularly spaced light pulses occurring at the round-trip time of the external cavity (1st column in Fig.6). If we observe the projection plane of the normalized carrier density and the phase delay ($\Phi(t)$-$\Phi(t-\tau)$), we can see that jumps occur when the output drops to zero. At this time the system settles in another external-cavity mode (ECM) before jumping in the direction of ECM with maximum gain (smallest phase difference)[1,3]. We have noticed that both the extinction and triggering levels of each ECM follow a downward carrier density trend, which explains the shift between different modes. The spectrum of cosΦ displays the same number of external-cavity modes present in the phase portrait. Finally, the temporal behavior of EcosΦ (Fig.7) shows a change in the frequency of oscillation within each pulse inside the same package, which corresponds to the shift to other ECMs. It may also be noted that there is a change in the shape of RPPs as the feedback level is increased to k=0.5 as shown in 2nd column in Fig.6. Clearly the number of ECMs visited in each package increases, corresponding to more light pulses within each. This trend of increasing number of modes continues for higher values of feedback than those used here.

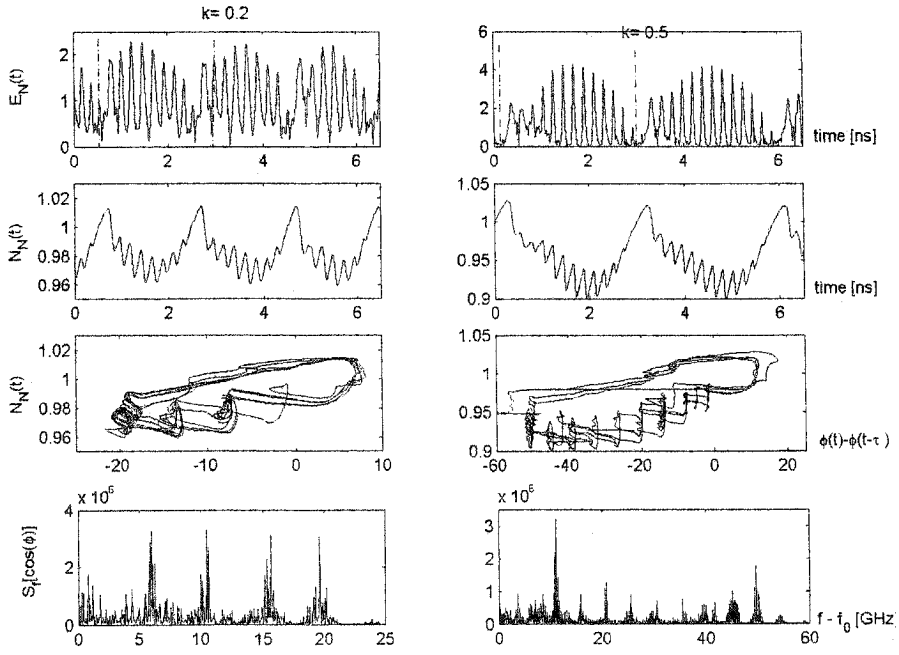


Fig.6: The dynamics of ECLD in the case of RPP at k=0.2 and 0.5.

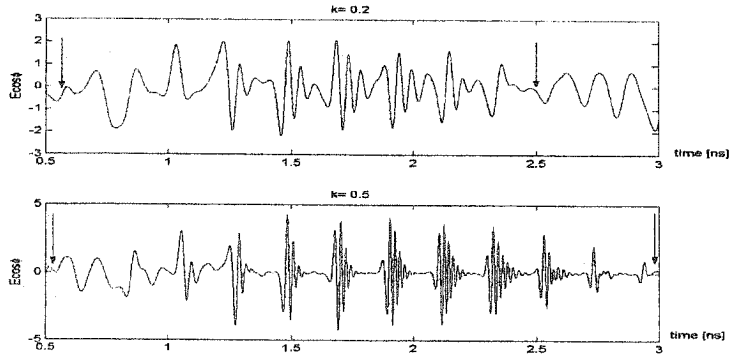


Fig.7: The temporal behavior of EcosΦ for k=0.2 and 0.5.

CONCLUSIONS

In this work we have studied the behavior of an extended-cavity semiconductor laser in the short cavity regime for an injection current slightly above the threshold lasing current and a varying amount of feedback. We presented the route to chaos, which showed subharmonic and later on a quasiperiodic behavior. In the RPP regime we showed how the different external-cavity modes appear in cascade and also how the spectrum widens as the feedback fraction increases.

REFERENCES

(1) J. Mork, B. Tromborg and J. Mark, "Chaos in semiconductor lasers with optical feedback: theory and experiment", *IEEE J. Quantum Electron.*, 28, 93-108, (1992).

(2) D. Pieroux and P. Mandel, "Low frequency fluctuations in the Lang- Kobayashi equations", *Phys. Rev.* E 68, 36204 (2003).

(3) T. Heil, I. Fischer and W. Elsäßer, "Dynamics of semiconductor lasers subject to delayed optical feedback; the short cavity regime", *Phys. Rev. Letters*, 87, 243901, (2001).

(4) A. Tabaka, M. Sciamanna, I. Veretennicoff and K. Panajotov, "Bifurcation study of regular pulse packages in the laser diodes subject to optical feedback", *Proceedings Symposium IEEE/LEOS Benelux Chapter*, 2002.

(5) "Special issue on applications of chaos in modern communication systems", *IEEE Trans. Circuits Syst. I*, vol.48, Dec.2001.

Large Plasma Set – Up For Modeling Space Phenomena And Technological Applications

A.V. Kostrov
Institute of Applied Physics, Russian Academy of Sciences, Ulyanov str. 46, 603950
Nizhny Novgorod, Russia
kstr@appl.sci-nnov.ru

ABSTRACT

The paper presents basic characteristics of the unique large-size experimental set-up "Krot", which makes it possible to study many problems of plasma physics within the unbounded-medium approximation. Describes recent experimental investigation of interaction of electromagnetic intense waves with magnetized plasma.

Key Words: Whistler Wave, Lower – Hybrid Turbulence, Parametric Transformation

INTRODUCTION

Modern intense progress in investigation of the near and far space has made laboratory modeling of some space phenomena most important. The scientific results of such studies can help solve the fundamental problems of plasma physics and realize some practical application, such as the active space experiments and satellite communications.

In this problem the nonlinear effects of importance when strong electromagnetic waves radiate and propagate in Earth's ionosphere and magnetosphere and these effects give rise to waves self-focusing and self-defocusing, stimulating scattering, modulation instability, wave ducts formation, anomalous absorption and plasma enlightenment. Prediction and quantity description of these phenomena are difficult, because ionospheric magnetoactive plasma is highly complex matter both due to electrodynamics and for transport process. That is why the laboratory modeling experiments are needed for creating the programs of active influence electromagnetic waves to Earth's ionosphere and magnetosphere. Such experiments allow to reveal and to study characteristic plasma-field self-consistent structures, whose properties should be known for natural experimentation.

In order to solve these problems, the IAP has developed and builds the large – scale plasma set-up (called "Krot").

The plasma device "Krot" (fig. 1) for experiments on wave – plasma interaction in large magnetized plasma consists of the following:

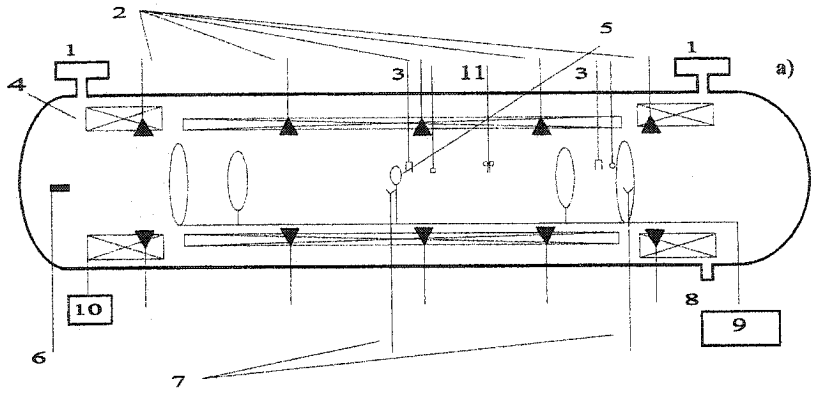
The solenoid (1.5 m in diameter, 3.5 long) to provide the pulsed magnetic mirror (mirror rate ~ 2.5, max magnetic field ~1000 G, $\tau \sim 20 \cdot 10^{-3}$ s) is situated inside the vacuum chamber (3 m in diameter, 10 m long). The plasma is produced with pulsed inductore RF- discharge. To get the uniform axial plasma profile, six current loops (1.2 m in diameter) are placed in the magnetic mirror and fed with three RF – power supply ($\tau \sim 10^{-3}$ s, $f \sim 5$ MHz). Most measurements are performed in the afterglow plasma (density time decay $\sim 7 \cdot 10^{-3}$ s, $N_{e\,max} \sim 10^{13}$ cm^{-3}, temperature of electrons $T_e \sim 10$ eV). The radial density profile is close to the parabolic one.

Thus, the "Krot" set – up magnetized plasmas in the volume of 8 m^3. Such a great volume of pleasures provides the unique possibility of studying physical phenomena in unbounded plasma.

The main problems which to investigate on experimental set-up "Krot" were:

1. Investigation of transport processes in magnetized plasmas (thermodiffusion, thermoforce).
2. Control radiation efficiency of the dipole antenna in plasma.
3. Radiation and channeling of waves in the whistler frequency range within nonuniform plasma structures.
4. Nonlinear processes of the lower – hybrid turbulence.
5. Whistler wave frequency transformation in nonstationary magnetized plasma.

We are represents in these report two last results (4 and 5).



1. vacuum pumps, 2. 5 - channel 8 mm interferometer, 3. rf antennas, 4. solenoid, 5. current loop, 6. grids probe, 7. system of moving double probes across chamber, 8. gas injector, 9. rf-generators, 10. generator of pulse magnetic field, 11. Hf - probe

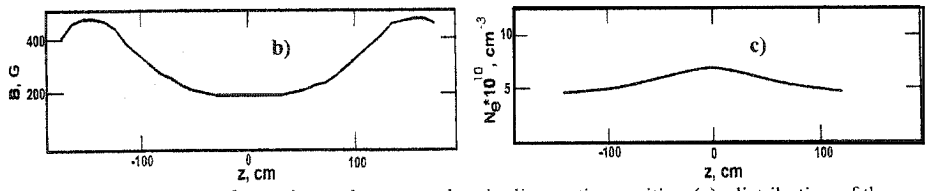


Fig. 1. The scheme of experimental set-up and main diagnostics position (a); distribution of the magnetic field (b) and plasma density (c) along the axis of the trap

RESULTS

1. Nonlinear processes of the lower – hybrid turbulence.

It is a widespread point of view that lower – hybrid waves are essential for the processes of collisionless particle acceleration in space physic. The most important consequence of lower – hybrid turbulence is formation and collapse of cavitons leading to particle acceleration.

Lower – hybrid waves were excited with a pulse of the high-frequency pump (frequency 3 MHz, pulse duration 1 ms), which was applied to the magnetic loop (R=10 cm) placed at the center of the solenoid at 12 ms after switching off the generator creating plasma. Initial temperature of electrons and ions was about 1 eV, plasma density - $5 \cdot 10^{10}$ cm^{-3}. The condition $\omega_{pe}/\omega_{He} >> 1$ was fulfilled in the experiment. In this case the frequency of lower – hybrid resonance does not depend on the temperature and is determined only by value of magnetic field.

In fig.2 radial distributions of plasma density at the various moments of time are given (U_{pump}=200V). During the first 300 μs after switching on the pump we observed formation of small – scale plasma structures with characteristic depth of density modulation of the order 10 – 20 % and its size about several centimeters. Later small – scale plasma density depression blurred and merged, forming at times $t \geq 500$ μs a global failure of plasma density at the center of the chamber (R<10 cm). At R>10 cm an increase of plasma density was observed, as compared with its unperturbed value (fig. 2e,f).

In dynamic of system development two characteristic temporary scale are traced: 1 – first 300 μs of the pump pulse; 2 – times >500 μs. Quasiperiodical modulation of plasma density (fig. 2b,c) with the characteristic spatial period L ~ 3 cm arising already during the first 300 μs after switching the pump on testifies to development a modulation instability in plasma.

Thus, in first 300 μs after switching on the pump formation of cavitons as the result of modulational instability development was observed. However, the collapse predicted in the collisionless case was not observed. Obviously, in the condition of a real experiment, the intense

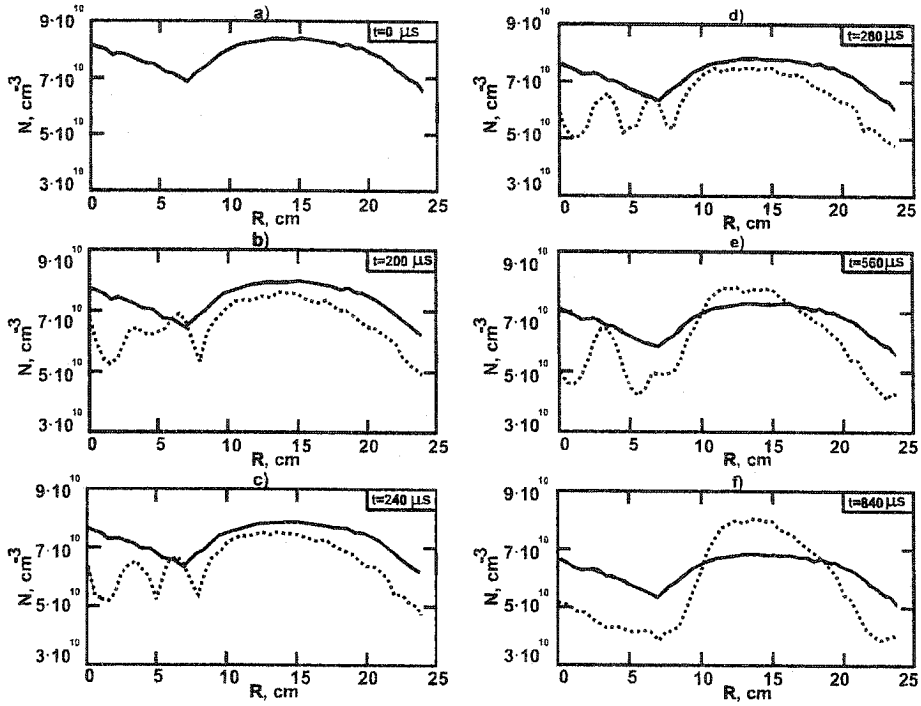


Fig. 2. Radial distribution of plasma density in the various moment of time

——— Without pump

..... With pump

lower-hybrid field trapped in cavitons results, along with strictional effects, in heating of plasma electrons in the field of cavities. In this case, thermal nonlinearity results in stabilization of the collapse process and, further, in blurring of cavities (fig. 2d,e,f).

2. Whistler wave frequency transformation in nonstationary magnetized plasma.

Parametric processes in whistler frequency range are of great interest in space and near-earth magnetized plasmas. In appearance of low-frequency ionic waves, low-hybrid oscillations or quasi-electrostatic whistler waves the frequency spectrum of whistler propagating in plasma can be transformed. Quasi-longitudinal whistlers interact with naturally occurring perturbations sometimes. Low frequency variations of plasma parameters provide spectrum broadening and side-band generation.

We are represents experimental results about parametric frequency transformation of ducted high-frequency whistler in appearance of intense low-frequency wave localized in the same duct.

Experiments were performed in afterglow plasma when electron density reached $n_e \sim 10^{12}$ cm^{-3}. Plasma duct was created by using additional RF-heating source. RF-pulse (T_{pulse}=1 msec, F_0=3 MHz, P=1÷9 kW) was applied to the loop antenna (Ø20 cm) placed in the center of plasma column. Electron heating near the loop and subsequent thermodiffusion process led to formation of field-aligned plasma channel with depressed plasma density (density on the duct axis was about 1.5×10^{11} cm^{-3}). Intense low-frequency waves (F_0=3 MHz) were radiated into duct simultaneously with plasma heating in antenna near-field. Amplitude of AC field was rather large, permanent magnetic field perturbation (B_0=100 G in minimum) reached $\delta B/B_0 \sim 1 \div 5\%$. High-frequency whistler pulse (τ_{pulse}=1÷3 μsec, f_0=160 MHz, P=0.01÷100 W) was radiated into duct by using small (Ø2 cm) magnetic loop antenna. Amplitude-phase modulation of ducted high-frequency wave (f_0=160 MHz) is the main experimental result (fig.3). Periodic plasma parameters variation can lead to 100% modulation of whistler pulse, signal can be shattered into short wave packets (fig.3,b). Signal frequency is modulated with frequency F_0=3 MHz also.

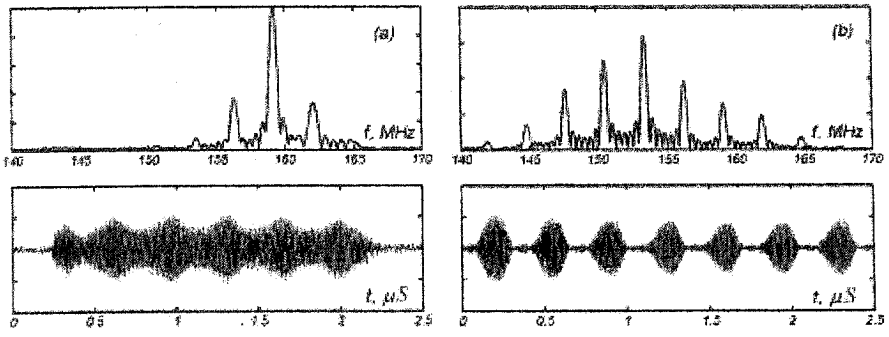


Fig.3. High-frequency pulse spectra and signal oscillograms in appearance of plasma nonstationary perturbation (F_0=3 MHz) – two cases: (a) – 25 cm, (b) – 250 cm between radiating and receiving antennas

Plasma parameters perturbation by low frequency wave (F_0=3 MHz) leads to hard-driving modulation of high-frequency signal (f_0=160 MHz) propagating in plasma. Initial signal can be shattered into the separate short wavelets. Periodic frequency modulation (phase modulation) took place.

Frequency spectrum broadening is observed, increasing of wave propagation length leads to spectrum down-converting also.

Spatial structure of parametrically exited whistler modes is different. Low-frequency satellite modes prevail, on the large distance from the transmitting antenna their amplitude is higher then amplitude of the main mode f_0=160 MHz.

3. Technological applications

Except the set-ups for fundamental plasma problems investigations the large-scale plasma arc devices are constructed. These devices are designed for different technological applications like thin films of Ti, TiN, Al, Cu deposition. The protective and decorative coatings can be deposited on turbine blades, aircraft propellers, tools, medicine equipment etc.

The work was performed under the support of RFBR (grants 01-02-16578), and with financial support of Russian Department of Science on "KROT" set-up (registr. 01-18).

Planetary Electromagnetic Waves in the Ionospheric E-layer

T. D. Kaladze
I. Vekua Institute of Applied Mathematics of Tbilisi State University,
2 University str., 0143 Tbilisi, Georgia
kaladze@viam.hepi.edu.ge

ABSTRACT

The linear theory for the large-scale ($\lambda > 10^3$ km) electromagnetic (EM) waves in the middle-latitude ionospheric E-layer is developed. The general dispersion relation for these waves is derived. It is shown that the latitudinal inhomogeneity of the geomagnetic field and the angular velocity of the Earth's rotation can lead to the appearance of wave modes in the form of slow and fast EM planetary waves. The slow mode is produced by the dynamo electric field and it represents a generalization of the ordinary Rossby type waves in a rotating atmosphere when the Hall effect in the E-layer is included. The fast mode is associated with the oscillations of the ionospheric electrons frozen in the geomagnetic field. It represents the variation of the vortical electric field and it arises solely due to the latitudinal gradient of the external magnetic field. The basic characteristics of the wave modes, such as the wavelength, the frequency and the Rayleigh friction are estimated. Other types of waves, termed slow magnetohydrodynamical (MHD) waves, which are insensitive to the spatial inhomogeneity of the Coriolis and Ampere forces are also reviewed. It is shown that they appear as an admixture of slow Alfven (SA) and whistler type waves. Such waves can generate variations in the magnetic field from a few tenth to a few hundreds *nT*. It is stressed that the basic features of the considered waves agree with the general properties of the magnetic perturbations observed at the world network of magnetic and ionospheric stations.

Key words: Ionospheric E-layer, planetary waves, inhomogeneity of the geomagnetic field

INTRODUCTION

The presence of charged particles in the ionosphere may substantially enrich the class of possible low-frequence wave modes in the ionosphere. In this paper it is shown that the spatial inhomogeneity of the geomagnetic field with respect to latitude also causes additional wave motions in the ionosphere which are magnetic analog of the long Rossby waves.

Up to now, a large amount of magnetometer and ionospheric observations has been collected which confirm the evidence of slow long-period planetary waves with phase velocities of the order of the velocity of the local ionospheric winds (1-100 m/s). At middle-latitudes their wavelengths are of the order of $10^3 - 10^4$ km and the wave periods constitute a few days at any season (1-2). Contrary to the ordinary Rossby waves, these slow waves are associated with a strong perturbation of the geomagnetic field (from a few to several tenths of *nT*). This fact shows their EM origin. Apart from the slow waves, there is evidence for the existence of fast large-scale EM perturbations in the middle-latitude ionosphere (3-5). Such waves propagate along the Earth's surface with the velocity 2 - 20 km/s. Their periods vary from a few to a few tenths of minutes, the wavelength is of the order 1000 km or larger and the wave amplitude is between ten to hundred *nT*. The phase velocity of the fast perturbations differs for the day- and night-time ionospheric conditions. The relatively low phase velocities and strong diurnal variations exclude the possibility of their identification with the ordinary magnetohydrodynamic (MHD) waves.

In this respect the study of possible mechanisms of generation and evolution of such EM planetary waves in the E-layer is of great importance for the interpretation of ground based and ionospheric observations. For that purpose it is necessary to elucidate the relevant physical factors which govern the generation and existence of such perturbations.

1. Basic Equations

Let us consider the ionospheric plasma which is immersed in a dipole magnetic field $\vec{B}_0$, assuming that the wave motions in the E-layer are localized in the vicinity of a given latitude $\lambda = \lambda_0$. We introduce a local Cartesian system of coordinates (x, y, z) with longitudinal, $x = \varphi R \cos\lambda_0$, and latitudinal, $y = (\lambda - \lambda_0) R$, coordinates. The z-axis of our system coincides with the local vertical direction. Furthermore, φ is the longitude and R is distance from the Earth's center. In this coordinate system the x-axis is directed from the west to the east and the y-axis is directed from the south to the north. The modulus of the dipole geomagnetic field is defined by the well-known expression $B_0 = B_{eq}(1+3\sin^2\lambda)^{1/2}$, whereas the components of the geomagnetic field vector are: $B_{0x} = 0$, $B_{oy} = B_{eq}\cos\lambda$, $B_{0z} = -2B_{eq}\sin\lambda$, where B_{eq} is the equatorial value of the geomagnetic field at a distance R from the Earth's center.

The plasma conditions in the E-region allow us to make some simplifications of the expression for the electric current. First, $\omega_{ci}/\nu_i << 1$ ($\omega_{ci,e} = eB_0/m_{i,e}$ is the ion or electron cyclotron frequency, ν_e and ν_i are the electron-neutral and ion-neutral collision frequencies), and thus the ions can be considered as unmagnetized. According to (6), their velocities across the magnetic field coincide with the wind velocity, $\vec{v}_i = \vec{v}$, and thus the ions are completely dragged by the ionospheric winds. In this limiting case the Hall conductivity is $\sigma_H \approx en/B_0$ (n is the equilibrium charged particle number density) while the Pedersen conductivity is small, i.e. $\sigma_P \approx \sigma_H \omega_{ci}/\nu_i << \sigma_H$. This allows us in the E-layer to neglect the ion friction caused by the Pedersen conductivity. On the contrary the electrons are magnetized, $\omega_{ce}/\nu_e >> 1$, and thus they are frozen in the external magnetic field. The electrons undergo solely the $\vec{E}\times\vec{B}_0$ drift perpendicular to the magnetic field, i.e. $\vec{v}_e = \vec{v}_E = \vec{E}\times\vec{B}_0/B_0^2$. Thus for the electric current in the E-layer we get $\vec{j} = en(\vec{v} - \vec{v}_E)$ or

$$\vec{E} + \vec{v}\times\vec{B}_0 = \frac{\vec{j}\times\vec{B}_0}{en} \equiv \frac{\vec{F}_A}{en}, \tag{1}$$

where $\vec{F}_A$ stands for the Ampere force, $\vec{F}_A = -\mu_0^{-1}\vec{B}_0\times\nabla\times\delta\vec{B}$, μ_0 is the permeability of free space, $\delta\vec{B}$ is the perturbation of the magnetic field.

Taking the curl from the electric field $\vec{E}$ given by the generalized Ohm's law (1) and substituting the result into Faraday's law $\nabla\times\vec{E} = -\partial\delta\vec{B}/\partial t$ we find the equation for the magnetic field $\delta\vec{B}$

$$\frac{\partial\delta\vec{B}}{\partial t} = (\vec{B}_0\cdot\nabla)\vec{v} - (\vec{v}\cdot\nabla)\vec{B}_0 - \frac{\nabla\times\vec{F}_A}{en}, \tag{2}$$

which differs from the ordinary frozen in condition for a conducting fluid by the additional term on the right-hand side. It is caused by the action of the Ampere force on the ionized plasma component (the Hall effect).

A qualitative understanding of the role of the internal dissipation may be obtained by representing this process very simply as a linear drag force (Rayleigh friction) in the momentum equation by adding a term proportional to the fluid velocity $\vec{v}$, i.e. $\vec{F}_R = -\Lambda\vec{v}$ (7-8). Here Λ is the coefficient of Rayleigh friction which at the altitude of the E-layer has a value of $10^{-5}\ s^{-1}$.

Considering the ionosphere as a weakly ionized gas, the neutral gas momentum equation reduces to

$$\frac{d\vec{v}}{dt} = -\frac{\nabla p}{\rho} + \frac{\vec{F}_A}{\rho} + 2(\vec{v}\times\vec{\Omega}) + \vec{g} - \Lambda\vec{v}\,, \tag{3}$$

Here $\rho = Nm_N$ is the neutral gas mass density, N and m_N are the number density and mass of the neutrals, p is the gas pressure and $\vec{g}$ is the gravitational acceleration. The third term on the right-hand side of Eq. (3) stands for the Coriolis force where $\vec{\Omega}$ is the angular velocity of the Earth's rotation. In our local system of coordinates, it is $\vec{\Omega}=(0,\Omega_y,\Omega_z)=(0,\Omega\cos\lambda,\ \Omega\sin\lambda)$. In the E-layer the wave motions are basically two dimensional, i.e. $\vec{v}=(u,v,0)$, with $u=-\partial\psi/\partial y$ and $v=\partial\psi/\partial x$, where ψ is the stream function.

From equations (2) and (3), in the linear approximation we get the following closed set of equations that describes the low-frequency perturbations in the ionospheric E-layer:

$$\left(\frac{\partial}{\partial t}+\Lambda\right)\nabla_\perp^2\psi + \beta\frac{\partial\psi}{\partial x} = \frac{1}{\mu_0\rho}\left[\frac{\partial B_{0z}}{\partial y}\frac{\partial \delta B_z}{\partial x} - \left(\frac{\partial B_{0y}}{\partial y} + B_{0y}\frac{\partial}{\partial y}\right)\nabla_\perp^2 A\right], \tag{4}$$

$$\left(\frac{\partial}{\partial t} - c_B\frac{\partial}{\partial x}\right)\nabla_\perp^2 A = -B_{0y}\frac{\partial}{\partial y}\nabla_\perp^2\left(\psi + \frac{\delta B_z}{en\mu_0}\right) + \frac{\partial B_{0y}}{\partial y}\left(\frac{\partial^2}{\partial x^2} - \frac{\partial^2}{\partial y^2}\right)\left(\psi + \frac{\delta B_z}{en\mu_0}\right), \tag{5}$$

$$\left(\frac{\partial}{\partial t} + c_B\frac{\partial}{\partial x}\right)\delta B_z = -\frac{\partial B_{0z}}{\partial y}\frac{\partial\psi}{\partial x} + \frac{1}{en\mu_0}\left(\frac{\partial B_{0y}}{\partial y} + B_{0y}\frac{\partial}{\partial y}\right)\nabla_\perp^2 A. \tag{6}$$

Here A is the z-component of the vector potential of the magnetic field $\delta\vec{B}$, $\beta = 2\partial\Omega_z/\partial y = 2\Omega\cos\lambda_0/R > 0$, $c_B = (en\mu_0)^{-1}\partial B_{0z}/\partial y = -2B_{eq}\cos\lambda_0/en\mu_0 R < 0$, which are evaluated in the vicinity of the latitude λ_0.

Considering all perturbed quantities to very as $\exp i(k_x x + k_y y - \omega t)$, from Eq. (4)-(6) one readily finds the following general dispersion relation

$$\omega + k_x\frac{\beta}{k_\perp^2} + i\Lambda = \frac{\omega + k_x c_B}{k_\perp^2}\quad \frac{k_x^2\alpha c_B + (-i\omega_* + k_y v_{Ay})(k_y k_\perp^2 v_{Ay} - i(k_y^2 - k_x^2)\omega_*)}{\omega^2 - k_x^2 c_B^2 - \omega_H^2 + (k_y^2 - k_x^2)c_{B1}^2 + 2ik_y^2 c_{B1} v_*}, \tag{7}$$

which is the third-order equation for the frequency ω. Here $\vec{k}(k_x,k_y,0)$ is the wave-number, $\alpha = en\rho^{-1}\partial B_{0z}/\partial y = -2enB_{eq}\cos\lambda_0/\rho R < 0$, $v_{Ay} = B_{0y}/\sqrt{\mu_0\rho} = v_{AS}\cos\lambda_0$, $v_{AS} = B_{eq}/\sqrt{\mu_0\rho}$, $\omega_* = (\mu_0\rho)^{-1/2}\partial B_{0y}/\partial y$, $c_{B1} = (en\mu_0)^{-1}\partial B_{0y}/\partial y$, $v_* = k_y B_{0y}/en\mu_0$. Furthermore, $k_\perp^2 = k_x^2 + k_y^2$ and ω_H^2 is the square of the helicon (whistler) frequency, i.e. $\omega_H^2 = \omega_{cy}^2 k_y^2 k_\perp^2 c^4/\omega_p^4$, where $\omega_{cy} = eB_{0y}/m_i$, $\omega_p = (ne^2/\varepsilon_0 m_i)^{1/2}$ is the ion plasma frequency, c is the velocity of light and ε_0 is the permittivity of free space.

Below for the simplicity we will consider such latitudes where the terms containing $\partial B_{0y}/\partial y$ are small and thus neglected.

2. Slow MHD Waves in the E-layer

At present a large amount of collected data verifies the existence of quasi-horizontal long period (with typical time scales 0.5-2 h) waves in the ionospheric E-layer propagating at distances up to tenths of thousands of kilometers with the velocity 1-2 km/s. These perturbations are known as slow MHD waves (2).

The slow MHD waves are insensitive to the Coriolis force as well as to the latitudinal gradient of the geomagnetic field. Decomposing the frequency ω into real and imaginary parts, $\omega = \omega_0 + i\gamma (\gamma << \omega_0)$, in this limiting case we find from the dispersion Eq. (7)

$$\omega_0 = (k_y^2 v_{AS}^2 \cos^2 \lambda_0 + \omega_H^2)^{1/2}, \qquad \gamma = -\Lambda \frac{k_y^2 v_{AS}^2 \cos^2 \lambda_0}{2\omega_0^2}. \tag{8}$$

In the long wavelength limit, when $k_\perp^2 c^2 / \omega_p^2 << \rho_i / \rho$ ($\rho_i = nm_i$), the waves propagate as slow Alfven, SA waves

$$\omega_0 = k_y v_{AS} \cos \lambda_0, \qquad \gamma = -\frac{\Lambda}{2}, \tag{9}$$

exhibiting a weak damping due to Rayleigh friction.

In the short wavelength limit the perturbations propagate as helicons (whistlers), i.e.

$$\omega_0 = \omega_H = \frac{\omega_{cy} k_y k_\perp c^2}{\omega_p^2}, \qquad \gamma = -\frac{\Lambda \rho_i \omega_p^2}{2\rho k^2 c^2}. \tag{10}$$

The existence of slow MHD waves with speeds of the order of 1-2 km/s in the dynamo region (2) cannot be explained in terms of ordinary atmospheric gravity waves (AGW) since their typical speeds at ionospheric altitudes do not exceed 700 m/s. Although these speeds are larger than those for AGWs in the ionosphere, for ordinary MHD type waves they are still small. The physical reason for such properties of the MHD perturbations in the ionosphere is that the plasma in the E-region is not completely frozen into the magnetic field. Due to the fact that the ions are completely dragged by the neutral particles ($\vec{v} = \vec{v}_i$), any perturbation that arises in the ionized component immediately exchanges energy with the neutral component and thus starts to propagate with an Alfven speed that is loaded by the heavy and dense neutral population, i.e. with the speed $B_{0y} / (\mu_0 \rho)^{1/2}$. The value of that decelerated Alfven speed is apparently much smaller than that for E-layer $\rho_i / \rho \approx n / N \approx 10^{-8} - 10^{-9}$ and owing to this fact the loading effect is quite substantial. As one sees from Eq. (9) the phase velocity of the SA wave is $v_{ph} = \omega_0 / k_y = B_{0y} / (\mu_0 \rho)^{-1/2} = v_{AS} \cos \lambda_0$. For typical values of the neutral particle number density N in the ionospheric E-layer, $N = (10^{18} - 10^{19}) m^{-3}$, and $B_{eq} = 0.6 G$ at middle latitudes, we obtain $v_{ph} \approx 1$ km/s. One can also estimate the typical wavelength to $\lambda \sim 2\pi c \omega_p^{-1} (\rho / \rho_i)^{1/2} \sim 10^4 km.$.

Thus, the slow MHD waves with phase velocity 1-2 km/s (2) can be identified with the SA waves that smoothly convert to helicons governed by the neutral component of the E-layer. According to Eq. (9) they propagate northwards along the meridian, induced by the y-component of the geomagnetic field.

3. Fast and Slow EM Planetary Modes

For wave perturbations with periods of the order of a few hours and more, the effects due to the inhomogeneity of both the Coriolis force and the latitudinal gradient of geomagnetic field becomes

inevitably important. In order to exclude the slow MHD waves from our further consideration, we get $k_y = 0$. Then from the dispersion relation (7) we find

$$\omega_0 = \frac{1}{2}[k_x c_B - \frac{\beta}{k_x} \pm \sqrt{(k_x c_B + \frac{\beta}{k_x})^2 + 4\alpha c_B}], \qquad \gamma = -\frac{\Lambda}{1 + \alpha c_B (\omega_0 - k_x c_B)^{-2}}, \tag{11}$$

where $\alpha c_B > 0$, and thus the expression in the square root is always positive.

In the short wavelength limit, when the condition $k_x^2 >> \beta / |c_B|$ is satisfied, from Eq. (11) one finds simplified dispersions for the fast

$$\omega_0^+ = k_x c_B (1 + \frac{\alpha}{k_x^2 c_B}), \qquad \gamma^+ = -\Lambda \frac{\alpha}{k_x^2 c_B} \tag{12}$$

and slow (Rossby type) modes

$$\omega_0^- = -\frac{\beta + \alpha}{k_x}, \qquad \gamma^- = -\Lambda. \tag{13}$$

Here the value $\beta + \alpha$ represents the generalized Rossby parameter where α corresponds to the additional contribution due to the Hall effect (the α-effect). Since $\alpha < 0$, the Hall effect leads to a deceleration of the Rossby waves in the E-layer due to the interaction with the ionized ionspheric component. We note that in the dynamo-region the β and α terms are comparable in value, i.e. $\beta \approx -\alpha \approx 10^{-11}\, m^{-1} s^{-1}$. One can easily verify that the dispersion relation (13) is identical to that for the hydromagnetic gradient (HMG) mode (9) and to those for the so-called magnetized Rossby waves (10), which represent, in a sense, the hydromagnetic analogue of the traditional Rossby wave.

The fast mode, described by the dispersion relation (12), is an additional new mode which has an EM origin and which can exist only in the presence of the latitudinal gradient of the magnetic field which is inevitably inherent in a dipole type magnetic configuration such as that of the Earth's magnetosphere. At middle latitudes the mode propagates practically without damping ($\gamma^+ << \Lambda$) along the parallel from the east to the west ($v_{ph}^+ = \omega_0^+ / k_x = c_B < 0$). Since the phase velocity of the fast waves c_B is inversely proportional to the charged particle number density n, the phase velocity of this mode during night-time conditions should exceed the value at the day side by two orders of magnitude. Taking the number density of the charged particles in the E-region to be $n \sim 10^{10} - 10^{11}\, m^{-3}$ we find for the day-time conditions $v_{ph}^+ = c_B \approx -0.5 - 5\, km/s$. When the wavelength varies from 10^3 to 10^4 km the period of the fast mode $T^+ = 2\pi / \omega_0^+$ changes from 2 to 20 min during night-time and from 20 min to 3 h during day-time.

In the long wavelength limit, when $k_x^2 << \beta / |c_B|$ the dispersion relation (11) for the two modes reduces to

$$\omega_0^+ = k_x c_B (1 + \frac{\alpha}{\beta})(1 - \frac{k_x^2 \alpha c_B}{\beta^2}), \qquad \gamma^+ = -\Lambda \frac{\alpha k_x^2 c_B}{\beta^2} \tag{14}$$

for the fast mode and

$$\omega_0^- = -\frac{\beta}{k_x}(1 + \frac{\alpha c_B k_x^2}{\beta^2}), \qquad \gamma^- = -\Lambda \tag{15}$$

for the slow mode.

From Eqs. (14) and (15) we conclude that the damping of the fast mode is considerably weaker than that for the slow mode. The dispersion relation for the fast mode (14) is similar to Eq. (12). However, in the long wavelength limit it is substantially influenced by the β- and α-effects.

The dispersion relation for the slow mode (15) is similar to Eq. (13) but contains the additional small term $k_x c_B$ that originates from the fast mode. Thus, in this limiting case both modes are interconnected. For typical values of the parameters of the E-layer we find that $c_B \sim -5\times10^2 - 10^3$ m/s.

DISCUSSION AND CONCLUSIONS

In the present paper it has been shown that the dynamo region (E-layer) of the ionosphere with its S_q current and wind system is capable to sustain a wide class of low-frequency wave perturbations. Among them are the SA waves. In the long wavelength limit they propagate along the meridian with a decreased Alfven speed loaded by the dense neutral component. The reason for that loading is that the ions in the E-layer are completely dragged by the neutral particles. Owing to that fact, any perturbation in the ionized components is immediately transferred to the neutral component. In the short wavelength limit these waves smoothly convert to helicons or gyrotropic waves. The SA waves have typical periods of 0.5-2 h and wavelengths of the order of 10^4 km. The typical phase velocities of these waves are of the order of 1-2 km/s.

With the decrease in the wave frequency the effects due to the latitudinal gradient of the Coriolis and Ampere forces become important. This leads to the fast and slow EM planetary waves described by the dispersion relation (11). The period of these waves stretches from a few hours to tenths of hours. In the short wavelength limit, the slow EM mode (see Eq. (13)) reduces to the well-known HMG mode (9) which serves as a hydromagnetic analogue of the ordinary Rossby wave in a rotating atmosphere. This mode can propagate westward or eastward along the parallel and can be excited by the dynamo electric field. The frequency of the slow mode varies in the range $10^{-5} - 10^{-4}\ s^{-1}$ whereas its wavelength is of the order 10^3 km and larger, and the phase velocity is of the order of the velocity of the local winds, i.e. ~1-100 m/s. In the long wavelength limit this wave couples to the fast mode. The damping of the slow mode is associated with the Rayleigh friction of the layers of the local ionosphere with a damping rate of the order of $10^{-5}\ s^{-1}$. The slow mode can produce a substantial change in the magnetic field. This follows directly from Ampere's law, $\nabla\times\delta\vec{B} = \mu_0\vec{j}$, and the expression for the electric current in the dynamo region, $\vec{j} \approx -i\omega en\vec{\xi}$, where $\vec{\xi}$ is the perpendicular plasma displacement. For the vertical component of the perturbed magnetic field one can use the estimate $\delta B_z \approx en\mu_0\xi_x\omega/k_x$, where ξ_x is the x-component of the plasma displacement. Taking $n = 10^{11} m^{-3}$ and $\omega/k_x \approx 10 - 10^2 m/s$ for a 10-km plasma displacement we find that $\delta B_z \approx 1 - 10\ nT$ within the E-layer. Thus, the slow mode in the dynamo region can be accompanied by a substantial variation of the geomagnetic field which has the same order of value as the geomagnetic pulsations, induced, for example, by the S_q current in the dynamo region.

On the contrary the fast mode, described in this limit by the dispersion relation (12) , can propagate practically without damping. The phase velocity of this mode is proportional to the latitudinal gradient of the magnetic field. Clearly, due to the short period, this mode does not belong to the Rossby or HMG type waves. The electrons in the E-layer for this motion are frozen in the magnetic field. In the fast EM mode, similar to helicons, the plasma oscillates with practically immobile ions and neutral particles, i.e. $\bar{\nu}_e >> \bar{\nu}_i = \bar{\nu}$. The fast electromagnetic wave with the dispersion $\omega = k_x c_B$ is driven by the latitudinal gradient of the geomagnetic field gradient and the Hall effect and represents a variation of the vortical electric field. It propagates westwards along the parallels with a speed of a few km/s. This mode has a relatively high frequency of the order of $10^{-1} - 10^{-3}\ s^{-1}$ and thus it is not influenced by the Coriolis force. The typical wavelength of the mode is of the order of $10^3\ km$ or longer. Both in

the long and short wavelength limit it is weakly damped. Since the phase velocity of the fast mode is much larger than that for the slow mode, a similar estimate for the magnitude of δB_z gives a value of the order of $10^3\ nT$.

References

(1) E. Gossard and Y. Hooke; "Waves in the Atmosphere", Elsevier, Amsterdam (1975).
(2) V.M. Sorokin and G.V. Fedorovich; "Physics of Slow MHD Waves in the Ionospheric Plasma", Nauka, Moscow (1982).
(3) M. Hayakawa (Edit); "Atmospheric and Ionospheric Phenomena Associated with Earthquakes", Terra Sci. Publ. Comp., Tokyo (1999).
(4) L.D. Shaefer, D.R. Rock, J.P. Lewis, et al.; "Detection of Explosive Events by Monitoring Acoustically-Induced Geomagnetic Perturbations", Lawrence Livermore Laboratory, CA USA, 94550, Livermore (1999).
(5) L.A. Haykowicz; Planet. Space Sci., 39, 583 (1991).
(6) Y. Kamide; "Electrodynamic Processes in the Earth's Ionosphere and Magnetosphere", Kyoto Sangyo University Press, Kyoto (1988).
(7) R.E. Dickinson; J. Atmospheric Sci., 26, 73 (1969).
(8) J.R. Holton; "An Introduction to Dynamic Meteorology", Academic Press, New York (1979).
(9) I. Tolstoy; J. Geophysical Research, 72, 1435 (1967).
(10) T.D. Kaladze and L.V. Tsamalashvili; Physics Letters A, 232, 269 (1997).

Nonrelativistic Plasma Electronics

I.N. Onishchenko
National Science Center "Kharkov Institute of Physics and Technology"
Academic St. 1, 61108 Kharkov - Ukraine
onish@kipt.kharkov.ua

ABSTRACT

The main physical principles for the elaboration of plasma and hybrid plasma-filled microwave devices based on the beam-plasma interaction are formulated. The theoretical and experimental results of the investigations of electromagnetic oscillations excitation in beam-plasma systems carried out in National Science Center "Kharkov Institute of Physics and Technology" are presented. The electrodynamics of plasma-filled slow wave structures, nonlinear stage of beam-structure interaction, and stochastization mechanism are studied. Some experimental installations created are described and obtained results on power level, efficiency, and spectra are represented.

Key Words: ***Beam-Plasma Interaction, Slow-Wave Structure, Generator, Electrodynamics, Stochastization***

INTRODUCTION

Prediction of the beam-plasma instability (1,2), discovery of the beam-plasma discharge (3-5), and investigation of plasma waveguide electrodynamics (6) have laid the foundation of the new branch of plasma physics – the plasma electronics. Numerous theoretical and experimental investigations carried out in NSC "KIPT" on this subject brought to the elaboration of the new kind of HF-devices of regular and stochastic electromagnetic oscillations, so called beam-plasma generators and amplifiers (BPG). The physical principles for the creation of such devices were firstly formulated in NSC "KIPT" in 1965. Only later they were partly published by the researches of NSC "KIPT" (7-9) and by authors from other places (10-11).

The theoretical efforts were undertaken to the investigation of plasma filled conventional slow wave structures (hybrid structures) electrodynamics, stochastization mechanisms, and spectrum evolution in such strong nonlinear and nonequilibrium systems as BPG's are.

Experiments were performed both for relativistic and nonrelativistic electron beams. The first ones in plasma waveguides (12,13) and in corrugated vacuum waveguides, filled with plasma (14,15) showed the impressive enhancement of the efficiency. "KIPT" experiments on nonrelativistic beams interaction with hybrid plasma structures were firstly represented in (16) demonstrating some merits of beam-plasma devices. The essential advanced elaboration and technological perfection of amplifier type were made in VEI (17). Some experiments with BPD were fulfilled in MRTI (18).

The idea of using plasma as a slow wave structure concludes to the high gain parameter in beam-plasma interaction reaching to 15 dB/cm (19). The frequency of excited oscillations can be tuned simply by plasma density changing. As an electromagnetic noise source, the beam-plasma system is a good approach due to the strong nonlinearity and nonstationarity of plasma, needed for dynamic chaos development, and abundance of plasma eigen modes. The problem of extracting of excited plasma oscillations is solved comparatively simply for the relativistic beam as their phase velocity is close to the speed of radiated electromagnetic waves (12-15). In the nonrelativistic case, more attractive one because of compact electron beam sources, plasma oscillations are trapped in plasma. So, special

measures and tools should be used to match the electrodynamics of nonrelativistic beam-plasma system with vacuum waveguide tract or open space. For this goal the conventional slow wave structures filled with plasma were used (20,21). As it was established in (7) optimal configuration is the partial filling with plasma, i.e. plasma is produced (for example by electron beam collisions with neutral gas) only in beam transit channel. It provides the interaction of the electron beam with vacuum eigen mode modified with plasma in such a way that the wave field in plasma has volumetric topography and, hence, beam-wave coupling is effective and gain parameter is high. Electron beam is efficiently interacting with plasma in transit channel and excited HF-power is being extracted and transported in surrounding vacuum region of waveguide.

The main advantages of the beam-plasma devices using plasma-filled slow wave structures are:

- possibility of power increase by rising of the vacuum limit current due to the compensation of the beam space charge;
- volume character of the excited wave that leads to the considerable increasing of the growing rate and consequently efficiency enhancement in comparison with the vacuum case;
- tuning of the excited frequency by plasma density changing;
- possibility to realize the interaction in a large volume and, hence, to obtain high power output;
- great number of the eigen modes in plasma-filled structures vary and enrich obtained spectra without losing the possibility of their governing.

THEORY

Electrodynamics (7, 16, 22, 23)

Theoretical investigations involved the study of the electrodynamics of hybrid plasma structures and stochastization processes. The gain, start current, nonlinear saturation and efficiency, and thresholds of bifurcation should be estimated. Some conventional slow wave structures (SWS) – helix, chain of coupled cavities, corrugated waveguide, ring-bar SWS, sequence of rings, and coaxial grate – were investigated under plasma filling to apply for various frequency bands. The main feature of these devices filled with plasma is the essential modification of dispersion properties and field topography that leads to the efficiency enhancement, activation of dynamic chaos evolution, and enriching of excited spectra. Below we present theoretical investigations of the hybrid SWS consisting of the chain of inductively coupled cavities in which the transit channel for electron beam is filled with plasma. The cross-section of this structure is represented in Fig. 1.

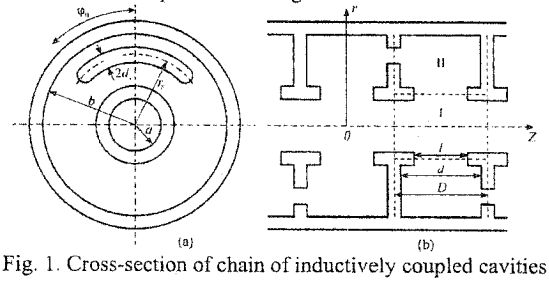


Fig. 1. Cross-section of chain of inductively coupled cavities

Dispersion equation (DE) for such hybrid structure was obtained in (22,23) by the method of partial regions (24) and the theory of the slit antenna (25). Due to the periodicity of the structure and plasma filling a great number of radial plasma waves (Trivelpiece-Gould modes) multiplied by system periodicity (spatial Flouquet modes) cover densely the plane longitudinal wave vector-frequency (k_z, ω) in the frequency region $(0 - \omega_p)$, where ω_p is the plasma frequency. In Fig. 2 the noninteracting dispersion curves corresponding to the mentioned modes are represented on (k_z, ω) plane only for four radial modes (to illustrate of the phenomenon). The interaction of electron beam with such structure leads to the excitation of so-called "dense" spectrum (26).

The left side of obtained dispersion equation in absence of the beam (cold system) $F(\omega)=0$ is pictured in Fig. 3 as a function of frequency ω at fixed geometric parameters and plasma frequency $\omega_p = 0.5\ \pi\ c/D$ (c is speed of light, D is structure period). It is seen the abundance of spatial

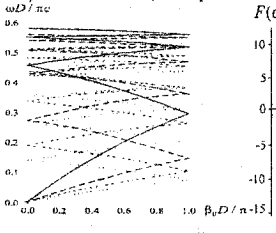


Fig. 2. Eigen radial and spatial modes

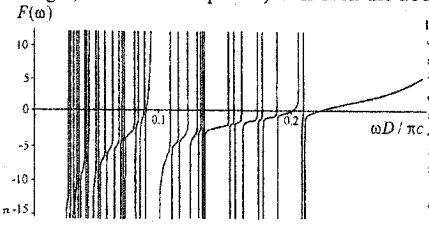


Fig. 3. Dependence of function F of DE upon frequency

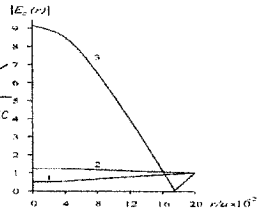


Fig. 4. Radial topography of ε_z

harmonics of many radial modes of the low frequency plasma wave ($\omega < \omega_p$) and clearly expressed principal TE-mode of the vacuum coaxial resonator, modified by plasma assistance. We should note that the eigen frequencies of noninteracting vacuum modes (the roots of $F(\omega)$) become the poles with vertical lines-asymptotes, when modes interact and the roots of $F(\omega)$ displace. It is important that roots displacement is also caused by plasma presence and depends on plasma density. It means that excited frequency can be tuned by plasma density changing. The value of the displacement from vacuum noninteractive case for the principal mode can be seen in Fig. 3 as the most right cross point of the dispersion curve with a small incline.

The evolution of the radial topography of the longitudinal field ε_z inside transit channel filled with plasma when plasma density grows is shown in Fig. 4. The curves *1,2,3* correspond to the plasma frequencies $\omega_p = (0;0.5;1.5)\ \pi\ c/D$. Volume property of the field inside the channel is evident for higher plasma densities.

Stochastization (27-30)

The preliminary experimental of beam-plasma HF-generator with the SWS described above have shown the following scenario. With beam current growth the change of generator operation regimes takes place: regular monochromatic generation is being changed by automodulation regime with a lot of satellites and noise component, which makes each spectral component wider. With further increase of beam current "natural" width of spectral lines becomes so wide that satellites overlap. Noise spectrum becomes uniform, its band coincide with the passband of SWS. Such evolution of spectra is typical for the majority of HF-devices (TWT, gyrotron etc.), however such peculiarities as spectral line widening and uniformity of noise spectrum indicate that hybrid SWS possesses new qualities not typical for vacuum devices. Stochastization mechanism in vacuum devises is based on phenomenological point map, that is treated as amplitude transformation for synchronous wave after one propagation along feed-back circle. Meanwhile the conception of "function of mapping" for amplitude can be introduced exactly only for monochromatic signal as such function depends strongly on signal frequency in amplification band. So for description of noise regime with wide band the new theory (functional map) was required, that would be based on the peculiarities of solutions for nonstationary equations of TWT with delayed feedback. Nonstationary equations of TWT-amplifier have two families of characteristics. Information from the entrance of amplifier of L length transmitted to its exit by beam particles and synchronous wave with velocities v_b and v_g, correspondingly. So the output signal $\varepsilon_{output}(\tau)$ is determined by input signal on the time interval $\Delta t = L(v_b - v_g)/(v_b v_g)$. By other words, output signal $\varepsilon_{output}(\tau)$ is not the function, as it was supposed in point map, but a functional of input signal $\varepsilon_{input}(\tau)$.

The plasma-beam microwave generator is considered as a circular system that consists of non-linear amplifier of HF-oscillations and feedback that maintains the excitation of the whole system. Non-linear amplifier is TWT, in which an electron beam interacts with synchronous wave of the structure. At analytical investigation we use the results, published in (27-30), and treat, in particular, the theory of circular generator with TWT as a non-linear amplifier. We consider also the influence of low-frequency non-stationary processes in plasma on a signal dynamics. The example of spectra of stochastic generation, obtained without and with taking into account the self consistent dynamics of plasma are pictured in Figs 5 and 6, correspondingly.

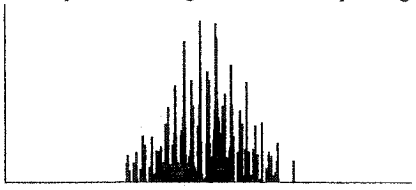


Fig. 5 Spectrum without plasma dynamics.

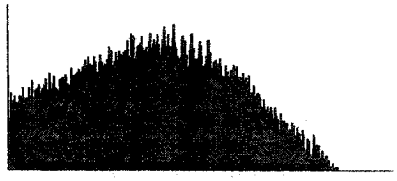


Fig. 6 Spectrum with plasma dynamics

The observation of spectrum enhancement due to low-frequency plasma instabilities may be difficult because this phenomenon is possible in the hybrid plasma-filled slow-wave structure if the microwave power is sufficiently high and generator operates in stochastic automodulation regime. Therefore the investigation of it is easily carried out in the regime in which the monochromatic external signal is applied to the TWT-generator input. In this case the generator may be driven from stochastic regime to monochromatic one without essential power change. The low-frequency instabilities may be identified as low-frequency oscillations of the phase shift $\Delta\alpha(\tau)$. The spectrum of such oscillations determines spectral line form of the plasma-beam microwave generator at high level of the power.

So due to the sufficiently large growing rate in the hybrid structure the threshold of stochastic generation are lower. The stochastization mechanism at high power levels is the alternating turbulence. Besides, the presence of a great number of radial modes and their space harmonics and also low frequency plasma motion (ion. sound, density modulation etc.) leads in the nonlinear regime to more homogeneous spectra of the stochastic automodulation comparatively to the vacuum case.

EXPERIMENT

Results of centimeter generation

Experimental realization of the generation in centimeter range has been carried out with slow wave structure of chain of coupled cavities (CCP) type with plasma filled transit channel. The scheme of the device is represented in Fig. 7.

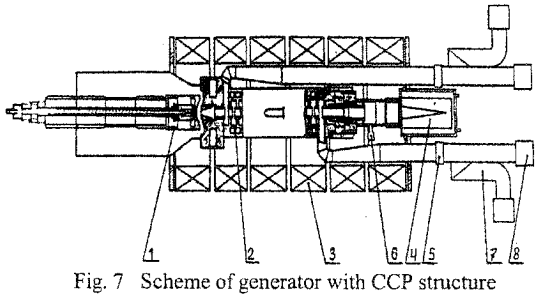


Fig. 7 Scheme of generator with CCP structure

Electron gun (1), injecting beam current 10 A at voltage 40 keV, is matched with compact high efficient ion-getter pump maintaining the pressure 10^{-6} Torr; slow wave structure (2) composed of

cupper cavities, inductively coupled with slits of lentil form, and drift tubes was placed in a solenoid (3) producing magnetic field 3 kG; cooled collector (4) was capable to dissipate the power up to 260 kW; the power output was realized by the waveguide of 74×36 mm sizes wideband sapphire window (5); the plasma of density $5 \cdot 10^{10} - 10^{12}$ cm^{-3} was produced by beam-plasma discharge in the transit channel under gas filling. The standing wave coefficient was 1.5 – 2.0 over the frequency band 2.4 – 5 GHz. The electron gun has the protection from the ion bombardment.

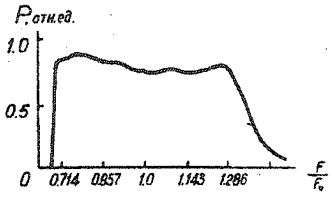


Fig. 8. Power spectrum

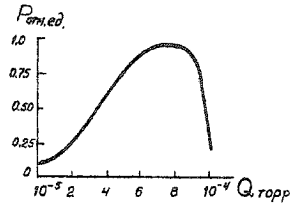


Fig. 9. Dependence of power on pressure

Start current was 100 mA and the stochastization threshold was 1.0 A in a good agreement with calculations.. With current increasing the generated frequency band overlapped the whole passband of the CCP structure.. Frequency spectrum is wide and homogeneous in the band of about a half of octave (Fig.8). The efficiency enhancement under plasma assistance and the existing of optimum of plasma density, that was discussed in theory is demonstrated in Fig.9.

The efficiency reached 40% for the optimum conditions in continuous operations. Varying phase velocity by the corresponding structure geometry the electronic efficiency was obtained 50% and output power 40 kW. For the pulsed operation during 4 ms the power 100 kW was achieved.

Results of decimeter generation

In decimeter range of wavelength the BPG of stochastic oscillations has been elaborated and created using plasma -helix structure with a single or modified contra-wound helix circuits that are operating in quasi continuous or continuous regimes.

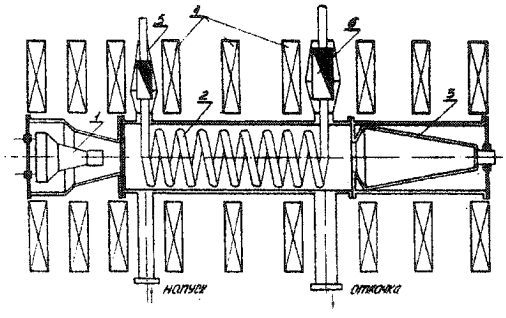


Fig. 10. Scheme of generator with helix structure

The generator (Fig.10) is consist of the following units: 1 — electron gun, 2 — helix structure, matched with beam-plasma interaction region, 3 — collector, 4 — solenoid, 5 — HF-load, 6 — HF power register. The beam current is 13 A, beam energy — 15 keV, magnetic field strength — 1100 G, plasma density — $6 \cdot 10^{10}$cm^{-3}. The total generated power was 80 kW and efficiency was 40%.

REFERENCES

(1) A.I.Akhiezer, Ya.B.Fainberg, Dokl. Acad. Sci. USSR, Vol.69, No.4, pp.555-556, 1949

(2) D.Bohm, E.Gross, Phys.Rev., Vol.75, No.12, pp.1861-1876, 1949

(3) A.K.Berezin, Ya.B.Fainberg, G.P.Berezina et al., Atomnaya Energija, Vol.11, No.6, pp.493, 1961.

(4) I.F.Kharchenko, E.A.Kornilov, Ya.B.Fainberg et al., J. Tech. Phys., Vol.31, No.7, pp.761, 1961.

(5) W.D.Getti, L.D.Smullin, J.Appl. Physics, Vol.34, No.12, pp.3421-3429, 1963.

(6) Ya.B.Fainberg, M.F.Gorbatenko, J. Tech. Phys., Vol.29, No.6, pp.549-562, 1961.

(7) Ya. B.Fainberg et al., Dokl. Acad. Sci. Ukr. SSR, Ser. A, No.11, pp.56, 1990.

(8) Electrodynamics of Helix-Plasma Structures /A.K.Berezin, V.A.Buts, I.K.Kovalchuk et al., Kharkov, 1991, Prepr./Acad. Sci. of Ukraine. KPTI; KPTI 91-52.

(9) E.A.Kornilov et al., Proc. IV Symp. On High Current Electronics, June 21-30, 1992, N.Novgorod: Gyperoks, 1992, p.132.

(10) K.G.Gureev, N.I.Karbushev, A.I.Lisitsin, et al., Proc. 8th Intern. Conf. on High Power Particles Beams, Novosibirsk, July 2-5, 1990. Singapure: world Sci., 1990, Vol.2, p.1173.

(11) V.I.Perevodchikov, M.A.Zavjalov, V.E.Martynov et al., Proc. 9th Intern. Conf. on High Power Particles Beams, Washington, May 25-29, 1992, p.1318.

(12) Theoretical and Experimental Investigations of Plasma Acceleration Methods/ A.K.Berezin, N.M. Zemlyanski, Ya.B.Fainberg et al, Kharkov, 1972, Prepr./Acad. Sci. USSR. KPTI; KPTI 72-07.

(13) M.V.Kuselev, A.A.Rukhadze, M.S.Rabinovich et al., JETP, Vol.63, pp.1358-1367, 1982.

(14) Yu.Tkach, Ya.B.Fainberg, I.I.Magda et al., Physica Plasmy, Vol.5, p.5, 1979.

(15) Y.Carmel, W.R.Low, T.M.Antonsen et al., Phys. Rev. Lett., Vol.62, pp.20, 1989; Proc. Inern. Workshop "Strong Microwaves in Plasmas", N.Novgorod, Aug. 15-22, 1993, p.34.

(16) A.N.Antonov, A.K.Berezin, Yu.P.Bliokh et al., "To the electrodynamics of the hybrid plasma-waveguide structures (theory and experiment)",Proc. 10th Intern. Conf. on High Power Particles Beams, San Diego, June 20-24, 1994, p.6-5.

(17) M.A.Zavjalov, V.E.Martynov, L.A.Mitin et al., ibid. p.40.

(18) K.G.Gureev, N.I.Karbushev, A.I.Komov et al., ibid. p.15.

(19) D.I.Trubetskov and L.A. Pishchik , "Nonrelativistic plasma HF-devices, based on Cherenkov radiation", Physica Plasmy, Vol.15, No.3, pp.342-353, 1989.

(20) M.Allen, C.Biechler, P.Chorney, "Tubes pour hyperfrequences", Fravaux du 5e Cong. Internat. Paris, 14-18 September 1964. P. 437.

(21) G.A.Bernashevski, E.V.Bogdanov, V.Ya. Kislov, E.S.Chernov, "Plasma and electron HF-amplifiers and generators", book Moscow: Sov. Radio, 1965.

(22) Ya.B.Fainberg et al., Proc. IX Winter School-Seminar on UHF Electronics and Radiophysics, Saratov, January 12-21 1993. Saratov, State Educational Centre, 1993, p.66.

(23) Ya.B.Fainberg, Yu.P.Bliokh, M.G.Lyubarskii et al., "Electrodynamics of Hybrid Plasma Slow-Wave Structures", Plasma Physics Reports, Vol.20, No.7-8, pp.681-690, 1994.

(24) A.D.Grigoryev, V.B.Yankevich, book "Resonators and slow wave UHF systems" Moscow: Nauka, 1984.

(25) M.L.Levin, J. Tech. Phys., Vol.21, No.7, pp.787-794, 1951.

(26) N.R.Lou, Y.Carmel, T.M.Antonsen et al., "New modes in a plasma with periodic boundaries: The origin of dense spectrum". Phys. Rev. Lett. Vol.67, No.18, pp.2481-2484, 1991.

(27) Yu.P.Bliokh, A.V.Borodkin, Ya.B.Fainberg et al., Izvestiya Vuzov. Ser. Appl. Nonlinear Dynamics, Vol.1, No.1/2, pp.34-49, 1993.

(28) Yu.P.Bliokh, M.G.Lyubarskii, L.A.Mitin et al., "Study of Signal Stochastization Mechanism in Plasma-Beam Generators", Physica Plasmy, Vol.20, No.7-8, pp.747, 1994.

(29) A.N.Antonov, A.K.Berezin, Yu.P.Bliokh et al., Ukr. J. of Physics, Vol.40, No.5, pp.413, 1995.

(30) Yu.P.Bliokh, V.A.Buts, M.M.Zemlyanski et al., Ukr. J. of Physics, Vol.43, No.9, pp.1167, 1998.

(31) M.Feigenbaum, Lecture Notes in Phys. Vol. 179, pp.131-148, 1983.

Tokamaks

Measurement of Electron Temperature Fluctuations with Tunnel Probe in the CASTOR Tokamak

J. P. Gunn 1), J. Stöckel 2), T. Van Rompuy 4), J. Adámek 2), P. Balan 5), O. Bařina 3), P. De Beule 4), I. Ďuran 2), R. Hrach 3), M. Hron 2), R. Pánek 2), R. Schrittwieser 5), G. Van Oost 4), M. Vicher 3), F. Žáček 2)

1) Association EURATOM-CEA sur la fusion contrôlée, Saint Paul Lez Durance, France
2) Institute of Plasma Physics, Association EURATOM-IPP.CR, Prague, Czech Republic
3) Charles University in Prague, Faculty of Mathematics and Physics, Czech Republic
4) Department of Applied Physics, Ghent University, Belgium
5) Institute for Ion Physics, University of Innsbruck, Austria
Jamie.Gunn@cea.fr

ABSTRACT

The tunnel probe is a new kind of Langmuir probe for use in the tokamak scrape-off layer. Two-dimensional kinetic analysis of the ion current distribution on the concave conductors is used to calibrate the probe for making fast dc measurements of ion flux and electron temperature. Qualitative agreement with classical Langmuir probe measurements is found, but the electron temperature given by the tunnel probe is several times lower. This discrepancy can be caused by secondary electron emission, or the presence of suprathermal electrons. Strong reduction of ion flux and electron temperature fluctuations is observed during electrode biasing.

Key Words: Plasma Diagnostics, Electrostatic Probes, Tokamak Edge Plasma

INTRODUCTION

The tunnel probe (TP)[1] is a new kind of Langmuir probe (LP) for use in the tokamak scrape-off layer. It consists of a hollow conducting tunnel a few millimetres in diameter and typically 5 mm deep that is closed at one end by an electrically isolated conducting back plate (see schematic in Fig. 1). The tunnel was split into two electrically isolated segments in order to study the axial distribution of ion current, but in this paper we only consider the total current flowing to the two segments shorted together. The conductors are biased negatively with respect to the tokamak chamber to collect ions and repel electrons. The tunnel axis is parallel to the magnetic field. Plasma flows into the open orifice and the ion flux is distributed between the tunnel and the back plate.[2] The self-consistent interaction between the charge distribution and the electric potential inside the tunnel gives rise to two concentric layers of strong radial electric field having different characteristic radial decay lengths. The first is the positively charged electrostatic Debye sheath that lies adjacent to the tunnel surface and shields the plasma column from most of the applied probe potential. It scales as the square root of the ratio of electron temperature T_e to local electron density n_e. The second layer is the quasineutral magnetic sheath that scales as the square root of T_e. This magnetic sheath owes its existence to the radial polarization drift of ions.[3] The magnetic sheath is broader than the Deybe sheath. The structure of the electric field

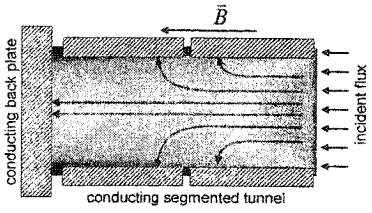


Fig. 1. Schematic of TP. The current collected by each of the three conductors is monitored separately. The ion guiding center trajectories are shown by black arrows.

layers determines the current path inside the tunnel. Ions that enter the strong radial electric field gradient in either of these two regions are demagnetized and attracted to the tunnel surface. Electrons remain strongly magnetized under all circumstances.

KINETIC MODELING OF THE TUNNEL PROBE

The current flow to the probe collectors is calculated by the two-dimensional kinetic code XOOPIC[4] in cylindrical geometry for a range of T_e and incident parallel ion current density $J_{//,i}$ (Fig. 2). Three parameter regimes have been identified. The first and most useful parameter regime occurs when $J_{//,i}$ is sufficiently high that the Debye sheath is much thinner than the tunnel radius (greater than about 1 A/cm^2 in CASTOR conditions), the potential drop between the tunnel surface and the plasma is efficiently shielded. In that case the potential distribution and plasma fluxes inside the tunnel are insensitive to variations of the applied potential, and the residual potential drop in the quasineutral magnetic sheath should only be sensitive to electron temperature for a given magnetic field. The probe can thus be operated in dc mode and therefore provides fast simultaneous measurements of $J_{//,i}$ and T_e. The ratio $R_c=I_{TUN}/I_{BP}$ increases with T_e because the magnetic sheath expands inward toward the cylindrical axis and diverts greater numbers of ions onto the leading edge of the tunnel. The analysis procedure is straightforward. One calculates $J_{//,i}$ from the sum of the two ion currents divided by the cross section of the tunnel, and their ratio is used to calculate T_e by interpolation within the numerical results. The second parameter regime occurs for intermediate values of $0.2<J_{//,i}<1.0$ A/cm^2. The density in the tunnel is low and the Deybe sheath thickness is significant with respect to the tunnel radius. The applied potential can penetrate into the plasma column, modifying the particle orbits. Simulations were performed in this regime for applied voltages of -100 V and -200 V with respect to the floating potential. For clarity we print the high voltage results only for T_e=20 eV in the figure, but the results for other temperatures behave the same way. It is observed that R_c is quite sensitive to applied voltage, as well as to the magnitude of $J_{//,i}$. Operation in dc mode is feasible in this regime but because fluctuations of floating potential, electron temperature, and ion current density all affect the current ratio, the floating potential must be measured simultaneously by small LP tips located near the tunnel entrance on the same magnetic flux surface. Finally, for extremely small $J_{//,i}<0.2$ A/cm^2, Debye shielding is weak and the potential distribution essentially is the same as the vacuum one. The current measurements give no information about $J_{//,i}$ or T_e. Fortunately such low densities only occur during the plasma current ramp-up phase at the beginning of the discharge. The typical evolution of the measurements is presented in Fig. 2 for CASTOR shot 13172. During the current ramp-up, the ratio is initially very high and the density low. The points smoothly follow the low temperature contours until the hot flat top phase when fully developed turbulence sets in.

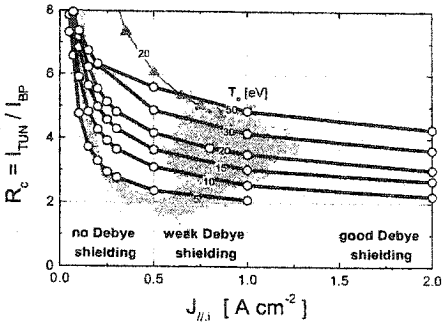


Fig. 2. The lines with open circles are simulated tunnel-to-back-plate ion current ratios for various values of $J_{//,i}$ and T_e assuming hydrogen, B=1 T, tunnel diameter 5 mm, and applied voltage -100 V. The gray points are measured (CASTOR shot 13172). Simulation results for T_e=20 eV, V=-200V are shown for comparison (full triangles).

EXPERIMENTAL VALIDATION OF THE NUMERICAL CALCULATIONS

The physics governing the TP is fundamentally different than that of a classical LP. The applied voltage on the LP is swept at 1 kHz in order to measure a restricted part of the electron distribution function. The TP, on the other hand, is biased to a fixed potential that is sufficiently negative to repel all electrons. The temperature of the electrons is measured even though none are collected. It is necessary to compare the two methods. In order to investigate the validity of the simulation results we built a prototype TP and installed it on the top of the CASTOR tokamak on a manipulator that could be displaced radially between discharges. Two copper tunnels were implemented, one facing the ion direction and the other the electron direction. The tunnel diameter was 5.0 mm and its depth was 5.0 mm. For this experiment (shots 16200-16221) the probe axis was aligned with the magnetic field and a radial scan was performed starting at r=91 mm and reducing the probe radius by 2 mm between shots. The voltage on all conductors was swept in order to measure current-voltage (I-V) characteristics. The averaged data that were acquired by the ion side TP on shots 16204 and 16214 during the bias or ohmic phase of the discharge, respectively, are shown in Fig. 3. On shot 16204 the probe was situated at r=83 mm, roughly the radius of the poloidal limiter (r=85 mm) and on shot 16214 it was placed at r=63 mm, near the radius of the biasing electrode (r=60 mm).

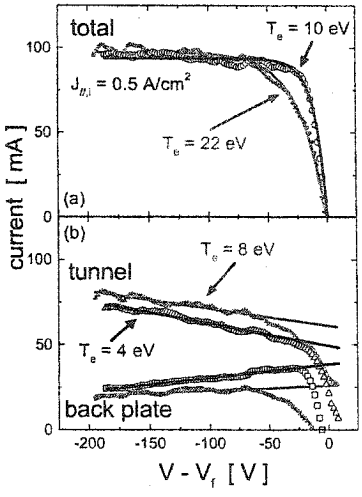


Fig. 3. (a) Total current collected by swept TP for two values of T_e. (b) Distribution of the current between the tunnel and back plate. The TP method gives lower T_e than the swept LP.

We focus on these specific data because $J_{//,i}$ was found to be roughly 0.5 A/cm^2, a value that we simulated with the XOOPIC code, while the electron temperatures differed by about a factor of two. The sum of the currents collected by the back plate and tunnel segments gives an I-V characteristic that is equivalent to that of an ideal disk probe with cross section equal to that of the tunnel entrance. The ion current for highly negative voltages is almost perfectly saturated, demonstrating the immunity of concave probes to sheath expansion effects, a problem that has always plagued convex LP applications. An exponential function of the form

$$I = I_{SAT}\left(1-\exp\left(\frac{V-V_f}{T_e}\right)\right) \tag{1}$$

is fit to the data to obtain estimates of T_e=10 eV and T_e=22 eV using the classical swept LP technique. Then the ion current to the back plate and the total of the two tunnel segments are measured at -100 V and -200 V with respect to floating potential. From the low temperature characteristic (open symbols on the figure) the ratios of those currents are R_c=2.1 and 3.3 respectively, and interpolation within the XOOPIC results gives T_e values of 3.6 eV and 4.2 eV. From the high temperature characteristic (full symbols on the figure) the ratios are R_c=3.1 and R_c=4.1, giving T_e=9.9 eV and 7.3 eV. From each characteristic we get three simultaneous and independent estimates of T_e that may be compared. The two values derived from the TP technique agree reasonably well with each other but they are generally a few times lower than the LP value. LPs are often accused of producing falsely high T_e measurements. If the electron distribution is not thermal, a small population of suprathermal electrons may be collected, and it is the characteristic energy of those electrons to which a swept LP is sensitive.[5] Further problems can arise due to rectification of plasma fluctuations and plasma

resistivity in the current channel between the probe and the reference electrode. On the other hand, secondary electron emission from ion bombardment of copper would lead to apparently high values of back plate ion current, which would cause the TP to underestimate the electron temperature. If we assume that the LP value is correct and calculate the secondary emission coefficient γ that would be needed to make the TP agree, we find $\gamma \approx 0.5$. This value is of the correct order of magnitude if we compare with published experimental studies.[6] More XOOPIC simulations are needed to quantify the effect of additional electrons, whether they be suprathermals emitted by the plasma or cold secondary electrons emitted by the back plate, on the electric field distribution inside the tunnel.

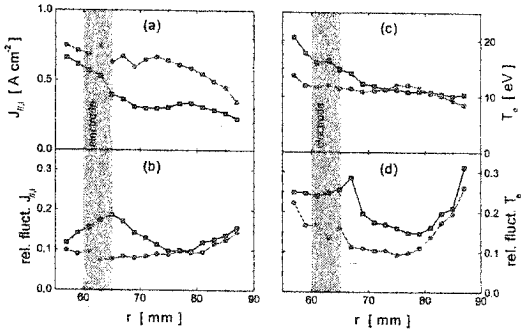


Fig. 4. Tunnel probe measurements from ion side during ohmic phase (squares) and bias phase (circles) of the discharge. The biasing electrode was placed at r=60 mm. The displayed quantities are (a) parallel ion current density and (b) its relative fluctuation amplitude, and (c) electron temperature and (d) its relative fluctuation amplitude. A secondary electron emission coefficient γ=0.5 was assumed.

The first analysis of electron temperature and ion current density fluctuations measured by the TP operating in dc mode indicates a strong reduction of the level of turbulence during electrode biasing (Fig. 4). In this experiment, the biasing electrode was placed inside the plasma (r=60 mm) and biased to +100 V. The strongest reduction is observed in the vicinity of the electrode radius with further reduction in the SOL behind the electrode.

CONCLUSIONS AND FUTURE WORK

Because of the simple geometry of theTP, it is possible to carry out precise kinetic simulations in order to calibrate it. Even with a highly idealized model, we have seen that the simulation results behave remarkably like the experimental measurements, indicating that we have correctly identified the essential physics. Further simulations including suprathermal electrons and secondary electron emission are expected to explain the discrepancy between LP and TP T_e measurements. Preliminary measurements of the radial profiles of ion current density and electron temperature fluctuations reveal a strong reduction of ion and electron turbulence in the EXB shear layer during electrode biasing.

ACKNOWLEDGEMENT

Parts of this work were performed in the frame of contracts No. 202/03/0786 and No. 202/03/P062 of the Grant Agency of the Czech Republic and by INTAS project no. 01-2056.

REFERENCES

(1) J. P. Gunn, P. Devynck, J. -Y. Pascal, J. Adámek, I. Ďuran, M. Hron, J. Stöckel, F. Žáček, O. Bařina, R. Hrach, M. Vicher, G. Van Oost, Czech J. Phys. **52**, 1107 (2002).
(2) J. P. Gunn, Phys. Plasmas **8**, 1040 (2001).
(3) J. P. Gunn, Phys. Plasmas **4**, 4435 (1997).
(4) J. P. Verboncoeur, A. B. Langdon, N. T. Gladd, Comp. Phys. Comm. **87**, 199 (1995).
(5) P. C. Stangeby, Plasma Phys. Contr. Fusion **37**, 1031 (1995).
(6) A. I. Kysljakov, J. Stöckel, K. Jakubka, Журнал Технической Физики 7, 1545 (1975).

EGYPTOR Tokamak: Modification of the Original Design Using Permanent Compensation Coils and First Results of the Breakdown Discharge

A.B. El Sisi and H. Hegazy
EGYPTOR Project, Plasma Physics Dept., NRC, Atomic Energy Authority, 13759 Enshass, Egypt

ABSTRACT

The EGYPTOR tokamak is a small device of rectangular cross section 25cm by 20cm. Modification of the original design is done by adding compensation coils connected to the toroidal field (TF) coils and ohmic heating (OH) coils. These compensation coils are used to compensate most of the stray magnetic field components that prevent a breakdown discharge. First results of the breakdown discharge are reported. A gated ICCD camera is used to obtain side view images of the visible light emitted from the plasma.

Key words: Tokamak, breakdown, stray magnetic field

INTRODUCTION

EGYPTOR is a small tokamak acquired from the Heinrich-Heine Universität Düsseldorf, Germany [1] after thirteen years from the first discharge. It was re-installed in Egypt during the end of the past decade. We have set all subsystems of the tokamak correctly and tested them successfully [2]. Breakdown in the discharge vessel, however, failed because of damage in one of the compensation coils of Ohmic heating(OH). Furthermore, the original design did not contain a return coil with the toroidal field (TF) coil to compensate the vertical field component resulting from the toroidal field. Damaged compensation coils are now replaced by new coils, and based on a recommendation by N. Brevenov and Yu. Gott[3] we added a temporary return coil with the toroidal field to compensate the obtained stray magnetic field. The coils are tested and breakdown discharges are successfully obtained at gas pressures of $3\sim5x10^{-4}$ mbar. In this paper we report details of the permanent compensation coils used and first results of the discharges.

1. Description of the EGYPTOR tokamak

Essential parts of the EGYPTOR tokamak are the stainless-steel discharge vessel, different coil systems(TF, OH, and vertical field VF), control system, and cleaning discharge system. The vessel consists of two half-torus separated by two viton O-rings. The chamber is of rectangular cross section 25cm by 20cm. The major radius (R) and the minor radius (a) are 30 cm and 10 cm, respectively. The aspect ratio is 3. Six large lateral ports and 12 smaller windows at top and bottom of the vessel allow good optical access to the entire plasma cross section for diagnostics. Figure (1) shows a sectional view of the vacuum chamber. The temperature of the vacuum vessel and the turbo-molecular pump can be controlled by external cooling. The working gas (hydrogen) pressure is controlled via a piezo-valve. For switching the high currents of the different coil systems an ignitron switching system is used. Triggering of the ignitrons is controlled by delay units, which easily allows to change timing of the triggers.

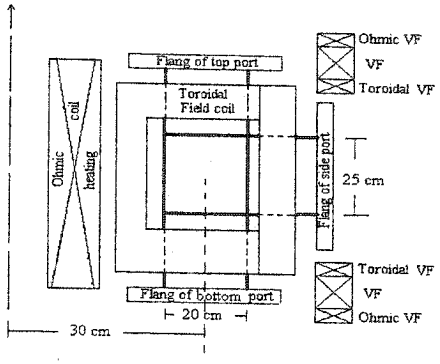


Fig. (1) Cross section of the EGYPTOR tokamak

2. Permanent Compensation Coils and Breakdown

A tokamak plasma is generated as the result of an electric breakdown in a toroidal geometry. The breakdown possibility severely depends on the stray, mainly vertical magnetic fields, which arise from ohmic and toroidal magnetic fields[4]. Two temporary return coils are used to compensate the stray magnetic field obtained from the toroidal field which was absent in the original design. These coils in parallel are then connected in series with the toroidal field coil. For ohmic heating we found that one of the compensation coils was damaged and we changed the old compensation coils by new coils which were prepared temporarily and positioned symmetrically on the lower and upper rim of the torus. At each rim we used two coils that were connected in series with ohmic heating coils. After achieving successfully breakdown[5] we exchanged these temporary stray magnetic field coils with permanent ones which were glued and fixed symmetrically to both rims of the torus. A comparison of stray magnetic field measurements for toroidal and ohmic heating in both cases will be discussed. Moreover a hot tungsten filament is used to ease breakdown.

3. Power Supply and Diagnostics

Power supply systems have fast and slow capacitor banks for respective discharges, a toroidal field capacitor bank for the toroidal magnetic field, and vertical field bank for the vertical magnetic field with firing circuits. The following diagnostics equipment is used at the moment:

1- Rogowsky coil for plasma current and discharge currents
2- Loop voltage
3- Gated ICCD camera for monitoring the plasma

EXPERIMENTAL SETUP

Figure (2) shows the block diagram of the experimental setup of the EGYPTOR tokamak. Up to now we obtain breakdown by discharging the fast and toroidal capacitor bank at a certain time and gas pressure. We charge the fast bank in the range 4 kV to 9 kV and the TF battery in the range 700 V to 1 kV. We adjust the pressure inside the vessel to 3-5 $x10^{-4}$ mbar by puffing in hydrogen via an electrical piezo-valve.

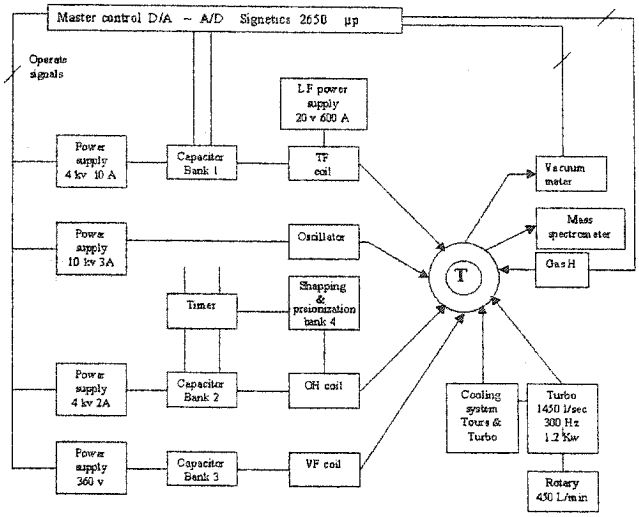


Fig. (2) Block diagram of experimental setup of EGYPTOR tokamak

EXPERIMENTAL RESULTS

First we tested the permanent compensation coils by using pick-up coils to measure the stray magnetic field of the ohmic and toroidal systems. Figure (3-a) shows the value of the stray magnetic field without temporary return coil (1) and with temporary return coil (2), and Fig. (3-b) displays the value of the stray magnetic field with permanent return coil. Figure (4-a) shows the value of the stray magnetic field without ohmic heating compensation coil (1) and with temporary compensation coil (2), and fig.(4-b) gives the value of the stray magnetic field for ohmic heating with the permanent compensation coil.

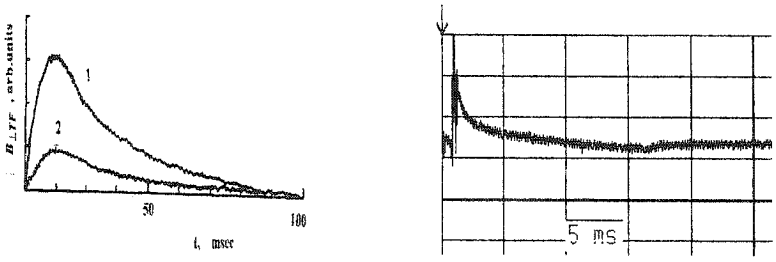
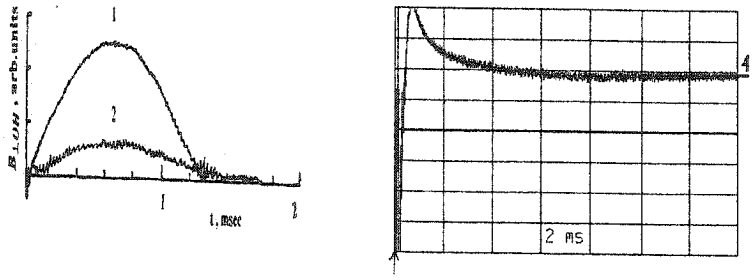


Fig.(3) Measurements of the compensation of the stray magnetic field of the Toroidal field in two cases:

a- temporary return coil (1- without compensation, 2- with compensation)

b- permanent return coil (with compensation)



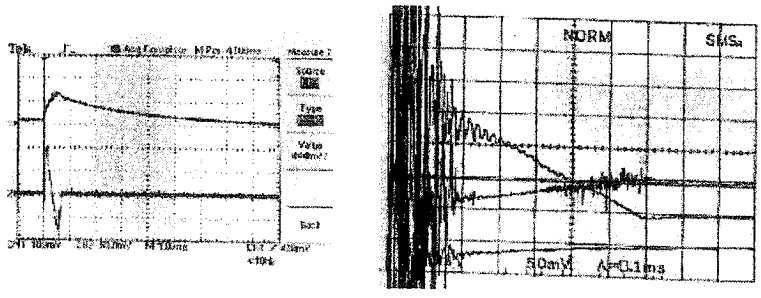
(a) (b)

Fig.(4) Measurements of the compensation of the stray magnetic field for ohmic heating in two cases:
a- temporary return coil (1- without compensation, 2- with compensation)
b- permanent return coil (with compensation)

The total current is measured with a Rogowsky coil consisting of a solenoid bent to form a loop. One end of the solenoid is connected back through its center. The total current is calculated using Ampere's law

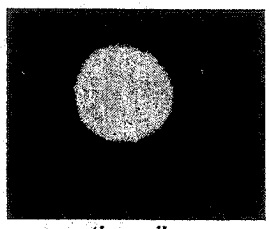
$$dI/dt = [(2\pi a)/(nA\mu_o)]\ V \qquad (1)$$

where a is the radius of the Rogowsky coil of n turns and V is the voltage induced. An integration circuit connected to the coil will thus give a direct reading of plasma current. The loop voltage V_l is measured with a single wire placed toroidally around the machine. Under steady state conditions $V_l = IR$, where R is the plasma resistance which depends on the plasma temperature and impurity concentration. Figure (5-a) shows voltage loop and output of the Rogowsky coil when charging the fast capacitor bank to 8 kV and the toroidal bank to 1 kV at a gas pressure of $5x10^{-4}$ mbar, for the case with permanent compensation coils. Figure (5-b) displays the same measurements under the same conditions but with the temporary compensation coils. We can observe the purity of the signals in the case of the permanent compensation coils. An intensified CCD camera (ICCD) gated at 20 ms exposure time is available and, synchronized with the discharge, has been used to obtain side view images of the plasma utilizing the visible light emitted by the plasma. An image of the plasma is shown in Fig.(6).



(a) (b)

Fig.(5) Oscillogram of loop voltage and plasma current for a charging voltage of the fast battery of 8 kV and of the toroidal battery of 1 kV, at a gas pressure $5x10^{-4}$ mbar
a- in case of permanent compensation coils.
b- in case of temporary compensation coils.



b- in case of temporary compensation coils.

Fig.(6) ICCD camera side view image of visible light emitted from the plasma.

CONCLUSION

Compensation of the stray magnetic fields is very important for normal Tokamak operation. A well-conditioned wall surface is necessary for attaining stable plasma with low impurity concentrations. The discharge characteristics were drastically improved in the initial several hundreds shots of discharge cleaning. After that, stable reproducible plasma will obtain.

ACKNOWLEDGMENT

The authors are very grateful to the EGYPTOR tokomak team for excellent and valuable assistances for fulfilling this work.

REFERENCES

(1) J. Uhlenbusch; in "3rd Workshop on Plasma and Laser Physics", Ismailia, Oct. 3-7, p49, (1993).
(2) A.B. El Sisi, and M.M. Masoud, "Egyptor Tokamak Reconstruction Development and Operation", AREAEA/Int. Rep. No. 313, (2001).
(3) N. Brevenov and Yu. Gott; "The Tokamak Egyptor Problem Analysis and Recommendations Concerning its Smooth Operation" RRC, Kurchatov Institute, Russia, October (2000).
(4) T. Sometani, N.Fujisawa; Plasma Physics; 20, 1101, (1978).
(5) A.B. El Sisi; Ph.D Thesis, Faculty of Engineering, Zagazig, University, (2001).

Study of the Formation of a Charge Separation and Electric Field at a Plasma Edge Using Eulerian Vlasov Codes

M. Shoucri[1], H. Gerhauser[2], K.-H. Finken[2]
[1]Institut de recherche d'Hydro-Québec
1800, boul. Lionel-Boulet, Varennes, Québec, Canada J3X 1S1
[2]*Institut für Plasmaphysik, Forschungszentrum Jülich GmbH*
EURATOM Association, Trilateral Euregio Cluster, D-52425 Jülich, Germany
shoucri.magdi@ireq.ca

ABSTRACT

One-dimensional (1D) Eulerian Vlasov codes are used to study the problem of the formation of charge separation, together with the self-consistent electric field, in the presence of a density gradient. The codes apply a method of fractional steps for the solution of the Vlasov equation. Comparison of the results obtained using a cylindrical geometry code and a Cartesian slab geometry code are presented.

Keywords: Numerical Simulation, Eulerian Vlasov Codes, Plasma Edge

INTRODUCTION

The problem of the formation of a charge separation at a plasma edge in the presence of a steep density gradient is of major importance in tokamak physics. It strongly affects the physics associated with the high confinement mode (H mode) and the reversed shear equilibria. In the present work, we study the formation of a charge separation, together with the self-consistent electric field at a plasma edge, using Eulerian Vlasov codes. These codes have the advantage of a very low noise level, which makes it possible to measure accurately a small charge separation. The results we present are obtained by solving the Vlasov equation in cylindrical geometry. In this case, the presence of centrifugal and Coriolis forces requires a 2D-interpolation in velocity space effected by using a tensor product of B-splines. In the limit of very large plasma radius the cylindrical geometry method yields results identical to the solution of the Vlasov equation in Cartesian geometry[1]. We compare the electric field calculated along the gradient with the macroscopic values calculated from the same kinetic code for the gradient of the ion pressure and the Lorentz force term, and we find that these quantities balance the electric field, a result similar to what has been presented in Cartesian geometry[1].

THE PERTINENT EQUATIONS AND THE NUMERICAL METHOD

The notation is the same as in Ref. (2). The inhomogeneous direction in the 1D cylindrical plasma is the radial direction r, normal to a vessel surface located at $r = R$. The constant magnetic field is in the z direction which represents the toroidal direction, and θ is the poloidal direction. The ions are described by the (normalized) 1D Vlasov equation for the distribution function $f_i(r, v_\theta, v_r, t)$:

$$\frac{\partial f_i}{\partial t} + v_r \frac{\partial f_i}{\partial r} + \left[E_r + v_\theta \omega_{ci} + \frac{v_\theta^2}{r} \right] \frac{\partial f_i}{\partial v_r} - \left(\omega_{ci} v_r + \frac{v_r v_\theta}{r} \right) \frac{\partial f_i}{\partial v_\theta} = 0 \qquad (1)$$

This equation is solved by a method of fractional steps[2]. To advance Eq. (1) for one time-step Δt, we split equation and solve for $\Delta t/2$ the equation:

$$f_i^*(r, v_\theta, v_r, t + \Delta t/2) = f_i^n(r - v_r\, \Delta t/2, v_r, v_\theta, t) \qquad (2)$$

where the shift in Eq. (2) is done using cubic spline interpolation. We then solve for Δt:

$$f_i^{**}(r, v_\theta, v_r, t+\Delta t) = f_i^{*}(r, v_r - 2a, v_\theta - 2b, t) \tag{3}$$

where the 2D interpolation is effected using a tensor product of B-splines[2], and a and b are given, to an order $O(\Delta t)^2$, by the expressions:

$$a = \frac{\Delta t}{2}\left\{E_r + \omega_{ci}\left(v_\theta + \frac{\Delta t}{2}\left(\omega_{ci}\, v_r + \frac{v_r\, v_\theta}{r}\right)\right) + \frac{v_\theta^2}{r} + \Delta t\,\frac{v_\theta}{r}\left(\omega_{ci} v_r + \frac{v_r\, v_\theta}{r}\right)\right\} \tag{4}$$

$$b = -\frac{\Delta t}{2}\left\{\omega_{ci}\left(v_r - \frac{\Delta t}{2}\left(E_r + v_\theta \omega_{ci} + \frac{v_\theta^2}{r}\right)\right) + \frac{v_r v_\theta}{r} + \frac{\Delta t}{2}\,\frac{v_r}{r}\left(\omega_{ci} v_r + \frac{v_r v_\theta}{r}\right) - \frac{\Delta t}{2}\,\frac{v_\theta}{r}\left(E_r + v_\theta \omega_{ci} + \frac{v_\theta^2}{r}\right)\right\}$$

We then repeat Eq. (2) to calculate f^{n+1} from f^{**}. Time is normalized to the inverse plasma frequency ω_{pi}^{-1}, velocity is normalized to the acoustic velocity $c_s = \sqrt{T_e / m_i}$, and length to the Debye length $\lambda_{De} = c_s / \omega_{pi}$. The potential is normalized to T_e / e, and the density to the peak initial central density. The system is solved over a length L = 175 Debye lengths in front of the vessel surface, with an initial ion distribution function and density profile over the domain {*R-L, R*} given by:

$$f_i(r, v_r, v_\theta) = n_i(r)\,\frac{e^{-\left(v_r^2 + v_\theta^2\right)/2\,T_i}}{2\pi T_i} \quad ; \qquad n_i = n_e = 0.5\left(1 + \tanh\left((R - r - L/5)/7\right)\right) \tag{5}$$

The magnetized electrons are frozen along the magnetic field lines, with a constant profile given by Eq. (5). In this case the electrons cannot move across the magnetic field in the gradient region to compensate the charge separation which is built up due to the finite ion orbits. For determining this charge separation along the gradient, it is important to calculate the ion orbits accurately by using an accurate Eulerian Vlasov code. The larger the ion gyroradius, the bigger the charge separation and the self-consistent electric field at the edge. (Hence the important role played by even small fractions of impurity ions). The electric field is calculated from the Poisson equation:

$$\frac{1}{r}\frac{\partial}{\partial r} r \frac{\partial \phi}{\partial r} = -\left(n_i - n_e\right), \qquad E_r = -\frac{\partial \phi}{\partial r} \tag{6}$$

The following parameters are used for deuterium ions:

$$\frac{\omega_{ci}}{\omega_{pi}} = 0.1; \qquad \frac{T_i}{T_e} = 1; \qquad \frac{\rho_i}{\lambda_{De}} = \sqrt{\frac{2T_i}{T_e}}\,\frac{1}{\omega_{ci}/\omega_{pi}} = 10\sqrt{2} \tag{7}$$

We assume that the deuterons hitting the wall surface at $r = R$ are collected by a floating cylindrical vessel. Since the magnetized electrons do not move in the r direction across the magnetic field, there is no electron current collected at the floating vessel. Therefore we have at $r = R$ the relation:

$$\left.\frac{\partial E_r}{\partial t}\right|_{r=R} = -J_{ri}\big|_{r=R} \qquad \text{or} \qquad E_r\big|_{r=R} = -\int_0^t J_{ri}\big|_{r=R}\, dt \tag{8}$$

Integrating Eq. (6) over the domain (*R-L, R*), we get the total charge σ:

$$R\, E_r\big|_{r=R} - (R-L) E_r\big|_{r=R-L} = \int_{R-L}^{R} (n_i - n_e) r\, dr = \sigma \tag{9}$$

We assume that the gyrating plasma ions are allowed to enter at the left boundary. So the electric fields at the left boundary $r = R - L$ and at wall $r = R$ in Eq. (8) must be such that Eq. (9) is satisfied.

We use a very large value of R ($R = 20000$ Debye lengths in the present calculation), so that the system behaves essentially as a Cartesian system. Indeed we recover results similar to those which have been found in Cartesian geometry in Ref. (1).

RESULTS AND CONCLUSIONS

Fig. (1) shows at $t = 500$ the plot of the electric field E_r (solid curve, we concentrate on the region less than 100 Debye lengths from the boundary to emphasize the edge region). To position the profiles in Fig. (1) with respect to the gradient we also plot $-n_i/2$ in the same figure. The electric field is pushing the ions back to the interior of the plasma. The dash-dotted curve gives the Lorentz force, which in our normalized units is given by $-<v_\theta>\omega_{ci}/\omega_{pi}$, and the dotted curve gives the pressure force $\nabla P_i/n_i$, $P_i = 0.5\,n_i(T_{ir}+T_{i\theta})$, with:

$$T_{ir,\theta}(r) = \frac{1}{n_i}\int dv_r\, dv_\theta\, (v_{r,\theta} - <v_{r,\theta}>)^2\, f_i(r, v_r, v_\theta) \tag{10}$$

$$<v_{r,\theta}> = \frac{1}{n_i}\int dv_r\, dv_\theta\, v_{r,\theta}\, f_i(r, v_r, v_\theta)\ ; \qquad n_i(r) = \int dv_r\, dv_\theta\, f_i(r, v_r, v_\theta) \tag{11}$$

In steady state the transport $<v_r>$ vanishes. The broken curve in Fig. (1) gives the sum $\nabla P_i/n_i - 0.1<v_\theta>$, which shows a very good agreement along the gradient with the solid curve E_r. In the region less than 20 Debye lengths from the wall, we have small oscillations in space (and time), the accuracy being degraded by the low density n_i and large ∇T_i appearing close to the surface. We plot in Fig. (2) the quantities $n_i E_r$, ∇P_i, $-0.1\,n_i<v_\theta>$ and the sum $\nabla P_i - 0.1 n_i<v_\theta>$. We see that there is a very nice agreement for the relation $n_i E_r = \nabla P_i - 0.1\,n_i<v_\theta>$ (the density $-n_i/10$ is also plotted to locate the profiles with respect to the gradient). The charge σ/R appearing in the system and calculated by the code from Eq. (10) amounts to -0.360 at $t = 500$. The collected charge calculated from Eq. (8) at $r = R$ is 0.364, hence $E_r|_{r=R} = -0.364$. The difference $E_r|_{r=R} - \sigma/R$ as calculated from Eq. (9) gives for $E_r|_{r=R-L}$ the value of -0.004, which is very close to the value obtained by the code at $R - r = 175$ (see Fig. (2)). We see also from Fig. (2) that at the left boundary, inside the plasma in the flat part of the density where $\nabla P_i = 0$, the electric field is compensated by the Lorentz force due to the poloidal drift $-0.1<v_\theta>$, while along the gradient the electric field is essentially balanced by $\nabla P_i/n_i$. Fig. (3) shows the charge density $n_i - n_e$ at $t = 500$, which illustrates how the combined effect of the steep profile at a plasma edge and the large ion orbits (large ratio ρ_i/λ_{De}) leads to a charge separation at a plasma edge. The electrons, which are frozen to the magnetic field lines, cannot compensate along the gradient the charge separation caused by the finite ion gyro-radius. Fig. (4) shows the potential. Fig. (5) shows the result for the electric field (full curve) E_x obtained in Cartesian geometry, the dash-dotted curve gives the Lorentz force, which in our normalized units is $0.1<v_z>$ and the dotted curve gives the gradient of the pressure ∇P_i, $P_i = 0.5 n_i(T_{ix}+T_{iz})$. The broken curve in Fig. (5) gives the sum $\nabla P_i/n_i + 0.1<v_z>$, which shows a very good agreement along the gradient with the solid curve E_x. $ni/2$ is plotted in the same figure (dash-and-three-dots curve). Finally we plot in Fig. (6) the quantities $n_i E_x$, ∇P_i, $0.1\,n_i<v_z>$ and the sum $\nabla P_i + 0.1\,n_i<v_z>$, similar to what we present in Fig. (2). We note the nice agreement between the curves of $n_i E_x$ and $\nabla P_i + 0.1\,n_i<v_z>$.

REFRENCES

(1) M. Shoucri, H. Gerhauser, K.H. Finken, in Proc. 30th EPS Conf. PPCF, St Petersburg (July 2003).
(2) M. Shoucri, H. Gerhauser, K.H. Finken, Comp. Phys. Comm 154 (2003) p.65.

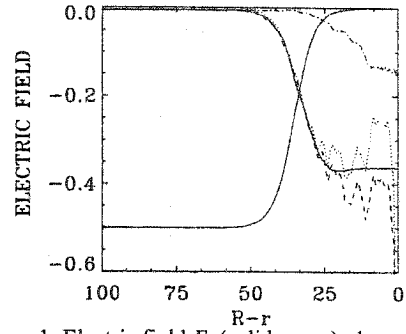


Figure 1: Electric field E_r (solid curve), the Lorentz force $-0.1 < v_\theta >$ (dash-dotted curve), the pressure force $\nabla P_i / n_i$ (dotted curve), and $\nabla P_i / n_i - 0.1 < v_\theta >$ (broken curve). The density $-n_i / 2$ is also plotted

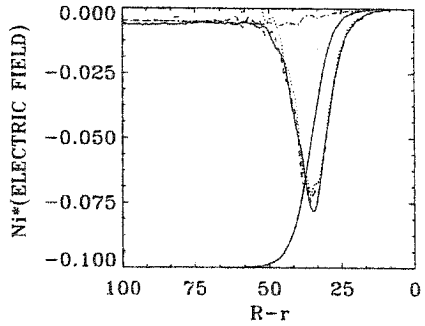


Figure 2: Plot of $n_i E_r$ (solid curve), $-0.1 n_i < v_\theta >$ (dash-dotted curve), ∇P_i (dotted curve), and $\nabla P_i - 0.1 n_i < v_\theta >$ (broken curve). ($-n_i / 10$ is also plotted for reference)

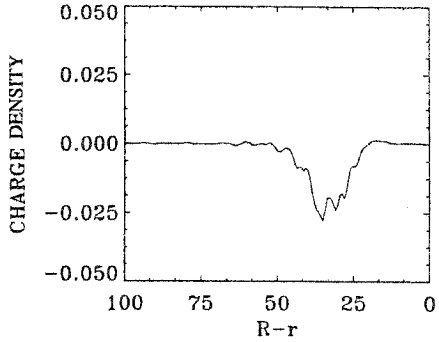


Figure 3: Charge density $(n_i - n_e)$

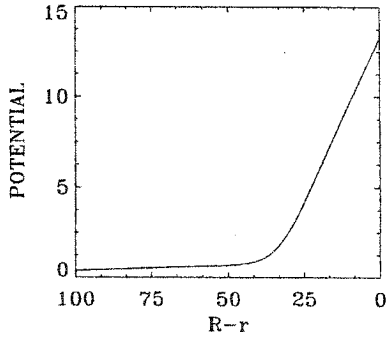


Figure 4: Potential

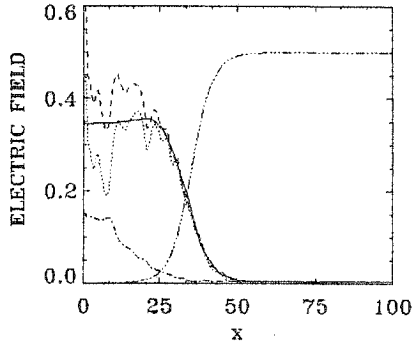


Figure 5: Plot, for the Cartesian geometry, of the electric field E_x (solid curve), the Lorentz force $+0.1 < v_z >$ (dash-dotted curve), the pressure force $\nabla P_i / n_i$ (dotted curve), and $\nabla P_i / n_i + 0.1 < vz >$ (broken curve). The density $n_i / 2$ is also plotted

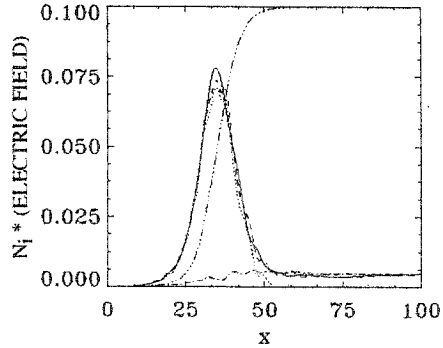


Figure 6: Plot of $n_i E_x$ (solid curve), $+0.1 < v_z >$ (dash-dotted curve), ∇P_i (dotted curve), and $\nabla P_i + 0.1 n_i < v_z >$ (broken curve). ($+n_i / 10$ is also plotted for reference)

Modelling of Rotating Plasma States and their Stability under the Influence of Helical Perturbations in TEXTOR and JET

A. Nicolai[1], U. Daybelge[2], C. Yarim[2]
[1]*Institut für Plasmaphysik, Forschungszentrum Jülich GmbH, Euratom Association, Trilateral Euregio Cluster, D-52425 Jülich, Germany*
[2]*Istanbul Technical University, Faculty of Aeronautics and Astronautics, 80626 Maslak, Istanbul, Turkey*
Email: A.Nicolai@FZ-Juelich.de

Abstract

The ambipolarity constraint and the parallel momentum equation of the revisited neoclassical theory allow to predict the parallel and poloidal flow speeds, $v_{\|}$, and v_{Θ}, respectively, and therefore the radial electric field E_r via the usual radial momentum balance equation.
The theory also accounts for the anomalous viscosity due to the plasma turbulence (ITG), the friction due to the recycled neutral gas, the momentum deposition due to NBI and due to a static or revolving helical perturbation field. A two time scale analysis allows to predict the stability of the asymptotic solutions, which depend on the initial values.

Key Words: Transport, Plasma Rotation, Perturbation Fields

Introduction

Anomalous plasma transport and the concomitant deterioration of the confinement times of tokamaks much below the neoclassical prediction, in particular if auxiliary heating is applied, are key issues in fusion research.
Therefore the surprising experimental discovery of the transition to a high confinement mode above a certain heating power has evoked considerable interest in improved confinement regimes.
The theory is valid in collision dominated plasmas with steep gradients and was able to reproduce the toroidal spin up in ALCATOR-C-MOD [1]. Here we concentrate on the influence of various source terms due to NBI, recycling and helical perturbation fields.

Plasma Rotation

The main result of the revisited neoclassical theory [1] is an equation describing the radial transport of toroidal momentum in a collisional subsonic plasma with steep gradients:

$$\frac{1}{\eta_2}\frac{\partial}{\partial x}[\eta_2(\frac{\partial g}{\partial x} - \frac{0.107q^2}{1+\frac{Q^2}{S^2}}\frac{\partial ln\, T}{\partial x}\frac{B_\phi}{B_\theta}h)] = \frac{\partial}{\partial t_T}g + T_{CX} + T_{NBI} + T_{ANI} + T_{j\times B} \qquad (1)$$

Here $t_T = \frac{t\hat{n}}{t_{ct}\hat{\eta}_2}$ is the normalized time used to evolve g (defined below). $T_{CX} = t_{ct}\frac{\hat{n}}{\hat{\eta}_2}\nu_{cx}g$ accounts for the friction caused by the neutral gas, $T_{NBI} = t_{ct}\frac{\hat{n}}{\hat{\eta}_2 v_T}\dot{v}_i$ for the momentum source due to neutral beam injection, $T_{ANI} = t_{ct}\frac{\hat{n}}{\hat{\eta}_2\tau_{ani}}g$ for the braking of the velocity field due to pressure anisotropization evoked by helical perturbation fields and $T_{j\times B} = \alpha_{j\times B}t_{ci}\frac{v_T}{b_s}$ for the force density due to the $\vec{j}\times\vec{B}$ force at the singular layer. The reciprocal braking time [2] $\frac{1}{\tau_{ani}} = \frac{\sqrt{\pi}\,10^4\sqrt{T_i[eV]/A}}{R_0[m]}[\sum_{m,n}\frac{n^2q}{|m-nq|}\frac{(B_{0,\theta}b_{\theta_{m,n}}+B_{0,\phi}b_{\phi_{m,n}})^2}{B_0^4}]$ accounts for the poloidal and toroidal components of the helical perturbation field, $b_{\theta_{m,n}}$ and $b_{\phi_{m,n}}$, respectively. The coefficient $\alpha_{j\times B} = \frac{nn_i4m^3r}{r_s\beta_{fi}}\frac{\omega\tau_s}{(-\Delta')^2+(\omega\tau_s)^2}v_T$ with $\beta_{fi} = \frac{nm_iv_T^2\,2\mu_0}{B_{hel}^2}$ accounts for the slip frequency ω between the the rotating plasma and the helical field, the radial component of which is B_{hel}. The quantities Δ', τ_s, δ_s are given [3]. The characteristic time t_{ct} at a point P_i (defined below) is given by $t_{ct}^{-1} = \frac{1}{m_jn_iL_\psi^2}\eta_{2i}$. m_j is the ion mass, n_i the ion density at P_i, $L_\psi = |(\frac{\partial ln\,T}{\partial r})_i^{-1}|$ the scale length of the ion temperature T at P_i. $x = \frac{r-r_i}{L_\psi}$ the radial coordinate, r_i the radius of P_i, and η_2 the perpendicular viscosity coefficient [1]. In the case of Alcator P_i was the 'inflexion' point of the temperature pedestal [1]. In the case of TEXTOR P_i is assumed to coincide with the plasma edge (r_i=r_s, r_s is the minor plasma radius). g and h are the normalized and poloidally averaged toroidal and poloidal velocities, $g = \int\frac{d\theta}{2\pi}\frac{u_\phi(\theta)}{v_T}$ $h = \int\frac{d\theta}{2\pi}\frac{u_\theta(\theta)}{v_T}$, respectively. v_T is the constant positive velocity $v_T = \frac{1}{eB_\phi}\frac{T_i}{L_\psi}$ [e is the elementary charge, $T_i = T(r_i)$]. B_ϕ is the toroidal field and B_θ the poloidal field. The velocities Q, S are defined in [1], η_2 is the perpendicular viscosity. $\hat{n}$ and $\hat{\eta}_2$ are given below.

Combining the ambipolarity condition with the parallel momentum equation [1] we get in the case of large aspect ratio and circular cross - section an evolution equation for the poloidal plasma velocity.

$$(1+2q^2)\frac{\partial h^*}{\partial t_P} = -(h^*+1.833) + \{\frac{0.45\Lambda}{1+\frac{Q^2}{S^2}}\tilde{v}_T[-\frac{B_\varphi}{B_\theta}]^2\{\frac{0.107q^2}{1+\frac{Q^2}{S^2}}h^* + \frac{1}{2}\frac{1}{[\frac{\partial\hat{T}}{\partial x}]^2}(g^*)^2$$

$$-\frac{1}{\frac{\partial\hat{T}}{\partial x}}g^*[h^*-(1+\frac{2}{\eta})] + 1.9[h^*-0.8(1+\frac{1.6}{\eta})]^2\}\} \qquad (2)$$

Here the definitions $t_P = \frac{t}{t_{cp}}$, $t_{cp} = \frac{R^2\nu_j}{0.96v_{T_i}^2}$, $g^* = \frac{B_\theta}{B_\phi}g$, $h^* = \frac{u_\theta}{\tilde{v}_T}$ and $\eta = \frac{L_n}{L_T}$ with $\tilde{v}_T = \frac{T}{eB_\varphi}\frac{\partial ln\,T}{\partial r}$ and $L_n = (\frac{\partial ln\,n}{\partial r})^{-1}$ are used, to cast equation (2) in a convenient form. The parameter Λ (crucial in the case of ALCATOR where finite Larmor radius effects are important) can be written as $\Lambda = \frac{\nu_j}{\Omega_j}\frac{q^2R^2}{L_TT}$. L_T is the radially varying decay length $L_T = (\frac{\partial ln\,T}{\partial r})^{-1}$, ν_j the ion - ion collision frequency, Ω_j the ion Larmor frequency, q the safety factor, R the major radius, $\hat{T} = \frac{T}{T_i}$ is the relative temperature, $\hat{n} = \frac{n}{n_i}$ the relative density and $\hat{\eta}_2 = \frac{\eta_2}{\eta_{2i}}$ the relative viscosity. Neglecting the time derivatives in (1) and (2) we obtain stationary equations [1] which are used in the next chapter exclusively. The characteristic time t_{cp} for the evolution of h^* is considerably smaller than t_{ct} for the evolution of g.

A two time step analysis, using an expansion with respect to $\frac{t_{cr}}{t_{ct}}$, allows to determine the dependence of the stability of the solution on the initial values [4].

Solution Method, Results and Discussion

The stationary equation (1) is a second order equation for g, the normalized toroidal velocity. This equation is replaced by two first order equations [1].
In addition we have the (stationary) equation (2) for the poloidal rotation. For a given temperature and density and normalized toroidal velocity g this equation is solved for h by means of a solver for transcendental equations. The boundary conditions are given in [1]. The viscosity η_2 accounts for the ITG - turbulence [1].
The input data are those of TEXTOR [1] and JET. The TEXTOR data are: $r_i = r_s$=46 cm, R=175 cm, T_{imax} = 1500 eV, T_{emax} = 1200 eV, n_{max} = 5.4 $10^{13} cm^{-3}$, η_i=1.6, B_ϕ = 2.23 T. NBI is charaterized by P_{MW} = 0.72, E_{keV} = 40 (deuterons). The plasma current is I_p = 351 kA.
Figs. 1 and 2 show the temperature profiles of TEXTOR [1] and JET (shot # 53298), respectively. Fig. 3 shows the toroidal speed for vanishing neutral gas density and Fig. 4 the analogous curve for $n_0 = 4\ 10^{16} m^{-3}$. Whereas in Fig. 3 the toroidal speed is too large by around 50 $\frac{km}{sec}$, in Fig. 4 the maximum toroidal speed $v_{\phi_{max}}$ =110 $\frac{km}{sec}$ is reproduced with an accuracy of 10%. The ITG - turbulence accounts approximately for the enhancement of the classical momentum transport. The ratio of turbulent viscosity to the classical viscosity is around 100.
At the resonant surface which is located at the effective radius $\rho_{q=2}$ = 25 cm the toroidal velocity (Fig. 5) has a local minimum due to the braking term. Here it is assumed that the slip frequency vanishes i. e. the beam power and the rotation speed of helical field are adjusted to synchronize the plasma with the perturbation field.
At JET the large slip frequency ω prevented the penetration of the the helical field what is well described by $\alpha_{j \times B} \approx 0$. However, in the case of a synchronization (by AC - operation), the toroidal velocity profile of Fig. 6 could be obtained. The minimum is located at $\rho_{q=2}$ = 90 cm.

References

[1] A. Nicolai et al., Theory of Fusion Plasmas, Proceedings of the Joint Varenna-Lausanne International Workshop, Varenna (2002), p.269

[2] E. Lazzaro, R. J. Buttery, T. Hender, P. Zanca et al. Phys. of Plasmas, 9 (2002) 3906

[3] R. Fitzpatrick, Theory of Fusion Plasmas, Proceedings of the Joint Varenna-Lausanne International Workshop, Varenna (1992), p.147 Phys. Plasmas 2 (1995) 1648

[4] U. Daybelge et al. to be published in Nucl. Fus.

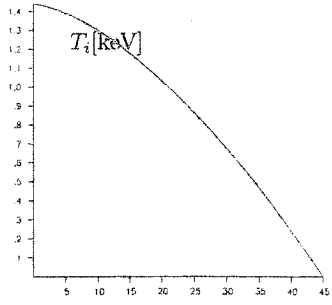


Fig. 1

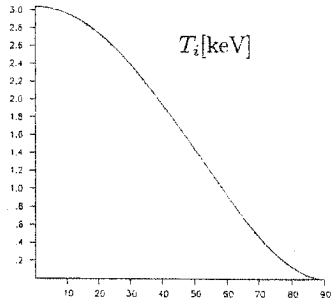


Fig. 2

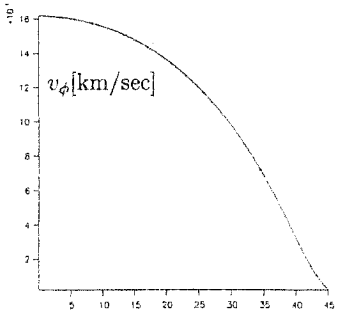


Fig. 3

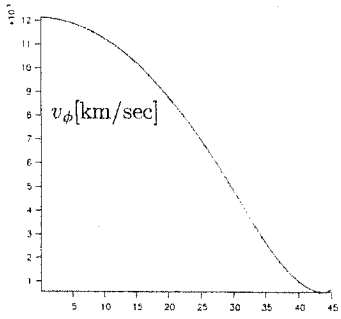


Fig. 4

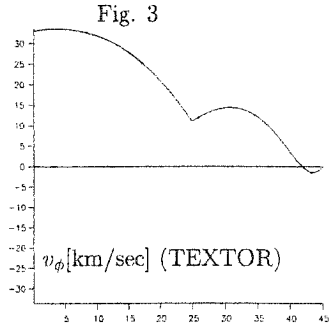


Fig. 5

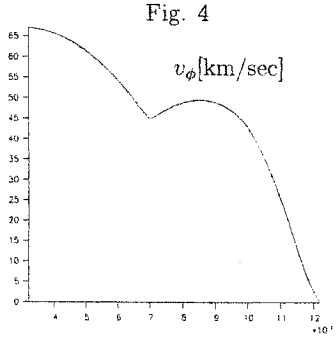


Fig. 6

Temperature profiles in TEXTOR and JET (Figs. 1, 2).
Toroidal velocity v_ϕ (TEXTOR) for $n_0 = 0$ and $n_0 = 4\,10^{16} m^{-3}$ (Figs. 3, 4).
Toroidal velocity at synchronized operation (TEXTOR: Fig. 5, JET: Fig. 6).

Plasma Separatrix in Toroidal Pinch

S.A.Shalaby, A.B.Beshara, A.B.EL - Bialy and M.M.Masoud
Plasma and Nuclear fusion Dept., N.R.C., Atomic Energy Authority,
Atomic Energy 13759 Cairo Egypt.
Safaa_Shalaby @ Yahoo.Com

ABSTRACT

The flux excluded method which include the flux loop and a small magnetic pick up coil located at the mid plane of the discharge vessel, had been used to determine the separatrix radius in toroidal pinch experiment at the confinement phase of the discharge. Experimental results show that the plasma separatrix radius is around 2 cm and stable for a period of time from 20 60 s independently on the helium gas pressure.

INTRODUCTION

The toroidally pinch was the first closed confinement system studied because of its apparent simplicity. The first worked out proposal for a magnetic system is the toroidal pinch of Thomson and Blackman (1964)[1]. In this experiment, the condenser bank is discharged into the primary poloidal winding to create a large secondary toroidal current induced in low-pressure gas inside a toroidal vessel.

This toroidal current I_Φ heats the plasma and provides a confining magnetic field due to B_θ to isolate the plasma from the inner walls of the torus.

In a simple torus which consisting of closed field lines is unstable to confine plasma. The curvature drift and gradient B drift of the particle produce the charge separation. The resulting electric field drives an outgoing plasma flow due to the $E_\theta \times B_\Phi$ drift across the toroidal field. The processes are the same as the flute instability and can be suppressed by introducing a poloidal magnetic field inside the torus. The net magnetic field line (having toroidal and poloidal component) is helically twisted. The particles moving along the helical field lines short circuit the perpendicular electric field, which does not grow. Thereby the flute instabilities are suppressed[2].

EXPERIMENTAL SETUP

The Toroidal discharge chamber of the theta Pinch is composed of two cylinder tubes made from stainless steel, the smaller cylinder is of 10 cm and the larger one has the diameter 31 cm. The length of both cylinders is equal, being 10 cm. The two cylinders are covered at both ends by two glass disks of 8-mm thickness. The resulting toroidal vessel has a rectangular cross section 10 x 10 cm. The picture of the toroidal theta pinch experiment is shown in Fig. 1a. (43 turns), which is wrapped on the toroidal vessel is apparent from the picture

The toroidal vessel is equipped by four ports. The first two ports are used for pumping and for measurement of the pressure in the discharge chamber. The last two ports are used for magnetic and electric probes and for gas feeding. Helium gas is used as a working gas.

The poloidal cross section of the discharge chamber is schematically in fig.1b. Here, the main dimensions are noted.

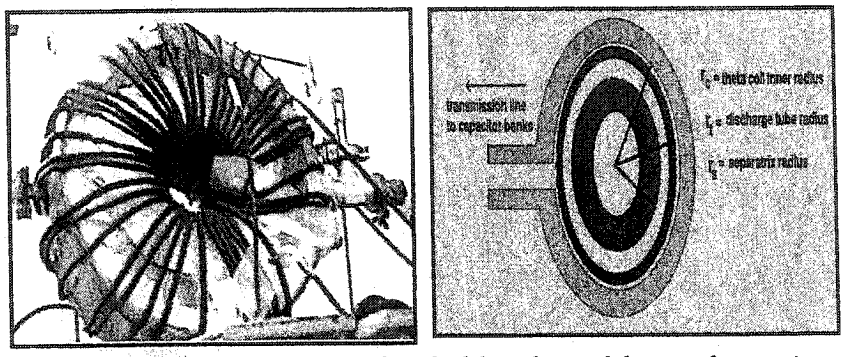


Fig. 1a:Picture of the torus is showing the poloidal winding and the ports for pumping and diagnostics.

Fig. 1b: Poloidal cross – section of the theta pinch (schematically).

Figure 2 shows the circuit diagram of the system. The electrical circuit is, in fact, compose of two schemes. The first scheme is the preionization circuit to fill the discharge chamber by cold plasma. For that, a high voltage (~ 6 kV) is applied between the inner and outer cylindrical electrode and the glow discharge is created. After this pre–ionization phase (with some delay in the range of microseconds), the main capacitor bank is discharged to the poloidal winding to compress and heats the plasma column

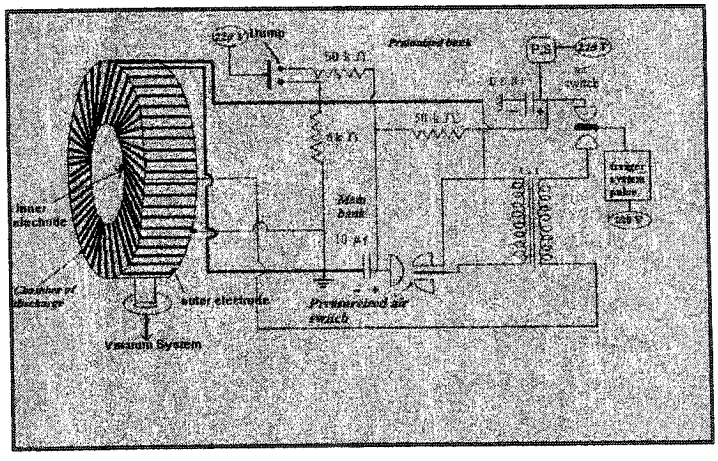


Fig. 2: Circuit Diagram of the toroidal system.

The charging voltage of the main capacitor bank used is 6 – 8 kV, which provides the peak current equal to 2.14 kA. The discharge period is about 185 μs.

FLUX EXCLUDED METHOD

The Separatrix radius of the plasma column, r_s is determined by the flux excluded method, which is based on comparison of the magnetic flux as measured either without (vacuum case) or with plasma in the discharge chamber. Such comparison allows finding how much flux is "excluded" by the plasma.

The background of the method is apparent from Fig. 3. The upper picture of this figure shows the vacuum case in which the magnetic flux Φ_v is distributed in the whole cross – section of the discharge vessel, πa^2. The lower picture refers to plasma case, when the magnetic flux is excluded by existing plasma. Thus the flux Φ_p included in a smaller area between the separatrix and the compression coil, $\pi (a^2 - r_s^2)$, and becomes higher.

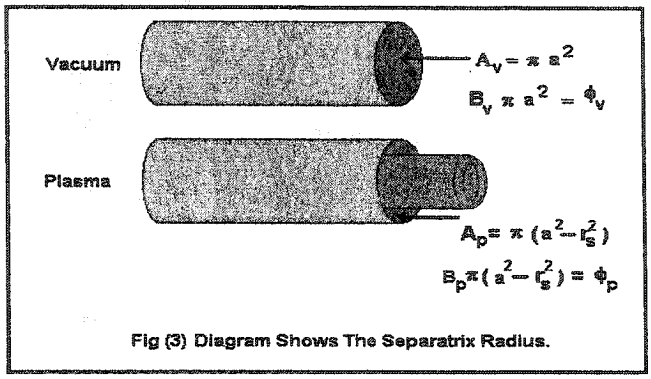


Fig (3) Diagram Shows The Separatrix Radius.

The separatrix radius r_s can be now easily calculated by using the expressions, which are given in Figure 3:

$$r_s = a \left(1 - \frac{\phi_p B_v}{\phi_v B_p}\right)^{\frac{1}{2}},$$

Where B_v is the axial magnetic field in vacuum, B_p is the axial magnetic field with plasma.

The magnetic flux Φ is measured by one turn loop wrapped around the discharge tube in the poloidal direction. The radius of the flux loop is $r_t = r_c$ The axial magnetic field B_Φ is measured by a small magnetic pick – up coil which is located between the two turns of the compression coil which fixed at the mid plane.

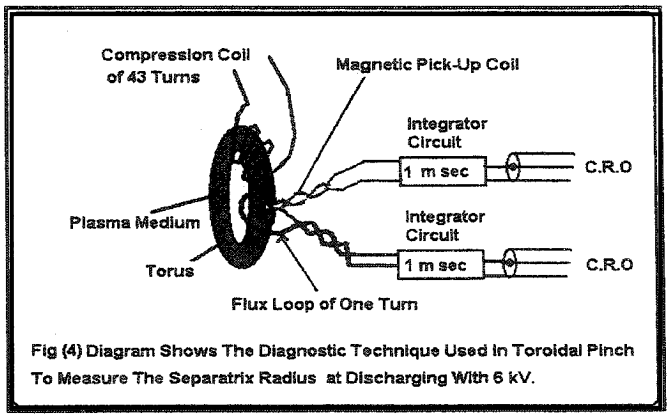


Fig (4) Diagram Shows The Diagnostic Technique Used In Toroidal Pinch To Measure The Separatrix Radius at Discharging With 6 kV.

As seen from Fig. 4, these two probes are connected to two integrating circuits of the same rise time, 1.1 ms.

The experiment has been carried out at different values of initial helium gas pressure. The excluded flux radius has been measured as a function of discharge time, which showed that, the plasma column have the same behavior for the different pressures.

EXPERIMENTAL RESULTS

Figure 5 shows the temporal evaluations of the separatrix radius during the compression phase of several helium discharges.

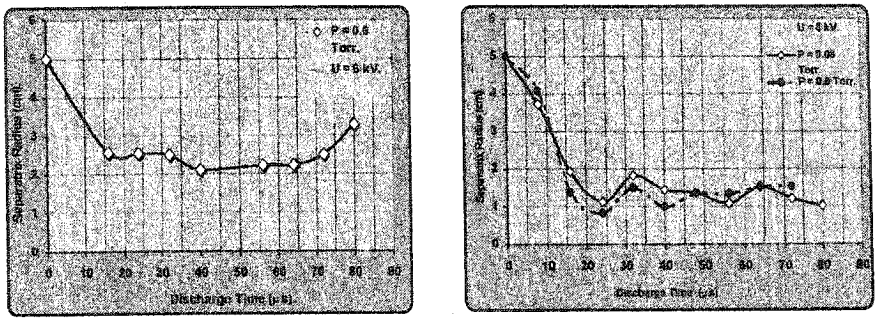


Fig. 5: Temporal evolutions of the separatrix radius at three discharges with different discharge conditions. Left panel – the discharge voltage 6 kV and helium pressure 0.6 Torr. Right panel – a higher discharge voltage (8 kV) and two values of helium pressure 0.08 and 0.8 Torr.

It is well seen from the figure that the plasma column is significantly compressed during a relatively short time period. The separatrix radius decreases from its maximum value (r_s = 5 cm) at the start of discharge down to 1 – 2 cm in 15 – 20 μs, independently on the discharge conditions. It is also evident that the compression phase of the discharge is quite stable and lasts of about ~ 60 μs. In the right panel, two discharges with the significantly different pressure of the working gas are compared. One can easily see that the degree of the compression is practically independent on the pressure. On the other hand, the separatrix radius seems to be inversely proportional to the discharge voltage, as it is apparent from comparison of the left and right panels of Fig 5. It is seen that the separatrix radius is significantly reduced by a factor of 2, when the discharge voltage is increased from 6 kV to 8 kV. This indicate that, the plasma column still in the steady state for a certain time and after that start to be decrease which may due to MHD instability which affects on the plasma stability. Also the conductivity of the medium, which varies by the variation of the temperature according to the relation $\eta \alpha 1/T$, can be source of instability. This temperature affects also by the power dissipated from the plasma due to MHD instabilities and the electron density, which inversely proportional to its temperature. This density tends to increase towards the outer wall as the temperature tend to be minimum at the same position at r = 3.5 cm at each wall. This state called the minimum relaxed state as Taylor described[3].

CONCLUSION

We demonstrated in this distribution that a steady state compression of the plasma column could be achieved in a small theta pinch experiments for time period of about 50 μs. The separatrix radius, derived from magnetic measurements depends on the discharge voltage, being independent on the initial gas pressure.

REFERENCES

(1) Deney, R.O., Culham Laboratory, an introductory course of plasma physics, Abingdon Oxfordshire, 495, (1993).

(2) Glaston, S. and Lovberg, R.H., Controlled thermonuclear reactions, University of California, Los Alamos Scientific Laboratory, (1960).

(3) Bodin, H.A.B and Newton, A.A, Nuclear fusion, 20,10, 1301 (1980).

Energy Confinement Analysis on the Libtor Tokamak

A. M. Alabyad, B. M. Esmail and R. M. Al-Habashi
Plasma Section, Physics Department.
Tajoura Nuclear Research Center, Tajoura, Libya
Alabyad@yahoo.com

ABSTRACT

We analyze a typical plasma discharge in the Libtor tokamak with a toroidal magnetic field of 2T, a plasma current of 40KA and a central plasma density of $6.0\times10^{13}cm^{-3}$, a central electron temperature of 400ev and a central ion temperature of 200ev. The global energy confinement time estimated experimentally is in the order of 1ms.
We make a comparison between the radial averaged confinement time calculated theoretically based on the classical transport models and the modified classical model (MCM) which had been recently introduced by Alabyad.
We find a close agreement between MCM and experimental values of the energy confinement time.

Key Words: Tokamak, plasma, transport, confinement.

INTRODUCTION

Plasma transport is a major concern of research groups in plasma physics for many reasons. First, plasma transport is a decisive factor in characterizing the plasma behavior in general: plasma transport coefficients enter the equations of power balance, the plasma diffusion and ohmic heating. Second, there has been a lack of understanding of plasma transport in major magnetic fusion experiments. In this work we analyze plasma transport on Libtor tokamak from the point of view of energy confinement. In the following discussion we introduce the machine, the operation mode and the data obtained from this machine during the period of initial operation. Then we analyze the data according to classical, neoclassical and MCM.

EXPERIMENT

The Libtor tokamak has a major radius R=53 cm, a minor radius a=11.5 cm, a maximum toroidal magnetic field B_t=4 Tesla and a maximum plasma current I_p=120 kA[1].
The data shown in Fig.1 was obtained during the operation of the tokamak with a plasma current of 40 kA and a magnetic field of 2 T[2]. The electron temperature T_e was measured by the Thompson scattering technique. The ion temperature T_i was measured by neutral beam analyzer diagnostic. The electron density n_e was measured using microwave interferometer and Thompson scattering techniques.

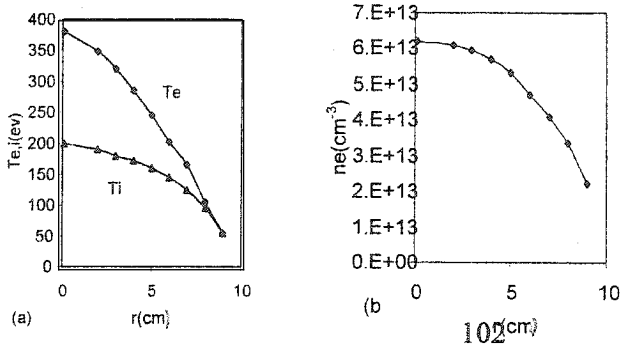


Fig.1-Experimentally measured radial profiles of **Libtor** plasma.
a) Electron and ion temperature profiles.
b) Electron density profile.

The experimentally estimated average energy density is $\sim 1.3\times10^{-3}$ J/cm^3 and the ohmic heating power is ~ 160 kW from which the experimental energy confinement time was estimated as $\tau_E^{exp} \approx 0.8$ ms.

TRANSPORT

In this section we analyze the data according to classical and neoclassical theory[3,4] and the MCM[5]. We calculate the energy confinement time for the bulk plasma τ_E as average value of the local energy confinement time:

$$\tau_E(r) = \frac{1}{4}\frac{r^2}{\chi_e(r)+\chi_i(r)} \quad , \qquad (1)$$

where r is the distance from the axis of the torus and χ_e and χ_i are the local electron and ion heat conductivity coefficients respectively. The average energy confinement time is obtain by calculating the local χ_e and χ_i and calculating the local τ_E from equation (1).
The radial averaged energy confinement time for the plasma is calculated on the basis of the radial points from 3 to 9 cm to avoid the central region where neoclassical coefficients are poorly determined and the edge region where non-collisional transport may play a major role.

Classical Transport

The classical heat conductivity for a fully ionized plasma can be written in the following way[6]:

$$\chi_i^c = \frac{5}{2}(r_i)^2 \nu_i \qquad (2) \qquad\qquad \chi_e^c = \frac{5}{2}(r_e)^2 \nu_e \qquad (3)$$

where $r_{e,i}$ are the electron and ion gyro-radii (Larmour radii) and $\nu_{e,i}$ are the classical electron-electron and ion-ion collision frequencies. The results of calculated electron and ion heat conductivity coefficients χ_e^c and χ_i^c are shown in Fig. 2. The average energy confinement time estimated in this way is $\tau_E^c \approx 75$ ms, which is substantially well above the experimental value.

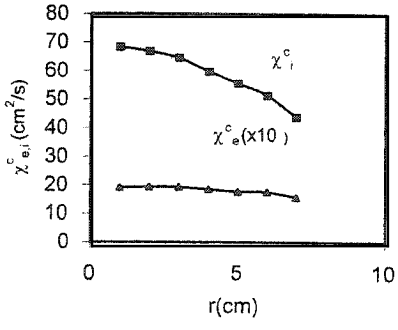


Fig.2 Classical electron and ion heat conductivity profiles.

It is well recognized that the classical theory is inadequate for prediction of transport properties of magnetized plasmas and we include it here because it provides the basis for our new model MCM.

Neoclassical Transport

The calculations of neoclassical transport coefficients are based here on the Hinton-Hazeltine theory, c.f.[3], which covers all regimes of neoclassical transport[7]: namely banana, Pfirsch-Schluter and plaeau regions. The neo-classical coefficients, which are based on classical calculations takes into account the tokamak concept and geometry, are given by:

$$\chi_e^{Nc} = \varepsilon^{\frac{1}{2}} \rho_e^2 \nu_e K_{22} \qquad (4) \qquad\qquad \chi_i^{Nc} = \varepsilon^{\frac{1}{2}} \rho_i^2 \nu_i K_2 \qquad (5)$$

Where $\varepsilon = 1/R$ is the inverse aspect ratio, $\rho_{e,i}$ are the electron and ion gyro-radii in the poloidal field and $K_{22,2}$ are the neoclassical constants.

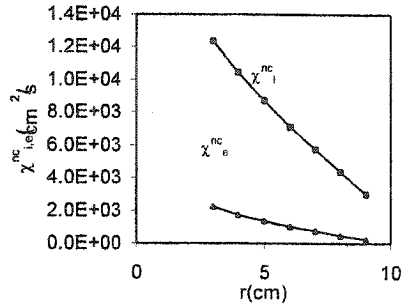


Fig.3 Calculated radial profiles of neo-classical transport coefficients.

Figure 3 shows the calculated profiles of neo-classical transport coefficients χ_e^{nc}, χ_i^{nc}, which are used to estimate an average confinement time $\tau_E^{nc} \approx 2$ ms. We notice that the profiles in Fig. 3 are steep towards the edge of the plasma, which is contrary to the expected behavior looking at the profiles of plasma parameters shown in Fig. 1.

We believe that even this kind of agreement between neoclassical estimate and the experimental confinement time is only coincidental and is due to the large magnitude of χ_i^{nc}. The character of transport is very poorly predicted by neoclassical theory because it is based on the classical theory, which in turn contains a very fundamental missconcept that has to do with the effect of magnetic field on the plasma relaxation times.

Modified Classical Model Transport

The Modified Classical Model (MCM) that was introduced recently by Alabyad[5], is a phenomenological semi-imperial model developed with the major assumption that the magnetic field has a very strong effect on the collision processes of charged particles.

The classical theory assumes that the collision frequencies $\nu_{e,i}$ in equations (2) and (3), calculated for a plasma without magnetic field, remain nearly unaffected by the magnetic field, and that the guiding center of the particle makes random translations during a collision time leading to an average translation of the center of the order of Larmor radius, $r_{e,i}$.

The new model (MCM) assumes that the magnetic field drastically changes the collision frequencies for particles of the same charge sign (electron-electron and ion-ion collisions) where as the effect is very weak for particles of different charge signs (electron-ion collisions).

The reason for such an assumption is that the magnetic field forces the colliding particles to re-encounter each other over and over again for many cycles during a collision which effectively increases the time of interaction and the exchange of momentum and energy. The charged particles are envisaged approaching each other along the field lines in helical orbits with a certain pitch depending on their parallel velocity. As the particles come close to each other their parallel velocity decreases because of repulsion if they are like-particles and increases because of attraction if they are unlike-particles. Slowing down makes the cycles closer and speeding up makes the cycles farther until they pass each other and start to accelerate or decelerate to return to their original parallel velocity before the collision. This means that the colliding particles of the same type make many cycles during the time of their interaction where as the unlike particles make few cycles during their interaction.

Each cycle is considered as a classical small angle scattering process or collision which means that the test particle in a plasma sees the same target particle over and over again as many times as the number of cycles it makes during the effective collision time. The collision frequency is assumed to increase by the number of cycles N that the charged particle makes during the effective collision time τ_{eff} that is $N = f\tau_{eff}$ where f is the cyclotron frequency. Therefore; an effective collision frequency $\nu_{eff} = 1/\tau_{eff}$ can be written as $\nu_{eff} = N\nu$, which leads to:

$$\nu_{eff} = \sqrt{f\nu} \qquad (6)$$

The second assumption in MCM is to think of the random step of the guiding center of the particle as not just the Larmour radius but added to it the Debye length. This assumption is not very crucial for the model but important if the character of transport is to be investigated in low density plasma under relatively high magnetic field. The rest of the model is classical and the results are shown in equations (7) and (8) below.

$$\chi_e^m = \frac{5}{2}(r_e + \lambda_D)^2 (f_e \nu_e)^{\frac{1}{2}} \qquad (7) \qquad \chi_i^m = \frac{5}{2}(r_i + \lambda_D)^2 (f_i \nu_i)^{\frac{1}{2}} \qquad (8),$$

where $\chi_{e,i}^m$ are the electron and ion heat conductivity coefficients according to MCM, λ_D is the Debye length and $f_{e,i}$ are the electron and ion cyclotron frequencies.

The electron and ion heat conductivity coefficients χ_e^m and χ_i^m, calculated according to MCM are shown in Fig.4. The resulting energy confinement time is $\tau_E^m \approx 0.88$ms.

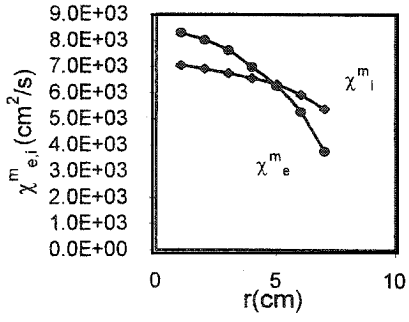


Fig.4 Radial profiles of electron and ion heat conductivity coefficients calculated on the bases of MCM.

CONCLUSION

Libtor tokamak data were analyzed using classical, neoclassical, and the modified classical models. An average energy confinement value is obtained in each case. The experimental values found to be in close agreement with MCM in further support for the model.

REFERENCES

(1) Libtor Tokamak Technical Documentation.
(2) First Results of Libtor Tokamak, TNRC Report (1983).
(3) Hinton, F. L., Hazeltine, R. D., Rev. Mod. Phys. 48 (1976) 297.
(4) Dolan, T. J., Fusion Research; Principles, Experiments and Technology, (1982) 204.
(5) Alabyad A. M., Modified Classical Model for Collisions and Transport in Magnetized Plasma. Proceeding of Workshop on Plasma and Laser Physics, Cairo, 1996.
(6) Fundamentals of Plasma Physics, V. E. Golant, A. P. Zhilinsky, I. E. Sakharov, John Wiley and Sons. New York (1977).
(7) TNRC Report, P.P.D. 2002.

Plasma Diagnostics

Laser Scattering for Plasma Diagnostics in Gas Liner Pinch

H. Hegazy[1], S. Seidel[2], Th. Wrubel[2], and H.-J. Kunze[2]
[1] *Plasma Physics Department, Atomic Energy Authority, 13759 Enshass, Cairo, Egypt*
[2] *Institut für Experimentalphysik V, Ruhr-Universität, 44780 Bochum, Germany*
hos_heg@yahoo.com

ABSTRACT

To illustrate the power of collective Thomson scattering for the diagnostics of high density discharge plasmas, respective experiments are described in which electron density and temperature are obtained spatially resolved in axial and radial direction simultaneously with spectroscopic observations of line profiles. The experiments were performed on the gas-liner pinch facility at Bochum. In most cases the device is used for accurate measurements of line shapes of multiply ionized atoms and can be operated in a stable and an unstable condition.

Keywords: Laser scattering; Thomson scattering; Plasma diagnostics

EXPERIMENTAL SETUP

The experiments were carried out at the Bochum gas-liner pinch facility which has been described in detail previously[(1)]. The device is, in principle, a large aspect ratio Z-pinch. The diameter of the electrodes is 18 cm and their distance is 5 cm; both are not variable (see Figure 1). A capacitor bank of 11 μF is switched by a rail-gap switch and can deliver energies of up to 10 kJ to the discharge channel. The discharge is operated in the gas-puff type mode, the gas (hydrogen or helium) is injected along the discharge wall through a circular orifice between upper electrode and wall by a gas inlet system, which is powered by a fast electromagnetic valve. The initial gas filling at the wall is pre-ionized by discharges underneath the lower electrode. This pre-ionization is crucial in achieving a cylindrically homogeneous implosion of the plasma shell since it keeps the initial amplitude of Rayleigh Taylor instabilities small. The period of the discharge is about 6 μs. After the implosion a plasma column is formed about 5 cm in length and 2 cm in diameter. Typical densities are n_e= (0.5-5)×10^{18} cm^{-3} and temperatures are in the range kT_e=(5-60) eV.

The unique feature of the device is the possibility to inject a so-called test gas along the axis through a nozzle in the center of the upper electrode. This gas inlet system is also powered independently by a fast electromagnetic valve. The test gas ions are confined to the homogeneous central part (a few mm in diameter) of the final plasma column. This has the advantage that neither emission nor absorption by cold boundary ions influence the profiles of emitted lines. Possible effects of optical thickness are readily identified since the concentration of the test gas ions is easily varied. The contribution of the test gas ions to the continuum emission is usually negligible at low test gas concentrations, and hence the continuous background (or at least its shape) underneath any line profile is identified by simply turning off the injection of the test gas. This possibility greatly assists in deriving the true width of line profiles.

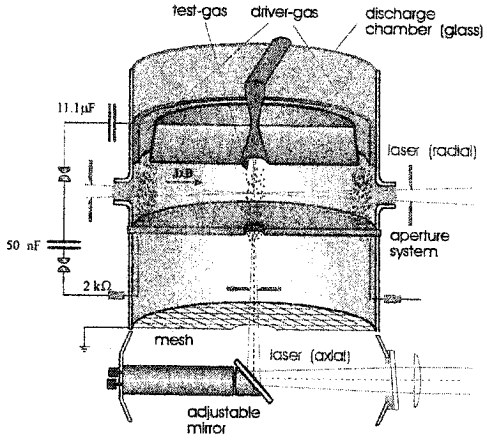


Figure 1. Schematic of the discharge vessel

Independent from, but concomitantly with, spectroscopic observations the plasma column has been diagnosed spatially resolved in radial and axial direction by collective Thomson scattering[2], which yields the local plasma parameters along a diameter in the mid-plane or along the axis. For the analysis of the scattered spectra usually 20 neighboring channels were averaged in order to improve the intensity to noise ratio. This resulted in a spatial resolution of about 0.5 mm. Thomson scattering as well as axially resolved spectroscopic studies clearly showed[2,3] that at high test gas concentrations severe modulations of density and temperature develop along the z-axis as consequence of an instability. On the other hand, homogeneity can be assured if the test gas concentration is kept low, i.e., if it does not exceed the level of about a few percent.

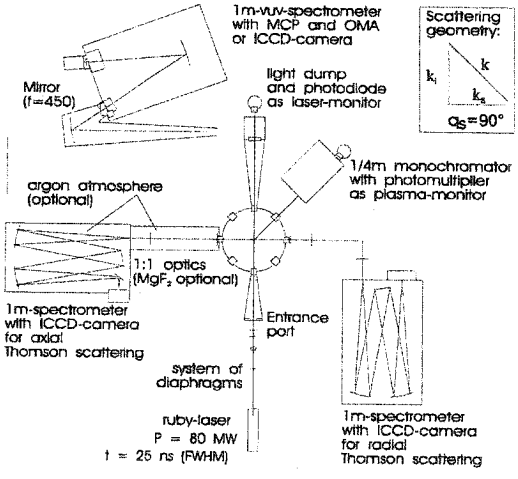


Figure 2. Schematic of the experimental setup

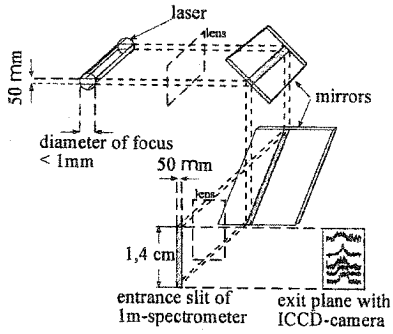


Figure 3. Setup of the two mirrors used for rotating the horizontal scattering volume

THOMSON SCATTERING RESULTS

Radially resolved Thomson scattering was employed in order to study plasma parameters and pinch dynamics. At the high densities of the pinch, the scattering parameter $\alpha=1/k\lambda_D$ is larger than 1 and scattering by the plasma electrons is in the collective regime, i.e. the scattered laser light is essentially in a narrow spectral region called the ion feature, which reflects the collective motion of the plasma ions. The laser beam (Kord K1-Q, 1 J, 25 ns FWHM) is focused either into the center of the discharge vessel passing perpendicularly the plasma axis (see Figure2) or along the axis (see Figure 1). The scattered light is focused onto the entrance slit of a visible 1-meter monochromator, the width of the entrance slit was 50 μm, in such manner that every point along the height of the entrance slit corresponds to a radial position in the midplane of the plasma whereby the rotation of the image is achieved by two mirrors (see Figure 3). An ICCD-camera (Princeton Instruments) with 384×578 pixels is positioned at the exit plane of the spectrograph. A grating with 1200 l/mm blazed at 1000 nm is fitted to the spectrograph giving a linear dispersion of 6.3 pm/pixel in second order. The apparatus profile of the system has a FWHM of 3 pixel and was determined from Rayleigh scattering spectrum.

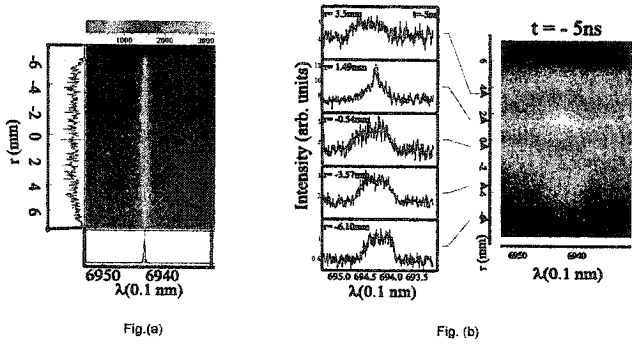


Figure 4. (a) Radially resolved Rayleigh scattering and (b) Radially resolved Thomson Spectra

An example of a measured ICCD spectrum is shown in Figure 4. Each recorded Thomson spectrum consists of 578 radial channels and we take a mean of 20 channels in order to improve intensity to noise ratio. These spectra are fitted with a theoretical form factor[4]. A detailed description of the form factor, the fitting procedure and the calibration via Rayleigh scattering on propan as well as a summary of the theory are given in (5). Examples of radially resolved plasma parameters obtained

from this procedure at different times of the discharge are shown in Figures 5.The time evolution of the electron density (Figure 5(a)) and the bulk velocity (Figure5(b)) are suited to investigate the dynamic of the pinch. The radial resolved distribution of the impurity concentration and the electron temperature at times shortly before maximum pinch compression is shown in Figure 5(c), 5(d).

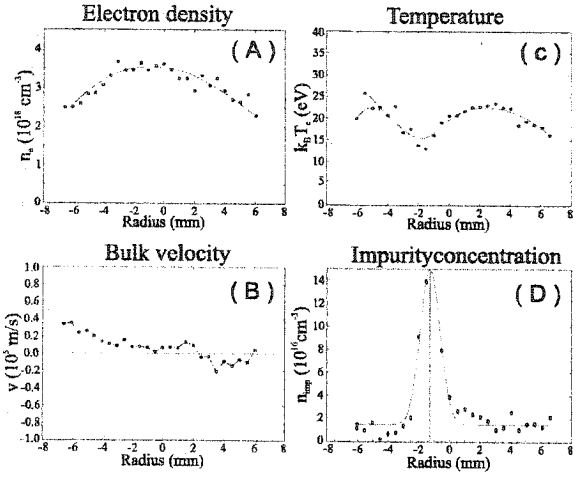


Figure 5. Results of radially resolved electron density, electron temperature, bulk velocity, and impurity concentration

The test gas ions are concentrated in a plasma volume shifted slightly out of the geometrical center of the discharge, but are still within the region of homogeneous electron density. The electron temperature normally increases with increasing density. Its behaviour is similar to that of the density and it is constant in the central part of the plasma. Nevertheless at times shortly before maximum pinch compression and in cases where the impurity ions are located in a very narrow central plasma region we find that the electron temperature is significantly decreased exactly at the position of the impurity ions as shown in Figure 5(c) and Figure 5(d). This behaviour is caused by enhanced radiative losses which are a function of Z. Due to the charge number of impurity ions Z and their high local concentration the plasma cools locally and the electron density is increased.

AKNOWLEDGMENT

H. Hegazy is very grateful to S. Seidel, Th. Wrubel, and H.-J. Kunze for excellent and valuable assistances during his visit to Institut für ExperimentalPhysik V, Ruhr-Universität Bochum, and to the International Office of the Forschungszentrum Jülich for supporting the visit.

REFERENCES

(1) Büscher S, Wrubel Th, Kunze H-J, Technical setup and physical properties of a gas-liner pinch, Nukleonica 2000; 45:167-172.
(2) Wrubel Th, Büscher S, Kunze H-J, Radially and axially resolved Thomson scattering in a gas-liner pinch, Plasma Phys. Contr. Fusion 2000; 42:519-528.
(3) Ahmad I, Büscher S, Wrubel Th, Kunze H-J, Experimental Stark widths of KrIII, Phys. Rev. E (1998); 58:6524-6530.
(4) Evans DE, Plasma Phys. 1970; 12:573-584.
(5) Wrubel Th, Glenzer S., Büscher S, Kunze H-J, J. Atoms. Terr. Phys. 1996; 58:1077-1087.

Comparison of Low Density Plasma Property Measurements in a Magnetic Multipole Source by Langmuir Probe and Laser Thomson Scattering Techniques

Ahmed A. I. Khalil[1], **S. Maurmann**[2] **and H.-J. Kunze**[2]
1 National Institute of Laser Enhanced Science (NILES), Cairo University, Giza – Egypt.
2 Institut für Experimentalphysik V, Ruhr-Universität Bochum, 44780 Bochum, Germany.
Ahmedasaad@hotmail.com

ABSTRACT

Langmuir probes and Thomson scattering are two independent methods of measuring electron properties in a magnetic multipole source. First results of measurements of electron density and temperature of helium plasmas in a cw running magnetic multipole plasma source by repetitively laser-pulsed 90^0 Thomson scattering are reported. The detection sensitivity of the Thomson experiment is higher than 10^{11} electrons and the accuracy of the electron temperature is specified to 20 % and of the electron density to 30%, respectively. In comparison with probe measurements the obtained electron temperature is in good agreement within the error margin but the density is found to be higher.

Key Words: Low density plasma, Magnetic Multipole Source, Langmuir probe, Laser.

INTRODUCTION

Thomson scattering is a very powerful plasma diagnostic technique[1,2] and it is well established for a wide variety of plasmas ranging from those in θ-pinch devices[3,4] and in tokomaks[5] (10^{13} cm^{-3} $\leq n_e \leq 10^{16}$ cm^{-3}) to high-density plasmas like in the plasma focus[6] and in z-pinch devices[7,8] ($n_e \approx 10^{18}$ cm^{-3}) and recently even to laser target plasmas[9] ($n_e \geq 10^{20}$ cm^{-3}). During the last few years, this technique has also been introduced to low-density glow discharge plasmas[10,11] ($n_e \leq 10^{11}$ cm^{-3}). Without perturbing these plasmas this development makes it possible to investigate locally resolved the properties of the discharge electrons, their density, temperature and energy distribution function, which are essentially for the understanding of the plasma behaviour. Steady-state plasmas of magnetic multipole source devices are characterized by an electron temperature of a few eV and an electron density in the range of 10^{11} cm^{-3} $\leq n_e \leq 10^{13}$ cm^{-3}, and hitherto these plasma parameters are measured using Langmuir probes[12,13]. The probe diagnostic technique has the advantage of simple experimental handling, but in many cases the data analysis can become difficult; moreover the presence of a metallic probe inside the plasma produces perturbations which have to be taken into account. Compared with electric probe diagnostics the interpretation of Thomson scattering measurements is straightforward and the results are unambiguous. We present here a 90^0-Thomson scattering technique designed for cw experiments, tested at our magnetic multipole plasma source device. The 90^0-Thomson scattered light is detected using a double monochromator and a multiplier with a high quantum efficiency at the wavelength of the scattered light. Electron density and temperature thus obtained are compared with those from Langmuir probe measurements.

EXPERIMENTAL SETUP

The experimental setup used for the 90^0-Thomson scattering is shown in figure 1. The main parts are the plasma source, the laser system and the detection unit. The helium plasma is produced in a magnetic multipole source which has been described previously in detail[13]. Briefly, the anode of the plasma source is a cylindrical vessel (diameter d = 15 cm, length l = 33 cm) made of non-magnetic stainless steel. To diagnose the plasma there are four ports with

windows (d = 3.5 cm) on each of three levels at the periphery of the discharge chamber. The directly heated cathode-filament is a small tube (1/4" in diameter and 1" in length) consisting of lanthanum-hexaboride (LaB6). A magnetic octopole structure (longitudinal line cusp configuration) on the vessel's external wall is used for the plasma confinement. The radial magnetic field at the inner wall of the discharge chamber (r = 7.5 cm) in front of the magnets is Br = 250 mT and at the position of the ports Br = 60 mT decreasing rapidly to a value of Br = 20 mT at r = 3 cm. The light source is a frequency-doubled Nd YAG laser (Quantel, type YG 481, 5 mm in diameter). Its special features for Thomson scattering measurements of cw plasma sources at λ = 532 nm are: high pulse-energy (0.2J), short pulse-duration (10 ns), high peak power (20 MW), low beam divergence (0.75 mrad) and high repetition rate (10 Hz). The laser beam is focused into the centre of the plasma column by lens L1 (f = 0.8 m), the beam diameter in the scattering volume being d = 0.6 mm. In order to reduce stray light to a tolerable level a diaphragm-system with Brewster-windows and a light dump for the laser beam consisting of four neutral glass filters at Brewster-angle is installed. The outgoing laser beam is monitored by a photodiode (EG&G, type FND 100Q) using the residual laser light from a Brewster-window. The scattered light is collected into a solid angle of 0.03 sr by a lens L2 (f = 0.1 m) and focussed onto the entrance slit (width: 500 µm, height: 10 mm) of a double monochromator (two single monochromators, Jarrell & Ash, model 82-410, in tandem operation, f = 0.25 m, grating 1180 grooves/mm, blaze-wavelength 0.5 µm, inverse linear dispersion 3.3 nm/mm). At the monochromator-exit-slit (width: 500 µm) a photomultiplier (RCA, type 4526) detects the transmitted scattered light. An 100 MHz transient digitizer oscilloscope (Gould, model 4074) recorded the signal of the scattered light.

SCATTERING LIGHT MEASUREMENTS, RESULTS AND DISCUSSION

Thomson scattering measurements are performed in the centre of the magnetic multipole plasma source running at a filling pressure of p_0 = 50 µbar helium gas, a discharge current of I_d = 20 A, a discharge voltage of U_d = 70 V and a cathode heating current of I_c = 120 A. Langmuir-probe measurements[13] give kT_e = 5.8 eV and $n_e = 1.3 \times 10^{12}$ cm^{-3}. The scattering parameter is $\alpha << 1$ at the laser wavelength λ_L = 532 nm and a scattering angle of $\theta = 90^0$, and we are dealing with incoherent Thomson scattering. Figure 2 shows as an example a measured scattering spectrum, which was obtained running the Nd YAG laser with a repetition frequency of prf = 10 Hz and setting the monochromator wavelength stepwise ($\Delta\lambda \approx 1$ nm) over a wavelength range of $-1 \text{ nm} \leq \Delta\lambda \leq 6$ nm in the vicinity of the laser line; the scattered signal normalized by the laser-monitor-signal is averaged over 128 laser pulses at every point of the spectrum. However, for plasmas of an electron temperature of a few eV, the spectral width of the Thomson component is larger due to the much higher velocity of the discharge electrons. Therefore, even in our case of a high stray light level the Thomson component can be determined by interpolation from a spectral range without contributions of Rayleigh- and stray light components. In the case of incoherent Thomson scattering and a Maxwellian velocity distribution the scattering spectrum is described by a Gaussian profile and the electron temperature can be evaluated from the total half-width of the spectrum[1,2]

$$\Delta\lambda_{1/2} = 4 * \sin\theta/2\,(2\,kT_e / mc^2 * \ln 2)^{1/2} \quad \ldots\ldots (1)$$

The analysis of the Thomson spectral profile, given in figure 2, reveals a total half-width of $\Delta\lambda_{1/2}$ = 6.0 nm (FWHM). Therefore the true width of the Thomson spectrum is given as $\Delta\lambda_{1/2}$ = 5.7 nm and the corresponding electron temperature is found to be kT_e = 5.3 eV.

The electron density can be evaluated by measuring the total Thomson scattered light which is directly proportional to the electron density. Therefore the calibration of the entire scattering set-up is performed by Rayleigh scattering from helium gas, the electron density is given by[1]:

$$n_e = n_R * \sigma_R/\sigma_{Th} * W_{Th}/W_R * \int_\lambda I_{Th} / \int_\lambda I_R \quad \ldots\ldots (2)$$

The electron density is obtained by the ratio of the spectrally integrated Thomson scattering intensity $\int_\lambda I_{Th}$ to that of Rayleigh scattering, $\int_\lambda I_R$, at a known neutral particle density n_R from

the gas filling pressure and the ratio of the laser power W_{Th} at Thomson scattering to W_R of Rayleigh scattering, taking into account the ratio $W_{Th}/W_R = 9537$ at the laser wavelength of λ_L = 532 nm. From figure 2 the electron density is determined to $n_e = 3.5 * 10^{12}$ cm^{-3}. As a result of pressure scanning the *stray light* level is found to be equivalent to a Rayleigh scattering signal from $p_R = 22.7$ mbar helium gas, corresponding to a Thomson scattering signal from an electron density of $n_e = 6.4 * 10^{13}$ cm^{-3}. In the case that no additional scattering processes are present in the plasma (see (10)), the procedure to obtain the neutral density is to determine precisely the contributions of Thomson scattering and stray light in the centre region of the scattering spectrum with an accurately calibrated experimental set-up. The uncertainty of the obtained electron parameters from the present Thomson scattering experiment due to statistical fluctuations of the photo-current is given by the signal-to-noise ratio[1]:

$$SN = [T * A / 2 e \Delta f * W_\lambda \Delta\lambda / (1 + P_\lambda / W_\lambda)]^{1/2}, \quad \ldots\ldots\ldots\ldots (3)$$

with $W_\lambda \Delta\lambda$: scattered intensity / $\Delta\lambda$: $2*10^{-9}$ W,
A : photo-cathode sensitivity of the multiplier: $8.9 * 10^{-2}$ A/W,
Δf : band width of the amplifier: 100 MHz,
T : transmission of the detection system: 0.03,
P_λ/W_λ : ratio of plasma radiation to scattered radiation: ≈ 1.

For one laser pulse the signal-to-noise ratio is SN $\approx$ 0.6 and averaging over 128 laser pulses the SN amounts to SN $\approx$ 6.8 resulting in an averaged error-bar of Thomson scattering signals of about 15%. The fitting procedure outlined above to obtain the electron parameters lead finally to $kT_e = (5.3 \pm 20\%)$ eV and $n_e = (3.5 \pm 30\%) * 10^{12}$ cm^{-3}, respectively. Fig. 3 shows the electron temperature and density versus the discharge current I_d at a helium gas pressure of p_g = 50 µbar and a cathode heating current of I_c = 120 A; Langmuir probe measurements are specified by a full square and results of the Thomson scattering are denoted by an open circle. A comparison of the two diagnostic techniques leads to the statement that there is a good agreement within the error bars for the electron temperature but the Thomson scattering provides a two times higher density. In conclusion we present first results of electron temperature and density of helium plasmas in a cw running magnetic multipole source obtained from 90^0 Thomson scattering diagnostic technique. Since the stray light level in the centre of the scattered spectrum is high the determination of the electron density became difficult but the electron temperature is in fairly good agreement with probe measurements. For further investigations of multipole plasmas using Thomson scattering the stray light level has to be reduced by a factor of ten and the scattering signal should be averaged over more laser pulses to improve the signal-to-noise ratio.

REFERENCES

(1) H.-J. Kunze, in *Plasma Diagnostics*, edited by W. Lochte-Holtgreven, (North Holland, Amsterdam), 550 (1968).
(2) J. Sheffield, *Plasma Scattering of Electromagnetic Radiation* (Academic Press, New York),(1975).
(3) H.-J. Kunze, E. Fünfer, B. Kronast, and W.H. Kegel, Phys. Letters 11, 42 (1964).
(4) S. Maurmann, K.H. Finken, H.-J. Kunze, Phys. of Fluids 19, 1551 (1976).
(5) H.R. Hr, K.H. Steuer, IPP Report Garching III/121 (1987).
(6) N.J. Peacock, D.C. Robinson, M.J. Forrest, P.D. Wilcock, and V.V. Sannikov, Nature (London) 224, 488 (1968).
(7) S. Maurmann, H.-J. Kunze, Phys. of Fluids 26, 1630 (1983).
(8) Th. Wrubel, S. Büscher, H.-J. Kunze, Plasma Phys. Contr. Fusion 42, 519 (2000).
(9) S. Glenzer, C.A. Back, K.G. Estabrook, R. Wallace, K. Baker, B.J. Maccowan, B.A. Hammel, R.E. Cid, and J.S. Degroot, Phys. Rev. Lett. 77, 1496 (1996).
(10) H.J. Wesseling, B. Kronast, J. Phys. D: Appl. Phys. 29, 1035 (1996).
(11) M.D. Bowden, Y. Goto, T. Horri, K. Uchino, K. Muraoka, M. Naguchi, Jpn. J. Appl. Phys. 38, 3723 (1999).
(12) M.B. Hopkins, W.G. Graham, J. Phys. D: Appl. Phys. 20, 838 (1987).
(13) S. Maurmann, P. Drepper, S. Ferrie, N. Petershagen, Contrib. Plasma Phys. 40, 152 (2000).

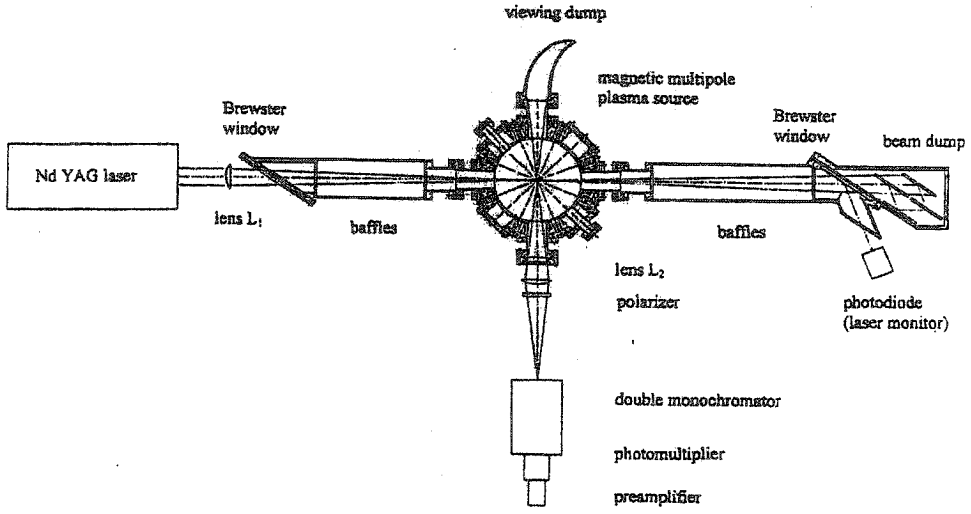


Fig. 1: Experimental set-up of the scattering experiment

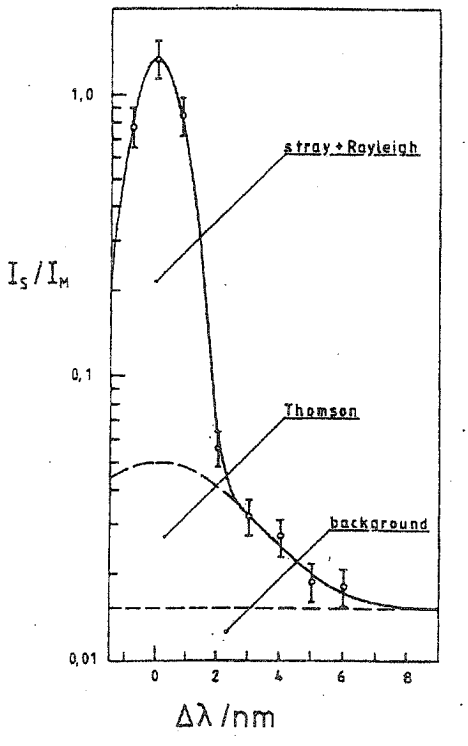


Fig. 2: Typical scatter spectrum with the components: stray light, Rayleigh scattered light, Thomson scattered light and background emission

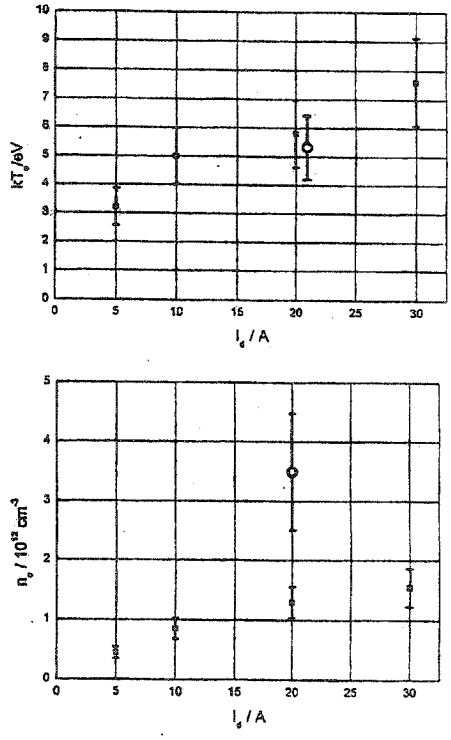


Fig. 3: Plasma parameter vs discharge current,
□: probe measurements,
O: Thomson light scattering measurements

Observation of Non Thermal N_2 Second Positive Emission in Quasi Thermal Air Plasma

S. Saloum[1], A.M. Gomes[2] and J.P. Sarrette[2]
[1] *Atomic Energy Commission of Syria, Physics Department, P.O. Box 6091, Damascus- Syria*
[2] *Centre de Physique des Plasmas et de leurs Applications de Toulouse, 118 Route de Narbonne, 31062 Toulouse Cedex 4- France*
ssaloum@aec.org.sy

ABSTRACT

During the diagnosis by optical emission spectroscopy of an inductively coupled air thermal plasma at atmospheric pressure, a non volume process was observed; it is the nitrogen ($C^3\Pi_u$- $B^3\Pi_g$) second positive emission, this phenomenon is in contradiction with the measured plasma temperature. One possible interpretation of this observation was given. This non-equilibrium phenomenon is characterized by an emission at wall such as: recombination of the nitrogen atoms $N(^4S)$ and $N(^2D)$, diffusion of the excited molecules $N_2(C)$ toward the center and de-excitation by radiation. The density of the excited molecules of $N_2(C)$ was evaluated near the wall of the plasma tube.

Key Words: ***Thermal Air Plasma, Optical Emission Spectroscopy, Nitrogen Second Positive, Emission at Wall.***

INTRODUCTION

Optical emission spectroscopy is a very common technique for understanding the physical and chemical properties of the plasma. Studies on natural air and O_2/N_2 plasmas have importance in various fields, such as: air de-pollution[1], continuous monitoring of trace metals in air[2]. Among the key species in such plasmas are the active nitrogen atoms, metastables and molecules having radiative states. Previously, we have characterized a natural atmospheric air plasma in terms of temperature, by optical emission spectroscopy where the diagnosis methods[3] were based on the calculation of the emission coefficients $\varepsilon(T)$ of the most intense molecular spectra (second positive of N_2, Gamma of NO, A-X of OH and NH, Schumann- Runge of O_2), as a function of plasma temperatures. The preliminary calculation of air plasma composition had taken into account the non thermal equilibrium $X = T_e/T_g$ (T_g and T_e kinetic temperatures of gas and electrons). The temperatures were determined with an accuracy of 50 K, under the condition of Local Thermodynamic Equilibrium (LTE) and the hypothesis of a moderate non thermal equilibrium ($X<1.2$), which was validated by an absolute optical calibration of air spectra[4]. In this paper, we study a non equilibrium phenomenon which was observed during the diagnosis of the plasma. It is the emission of second positive nitrogen system near walls.

EXPERIMENTAL

Set - Up

The ambient air, with about 2% humidity at 300 K, is channeled by direct suction from a high throughput pump placed downstream, into a quartz confinement tube, whose internal diameter is 22 mm with tangential injection of the gas to the torch. The generator frequency was 64 MHz, the power between 1.5 and 2.5 kW, the inductor was a 7-turn water-cooled coil, and 35 mm in length. The flow rate of air was 15 l/min. Signal analysis was performed using a 640 mm focal length monochromator,

a focusing lens and a photodiode array detector. Abel Transformation was used to obtain the local emission coefficients J(r) from the measured intensities I(x). Fig.1 shows the discharge geometry.

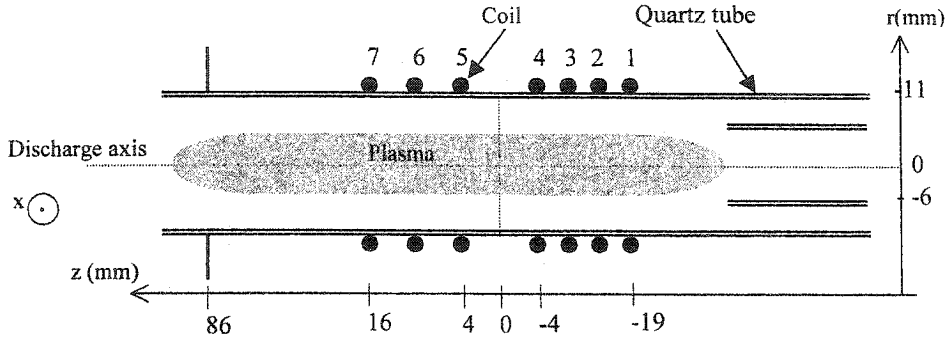


Fig.1. Schematic of air plasma torch.

Temperature Measurements

The explored zones of the discharge were :

- The central zone (between the coils 4 and 5), labeled $Z_0(z = 0)$.
- The end of coil, labeled Z_1 ($z = 18$ mm)
- The jet zone, from $z = 18$ mm to $z = 80$ mm.

In the two zones Z_0 and Z_1, the radial profile of gas temperature T_g was deduced from the local emission coefficients J(r) of air molecular spectra (Fig.2a.). In the jet the axial profile (Fig.2b.) was deduced from the intensities I(x).

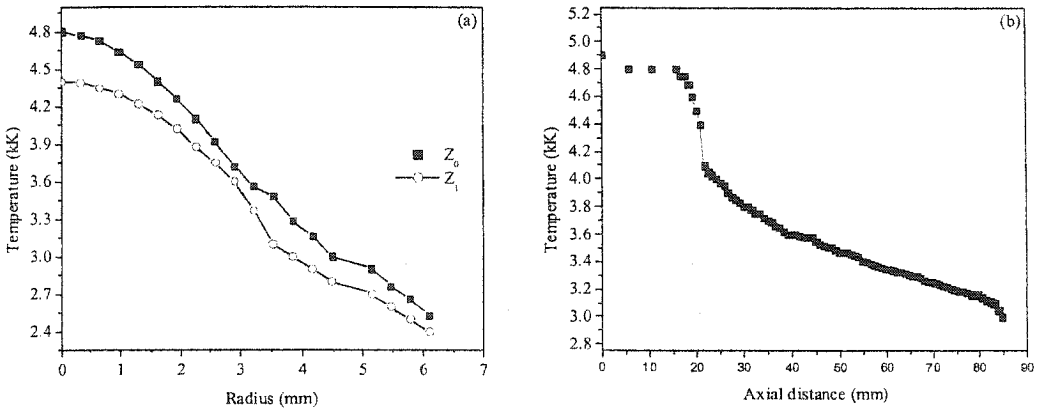


Fig.2. : a- Radial profile of T_g in Z_0 and Z_1. b- Axial profile of T_g in the plasma jet.

N_2 EMISSION OBSERVATION

In the discharge centre (Z_0) the emission intensity of N_2 is very weak; while it becomes important at the end of coil (Z_1) and over a distance up to 30 mm in the jet, particularly in the high zones of the quartz tube, near the wall. The head band (0-0) of N_2 second positive is situated at λ= 337.1 nm, close to the head band (0-0) of NH. N_2 emission shows an asymmetric behavior relatively to the discharge axis, contrary to NH emission (Fig.3b.), and seems to be related to an out of equilibrium phenomenon. The modeling of N_2 (0-0) and NH (0-0) bands allow to calculate the ratio of emission coefficients of the two head bands. The evolution of the ratio $\varepsilon_{N2}/\varepsilon_{NH}$ as a function of T_g is presented in Fig.3a.

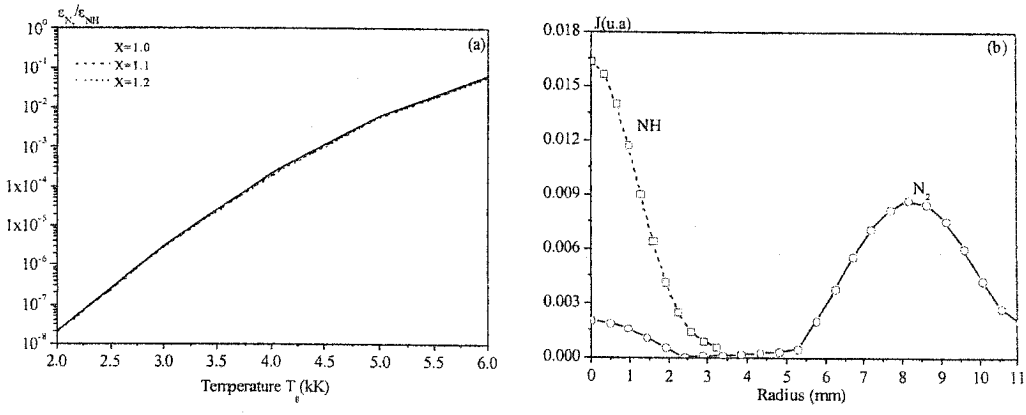


Fig.3. Emission coefficients of N_2 and NH:
a- Calculated ratio, as a function of temperature and $X=T_e/T_g$.
b- Experimental radial profiles in Z_1.

Fig.3a. shows that the ratio $\varepsilon_{N2}/\varepsilon_{NH}$ increases with temperature. From Fig.2a. The plasma temperature in Z_1 at r=6mm equals to 2400 K, at the same temperature Fig.3a gives the ratio $\varepsilon_{N2}/\varepsilon_{NH}$ = 1.6 10^{-7}, whereas Fig.3b shows that the emission of NH is null in r=6 mm and the emission of N_2 is more important. This observation indicates a non equilibrium emission of N_2 since we have:

$$\frac{\varepsilon_{N2}}{\varepsilon_{NH}}(T_g(r)) \neq \frac{J_{N2}}{J_{NH}}(r)$$

PHENOMENON INTERPRETATION

The observed intensity profile seems perfectly to be characteristic of molecular spectra emission at wall, followed by excited molecules diffusion toward the axis of the discharge and de-excitation by radiation.

We can give the hypothesis that the radiative state $N_2(C)$ results from the re-formation (inverse dissociation) of nitrogen atoms in the fundamental state $N(^4S)$ and in the metastable state $N(^2D)$ situated at 3.28 eV from the fundamental :

$$N(^4S) + N(^2D) + \text{Wall} \rightarrow N_2(C) \qquad (1)$$

Followed by the radiative emission of second positive:

$$N_2(C) \rightarrow N_2(B) + h\nu \quad (2)$$

The reaction (1) necessitates that the two states $N(^4S)$ and $N(^2D)$ have high densities near the wall whereas their densities must by quasi null according to ref. (5) in which it is showed that in the LTE conditions the $N(^2D)$ density is negligible at the accessible temperature at quartz wall whose fusion temperature is about 1883 K.

The metastables $N(^2D)$ have a long life-time : 1-3 seconds[6], so they are capable of diffusion in the plasma radially and axially.

It is possible to evaluate approximately the local density of $N_2(C)$ state if we compare the measured emission coefficients of NH and N_2 with the coefficients calculated in LTE conditions. In fig.3b. one notices that in the zone near the wall ($r \cong R$) the head band of N_2 second positive presents an emission of the same order of magnitude of NH head band in the centre ($r=0$) where the temperature is of the order of 4200 K. Fig.3a shows that, for this same temperature, $N_2(C)$ density near the wall is 2.10^3 times the value of $N_2(C)$ density which is calculated at LTE and at 4200 K, let us say a density of 7.10^8 cm^{-3} approximately near the wall.

The interest of this study is that the emission of N_2 could serve like indicator in order to localize the presence of the atoms of nitrogen for some applications in the domain of treatment and cleaning of surface in the case where the elevated temperature 2000 K is not inconvenient.

REFERENCES

(1) M. Jasinki, P. Szczucki, M. Dors, J. Mizeraczyk, M. Lubanski, Z. Zakrzewski; Czechoslovak Journal of Physics; 50, 285 (2000).
(2) A.M.Gomes, A. Almi and J.P. Sarrette; Spectrochem.Acta Part B; 1567 (1998).
(3) A.M. Gomes, J.P. Sarrette and S. Saloum; High Temp. Material Processes; 5, 169 (2001).
(4) S. Saloum; PhD Thesis, Univ. of Paul Sabatier, France (2002).
(5) P. Teulet; PhD Thesis, Univ. of Paul Sabatier, France (1998).
(6) M. Capitelli, C.M. Ferreira, B.F Gordiets and A. Iosipov; Plasma Kinetics in Atmospheric Gases, Springer Series on Atomic, Optical and Plasma Physics, 31, (2000).

Temperature Distribution Induced by Electron Beam in a Closed Cavity

A.G. Molhem and S.Sh. Soulayman
Department of Applied Physics, Higher Institute of Applied Sciences and Technology, Damascus, P.O. Box 31983, Syria
Email: ssoulayman@netcourrier.com

ABSTRACT

In order to investigate heat transfer phenomena induced by EB in a closed cavity an experimental arrangement, which allows generating and focusing an electron beam in to closed cavity within 1 mm in diameter and measuring temperature all over any perpendicular section to the EB, is used for this purpose. Experimental data show that the radial distribution of current density and temperature is normal with pressure and location dependent parameters. Moreover, there is two distinguishable regions in the EB: one is central while the other surrounds the first one.

Key Words: ***EB Plasma, Current Density Spatial Distribution, Temperature Radial Distribution***

INTRODUCTION

Electron beam (EB) has a wide field of applications in modern scientific investigations and new technologies. One can mention here, smog radiation cleaning, thin film deposition, etching, laser medium and radicals generation, gas stream diagnostic and surface treatment. In spite of that the optimization of these processes is still demanded because it allows obtaining a greater control over plasma parameters and a higher plasma density and uniformity. Nowadays, there is in use a number of new high-density plasma sources, electron cyclotron resonance[1], inductively coupled plasma[2], helicon reactors[3,4] and large area plasma processing system[5].

Up to date, it is well known that the collision of electron beam with gas's atoms and molecules is of fundamental interest in plasma physics and many researchers pay their attention to study the radial temperature distribution across the EB plasma in order to deeply understand the mechanism of heat transfer from EB to working gas. This mechanism is a very complex self-consistent problem as the propagating of EB in gases involve many physical processes like excitation and ionization, diffusion, generation of electromagnetic waves, heterogeneity of the medium, non-equilibrium state of the EB plasma, ...etc which are in their role strongly dependent on temperature. So, the heat transfer, which is largely influenced by these processes, strongly depends on the temperature also. The theoretical complete solution of the mentioned problem requires powerful computer. Moreover, when injecting an EB in a gas the angular and energy distribution of electrons as well as the properties of the gas will be changed.

On the other hand, long time ago Shoumakher[6] studied, experimentally, the spatial distribution of EB current density at some EB cross sections according to working air pressure of 30 Torr and electron initial energy of 16.5 keV. Then, he concluded that the distribution is Gaussian all over the cross section. Later on, the researchers cited this result as a non-disputable fact (see, for example, references (7-9)). Moreover, it was supposed[9] that EB current density decreases with distance exponentially and the EB energy converted into heat obtained by a metallic body located at distance z from the injection point is but a simple function of pressure ($1/P^2$). However, EB current density distribution, electron energy distribution and temperature distribution are still subjects of numerous theoretical and experimental investigations (see, for example, references (10-13)).

This work is intended to study experimentally the EB plasma (EBP) temperature and EB current density over two cross sections of the EB, at different pressures, in order to obtain useful information about the radial distribution of these quantities. The temperature in EBP and the heat flux of EB as function of pressure is also studied in the central region of EB located at distance 280 mm far from the injecting aperture.

EXPERIMENTAL ARRANGEMENT

Experiments have been carried out on a setup, which consists of the following basic components: 1) Electron gun, 2) Introductory device ID, 3) Cavity filled with a gas (air in our case) and 4) Vacuum pumps. Experimental setup is described in detail previously[14]. In this arrangement the electron beam of initial radius r_0 enters the so-called working camera (closed cavity), where it can generate EBP. One can watch the EBP through a window, designed for this purpose (see the photo of the beam on Fig.1). Moreover, the equipment allows to regulate the beam current, initial energy and the pressure of gas in the cavity. For measuring the temperature, a copper sphere of small diameter supplied with thermocouple is used (see Fig. 1).

Additionally, we used a simple arrangement for measuring the heat flow from the EB. A schematic construction is shown in Fig. 2.

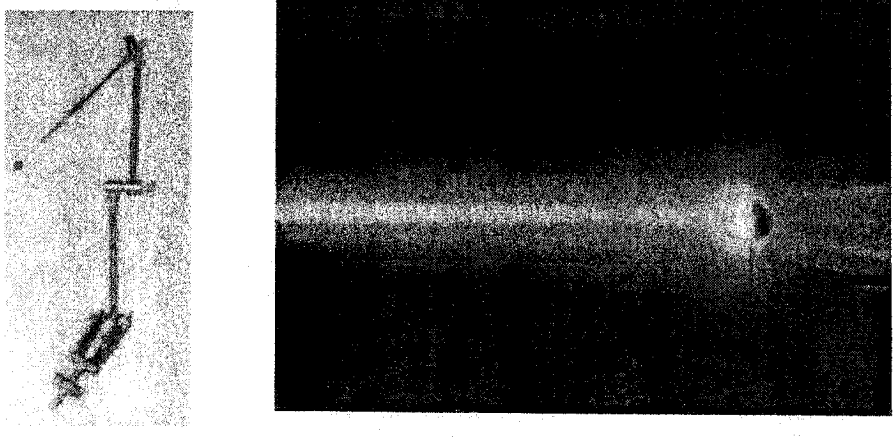


Fig. 1: The photo of EB incident on the copper sphere (on the right) and the arrangement of measuring temperature (on the left).

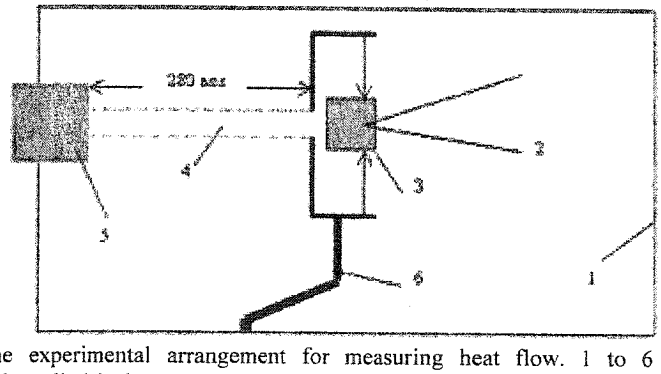


Fig. 2: The experimental arrangement for measuring heat flow. 1 to 6 denote the camera, thermocouple, cylindrical sensor, EB, ID and arm for controlling sensor respectively. Sensor is located 280 mm far from the ID.

RESULTS AND DISCUSSIONS

First of all, we have noticed (see Fig. 1) that the EB, a little far from the places of injection (ID) and incidence (copper sphere), consists of two clearly distiguishable regions: a central one with relatively small dimensions in relation to the surrounding one. The radial dimensions of each of them depend on the gas pressure in the cavity as well as on the location of cross section in relation to the

injection point ID. For example, the radius of the central region, at z=210 mm, equals 5.5 mm, 6 mm and 7 mm at pressure value of 0.66 Torr, 1.1 Torr and 2.6 Torr respectively. This division appears clearly when measuring EBP temperature or current EB density radialy and more clearly when analysing these results. Here, it was found that each of the measured EBP temperature and EB current density could be fitted well by normal radial distribution (see Figs (3) and (4)) in each of these regions. These Figures give also measured data of EBP temperature and EB current density at z =210 mm and 130 mm. It is clear from these Figures that, for low pressures, the temperature of the EBP undergoes a sudden change after moving away some mm from the axis of the EB, and this change becomes smooth for higher pressures. The same is observed for EB current density.

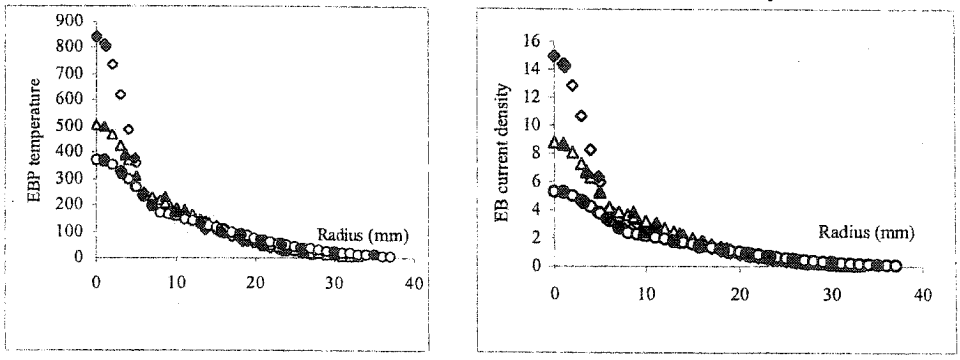


Figure 3: Radial dependence of measured (closed symbols) and fitted (open symbols) EBP temperature ($T - T_a$, T_a ambient temperature) (left in K) and EB current density (right in A/m^2) at z =210mm. Square, triangle and circle denote pressure of 0.66 Torr, 1.1 Torr 2.6 Torr respectively.

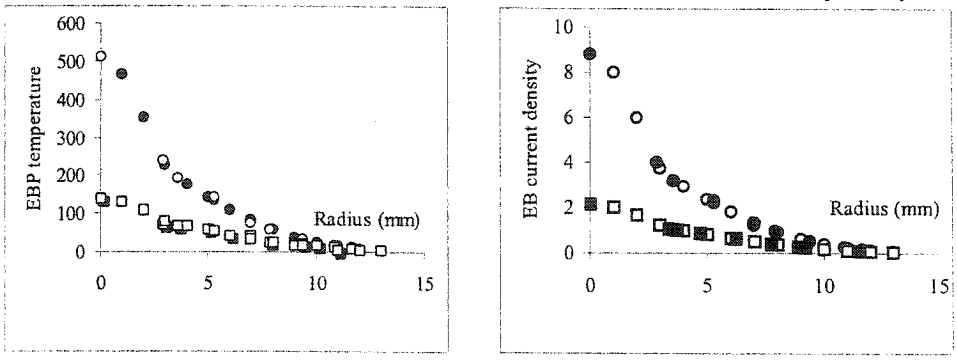


Figure 4: Radial dependence of measured (closed symbols) and fitted (open symbols) EBP temperature (left in K) and EB current density (right in A/m^2) at z =130 mm. Square and circle denote pressure of 8 Torr and 2.6 Torr respectively.

Here, it should be mentioned that we used, in our experiments the aperture radius r_0=0.5 mm, the initial electron energy of 25 keV and the initial EB current intensity of 10 mA. So, the initial EB current density equals 12739 Am^{-2}. This means that our working conditions satisfy the conditions of producing quasi-stationary plasma (namely: the density of the current of beam $10^3 < j_b < 10^6$ A/m^2, and the pressure of the gas $P \sim 1-100$ Torr). So, the space charge is compensational and the density of secondary electrons equals to the density of ions (9). We must also mention that the quasi-stationary state of plasma can be realized by the continuous injection of electron beam, that leads to a balance in formation and annihilation of charged particles by many physical mechanisms (basically by diffusion)[9]. Therefore, the steady distribution of temperature in the cavity could be easily interpreted according to these reasons. Moreover, this result enables us to use steady-state equation for describing the heat transfer.

For the EBP temperature and the heat flux of EB as function of pressure in the central region of EB cross section, located at distance 280 mm far from the injecting aperture, an arrangement shown in Fig. 2 is used. The sensor is a copper cylinder, of 1cm in diameter and 1 cm in height, equipped with a thermocouple, is used. The obtained results are shown in Fig. 5. On the contrary to (9), it was found that the dependence of all quantities shown in Fig. 5 on pressure up to 1.1 Torr could be well approximated by an exponential function. Moreover, the measured radius of enlargement of EB, for pressures more than 1 Torr, differs largely (see Figs 3 and 4) from the proposed theoretical values.

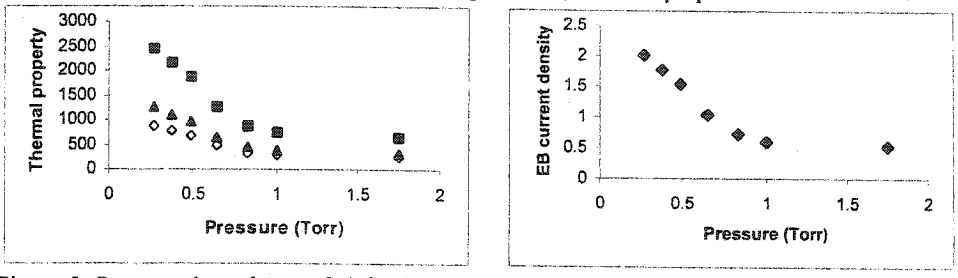


Figure 5: Pressure dependence of (left Fig.) EBP temperature increase (open symbol), EB energy (triangle) in J, heat flow, which is the beam energy flow rate to the metallic stopper, (square) in kWm^{-2} and EB current density (right Fig.) at z =280 mm.

Here it should be mentioned that the EB energy is calculated by:

$$E = 2\pi \int_0^{0.005} N_e(z,r) E_e(z,r) r dr$$

where z is the distance from the ID (see Fig. 2) which equals 280 mm in the case of Fig. 5, $N_e(z,r)$ is the radial distribution of incident electrons at z distance and $E_e(z,r)$ is the radial distribution of the energy of incident electrons. The number 0.005 denotes the radius (in m) of copper cylinder used in experimental arrangement (see Fig. 2).

REFERENCES

(1) M. Lampe, G. Joyce, W. M. Manheimer and S. P. Slinker; IEEE Trans. Plasma Sci.; 26 (1998) 1592 – 1596.

(2) J. H. Keller; Plasma Sources Sci. Technol.; 5 (1996) 166 – 172.

(3) R. W. Boswell and F. F. Chen; IEEE Trans. Plasma Sci.; 25 (1997) 1229 - 1244.

(4) F. F. Chen and R. W. Boswell; IEEE Trans. Plasma Sci.; 25 (1997) 1245 - 1257.

(5) W. M. Manheimer, R. F. Fernsler, M. Lampe and R. A. Meger; Plasma Sources Sci. Technol.; 9 (2000) 370 – 386.

(6) B. Shoumakher; in: "Electron-Beam and Ion-Beam Technology"; MPTI, Moscow (1968) 7 – 43 (in Russian).

(7) N. N. Rykalin, I. V. Zuev and A. A. Uglov; " The Fundamentas of Electron-Beam Material Treatment"; Moscow (1978) (in Russian).

(8) V. L. Bychkov, M. N. Vasilev and A. C. Koroteev; " Electron-Beam Plasma"; MGOU, Moscow (1993) (in Russian).

(9) M. N. Vasilev; " Electron-Ray and Electron-Beam Vacuum-Free Plasma Technologies"; MPTI, Moscow (1999) (in Russian).

(10) V. I. Poznyak, D. V. Kalupin, A. V. Khramenkov, N. A. Kirneva, T. V. Myalton, Yu. D. Pavlov, V. V. Piterskii, E. G. Ploskirev, D. V. Shelukhin and V. A. Vershkov; ECA C; 22 (1998) 607 – 610.

(11) N. Nickles, R. E. Davies and J. R. Dennison; 6th Spacecraft Technology Conference; AFRL-VS-TR-20001578, 1 September (2000) 275 – 280.

(12) N. G. Lehtinen, U. S. Inan and T. F. Bell; Geophys. Res. Letters; 27 (2000) 1095 – 1098.

(13) Sh. Yonemura and K. Nanbu; Jpn. J. Appl. Phys.; 40 (2001) 7052- 7060.

(14) A. G. Molhem; Electron Beams in Vacuum and Plasma Systems; MS Thesis, MPTI, Moscow (2001).

Electron Temperature in Ar Glow Discharge

A.A. Garamoon, F.F. Elakshar, E.F. Kotp*, and A. Samir
Center of Plasma Technology, Faculty of Science, Alazhar University, Nasr City, Cairo, Egypt.
** Phys. Dept., Faculty of Science, Alazhar University, Assuit Branch, Assuit, Egypt.*
ahmed_samir_aly@yahoo.com

ABSTRACT

The electron temperature (T_e) has been measured using three different methods; single probe, double probe, and optical emission spectroscopic techniques. It has been found that, T_e decreases by increasing the gas pressure and attains a maximum value at the end of the cathode fall. Two groups of electrons have been detected by single probe in both the cathode fall and negative glow regions .The high and low energy groups were found in the range of 6-15 eV and 3-5 eV respectively. In positive column, however, only one group of electrons has been detected and has been found to have a Maxwellian distribution. A comparison between the results of the three used techniques has given a reasonable agreement.

Key Words: DC glow discharge, electron temperature, groups of electrons, electric probes, optical emission spectroscopy.

INTRODUCTION

DC glow discharge applications have been developed extensively through the last century. Its technology has covered a vast range of industrial applications. In this paper, the electron temperature (T_e) in different regions of glow discharge has been studied under different conditions of the discharge. The present work has been carried out in the normal glow discharge region. In the normal glow region, the potential difference across the tube becomes almost independent of the current flowing through it [1,2].

EXPERIMENTAL SETUP

The discharge cell consists of two movable parallel electrodes enclosed in a pyrex tube. The two electrodes were made of copper brass discs of 3 cm diameter and their edges were rounded in hemi-sphere of radius equal to the electrodes half thickness . The pyrex glass tube was 4 cm in diameter. After pumping down the discharge tube a continues dynamic flow of argon gas (of purity 99.98 %) was let in the system through a needle valve at the desired pressure.

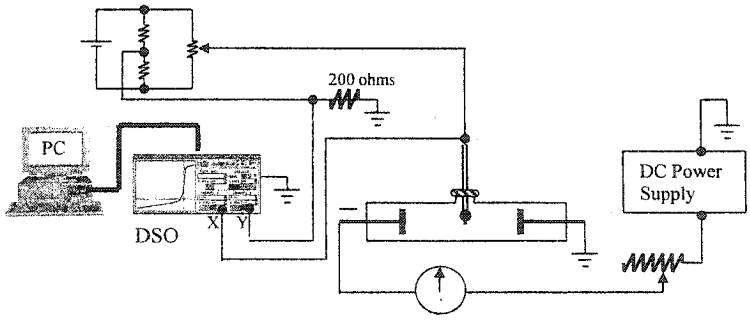


Fig. (1) Circuit diagram of single probe I-V curve measurement.

Fig. (1) shows the electric circuit used to measure the single probe I-V curve. Digital storage oscilloscope (DSO) (type HM-407) has been used to measure the I-V curve of the discharge. The

oscilloscope has RS232 card, built in, which was able to connect the oscilloscope to a personal computer. Fig. (2) shows the electric circuit used to measure the double probe I-V curve. McPherson scanning monochromator [model 270] with 35 cm focal length and a grating of 1200 grooves/mm, has been used to analyze the spectra of the discharge. The intensity of the light has been measured using a photomultiplier tube (type 9558QB) placed after the monochromator.

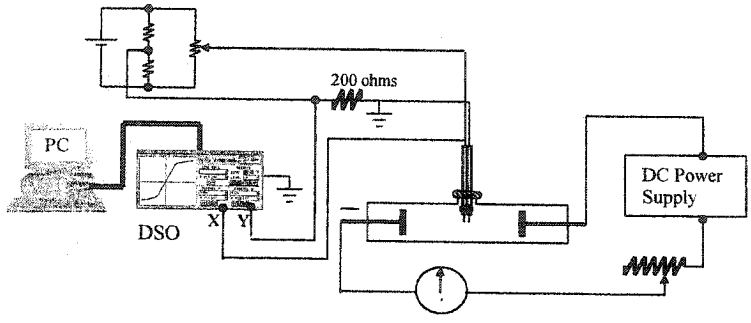


Fig. (2) Circuit diagram of double probe I-V curve measurement.

RESULTS AND DISCUSSION

The measured values of T_e (using the three techniques) at different currents show that, T_e is independent of the discharge current in the normal glow region. This is related to the constancy of potential and electric field at different discharge currents in the normal glow region[3].

Fig. (3) shows values of T_e measured by the double probe as a function of P at different axial positions. T_e decreases by increasing the gas pressure (P), which can be explained in the light of the fact that the mean energy of an electron, gained by the electric filed E, is $eE\lambda_e$, where λ_e is the electron mean free path, so T_e is proportional to λ_e and hence inversely proportional to P.

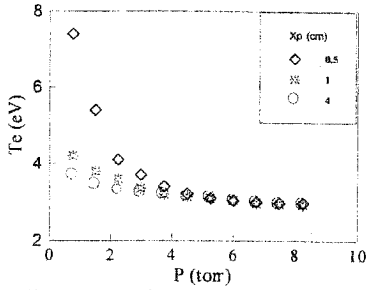


Fig. (3) Te as a function of P, using double probe at different distances form cathode.

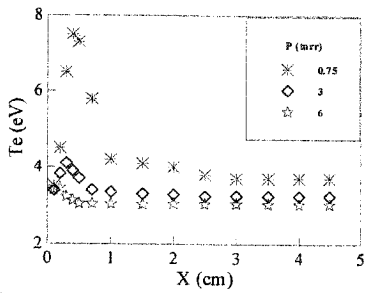


Fig. (4) Te as a function of x at different pressures.

Fig. (4) describes the axial distribution of T_e at different pressures. T_e increases sharply by increasing the distance from the cathode (x) and it reaches a maximum value at the edge between the cathode fall and the negative glow, then it decreases sharply in negative glow and finally it nearly saturates in positive column. This behavior of T_e with the axial distance is related to the axial distribution of the electric field. In the cathode fall region, the electric field is very high[3] and electrons are accelerated by this field, so T_e increases by increasing x. As soon as the electrons enter the negative glow region their energies are lost in inelastic collisions, also their energies are continuously lowered due to the deceleration in the reversal electric field that exist in this region. As a result of these factors, electrons enter the Faraday dark space region with very low energies, inelastic collisions are negligible. In fact, electrons in Faraday dark space, move by diffusion[1], as a result of the weak electric field, T_e begins to saturate. In the positive column region a very low increase in the electric field exists, and the gain of

small energies in this region is lost by the few inelastic collisions, and therefore T_e saturates in this region or increases in a very slow rate.

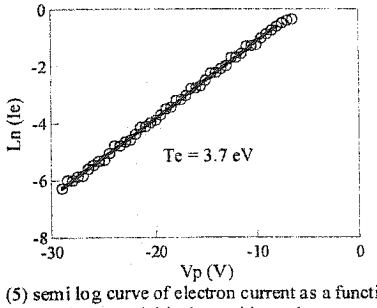


Fig. (5) semi log curve of electron current as a function of single probe potential in the positive column.

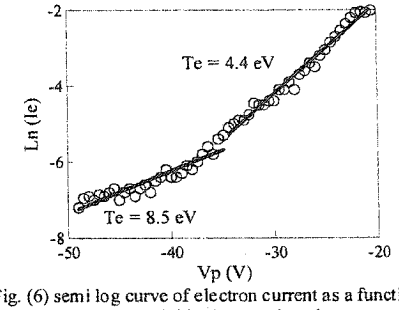


Fig. (6) semi log curve of electron current as a function of single probe potential in the negative glow.

Fig. (5) represents the semi-log curve of the electron current of the single probe (I_e) as a function of the probe potential (V_p) in the positive column region. This straight line confirms that, the positive column contains only one group of electrons with a Maxwellian distribution. Fig. (6) shows the corresponding semi-log curve in the negative glow region. Two straight lines are obtained in this case, which confirms the presence of two groups of electrons with two different temperatures. Also measurements in the cathode fall region has shown the existence of the two groups (high energy group and low energy group).

Figures. (7a) and (7b) show the axial distribution of the electron temperature for high energy group, T_{eh}, and low energy group, T_{el}, at different pressures.

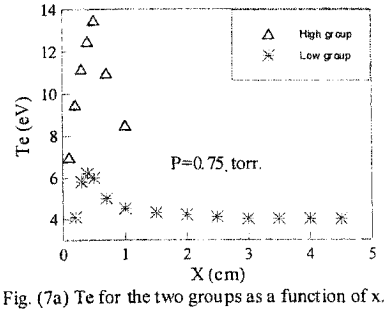


Fig. (7a) Te for the two groups as a function of x.

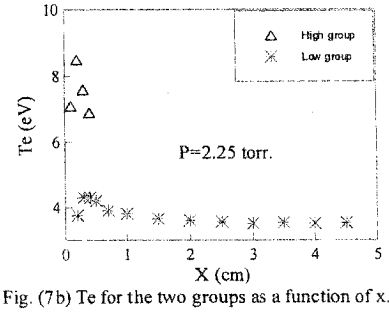


Fig. (7b) Te for the two groups as a function of x.

The general behavior of the electron temperature with the axial distribution for both T_{eh} and T_{el} is the same as that of T_e measured by the double probe. Also the position of the peak on the x-axis of each group is the same and it moves toward the cathode as the pressure increases. It is also noticeable that, high energy group disappears at a certain distance from the cathode. This distance decreases as the pressure increases. Disappearance of high energy group of electrons can be explained in view of the fact that they enter the negative glow with their maximum energy and therefore start to lose their energy in the inelastic collisions. At a certain distance from negative glow edge (relaxation length), the energy of this group of electrons will be consumed by inelastic collisions; and hence their energy becomes low and the whole swarm of electrons becomes a low energy group. At this point Faraday dark space region begins to be formed where electrons are unable to perform inelastic collisions.

The relative intensity of the argon glow discharge spectra has been measured using optical emission spectroscopic technique. The ratio of the relative intensity of two lines technique has been used in the present work to determine T_e . For high accuracy it's desirable to choose two spectral lines whereas the ratio of the relative intensity of the two lines is a strong function of T_e . This will be the case if the difference between the transition energy levels of the two lines is large enough. However for neutral atoms, the greatest attainable energy difference still yields a minimum uncertainty in temperature of 70 % for argon gas in the range of 0.5 to 1.5 eV[4]. The accuracy may be improved somewhat by measuring several pairs of spectral lines and averaging the resulting temperatures. However this rather time-consuming technique is only partially successful in reducing the experimental uncertainty. A larger

energy difference can be obtained if one of the transitions occurs in singly ionized atom, and the other occurs in a neutral atom. The relative intensity of argon neutral atom (4159 and 4259 Å) and argon singly ionized atom Ar^+ (4348, 4765, and 4880 Å) have been measured at different pressures and discharge currents in both negative glow and positive column. Steady state corona model has been assumed to estimate T_e. The ratio of two lines intensity T_e is expressed in the form[5]:

$$kT_e = [(7.87\times10^{-9})E_\infty^{'7/4}\frac{fgI'\lambda'^3}{f'g'I\lambda'^3}\exp(\frac{E'+E_\infty-E}{kT_e})]^{4/3}$$

This equation shows that, T_e can not be written as an explicit function of the ratio of lines intensity [i.e. $T_e \neq f(I'/I)$]. The implicit function [$T_e=f(I'/I,T_e)$] can be solved numerically. Successive iteration has been carried out to solve the equation. The ratios of two lines intensities I'/I, one from single ionized atom and the other from neutral atom, have been measured for six pairs of lines (4159/4348, 4159/4765, 4159/4880, 4259/4348, 4259/4765, and 4259/4880 Å).

Figures (8) and (9) show values of T_e as a function of the gas pressure, using the six pairs of lines, in positive column and negative glow respectively. Figures (8) and (9) indicate a reasonable agreement of the measured values of T_e using the different pairs of lines.

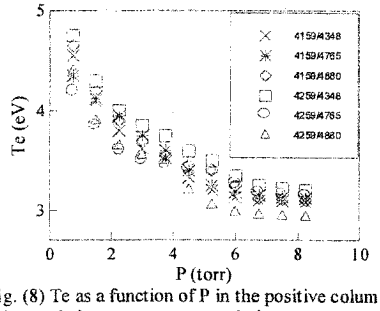


Fig. (8) Te as a function of P in the positive column, using emission spectroscopy technique.

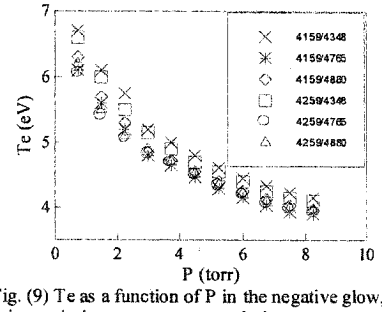


Fig. (9) Te as a function of P in the negative glow, using emission spectroscopy technique.

Figures (10) and (11) represent values of T_e as a function of the gas pressure in positive column and negative glow regions, respectively, using the average values measured by the three techniques (i.e. single probe, double probe, and optical emission spectroscopy). A good agreement between the three techniques is observed.

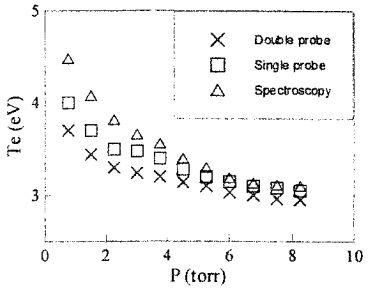


Fig. (10) Te as a function of P measured by different techniques in positive column.

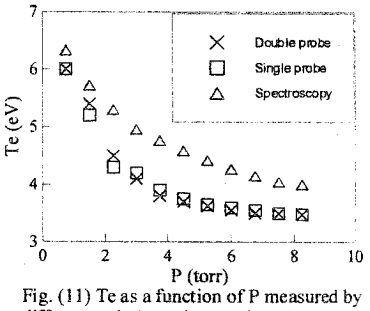


Fig. (11) Te as a function of P measured by different techniques in negative glow.

REFERENCES

(1) Lisovskiy V.A., Yakoven S.D., and Yegorenkov V.D., J. Phys. D: Appl. Phys. 33, 2722 (2000).
(2) Phelps A.V. and Petrovic Z.Lj., Plasma Sources Sci. Technol. 8, R21 (1999).
(3) Garamoon A.A., Samir A., Elakshar F.F., and Kotp E.F., Plasma Sources Sci. Technol. 12, 417 (2003).
(4) Schmidt P.S., Inst. Tech. 22, 35 (1975).
(5) Griem H.R., "Plasma Spectroscopy", McGraw-Hill, New York (1964).

A Practical Method Using Labview® for Measurements of The Electron Temperature in a Helium Glow Discharge by Optical Emission Spectroscopy

Eynas Amer, L. Z. Ismail* and M. El Shaer.
Faculty of Engineering, Zagazig University, Zagazig, Egypt.
**Faculty of Science, Cairo University, Cairo, Egypt.*
MELSHAER@LINK.NET

ABSTRACT

A practical homemade system is used to measure the electron temperature of a DC helium glow discharge by optical emission spectroscopy. The system consists of standard laboratory equipment, such as monochromator equipped with stepper motor, photomultiplier, and calibration lamp. The output of the photomultiplier is recorded using a data acquisition card. The electron temperature is calculated by three methods: line intensity versus excitation energy, and relative intensities of two lines with and without taking into consideration the plasma depth. The LTE model is assumed to be valid. Reasonable values for the electron temperature are obtained. The electron temperature is found to decrease with the discharge pressure, and increase with the discharge current density.

Key Words: Plasma Diagnostic, Glow Discharge, Spectroscopy Technique.

EXPERIMENTAL SET-UP

The experimental set-up is shown in figure (1). A DC glow discharge is built using a cylindrical Pyrex glass tube about 83 cm long and 4 cm diameter, at its two ends we introduce two movable cylindrical brass electrodes of 2.5 cm diameter, the inter-electrode distance can vary and is set in these measurements to a value of 23 cm. The plasma emission light is observed using a monochromator (model Bausch and Lomb) equipped with a photomultiplier tube (1P28). The output of the photomultiplier tube is recorded using a data acquisition card, (super 12 bits A/D-D/A card). This card is a high precision data conversion system for PC/XT, PC/AT, or compatible computer.
A simple program is written with LabView® standard software. LabView® is short for laboratory virtual instrument engineering workbench; it is a powerful and flexible instrumentation and analysis software using a graphical programming language, known as the G programming language to create programs relying on graphic symbols to describe programming actions.

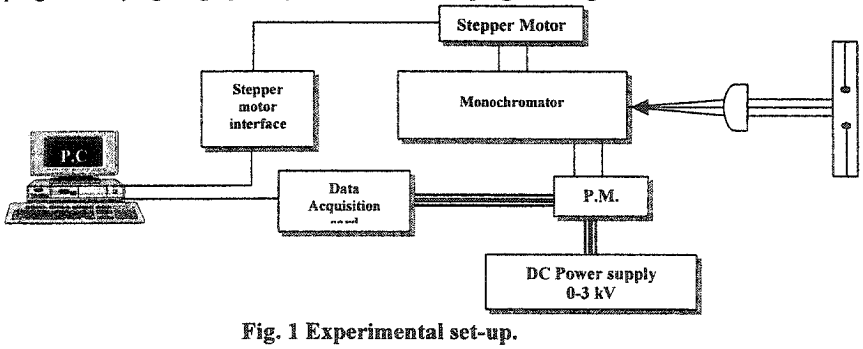


Fig. 1 Experimental set-up.

Experimental Results

Electron temperature of DC helium glow discharge has been evaluated using optical emission spectroscopy technique assuming local thermodynamics equilibrium (LTE) model at different conditions of gas pressure and discharge current density. The discharge current density varies from $1.018\text{x}10^{-3}$ A.cm^{-2} to $2.8\text{x}10^{-3}$ A.cm^{-2}, and the pressure of the working gas varies from 2 mbar to 11.5 mbar. In order to calculate the electron temperature assuming LTE model, we use the line intensity versus excitation energy method. The intensity (I) of the line having a wavelength (λ) is given in reference (1):

$$I_{ij} = \frac{h\upsilon}{4\pi} g_i A_{ij} \frac{N_o}{U(T)} e^{-\frac{E_i}{kT}} = \frac{2h\pi e^2}{m} \frac{g_i f_{ij}}{\lambda^3} \frac{N_o}{U(T)} e^{-\frac{E_i}{kT}} \qquad [1]$$

Where g_i is the statistical weight for level i; f_{ig} is the oscillator strength between two levels i, g; E_{ig} is the excitation energy from level i to g; k is the Boltzmann constant; T is the electron temperature. This formula is used to calculate the plasma electron temperature using a fitting program with the experimental measured lines intensities and the spectroscopic data. The data fitting to the LTE model at pressure P equal to 2.34 mbar and current density J equal to $2.8\text{x}10^{-3}$ A.cm^{-2} is shown in figure (2).

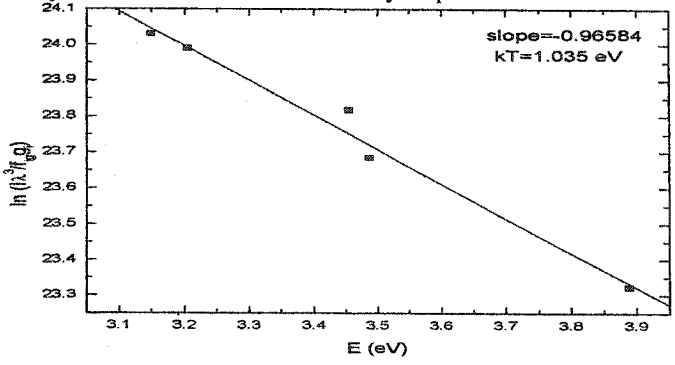


Fig. 2 Electron temperature at P=2.34 mbar. J=$2.8\text{x}10^{-3}$ A.cm^{-2}.

The behavior of the calculated electron temperature as function of gas pressure at constant current density J=$2.8\text{x}10^{-3}$ A.cm^{-2} and at J=$1.273\text{x}10^{-3}$ A.cm^{-2} is shown in figure (3). Figure (4) shows the behavior of the discharge current density at constant pressure P= 2 mbar.

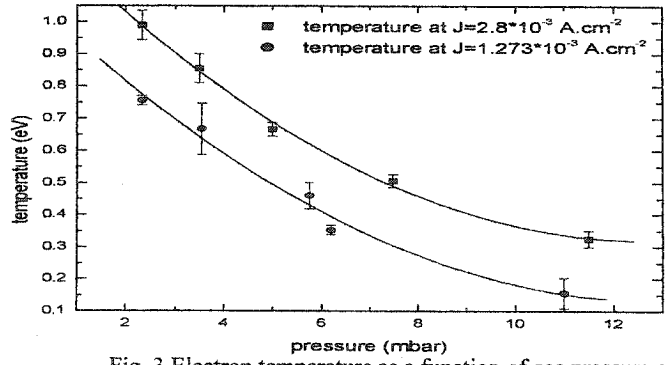


Fig. 3 Electron temperature as a function of gas pressure at J=$2.8\text{x}10^{-3}$ A.cm^{-2} and at J=$1.273\text{x}10^{-3}$ A.cm^{-2}.

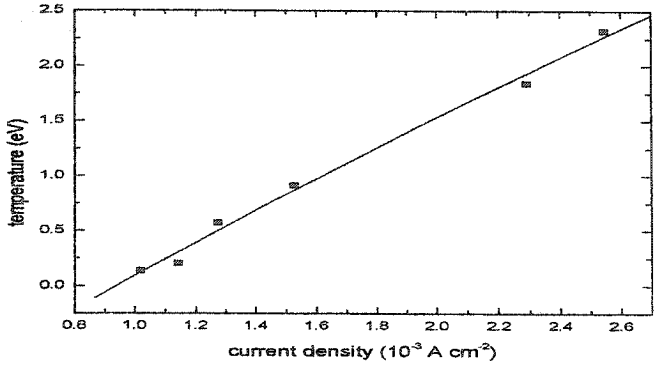


Fig. 4 Electron temperature as a function of discharge current density at constant pressure P=2 mbar.

The electron temperature has been estimated using relative intensities of two lines with and without taking the plasma depth into consideration method, which are given in references (2) and (3) respectively. The comparison between the behaviors of the electron temperature calculated by the three used methods as a function of gas pressure at J=2.8x10^{-3} A.cm^{-2} is shown in figure (5).

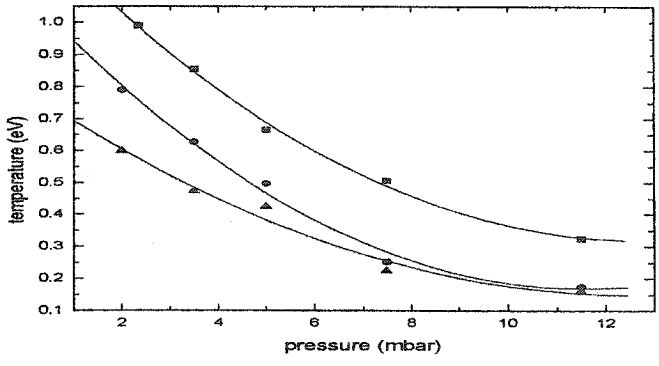


Fig. 5 Comparison between behavior of electron temperature calculated by the three used methods as a function of gas pressure at J=2.8x10^{-3} A.cm^{-2}.

- Electron temperature calculated by using line intensity versus excitation energy method.
- Electron temperature calculated by using relative intensities of two lines method taking plasma depth into consideration.
- Electron temperature calculated by using relative intensities of two lines method without taking plasma depth into consideration.

INTERPRETATION OF THE RESULTS

The results reveal that the electron temperature decreases with increasing the gas pressure this behavior is interpreted using the time dependent electron balance equation is given in reference (4):

$$\partial n_e/\partial t = n_e n_o k_{ion} - n_e D_a/\Lambda^2 - n_e^2 k_{rec}^{rad} - n_e^3 k_{rec}^{(3)} \quad [2]$$

The first term of the R.H.S. of equation [2] expresses the electron production by ionization of atoms with number density n_o in the ground state where k_{ion} is the ionization rate coefficient. The second term describes electron losses through ambipolar diffusion of electron-ion pairs to the wall where they recombine. The ambipolar diffusion coefficient is given by:

$$D_a = (\mu_i D_e + \mu_e D_i) / \mu_e + \mu_i \quad [3]$$

Where D_e, D_i are the electron and ion diffusion coefficients and μ_e, μ_i are the respective mobilities. For a parallel plate reactor with cylindrical geometry the diffusion length Λ is given by:

$$\Lambda = ((\pi/L)^2 + (2.405/\overline{R})^2)^{-1/2} \quad [4]$$

Where L is the distance between the plates and $\overline{R}$ is the mean radius of the vessel. The last two terms of the R.H.S. of equation [2] describe bulk recombination processes, radiative recombination (k_{rec}^{rad}) and three-particle-recombination ($k_{rec}^{(3)}$). These recombination terms can be neglected and it is assumed that the ambipolar diffusion is by far the most important electron loss mechanism. For a DC glow discharge the electron density can be taken as a constant, $\partial n_e/\partial t = 0$. Thus the equation [2] yields:

$$n_o k_{ion} - D_a/\Lambda^2 = 0 \quad [5]$$

D_a can be written as:

$$D_a = \tilde{D}_a(T_e) / n_o \quad [6]$$

Where $\tilde{D}_a$ is weakly dependent on electron temperature, it will be replaced by a constant value, accordingly:

$$k_{ion}(T_e) = (1/n_o^2)(\tilde{D}_a/\Lambda^2) \quad [7]$$

Equation [7] illustrates that the increasing of n_o is associated with decreasing in k_{ion}, accordingly T_e decreases. We conclude that electron temperature decreases with increasing gas pressure.

CONCLUSION

The linear behavior of LTE parameters as a function of the emitted photon energy (eV) reveals the ability of applying LTE model for the considered helium glow discharge in the applied range of gas pressure and discharge current density.

Accordingly the behavior of the estimated plasma temperature T_e as a function of the gas pressure and discharge current density reveals an agreement with the expected behavior for both the pressure and the current density. This shows the possibility of applying this method, in situ, for glow discharge processing. The advantage of this method with respect to the other electric probe methods is that it neither disturbs nor pollutes the plasma.

REFERENCES

(1) Lotfi Z. Ismail and Atef Eljoundi, "Spectroscopic studies of mercury plasma under differet metallic vapour", Indian Journal of Pure & Applied Physics, Vol. 34, November 1996, pp. 876-879.

(2) A. B. Rodrigo, "Collisional-radiative processes in plasmas and plasma spectroscopy", 1991 spring school on plasma physics, International Centre for Theoretical Physics, Trieste, Italy.

(3) Bekefi G., Deutsch C., and Yakkobi B., "spectroscopic diagnostic of laser plasmas, in: principle of laser plasmas", Wiley, New York (1976), chapter 13.

(4) R. J. Seebock, W. E. Kohler and M. Romheld, "Pressure dependence of the mean electron energy in the bulk plasma of an RF discharge in argon", Contrib. Plasma Phys. 32 (1992) 6, pp. 613-622.

Measurement of the Formative Time Lag of Argon Using Magnesium Electrode

E. F. Kotp[1], A. H. Saudy, F.F. Elaksher, A.M. Bakry and A. A. Garamoon
Center of Plasma and Technology, Alazhar Univ., Nasr City, Cairo, Egypt.
1-Physics Dept. Alazhar Univ., Assuit Branch, Assuit, Egypt.
Eizaldeen@yahoo.com

ABSTRACT

First and secondary ionization coefficients, ηand ω/α, have been estimated using magnesium as a cathode in the range of 80 ≤ E/p ≤ 300 V/torr.cm of the argon discharge. The first ionization coefficient (η) estimated using empirical equation and the secondary ionization coefficient (ω/α) has been estimated using the measured values of the breakdown potentials V_B and the values of η calculated.

The formative time lag, τ_f, of argon gas has been measured as a function of (E/p) and over-voltage percentage. For over-voltage the measurements is in the range of 0.25 to 3% above the breakdown voltage and for E/p in the range of 80 ≤ E/p ≤ 300 V/torr.cm. The results show that τ_f is in the range of microseconds.

Key Words: ***Formative Time Lag, Plasma Phys., First and second ionization.***

INTODUCTION

The importance of studying the physical processes that initiate electrical breakdown to generate low temperature plasma at low gas pressures is that it has numerous gas applications. Studying the physics of the electrical breakdown in gas illuminate understanding of physical process that takes place in the discharge. Many authors have studied the effect of different electrode materials, gases and pressures on the electrical breakdown voltage, first and secondary coefficients and the formative time lag in gas discharge[(1)]. A study of formative time lags should make it possible to estimate the relative importance of different ionization processes. The formative time lag (t_f) plus statistical time lag (t_s) equal to the electrical time delay (t_d) that takes place between the moment of applying dc voltage on the electrodes to the moment electrical breakdown starts to takes place [(2)].The formative time lag depend on the gas pressure, E/p (E is the electric field between two electrodes, p is the gas pressure), ratio D/d (where D is the diameter of the electrode and d is the distance between two electrodes) and the over-voltage, Δv/v, where over-voltage is the voltage that exceeds the electric breakdown voltage [(3)].

The aim of this paper is to determine the electric breakdown voltage, the secondary ionization coefficient and the formative time lag in argon gas discharge using magnesium as a cathode.

EXPERIMENTAL SETUP

The experimental setup consists of discharge tube, electric circuits and high vacuum system. The discharge tube consists of pyrex glass tube of diameter 10 cm and length 40 cm. the cathode was made from magnesium and the anode was made from aluminum. The diameter of electrodes was 5 cm and the distance between was fixed at 1 cm a continuum flow of argon gas was used in the pressure range of 0.2 to 4 torr. The cathode was irradiated by intense UV from

high pressure mercury discharge through quarts window to provide an efficient source of photoelectrons (I_o) passing through the quartz windows Figure (1) shows the diagram of the discharge tube and SCR electric circuits used to measure the breakdown voltage and the formative time lag.

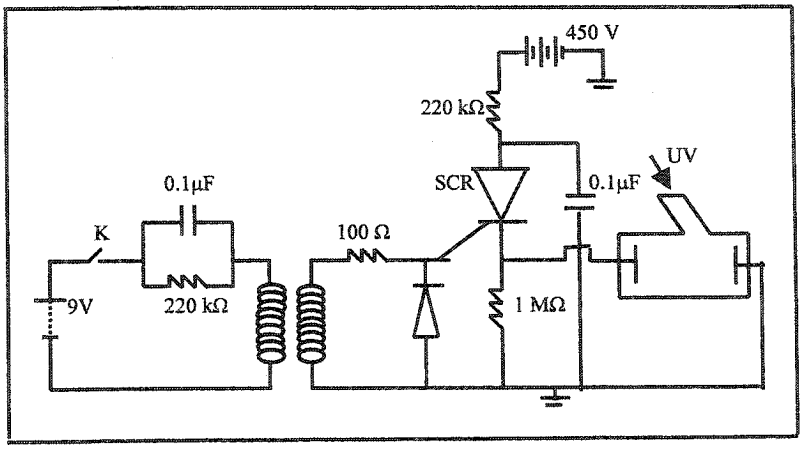


Figure (1)

RESULTS AND DISCUSSION

The first ionization Coefficient, η, was estimated as a function of (E/p), using the relation mentioned in[3].

$$\eta = \frac{A}{(E/p)} \exp -[B/(E/p)] \qquad (1)$$

Where A, B are constants depend on the gas type, for argon A=14 V/torr.cm and B =180 V/torr.cm, when (E/p) is in the range 100-1000 V/torr.cm[4], E is the electric filed between the electrodes and p is the pressure.

Figure (2) shows the values of η as a function of (E/p) for argon. In the range of E/p <180 V/torr.cm, η increases until it reaches a maximum value of (E / p) = B, where at this point

η = A / B exp, and then the values of η decreases.

Figure (3) shows the Paschen curve for argon discharge, the decrease in V_{Br} by increasing p.d may be attributed to the increasing of collision frequency between electrons and neutral atoms. Above $(V_{Br})_{min}$ the breakdown voltage increases gradually. This can be attributed to the decrease of the ionization coefficient at low (E/p) values.[5].

Fig (2)

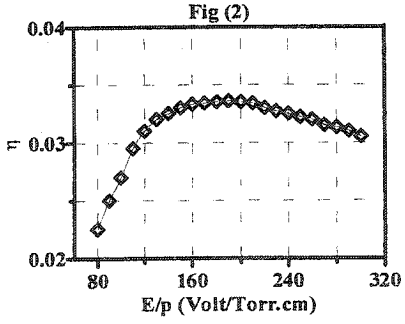
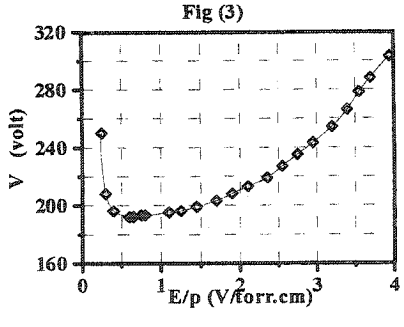


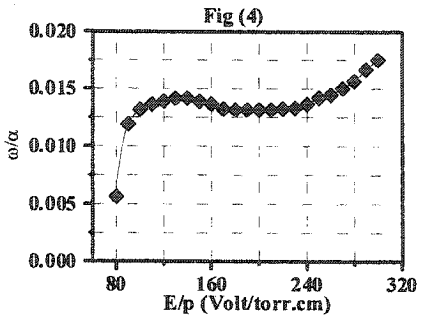
Fig (3)



The number of secondary electrons emitted in the discharge by the different secondary electron processes per ion pair produced in the discharge is known as the total secondary Townsend electron coefficient ω/α.

Values of the secondary ionization coefficient ω/α are estimated using the equation(6).

$$\frac{\omega}{a} = \frac{1}{e^{\eta V_{Br}}} \qquad (2)$$



Values of ω/α at a certain (E/p) is determined using the estimated values of η and the measured values V_{Br} , at the same value E/p. Values of ω/α as a function of (E/p) are shown in figure (4) for argon discharge. At low E/p < 120 volt/torr.cm, ω/α increases rapidly to a maximum value then decreases very slowly, and followed by an increases once more at a medium rate. The curve in this figure can be subdivided into three regions. In the first region E/p=80 to 120 V/torr.cm, (ω/α) rises sharply and this may be attributed to the photoelectric emission by photon bombardment on the cathode surface [5]. In the second region (E/p) = 120 to 200 V/torr.cm, ω/α decreases slowly by increasing E/p and this is due to the decrease in the photoelectric effect as a result of the decrease in the number of excited atoms in this region. In the third region E/p > 200 V/torr.cm where ω/α increases by increasing (E/p), this is well known to the increasing contribution of ions i.e. the dominant secondary process in the discharge in this region of E/p is due to the impact of ions on the cathode[5]. The maximum of this curve may be attributed to the maximum of a certain active secondary process, at low (E/p). Also the minimum of this curve may be attributed to the beginning of another different secondary process. At high (E/p). Identification of such secondary process needs the determination of the formative time lags.

Figure (5) shows the signal oscillogram obtained for the breakdown voltage as a function of time at different over-voltage percentage. The formative time lag at any given (E/p) will be related to the active secondary processes.

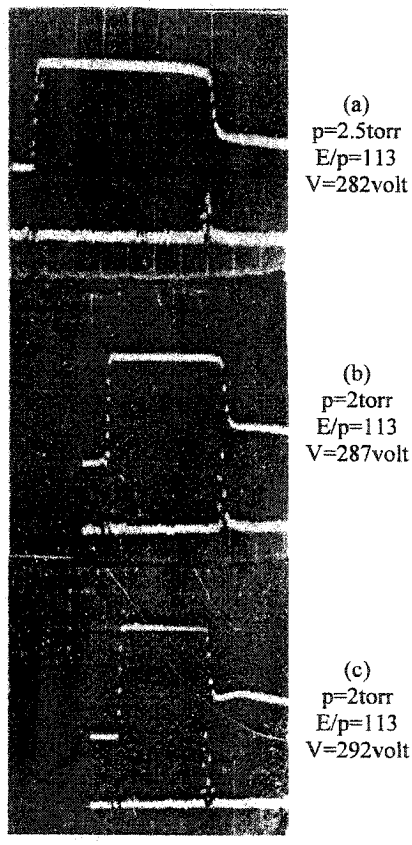


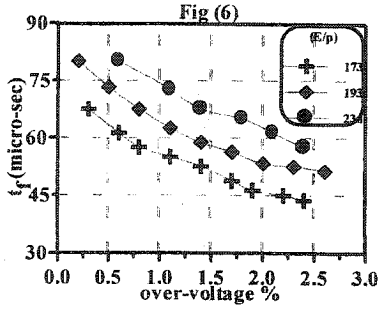
Figure (5): Show that Three actual oscillograms showing voltage vs. time in argon for Mg cathode. Time scale 1 μs/div, 100 volt/div

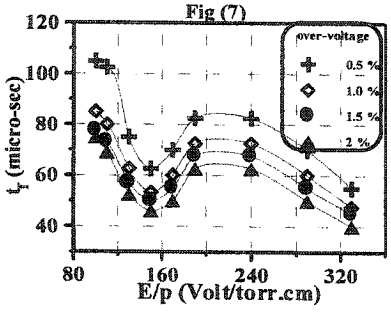
Figure (6) shows the relation between the formative time lag, tf , and the percentage over-voltage (100 ΔV/VBr) for argon gas discharge at different E/p. By increases of (100 ΔV/VBr) the acceleration of the charged particles increases, which effects the secondary processes and hence decreases the formative time lag. When the over-voltage percentage changes from 0.6 to 2.4, the formative time lag decreases from 80 to 65 μses at (E/p) = 236 V/torr, from 70 to 52 μsec at (E/p)

=193 V/torr.cm and from 60 to 46 μsec at (E/p) =173 V/torr.com.

Figure (7) shows the values of the formative time lag as a function of E/p. The figure can be subdivided into three regions. In the first region, where (E/p) changes from 90 to 140 V/torr.cm, the formative time lag decreases by increasing E/p, this may be related to the decrease of the absorption of photons in the bulk of gas, its effect at the cathode photoelectric emission (4), leading to increase of ω/α and then decreases of the formative time lag. It could also be caused by the increase of the number of excited atoms in this region. In the second region, 140 < (E/p) < 200 V/torr.cm, the formative time lag increases by increasing (E/p). This may be due to the gradual decrease of the number of photons and the increase of excited atoms that reach the cathode because the secondary ionization.

In the third region, 200 < (E/p) < 320 V/torr.cm, the formative time lag decreases slowly as E/p increases and it can be related to the increase in positive ions and the role of the positive ions as a secondary ionization process.





CONCLUSION

The measurement of (ω/α) and t_f as functions of (E/p) is an effective way for distinguishing secondary ionization cathode processes in gas discharge. Formative time lag has been measured as a function of E/p in the range of 90 to 330 Volt/torr.cm in argon gas discharge. The results have indicated that in the E/p range less than 160 V/torr.cm formative time lag measurement reflects the importance of photons and excited atoms as a secondary electron process from the cathode. Also when E/p is higher than 180 volt/torr.cm the positive ions play an important role as secondary process in argon discharge. The results show that the increase of over voltage percentage decreases the formative time lag, due to the acceleration of the charged particles under the electric field.

REFERENCES

(1) Momcilo M. Pejovic, Goran S. Ristic and Jugoslav P. Karamarkovic, J. Phys. D: Appl. Phys.; **35**, R91-R103, (2002)

(2) Radovic M.K., Stepanovic O.M. and Maluckov C.A., J. Phys. D: Appl. Phys.; **31**, 1206-1211, (1998)

(3) Loeb L.B, "Basic processes of Gaseous Electronics. Univ. California Press, (1961)

(4) Nasser E., "Fundmental of Gaseous Ionization and Plasma Electronics", Wily-Interscience, New Yourk, (1971)

(5) Pheleps A.V. and Petrovic Z.Lj, Plasma Source Sci. Technol.; **8**. R21-R44, (1999)

(6) Llewellyn-Jones F. Ionization and breakdown in gasses, London, Methuen Co., (1956)

VUV Spectrum and Plasma Dynamics in a Small and Fast Capillary Discharge Operating in Argon. Observation of the ArIX 46.9 nm Line

Leopoldo Soto[1], Andrey Nazarenko[2], Cristian Pavez[1,3], and Patricio Silva[1]

1 Comisión Chilena de Energía Nuclear, Casilla 188 D, Santiago, Chile
2 Institute of Spectroscopy, RAS, Troitsk, Moscow Region, 142090 Russia
3 Universidad de Concepción, Chile

ABSTRACT

Experiments in a small and fast capillary discharge were performed The discharge was operated in argon, with a cathode pressure of 0.1-1 torr. The system works with differential vacuum, thus the anode pressure is around five to ten times less than the cathode pressure. Experiments in capillaries with 0.8 and 1.5 mm internal diameter, and 8 to 40 mm were performed. For an applied voltage of 10 to 15 kV, a peak current of 3 to 5 kA with a rise time of 2 to 5 ns is obtained (~10^{12} to 5x10^{11} A/s). In addition to usual electrical diagnostics, time resolved spectra in the region of 30 to 100 nm and time resolved pinholes images from the plasma have been obtained. The ArIX (46.9 nm) line was detected. From the plasma images compression was observed close to the moment of maximum emission of the ArIX (46.9 nm) line.

Keywords: Capillary discharge, VUV laser, VUV spectroscopy

INTRODUCTION

In order to produce high brightness radiation with an electrical discharge, high energy densities should be provided to the plasma, ~10^{12} J/m^3 (i.e. some MJ into a plasma column of a centimeter in length and radius). This is usually done by means of huge facilities such as the Sandia National Laboratory in the USA. Intermediate devices have been used to produce vacuum ultraviolet (VUV) to soft X ray radiation[1-4] and VUV lasing has been also reported[1]. Interestingly, 10^{12} J/m^3 can also be provided using small devices. In effect, by confining the plasma to submillimetric volumes, less than 1 J is required to reach high energy densities (as an extreme example 0.1 J is enough for a 60 μm diameter sphere). The key point to produce those conditions in small devices is the current rate, which should reach about 10^{13} A/s [5]. Consequently, the inductance should be very low.

To allow studies on the physical mechanisms related to population inversion and high brightness emission in the VUV to soft X-ray region in a table-top device, a fast and small capillary discharge was constructed at the *Comisión Chilena de Energía Nuclear*, CCHEN[6, 7]. Our device follows the design reported by P. Choi and M. Favre (0.1 - 1J, $dI/dt \sim 10^{12}$ A/s)[8].

EXPERIMENTAL SETUP AND DIAGNOSTICS

A pair of 90 mm diameter brass electrodes forms the anode and the cathode of the discharge, as well as a parallel plate capacitor. The insulator (polyvinylidenefluoride, PVDF) between the electrodes is also the capacitor dielectric. A 1 - 1.5 mm inner diameter capillary tube, 0.8, 2.8, 5.0 cm long, is placed at the axis. The discharge is produced inside the capillary. A primary 7 nF capacitor charges the storage capacitor by means of a pulse. The length of the cable connections between the spark gap and the capacitor of the main discharge is calibrated to obtain the required timing between the discharge and the diagnostics. Ionization in the interelectrode space is assisted by a high-energy electron beam,

which is originates in the plasma inside the hollow cathode region. The discharge operates in argon with a cathode pressure of 0.1-1 torr. The anode pressure is around five to ten times less than the cathode pressure. Current rates about of $5x10^{11}$-10^{12} A/s were obtained applying voltages of –10 to –15 kV.

The voltage in the capillary capacitor, the current and the current derivative were measured in our experiments. Also VUV diagnostics have been developed and applied in previous experiments[6, 7]. A coaxial cable was biased at –200V and located at the discharge axis, behind the anode, in order to detect electrons (negative signal) or photons with energy above 4.3 eV (positive signal, like a X ray diode). A multipinhole camera with a magnification of m=3, attached to a microchannel plate (MCP) sensitive to X rays and VUV radiation is used to register 1 frame every 4 ns. VUV spectra of the capillary discharge were obtained by means of a grazing incidence spectrograph GISVUV1-3S attached to a MCP. A gold-coated replica grating of 300 lines/mm, with 1 m curvature radius, was used. The grazing angle was 4°. Results obtained in our previous experiments [6, 7] shown negative signals in the diode detector before breakdown indicating electron beams. About 2-3 ns after the peak current there were indications of photon radiation impacting on the diode, which produced positive signals. Pinhole images taken during a discharge along an 8 mm length capillary and 500 mtorr suggested the existence of a homogeneous plasma column at early time and after a possible compression in the plasma column. Time-integrated spectrum over ten discharges along an 8 mm length capillary were obtained (a single shot did not show enough intensity under these set up conditions to register a spectrum). Several lines are attributed to ArVIII , ArIX and ArX ions (second and higher orders were identified: ArIX-2, ArIX-3, ArIX-5). The ion temperature was roughly estimated at about 40-60 eV.

The research also has been complemented with numerical simulations. A one-dimensional model derived from the magnetohydrodynamics (MHD) equations was applied by A. Esaulov to study the plasma dynamics and temperature evolution during the discharges[9]. The calculations predict a final radius of 100-200 microns and electron densities of 2×10^{24} m^{-3} occurring three nanoseconds after the peak current. The corresponding electron and ion temperatures are 80 and 40 eV. Under these conditions, theoretically soft X-ray lasing can occur at 46.9 nm, due to population inversion by collisional electron excitation of Ne-like ArIX ions.

Recently the VUV spectroscopy diagnostic was improved in order to obtain time resolved spectra and the ArIX (46.9 nm) line was detected[10]. In this work time resolved pinholes images from the plasma have been obtained for the conditions at where ArIX (46.9 nm) line was detected. Four end-on plasma images were obtained from the same discharge with a 4-pinhole camera with a magnification of m=2, attached to a microchannel plate (MCP) sensitive to X rays and VUV radiation. Four frames (4 ns between frames) with a time of exposure of 5 ns were obtained in the same discharge.

RESULTS AND DISCUSSION

Experiments for capillary lengths of 8, 28 and 40 mm, with a internal diameter of 1.5 mm, were performed in Ar with a cathode pressure of 300, 450, 600, 900 mtorr. Voltage of charge was –13 kV. Interesting spectra were obtained in discharges with capillary length of 28 mm. At these conditions a peak current of ~3 kA, with a half period of 12 ns is observed. Figure 1 shows the corresponding current trace and spectra at different stages of the discharge. The spectra were obtained from different discharges and the gating pulse in the MCP was 5 ns. From the plasma images, 4 frames (4 ns between frames) with a time of exposure of 5 ns obtained in the same discharge, a slow compression of the plasma column was observed. It is important note that the minimum radius measured is an average radius over 5ns. It is probable that 5 ns exposure time is long in order to register the compression stage and the minimum radius could be less.

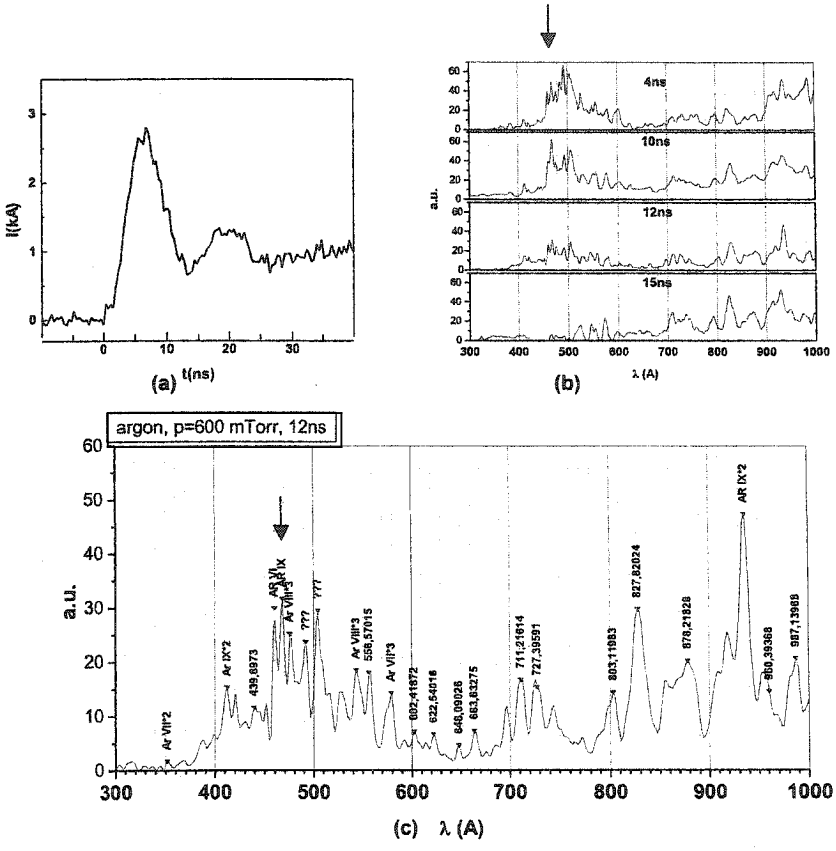


Figure 1. Current trace and spectra for discharges operating in Ar at 600mtorr. a) Current trace, b) spectra at 4, 10, 12 and 14 ns. c) Some lines have been identified. In b) and c) the arrow indicates the Ar-IX (46.9nm) line [19].

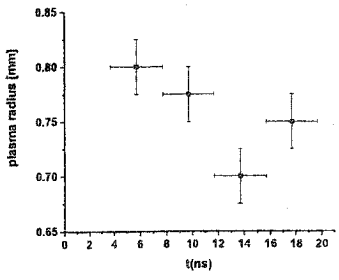


Figure 2. Plasma radius evolution from 4 plasma images obtained from the same discharge with a 4-pinhole camera attached to a microchannel plate (MCP) sensitive to X rays and VUV radiation. One frame every 4 ns with a gating pulse of 5 ns was obtained in the same discharge.

In summary the ArIX (46.9 nm) line was detected. The maximum emission of this line occurs 2-4 ns after the peak current, 7-10 ns after the peak current the line was not observed. These results are in agreement with predictions from theoretical simulations performed by A. Esaulov[9]. From the plasma images a compression of the plasma column was observed close to the moment of maximum emission of the ArIX (46.9 nm) line.

ACKNOWLEDGEMENT

This work has been funded by a *Cátedra Presidencial en Ciencias* awarded to L. Soto by the Chilean Government by the grant CCHEN 563, and by FONDECYT grant 1030062. The authors are thankful to Prof. K.N. Koshelev and Dr. P. Antsiferov (ISAN, Troitsk, Russia) and to Prof. H. J. Kunze (Ruhr Universitat, Germany), for fruitful discussions and comments.

REFERENCES

(1) J.J. Rocca, *Rev. Sci. Instrum.* 70, 3799 (1999).
(2) J.J. Rocca, v. Schlyaptsev, F.G. Tomasel et al, *Phys. Rev. Lett.* 73,2192 (1994).
(3) C.H. Moreno, M.C. Marconi, V.N. Shlyaptsev, B.R. Benware, C.D. Macchietto, J.L.A. Chilla, and J.J. Rocca, *Phys. Rev. A* 58, 1509 (1998).
(4) P.S. Antsiferov, L.A. Dorokhin, E.Yu. Khautiev, Yu.V.Sidelnikov, D.A. Glushkov, I.V. Lugovenko, and K.N.Koshelev, *J. Phys. D: Appl. Phys.* 31, 2013 (1998).
(5) P. Choi, J. G. Lunney, A. Engel, C. Dumitrescu-Zoita, T. N. Hansen, I. Krisch, J. Larour, J. Rous, Proceedings IEEE Pulse Power Conference, p. 287 (Piscataway, NJ, USA, 1999)
(6) L. Soto, A. Esaulov, J. Moreno, P. Silva, G. Sylvester, M. Zambra, A. Nazarenko, and A. Clausse, Physics of Plasma 8, 2572 (2001).
(7) L. Soto, A. Esaulov, P. Silva, G. Sylvester, J. Moreno, M. Zambra and A. Nazarenko, IX Latin American Workshop on Plasma Physics, (Nov., La Serena, Chile, 2000). AIP Conf. Proc. 563, 264 (2001).
(8) P. Choi and M. Favre, Rev. Sci. Instrum. 69, 3118, (1998).
(9) A. Esaulov, P. Sasorov, L. Soto, M. Zambra and J. Sakai, Plasma Physics and Controlled Fusion, 43, 571 (2001).
(10) L. Soto, A. Nazarenko, C. Pavez, P. Silva, J. Moreno, K. Aubel, and T. Vucina, 14th International Conference On High Power Particles Beams and 5th International Conference on Dense Z-pinches (June 23-28, Albuquerque, USA, 2002). AIP Conf. Proc. 651, 161 (2002).

Proportional Counter of ^{3}He Adapted to Measure Neutron Pulses of Low Total Yield in Pinch Devices

José Moreno, Lipo Birstein, Roberto Mayer[1], Patricio Silva, and Leopoldo Soto
Comisión Chilena de Energía Nuclear, Casilla 188 D, Santiago, Chile
1 Centro Atómico Bariloche and Instituto Balseiro, Comisión Nacional de Energía Atómica y Universidad Nacional de Cuyo and associate member of PLADEMA, Argentina
lsoto@cchen.cl

ABSTRACT

A conventional technique is adapted to measure neutron production of very short and low total yield pulses from D-D fusion reactions. This method uses a ^{3}He proportional counter polarized with high voltage and surrounded by a paraffin moderator. An analog signal is registered through a preamplifier whose output is directly connected to a digital oscilloscope. The time-integrated signal is proportional to the neutron yield. The system was used to measure the neutron yield (< 10^6 neutron/pulse) generated in a fast and very small plasma focus device designed to operate with energies of tens to hundreds of joules.

Keywords: neutron pulses, z-pinch, plasma focus

INTRODUCTION

The generation of pulsed neutrons is a common process of many dense transient pinch plasmas (Z-pinches, plasma foci, etc.). The pinch also generates beams of ions, electrons, and ultra-short X-ray pulses. When using deuterium gas, plasma focus devices produce D-D fusion reactions, generating fast-neutron pulses (~ 2.5 MeV) and protons (leaving behind ^{3}He and ^{3}H ions). The neutron bursts usually last about tens to hundreds of nanoseconds.

The great majority of neutron detectors have been designed for measurements in continuous mode of emission and its use is generally not applicable in the same manner to the case of very short bursts. Nevertheless, some of these detection systems are compatible with the detection of short neutron bursts (~100ns), for instance the silver activation counter, the scintillation counter system, the bubble counter system and, different types of nuclear emulsions.

Neutron emission from plasma foci have been found ranging from 10^7 neutrons per pulse with 1 kJ driver up to 10^{12} neutrons per pulse with 1000 kJ. The region corresponding to total neutron yield of less than 10^6 neutrons per pulse, is unexplored. The consequence of this is that measurement of very low levels of fast neutron emission becomes very important to consider.

As a first stage of a program to design a repetitive pulsed radiation generator for industrial applications we constructed a very small plasma focus operating at an energy level of the order of ~ 100 joules or less (160 nF capacitor bank, 38 nH, 20-35 kV, 32-100 J, ~150 ns quarter of period). The design calculations indicate that neutron yields of 10^4 – 10^5 neutrons per shot are expected with discharges produced in deuterium gas[1,2]. It is therefore expected that techniques capable of detecting total neutron yields less than 10^6 neutrons per pulse would be required. For neutron yields of less than 10^6 neutron/pulse, the well known techniques (activation counter, bubble counter system, etc.) are not effective. Nevertheless, references of measurements made with a ^{3}He proportional counter exposed to a plasma focus device that generates ~ 10^8 neutrons per pulse[4] at different distances, showed better possibilities of applying this technique for lower level neutron emission.

THE DETECTOR

^{3}He proportional counters are well known neutron detectors whose detection principle is based on the nuclear reaction, n(He^3, H^3)p. They show a high sensitivity (~3000 barn) to thermal neutrons (< 0,1 eV). The detection system used in this work consists of an ^{3}He proportional counter with the following characteristics: gas encapsulated in a cylinder (ϕ = 25.4 mm, l = 300 mm) to high pressure (~ 7000 bar), polarized with high voltage (~ 4 kV) through a preamplifier (Canberra 2006E) whose output is directly connected to a digital oscilloscope, which registers the signal (Fig. 1).

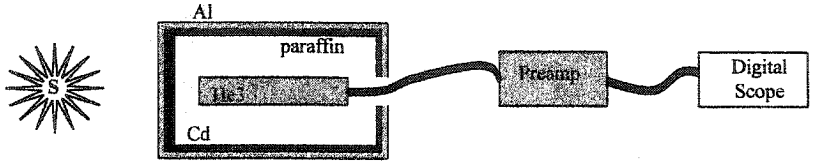


Figure 1.- Detection system based on a ^{3}He proportional counter. The moderator is solid paraffin of 45x15x15 cm^3 with an axial hole of 1 inch diameter (the detector diameter) and 39 cm length. The paraffin moderator is surrounded with aluminum and cadmium layers.

We will see that the time integrated signal is proportional to the neutron yield. This is so because neutrons, which react with the active gas filling, produce a number of free electrons and corresponding positive ions. In the so called proportional regime, the free electrons are accelerated by the applied electric field and through inelastic collisions knock off new secondary electrons. The whole process renders an electric charge proportional to the energy deposited in the detector by the exothermal ^{3}He(n, p) ^{3}H reaction. This energy is much greater than the neutron kinetic energy, as it is usually employed to detect slow neutrons, thus taking advantage of the high 1/velocity neutron reaction cross section. The energy deposited in the detector is by no means a constant, although the reaction energy Q is constant. This is due to wall effects, for those reaction products (p and ^{3}H) which upon collision transfer part of their kinetic energy to the tube wall, will not produce the same amount of primary ionization. Finally, this wall effect has a constant probability distribution for an approximately constant neutron spectrum. This brings about that neutrons detected do not produce equal energy output per neutron, generating instead a spectrum characteristic of detector filling pressure and geometry. Bearing in mind these considerations, it is possible to see that when many neutrons interact within the resolution time of the detector, the overall integrated electric charge will be proportional to the number of neutrons.

In deuterium pinch plasmas the energy of the emitted neutrons is centered at 2.45 MeV which makes moderation for efficient neutron detection necessary. Moderation in a small volume is best achieved through a hydrogenated substance such as solid paraffin for example, due to hydrogen's high scattering cross section and its nuclear mass quite similar to the neutron mass. Thus, the moderator used was solid paraffin of 45x15x15 cm^3 with an axial hole of 1 inch diameter (the detector diameter) and 39 cm length. The neutrons generated in the PF pulse (~ 10-100 ns) are dispersed in time (~ 300 μs) depending on moderator volume and geometry, reducing saturation effects in the detector.

CALIBRATION

To calibrate the ^{3}He detection system (with moderator included) a silver activation counter (previously calibrated with an Am-Be source) is used as a neutron calibration reference. This system has an active area of 15x20 cm^2 with a paraffin moderator 7cm thick and a plane Geiger counter. Simultaneous measurements with the ^{3}He detector and the activation counter were performed in two very small plasma focus devices. The plasma foci devices for which the measurements were made have energies between 50 and 400 Joules (PF-50J and PF-400J) with an expected yield between 10^4

and 10^6 neutrons per pulse respectively[1-3]. Figure 2 shows signals obtained from the ^{3}He detector and count-rate characteristics for both devices. For the case of the PF-400J (Fig. 2a), in which the activation detector was placed 41 cm from the emission point, the mean counting rate was around 80 count/30s above the background; however for the case of the PF-50J (Fig. 2b), where the activation detector was positioned at 24 cm distance, the count rate did not exceed the background level. If we compare this last result with the ^{3}He signal for the same PF device (PF-50J), it is possible to say that under similar measurement conditions (active area), the gaseous detector will provide useful

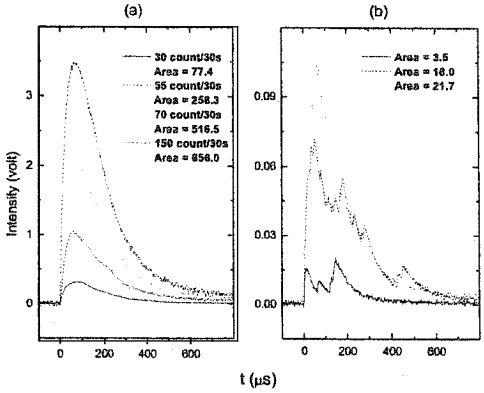


Figure 2.- Characteristic signals of the ^{3}He detector. a) PF-400J with the ^{3}He detector at 41 cm from the emission point, b) PF-50J with the ^{3}He detector at 24 cm from the emission point.

information about neutron emission in a range where the reference system will not. To turn this information into a value for the neutron yield at this emission level (< $5x10^5$ neutron/pulse), the ^{3}He based system must be studied in contrast with the preexisting detector which will thus be taken as a reference.

The existence of simultaneous measurements with both neutron detectors exposed to the PF-400J device allows for this direct comparison. The plots of count rate v/s area under the curve (Fig. 3a) and the count rate v/s the maximum intensity of the signal (Fig. 3b), show that a linear relation exists for both cases. Therefore, by using the calibration of the reference detector, we may obtain the calibration for the ^{3}He detector (figure 3c), i.e., Yield v/s Intensity or Yield v/s Area. In this manner, the neutron yield of a pulsed source is obtained by direct measuring the maximum intensity of the signal of the ^{3}He detector (or area under curve) and using the calibration, for a particular plasma focus shot. An additional result corresponds to the lower limit of detection for the previous activation system at approximately $5x10^5$ neutron/pulse as it is shown in the Fig. 3c. By using now the proportional relation between the neutron count and the area under the curve, is it possible to extrapolate these results to obtain the neutron yield for low yield cases like the plasma focus device PF-50J.

In effect using the proportional relation between neutron yield N_n and area A (N_n=(482.1±9.2)A), it was possible to obtain a measurement of the neutron emission in a very small plasma focus of only tens joules, PF-50J, resulting in the order of $2x10^4$ when operated in D_2 at 8-9 mbar with an initial energy stored of 70 joules.

It must be mentioned that the 'height' or 'intensity of the signal method' cannot be carried too far into the very low neutron intensity region, because as it becomes evident in Fig.2 (b), independent pulses may not contribute to the 'height' of the recorded signal, in which case it should be possible to identify independent neutron pulses, whose one-by-one counting would render a much more precise result.

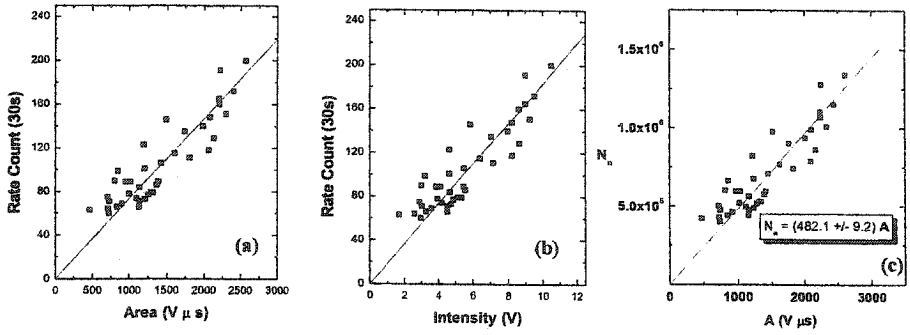


Figure 3.- a) Plot of the count rate v/s the area under curve of the ^{3}He detector signal, and b) count rate v/s the maximum intensity of the ^{3}He detector signal. c) Calibration curve obtained for the ^{3}He detector: Neutron Yield (N_n) v/s Area (A) under the curve.

CONCLUSIONS

In summary, a detection method based on the well known ^{3}He proportional counter was adapted to measure neutron yields from sources of a short pulsed nature of emission. It was applied in the detection of neutrons produced by plasma foci devices with low level of neutron emission (< 10^6 n/pulse)[5]. This development allows to have an additional technique to be used in the measurement of low level neutron yields produced in transient plasma devices.

ACKNOWLEDGEMENTS

This work is part of the Bilateral Agreement: Comisión Chilena de Energía Nuclear, (CCHEN, Chile) - Comisión Nacional de Energía Atómica (CNEA, Argentina). The authors greatly appreciate the fruitful discussions and valuable comments of Dr. Alejandro Clausse of the CNEA and PLADEMA network of Argentina. This work has been funded by CCHEN, by a Presidential Chair in Sciences awarded to L. Soto by the Chilean Government, and by the FONDECYT grant 1030062.

REFERENCES

(1) L. Soto, A. Esaulov, J. Moreno, P. Silva, G. Sylvester, M. Zambra, A. Nazarenko, and A. Clausse, Phys. Plasmas 8, 2572 (2001).
(2) P. Silva, L. Soto, J. Moreno, G. Sylvester, M. Zambra, L. Altamirano, H. Bruzzone, A. Clausse, and C. Moreno, Rev. Sci. Instrum. 73, 2583 (2002).
(3) P. Silva, J. Moreno, L. Soto, L. Birstein, R. Mayer, and Walter Kies, App. Phys. Lett. 83, 3269 (2003)
(4) R. E. Mayer, Internal report Comisión Nacional de Energía Atómica, Tandil, Argentina (1996).
(5) J. Moreno, L. Birstein, R. Mayer, P. Silva, L. Soto, "Measurements of low yield neutron pulses from D-D fusion reactions using a ^{3}He proportional counter", submitted for publication.

Density Diagnostic of Hot Plasmas Using Intensity Ratios of Emission Lines from Be-Like Fe^{22+} Ions

S.W. Rachedi and M.K. Inal

Université Aboubekr Belkaïd, Département de Physique, B. P. 119, 13000 Tlemcen, Algeria

rachedi_w@yahoo.fr

ABSTRACT

The intensity ratios for the two couples of lines ($2s2p\ ^3P_2 \rightarrow 2s2p\ ^3P_1$, $2s2p\ ^3P_1 \rightarrow 2s^2\ ^1S_0$) and ($2p^2\ ^3P_2 \rightarrow 2s2p\ ^3P_1$, $2s2p\ ^1P_1 \rightarrow 2s^2\ ^1S_0$) emitted by FeXXIII ions in the 131–900 Å wavelength range have been calculated as a function of the plasma electron density. A collisional-radiative model has been used for determining the upper-level populations in order to calculate the intensities of these lines. Twenty levels associated with the six configurations $2s^2$, $2s2p$, $2p^2$ and $2s3l$ (l=s,p,d) have been taken into account. The required collisional excitation and de-excitation rate coefficients between all of the twenty levels were computed for two values of the electron temperature, 9.7×10^6 K and 1.3×10^7 K, adopting collision strength data obtained in the distorted wave approximation. We have also included collisional transitions between the three fine-structure $2s2p\ ^3P$ levels induced by proton impact. Our results show that the two selected intensity ratios are highly sensitive to the electron density in the 10^{12}-10^{16} cm^{-3} range. Because of its weak dependence on temperature, the first one is quite good for density diagnostic.

Key Words: Fe^{22+}, Excitation Rate Coefficients, Population Densities, Intensity Ratios, Plasma Diagnostics.

INTRODUCTION

The Be-like iron ions Fe^{22+} are observed in fusion plasmas at around 1 keV, as well as in astrophysical plasmas, such as the solar corona and flares[1,2] in which the electron density is lower than 10^{14} cm^{-3}. At such conditions of temperature and density, population of the different ionic levels violate local thermodynamic equilibrium and the presence of metastable $2s2p\ ^3P_{0,2}$ levels in the case of Fe^{22+} ion make that the coronal model cannot be used even when the density of electrons is as low as 10^{10} cm^{-3}. So, in order to determine the population density of excited levels we have developed a collisional-radiative model which includes the first twenty levels belonging to $2s^2$, $2s2p$, $2p^2$ and $2s3l$ (l=s,p,d) configurations. Population of each level is determined by taking into account all processes that contribute to populating and depopulating the level, in particular excitation from the metastable levels $2s2p\ ^3P_{0,2}$ and radiative cascades from upper levels, in addition to excitation from the ground level $2s^2\ ^1S_0$. Collisional transitions between the fine-structure levels due to proton impact were also included. Because of their weak contribution to the population of excited levels, ionization processes are ignored. We have evaluated the intensity ratio of two couples of spectral lines ($2s2p\ ^3P_2 \rightarrow 2s2p\ ^3P_1$, $2s2p\ ^3P_1 \rightarrow 2s^2$) and ($2p^2\ ^3P_2 \rightarrow 2s2p\ ^3P_1$, $2s2p\ ^1P_1 \rightarrow 2s^2\ ^1S_0$) emitted by Fe^{22+} ions. Interpretation of these intensity ratios represent a good diagnostic tool at the physical conditions occurring in astrophysical plasmas as well as those produced in laboratory plasmas in fusion devices for magnetic confinement.

ATOMIC DATA AND METHODS OF CALCULATION

1. Energy Levels and Transition Probabilities

In our calculations we have taken into account the first twenty levels that belong to the configurations $2s^2$, 2s2p, $2p^2$, 2s3s, 2s3p and 2s3d of Fe^{22+} ions. All of these energy levels and radiative transition probabilities have been taken from Ref.[2] in which the atomic structure code *SUPERSTRUCTURE* was used.

2. Collisional Excitation and De-Excitation Rates

Electron collisional excitation rate coefficients $C_{ij}^e = C(i \rightarrow j)$ (expressed in cm^3/s) are determined by averaging collision strength $\Omega(i,j)$ over the energetic distribution $F(E)$ of incident electrons which are generally Maxwellian in astrophysical and fusion plasmas. That allows us to write the following relation

$$C_{ij}(T_e) = \frac{8{,}63 \times 10^{-6}}{\omega_i T_e^{1/2}} \int_1^{\infty} \Omega_{ij} \exp(-\varepsilon \Delta E_{ij} / kT_e) d\varepsilon \qquad (1)$$

where the electron temperature T_e is expressed in Kelvin, ω_i is the statistical weight of the initial level ($\omega_i = 2J_i+1$) and $\varepsilon = E_i / \Delta E_{ij}$ represents the ratio of the incident electron energy E_i over the threshold excitation energy ΔE_{ij}.

In order to determinate collisional excitation rates coefficients among the first ten levels originating from $2s^2$ 2s2p and $2p^2$ configurations of Fe^{22+} ions, we have adopted collision strengths $\Omega(i,j)$ evaluated by Zhang and Sampson[3]. These authors had used a fully relativistic distorted-wave approach. For the other transitions involving upper levels $2s3l$, we have used the values of collision stre0ngths given by Bhatia and Mason[4]. They were calculated in a semi-relativistic distorted-wave approximation where relativistic corrections in the target ion were included perturbatively through the Breit-Pauli Hamiltonian.

Due to microreversibility, the de-excitation rate coefficient C^d is related to C^e by:

$$C_{ji}^d(T_e) = \frac{g_i}{g_j} C_{ij}^e(T_e)\, e^{\frac{\Delta E_{ij}}{kT_e}} \qquad (2)$$

Collisional transition rates from level i to level j are given by the product $n_e C(i \rightarrow j)$, where n_e is the electron density.

3. Population Density and Line intensity Ratios

We have calculated the relative population densities for the different levels considered in Fe^{22+} by using a collisional-radiative-model. In this model, the level populations are given by solution of following equations.

$$N_j \left[n_e \left(\sum_{k>j} C_e(j \rightarrow k) + \sum_{i<j} C_d(j \rightarrow i) \right) + \sum_{i<j} A(j \rightarrow i) \right] = \sum_{k>j} N_k A(k \rightarrow j) + n_e \left[\sum_{i<j} N_i C_e(i \rightarrow j) + \sum_{k>j} N_k C_d(k \rightarrow j) \right] \qquad (3)$$

where n_e is the electron density, N_i is the population of level i, $C(i \rightarrow j)$ is the rate coefficient for the transition (excitation or de-excitation) from the level i to the j level consisting of the sum of two terms

corresponding to electron and proton impact and $A(j \rightarrow i)$ is the radiative spontaneous emission rates from level j to level i. Let us mention that the population densities N_j satisfy the following normalisation:

$$\sum_j N_j = 1 \quad (4)$$

In this model, we assume that the plasma is optically thin and neglect the contributions to the level populations due to ionisation and recombination processes. Collisions induced by protons can be as efficient as those induced by electrons for transitions between fine structure levels 2s2p ^{3}P and 2p^2 ^{3}P [5].

The metastable 2s2p ^{3}P levels and other triplet levels have varying electron density dependence and this is utilised for density diagnostics by the line ratio method. The population of the triplet levels are mainly excited from the metastable levels 2s2p ^{3}P where the population of the metastable levels are comparable to that of the ground level, since the excitation rate coefficients from the 2s^2 ^{1}S ground level to the triplet levels are small. At this densities range, the population densities of such levels are approximately proportional to n_e^2, while at higher densities where the populations of the metastable levels are determined only by collisional processes, this changes to a linear dependence. Then the ratio of the intensity of a line excited from the métastable levels to a line excited from the ground level is density dependent because the difference on the variation of her emissivity with density n_e.

Let us mention that the emissivity of the ion line transition from level j to the lower level i at frequency ν_{ij} is defined as:

$$\varepsilon(j \rightarrow i) = N_j A(j \rightarrow i)\, h\nu_{ij} \quad (5)$$

RESULTS AND DISCUSSIONS

We calculate the populations of 20 levels belonging to the configuration 2s^2, 2s2p, 2p^2, 2s3s, 2s3p and 2s3d. In Fig. 1. We plot the relative population of the metastable level 2s2p ^{3}P$_1$ to the ground level.as a function of electron density at two values of electron temperature T_e= 9.7×10^6 and 1.3×10^7 K. From this figure, we see the population densities of the metastable level increase with the electron density until they become comparable to the population density of the ground level 2s^2 ^{1}S at n_e ~10^{18} cm^{-3}. Between 10^{20} and 10^{24} cm^{-3}, this population densities become independent of electron density because of the small value of the transition probability from 2s2p ^{3}P to the 2s^2 ^{1}S ground level.

From Fig.2, the reduced population densities divided by an electron density are plotted as a function of the electron density for several levels. They indicate the density dependence of the spectral line intensities. This figure shows that the population density of 2p^2 levels increase at n_e~10^{12} cm^{-3}, according to the change of the population density of 2s2p ^{3}P$_2$. The density effects are also seen at 10^{12}<n_e<10^{20} cm^{-3}. Increase of the reduced population densities of higher levels is related to the decrease of those of lower levels.

In figures 3(a) and 3(b), we plot the line intensity ratios for the two couples of lines (2s2p ^{3}P$_2$ →2s2p ^{3}P$_1$, 2s2p ^{3}P$_1$ →2s^2 ^{1}S$_0$) and (2p^2 ^{3}P$_2$ → 2s2p ^{3}P$_1$, 2s2p ^{1}P$_1$ →2s^2 ^{1}S$_0$) emitted by Fe^{22+} ions in the 131–900 Å wavelength range as a function of electron density at electron temperature of 9,7·10^6 and 1,3·10^7 K. There is no density dependence seen at n_e<10^{11} cm^{-3}. From figures 3a and 3b, we see that the ratios are strongly sensitive to the electron densities from 10^{12} to 10^{15} cm^{-3} therefore, are useful density diagnostics for tokamak plasmas at electron density around 10$^{13\text{-}14}$ cm^{-3}. Because of its very small temperature dependence, the first ratio is quite good for density diagnostic.

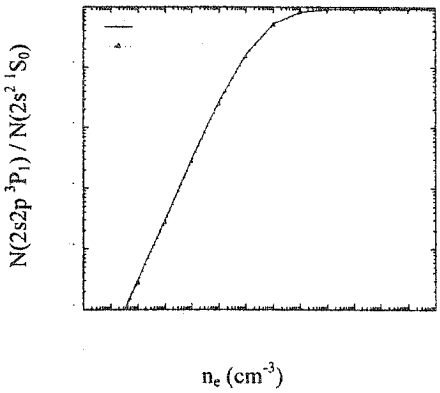


Fig. 1 : Population density of the metastable level 2s2p $^3P_1$ for Fe^{22+} ion for T_e = 9,7·10^6 et 1,3·10^6 K as a function of electron density.

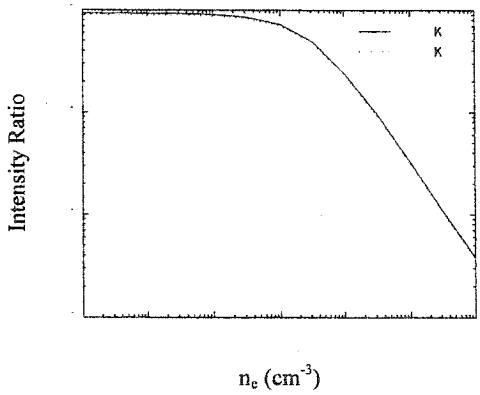


Fig. 3(a): Density dependent line ratio for 2s2p $^3P_2$→2s2p $^3P_1$ and 2s2p $^3P_1$→2s^2 ^1S for T_e = 9,7·10^6 and 1,3·10^7 K.

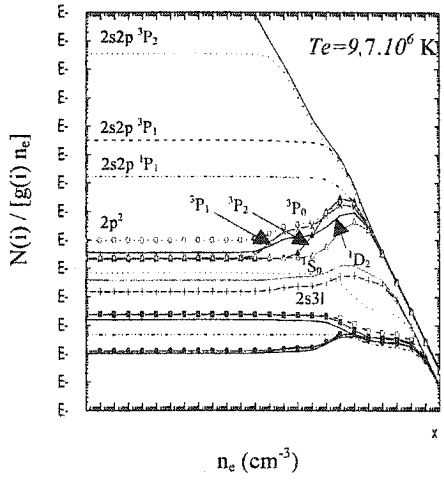


Fig. 2: reduced population densities divided by an electron density as a function of the electron density for the lowest 20 levels for T_e = 9,7·10^6 K.

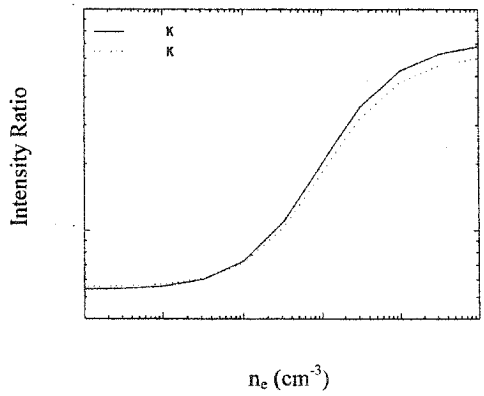


Fig. 3(b): Density dependent line ratio for 2p^2 $^3P_2$ → 2s2p $^3P_1$ and 2s2p $^1P_1$→2s^2 ^1S for T_e = 9,7·10^6 and 1,3·10^7 K.

REFERENCES

(1) K. Masai, J. Quant. Spectrosc. Radiat. Transfer **51**, 211 (1994).
(2) I. Murakami, T. Kato and J. Dubau, NIFS-DATA-35 (National Institute for Fusion Science, Nagoya, Japan 1996).
(3) H.L. Zhang and D.H. Sampson, At. Data Nucl. Data Tables **52**, 143 (1992).
(4) A.K. Bhatia and H.E. Mason, Astron. Astrophys. **155**, 413 (1986).
(5) J.G. Doyle, At. Data Nucl. Data Tables **37**, 441 (1987).

Polarization Spectroscopy of Anisotropic Hot Plasma

Z. Bedrane* **and M. K. Inal**

Theoretical Physics Laboratory, Abou-Bekr Belkaid University, Sciences Faculty B.P. 119, 13000 Tlemcen – Algeria.
zeyneb_bedrane@hotmail.com

ABSTRACT

In laser produced plasmas non-thermal electrons could be generated with an anisotropic velocity distribution. Spatially anisotropic collisions induce unequal population of some magnetic sublevels within an atomic level. This alignment gives rise to a linear polarization of the radiation emitted during the decay of these magnetic sublevels. The purpose of the present work is to explore a tool to diagnose the angular distribution of these non-thermal electrons based on the polarization degree of the resonance line, noted *w*, $1s2p\ ^1P_1 \rightarrow 1s^2\ ^1S_0$, emitted from He-like aluminium ions.

Key Words: Hot and dense plasma, non-thermal and anisotropic electron distribution, collisional excitation of the ions, diagnostic of angular distribution, X-ray polarization.

INTRODUCTION

When ions are excited by collisions with electrons whose velocity distribution is anisotropic, the resulting emission lines are partially polarized [1-4]. The fundamental asymmetry in the problem is in the orbital motion of the colliding electrons. Taking the direction of spatial gradients as the axis of reference for the quantization of angular momentum, it can be shown [1-4] that some magnetic sublevels are preferentially populated giving rise to significant linear polarization P for the radiation emitted during the decay of these sublevels. Plasma Polarization Spectroscopy (**PPS**) is a powerful tool to investigate the anisotropic, and thus non-thermal, features of the plasma.

The first **PPS** experiment on a laser produced plasma has been reported by Kieffer *et al* [5, 6]. A laser pulse of 1 ps with wavelength 1.05 μm and intensity 8×10^{14} W cm^{-2} illuminated an aluminium target. This pulse was preceded by a pre pulse with the intensity ratio of 10^{-3}. The helium-like ion lines of the $2 \rightarrow 1$ transitions were observed with a crystal spectrometer. This crystal (ADP) reflected preferentially the light polarized perpendicular to the plane of incidence. By rotating the spectrometer around the optical axis by 90° and recording spectra, they obtained the polarization degree of the lines. The resonance *w* line $1s2p\ ^1P_1 \rightarrow 1s^2\ ^1S_0$ was found polarized with polarization degree $P = -0.25 \pm 0.07$. Here the polarization degree is defined as $P = (I_\pi - I_\sigma)/(I_\pi + I_\sigma)$, where I_π and I_σ are the intensity of the light polarized in the direction of the quantization axis and perpendicular to that, respectively. In the present case, the quantization axis is taken in the direction normal to the target surface.

Furthermore, Al has an $I = \frac{5}{2}$ nuclear spin, so the intercombination *y* line, $2\ ^3P_1 \rightarrow 1\ ^1S_0$, which is expected to be unpolarized due mainly to hyperfine interactions (the coupling of the orbital angular momentum with the nuclear magnetic momentum)[7], can be used to monitor the efficiency of the detection system.

They simulated the plasma with the one-dimensional hydrodynamic code and the electron kinetic code, and calculated the velocity distribution as the result of the non-local electron heat flow, depending on the location of the plasma. The polarization degree of the w line was calculated to be –0.1 to –0.15. Thus the observed polarization degree is higher in absolute value than the model prediction. The reason of the discrepancy is not known.

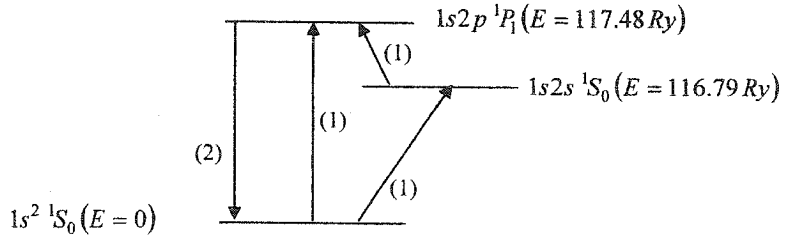
Fujimuto T. and Kazantsev S.[8] noted a very important remark concerning this experiment. They mentioned that Kieffer *et al.* assume the population kinetics to be corona equilibrium. However, the electron density is of the order of 10^{21} cm^{-3}. For such higher-density plasma this assumption may not be valid, and the collisional-radiative model should be employed for the analysis of the population and, therefore, polarization characteristics.

Let us mention that, for this reason, the purpose of the present work is to study theoretically the polarization of the resonance line w taking into account both the excitation from the excitation from the $1s^2\ ^1S_0$ ground level and $1s2s\ ^1S_0$. metastable level.

THEORY

In this paper we are interested in the polarization of the $1s2p\ ^1P_1 \rightarrow 1s^2\ ^1S_0$ resonance line. It is an electric dipole transition. For the helium-like aluminium ions, the transition probability is 2.74×10^{13} s^{-1} [9]. Let us mention that the $1s2p\ ^1P_1 \rightarrow 1s2s\ ^1S_0$ decay probability is 5.39×10^{7} s^{-1} [9] and it can be neglected.

In the **figure 1** we represent the formation process of the *w* line



(1) collisional excitation of the ions

(2) Radiative decay of the ions to the ground level

Figure 1: Scheme of the formation process of the resonance line

The linear polarization degree of the *w* resonance line can be written as a function of the population of the magnetic sublevels $M_J = 0$ and $M_J = 1$.

$$P(w) = \frac{N\left(2\,^1P_1,0\right) - N\left(2\,^1P_1,1\right)}{N\left(2\,^1P_1,0\right) + N\left(2\,^1P_1,1\right)} \qquad (1)$$

COLLISION STRENGTHS

The required collision strengths for the transitions between magnetic sublevels were computed using semi-ralativistic distorded-wave approximation [10, 11]. For partial waves with angular momenta up to 20 the collision strengths were calculated with the Coulomb-Bethe approximation [12].

In **Table I** and **II** are tabulated the collision strengths for populating magnetic sublevels of $1s2p\ ^1P_1$ of aluminium helium-like ions due to the direct excitation from the ground level and the metastable level, respectively, for various incident electron energy k_j^2 . In **Table III** is given collision strengths for the $1s^2\ ^1S_0 \rightarrow 1s2s\ ^1S_0$ transition for various incident electron energy k_j^2.

		k_j^2 (Ry)						
	M_J	120	160	180	240	350	480	960
$1s2p\ ^1P_1$	0	5.47[-3]	9.26[-3]	1.07[-2]	1.44[-2]	1.83[-2]	2.08[-2]	2.41[-2]
	1	1.41[-3]	2.29[-3]	2.76[-3]	4.27[-3]	6.95[-3]	9.72[-3]	1.74[-2]
	$\Omega_0+2\Omega_1$	8.30[-3]	1.38[-2]	1.63[-2]	2.29[-2]	3.22[-2]	4.02[-2]	5.89[-2]

Table I: collision strengths for the $1s^2\ ^1S_0 \rightarrow 1s2p\ ^1P_1 M_J$ transition of Al^{11+} for various incident electron energy k_j^2.

		k_j^2 (Ry)				
	M_J	120	160	180	240	350
$1s2p\ ^1P_1$	0	0.186	0.156	0.141	0.104	0.0645
	1	0.802	0.799	0.797	0.790	0.776
	$\Omega_0+2\Omega_1$	1.79	1.753	1.734	1.685	1.616

Table II: collision strengths for the $1s2s\ ^1S_0 \rightarrow 1s2p\ ^1P_1 M_J$ transition of Al^{11+} for various incident electron energy k_j^2.

		k_j^2 (Ry)						
	ΔE(Ry)	120	160	180	240	350	480	960
$1s2s\ ^1S_0$	116.79	2.98[-3]	3.73[-3]	3.96[-3]	4.48[-3]	4.98[-3]	5.28[-3]	5.70[-3]

Table III: collision strengths for the $1s^2\ ^1S_0 \rightarrow 1s2s\ ^1S_0$ transition for various incident electron energy k_j^2. The threshold energy ΔE is also given.

For He-like aluminium ions excited by collisions with monoenergetic unidirectional electron beam, the polarization degree for the resonance line can be written as:

$$P(w) = \frac{A - B}{A + B} \tag{2}$$

$$A = \Omega\left(1\ ^1S_0 \rightarrow 2\ ^1P_1\ 0\right) + \Omega\left(1\ ^1S_0 \rightarrow 2\ ^1S_0\right) \times \frac{\Omega\left(2\ ^1S_0 \rightarrow 2\ ^1P_1\ 0\right)}{\Omega\left(2\ ^1S_0 \rightarrow 2\ ^1P_1\right)}$$

$$B = \Omega\left(1\ ^1S_0 \rightarrow 2\ ^1P_1\ 1\right) + \Omega\left(1\ ^1S_0 \rightarrow 2\ ^1S_0\right) \times \frac{\Omega\left(2\ ^1S_0 \rightarrow 2\ ^1P_1\ 1\right)}{\Omega\left(2\ ^1S_0 \rightarrow 2\ ^1P_1\right)}$$

RESULTS AND DISCUSSION

It is clearly seen in **Table IV**, where the polarization degree of the $1s2p - 1s^2$ of Al^{11+} as the function of the incident–electron energy k_j^2 is given, that the inclusion of the excitation from the metastable level in the $2\ ^1P_1$ population has a strong depolarization effect. For an energy of 123 Ry the polarization degree decreases noticeably varying from 60% to 37%. The depolarization effect decreases with increasing impact energy. The reason for this is that for higher electron energy the contribution of the $2\ ^1S_0$ metastable level to the population of the $2\ ^1P_1$ decreases with respect to that of $1\ ^1S_0$ ground level because of $\Delta E_{2\ ^1P_1 - 2\ ^1S_0} << \Delta E_{2\ ^1P_1 - 1\ ^1S_0}$. For example, at energy of 233 Ry, the polarization degree is varying from 55.5% to 39.8% i.e. a depolarization of 15.7%. It's should be mentioned that if we don't include the contribution of the $2\ ^1S_0$ metastable level the depolarization is of 12.2% when the energy is varying from 233 Ry to 363 Ry.

The linear polarization degree is expected to be near zero for approximately 12 times the threshold energy.

	k_i^2 (Ry)						
	120	160	180	240	350	480	960
$P_0(w)$	0.590	0.603	0.590	0.543	0.450	0.363	0.161
P(w)	0.356	0.412	0.412	0.392	0.329	/	/

Table IV: polarization degree of $1s2p - 1s^2$ of Al^{11+} as o function of the incident – electron energy k_j^2 considering only direct excitation from the ground level (first row) and including the contribution of the metastable level (second row).

CONCLUSION

We have calculated the polarization degree of the $1s2p\ ^1P_1 \rightarrow 1s^2\ ^1S_0$ resonance line emitted from helium-like aluminium ions. The population of the magnetic sublevels $2\ ^1P_1\ M_J = 0, \pm 1$ were assumed to be in collisional-radiative equilibrium. It means that both the excitation from $1s^2\ ^1S_0$ ground level and $1s2s\ ^1S_0$ metastable level were included. Our results show a noticibly depolarization which arises from the fact that there is preferential population of the $2\ ^1P_1\ M_J = \pm 1$ sublevels by excitation from the metastable level, contrary to excitation from the ground level. The depolarization effect decreases with increasing impact energy because for higher electron energy the contribution of the $2\ ^1S_0$ metastable level to the population of the $2\ ^1P_1$ decreases with respect to that of $1\ ^1S_0$ ground level.

REFERENCES

(1) Oppenheimer J.R., Z. Phys. 34, 27 (1927).
(2) Percival I.C. and Seaton M.J., Philos. Trans. R. Soc. London; 251, 113 (1958).
(3) Inal M.K. and Dubau J., J. Phys. B. 20, 4221 (1987).
(4) Inal M.K. and Dubau J., J. Phys. B. 22, 3329 (1989).
(5) Kieffer J.C, Matte J.P., Pépin H., Chaker M., Beaudoin Y., Johnson T.W., Chien C.Y., Coe S., Mourou G. and Dubau, J. Phys. Rev. Lett. 68, 480 (1992).
(6) Kieffer J.C, Matte J.P., Pépin H., Chaker M., Beaudoin Y., Johnson T.W., Chien C.Y., Coe S., Mourou G., Dubau J. and Inal M.K., Phys. Rev. E. 48, 4648 (1993).
(7) Henderson J.R., Beierdorfer P., Bennett C., Chanternne S., Knapp D., Arrs R.E., Schneider M.B., Wong K.L., Doschek G., Seely J.F., Brown C.M., La Villa R.E., Dubau J. and Levine M., Phys. Rev. Lett. 65, 705 (1990).
(8) Fujimoto T. and Kazantsev S.A., Plasma Phys. Control. Fusion 39, 1281 (1997).
(9) Johnson W.R., Plante D.R. and Sapirstein, J. Adv. At. Mol. Opt. Phys. 35, 255 (1995).
(10) Eissner W. and Seaton M.J., At. Mol. Phys. 5, 2187 (1972).
(11) Saraph H.E., Comput. Phys. Commun. 15, 247 (1978).
(12) Burgess A. and Sheorey V.B., Atom. Mol. Phys. 7, 2403 (1974).

Polarization of the Line *x* Emitted by Nb^{39+} Ions From Anisotropic Hot Plasmas

R. Bensaïd and M.K. Inal
Laboratoire de Physique Théorique, Université Aboubekr Belkaïd, B.P. 119, 13000 Tlemcen, Algérie
rahma_ben@wissal.dz

ABSTRACT

Owing to hyperfine interaction, in ions with non-zero nuclear spin, the $(1s2p)_{J=2}$ decays to $(1s^2)_{J=0}$ with electric dipole (E1) transition, besides its usual magnetic quadrupole transition (M2). This admixing E1 transition together with the hyperfine splitting of $1s2p\ ^3P_2$ upper level can lead to a strong depolarisation to the line x. In the present work the linear polarization of helium like Niobium for which the nuclear spin equal to 9/2, excited by directive electron beam of impact energy of 17.2 keV just above the excitation threshold, is theoretically studied. The hyperfine splitting of the excited level and the transition probabilities for hyperfine-induced E1 decay 2^3P_2(F=7/2, 9/2 and 11/2) $\rightarrow 1s^2$ have been calculated using the First-order perturbation approach. Distorted waves approach has been adopted in determining the magnetic sublevels M_J = 0,1 and 2 excitation collision strengths. Our results for the polarization degree of the line x have shown that the allowance for the combined effect of hyperfine splitting and interference between the two modes of decay M2 and E1 result in drastic decrease of the polarization from –51.5% to –7.5%.

Key words: X-ray polarization spectroscopy, Helium-like ions, hyperfine interaction, M2- E1 interference.

INTRODUCTION

Polarization spectroscopy of x-ray lines represents a diagnostic tool to ascertain the presence of electron beams in hot and thin plasmas[1,2]. Indeed, the collisional excitation of ions by a directive electron beam leads in general to a selective population of specific M_J-sublevels, which is manifested in the linear polarization of radiation subsequently emitted.

When the ion in plasma has nonzero nuclear spin, the hyperfine interaction can significantly alter the polarisation degree. Such an interaction not only shifts and splits the individual *J*-levels, but also mixes different *J*-levels. Because of the mixing with the nearby $^3P_1$ and $^1P_1$ states, the level $^3P_2$ undergo an E1 transition to the $^1S_0$ state, and mixture of M2 and E1 radiation occurs in the line x[3]. For the ion Nb^{39+} which has a nuclear spin I=9/2 and a magnetic moment 6.17, the $^3P_2$ level splits into five components with total angular momentum between F=5/2 and F=13/2. Because the hyperfine interaction is diagonal in F the lines from F=5/2 and 13/2 are not altered by the E1 hyperfine induced transition however, those from F=7/2, 9/2 and 11/2 will be.

The purpose of the present paper is to calculate the degree of polarization of the x line and its hyperfine components of the helium-like Niobium Nb^{39+}. The choice of the Niobium element which is a naturally mono-isotopic, is based on its relatively large nuclear g-factor (g=1.37) and mainly on the highly contribution of the hyperfine induced E1 decay to the x line transition rate. This contribution is found to reach 45%[4].

THEORY

The expression of linear polarization degree is completely derived in ref. (5) using the density matrix formalism for ions with zero nuclear spin excited by a directive electron beam. In the presence of hyperfine interaction the matrix element for photon emitted in $\alpha F_i \rightarrow \alpha' F_f$ decay allowed by both E1 and M2 transitions can be expressed in terms of the population N_{MFi} of the magnetic sublevel αFiM_{Fi} by equation (6). In which A1 and A2 are the transition probability for the E1 and M2 decay respectively.

$$\rho_{\lambda\lambda'}^{ph} = -2\sqrt{\pi}\sum_{Jpair}\sqrt{2J+1}\,Y_J^{\lambda-\lambda'}(\eta)\sum_{M_{Fi}}N_{M_{Fi}}(-1)^{-M_{Fi}-F_f}\begin{pmatrix} J & F_i & F_i \\ 0 & -M_{Fi} & M_{Fi}\end{pmatrix}\left[3\begin{pmatrix} 1 & 1 & J \\ \lambda & -\lambda' & \lambda'-\lambda\end{pmatrix}\begin{Bmatrix} J & F_i & F_i \\ F_f & 1 & 1\end{Bmatrix}A1 + 5i^{\lambda-\lambda'}\begin{pmatrix} 2 & 2 & J \\ \lambda & -\lambda' & \lambda'-\lambda\end{pmatrix}\begin{Bmatrix} J & F_i & F_i \\ F_f & 2 & 2\end{Bmatrix}A2 + -2\sqrt{15}\lambda i^{\lambda-\lambda'}\begin{pmatrix} 2 & 1 & J \\ \lambda & -\lambda' & \lambda'-\lambda\end{pmatrix}\begin{Bmatrix} J & F_i & F_i \\ F_f & 2 & 1\end{Bmatrix}\sqrt{A1A2}\right] \tag{6}$$

In terms of the density matrix elements. The linear polarization degree is given by:

$$\eta_3 = -\frac{\rho_{1-1} - \rho_{-11}}{\rho_{11} + \rho_{-1-1}} \tag{7}$$

considering equations (6) and (7), and by separating terms with different transition mode and cross terms, the polarization degree for F value can be written in the form.

$$\eta_3(F) = \frac{N_{E1} + N_{M2} + N_{12}}{D_{E1} + D_{M2} + D_{12}} \tag{8}$$

Where N_{E1} and D_{E1} refer to the E1 transition, N_{M2} and D_{M2} refer to the M2 transition, N_{12} and D_{12} correspond to interference terms. By assuming that the observation direction is at right angles to the axis of symmetry (which can be the incident electron beam), for a transition Δ JIF $\rightarrow \Delta'$(J'=0)I(F'=I), the six terms entering the previous equation are given by:

$$N_{E1}(F) = \frac{3\sqrt{15}}{2\sqrt{2}}(-1)^{I-F}\sqrt{2F+1}\,W(11FF;2I)R_{E1}^{hf}\sum_{MF}\Omega_{MF}C^{2\ F\ F}_{0-M_FM_F} \tag{9a}$$

$$N_{M2}(F) = \frac{15}{2}\sqrt{\frac{5}{14}}(-1)^{I-F}\sqrt{2F+1}\,R_{M2}\sum_{MF}\Omega_{MF}\times \left[W(22FF;2I)C^{2\ F\ F}_{0\,M_FM_F} + W(22FF;4I)C^{4\ F\ F}_{0M_FM_F}\right] \tag{9b}$$

$$N_{12} = \frac{5}{2}\sqrt{6}(-1)^{I-F}\sqrt{R_{E1}^{hf}(F)R_{M2}(F)}\,W(112FF;2I)\sum_{MF}\Omega_{MF}C^{2\ F\ F}_{0M_FM_F} \tag{9c}$$

$$D_{E1}(F) = R_{E1}^{hf}(F)\left[\sum_{MF}\sigma_{MF} + \frac{\sqrt{15}}{2\sqrt{2}}(-1)^{I-F}\sqrt{2F+1}\,W(11FF;2I)\sum_{MF}\Omega_{MF}C^{2\ F\ F}_{0M_FM_F}\right] \tag{9d}$$

$$D_{M2}(F) = R_{M2}(F)\left[\sum_{MF}\sigma_{MF} + \frac{1}{2}\sqrt{\frac{5}{14}}(-1)^{I-F}\sqrt{2F+1}\times \sum_{MF}\Omega_{MF}\left(5\,W(22FF;2I)C^{2\ F\ F}_{0M_FM_F} - 9\,W(22FF;4I)C^{4\ F\ F}_{0M_FM_F}\right)\right] \tag{9e}$$

$$D_{12}(F) = -\frac{5}{2}\sqrt{6}(-1)^{I-F}\sqrt{2F+1}\,\sqrt{R_{E1}^{hf}(F)R_{M2}(F)}\;W(12FF;2I)\sum_{MF}\Omega_{MF}C^{2\ F\ F}_{0M_FM_F} \tag{9f}$$

Since the incident beam is assumed to have one impact energy 17.2 keV, Just above the excited threshold , the population of upper level is assured mainly by collisional excitation from the $1s^2\ ^1S_0$ ground level. In this case we can substitute N_{MF} by collision strength Ω_{MF}:

They have been shown that the hyperfine mixing of levels can alter the radiative lifetime of the $^3P_2$ long-lived state in a significant way[3]. But because of its weakness and the instantaneity of the collisional excitation process, hyperfine structure can be taken into account in the collision strength just trough angular momentum recoupling. Assuming that the nuclear spins are initially randomly oriented, the collision strength for the $1^1S_0 \rightarrow \Delta JIFM_F$ excitation can be determined from the $1^1S_0 \rightarrow \Delta JM_J$ collision strengths by using only the square of Clebsch-Gordan coefficients according to the formula given in ref. (6):

$$\Omega(1_1S_0 \rightarrow \Delta JIFM_F) = \frac{1}{2I+1}\sum_{MJ}\left[C(JIM_JM_F - M_J; FM_F)\right]^2 \times \Omega(1_1S_0 \rightarrow \Delta JM_J) \qquad (10)$$

Since the $^3P_2$ level is completely resolved, as we will see below, one can neglect the interference between all hyperfine components so the degree of polarization of the whole line x can be written as fellow:

$$\eta_3(x) = \frac{\sum_{F=5/2}^{13/2} N_{M2} + \sum_{F=7/2}^{11/2} N_{E1} + \sum_{F=7/2}^{11/2} N_{12}}{\sum_{F=5/2}^{13/2} D_{M2} + \sum_{F=7/2}^{11/2} D_{E1} + \sum_{F=7/2}^{11/2} D_{12}} \qquad (11)$$

RESULTS AND DISCUSSIONS

To calculate the hyperfine splitting, for each F value of the level $1s2p\ ^3P_2$, we have adopted values of reduced matrix elements given by Johnson[4], Our results of energy splitting $\Delta E_{FF'}$ between consecutive hyperfine components F and F' =F+1 varies from 3.72 10^{-3} (au) and 6.910^{-3} (au), show that the hyperfine structure of the level $^3P_2$ is completely resolved since its natural width Γ which equal 7.23 10^{-6} (au) remain very small. This allows us to adopt the first order perturbation approach to evaluate the hyperfine induced transition probability *A1*. From our results of our calculation concerning hyperfine induced transition probabilities for each F value we found that the total hyperfine-induced decay probability reach 131.41 ns^{-1} that is 44% of the $2\ ^3P_2 \rightarrow 1\ ^1S_0$ transition rates. this value differ by 2.6% from the value given by Johnson and al in [4] using the radiation damping theory. We found that the branching ratios for hyperfine-induced *E*1 transitions from hyperfine components *F*=7/2, 9/2 and 11/2 are about 43%, 4% and 10% lower than those for *M2* transitions, respectively. The probabilities of E1 and M2 transitions from $1s2p\ ^3P_2$ other than those made possible by the hyperfine interaction have been taken from paper[7].

Collision strengths for excitation of Nb^{+39} ion by directive electron beam from the $1s^2\ ^1S_0$ ground level to deferent $|M_j|$ magnetic sublevels of $1s2p\ ^3P_2$ those appear in the table 1 have been calculated using distorted-wave method. The direction of the electron beam is taken as the quantization axis (z-axis). And in order to avoid the contribution of other atomic processes than the excitation from the ground level, the electron beam is assumed to have one impact energy, 17.2 keV, just above the excitation threshold.

Values reported In table 2 have been evaluated via computation program. Calculation of collision strengths for each F value, have been achieved in basing on values given in table 1 and the equation (10). We can see that the hyperfine interaction result in a strong depolarisation of the x line and the inclusion of the interference between E1 and M2 decay modes leads to a very slight increase of η_3.

$\|M_J\|$	+2	+1	0
$\Omega_{Mj}(10^{-4})$	0.368	1.15	1.41

Table I : collision strength for excitation from ground level to the different $|M_J|$ magnetic sublevels of $^3P_2$ at the incident electron energy of 17.2 keV.

	$\Omega_{Fj}(10^{-4})$	η_3 (%)				
		$E1M2^i$	$E1M2^{ni}$	E1	M2	$M2^{nhf}$
x	/	-7.46	-6.93	/	-9.86	-51.5
F=5/2	5.335	-4.55	-4.55	/	-4.55	/
F=7/2	7.114	-16.62	-9.18	-5.67	-11.20	/
F=9/2	8.892	6.11	2.53	14.21	-9.63	/
F=11/2	10.67	.32	-.28	-.56	-.04	/
F=13/2	12.449	-20.65	-20.65	/	-20.65	/

Table II: collision strengths for excitation from ground level to the different hyperfine sublevels of the level $^3P_2$ ($\Omega_F(10^{-5})$) are listed in the second column. In the remainder of table degree of linear polarization η_3 (in %) for the line x and its hyperfine components emitted by directive electron beam at the incident energy of 17.2 keV which is just above the excitation threshold are given: The third and the fourth column show results with ($E1M2^i$) and without ($E1M2^{ni}$) including the E1-M2 interference effect. The fifth and the sixth column show η_3 calculated with considering E1 and M2 radiations separately in the last column we can see the values of the linear polarization when we neglect the nuclear spin.

CONCLUSION

We have calculated the degree of linear polarization of the line $2\ ^3P_1 \rightarrow 1\ ^1S_0$ and its hyperfine components. It can be see that the hyperfine interaction result in a drastic depolarisation of the line x whereas the inclusion of the interference between E1 and M2 transitions has the effect of increasing significantly the absolute value of the η_3 for the individual hyperfine components of x originating from F=7/2 and F=9/2. For the whole line x, inclusion of the E1-M2 interference results in a very slight increase of η_3 because of large cancellation between the contributions from the F=7/2 and F= 9/2 components. We can conclude that to better interpret the linear polarization of radiation excited by electron impact me must taking into account all effect issued from nuclear spin.

REFFERENCES

(1) Haug E., Solar Phys 71(1981).
(2) Akita K. et al., Solar Phys 86 (1983) .
(3) H. Gould, R. Marrus and P.J. Mohr, Phys. Rev. Lett. 33, 676 (1974) .
(4) Johnson W. R. et al., Phys. Rev. A 55, 2728 (1997).
(5) M.K. Inal and J. Dubau, J.Phys. B 20, 4221 (1987).
(6) Rercival I. C. and Seaton M.J., Phil. Trans. Roy. Soc. 251, 113 (1958).
(7) Johnson W.R. et al., Advanced in Atomic, Molecular and Optical Physics, Vol.35 eds. B. Bederson and H. Wlther (Addision-Wesley, New York, 255 (1995)).

Small Plasma Devices

Route to Soft X-ray Laser Pumped by Gas-Filled-Capillary Discharge

K. Koláček, J. Schmidt, V. Boháček, V. Prukner, M. Řípa, O. Frolov, J. Štraus, and P. Vrba
Pulse Plasma Systems Department, Institute of Plasma Physics, Academy of Sciences of the Czech Republic, Za Slovankou 3, P.O.Box 17, 182 21 Prague 8, Czech Republic
kolacek@ipp.cas.cz

ABSTRACT

Key points for the design and development of the capillary-discharge-pumped soft X-ray laser working according to the electron-collisional excitation pumping scheme are discussed. They include the design of the apparatus capable to deliver currents with sufficient rise-rate, role of pre-pulse, test of plasma parameters and finally proof of lasing. (47+5)

Key Words: ***fast capillary discharge, soft X-ray laser***

INTRODUCTION

Gas-filled capillary pulse discharges belong to the most perspective devices in the group of discharge-pumped soft X-ray lasers: in Rocca's laboratory at Colorado State University (USA) strong amplification [1] (according to **electron-collisional excitation pumping scheme**), lasing [2] and achievement of saturation limit [3] with neon-like argon (46.9 nm) were declared in the mid nineties. At present such laser is in routine operation and in repetitive regime (4 Hz) it achieves an average power ≈3.5 mW and an output energy of 880 μJ/pulse[4]. Rocca and his co-workers have already thoroughly investigated the laser itself (e.g. the dynamics of plasma implosion [5], the laser beam characteristics {near-field and far-field patterns} [6], and spatial coherence [7, 8]) as well as tested some soft X-ray laser applications listed e.g. in [9]. Besides that they published lasing on neon-like sulphur (60.8 nm) [10] and neon-like chlorine (52.9 nm) [11].

Conditions for achievement of population inversion seems to be very easy to fulfil: the discharge with fast current rise-rate, if starting in a pre-ionised gas, detaches very rapidly from capillary walls (by Z-pinch effect) and, hence, due to small wall ablation only a limited number of particles is heated and compressed to create abundance of neon- (or nickel-)like ions. Collisions of these ions with energetic electrons excite their valence-electrons from the initial ground state i of a given ionization stage (e.g. $1s^2 2s^2 2p^m$ (neon-like closed shell with $m = 6$ being the most successful)) to the upper state u ($2p \rightarrow 3p$), which is metastable with respect to radiative decay to the ground state, while the lower state l of the lasing transition is efficiently de-populated by the dipole-allowed transition ($3s \rightarrow 2p$). In this way a population inversion between $3p$ and $3s$ levels appears, which enables lasing on the transition between them ($3p \rightarrow 3s$).

Fact, that first lasing in a gas filled capillary outside Rocca's laboratory was announced [12] only seven years after the demonstration by Rocca (in spite of endeavour of a few laboratories) witness for the complexity of the problem. In the following we pay attention to some (in our opinion) key points of the design and realisation/development of the gas-filled-capillary-discharge pumped soft X-ray laser based on the excitation pumping scheme.

DRIVER DESIGN

The apparatus design should minimise the current rise-time (minimising the capacitance and the inductance of the circuit) at maintaining sufficient energy for ionisation of the gas atoms up to their K-shell (elevating charging voltage and scaling up insulators).

A typical driver (see Fig. 1) consists of a high voltage (HV) pulse generator (HV pulse transformer or Marx generator), a fast capacitor (pulse forming line) with a closely coupled main spark gap and a capillary. Attached are the gas filling and pumping assembly and the diagnostic part. Prior to

manufacturing it is worth to calculate and test a preliminary design. First to solve the Laplace-Poisson equation in the most exposed regions that helps to determine not only the minimum save dimensions of insulators and the optimum roundness of the conductor edges (Fig. 2), but also the mutual capacitance of individual components [13]. Second to solve transient characteristics of an equivalent circuit (Fig. 3) comprising HV pulse generator, pulse forming line (circuit part with distributed parameters), spark gap and capillary (with different switching times and with different parameters before and after their breakdowns) that predicts among others the capillary current amplitude and rise rate [14] (see Fig. 4).

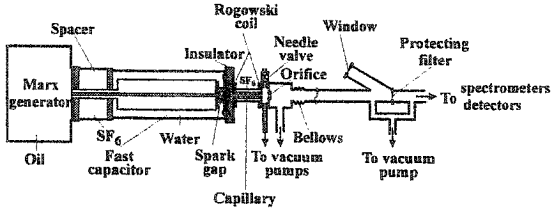


Fig. 1 Apparatus CAPEX 1

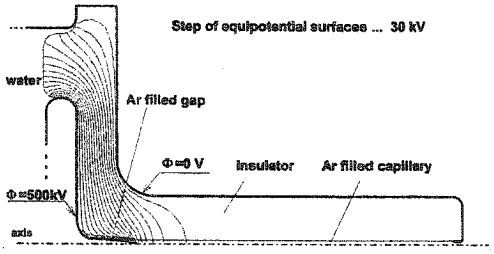


Fig. 2 Electrostatic potential distribution in the region of output insulator and capillary

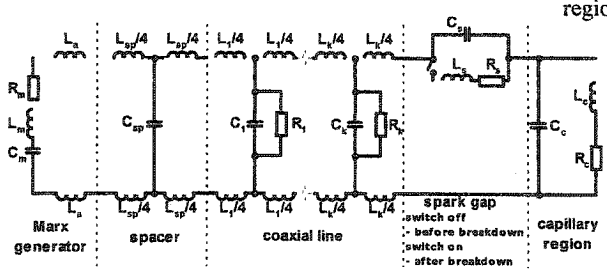


Fig. 3 Example of the equivalent circuit of the capillary driver

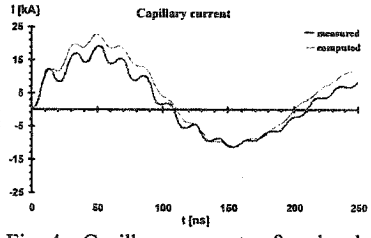


Fig. 4 Capillary current after breakdown – the measured curve and the result of simulation

PRE-PULSE AND ITS INFLUENCE ON PLASMA DYNAMICS

It was generally understood, thatplasma dynamics plays one of key roles for capillary-discharge-pumped lasing. A methodical way, how to achieve the conditions for soft X-ray amplification in capillary discharge experiments, was published by colleagues of Technion – Israel Institute of Technology, Haifa [12]. Also they first attracted attention to the decisive role of the pre-pulse, showing (with the help of on-axis soft X-ray quadri- pinhole camera) that a stable radial plasma column collapse is achieved for pre-pulse currents between 10 A and 50 A.

A more detailed study of the pre-pulse and its influence on the main discharge was presented by the Tokyo Institute of Technology [15, 16]. Their study, based on side-on photographs of Pyrex capillary taken by a high-speed camera, showed that the initial stable pre-discharge develops (after 40 μs) into an unstable one with moving striations. Similar photographs of the main discharge without pre-pulse show a very irreproducible regime with helical instabilities while the same discharge with the pre-pulse 10 A is very repeatable.

A summary of various techniques of pre-pulse generation and theoretical explanation of the pre-pulse limits has been recently given by us [17]. It was shown that a partially ionised plasma has a conductivity directly proportional to the plasma density and, because the Bessel function J_0-like radial density profile has maximum density on the discharge axis, the main current starts to flow along the axis,

heating the plasma there, but not causing any compression. On the other hand, the conductivity of a fully ionised plasma does not depend on the plasma density. In the beginning the main current is skinned in the vicinity of the capillary wall and, then it compresses and heats the whole plasma column (by Z-pinch effect). The upper pre-pulse limit can be inferred from an estimate, how much pre-heated plasma can still be efficiently compressed by the available main current.

While other laboratories use a combined pre-pulse (generated by external circuit as well as by capacitance of the spark gap), our pre-pulse is generated purely internally (by carefully adjusted capacitance of the spark gap - see Fig. 5).

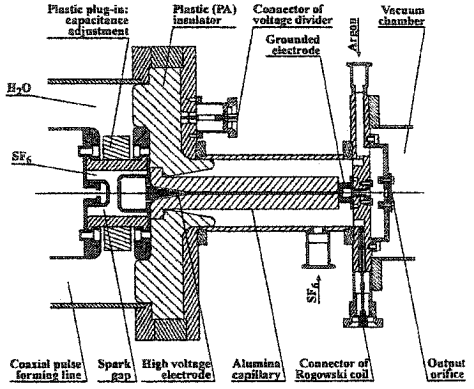


Fig. 5 Detail of the end of coaxial pulse forming line, spark gap, capillary and its gas filling and pumping assembly.

PLASMA PARAMETERS

In parallel to the pre-pulse also other boundary and initial conditions (e.g. main current amplitude, capillary diameter, initial gas pressure) must be tuned in. The first test of efficiency of plasma pinching may be time-resolved axial emission in the spectral band of interest (registered e.g. by PIN diode or vacuum diode behind an appropriate filter): efficient compression and heating is characterised by a sharp narrow peak on the time curve of soft X-ray intensity (see Fig. 6) that need not be necessarily lasing [18].

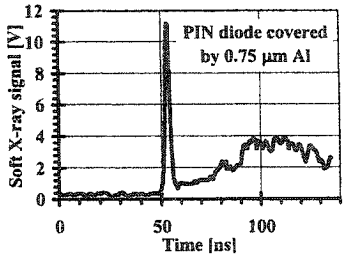


Fig. 6 Signal of PIN diode filtered by 0.75 μm Al filter

The second step should confirm, that the electron temperature of such plasma is sufficient for desirable ionisation stage. The only proof can render the time-resolved spectroscopy in the spectral range with prevailing lines of ions of this ionisation stage. For example Rocca demonstrated [19] efficiency of capillary discharge comparing its spectra in the range of 15-19 nm (see Fig. 7) with spectra of Gamble II generator (1 MA current implosion), where exactly the same lines were present.

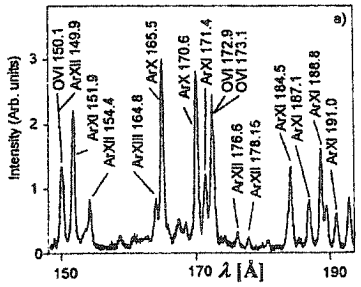


Fig. 7 Rocca's Ar filled capillary spectra [1]

PROOF OF LASING

Proof of exponential scaling of the laser line intensity with the capillary length (Fig. 8) is difficult (see e.g. [3, 12, 20]): it is necessary to maintain plasma conditions, alignment, and linearity of the detector over a few orders of magnitude. Besides that one has to respect short duration of gain and

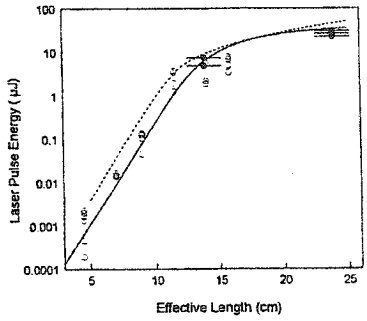


Fig. 8 Measured and computed laser output energy as a function of plasma column length [3];
° single pass measurements,
• double pass measurements,
— radiation transport calculation,
--- hydrodynamic/atomic physics code

intrinsic refraction effects. An application of mirror helps to test double-pass amplification [3]. A fit of the data (below a knee to saturation) with the Linford formula yields the gain coefficient.

CONCLUSION

This contribution specifies the role of pre-pulse for soft X-ray lasers pumped by gas-filled capillary discharges and adds it to earlier known necessary conditions. However, even if processes running in this type of laser are more and more understood, there still remain some items that should be clarified (e.g. capillary wall material, current rise rate, external longitudinal magnetic field controlling density gradients near the axis, etc.).

Acknowledgement. This work was performed under the auspices and with the support of the Grant Agency of the Czech Republic (Grant 202/03/0711) and the Ministry of Education, Youth, and Sports of the Czech Republic (Contract LA 055).

REFERENCES

(1) J.J. Rocca, O.D. Cortázar, B. Szapiro, K. Floyd, and F.G. Tomasel; Phys. Rev. E; **47**, 1299 (1993).

(2) J.J. Rocca, V. Shlyaptsev, F.G. Tomasel, O.D. Cortázar, D. Hartshorn, and J.L.A. Chilla; Phys. Rev. Letters; **73**, 2192 (1994).

(3) J.J. Rocca, D.P. Clark, J.L.A. Chilla, and V.N. Shlyaptsev; Phys. Rev. Letters; **77**, 1476 (1996).

(4) C.D. Macchitto, B.R. Benware, and J.J. Rocca; Opt. Lett.; **24**, 1115 (1999).

(5) F.G. Tomasel, J.J. Rocca, and V.N. Shlyaptsev; IEEE Trans. Plasma Sci.; **24**, 49 (1996).

(6) C.H. Moreno *et al.*; Phys. Rev. A; **58**, 1509 (1998).

(7) M.C. Marconi, J.L.A. Chilla, C.H. Moreno, B.R. Benware, and J.J. Rocca; Phys. Rev. Lett.; **79**, 2799 (1997).

(8) Y. Liu, M. Seminario, F.G. Tomasel, C. Chang, J.J. Rocca, and D.T. Attwood; Phys. Rev. A; **63**, 033802 (2001).

(9) K.Kolacek; Proc. 27th ECLIM 2002, Moscow, Russia, October 7-11, 2002, *to be published*

(10) F.G. Tomasel, J.J. Rocca, V.N. Shlyaptsev, and C.D. Macchietto; Phys. Rev. A; **55**, 1437 (1997).

(11) M. Frati, M. Seminario, and J.J. Rocca; Optics Letters; **25**, 1022 (2000).

(12) A. Ben-Kish, M. Shuker, R.A. Nemirovsky, A. Fisher, A. Ron, and J.L. Schwob; Phys. Rev. Lett.; **87**, 015002 (2001).

(13) K. Koláček, V. Boháček, J. Schmidt, P. Šunka, J. Ullschmied, M. Řípa, and P. Kotalík; Proc. 18th Symp. Plasma Phys. and Techn.; Prague, Czech Rep., June 17-20, 1997, p.86 (1997).

(14) K. Koláček, V. Boháček, J. Schmidt, P. Šunka, J. Ullschmied, and M. Řípa; Proc. 12th Int. Conf. High Power Particle Beams, BEAMS'98; Haifa, Israel, June 7-12, 1998, Vol.II, p.619 (1998).

(15) G. Niimi, Y. Hayashi, A. Okino, M. Watanabe, and E. Hotta; Proc. 28th Int. Conf. Plasma Sci. and 13th Int. Pulsed Power Conf, PPPS-2001; Las Vegas, Nevada, USA, June 17-22, 2001, 746 (2001).

(16) G. Niimi, N. Sakamoto, M. Nakajima, Y. Hayashi, M. Watanabe, A. Okino, K. Horioka, and E. Hotta; X-Ray Lasers 2002, 8th Int. Conf. X-Ray Lasers; Eds. J.J.Rocca, J.Dunn, and S.Suckewer, Aspen, Colorado, USA, May 27-31, 2002, AIP Conference Proceedings, Vol. **641**, p.103 (2002).

(17) K. Kolacek, J. Schmidt, V. Prukner, V. Bohacek, M. Ripa, P. Vrba, and O. Frolov; Proc. 30th IEEE Int. Conf. on Plasma Sci., Jeju, Korea, June 2-5, 2003, *to be published.*

(18) P. Vrba, K. Koláček, J. Schmidt, M. Řípa, V. Boháček, N.A. Bobrova, P. Sasorov, and M. Vrbová; Int. Symposium on Plasma Research and Application (PLASMA-2001); Warsaw, Poland, September 19-21, 2001, Paper 3.23 (2001).

(19) J.J. Rocca, F.G. Tomasel, M.C. Marconi, V.N. Shlyaptsev, J.L.A. Chilla, B.T. Szapiro, and G. Giudice; Phys.Plasmas; **2**, 2547 (1995).

(20) G. Tomassetti, A. Ritucci, A. Reale, L. Palladino, L. Reale, S.V. Kukhlevsky, F. Flora, L. Mezi, J. Kaiser, A. Faenov, and T. Pikuz; Eur. Phys. J. D; **19**, 73 (2002).

Spectroscopic Measurement of Radiation Generated by Discharge in Alumina Capillary

J. Schmidt, K. Kolacek, V. Bohacek, M. Ripa, V. Prukner, O. Frolov, and J. Straus
Institute of Plasma Physics, Academy of Sciences of the Czech Republic,
Za Slovankou 3, P.O.Box 17, Prague 8, Czech Republic
schmidt@ipp.cas.cz

ABSTRACT

Recently we have started to study an influence of capillary pre-ionization on the soft X-ray emission from the fast capillary discharge device CAPEX 2. For this purpose we used both the home-made flat field spectrograph, and for the first time also the McPherson's XUV grazing incidence spectrograph. A strong laser transition line (*Ne*-like *Ar* line, λ=46.9 nm) was found in the time-resolved spectrum of both spectrographs.

Key Words: ***Capillary discharge, soft X-ray spectroscopy, soft X-ray laser***

INTRODUCTION

The main motivation for developing discharge pumped soft X-ray lasers is their relative simplicity in comparison with pumping mechanism based on extremely expensive and complex laser facilities. A significant progress in different types of capillary discharge devices has been made in the last decade of the 20th century. The demonstration of a large soft X-ray amplification in a discharge-created plasma opened a new path towards the development of compact and practical soft X-ray lasers [1]. Mainly devices based on capillary discharge are able to find widespread use in applied research and practical applications.

There are currently three principal approaches to achieve a population inversion in a capillary discharge: electron-collisional recombination pumping, charge-exchange pumping and electron-collisional excitation pumping. The electron-collisional excitation-pumping scheme to achieve a population inversion in a gas-filled-capillary discharge is the most favorable. A great progress has been made since the first observation of the large amplification in a discharge-created plasma to the demonstration of a saturated table-top soft X-ray laser, in *Ne*-like *Ar* on the line λ=46.9 nm [2-4].

It is obvious that the capillary discharge is a multi-parametric system. Driver characteristics (capillary current amplitude, rise-time), initial conditions (initial gas pressure, pre-pulse capillary current) and boundary conditions (capillary length and diameter, wall material) are important for achieving an efficient population inversion in gas-filled capillary discharges. It is desirable to find optimal conditions, especially initial conditions of the capillary discharge, to get from the device a coherent soft X-ray radiation with a good repeatability.

EXPERIMENTAL SET-UP

A capillary discharge device (CAPEX 2) was used for generating the soft X-ray radiation. CAPEX 2 apparatus consists of five main parts: a Marx generator, a coupling section (spacer), a fast coaxial cylindrical capacitor (pulse forming line), a main spark gap and a capillary. The experimental set-up is shown in Fig.1.

The fully screened oil-insulated Marx generator is used as a power supply for the capillary discharge experiment. At present the Marx generator has 8 stages and its erected voltage is typically up to 450 kV. The coupling section (spacer) is a short coaxial cylindrical line and it functions only as a

safe interface between the oil-insulated Marx generator and the water-filled fast capacitor. The pulse forming line (fast capacitor) is a coaxial cylindrical line as well. At present we use de-ionized water as a dielectric.

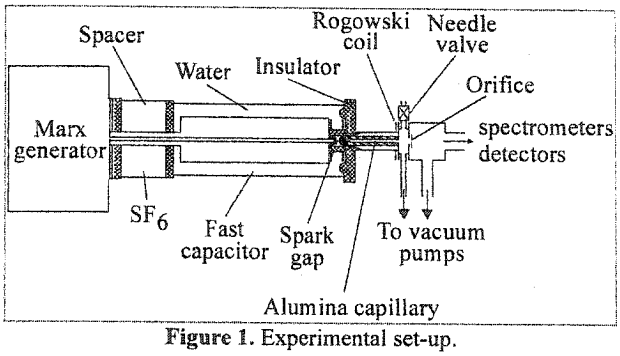


Figure 1. Experimental set-up.

At the end of the line the main spark gap is placed. The inner part of the spark gap is filled with SF_6 gas, while its outer part is filled with water. The CAPEX 2 device hasn't been equipped with an external driver of the capillary pre-pulse. Therefore, the pre-pulse was very roughly controlled by changing capacity and conductivity of the main spark gap. The quantity of water in the outer part of the spark gap can be changed by a suitable plastic circular ring. The schematic drawing of the spark gap region is shown in Fig. 2.

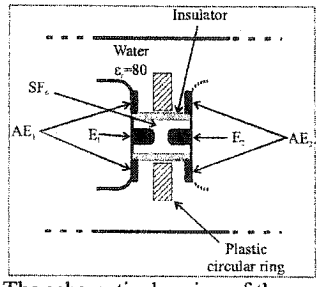


Figure 2. The schematic drawing of the spark gap (electrodes E_1, E_2 and auxiliary electrodes AE_1, AE_2).

We have tested several arrangements of the spark gap:

- no plastic circular ring (pre-pulse > 50A)
- plastic circular ring of medium thickness (pre-pulse ~ 10-50 A)
- plastic circular ring of full thickness (outer part of the spark gap without water) (pre-pulse 0.5-1 A)
- plastic circular ring of full thickness with suitably reduced outer diameter (pre-pulse 1-30 A)
- without auxiliary electrode AE_2 (see Fig. 2) located in water (no observed pre-pulse)

In the last case the capacity of the spark gap was very small (approx. 10 times smaller that the original one without the plastic circular ring) and its conductivity was converging to zero. The electrical conductivity of the de-ionized water was approximately constant (~2 μS/cm) for all measurements. The plastic circular ring of medium thickness was not suitable, because electrical breakdowns in

plastic material of the ring relatively frequently occurred. Modification of the plastic circular ring geometry (namely reduction of its outer diameter) was found to be more resistant.

The fully-ceramics capillary (ϕ3.2 mm) was filled with argon by a needle valve. The generated radiation was brought out through ϕ4 mm orifice in the outer electrode. The capillary discharge length was set to 180 mm. The diagnostic part was separated by another ϕ 0.8 mm orifice (~55 mm apart of the grounded capillary end). A more detail description of the apparatus can be found in [5].

SPECTROSCOPIC MEASUREMENTS

1. Flat field spectrograph

Recently we designed and assembled a survey soft X-ray flat field spectrograph based on Jobin Yvon grating (average groove density ~ 450 grooves/mm). The spectral interval of this spectrometer is 10-110 nm. The X-ray spectrum was registered with help of MCP detectors (tandem setup) and the lens-coupled cooled 12-bit CCD camera (1280x1024, PCO SensiCam). The survey flat field spectrograph was used for spectroscopy of the axially emitted radiation from the capillary and was placed approximately 2 m apart from the grounded capillary end. The more detail description of this spectrograph can be found in [5].

The MCP detector was gated by a 50 ns pulse in our experiments. We have tested several configurations of the spark gap (inserting various plastic circular rings) that helped us to control/adjust roughly the pre-pulse current. Up to now, the best result was obtained with full thickness plastic circular ring, which completely displaced the water between auxiliary electrodes of the spark gap (see Fig. 2). For this arrangement the measured pre-pulse amplitude was approximately 4 A and its duration was shorter than 0.9 μs. Fig. 3 shows a spectrum with a strong spectral line (*Ne*-like *Ar*, λ=46.9 nm) that dominates the whole survey spectrum 10-60 nm. The spectrum was obtained for a 35 kA capillary current amplitude (~230 ns period), an initial pressure of argon of ~80 Pa and for 1 kV/50 ns HV pulse opening the MCP detector approximately 5 ns before the main current onset.

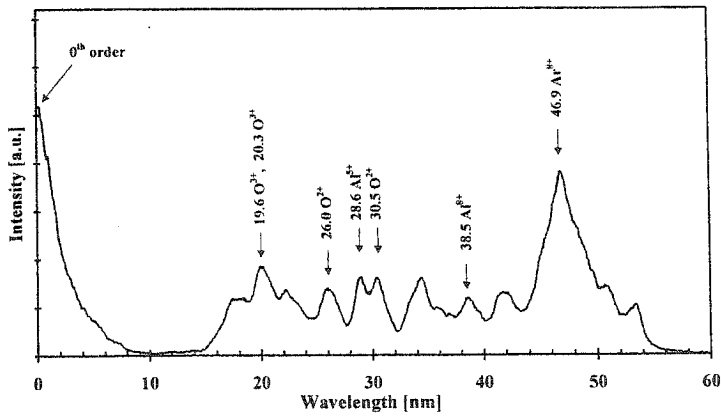


Figure 3. Spectrum of the flat field spectrograph.

2. McPherson spectrograph

The first spectroscopic measurements of the soft X-ray emission from capillary output were performed with the help of computer-controlled McPherson's XUV grazing incidence 1 m

spectrograph Model 248/310G (spectral range for 600 gr/mm grating is 7 to 70 nm). The time-resolved spectrum was registered similarly as in the case of the above-described flat field spectrograph. A more detail description of the McPherson spectrograph and its calibration can be found in [6].

We changed the pre-pulse current (its amplitude and duration) and observed its influence on the measured high-resolved spectrum (in surroundings of *Ne*-like *Ar* line, λ=46.9 nm). It was found (see Fig. 4) that the strong spectral line at the laser transition wavelength (*Ne*-like *Ar*, 3p-3s, J=0-1) clearly dominates the time-resolved (50 ns exposition) spectrum (λ=37-55 nm). In this case the amplitude of the pre-pulse was approximately set to 1 A with a duration of 0.8 μs. The main capillary current amplitude was as high as 38 kA (~230 ns period). In one particular case this dominating spectral line was found even when the MCP detector was opened 10 ns before the maximum of the second current half-period. This untypical behaviour is connected with the second pinching (observed sometimes also on the signal of the filtered PIN diode (multiple lasing was found earlier in Hotta's Laboratory, Tokyo Institute of Technology, Japan [7])).

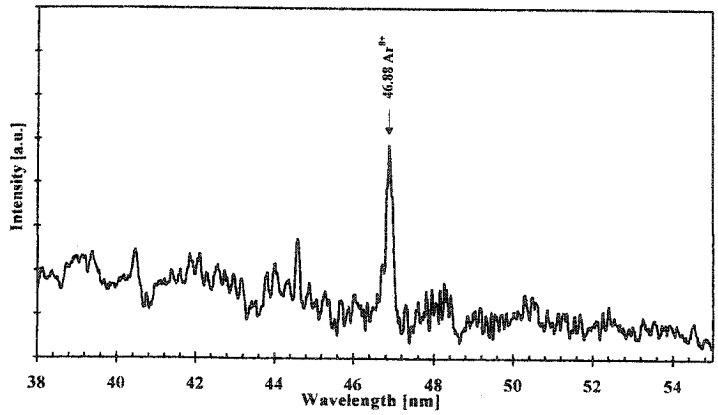


Figure 4. Spectrum of the McPherson's XUV 1 m spectrograph.

CONCLUSION

Our spectroscopic measurements performed by a flat-field spectrograph as well as by McPherson's grazing incidence 1 m spectrograph prove that our modified capillary discharge device CAPEX 2 emits in one particular moment the radiation with one dominating spectral line at the wavelength of the laser transition (46.9 nm).

Acknowledgement. This work has been performed under auspices and with the support in part by the Grant Agency of the Czech Republic under Grant 202/03/0711 and in part by the Ministry of Education, Youth, and Sports of the Czech Republic under Grant LA 055.

REFERENCES

[1] K. Kolacek; Proc. 27th European Conf. on Lasers Interaction with Matter (2002); *to be published.*
[2] J.J. Rocca *et al.*; Phys. Rev. E; Vol. 47, No. 2, 1299-1304 (1993).
[3] J.J.Rocca *et al.*; Phys. Rev. Letters; Vol. 73, No. 16, 2192-2195 (1994).
[4] J.J.Rocca *et al.*; Phys. Rev. Letters; Vol. 77, No. 8, 1476-1479 (1996).
[5] K. Kolacek *et al.*; Czechoslovak J. of Physics; Vol. 52, Suppl. D, 199-204 (2002).
[6] K. Kolacek *et al.*; Proc. German-Polish EURO Conf. on Plasma Diag. for Fusion and Applications; Greifswald, Germany, CD-ROM Publication, Paper A 02 (2002).
[7] G. Niimi *et al.*; J. Phys. D: Appl. Phys.; Vol. 34, No. 14, 2123-2126 (2001).

Ramp Discharge in Z-pinch

W.H. Gaber, A.B. Beshara, A.B. El-Bialy and M.M. Masoud
Plasma and Nuclear Fusion Dept., N.R.C., Atomic Energy Authority, 13759 Enshass, Egypt
wgaber2@yahoo.com

ABSTRACT

A ramp Z-pinch discharge is designed and built in order to increase the pinch ratio and obtain a maximum contraction, and to increase the temperature. The discharge chamber is a cylindrical Pyrex tube of 25 cm long, 18.5 cm, 20 cm inner and outer diameter and two circular Aluminum plates of radius 15 cm separated by 21 cm are inserted into the tube. The tube is filled with He gas at 0.1 mbar. Two capacitor banks are used, the first bank 30 μF and the second fast bank 1.3 μF. The charging voltage was 8 kV for both banks. The discharge current and voltage of each bank are measured by potential divider and Rogowski coil respectively. Also the plasma inductance and resistance are obtained for each case. The plasma inductance has its peak value 300 nH at 4μs, while the plasma resistance has it minimum 8 mΩ at the same time in the case of conventional discharge (single bank). In the case of ramp discharge, the inductance has two peaks 440 nH, 380 nH at 4μs, 9.5 μs respectively, while the resistance has two minimum 4 mΩ, 20 mΩ at at 4μs, 9.5 μs respectively. The temperature has been measure spectroscopicaly by using relative continuum intensity ratio method. The temperature has its peak value 38 eV at 4 μs for single bank case, while it larger peak value 55 eV for ramp case.

INTRODUCTION

In the Z-pinch system the plasma is produced by applying a high voltage pulse between two electrodes, where the space between them is filled with gas or an array of wires, then the discharge takes place by pre-ionizing the gas and becomes conducting. The current then follows in the gas between the two electrodes inducing a magnetic field perpendicular to it and generating a Lorentz force acting inward on the gas and compressing it. It will be compressed until the particle pressure reach the magnetic pressure, which is called pinch effect, then after the magnetic pressure become smaller and decreases, then the compressed dense hot plasma is expanded. Controlling the initial gas density, the current peak and its pulse width can control the maximum plasma temperature and density. The contraction time depends on the initial radius of discharge tube, the density of the gas and the initial rate of increase of the discharge current (dI/dt)[1]. There are many type of Z-pinch such as; slow, fast and super fast Z-pinch which are dependent on initial rate of increase of the discharge current (dI/dt).There are many application of Z-pinch such as; fusion research, X-ray lasers, soft X-ray source, magnetic field compression and high energy particle lens[2]. Artamonov[3] studied the structure of the current layer of radiating Z-pinch in the single compression regime. Christie[4] studied the effect of the wall current on the numerical simulation of the pinch formation. Lee[5] use the snow-plough equation coupled to a circuit equation to compute the trajectory of the pinch. Lee[6] designed a Z-pinch machine for the study of the current stepping technique. It relied on the fact that, when an equilibrium pinch radius was approached as defind by an energy balance condition, it was possible to shift the equilibrium pinch radius ratio to a reduced value by rapidly increasing or stepping up the driving current, since the equilibrium pinch radius ratio depended only on the time-form function of the current shape.

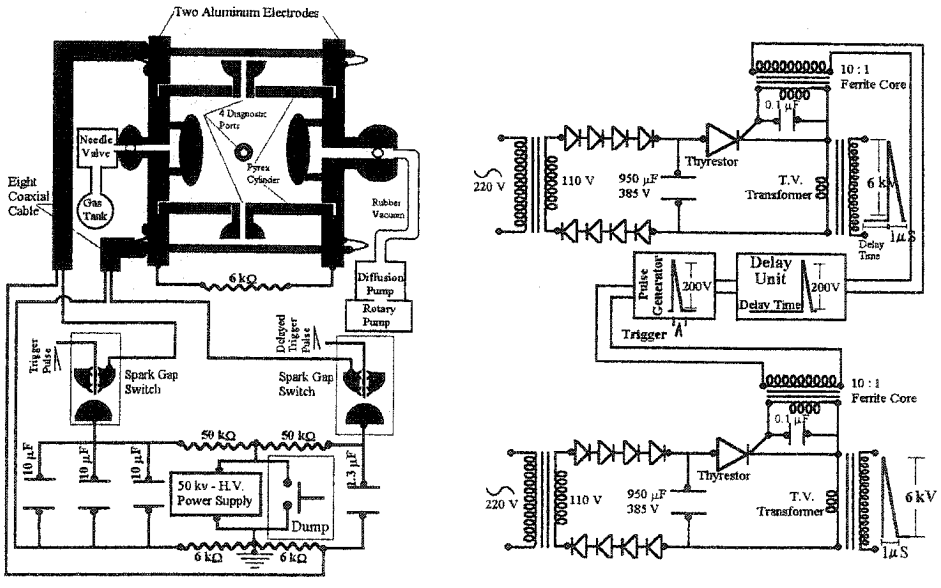
The main interest of this work is to increase of the plasma density and temperature in Z-pinch ,this will be carried out by an additional discharge ahead of the main discharge which will compensate the energy losses of the main bank for pre-ionizing the gas.This is known as ramp discharge or

cascade discharge. This is done by introducing and discharging a fast capacitor bank 1.3 μF, beside the main bank (30 μF), but with delay time, i.e, the fast bank begin the discharge when the main bank current reach its maximum value. This is known as a cascade discharge or ramp discharge.

EXPERIMENTAL SETUP AND MEASURING DIAGNOSTICS

A ramp Z-pinch discharge experiment has been designed and constricted specially for this study and its sketch diagram is shown in figure (1). The discharge chamber is a cylindrical Pyrex tube of 25 cm long, 18.5 cm, 20 cm inner and outer diameter and two circular Aluminum plates of radius 15 cm separated by 21 cm are inserted into the tube . The He gas is used and is injected through the discharge tube via needle valve , which can be used to control the gas pressure, on the other side a pumping unit is connected, it consists of rotary pump and an oil diffusion pump. A resistor (6 k Ω) is connected between the two electrodes to hold the voltage between the electrodes to ensure the discharge.

Two capacitor banks are used, the first bank "30 μF" consisting of three units of 10μF, 20 kV capacitor to minimize its total inductance and the second fast bank (as compared to the first) 1.3 μF. The charging voltage was 8 kV for both banks. This two bank is charged with "8kV" by the same power supply across a separated load resistance "50 kΩ" between the power supply and each bank, so that the resistance between two banks is high "100 kΩ", which prevent the two banks to discharge themselves by each other. The first main bank (30 μF) is discharged firstly through the system via its separate spark gap switch by triggering system. The second fast bank (1.3 μF) begins to discharge after the discharging of main bank by 3.2 μs (i.e. it reach its peak value when the main ionizing bank current reach its maximum value and begin to decrease) these time is adjusted by using the triggering system with its pulse delay time unit as shown in figure (2)



Two Rogowski coils have been used with its "RC" integrator to measure the discharge current, one around the discharge chamber (Pyrex cylinder) to measure the total discharge current and the other around the collector switch plate of the second fast bank. The first has these properties n = 400 turn , r_{maxi} = 10 cm , r_{min} = 0.4 cm, A = 5 × 10^{-5} m^2, R = 15 KΩ, C = 200 nF, so that $I_{discharge}$ =75000 V_{osc} . The second has these properties, n = 200 turn , r_{maxi} = 5 cm , r_{min} = 0.4 cm, R = 15 KΩ, C = 200 nF, so that $I_{discharge}$ =75000 V_{osc} . The discharge voltage is measured by special design of capacitive coupling potential divider with sensitivity "V_H= 720 V_{out}" .

EXPERIMENTAL RESULTS

The waveform signals of discharge current, voltage and power under a charging voltage 8 kV at 0.1 mbar , for single main bank case (conventional discharge) and for two banks case (ramp discharge) are shown in figure (3a) and figure (3b) respectively. The variation of plasma electron temperature with time has been measured by spectroscopy using relative intensity of continuum radiation ratio method[7]. The electron temperature is calculated from the measurements of the intensity ($I_{\lambda 1}$ and $I_{\lambda 2}$) of continuum radiation (recombination + bremsstrahlung) at two different wavelength λ_1 and λ_2 . The electron temperature is calculated from their ratio by using this equation

$$\frac{I_{\lambda 2}}{I_{\lambda 2}} = \left(\frac{\lambda_1}{\lambda_2}\right) \exp\left(\frac{-h C}{K T_e}\left(\frac{1}{\lambda_1} - \frac{1}{\lambda_2}\right)\right)$$

where; h : is the plank constant, C : is the velocity of light, K :is the Boltzman constant, T_e : is the temperature in Kelven and $I_{\lambda 1}$, $I_{\lambda 2}$: is the measured continuum intensity at wavelength λ_1, λ_2 respectively .We use two calibrated filter; violet filter which it transmit the violet light of wavelength λ_1 = 4018 ^{0}A and red filter which it transmit the red light of wavelength λ = 6830 ^{0}A. We measure the transmitted light intensity for the two filters, on the oscilloscope by using the photomultiplier and fiber optics

We can see from figure (3) that, the main bank current has its peak value 54 kA with rise time 4.8 μS and it has a dip at 4 μS, while a voltage shows a sudden peak at this time, the second fast current begins after 3.2μS from beginning of main current and it has peak value5 kA with rise time 1.5 μS. The power has its peak value 60 Mwatt at 4.8 μs in case of single bank, while the power has two peaks 64, 72 Mwatt at 3.5, 6 μS respectively in the case of ramp discharge. We can see from figure (4) that the plasma inductance increase vastly with time and it has a peak value 300 nH at 4 μS in the case of single bank, while it has two peaks 440 nH , 275 nH at 4 μS, 9 μS respectively in ramp discharge and the inductance peak width is greater in the ramp discharge than in case of single bank. This means that, the plasma column is pinched to a smaller radius in ramp discharge than single discharge, and the duration of the pinch is greater in case of ramp discharge than single bank. We can see from figure (5) that the plasma resistance has a smaller minimum value 4 mΩ in ramp discharge, than that in single discharge 8 mΩ. We can see from figure (6) that the plasma temperature has a peak value 55eV in ramp discharge, greater than its peak value 37 eV in single discharge with ratio 150 % approximately.

CONCLUSION

We can conclude that the out put power increase in the case of ramp discharge with 125 % more than in the case of single bank, and with successive pinches occurred. The plasma inductance increase in case of ramp discharge with 150 % more than in the case of single bank. and also its peak width increase for ramp discharge. This means that the pinch ratio and the duration of pinch is increased in the case of ramp discharge . Also the plasma temperature is increased in the case of ramp discharge with ratio 150% of its value in case of single bank.

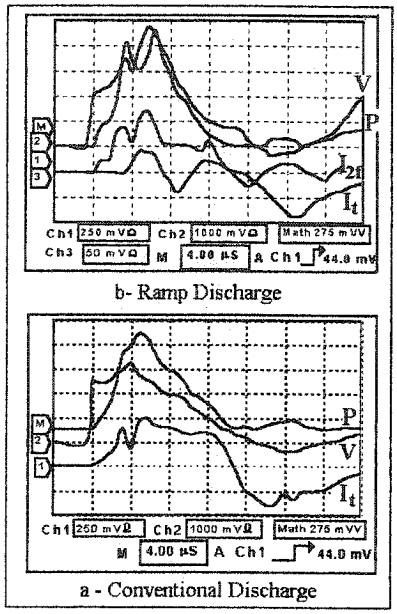


Fig.(3) Waveform Signals for Main Current I_t (27 kA/div), Voltage (750 v/div) , Second Fast Current I_{2f} (4 kA/div) and Power (16 Mwatt/ div) at 4 µs/div.

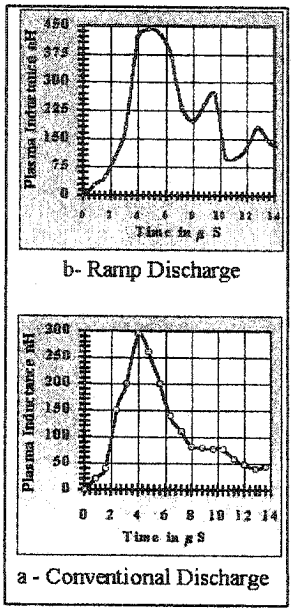


Fig.(4) Variation of Plasma Inductance with Time

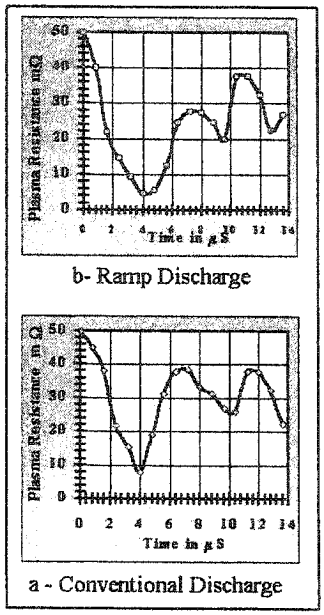


Fig.(5) Variation of Plasma Resistance with Time

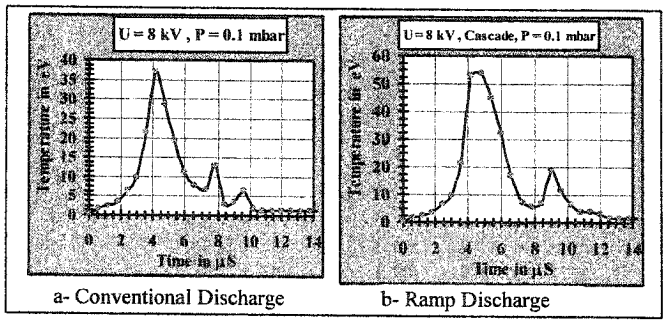


Fig.(6) Variation of Plasma Temperature with Time

REFERENCES

(1) Glaston S. and Lovbereg H.R., Controlled Thermonuclear Reaction, Von Norstrand Co., Inc. (1960).

(2) Dangor E.A., Plasma Physics and Controlled Fusion, 28, 1931, (1986).

(3) Artamonov I.A. and Timofeev B.I., Sov. J. Plasma Phys., 9, 553, (1983).

(4) Christie M.A., J.Phys. D: Appl. Phys., 14, 73, (1981).

(5) Lee S., J. Phys. D:Appl. Phys., 16, 2463, (1983)

(6) Lee S., J. Phys.D: Appl. Phys., 17 , 733, (1984)

(7) Rodrigo B.A., Spring College on Plasma Physics, 27 May-21 June, 1991, Argentina.

Magnetic Forces Distribution in a 4.4kJ Plasma Focus Device

G. M. El-Kashef and H. M. Soliman

Plasma Phys. and Nuclear Fusion Dept., Nuclear Research Center,
Atomic Energy Authority, Atomic Energy13759
Cairo - Egypt.

ABSTRACT

This paper presents results of experimental investigations of the magnetic forces distribution in a 4.4KJ plasma focus device of the Mather-type configuration. Investigations were carried out for a plasma generated in the PF device with parameters as follows: - charging voltage = 12kV, helium gas pressure in the range of 0.5 to 1.5 Torr, peak discharge current ≅ 116kA, and period quarter discharge (current rise time) =7μs. Magnetic probe signals of azimuthal and induced axial magnetic fields at various axial positions in the inter-electrode discharge region between the two coaxial electrodes system and at a fixed radial distance = average radii of inner and outer electrode =3.75cm are used to estimate the distribution of azimuthal F_θ , axial F_z and radial F_r forces along the coaxial electrodes system. The magnetic forces F_θ, F_z, and F_r dependencies on helium gas pressure in the range from 0.5 to 1.5 Torr are represented and the maximum forces are obtained at P=1 Torr. Axial distribution of F_θ , F_z and F_r along the coaxial electrodes have approximately the same profile. The inclination angle of the plasma current sheath with axial distance is estimated for different helium gas pressures.

Key Words: *Plasma Focus, Magnetic Forces, Plasma Current Sheath*

INTRODUCTION

In order to get good focusing, it is important to investigate the magnetic forces distribution, which affects the plasma current sheath during the acceleration phase of the discharge. Plasma current sheath dynamics have been investigated by many authors, some of them are reported here, Krompholz, et.al[1] studied the formation of the plasma layer in 2kJ plasma focus device of the Mather type. They observed that any prerunning filament or inhomogeneous plasma sheath will produce magnetic stray fields in front of the plasma layer which prevents maximum compression of the plasma on the focus axis..Kies et.al.[2] showed that necking (m=0 type) and micro-pinches appeared in the Speed-2 plasma focus, only if the atomic number of thedoping gas was $Z \geq 18$ whereas with $Z<18$ macroscopically stable pinch columns were formed. H.M. Soliman and M.M. Masoud[3] studied the dynamics of an expanded plasma focus of 4.5kJ, their experimental results showed that within the expansion chamber at an axial distance 3.5 times the length of the outer electrode a discontinuity occurred.. Patricio Silva et.al.[4] studied the characterization of very small plasma focus of 50J and observed that the shape of the current sheath running over the end of the coaxial electrodes and the pinch after the radial collapse were similar to the results obtained with devices operating at energies several orders of magnitude higher.

EXPERIMENTAL SET-UP

The schematic arrangement of theMather-type plasma focus electrode system is shown in Fig.(1). The electrode assembly consists of a stainless steel inner electrode 13cm long and 4cm in diameter, surrounded by eight stainless-steel rods fixed symmetrically around the inner electrode, They are screwed to a brass circular plate at the breech of the coaxial electrode system, the diameter of each rod being 0.8cm and its length 13.6cm, the inter electrode separation is 3.5cm. A teflon insulator ring is placed between the inner and the outer electrode at the breech. The inner and outer electrodes

system is enclosed in a stainless steel plasma chamber of length and diameter 40 cm and 38 cm, respectively. This device is powered by a capacitor bank of 61.68 μ F capacity, charged up to 12kV.

EXPERIMENTAL RESULTS AND DISCUSSION

The axial, azimuthal and radial magnetic forces F_z , F_θ and F_r distribution profiles along the coaxial electrodes and at the radial distance of 3.75cm from the inner electrode axis are estimated from the magnetic field induction and the plasma current density data. Figs. 2a,b present the variation of the axial magnetic force F_z against the axial distance Z for different filling helium gas pressure values These figures reveal that F_z decreases up to Z=7cm according to $F_z \propto Z^{-4.8}$ (for P=0.5Torr), $F_z \propto Z^{-3}$ (for P=1Torr) and $F_z \propto Z^{-8.2}$ (for P=1.5Torr) but after Z=7cm it increases and decreases as the relations $F_z \propto Z^6$for Z varied from 7cm to 10cm and then it decreases slowly as $F_z \propto Z^{-1}$ for Z varied from 10cm to 13cm, (for P=0.5Torr), also $F_z \propto Z^5$ and $F_z \propto Z^{-0.8}$ for Z varied from 7cm to 10cm and from 10cm to 13cm respectively, (for P=1Torr), while at P=1.5Torr, $F_z \propto Z^9$ and $F_z \propto Z^{-1}$ for the same axial distance as above. Variation of azimuthal magnetic force, F_θ with axial distance Z at different Helium gas pressures is shown in Fig.(3), these curves illustrate that, F_θ has the same behavior like F_z for Z varied from 4cm to 7cm and it decays with different rates at different Helium gas pressure according to the relation $F_\theta \propto Z^{-5.5}$, $F_\theta \propto Z^{-4.7}$ and $F_\theta \propto Z^{-6.5}$ for P=0.5, 1and 1.5Torr respectively. Afterwards, it increased sharply until Z=10cm according to the relation $F_\theta \propto Z^6$ (for P=0.5Torr), $F_\theta \propto Z^{4.1}$ for P=1Torr and $F_\theta \propto Z^8$ for P=1.5 Torr, then F_θ is increased with axial distance Z from 10cm to coaxial electrodes muzzle with a small rate according to $F_\theta \propto Z^{0.74}$, for P=0.5Torr, $F_\theta \propto Z^{0.3}$, for P=1Torr and $F_\theta \propto Z^{0.8}$ for P=1.5Torr. Fig.(4a, b) describe the axial distribution of radial magnetic force, F_r , these figures demonstrate that F_r remains almost constant for the axial distance near to coaxial electrodes breech, Z=4cm to Z=7cm, then it increases sharply with axial distance as the relation, $F_r \propto Z^{1.7}$, $F_r \propto Z^{2.5}$ and $F_r \propto Z^{2.2}$ for P=0.5,1and 1.5Torr respectively.

Figures ((2a,b),(3a,b),(4a,b)) can be seen that the maximum magnetic forces along the inter-electrode space is detected at Helium gas pressure = 1Torr.

The inclination angle of the plasma current sheath with axial distance in the inter-electrode space is computed from axial and radial magnetic forces data. Fig.(5) decribes the variation of inclination angle θ versus the axial distance Z. It clearly shows that the inclination angle θ has two minimum values, one at Z=7cm , the other at Z=13cm.

CONCLUSION

The experimental results of the axial, the azimuthal and the radial magnetic forces distribution profiles along the coaxial electrode system have been shown to depend on the helium gas pressure, and the maximum value of these forces is reported for a pressure of 1Torr. The axial distributions of F_z , F_θ and F_r have approximately the same profile for different helium gas pressures. These profiles may be attributed to the current shedding effect phenomena[5] i.e the plasma current sheath does not carry along with it the full discharge current and a slow moving diffuse layer current lags behind the main plasma current sheath. This phenomena is identified clearly at the axial distance Z=7cm from the coaxial electrodes breech, where a rapid drop of F_z , F_θ occurs, at this position a minimum inclination angle of plasma current sheath with z-axis is detected, then a collapse of plasma sheath may occur.

REFERENCES

(1) H. Krompholz, et al., Phys. Letters, 77A, 246 (1980).
(2) W. Kies, et al., Plasma Source Sci. Technol, 1, 21 (1998).
(3) H. M. Soliman and M.M. Masoud, Contrib. Plasma Physics, 33, 317 (1993).
(4) Patricio Silva, et al., Proc. of International Symposium; Research and Applications of Plasmas, (2001).
(5) P.S. Chow, S. Lee and B.C. Tan, J. Plasma Phys, 8, 1, 21 (1972)

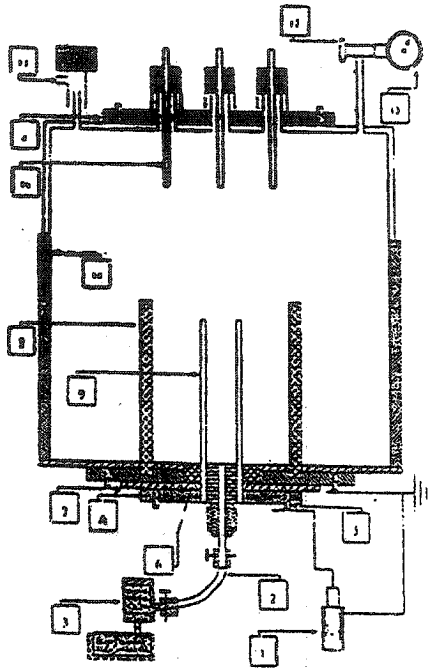
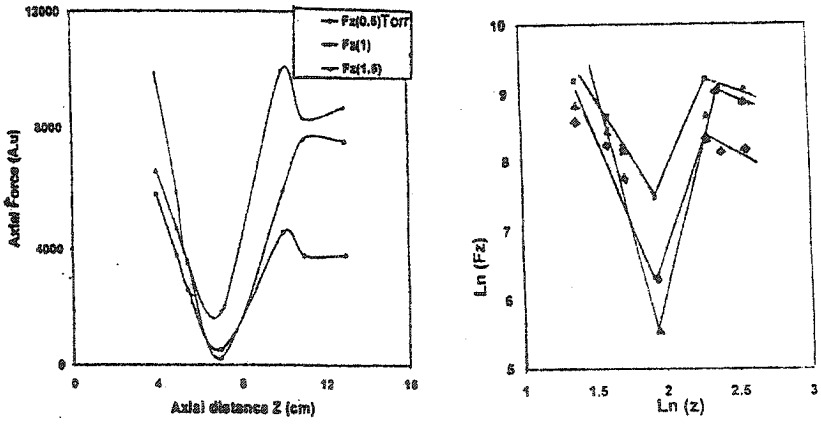


Fig. (1) Schematic diagram for the discharge Chamber of the plasma focus device.

1- Coaxial cables (24 cables) 2- Rubber tube 3- Rotary pump
4- Copper flange 5- Connection points 6- Teflon
8- Outer electrode 9- Inner electrode 10- Diagnostic tool
11- Gas inlet 12- Thermocouple gauge 13- Vacuum meter 14- Slit



(a) (b)

Fig.(2) Axial force versus axial distance

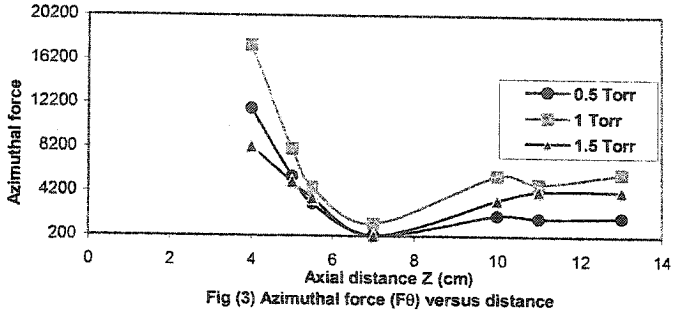


Fig (3) Azimuthal force (Fθ) versus distance

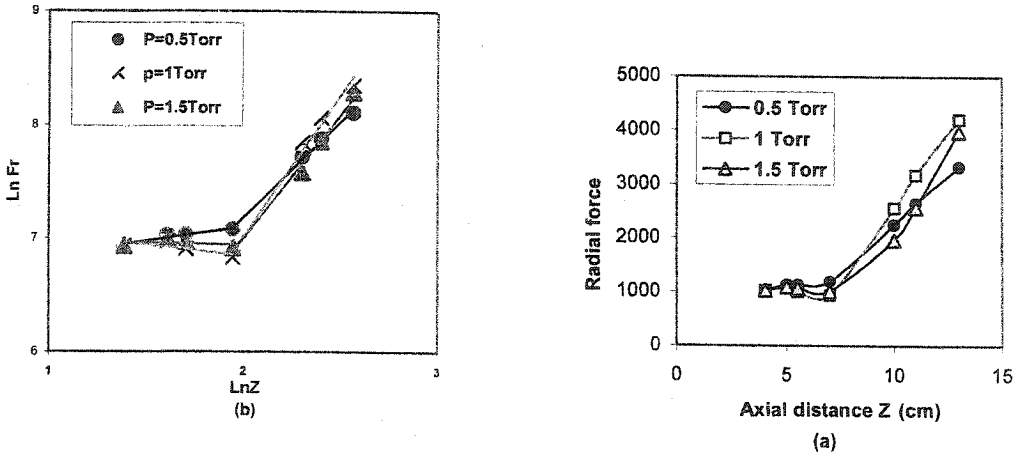


Fig. (4) Radial forces versus axial distance

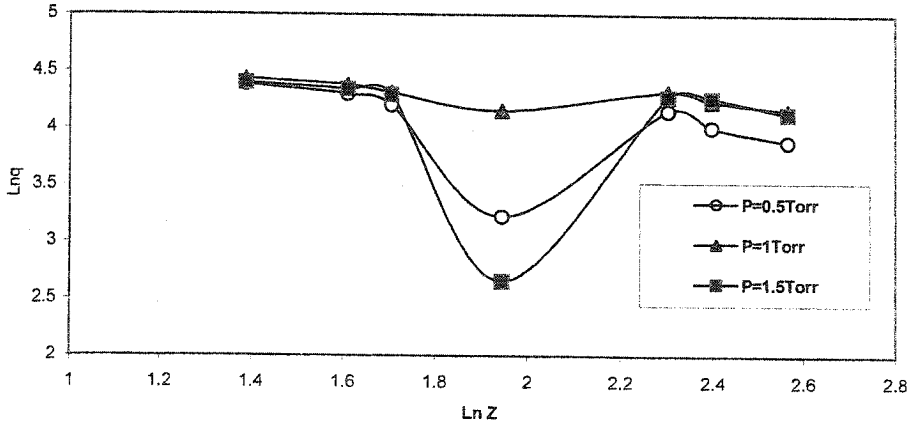


Fig. (5) Inclation angle, Lnθ versus axial distance Ln Z

Operation of a Plasma Focus Device with Energy of 2.8 kJ in Various Gases

Sh. H. Al-Hawat, O. Othman
Physics Department/ Plasma Laboratory,
Atomic Energy Commission, P. O. Box 6091, Damascus, Syria.
shhawatt@aec.org.sy

ABSTRACT

A 2.8 kJ plasma focus device has been constructed using a set of four storage capacitors which are connected in series and each of them has the specifications of 100 μF and 5 kV. The device was operated in various gases. The good focusing action was obtained for Ne between 0.6 and 1.5 mbar, for N_2 between 0.5 and 1.25 mbar and for He between 0.3 and 2 mbar.
A FORTRAN program was written for a three phase model of the plasma focus dynamics to calculate the main characteristics of the plasma. The theoretical results were compared with the experimental results and qualitative agreement was observed.

Key Words: ***plasma focus, numerical modeling, fast discharge***

INTRODUCTION

It is well known that the plasma focus device is a fundamental tool for research and applications as a source of x-rays, of neutrons and of electron beams, according to the design and geometry of the device and nature of the gas and its pressure[1].
The intensity of focus action is governed by the nature and pressure of the filling gas, the yield of the device depends on the strength of focusing action[2, 3].
In this paper we discuss operation of AECS PFF in various gases (Ne, N_2, He) in order to determine the operating conditions which give the best focus action, also to apply a theoretical model in purpose to specify this device.

EXPERIMENTAL SETUP

The structure of the plasma focus device which was constructed and operated locally is fully described in[3, 4] and the essential parts of the setup are shown in the Fig.1.
Energy from the charger with specifications of 0-20 kV and 0-100 mA is stored in a 25μF, 20kV capacitor which is charged to 15 kV and switched by means of a spark gap which is in turn switched by a high voltage negative pulse getting from TV transformer of a triggering unit.
The system is pumped down to a base pressure of 0.25 mbar and operated at pressures up to 5 mbar. The focus action is characterized by a distinctive dip in the current signal and a spike in the voltage signal, which indicate a rapid magnetic compression. Fig. 1 shows a schematic diagram of the experimental setup. As seen from the setup an Ohmic voltage divider 1:100 and Rogowski coil were used to determine the voltage and current signals vs. the time during the plasma focus process using a storage oscilloscope with 1:10 attenuator.

used to determine the voltage and current signals vs. the time during the plasma focus process using a storage oscilloscope with 1:10 attenuator.

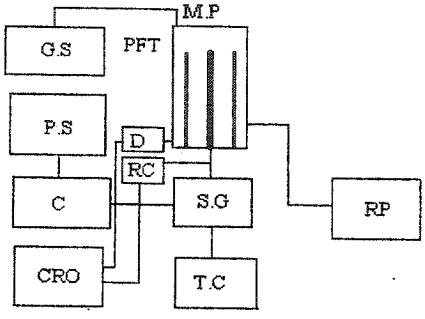


Fig.1 Experimental setup: PFT plasma focus tube, GS gas supplier, PS power supply, C bank capacitors, SG spark gap, TC triggering circuit, CRO storage oscilloscope, RP rotary pump, D-voltage divider, RC Rogowski coil.

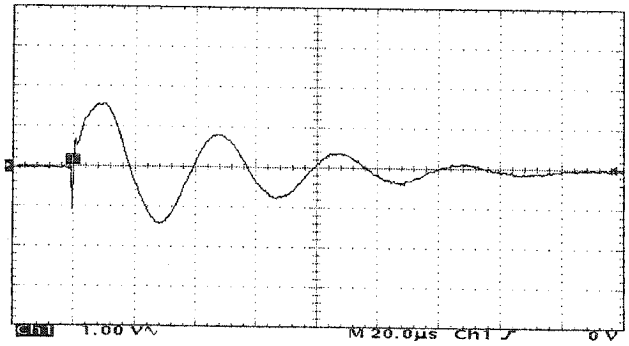


Fig. 2: The current waveform for calibrating the Rogowski coil taken at 3 mbar in N_2.

THEORY

The dynamics of the plasma focus is divided into three phases as follows:

- The axial phase which is described by a snow-plow model
- The compression radial phase which is described by a slug model
- And the expansion phase which is described by equations similar to those of the axial phase.

A FORTRAN program was written to solve numerically the differential equations of the plasma dynamics using a linear approximation method[5]. The calculated results for the cases of He, Ne and N_2 were obtained as shown in Fig 3 a, b, c respectively. As seen from results the focusing action

occurs during the radial phase and it can be seen by a spike on the voltage curve and a dip on the current curve.

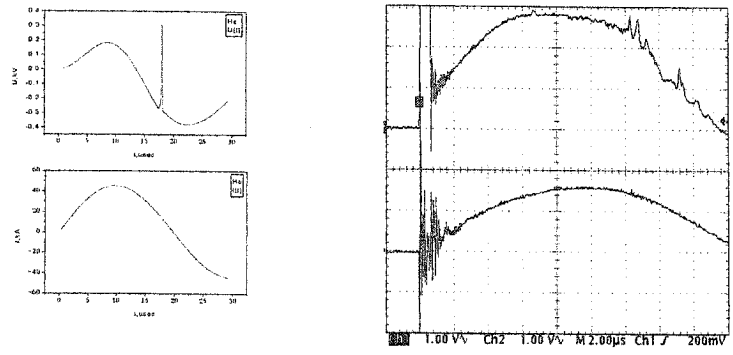


Fig.3a Theoretical (left) and experimental (right) voltage (upper) and current (lower) trace at a pressure of 0.6 mbar in the case of He.

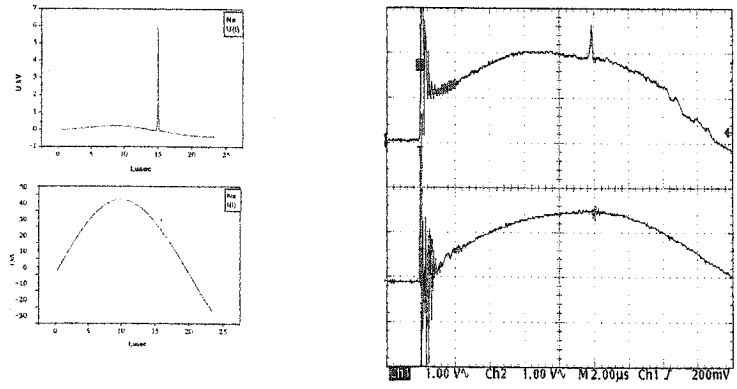


Fig.3b Theoretical (left) and experimental (right) voltage (upper) and current (lower) trace at a pressure of 0.9 mbar in the case of Ne.

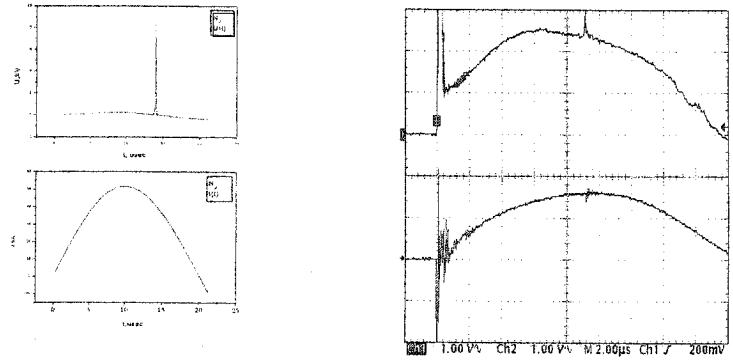


Fig.3c Theoretical (left) and experimental (right) voltage (upper) and current (lower) trace at a pressure of 0.75 mbar in the case of N_2.

RESULTS AND DISCUSSION

The plasma focus device was operated with three different gases; He, Ne and N_2.
The current waveforms were recorded using Rogowski coil at pressure of 3 mbar for each of the gases separately by a Tektronix oscilloscope. Fig.2 shows the current curve for N_2, which is used for calibration of the coil; this curve is similar to the curve of a damped current in a L-C-R circuit.

The calibration coefficient is calculated by $K = \frac{I}{V}$.

where V_1 is the amplitude of the first top of the voltage signal and I_1 is the maximum current. The calculation showed that the average value of the calibration constant of the coil is 32.23 kA/ V. The AECS PFF has been operated in helium, nitrogen and neon at 15 kV and at pressures between 0.5 mbar and 5 mbar in order to determine the regimes of operation for best focusing
In Fig. 3a, b, c a set of typical current and voltage waveforms are shown, one for each of the gases studied, theoretically and experimentally. It was shown that for gases with many electron atoms like Ne and N_2, the focus action tends to be strong and to occur after the current peak whereas for helium, a two electron atom, the focus tends to be less intense and to occur at or earlier than the current peak. Multiple focusing was also observed to occur more readily with the lighter gas He[6].
In helium, a good focus action was obtained for a pressure range of 0.3 to 2 mbar, with a best focus at 0.6 mbar (Fig. 3a). The good focus action pressure range for neon was found to be from 0.6 to 1.5 mbar with best focus action at 0.9 mbar (Fig.3b), where for nitrogen the pressure range for focusing action was from 0.5 to 1.25 mbar with a best focus action at 0.75 mbar (Fig.3c).
The intensity of the focus action could be measured by the size of the voltage spike.

CONCLUSION

AECS PFF has been operated in various gases including helium, neon and nitrogen; the optimum operating pressures in these gases have been established. They were 0.6 mbar for He, 0.9 mbar for Ne, and 0.75 mbar for nitrogen.
A FORTRAN program was written for a three phase model describing the plasma dynamics in three main phases (axial, radial and expansion) and run for the studied conditions.
The theoretical and experimental results were compared, and qualitative agreement was observed.

REFERENCES

(1) S. Lee, S.P. Moo, C.S. Wong and A.C. Chew; "Twelve years of UNU/ICTP PFF- a Review"; Kuala Lumpur, Malaysia, (1998).
(2) Sh. Al-Hawat and M. Al-Barhoum, "A Preliminary Study of a Plasma Focus Device"; AECS-PH/RSS 121, (July 1995).
(3) Sh. Al-Hawat, W. Al-Sadat and J. Assaf; "Construction of a Plasma Focus Device"; AECS-PH/RTW 74 (September 2000).
(4) B. Paosawatyanyong et al., "Proceedings of the Regional Conference on Plasma Research in 21th Century"; Bangkok, Thailand, May 7-12, 80 (2000).
(5) S. Lee; "Spring College on Plasma Physics, Experiments with the ICTP-UM 3.3kJ Plasma Fusion Facility"; (17 May-11 June 1993).
(6) A. J. Smith and A. V. Gholap, "Small Plasma Physics Experiments"; ICTP, Trieste, (25 May – 19 June 1987).

MAGNETIC FIELD AND PLASMA SHEATH VELOCITY PROFILES IN 2 KJ PLASMA COAXIAL ACCELERATOR

M.M. Masoud[1], H.M. Soliman[1], A.B. El-Bialy[2], F.A. Ebrahim[1]
[1]*Plasma Physics Dept., Nuclear Research Centre, Atomic Energy Authority, Cairo, Egypt.*
[2]*Physics Dept., Faculty of Girls, Ain Shams University, Cairo, Egypt.*

ABSTRACT

The purpose of this paper is to determine experimentally and theoretically the dynamical plasma sheath distribution in the plasma coaxial accelerator device of Mather type configuration. This device is powered by a single module capacitor bank of 38.55 μF capacity and maximum charging voltage of 10 kV. The discharge takes place in Argon gas with a pressure of 0.1 Torr.

Axial distribution of azimuthal magnetic field induction is detected in the annular space between two coaxial electrodes by using a magnetic probe technique. A snow-plough model is used to derive analytical solution of axial plasma sheath dynamics along the coaxial electrodes.

Experimental results of axial distribution of azimuthal magnetic field induction, B_θ and plasma sheath velocity, V_z showed that, B_θ had a peak value = 2.4 kG at axial distance z=6.5 cm from the coaxial electrodes breech and at discharge time t = 5.5 μs. V_z had a peak value = 6×10^6 cm/s at z = 11.8 cm and at t = 6.75 μs.

Theoretical calculations of axial plasma sheath velocity are demonstrated that, the maximum axial plasma sheath velocity = 4.7×10^6 cm/s at z = 20 cm and at t = 7 μs.

Comparison between the theoretical calculations and the experimental data are studied in this work.

Keywords: ***Plasma Gun, Plasma Dynamics, Coaxial Discharges***

INTRODUCTION

The purpose of the present work is to determine experimentally and theoretically the current plasma sheath (CPS) dynamics. The magnetic probe technique is used to measure the plasma sheath dynamics in the annular space between coaxial electrodes at radial distance a + b /2 = 2.45 cm.

The Snow- Plough model is used to investigate theoretically the plasma sheath dynamics along the coaxial electrodes of plasma coaxial accelerator device under consideration. Previously, Marchall et al.[(1)] showed that the investigation of the plasma sheath dynamics in a coaxial discharge accelerator (10 Kv – 50 KJ), a jet of plasma current with fast velocity ranging from 5x 10^7 to 10^8 cm/ sec. flowed from the muzzle. Soliman, H.M. et al.[(2)] showed that, the plasma sheath had its maximum thickness, near the inner electrode, and then it decreased in the radial direction.

EXPERIMENTAL SETUP

A schematic diagram of coaxial plasma accelerator device is shown in fig. (1). The device is a Mather type configuration. This device is powered by a single module capacitor bank (5x7.71 μF – 12Kv) and is switched by a pressurized spark gap switch. The plasma coaxial accelerator device is

operated with argon gas at ambient pressure = 0.1 Torr and condenser bank voltage = 10 Kv. The diagnostic tool used in this paper is a magnetic probe.

EXPERIMENTAL RESULTS AND DISCUSSION

Axial distribution of azimuthal magnetic field induction (B_θ) attached with the plasma sheath current is detected in the annular space between two coaxial electrodes at radial distance = average radius of inner and outer electrodes, by using a magnetic probe with 20 turns of enameled copper wire of 2mm inner diameter and the cross-section area of it = 3.5×10^{-2} cm^2. Fig. (2-a&b) shows the signals of azimuthal magnetic field induction for argon gas pressure of 10^{-1} Torr, charging voltage of 10Kv and at an axial distance= 5.5cm and 9.5 cm respectively from the coaxial electrode breech.

Variation of the peak value of azimuthal magnetic field induction, B_θ with time ,t, and axial distance, Z, from breech are shown in figures (3) and (4) respectively. Fig.(3) shows that at t = 5.5 μs, B_θ has a maximum value = 2.4×10^3 G. Fig. (4) shows that, the maximum value of B_θ. at Z = 6cm.

The axial plasma sheath velocity along the coaxial accelerator is detected from the relation between the arrival time of the peak value of the azimuthal magnetic field induction, associated with the plasma sheath and the axial distance from the coaxial electrodes breech.

Variation of axial plasma sheath velocity V_z with axial distance, Z and time, t, for argon gas pressure = 10^{-1} Torr and charging voltage = 10 Kv are shown in figures (5) and (6). These figures show that the maximum value $V_z = 6 \times 10^6$ cm/s is found at Z = 11.8 cm at t = 6.75 μs.

The Snowplough model is used to investigate theoretically the plasma sheath dynamics along the coaxial electrodes of plasma coaxial accelerator device under consideration. This model[3] assumes that the force accelerating the total mass of gas swept up by the current sheath equals to the electromagnetic driving force of the current sheath. Then, the rate of change of momentum is equal to the sum of forces acting on the plasma sheath, (Navier Stokes equation)[4]

$$\frac{d}{dt}\left(m\frac{dz}{dt}\right) = \left(J_r \times B_\theta\right) - \nabla P + \frac{\eta}{3}\nabla\left(\nabla.V\right) + \eta\nabla^2 v + mg \qquad (1)$$

Where: m is the mass of the argon gas within the sheath,

J_r is the radial current density of the sheath,

B_θ is the azimuthal magnetic field intensity formed by the current sheath,

∇P is the pressure gradient in the interelectrode gap of coaxial system.

dz/dt = V is the plasma sheath velocity.

η is the viscosity coefficient, and

mg is the gravitational force.

Figures (7) and (8) show the theoretical calculation of axial plasma sheath velocity versus the discharge time and axial distance respectively. Fig. (7) shows that, the plasma sheath has a maximum axial velocity = 0.0423 m/μs, 0.0473 m/μs for P = 10^{-1} Torr and P = 8×10^{-2} Torr respectively at t = 6 μs, i.e at the peak of discharge current. Fig.(8) shows that, the plasma sheath reaches the muzzle with axial velocity = 0.0375 m/μs, 0.045 m/μs for P = 10^{-1} Torr and 8×10^{-2} Torr respectively and the maximum axial velocity = 0.042 m/μs at z = 15.5×10^{-2} m, and 0.047 m/μs at z = 17.4×10^{-2} m, for P = 10^{-1} Torr and P = 8×10^{-2} Torr respectively.

CONCLUSION

Axial distribution of azimuthal magnetic induction B_θ and axial plasma sheath velocity V_z along the coaxial electrodes, showed that at V_{ch} = 10 Kv and P = 10^{-1} Torr, B_θ had one peak value = 2.4 KG at axial distance z = 6.5 cm, and at t = 5.5 us, V_z had a peak value = 6x106 cm/sec at z = 11.8 cm and t=6.75 us.

The axial plasma sheath propagation along the coaxial electrodes had been studied theoretically, using a Snow- Plough model. A comparison of of the prediction of the theoretical

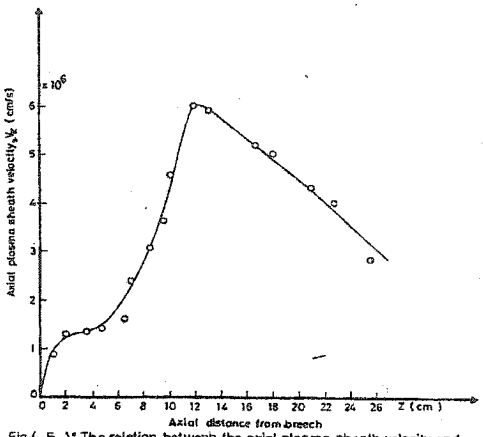


Fig (5) : The relation between the axial plasma sheath velocity and the axial distance from breech.

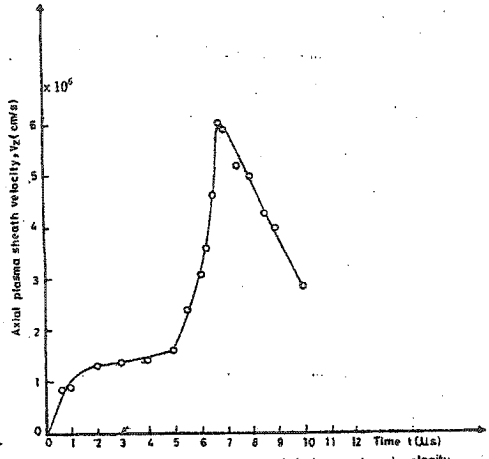


Fig.(6) : The relation between the axial plasma sheach velocity and the time.

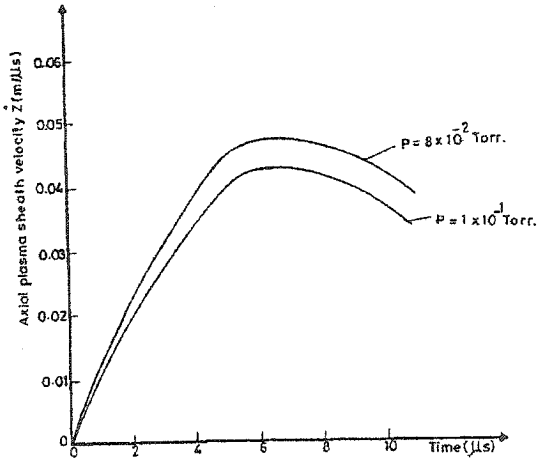


Fig (7) The relation between the axial plasma sheath velocity and the discharge time.

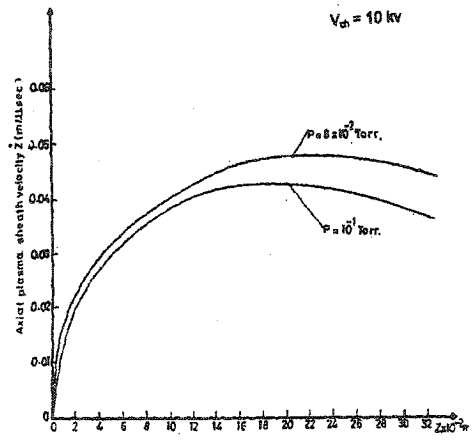


Fig. (8) The relation between the axial plasma sheath velocity and the axial distance.

calculation and the experimental results of plasma sheath dynamics had been carried out and it demonstrated that, the measured axial plasma sheath velocity is higher than that predicted theoretically, for V_{ch} = 10 Kv and P = 0.1 Torr. This result could be due to the inefficient Snow – Plough action by the plasma current sheath i.e experimentally, the plasma sheath does not carry along with it all the gas particles encountered, then the motion mass of the Snow- Plough model is greater than the actual one.

REFERENCES

(1) Marchall, J. and Henins, I.; XVII International Conference on Plasma and Controlled Fusion CN- 21/ 86, 449, (1965).

(2) Soliman.H.M. and Masoud, M.M.; 17th International Symposium on Rarefied Gas Dynamics, 2, 479 (1991).

(3) Tsagas, F.F.; Mair, G.L.R. and Prinn, A.E.;Phys. D. Appl. Phys. 11, 1263 (1978).

(4) Roserbluth, M.; Los Alamas Scientific Repot LA – P, 1850 (1954).

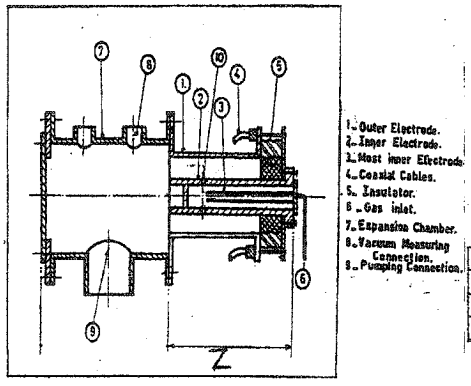


Fig.(1): Shows cross-section of the coaxial plasma accelerator device.

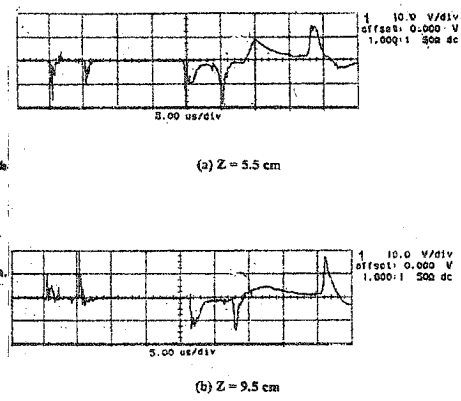


Fig.(2 a-b): Oscillogram of azimuthal magnetic field induction signals at charging voltage of 10 kV and argon gas pressure of 10^{-1} Torr.

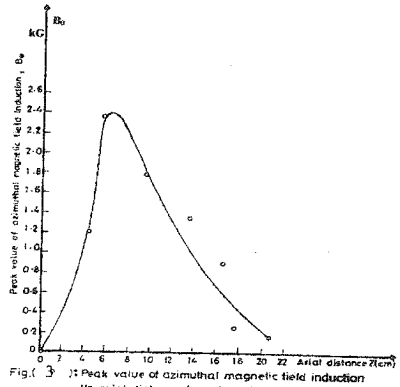


Fig.(3): Peak value of azimuthal magnetic field induction Vs axial distance from breech.

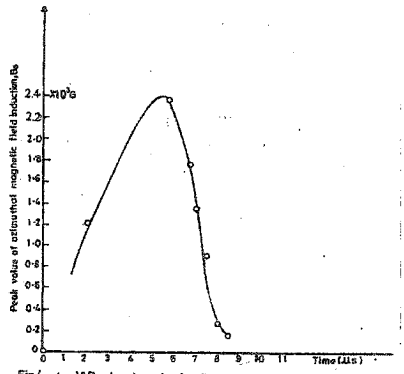


Fig.(4): Peak value of azimuthal magnetic field induction Vs time, at V = 8 Kv, P = 0.1 Torr.

INVESTIGATION OF PLASMA CURRENT SHEATH DYNAMICS IN A PLASMA FOCUS DISCHARGE

T. Y. Allam, G. M. Elkashef, H. M. Soliman
Plasma Physics and Nuclear Fusion Department, Nuclear Research Center, Atomic Energy Authority, Cairo, Egypt
tarekmya1@hotmail.com

ABSTRACT

This paper is concerned with the study of the plasma current sheath dynamics in Mather geometry plasma focus device. The condenser bank voltage is 10kV, which corresponds to capacitor bank storage energy of ~1kJ. Experimental measurements were detected with Nitrogen gas at 1.5 Torr base pressure. The experimental investigations were carried out using a magnetic probe and a miniature Rogowski coil. The plasma current sheath velocity in the inter-electrode space between the two coaxial electrodes in axial direction from the breech end to the muzzle end is estimated from analysis of the azimuthal magnetic field induction and plasma current sheath distribution profiles. The experimental results showed that the plasma sheath dynamics is important because the plasma focus formation depends on the state of plasma sheath just before the radial collapse phase.

Keywords: ***Plasma Focus, Current Sheath Dynamics, Coaxial Discharges***

INTRODUCTION

The study of plasma current sheath dynamics in axial phase is of interest in determining the actual behaviour of the collapsing current sheath during the focus phase. Plasma current sheath dynamics in plasma focus devices have been investigated by many authors[1-4]. M. Mathuthu et al[1] studied a simplified theoretical model for design of a new plasma focus device. They observed that the focus strength was shown to be coupled to the breakdown conditions via the initial radial velocity and the initial and final velocities of the axial rundown phase of the current sheath. S. Lee and A. Serban[2] found that the linear dimensions and time scales of the gross plasma focus pinch in 3kJ plasma focus device were shown to be related to the anode radius of the plasma focus device. A. Kasperczuk et al[3], showed that, in PF-1000 device, two kinds of plasma sheath disturbance, type I: classical MHD m=0 instability, type II: singular great scale disturbance. H. Soliman and M. Masoud[4] showed that the plasma sheath was split into two layers at the breech, which was referred to as a shock front and its magnetic piston and the two layers of plasma current sheath rotated around the inner electrode. The aim of the present work is to investigate the plasma current sheath dynamics along the coaxial electrodes of the plasma focus device system operated in Nitrogen gas.

DESIGN AND FABRICATION OF A PLASMA FOCUS DEVICE

1. The Focus Chamber

The discharge chamber used is a cylinder of 40cm diameter and 35cm length and is made of stainless steel with a volume of ~0.18m^3. Four cylindrical side ports each of 5.4cm inner diameter are welded to the side of the chamber, two of which is sealed with stainless-steel flanges and the other two ports are sealed with glass disks to allow viewing into the chamber. The two circular glass windows

are sealed with rubber by means of a stainless-steel flange and are fixed with its center at the same altitude of the nozzle of discharge. These four ports can be used for x-ray imaging, optical diagnostics or probes introduction. The chamber is fixed with its axis vertical on an isolating disk. On the top of the chamber, a stainless-steel flange is fixed and sealed with rubber. Eight small ports, each of 10mm inner diameter, are fixed to the top flange five of which are situated in front of the inter-electrode region and are designed for glass probes, one for vacuum measurement and the other two inlets are designed for using multiple gas mixtures. In the plasma focus assembly, shown in Fig.(1), the capacitor banks were connected to the plasma focus system via 30 1.5m-long coaxial cables. The discharge chamber is connected to a rotary pump capable of evacuating the chamber down to 10mTorr.

2. The Electrode System

The outer electrode consists of eight stainless-steel rods each of 1cm diameter and 13.4cm length. The eight rods are fixed to a copper flange of 15mm thickness on a circle of 10cm diameter around the inner electrode. This copper flange is fixed to a stainless-steel flange for sealing the focus chamber from the bottom. The inner electrode has 4cm outer diameter and 11.2cm length and is made of stainless steel. The inner electrode is fixed to a copper disk of 15mm thickness. A teflon disk of 30mm thickness insulates the two copper disks. 30 coaxial cables connect the two copper disks to the collecting plates of the capacitor banks. Two ports are made on the bottom of the focus chamber; one is used for vacuum pump connection and the other is used for gas inlet.

3. The Energy Storage System

The plasma focus device is energized by two capacitor-banks each consisting of 20 parallel capacitors of 1.5μF and 40kV maximum charging voltage. The total capacitance of each bank is thus 30μF. The two capacitor-banks are connected in a way similar to that used in Marx generators. The idea of using this circuit assembly is to be able to charge the two large capacitor-banks in parallel, by means of a single high-voltage power-supply, to equal amounts of charging voltage without using a higher voltage supply with a higher maximum rating for charging voltage and current. In contrast to the charging operation of the two capacitor-banks connected in parallel, they are then discharged in series by means of two spark gap switches, operated with compressed dry air, in a two-stage operation. The air gap inside the two switches controls the simultaneous discharge of the two capacitor-banks and need to be carefully adjusted. An illustration of the circuit connections is shown in Fig.(2).

The first air gap switch is triggered by a high voltage pulse of 15kV peak voltage using a triggering capacitor of 1μF and 25kV maximum charging voltage. Another high voltage power supply is used to charge the triggering capacitor to 15kV charging voltage. The triggering pulse is delivered to the triggering pin of the first air gap switch via a carefully isolated triggering circuit used to discharge this triggering capacitor. Fig.(2) also shows a connection diagram of the used trigger system. The maximum storage energy of the used capacitor banks is 48kJ corresponding to a bank charging voltage of 40kV on each of the two capacitor-banks.

RESULTS AND DISCUSSION

The maximum discharge current in the first half cycle of discharge was 17kA at a charging voltage of 10kV and Nitrogen gas pressure of 1.5Torr. The total circuit inductance was measured as 2.8μH while the discharge circuit resistance was 0.022Ω.

1. Focus Action

The experimental investigations were carried out using Nitrogen gas as a filling pressure in an

of the total voltage needed for discharging between the two coaxial electrodes. Experimental results show that the plasma current sheath forms a focus at maximum input power for a certain operating condition of 10kV banks charging voltage and 1.5Torr Nitrogen gas pressure. At this operating condition, all signals of miniature Rogowski coils or magnetic probes become clear and reproducible. Results of discharge current signal show that the typical dip of the focus phenomena in the discharge current signal does mot appear clearly but it appears as a very small drop at $t \approx 8\mu s$. This behaviour may indicate that the external circuit impedance is rather big in comparison with that of the pinch.

2. Axial Magnetic Field Induction and Plasma Current Sheath Density

Results of the magnetic probes measure the presence of an axial magnetic field as scanned along the axial length at mid-points between the two electrodes. Signal of the magnetic probe measuring the axial magnetic field component is formed of several spikes each lasting ~1-2μs starting with a spike of large amplitude formed directly after breakdown, for all values of operating gas pressure. This is perhaps due to the formation of vortices of moving charges encountered by the current sheath.

Measurements of the current density in the axial direction, using a miniature Rogowski coil, show a peak of ~850Acm^{-2} as the plasma current sheath passes by the point of measurement. In the opposite direction, a smaller peak of current density in the axial direction of amplitude ~130Acm^{-2} then follows this peak. A typical waveform is shown in Fig.(3). The signal amplitude continues to rise as the bank charging voltage is raised. The signal stays clear as we go down in value of initial gas pressure until the value of 0.8Torr is reached.

As a conclusion, the plasma current sheath actually consists of two layers. When any of these layers loses the azimuthal component of discharge current the other layer will force it to rotate in the opposite direction by the effect of mutual magnetic induction coupling. Then, we have two layers of axial plasma sheath current density each is moving in opposite direction to the other[4].

3. Axial Speed of the Plasma Current Sheath

A magnetic probe was used to measure the plasma current sheath velocity in the axial direction by detecting the peak time of azimuthal magnetic field. Results of the axial plasma current sheath velocity show a continuous increase of sheath velocity as the plasma propagates along the length of the inner electrode till it reaches a value of ~2.5cm/μs at focusing time $t \approx 8\mu s$, as shown in Fig.(4).

ACKNOWLEDGEMENT

The study was performed with the support of the International Atomic Energy Agency and the Egyptian Atomic Energy Authority.

REFERENCES

(1) M. Mathuthu, T.G. Zengeni and A.V. Gholap, IEEE Transactions on Plasma Science, Vol. 25, No. 6, p. 1382 (1997)

(2) S. Lee and A. Serban, IEEE Transactions on Plasma Science, Vol. 24, No. 3, p. 1101 (1996)

(3) A. Kasperczuk, R. Miklaszewski, M. Paduch, T. Pisarczyk and M. Scholz, Proc. of International Symposium, Research and Applications of Plasmas (2001)

(4) H.M. Soliman and M.M. Masoud, Physica Scripta, Vol. 50, P.406 (1994)

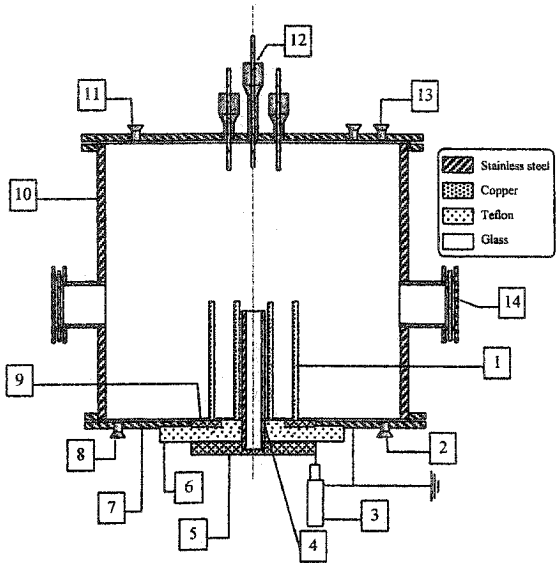


Fig.(1) Schematic diagram of the focus chamber

1- Outer electrode (8 rods)
2- Gas inlet
3- 30 coaxial cables
4- Inner electrode
5- Anode connecting plate
6- Teflon insulator
7- Bottom flange
8- Vacuum pump outlet
9- Cathode connecting flange
10- Focus chamber
11- Vacuum meter connection
12- Five diagnostics ports
13- Two extra gas inlets
14- Glass windows

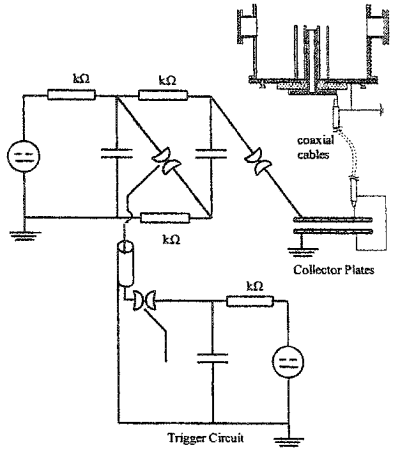


Fig. (2)

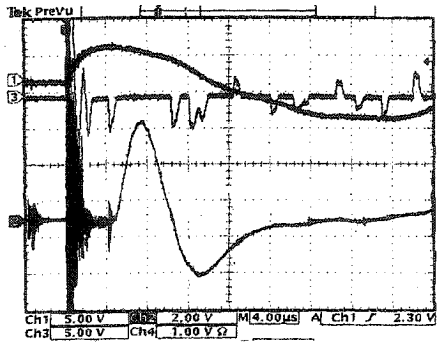


Fig.(3)

Upper trace: Discharge current
Middle trace: Axial magnetic field
Lower trace: Axial sheath current density

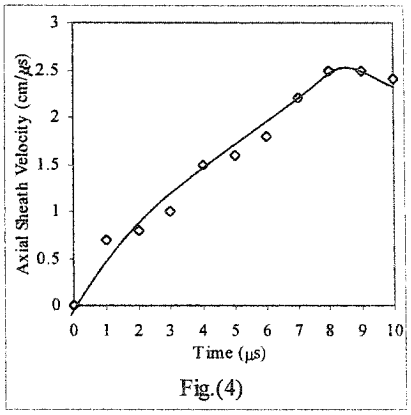


Fig.(4)

EFFECT OF APPLIED MAGNETIC FIELD VARIATION ON MICROWAVE RADIATION FROM COAXIAL DISCHARGES

T. Y. Allam
Plasma Physics and Nuclear Fusion Department, Nuclear Research Center, Atomic Energy Authority, Cairo, Egypt
tarekmyal@hotmail.com

ABSTRACT

Investigation of plasma dynamics inside the coaxial plasma gun systems for its use as a source of microwave radiation in gyrotron mode is of interest. A study of the effect of electrode configuration on the use of plasma guns as sources of microwave radiation in gyrotron mode had been made in prior work[1]. The introduction of a magnetization coil in the discharge circuit provides a strong axial magnetic field driving a rotational force, which in turn acts upon the coaxial accelerator current sheath and forces its gyration around the axis of discharge electrodes. As a result of the current sheath fast rotation inside the magnetic field, wave emission in the range of microwave frequencies is generated. This hypothesis had been investigated experimentally on a coaxial discharge chamber. Theoretical modeling describing this wave emission as a result of current sheath rotation around the axis and comparison of the model results with experimental results had been illustrated. In this work, a study is made on the effect of applied axial magnetic field strength variation on the emission of cm waves. Improvement of the previously designed analytical model describing the microwave emissions from such geometries to meet the desired specifications is necessary for development of this cheap source of microwave. The emission of microwave has a starting condition, which is markedly depending on sheath velocity of rotation around the axis of discharge. i.e. it depends on gas density and driving rotational Lorentz force.

Keywords: High-power Microwaves, Plasma Focus, Current Sheath Dynamics

INTRODUCTION

The field of high-power microwaves (HPM) has matured considerably in the last 30 years since the initial development of relativistic backward wave oscillators (BWOs) by researchers from the Institute of Applied Physics and the Lebedev Institute in Russia [2] and from Cornell University in the US [3,4]. Years of investigation have led to sharpening of the research focus, created a commercial supplier base, and generated international interest in the technology.

While earlier experiments have demonstrated very high power levels over a broad range of frequencies, users and the research community have fixed on several systems with very versatile features and relatively compact dimensions. Nevertheless, research continues on several other sources with attractive prospects. Looking into the future, the prospects for the near term appear to favor sources aimed at defense interests, with linear accelerators and ECRH plasma heating constituting additional technology drivers [5].

A simple and cheap design based on the modification of the well-known plasma gun experiment by simply introducing a magnetization coil into the discharge circuit is described here. The new design may be suitable as a laboratory cheap source for the generation of high-power microwaves. This paper is intended to describe the effect of changing the intensity of magnetic field

axial lines on the discharge circuit parameters and its contribution to the emission of microwave pulses.

EXPERIMENTAL SETUP

The plasma is produced by a capacitor bank of 195.8 μF. Discharge occurs between two coaxial electrodes with length 20 cm. The inner and the outer radii of the coaxial electrodes are 1.29 cm and 4.13 cm, respectively. The outer electrode is extended 40 cm to allow introduction of probes and diagnostics. For clean discharge, the inner surface of the insulator is covered with a 4mm-thick glass disk. To ensure the breakdown of the gas at the breech a stainless steel ring, of 5 cm diameter and 4 mm thickness, is welded to the inner electrode directly at the surface of the glass disk. The negative inner electrode is shorter in length than the outer electrode. Four orifices, each 0.6 cm in diameter, are drilled through the surface of the inner electrode and are equally distributed along a virtual circle drawn on the outer surface of the inner electrode directly in front of the stainless steel ring for gas inlet. Six small glass windows, each 1cm in diameter, are distributed on the surface of the outer electrode along a straight virtual line parallel to the cylinders' axis for optical observations. The inner electrode is sealed to ensure the flow of gas from the 4 orifices only. The end of the outer electrode is sealed with a Perspex flange for the fixation of the microwave detection assembly. The microwave horn is placed inside and on the axis of the discharge chamber facing the nozzle and 25 cm distant from the end of the inner electrode. An insulating sheet together with the Teflon rod is used to prevent charge carriers from reaching the microwave horn and affecting the detected signals while allowing waves to penetrate and reach the diode detector. Terminals of the diode detector are directly connected to the oscilloscope via a coaxial cable. Fig. 1 shows the experimental device.

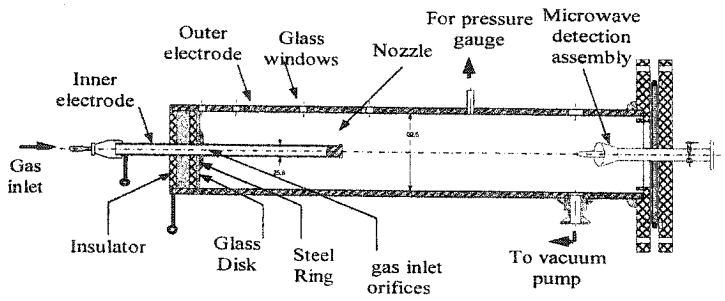


Fig. 1

The discharge takes place in Nitrogen gas with initial pressure of 0.7 Torr. The experiments are conducted with 2 kV maximum bank voltage. The magnetization coil arrangement consists of 9 sets of coils connected in series. Each set is formed of 8 turns of insulated copper wire of 6-mm diameter. The magnetization coil is wrapped around the outer electrode and distributed along the effective length of electrodes. The magnetization coil produces axial magnetic field lines with intensity reaching 8 kG. Measurements have been carried out using Rogowsky coil, magnetic probe and crystal diode detector for recording microwave emissions.

3. Experimental Results

Results obtained from measurements of discharge current and axial magnetic field shows that the introduction of the magnetization coil in the discharge circuit reduces the discharge current due to increase of total circuit impedance as shown in Fig. 2,3,4.

As the number of coils (each constituting 8 turns) is increased starting with 5 coils constituting 40 turns of magnetization coil up to 8 coils constituting 64 turns, the axial magnetic field intensity in the inter-electrode region increases almost linearly, as shown in Fig. 5.

For microwave detection, results show a continuous increase in the amplitude of the signals from the crystal diode detector. For case of 8 coils, microwave signal becomes very much reproducible and clear with a starting time depending on the charging voltage of capacitor bank so that no more than 1 kV charging voltage is needed to obtain a clear and sharp signal of microwave. Fig. 6 shows a typical microwave signal taken via the crystal detector at charging voltage of 1 kV in case of 8 coils constituting 64 turns of magnetization coil.

SUMMARY AND DISCUSSION

The plasma coaxial gun design is modified through the introduction of a magnetization coil in the discharge circuit which forces the current sheath to gyrate around the axial lines off magnetic flux producing microwave pulses. A study on the effect of magnetic field variation on the emissions of microwave has been made. Results maintained a good understanding of the effect of the axial magnetic field variation on the current sheath behaviour and results of detection of microwave signals show a continuous increase of microwave signal amplitude with increasing the number of turns of magnetization coil. Further development of this cheap source of microwave pulses requires a better understanding of the direct cause of these wave emissions.

REFERENCES

(1) T. Y. Allam, Ph.D. Thesis, Zagazig University, (2003).
(2) N. F. Kovalev, M. I. Petelin, M. D. Raizer, A. V. Smorgonskii, and L. E. Tsopp, ZhETF Pis. Red. 18, 232 (1973) [JETP Lett. 18, 138 (1973)].
(3) J. A. Nation, Appl. Phys. Lett. 17, 491 (1970).
(4) Y. Carmel, J. Ivers, R. E. Kribel, and J. Nation, Phys. Rev. Lett. 33, 1278 (1974).
(5) International Workshop on High Power Microwave Generation and Pulse Shortening -- Papers, Edinburgh International Conference Center, June 10-12, 1997, printed by the University of New Mexico and the Phillips Laboratory, Albuquerque, NM.

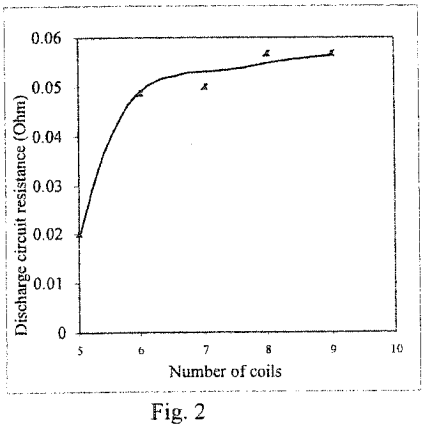


Fig. 2

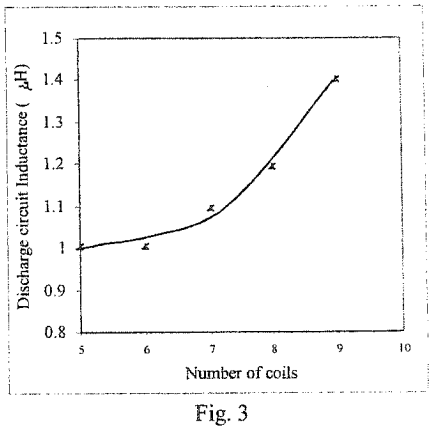


Fig. 3

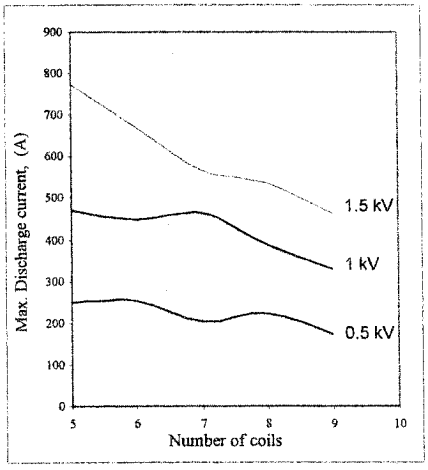


Fig. 4

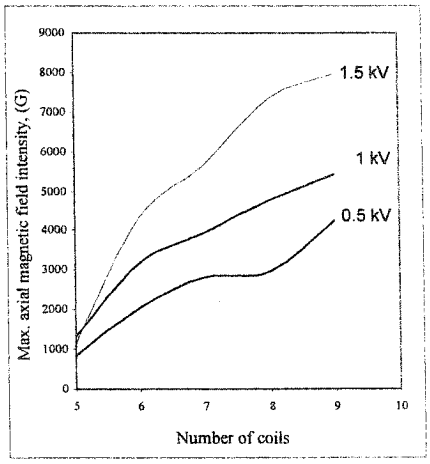


Fig. 5

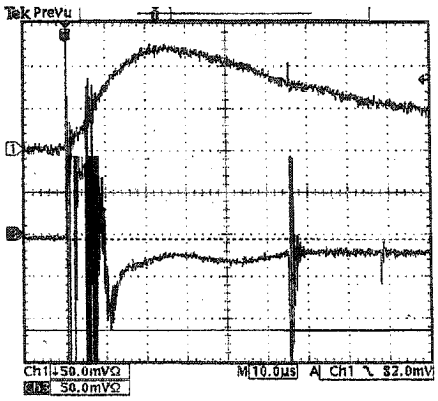


Fig. 6 : Upper trace: discharge current
Lower trace: microwave signal

Design Aspects of an Ion Injector

N. I. Bassal, M. S. Ragheb and S. G. Zakhary
Accelerators Dept., Nuclear Research Center, AEA, P. O. Box 13759, Cairo, Egypt

ABSTRACT

A study is made for the main factors that must be considered on the design of an ion injector. These factors are: the current intensity limits, plasma potential and beam emittance, The current intensity is limited by the beam perveance which depends on the geometry of the extraction system, the type of the ion species and beam aberration factor. We take into account the influence of the plasma potential in determining the actual beam energy. Study of the appropriate design of the Einzel lens is necessary in order to match the beam emittance with the accelerator acceptance. The study shows an optimal voltage ratio, which corresponds to the geometry of the lens. At this optimal voltage ratio the beam emittance at the output of the lens is minimum and the beam transport through the lens is without aberration and its intensity decreases with the increase of the atomic number of the ion species. The increase of the extraction voltage affects the increase of the extracted current and decreases the beam brightness which shows that an optimization is necessary to make a compromisation between the extracted current intensity and the beam brightness.

1-Accelerating Decelerating Extraction System

The accel./decel. extraction system is applied to avoid the compensation of the electrons being accelerated back into the source, thus destroying its rear side and leaving the ion beam uncompensated.. Also a shaped aperture[1,2] can decrease the beam aberration and beam emittance. as shown in Fig.2 To achieve zero normal component of the electric field, the cathode should have a suitable shape by forming Pierce electrode geometry. The zero equipotential occurs along a line passing through z = 0 and making an angle equal to 67.5° with the beam edge as shown in Fig.1.

2- Variation of the Beam Perveance with the Atomic Weight of the Gas Discharge:

The beam perveance is introduced in order to differentiate between the perveance of different beams particles and gases. Charged ion beams are usually drawn from a space charge ion source at zero initial velocity. The maximum beam current occurs when the electric field becomes zero at the plasma emitter surface. Let A be the distance coordinate between the two parallel plates, from Poisson equation:

$$\frac{d^2V}{ds^2} = -\frac{\rho}{\varepsilon_o} \qquad (1)$$

The maximum current density could be derived as:

$$J = \chi \frac{V_0^{3/2}}{A^2}$$

where $\chi = \frac{4\varepsilon_o}{9}\left(\frac{2e}{m}\right)^{1/2}$ is the perveance of the ion beam.Fig. 3 shows the calculated space charge perveance for electron, proton, deuteron, He^+, N^+ and Ar^+ ions. Where the microperveance is defined as: $1\mu P = 1\times10^{-6} A/V^{3/2}$.

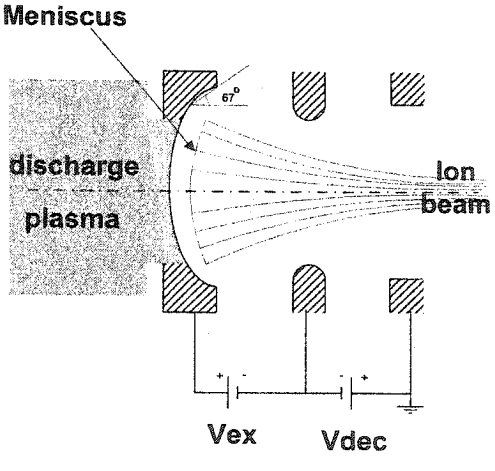


Fig.1 The basic features of the ion gun extractor system with the Einzel lens.

It shows the decrease of the beam perveance with the increase of the atomic number of the ion species. Keller[3,4] and others found that actually the transported ion current scale is: $I_{tr} = \chi \frac{S^2}{1+aS^2} V^{3/2}$ where a = aberration factor, χ perveance, S is the aspect ratio. The quoted study states a=3. For more refined two gap extraction system a=1.7 and $\alpha_o = 6 \times 10^{-8}$ A/V$^{3/2}$ gives best fit to the current values measured with α_o = 20 m.rad. Using these values one can conclude at once that the maximum normalized current to be obtained from one round aperture is obtained by the following equation:

$$I_{tr.n} = 7.03 \times 10^{-4} V^{3/2} \frac{S^2}{1+aS^2} \quad (\text{A/kV}^{3/2})$$

From which the influence of the aberration factor on the actual transported current could be shown as in Fig .4 .

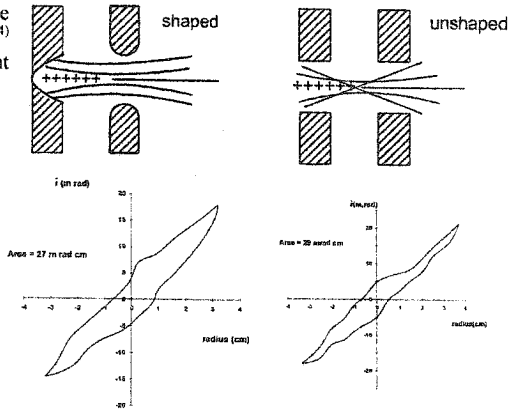


Fig.2The influence of aperture on shaping beam aberration (Thompson), Emittance diagram of (a) optimum shaped aperture ,(b) unshaped aperture.

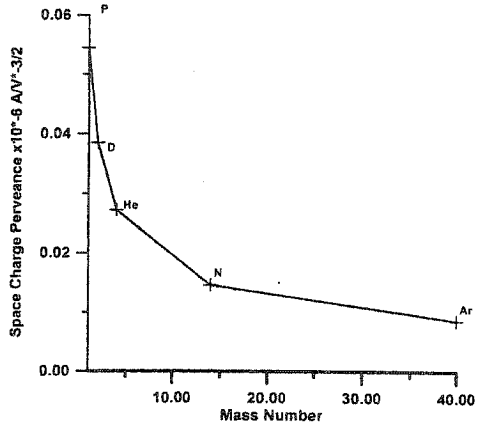


Fig. 3 Variation of the beam perveance with the atomic numer of the ion species

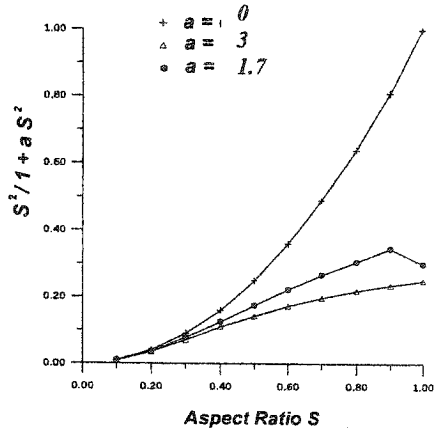


Fig.4 General shape of the actual extracted current considering the influence of the aberration factor with the aspect ratio.

4-Design Aspects of an Einzel Lens:

The use of an Einzel lens is necessary to match the output emittance characteristics of the ion source to the desired characteristics of an accelerating column. This transformation can be made without changing the input particle energy at the column entry.

In the beam transport system the operating regime is usually best represented by the paraxial ray equation with the space charge approximation. Each element of the transport system can be expressed by a transformation which relates the radius and the slope of the ion trajectories at the output to the input plan ends of these quantities. The paraxial ray equation for the axially symmetric electrostatic field can be written[5] as:

$$\frac{\partial^2 r}{\partial z^2} + \frac{V_o'}{2V_o}\frac{\partial r}{\partial z} + \frac{V_o''}{4V_o} = -Q\frac{r}{4V_o\varepsilon_o} \qquad (1)$$

where V_o is the potential on the Z axis and the primes denotes the derivatives with respect to Z axis , Q represents the space charge density (which is assumed to be uniform over the beam cross section) and ε_o is the dielectric permitivity of the free space. The solution could be written in the form:

$$\begin{bmatrix} r_4 \\ \sqrt{V_2}\, r_4' \end{bmatrix} = M_{14} \begin{bmatrix} r_1 \\ \sqrt{V_1}\, r_1' \end{bmatrix}$$

where M_{14} for the Einzel lens is[6]:

$$M_{14} = \begin{bmatrix} \frac{16 - 6\sqrt{K} - 6/\sqrt{K}}{4} & \frac{2d}{1/\sqrt{K}+1} \cdot \frac{3-\sqrt{K}}{\sqrt{V_1}} \\ \frac{3}{8}\frac{V_1 - 1}{d} & \frac{16 - 6/\sqrt{K} - 6/\sqrt{K}}{4} \end{bmatrix}$$

Where $K = V_1 / V_2$.

Tracing the beam line through the lens as shown in Fig.5.The dotted line indicates beam crossover and beam aberration. Fig.6 shows the variation of the output beam radius with the acceleration ratio for different gap lengths (d=1.5, 2 cm). It is clear that the focusing effect without beam aberration is defined with voltage ratio k =0.2 up to 0.3. The negative portion of the curve indicates beam crossover which means that the beam suffers aberration with the related voltage ratio 0.05 up to 0.18 . The transverse beam emittance ε shown in Fig.7 is determined from the relation $\varepsilon = r\, r'$ where r and r' are beam radius at waist and its divergence. The general view of the figure indicates a minimum beam emittance with the use of the Einzel lens.

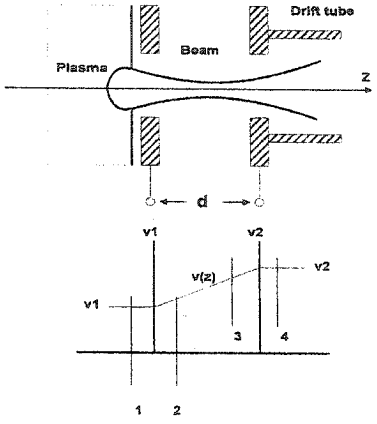


Fig. 5 Tracing the bean line through a double aperture lens.

5-Evaluation of the Current Intensity Capability of the Lens

By using a simple model of balancing the beam's space-charge force with the Einzel lens focusing force, is found to be[7]:

$$J = 2\chi \left(\frac{\delta V}{L}\right)\frac{1}{\sqrt{\phi}}$$

Where ϕ is the ion kinetic energy in volts, δV and L are the voltage difference and gap distance between the lens of the electrodes, respectively. Fig.8 shows the variation of the current density of the lens with the atomic number of the ion species. The current capability of the lens to be focused decreases with the increase of the atomic number of the gas discharge.

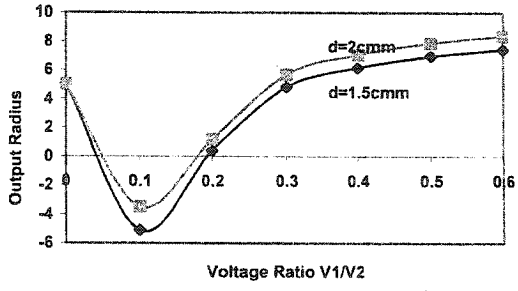


Fig.6 Variation of the output radius of the beam with the voltage ratio of the lens

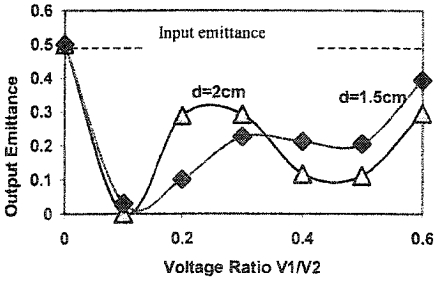


Fig.7 Variation of the transverse beam emittance with the voltage ratio of the lens.

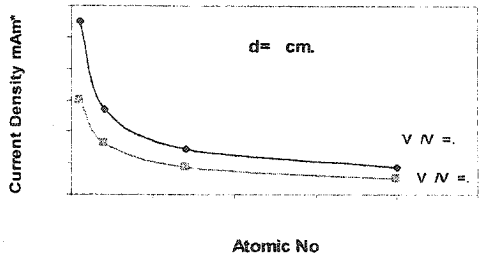


Fig. 8 Influence of the atomic number of the ion species on the current transported by the lens.

Fig.9 shows the current intensity for different ion species that increases with the increase of the electric field in the gaps of the lens.

6- Plasma Potential

Considering space charge effect, the Child-Langmuir law expresses the extraction ion current density as:

$$J_i = \frac{4}{9}\varepsilon_o \left(\frac{2e}{M}\right)^{1/2} \frac{V_o^{3/2}}{a^2} \qquad (2)$$

where V_o is the potential difference between the source and the extraction electrode, a is the distance from the plasma boundary to the extraction electrode, and ε_o is the dielectric constant of the vacuum. V_o is expressed as the summation of the plasma floating potential V_P and V_{ex} the potential difference between the cathode and the extraction electrode $V_0 = V_P + V_{ex}$. Also the ion current density J_i is expressed by the electron temperature T_e, ion mass M and electron density n_e as following[8]:

$$J_i = en_e \left(\frac{kT_e}{M}\right)^{1/2} \exp\left(-\frac{1}{2}\right) \qquad (3)$$

Where k is the Boltzmann's constant and e the absolute value of the electron charge. On the other hand, the electron current density J_e is dependent on the plasma floating potential V_p as

$$J_e = -en_e \left(\frac{kT_e}{2\pi\ m}\right)^{1/2} \exp\left(\frac{-eV_P}{kT_e}\right) \qquad (4)$$

where m is the electron mass. Since J_i+J_e equals zero in a state of equilibrium, the following equations are obtained:

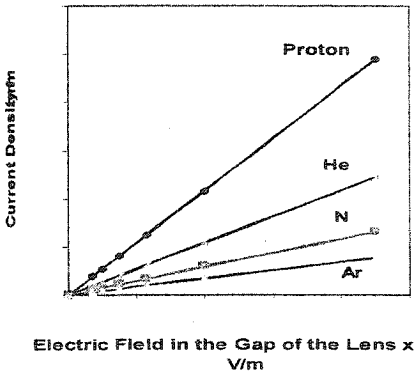


Fig. 9 Influence of the electric field in the gaps of the lens on the current transported by the lens.

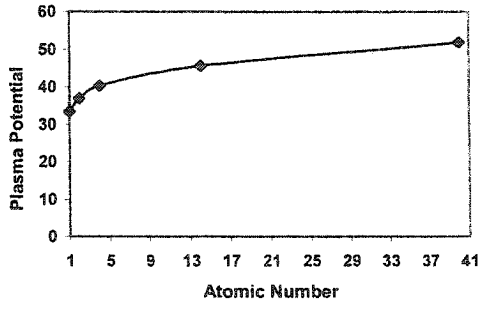


Fig.10 Influence of the atomic weight of the ion species on the plasma potential.

$$\therefore V_P = \frac{kT_e}{2e} \ln\left(\frac{A}{1.26x10^{-3}}\right) \qquad (5)$$

where A is the ion mass number. As a result one can conclude that the plasma floating potential V_P is proportional to the electron temperature T_e. Fig.10 shows the increase of the plasma potential with the atomic number of the ion species.

7- Optimization of the Ion Beam Characteristics (Intensity & Emittance) Produced from the Ion Source

To keep aberration as low as possible , the aspect ratio S (the ratio of aperture radius to the electrode distance)should be of the order. S = 0.5,With the breakdown limit in mind (d in mm,Vin kV); $d \geq 0.015\ V^{1/2}$, the extracted current is given by:

$$I_{Ch} = \frac{\pi}{9}\ \chi\ V^{3/2}$$

On the other hand the emittance ε can be estimated to first order by the aperture radius and a certain divergence angle of the beam if a waist is assumed at the exit of the extraction system; $\varepsilon = \alpha r_o$. As mentioned before the aperture radius depend on the extraction voltage with the aspect ratio; $\varepsilon = \alpha Sd$. Using the breakdown limit, the emittance can be estimated $\varepsilon = 2.37 \times 10^{-7} \alpha_o V^{1/2}$; the brightness is defined as $B = I / \varepsilon_x \varepsilon_y$. Plugging in numbers, we have[9]

$$B = \frac{1.24x10^{13} \varepsilon_o \sqrt{2q/m}}{\alpha_o^2 V^{3/2}} \qquad (6)$$

Fig. 11 shows the influence of the extraction voltage on both the beam current and beam brightness extracted from hydrogen discharge with assumed beam divergence α_o=20m.rad. It might be surprising that the current increases with the extraction voltage, whereas the brightness decreases with the extraction voltage. These dependences make clear why the optimization of extraction systems is necessary.

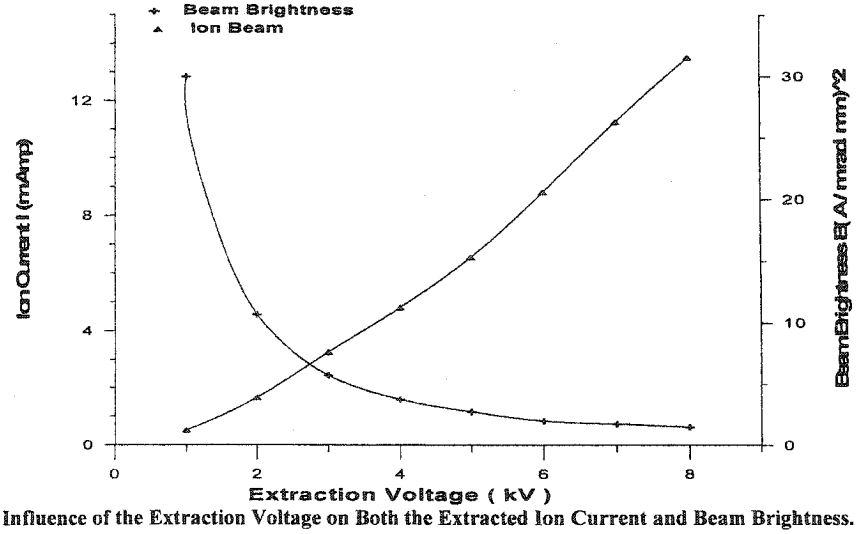


Fig. 11 Influence of the Extraction Voltage on Both the Extracted Ion Current and Beam Brightness.

CONCLUSION

Beside the geometry of the beam exit which includes aperture radius and gap distance between the extracting electrode and plasma surface , the source perveance depends on the type of the ion species and on the aberration factor. Minimization of the beam aberration necessitates shaping of the extracting electrode with Pierce shaping and avoid sharp edges of the extracting electrode. Also the gradient field inside the lens must be within certain limits in order to avoid beam crossover. Knowledge of the actual plasma potential helps the workers in the field of low energy <100eV to determine the exact applied beam energy. The increase of the extracting voltage affects the increase of the extracted ion current while it decreases the beam brightness and this necessitates the need to an optimization between both of them.

REFERENCES

(1) R.G. Wilson, G.R. Briewer "*Ion Beam Application to Ion Implantation*" John Wiley and Sons, New York (1973).
(2) E. Thompson, Proceedings of the 2nd Symposium on Ion Sources and of Ion Beams, Berkely, CA 11-3 (1974).
(3) R. Keller, American Institute of Physics, Conf. Proceedings 139 p. 1-15(1986).
(4) R. Keller, P. Spadtke, K. Hofmann, Springer Ser. Electrophys.11,Heidelberg, p.69 (1983).
(5) P.T. Kirstain, G.S. Kino and W.E. Waters, Space Charge Flow (Ma Graw-Hill, New York), (1967).
(6) K. Halabach, J.Amer. Phys.Vol.32, 90 (1964).
(7) J.W. Kwan, Rev of .Sci. Instrum., Vol.71 No 2, p. 807-809 (2000).
(8) N. Sakudo and K. Hyshi, Rev.Sci. Instrum 67 (3) 1218 (1996).
(9) P. Spadike, Rev. of Sci. Instrum.63 (4) 2647 (1992).

Phase Space Measurements at Non-Accessible Point on the Beam Path of an Accelerator Facility

A. Hassan
Accelerator and Ion Sources Dept., N.R.C., Atomic Energy Authority, Atomic Energy 13759 Cairo - Egypt.
E-mail: amein_hassan@hotmail.com

ABSTRACT

The optimization of beam lines for particles extracted from accelerator facilities requires the knowledge of beam parameters. A method for the measurement of phase space and beam intensity distribution is represented. This method depends on the setting of quadrupole lenses that allows the imaging of beam profiles at arbitrary positions along the beam path on the same multi-wire proportional chamber, where the intensity distribution can be evaluated. The necessary focusing powers for a certain imaging task are calculated in a thin lens approximation. The corresponding focusing power for thick quadrupole lenses are calculated using the PC transport program. A comparison of the calculated focusing powers for thin and thick lenses reveals deviations at the highest field strengths, due to saturation effect. The position of the beam waist in normal and angular space is directly calculated and visualized. The horizontal and vertical waist positions are found to be rather independent of the beam energy. Extensive calculation was done to study the effect of a reduced aperture on the maximum beam emittances $å_x$ and $å_y$ of the extracted particles. The main result shows that the maximum emittance passing through depends on the waist distant and the diameter of the reduced aperture.

INTRODUCTION

The beam in an accelerator facility starts in an ion source and goes through several intermediate stages prior to inject ions into the main accelerating structure. A set of optical elements is installed to hold the beam to the experimental target area forming the beam line. The economic way for particle beam transport is: the beam line is defined into individual sections, each has certain tasks. The first section is used to match the accelerated beam parameters to following sections. In the following sections the charged particle optics remains almost unchanged, i.e. the magnetic fields are scaled according to the particle momentum. The task in the last section is to adjust the beam parameters to the experiment requirements. Concisely, at both ends, the beam transport and adjustment have to take into account the actual beam properties on one side and the experiment requirements on the other.

PHASE SPACE OF THE BEAM

The beam line components which are often installed are drifts, bending magnets, quadrupoles, sextupoles, octupoles, solenoids, steering magnets and beam monitoring devices. For mono-energetic particles with corresponding trajectories in one transverse plane, the phase space is normally described by Twiss parameters method[1,2]. The Twiss parameters α, β, γ and beam emittance ε specify the beam phase ellipse at each position (fig.1.)

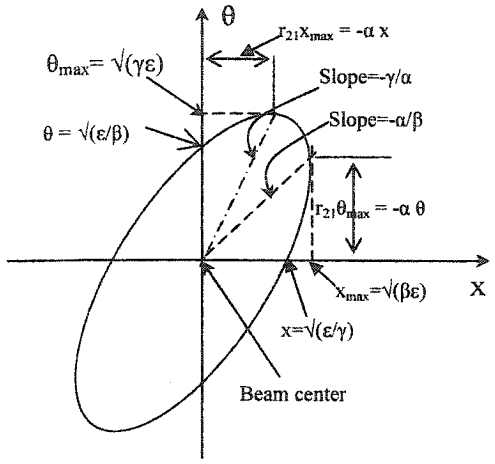


Fig. 1 A two dimensional beam phase space ellipse. The area of the ellipse A is given by: $A = \pi x_{max}\, \theta = \pi x\, \theta_{max}$, and the equation of the ellipse is: $\gamma x^2 + 2\,\alpha\, x\, \theta + \beta\theta^2 = \varepsilon$.

An equivalent but slightly different method is used here starting from the simple laws of imaging by a quadrupole lens which can be approximated by a thin lens. So it is often desirable to change the focusing in either the horizontal or the vertical direction independently. Furthermore by this method one gets additional and more detailed information on the intensity distribution in normal and angular space, and the possibility to cross check the results. We Assume that in the first section, two quadrupoles and steering magnets and beam monitoring are present.

Imaging method using thin lens approximation:

From light optics for a given distances g and b we have: $\frac{1}{g}+\frac{1}{b}=\frac{1}{f}$, where g, b are object G and image B distances in meter, Fig. 2a. Similarly in magnetic optics, $\frac{1}{g}+\frac{1}{b}=\frac{1}{f}=a\cdot\frac{I}{P}$, where I = quadrupole lens current [A], P = beam momentum [GeV/c]

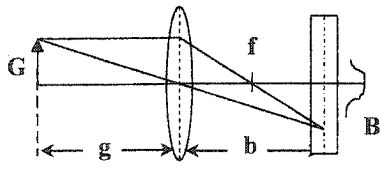


Fig 2a.

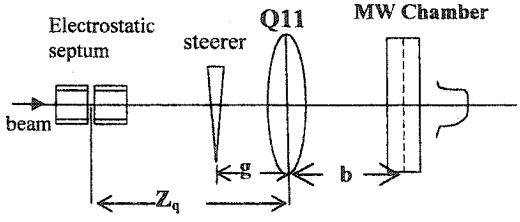


Fig. 2.b, $z = z_q - g$

and a is the calibration constant of the thin lens $[\frac{GeV/c}{m.A}]$. This calibration constant a, could be determined by imaging the steerer (thin dipole) magnet at the multi-wire chamber fig. 2b. The focal

length of the calibrated quadrupole is changed by setting the lens current I and the lens image extension at a well defined beam position z along the beam line:

$$z = z_q - g = z_q - \frac{1}{\frac{a.I}{p} - \frac{1}{b}}, \qquad (1)$$

Using the TRANSPORT notation the lens strength of a thick lens can be calculated by:

$$k_q \cdot \sin(k_q . L_{eff}) = a_q \cdot \frac{I}{P} \quad \text{, where } k_q = \sqrt{\frac{B_0}{r_l \cdot 33.356 \cdot P}} \; [m^{-1}], \quad (2) \quad \text{and}$$

r_l = radius of the lens aperture [m] , B_0 = magnetic field in [kG] at radius r_l , P = beam momentum [GeV/c], L_{eff} = the effective length of the lens and a_q = the calibration constant of the thick lens $[\frac{GeV/c}{m \cdot A}]$. With the transport at imaging condition of the steerer by the quadrupole in fig. 2b at the multi-wire chamber the magnetic field B_0 at r_l is calculated. Consequently using equation (2) k_q and a_q are determined.

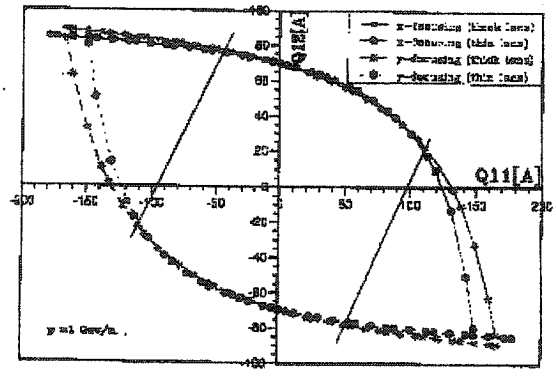


Fig. 3.

Extensive calculations have been done for imaging by thin and thick quadrupole lenses. The imaging of the thin steerer magnet at the multi wire chamber with two quadrupole lenses Q11 and Q12 (one quadrupole focuses in the x-plane and the other in the y-plane) has been obtained using the thin lens approximation Fig. 3. It shows that the thin lens approximation can be used with good accuracy along a wide range, except at higher current of the quadrupoles where the saturation of the magnetic field has to be taken into account. The imaging method is widely applicable at the COoler SYnchrotron COSY. The measurements of the beam extensions in the extraction region by the imaging method at three different momenta for the beam line of the time of flight spectrometer are shown in Fig. 4. Each point of these curves corresponds to one setting of the quadrupole with its separate beam profile on the Multi-wire chamber. The emittance is on the average 3 mm mrad, and the waist positions for the three different momenta is almost the same.

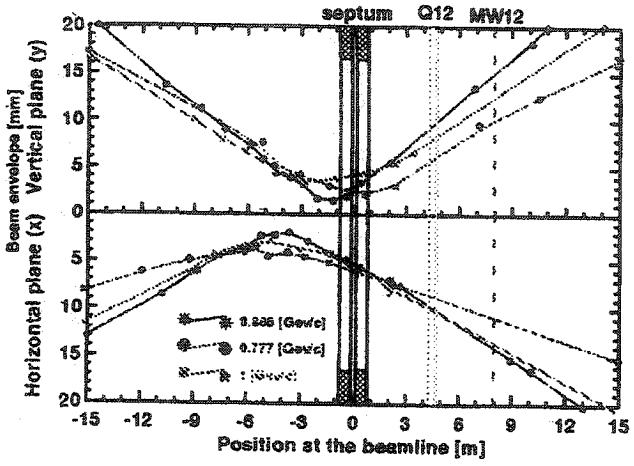


Fig. 4.

These curves in Fig. 4. also show the beam envelop along the z-axis, the beam extension in horizontal and vertical planes and the minimum beam radius or the waist positions.

MAXIMUM EMITTACE TRANSPORT THROUGH AN APERTURE

If there is a mechanical aperture of diameter R and $\mathbf{L_w}$ is the distance of the waist from the middle of the mechanical aperture to the imaging position (target). Assuming the waist in x- and y- planes place at the same position $\mathbf{Z_w}$, the radius x of the beam can be described as[3]:

$x^2 = x_w^2 + (Z - Z_w)^2 \cdot x_w'$, If $x = R$, $(Z - Z_w) = L_w$, and the beam emittance at the waist

$\varepsilon = x_w \cdot x_w'$, *then* $\varepsilon^2 = \dfrac{x_w^2 (x_w^2 - R^2)}{L_w^2}$, at maximum emittance ε , $\dfrac{d\varepsilon}{d x_w} = 0$;

This leads to the solutions: $x_w = \dfrac{R}{\sqrt{2}}$, and $x_w' = \dfrac{R}{\sqrt{2} \cdot L_w}$; This gives the emittance :

$\varepsilon_x = \varepsilon_y = \varepsilon_{max} = x_w \, x_w' = \dfrac{R^2}{2 L_w}$. The main result is that the beam extensions at the starting waist x_w and y_w are independently from the waist position. So experimentally it is listed to transport waist to waist on the target, one need to establish a waist position at a distance $2\,L_w$. This waist also can be imaged by the quadrupoles onto the target. Furthermore the maximum emittance that can be transported through an aperture of radius R is equal to $2R/L_w$, and the beam extension is limited to $R/\sqrt{2}$

REFERENCES

(1) Beam diagnostics: CERN Accelerator School, Aarhus, 1986, P. 99.
(2) Brown K. L. Nucl. Instr. & Methods 187 (1981) P. 51.
(3) TRANSPORT manual , Geneva, CERN 80-04 (1980).

Plasma Applications

Application of Dense Plasma Focus Device for Thin Film Deposition and Modification

R.S. Rawat[1], R.S.V. Joseph[1], W.L. Clarissa[1], L.Y Soh[1], P. Arun[2], A.G. Videshwar[2], W.M. Chew[1], V. Aggarwal[3], P.Lee[1] and S. Lee[4]

[1]*Natural Sciences, National Institute of Education, 1 Nanyang Walk, Singapore*
[2]*Department of Physics and Astrophysics, University of Delhi, Delhi, India*
[3]*Department of Metallurgical Engineering and Material Science, IIT Mumbai, India*
[4]*International Center for Dense Magnetized Plasma, Warsaw, Poland*
rsrawat@nie.edu.sg

ABSTRACT

The paper presents the details of application of dense plasma focus (DPF) device for thin film deposition and modification. The thin film deposition process is being understood by ion flux measurement using Faraday cup and by laser shadowgraphy study of post radial collapse phase. Desired stoichiometric changes on antimony telluride and stress and grain-size modification of cadmium iodide thin films have been achieved using energetic ions from DPF device. The successful deposition of thin films of TiN, TiC and sp^3 rich hydrogenated diamond like carbon (DLC) has been done using single shot DPF device. Recently we have also deposited nano-phase TiO_2 thin films using repetitive DPF device.

Key Words: Dense Plasma Focus, Thin Film Deposition and Processing, Film Characterization

INTRODUCTION

The dense plasma focus (DPF)[1] device is a coaxial plasma gun that uses a large electric current to heat and compress a gas to high temperatures (1-2 keV) and densities (10^{25-26} m^{-3}). Under such extreme conditions, the gas radiates copious ultraviolet, X-rays and particle beams such as relativistic electrons and ion beams. A compact plasma focus has been successfully used for electron microlithography[2] and soft X-ray lithography[3]. More recently, the energetic ions of the plasma focus device have been used for inducing a change of phase in thin films[4, 5] and for deposition of thin films[6, 7]. This paper presents the use DPF device for thin film deposition and modification at Plasma Radiation Source Lab at National Institute of Education in Singapore.

EXPERIMENTAL SETUP

Most of the thin film depositions and modifications have been done on a simple single shot, single-capacitor dense plasma focus device, designated as UNU/ICTP PFF. It is a 3.3 kJ Mather-type DPF device. Details of the device are provided elsewhere[1]. Conventionally, the electrode assembly of UNU/ICTP PFF uses a hollow copper anode which we also used for thin film processing with either argon or neon as the filling gas. For deposition of TiN and TiC thin films, the central hollow copper anode was changed to solid titanium. The working gas used was nitrogen for TiN film and argon-acetylene admixture for TiC thin films. The deposition of DLC thin films was done with the copper electrode top replaced by high purity graphite top. The charging voltage was always kept at 14 kV.
A low energy high performance high repetition rate plasma focus device, designated as NX2, was used for the deposition of TiO_2 thin film. The charging voltage was kept at 10.5 kV. The conventional copper-tungsten hollow anode of NX2 was replaced with a solid titanium anode and argon-oxygen mixture was used for the purpose of deposition of titanium oxide thin films. The device was operated at 0.2 Hz. The processed and deposited films were then characterized for their structure, surface

morphology, elemental distribution, optical properties, hardness and other properties by variety of techniques.

RESULTS AND DISCUSSIONS

It is important for us to understand the thin film modification or deposition process in DPF device. In low energy plasma focus devices, like that of ours, sausage instabilities (m=0) are seen to set in focused plasma column during radial collapse phase. This instability breaks the focused plasma column and accelerates the ions of filling gas species to very high energies (tens of keV to MeV) towards the top of the chamber and electrons to relativistic energies (100 keV and above) towards the anode. The high flux energetic ions of the filling gas species are the one that we use for processing/modification of thin films placed down the anode axis. Relativistic electrons cause the ablation of anode material. The ablated plasma, from the anode surface, has those ions required for the corresponding film formation. If the filling gas species is a reactive gas than the thin film can formed as a mixed phase of anode material and filling gas species like TiN (with Ti ions from the anode ablation and N ions from the filling gas) which is then deposited on substrate..

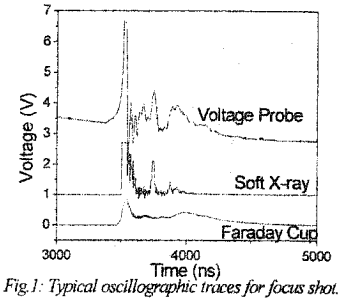


Fig.1: Typical oscillographic traces for focus shot.

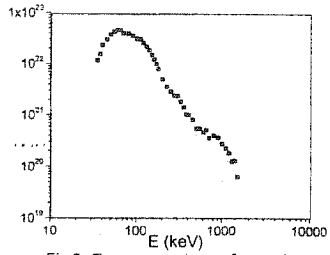


Fig.2: Energy spectrum of neon ions

Recently we used a Faraday cup, placed in a differentially pumped vacuum chamber, to measure the neon ion energy spectrum in DPF device. The typical oscilloscope traces are shown in Fig.1. The deduced ion energy spectrum of the filling gas species is shown in Fig.2. The neon ions were found to have energies in the range of 35 keV to about 1.5 MeV. The estimated ion flux for the ions in the entire energy range is about 9.6×10^{12} ions/stread.

A laser shadowgraphic setup consisting of an LN 203C N_2-dye (LD2S) (operated at 500 nm) is used to outline DLC thin films deposition process The first shadowgraph at t = 39 ns shows that the focused plasma column being just disintegrated and the ablation of the anode material can be seen to be just occurring at the center of the anode top. It is this ablated material that has the carbon ions required for the DLC film deposition. Fig. 3 shows the expansion of the ablated carbon plasma plume in the forward direction. The ablation continues for about 2 μs above the top of the anode. It may be noted that the ablation plume mainly expands from the center of the anode resulting in greater ablated ion energies and flux along the anode axis.

1. Thin Film Processing

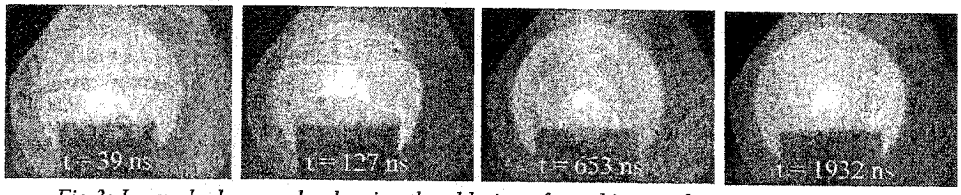


Fig.3: Laser shadowgraphs showing the ablation of graphite top during DLC deposition.

1.1 Modification of Antimony Telluride Thin Film

Thin films of Sb_2Te_3 were deposited on glass substrate at room temperature using resistive heating method at a vacuum greater than 10^{-6} Torr. The films were exposed at distances of 0.5 cm interval from 4.5 to 10.5 cm from the top of the anode. The chemical compositional analysis using XPS showed that exposure at shorter distances to higher energy argon ions broke the bonding of Sb_2Te_3 and promoted oxidation. The oxidation of tellurium however occurred at lower temperature and hence at

shorter distance of exposure the antimony-rich phase was created by decomposition of stoichiometric Sb_2Te_3. The ion energy decreases with increasing distance of exposure and so at higher distances the antimony-rich phase along with along with the free Te gave rise to single stoichiometric Sb_2Te_3 film. The XRD of the films also confirmed this preferred orientation of films. The full details of argon ion effects on Sb_2Te_3 film can be found in reference[8].

1.2 Cadmium Iodide Thin Film Processing

The as grown polycrystalline CdI_2 thin film, essentially with (002) orientation, were deposited by thermal evaporation method. The diffraction peaks of unexposed as grown film showed oriented growth parallel to (001) diffraction planes. At certain moderate irradiation distances the exposure was found to change the orientation to (110) plane as shown in Fig.4. The films exposed at 6, 7 and 8 cm became mainly (110) oriented and rest could still be treated as (001) oriented films. The XRD and SEM analysis confirms that the grain size increased linearly from about 1.5 to 4.8 μm with the increasing distance of exposure. The displacement of diffraction peaks, towards higher side, indicated uniform compressive stress which was found to increase with increasing irradiation distance. The estimation of grain size from SEM and residual stress from XRD showed a linear increase in grain size and residual stress with increasing irradiation distance (or decreasing ion energy) consistent with both structural and morphological observations.

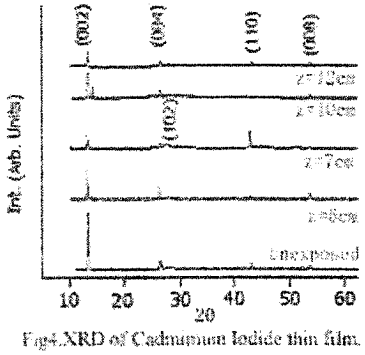


Fig4.XRD of Cadmium Iodide thin film.

2. Thin Film Deposition

2.1 Deposition of TiC Thin Films at Room Temperature Substrate

Thin films of titanium carbide (TiC) were deposited on 304-stainless steel substrates, at a distance of 11.5 cm, using different numbers of focus shots, like 10, 20 and 30, at room temperature substrates[9]. XRD patterns in all three cases were found to have diffraction peaks for (111), (200), (220), and (311) TiC crystalline planes. Surface morphological studies using SEM revealed increasing clustering of TiC grains with the increase in number of focus deposition shots. EDX spectra confirmed (shown in Fig.5) the presence of constituent elements with the gradual increase in TiK_α peak (of the TiC thin film) relative to FeK_α peak (of the substrate) with increasing numbers of focus deposition shots due to increasing film thickness.

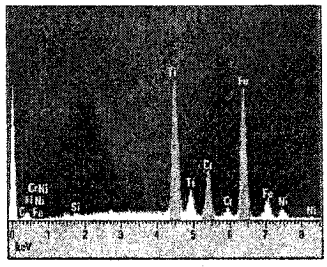
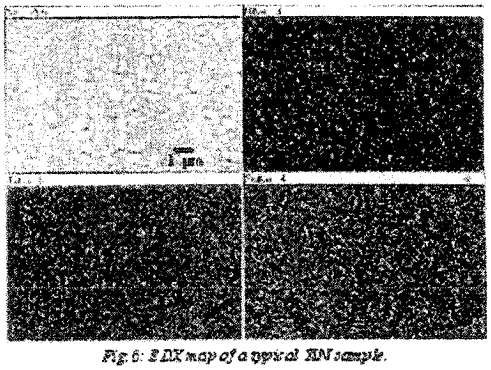


Fig.5: EDX of typical TiC film.

2.2 TiN Thin Film Deposition on Stainless-Steel Substrate


Fig.6: EDX map of a typical TiN sample.

Successful deposition of as grown polycrystalline TiN thin films onto stainless steel substrates was achieved at different distances from the top of anode and at different angular positions with respect to the anode axis and using different number of focus deposition shots[10]. In addition to TiN and substrate diffraction peaks, the diffraction patterns for films deposited along the anode axis showed the induction of a phase corresponding to Iron Chromium Nickel on the film-substrate interface. SEM pictures confirmed smooth film

surface with uniformly distributed TiN grains. EDX mapping (shown in Fig.6) confirmed the uniform distribution of TiN on the film surface.

2.3 TiO_2 Film Deposition

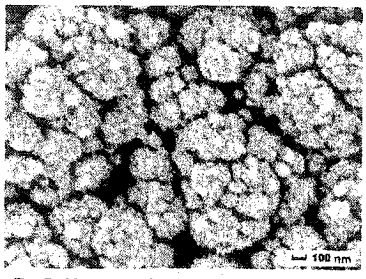


Fig.7: Nano-sized grains on titania film.

Thin films of titania (TiO_2) were deposited at room temperature onto silicon substrates using repetitive DPF device. XRD patterns showed that the as-deposited TiO_2 thin film was crystalline in anatase and rutile phase. The films were annealed for 1 h in air at 773. Annealing caused the onset of other anatase and rutile phase on thin films. Wide peak on XRD suggested the nano-phase titania thin film which was confirmed by SEM images. Grains with the sizes of 20-70 nm have been observed as shown in Fig.7. Raman results confirmed that deposited films consisted of anatase and rutile structure.

2.4 Deposition of DLC Thin Films

The thin films of DLC were deposited at a distance of 120 mm from the top of the anode and are deposited with different numbers of focus shots (5, 10, and 15), at neon filling gas pressure of 4.0 mbar. Raman results showed that films deposited at the outermost position have higher sp^3 content as compared with those deposited at the off-center position and the highest sp^3 content obtained is about 85%. Fig.8 shows the typical Raman spectra with G and D peaks. FTIR revealed that the deposited DLC films are hydrogenated. UV spectroscopy showed that the optical band gap energy of the deposited films ranges from 1.12 to 2.12 eV. XPS results indicated the presence of nitrogen, oxygen and silicon besides carbon. FSEM images that films deposited at the outermost are smoother than those deposited at the off-center position. Hardness of the deposited films obtained using the Nanoindenter and were found to be ranging from 3.2 to 13.6 GPa.

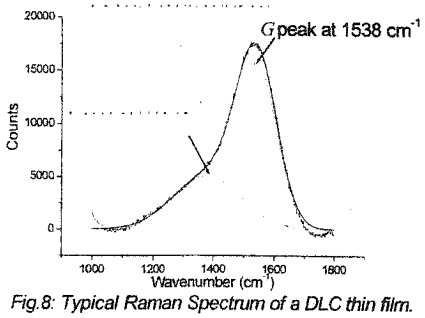


Fig.8: Typical Raman Spectrum of a DLC thin film.

CONCLUSION

The DPF is a simple pulsed plasma device that can be used effectively for thin film deposition and processing. Its potential in this field are enormous and should be explored further.

REFERENCES

(1) S. Lee, T.Y. Tou, S.P. Moo, M.A. Eissa, A.V. Gholap, K.H. Kwek, S. Mulyodrono, A.J. Smith, Surayadi, W. Usada, M. Zakaullah; Am. J. Phys.; 56, 62 (1988).

(2) P. Lee, X. Feng, G.X. Zhang, M.H. Liu, S. Lee; Plas. Sour. Sci. Tech.; 6, 343 (1997).

(3) S. Lee, P. Lee, G. Zhang, A. Serban, M. Liu, X. Feng, S.V Springham, C. Selvam, V. Kudryashov, T.K.S. Wong; Sing. J. Phys.; 14, 1 (1998).

(4) R.S. Rawat, M.P. Srivastava, S. Tandon, A. Mansingh; Phys. Rev. B; 47, 4858 (1993).

(5) Priti Agarwala, S. Annapoorni, M.P. Srivastava, R.S. Rawat, Pratima Chauhan; Phy. Lett. A; 231, 434 (1997).

(6) Chayya R. Kant, M.P. Srivastava, R.S. Rawat; Phys. Lett. A; 226, 212 (1997).

(7) Chayya R. Kant, M.P. Srivastava, R.S. Rawat; Phys. Lett. A; 239, 109 (1998).

(8) R.S. Rawat, P. Arun, A.G. Videshwar, Y.L. Lam, P. Lee, M.H. Liu, S. Lee, A.C.H. Huan; Mat. Res. Bull.; 35, 477 (2000).

(9) R.S. Rawat, P. Lee, T. White, Li Ling, S. Lee; Surf. Coat. Tech.; 138, 159 (2001).

(10) R.S. Rawat, W.M. Chew, P. Lee, T. White, S. Lee; Surf. Coat. Tech.; 173, 276 (2003).

Tailoring of Materials by Atomic Oxygen from ECR Plasma Source

Munzer Naddaf and S.V. Bhoraskar
Department of Physics, University of Pune, Pune-411007, India.
mnaddaf@aec.org.sy

ABSTRACT

Polyimide films have been exposed to atomic oxygen produced in Electron Cyclotron Resonance (ECR) plasma. A considerable improvement in the surface wettability after plasma exposure has been observed indicating improvement in the surface adhesion of plasma treated films. X-ray photoelectron studies showed that the atomic oxygen in the plasma is the main species affecting the surface chemistry and adhesion properties by producing highly cross-linked species and by producing of highly polar groups at the surface. The surface morphology changes were observed under an Atomic Force Microscope.

Key words: Atomic oxygen, ECR plasma, Polyimide.

INTRODUCTION

Atomic oxygen (AO) finds important applications in many areas of science, technology and industry. Atomic oxygen and its interaction with materials have a significant importance in space science and technology. Polyimides (PI) find extensive use in variety of applications in aerospace[1], and other industries[2]. Oxygen atoms of energies of 3-7 eV are the most common atmospheric species at altitudes between 150 km and 1700 km[3]. Polyimide is seen to get degraded at these altitudes. Tagawa et al[3], have studied the effect of AO generated by an ion beam type on PI films. They found that C-N bonding in PMDA was broken by AO attack. In our previous report[4], the density of atomic oxygen was measured and it was found to be of the order 10^{20} m^{-3}. The effect of AO in oxidizing the silver surface was also demonstrated. In the present work, the effect of AO produced by ECR oxygen plasma on some surface properties of polyimide (Kapton) films, has been investigated.

EXPERIMENTAL

The ECR plasma reactor used in the present work consisted of a cw magnetron (700W) with frequency of 2.45 GHz, and is described else where[4]. After evacuating the chamber to a base pressure of 10^{-6} Torr, thin films of PI of thickness of 40 μm were exposed to oxygen ECR plasma for different durations of time. The operating pressure during the plasma exposure was 8 x 10^{-3} Torr, which corresponds to ion energy of about 5 eV[4]. The contact angle formed by a drop of liquid (water) deposited on the surface of the sample was measured with the aid of a graduated eyepiece fitted into an optical goniometer. X-ray Photoelectron Spectroscopy (XPS) was used to study the changes in the chemistry of the surface due to plasma treatment. The surface morphology changes due to AO exposure was monitored by an Atomic Force Microscopy (AFM).

RESULTS AND DISCUSSIONS

Fig. 1 shows the variations in measured contact angles and the corresponding changes in the work of adhesion as a function of time of plasma exposure. The work of adhesion (energy of adhesion) is calculated using the following relation[5]:

$$W_A = \gamma_{lg}(1+\cos\theta) \quad (1)$$

where W_A is the work of adhesion, γ_{lg} is the surface tension corresponding to the liquid (l) – gas (g) interface and θ is the contact angle. $\gamma_{lg} = 72.8$ mJ/m^2 for water. The improvement in the surface wettability is also illustrated in the photograph in Fig.2 which shows the droplet of water on (a) surface of virgin PI, and (b) surface of PI exposed to oxygen plasma for 60 min. The reduction in the contact angle is seen clearly. The drop on the virgin PI film is semispherical whereas it has flattened after the plasma treatment of the PI film.

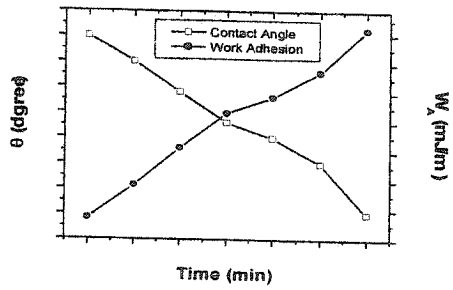


Fig. 1: Variation of contact angles (θ), and the work of adhesion (W_A) as a function of time of plasma exposure.

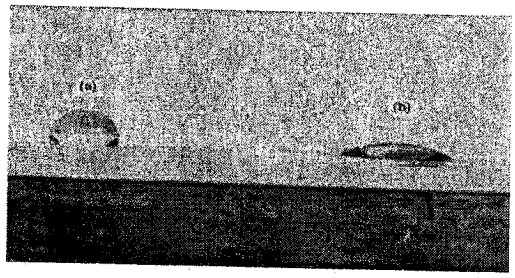


Fig.2: The droplet of water on (a) surface of virgin PI, and (b) surface of PI exposed to oxygen plasma for 60 min.

Fig. 3 (a), (b), (c), (d), (e) and (f) show the XPS spectra of Kapton films at angle of incidence of 25°. (a), (b) and (c) show the XPS spectra of C 1s, O 1s, and N 1s before exposure to oxygen plasma whereas (d), (e) and (f) show the spectra recorded after exposure (60 min) to the oxygen plasma. C 1s peaks positioned at 285.2 eV, 284.5 eV and 283.6 eV in virgin PI are assigned to C-C and C- H in benzene rings of PI molecule. These peaks show variations in their intensities and positions after the plasma treatment, which can be explained by modification of the imides structure and opening of benzene ring to form linear carbon-oxygen species. The peak at around 286.1 eV is assigned to the aromatic carbons bonded to oxygen. There is a reduction in its intensity by 36 %, after the plasma exposure. The peaks appear at 286.2 eV in virgin and 286.6, in the plasma treated PI respectively, are assigned to the imides carbonyls in the PI molecule. However, the peak at 288.6 eV in plasma treated PI could be associated not only with the carbonyl carbon but also with ester and acid groups[6].

It is seen from the XPS spectra of O 1s that the intensity of the peak at around 532 eV, which is assigned to (>C=O) is decreased and the intensity of the peaks: around 531, 533, which are assigned to peroxy C – O – C structure, and around 534.7 eV, which are assigned to polycarbonate OO>C=O, is increased, after plasma treatment. The >C = O structure is therefore changed into OO > C = O type structure after plasma treatment. These results can be interpreted as follows: the AO of the ECR plasma reacts with C-N bonds in PI, the weakest

bond in this polymer, and forms C – O – N bonding. Similar behavior has been observed[3] for PI exposed to the atomic oxygen during irradiation by a beam of OA of 5 eV.

N 1s for virgin PI film exhibited three peaks at 399.8 eV, 400.3 eV, and 401.8 eV, wherein the plasma treated PI film showed two peaks at 400.3 and 400.9 eV. The plasma treatment causes a significant reduction of the imidic nitrogen at 400.3 eV, whereas the peak around 401 eV, which is related to nitrogen-oxygen bonded species is seen to increase. The peak at 399.8 eV in virgin PI, which is assigned to >C=N- groups has disappeared after the exposure to the plasma.

Thus, the exposure of PI surface to the oxygen plasma leads to an increase in the polarity of the surface as a result of the interaction with AO. This is in good agreement with the increase in the wettability of the surface of PI observed after plasma treatment, since such polar species improve the hydrophilicity of the surface and enhance the wettability.

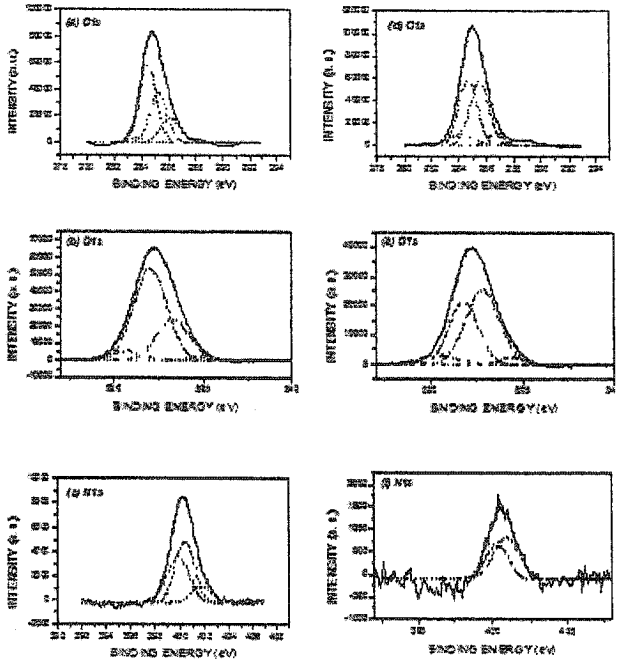


Fig. 3: XPS spectra of Kapton films of C 1s, O 1s, and N 1s, respectively: (a), (b) and (c) before exposure to oxygen plasma, and (d), (e) and (f) the spectra recorded after exposure (60 min) to the oxygen plasma. The angle of incidence is of 25°.

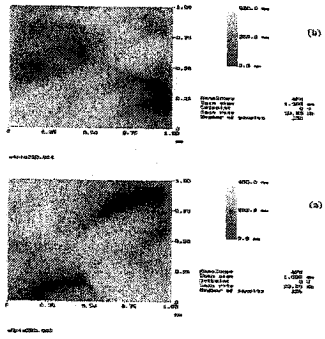


Fig. 4: AFM image for a) virgin PI film, b) PI exposed to AO for 60 min.

Fig. 4 shows the AFM image for a) virgin PI film, b) PI exposed to AO for 60 min. The root mean square (RMS) roughness is measured to be 15 nm for virgin PI films as compared to 18.6 nm for PI films exposed to the ECR plasma for 60 min. Hence the surface becomes slightly roughened after the plasma treatment. Therefore, the increase in the wettability of the PI films after the plasma exposure is attributed to mainly to effect of interaction of AO with the surface of PI and formation of the polar groups, which are characterized by their high hydrophilic properties as it is seen from the results of the XPS.

CONCLUSION

The effect of the atomic oxygen from ECR plasma on the surface properties of PI films has been investigated. It is shown from XPS studies and contact angle measurements that the AO in the plasma is the main species affecting the surface chemistry and wettability by producing of highly cross-linked species and highly polar groups at the surface.

ACKNOWLEDGMENT

SVB acknowledges the financial support from Department of Science and Technology India. M. Naddaf is thankful to the AEC of Syria for providing the study leave and fellowship.

REFERENCES

(1) D. Wilson, "Polyimides", eds. D. Wilson, H.D. Stenzenberger, and P.M. Hergenrother, Chapman and Hall, New York, p. 195, (1990).
(2) P.M. Hergenrother, "Polyimides", eds. D.Wilson, H.D. Stenzenberger, and P.M. Hergenrother, Chapman and Hall, New York, p. 178, (1990).
(3) M. Tagawa, M. Matsushita, M. Umeno, and N. Ohmae, "Proceedings of the Sixth Symposium on Materials in a Space Environment ESTEC ", Noordwijk, The Netherlands, p.165, 19-23 Sep., (1994).
(4) M. Naddaf, V.N. Bhoraskar, S.V. Bhoraskar, A.B. Mandale and S.R. Sainkar, Plasma Sources Sci. Technol. 11 (2002) 1-7.
(5) D.H. Kaelble and K.C. Wu, J. Adhes. 2, (1970) 50.
(6) D.T. Clark and H.R. Thomas, *J. Polym. Sci. Polym. Chem.* 16 (1978) 791.

Deposition of Different Thin Films Using Dense Plasma Focus

U. M. Rashed, A. H. Saudy, W. Sharkawy, M. A. Eissa
Phys. Department, Alazhar Univ. Faculty of Science, Cairo Egypt.
usamarahshed@yahoo.com

ABSTRACT

Thin films of different materials have been deposited on glass, silicon and metallic substrates using dense plasma focus device (DPF). The films are deposited using different numbers of focus shots. The deposited films have been studies using x-ray diffraction (XRD) and scanning electron microscope (SEM). Thin film thickness was measured using optical method.

Key Words; DPF, XRD, SEM, and TiN.

INTRODUCTION

The DPF device [1,2] is a simple device which generates a self magnetic field for compressing the plasma to high densities (10^{25}-10^{26} m^{-3}) and high temperatures (1-2keV). The DPF has been established as a source of highly energetic ions having energies in the range of 25keV to 8MeV [3,4], fusion neutrons, X-rays and relativestic electrons.

The preparation of carbon films has recently received a considerable attention due to the wide range of its applications. Thin amorphous carbon films are being used as an overcoat to protect the magnetic layers from the abrasive action of the reading head [5]. Crystalline highly conducting graphite films have a number of technological applications.

Vanes, turbine and various components in fuel conversion units, that are subjected to thermal fluctuations under normal operation conditions need protection from corrosion and high temperature degradation. This is usually performed by using a hard ceramic coating such as TiN. The aim of the present work is to use highly energetic ion and electron beam to deposit different thin films.

EXPERIMENTAL SETUP

The DPF used in this paper is a 3.3 kJ/15kV plasma focus device of Mather type. The condenser bank consists of a single Maxwell condenser bank of 30 μF capacitance , 27nH inductance, and maximum potential of about 15 kV. A simple parallel plate spark gap with a swinging cascade configuration was used as a high voltage switch. The gap was trigged via an isolating capacitor using HV SCR via a T.V transformer. The electrodes system consist of 16 cm long hollow copper tube of 1.9 cm diameter as anode (center electrode) surrounded by six 1cm thick copper rods of 16 cm long forming the cathode. An insulator sleeve of pyrex glass 3.2 cm in length is placed between the anode and the cathode. Argon and nitrogen plasma were used to prepare thin films.

In the present work, thin films have been deposited by two techniques. In the first technique, the argon ions were emitted preferably along the axis of anode taking a shape of fountain and spreading outward. A prespex box containing the target and the substrate holder was inserted by means of a brass rod from the top plate of the plasma chamber. A graphite target was stuck in the target holder such that it made an angle of 45^0 with respect to the anode axis. In the second technique, a cylindrical disc of the target was inserted in the anode tip and the substrate holder was incorporated inside the chamber by means of glass tube from the top plate of the chamber such that, facing the target and perpendicular to the axis of anode.

Analyzing of the thin films was performed using x-ray diffractometer (XRD) (PHILIPS analytical X-ray diffractionTypePW3710) and scanning electron microscope(SEM) (JSM-T20, JEOL, JAPAN).

RESULTS AND DISCUSSION

Carbon Thin Film

Carbon films were prepared using the two techniques which explained above. In each technique, films have been prepared by means of several shots. During each shot, the filling argon gas pressure and charging voltage of the capacitor were kept at 1 mbar and 13 kV respectively, which represent the condition of good focusing.

In the first technique, visual inspection of the deposited film shows that, the upper portion has a transparent uniform brownish thin film on the substrate and a lower portion having a grayish hazy patch due to the deposition of macro-particles[6].

XRD pattern of the carbon films shows no peaks on the glass substrate, this indicates that carbon may be present in an amorphous form in glass substrate.

Fig. (1A) shows SEM micro-graph of surface morphology of the carbon film deposited with 40 DPF shots at 1.3 cm distance of graphite target from the anode tip (the proper distance) [6]. This figure shows also the surface distribution of clusters having different shapes and sizes. The figure shows a number of destroyed cluster. This distortion is in conformity with the absence of the XRD peak.

On the other hand, carbon thin film was prepared using a second technique by means of a number of DPF shots and 7 cm distance from the target tip. Inspection of the films by naked eye shows a circular arched shape at the prefer portion of the glass substrate. It is of almost a uniform and a homogeneous distribution. This prefer portion contains a transparent brownish thin film. As directing to the central circular area, the grayish hazy patch due to deposition of macro-particles is appeared. This area has places of defects due to the ion beam sputtering of glass. In the central circular area of the substrate, the deposition is very weak and the ion beam sputtering of glass is mainly found.

Fig. (1B) shows SEM micro-graph of surface morphology of the carbon film deposited with 15 DPF shots at 7 cm distance from the graphite target tip. The micro-graph indicates that, the deposited carbon film has almost homogeneous structure and includes clusters of different shapes and sizes.

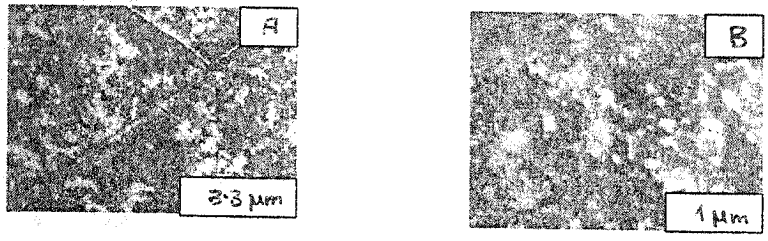


Figure (1) SEM micro-graph of surface morphology of the carbon film deposited with (A) 40 DPF shots on glass substrate at 1.3 cm distance of graphite target from the anode tip (first technique) and (B) 15 DPF shots on glass substrate at 7 cm substrate distance from graphite target. (second technique).

The carbon thin film thickness was measured using Michelson interferometer. The interference fringes produced by laser light (He-Ne laser 6328 A^0) reflected from the film surfaces and the substrate allows determination of the film thickness[7]. Figure (2) shows sample of the fringes system of carbon thin film deposited on glass substrate by 40 DPF shots. Fig. (3) shows the variation of carbon film thickness as a function of DPF shots. It was noticed that, the film thickness increases with increasing the number of shots due to the increasing of accumulated sputtered carbon atoms.

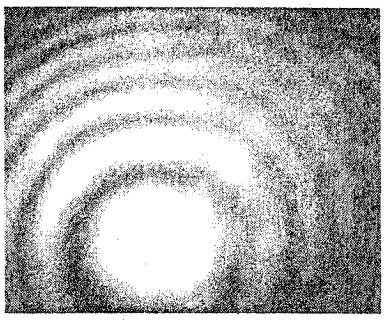


Figure (2) Sample of the fringes system carbon film deposited on glass substrate by 40 DPF shots.

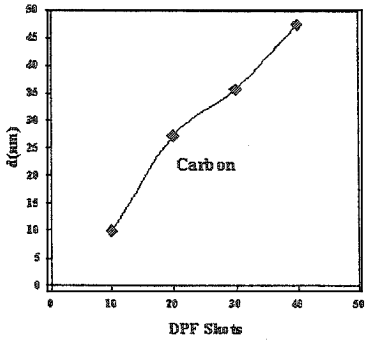
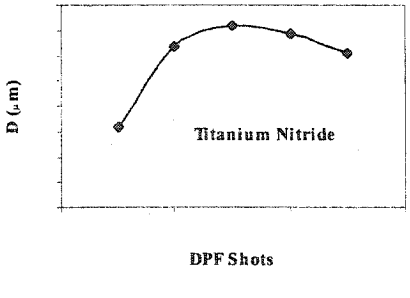


Figure (3) The variation of carbon of thickness as a function of DPF shots.

Titanium Nitride (TiN) Thin Film

A hard ceramic film of TiN was prepared using the second technique. Ti target was inserted into anode tip such that covering the rim of anode and the substrate holder was incorporated in the vacuum chamber facing Ti insertion. The stainless steel (AISI 304) substrates is a typically 3 cm length and 3 mm thick. These substrates were mechanically polished with SiC paper and cleaned before mounting in the holder. The plasma focus device was operated on a good focusing condition of Nitrogen gas (13 kV, 2 mbar gas pressure) and TiN was deposited on stainless steal substrate by means of a number of shots. In each shot N_2 ions and evaporated Ti were ejected in the forward direction toward the substrate to form a hard ceramic of TiN coat.

The coated TiN films thickness was measured using coating thickness gauge 6000-N4. Fig. (4) shows the variation of TiN film thickness with the number of shots. The figure indicates an increase in film thickness with the number of shots until 15 shots then, it weakly decreases. This decrease can be attributed to the balance between the rate of film build up and film removals due to the impact of the substrate surface by high energetic nitrogen ions.



Figure(4) The TiN film thickness as a function of DPF shots.

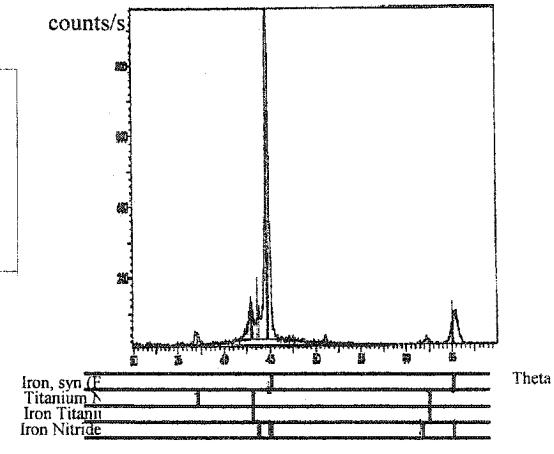
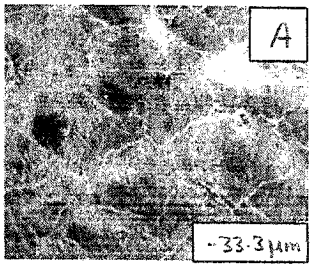
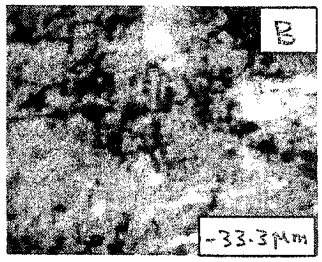


Figure (5) XRD pattern of coated TiO on AISI 304 stainless steel substrate prepared by 15 DPF shots.

The coated films was studied using XRD. Fig. (5) shows XRD pattern of coated TiN on stainless steel substrate. The figure shows peaks at 2θ equal 44.7^0 and 65^0 corresponding to Fe phase and three small peaks at 37.1^0, 46.1^0 and 62.4^0 corresponding to TiN . There are also peaks at 43^0 and 62.2^0 corresponding to FeTi.

The coated films were also studied using SEM. Fig. (6 A,B) shows the surface morphology of the stainless steel substrate before and after the deposition of TiN film respectively. Figure (6A) shows different sizes of stainless steel grains. The grain boundary appears very clearly in this figure. Fig. (6B) shows a successive layer of coated material on stainless substrate. In some regions, the grains of stainless steel appear but in a smaller sizes. This is due to the impinging N_2 ion beams of high energy to the substrate. This leads to increase the number of grain boundaries and consequently increase the ability of coat material and particles to diffuse interior the stainless steel substrate.





REFERENCES

(1) J. W. Mather, Phys. Fluids vol. 7, P. 5, 1964.
(2) S. Lee, T. Y. Tou, S.P. Moo, M. A. Eissa, A. V. Gholap, K. H. Kwka, S. Mulyodrono, A. J. Smith, Suryadi, W. Usada, and M. Zakaullah, J. phys., vol. 56, P. 62, 1988.
(3) R. L. Gullickson, and H. L. Sahlin, J. Appl. Phys., vol. 49, P. 1099, 1978.
(4) G. Gerdin, W. Stygar, and F. Veenneri, I, J. Appl. Phys., vol. 52, P. 3269, 1981.
(5) V. Raman, and K. R. Coffey, Appl. Phys. Lett., vol. 59, p. 25, (1991).
(6) R. K. Chhaya, M. P. Srivastava, and R. S. Rawat, Phys. Letters, A vol. 226, p.p. 212-216 (1997).
(7) L. Frank, L. Pedrotti, J. Leno and S. Pedrotti, "Introduction to Optics", Prentice-Hall Inc., 3269, (1987).

Carbonitriding of ASS by ICRF Discharge

M. A. Eissa, A.M. Nossair*, F.F. Elakshar, F.M. El-Hossary, and A.M. El Halafawy*****

Alazhar Univ., Science Fac , Physics Dept , Nasr City, Cairo, Egypt.

**Alazhar Univ., Science Fac., Physics Dept (Assuit branch), Assuit,Egypt.*

***South Valley Univ ., Science Fac , Physics Dept. Sohage, Egypt.*

****Central Lab of Quality Testing, GOEIT, Cairo Airport, Cairo, Egypt.*

mahmoudeisa@hotmail.com

Abstract

Carbonitriding of austenitic stainless steel (ASS) samples was carried out using inductive coupled radio frequency (ICRF) discharge system. The effects of plasma gases pressure on the crystal structure, surface hardness, surface, and profile morphologies of the treated samples were studied. The obtained results show that, the surface hardness value of the untreated sample increases from 220 Kg/mm^2 to 1070 Kg/mm^2 for the treated sample at 75 mtorr. X-ray diffraction was used to identify the carbonitriding phases formed in the sample surface. Optical microscope was used to study the change of the surface morphology of the treated samples and to determine the thickness of the treated layers. The thickness of the carbonitrided layer was in the range of 20 μm.

Key Words: Plasma Carbonitriding, ASS Treatment, ICRF Discharge, Microhardness, Phase structure

INTRODUCTION

Austenitic grades of stainless steels are widely used in the chemical and food industries[1,2]. These materials exhibit excellent resistance and resist oxidation at high temperatures, but their relatively low wear resistance and hardness is an impediment to their more widespread use. Consequently, several nitriding and carbonitriding techniques have been used to overcome these impediments by improving the surface hardness[3]. Among the different variants of the plasma processing, RF nitriding has also shown to enhance hardness[4]. The mechanism of carbonitriding using plasma-based methods has been explained in contradictory way. Ionic bombardment, neutral atomic and molecular absorption are the main models that have been explained for plasma nitriding mechanism[5]. The interpretation is based on a new approach that the microcracks in the surface, at a certain ambient temperature and plasma, can create traps for the active nitrogen species. The nitrogen concentration and temperature gradient can also drew some of the nitrogen species towards the bulk side. The microhardness can be explained in terms of the high concentration of nitrided phases created under the surface of the treated sample[6]. The carbonitrides also have superior anti-corrosion, anti-wear, and anti-scuffing properties and are commonly used for improvements in surface mechanical and chemical properties[7]. The increasing use of thermochemically-assisted carbonitriding technology is largely due to the fact that these processes are environmentally friendly. Typically, components such as gears, crankshafts dies, bearing, ...etc, are often carbonitrided[2].

In this paper the inductive coupled radio frequency (ICRF) plasma was used for carbonitriding (CN) the surface of austenitic stainless steel (304 ASS) samples at different gas pressures.

EXPERIMENTAL SETUP AND MEASUREMENTS

304 ASS samples are 1 mm thick rolled sheet, cut into pieces with small dimensions of order 1 cm x 2 cm. The carbonitriding processes of ASS were done using radio frequency (RF) inductively coupled glow discharge; with continuous mode of operation at 13.56 MHz. The system comprises a quartz tube with 500 mm in length and 41.5 mm in diameter evacuated by a two stage rotary pump to a base pressure of 10^{-2} torr. Figure (1) shows schematic diagram of (ICRF) discharge system. The ASS samples were treated using 50% nitrogen plus 50% acetylene and the total gases pressure was varied from 40 to 60 mtorr. The input plasma power was fixed at 450 watt for plasma processing time 10 min. An induction copper coil energized by Rf power generator type RF20, 13.65 MHz and 2.5 KW via a tunable matching network, generated the discharge. An inserted thermocouple probe close to the samples was devoted to measure the sample temperature. After treating process, samples were allowed to cool slowly in the evacuated reactor plasma tube. X-ray diffraction analyses of the carbonitrided surface were diagnosed using a Siemens model diffractometer unit. Vickers microhardness measurements were made perpendicular to the treated surface, using an E. Ltd Wetzlar microhardness tester at contact load 100 gm. Metallographic studies were performed using optical microscopy (OM).

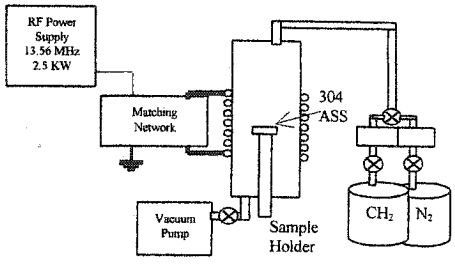


Fig. (1) Schematic diagram of the discharge cell

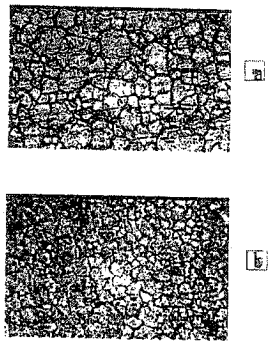


Fig. (2) Optical micrographs for the surface of an ASS sample (a) before and (b) after treatment by ICRF plasma

Fig. 2 (a,b) shows the optical micrographs for the surface of an ASS sample before and after treatment by ICRF discharge. The cross-section micrographs of the treated samples at 45 and 51 mtorr are shown in Fig. 3 (a,b). Examination of this Figure reveals that the formation of distinct homogenous carbonitried layers. From Fig (3) one can measure the thickness of the compound layers to be 10 μm and 15 μm for samples treated at 51 mtorr and 45 mtorr respectively.

In order to clarify the influence of RF plasma processing on the mechanical properties of carbonitrided samples, microhardness measurements of ASS and CNASS samples have been performed. The microhardness of ASS 304 sample has been found to be 220 Kg/mm^2. Table (1) shows the microhardness values of the treated samples at 450 W for plasma processing time equal 10 min versus the gas pressure. One can see that the microhardness value of the ASS sample is increased by a factor of 3.5 - 5 fold by exposing it to the RF plasma.

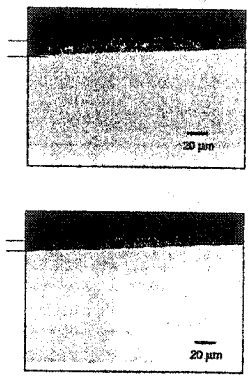


Table (1) The microhardness values versus gas pressure

Gas pressure (mtorr)	Microhardness (Kg/mm^2)
45	1020
52	1015
57	900
60	770
66	950
75	1070

Fig. (3) Optical micrographs of CNASS samples
treated at 450 watt. 10 min., for different pressures

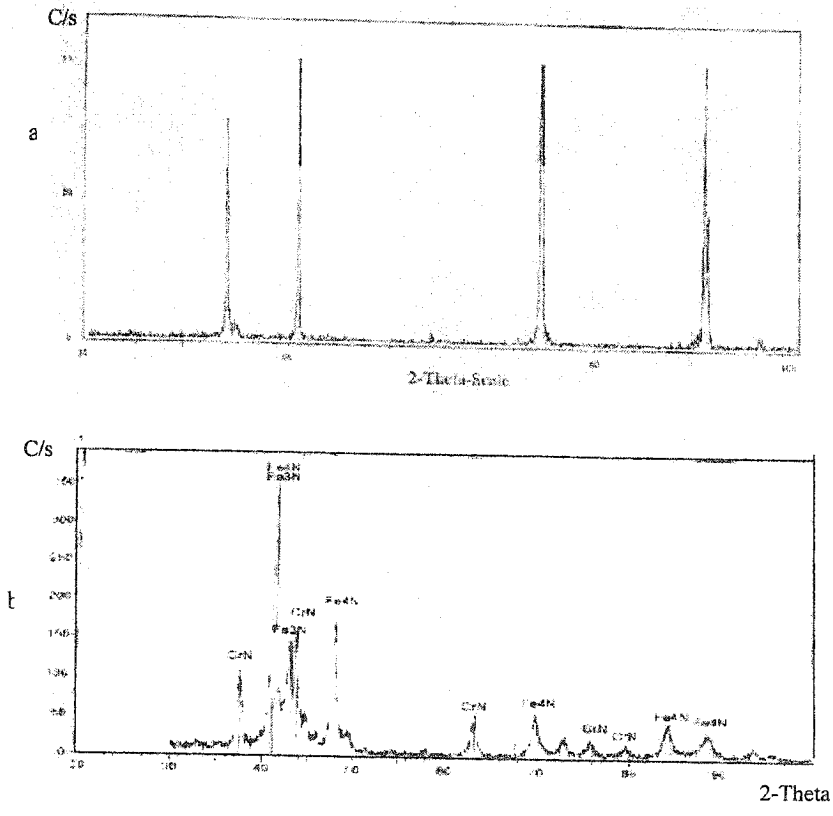


Fig. (4a,b) XRD spectra of ASS and CNASS samples treated by ICRF discharge

X-ray diffraction spectra of the untreated and treated sample are shown in Fig. 4(a,b). The most intense peaks for ASS sample characterise the austenite phase, while for the CNASS sample, the most intense peaks are corresponding to Fe_4N, Fe, C, FeC, and CrN. The existence of chromium nitride (CrN) precipitation at the grain boundaries might be interpreting the high values of hardness for the carbonitrided layers[8].

The surface morphology of original (ASS) is characterized by large non-uniform grains with thin boundaries. These grains are randomly packed, forming a porous microstructure and the link between the grains is weak. On the other hand the surface morphologies of (CNASS) samples have small grains and the boundaries are very thin.

DISCUSSION AND CONCLUSION

The high hardness of the CNASS shown in table (1) might be reveal to the high concentration of nitrogen in the compound layer. Moreover, the CrN precipitation near the grain boundaries and the smaller grain sizes after carbonitriding process could be another reasons[8]. Achieving compound layer of thickness 15 μm in 10 min means that the carbonitriding rate is high with respect to previous work published elsewhere[9]. To understand this high carbonitriding rate value, we have adapted the formed microcracks mechanism[10]. At certain temperature, depending on the treated material, and with high concentration and high energy of nitrogen and carbon species, the possibility for surface microcraks and high penetration of nitrogen and carbon species in the native material is high. The penetration nitrogen and carbon diffuses into native material through the sample surface (mainly through grain boundaries) and the wall of the formed microcraks, in which the interface between them is large enough for fast carbonitriding process due to concentration gradient.

REFERENCES

(1) Zanng Z.L. and Bell T., Surf. Eng. 1, 131 (1985).
(2) Staines A.M., Heat Treat. Metal. 17, 85 (1990).
(3) Baldwin M.J., Kumar S., Priest M.J., Fewell M.P., Prince K.E., and Short K.T., Thin solid Films 345, 108 (1999).
(4) Baldwin M.J., Fewell M.P., and Haydon S.C., Surf. Coat. Technol. 98, 1187 (1998).
(5) Parascandola S., Gunzel R., Grotzschel R., and Moller W., Nucl. Instrum. Meth. Phys. Res. B 136, 1281 (1998).
(6) El-Hossary F., Negm N.Z., Khalil S.M., and Abd Elrahman A.M., Thin Solid Films 405, 179 (2002).
(7) Borges C.F. M., Henneck S., and Pfender E., Surf. Coat. Technol. 123, 112 (2000).
(8) Metals Handbook, Vol. 13, Corrosion, 551 (1987), Metals Park, OH,ASM.
(9) Priest, J.M., Baldwin, M.J., Fewell, V, Haydon, V, Collins, V, Short, V, and Tendys, J., Thin Solid Films 113, 345 (1999).
(10) El-Hossary, F.M., Surf. Coat. Technol. 177, 150 (2002).

Characteristics of Plasma Etching Associated with a Multihollow Cathode Glow Discharge

Ahmad R. Galaly[3], M. Atta Khedr[1], F.F. El-Aksher[2], and Y. Badr[1]
1) National Institute of Laser Enhanced Sciences, Cairo University, Giza
2) Physics Dept., Faculty of Sciences, Azhar University, Nasr City, Cairo
3) Physics Dept., Faculty of Science, Cairo University Beniswaif, Beni Swaiv

ABSTRACT

The properties of a plasma producing cathode etching have been studied using different techniques such as single probe, double probe, and a Faraday cup. The plasma was produced employing a RF source and a mesh cathode, and its general properties such as electron temperature, ion temperature, plasma density, floating potential, ion velocity distribution function, and electron energy distribution function have been investigated using these techniques. In order to measure localized plasma parameters, Langmuir probes (single and double) were used. Plasma parameters in the discharge region above the mesh cathode such as the electron temperature, electron density, and the electron energy distribution (EEDF) have been determined. The electron density increased by increasing the gas pressure while the electron temperature decreased. We placed a grid (mesh) in the CCP (Capacitive Coupled Plasma) to control the plasma parameters in the region above the mesh and investigated plasma parameter variation as function of the mixing ratio in an Ar/O_2 plasma.

INTRODUCTION

Capacitively coupled plasmas have been widely used for silicon dioxide (SiO_2) etching. However, for high anisotropic and fast etching, other sources which have high density at low pressure are necessary. There has been much research on high density sources excited by electron cyclotron resonance[1,2], helicon waves[3-5], and inductively coupled plasmas (ICP)[6]. ICP has attracted interest due to its simple structure and the absence of a magnetic field. A few researchers have carried out SiO_2 etching in an ICP. However, most of them have reported that using ICP for etching introduces some problems, such as low etching selectivity, local side etching and charge build up damage. Plasma parameter variation as a function of mixing ratio in an electron temperature control system using a grid was investigated by Bai et al.[1]. Underneath the grid, the electron temperature as well as the electron density are a strong function of the mixing ratio. The electron temperature decreases with the admixture of molecular gases (O_2 and CF_4), and the large inelastic cross section for electrons in the molecular gas is the reason for this.

In the present experiment two kinds of dry etching (mainly physical etching, like e.g. sputtering), ion etching and ion chemical etching were used. In the simplest case, chemically active oxygen is added to the inert gas (argon) to change the etching rate and to provide a high selectivity of the etching. Moreover in chemical etching we have two sources of reactions, surface reactions and plasma reactions.

EXPERIMENTAL SETUP

The discharge system consists of two parallel, plane and circular electrodes enclosed in a vacuum vessel of cylindrical shape which has been evacuated and filled with the working gas (Ar) at continuous flow. The chamber was made of stainless steel and has a volume of approximately 5×10^4 cm^3. The chamber has several ports used for pumping, pressure gauges, gas inlet, movable single and

double probe, holder for a Faraday cup probe, and the input of two electrodes (anode and cathode); the anode was made of copper and has a diameter of 4.5 cm while the cathode was made of aluminum mesh and has the same diameter as the anode. The system of the two electrodes was able to move 360^0 to be compatible with radial and axial measurements. The cathode material can be changed according to the experimental requirements. The separation of the electrodes is 3 mm. An insulated material was placed around cathode and anode to provide a sheath around the two electrodes and to confine the plasma in the cathode-anode region, in addition to strengthen the plasma over the cathode mesh. When a voltage V_a was applied to the electrodes and the vacuum vessel was filled with the used gas, at a certain pressure the discharge took place and a glow discharge formed which we could be observed through quartz windows. A schematic diagram of the electrical circuit of the discharge system is shown in Fig. (1). The power supply was capable of delivering an output current up to 500 mA at a maximum output voltage of a several kV, with the cathode grounded. A single cylindrical probe of 1 mm diameter and a length of 3 mm, made of titanium, was used. The electrical circuit used for the single probe[6] consists of a DC-power supply, 10 turns potentiometer (50 kΩ), a load resistor (R_p=1 kΩ), and a 10 μF capacitor. This capacitor was placed in parallel with the measuring resistor R_p to filter out noise. The double probe consists of two identical cylindrical electrodes. Each electrode is 8 mm long and 1 mm in diameter and is made of titanium wire. The distance between the two electrode centers was about 3 mm. This separation was large enough to avoid interference of the sheaths around each electrode[6]; the sheath thickness is given by the Debye length λ_D which is

$$\lambda_D = 740\ (kT/n)^{1/2}\ \text{cm}, \quad kT \text{ in eV}$$

For a temperature of 10 eV and a density of 9×10^9 cm^{-3}, the Debye length equals 0.025 cm, and hence the distance between the two electrodes is larger than twice the Debye length. The two electrodes were placed normal to the formed plasma so that the plasma arrived at both at the same instant. The double probe electrical circuit consists of a DC power supply, a 10 turns potentiometer (50 kΩ) to allow accurate measurements of the I-V characteristic curve, and a load resistor of 1kΩ. The I-V characteristic curve was obtained by varying the probe bias from +100 to –100 V between the two probes by using a potentiometer. The Faraday cup probe was used to measure the velocity distribution function of the plasma observed above the mesh (intense glow cylinder zone); we place the Faraday cup probe facing the mesh at a distance of 4.5 cm from the mesh and 4.3 cm from the anode, at their axial axis. The Faraday cup probe consists of a cup made of brass 1.5 cm in diameter and 1 cm long. It was connected to the negative terminal of a DC power supply. The circuit consists of a DC power supply adjusted to 60 V across a resistance 110 Ω, a 10 turn potentiometer (50 kΩ) to vary the probe bias from +100 to –100 V; in our case we determined the negativity of the Faraday cup. In addition, the brass cup was covered by a grounded closed cylindrical cup (with a hole 2 mm diameter at its center) to avoid the noise and to achieve filtering. The negative polarity of the Faraday cup attracts the positive ions emitted from the mesh and repels the electrons. The electron temperature is a strong function of the admixture of molecular gas, the decrease of the electron temperature being mainly due to the large inelastic cross sections of the electrons with the molecules; this increases the sheath length around the grid (mesh) wires and causes dissociation of the molecular oxygen gas (O_2) by argon atoms besides the ionization. The electron energy distribution function (EEDF) was investigated using different methods e.g. by a graphical method (i.e. drawing the semi-log of the electron current) and by estimating the second derivative of the electron current. The EEDF was found to be a Maxwellian distribution for pure argon and non-Maxwellian for Ar/O_2 mixtures whereby two or many well-defined maxima are observed. Sources of these maxima are also discussed. The etching process of Si (100) wafers has been studied using two different techniques, namely: ion etching using the inert gas only (e.g. argon), and ion chemical etching using an active gas (besides the inert gas) such as oxygen. The characteristics of the etched sample (e.g. width, depth, etching rate) have been investigated. In the following we discuss the experimental data which were obtained in the low-density plasma generated by a capacitive RF discharge. Ion chemical etching (chemically active oxygen is added to the inert gas

(argon)) changes the etching rate and provides a high selectivity of the etching, where we have two sources of reactions (surface reaction and plasma reaction). We will deal with a Si wafer only without any substrate to confirm the plasma etching process, and then with substrate (silicon wafer coated with photoresist) to confirm the measurements of the width of the holes, of the average distance between the holes, of the depth, and of the etching rate, also when special media are being offered for the etching of the Si wafer. Moreover, we used scan size of the Jeol scanning microscope figures, and studied the effect of the plasma etching time on the sample weight to confirm the parameters of the etching processes for ion etching by pure Ar and by ion chemical etching by Ar/O_2 mixtures. We used the Jeol Scanning Electron Microscope (SEM) to study the surface morphology of the Si-wafer after placing it into the plasma and to obtain the width of the holes produced by plasma etching.

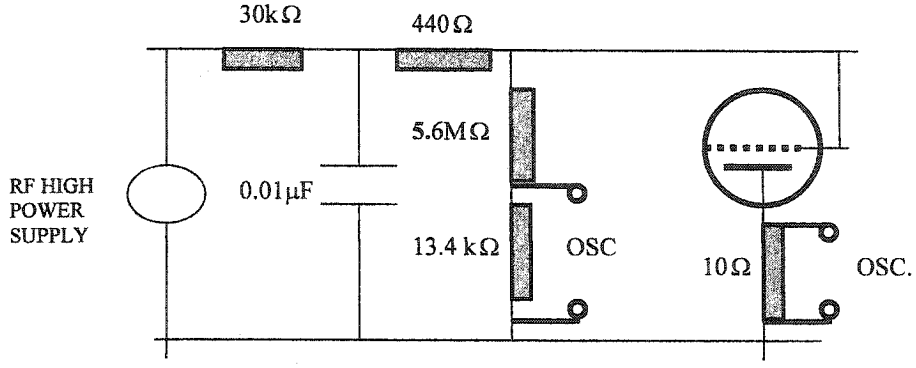


Figure (1) The electrical discharge circuit.

RESULTS AND DISCUSSION

Figure (2) shows that the density has maximum values near the mesh and begins to decrease away from the mesh. This is derived from the ion saturation current of the double probe which has also

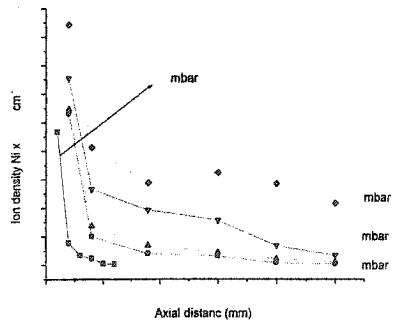


Figure (2) Axial Ar ion density distribution

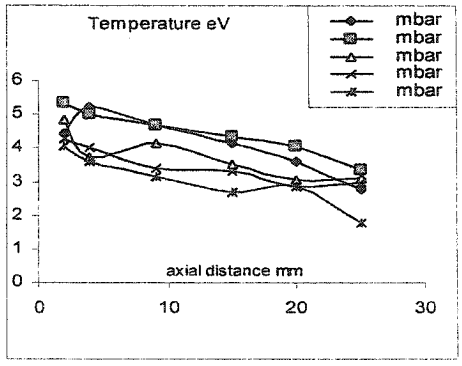


Figure (3) Axial electron temperature distribution

a maximum value near the mesh and decreases sharply away from the mesh, where the ion density N_i is directly proportional to the ion saturation current. Figure (3) shows the temperature distribution

from the center of the cathode mesh in axial direction for different Ar pressures. The electron energy distribution function (EEDF) was determined for pure argon, and for different mixing ratios of Ar/O_2, A comparison between the experimental electron energy distribution function for 100%, 75% and 50% argon with oxygen mixing is shown in Fig. (4). The dissociation of the molecular oxygen gas (O_2) by argon atoms besides ionization by electrons is a very important factor; when the mixing ratio with molecules is increased the temperature decreases. The decrease in the electron temperature with mixing ratio is mainly due to large inelastic cross sections of the electrons with the molecules and also due to the increase of the sheath length around the grid wire. We concluded that the electron temperature is a strong function of mixing ratio. The velocity of the ion flux from the mesh (cathode) is crucial for ion sputtering of a sample (Si-wafer) and therefore we measured it by a Faraday cup probe to give the respective information averaged over a large volume of plasma. The ions have velocities in the range of 10^5 cm/s which leads to T_i in argon of about 0.2 eV. This confirmed the assumption that $T_e > T_i$ which has been used in the present work. The Langmuir probe proved that the electron temperature was about 2.6 eV. The etching process of a Si (100) wafer has also been studied using two different techniques, namely ion etching using an inert gas, e.g argon, and ion chemical etching using an active gas (besides the inert gas) such as oxygen. The characteristics of the etched sample (hole depth, width, etching rate) were also investigated. The width of the holes produced on the sample by pure Ar discharge etching over the center of the mesh region increased with etching time. The hole width increased from 1 μm to 6.5 μm when increasing the etching time from 20 minutes to 120 minutes. The hole depth was in the range 0.5 – 3 μm, the etching rate took on values in the range 50 – 250 μgm/coul.

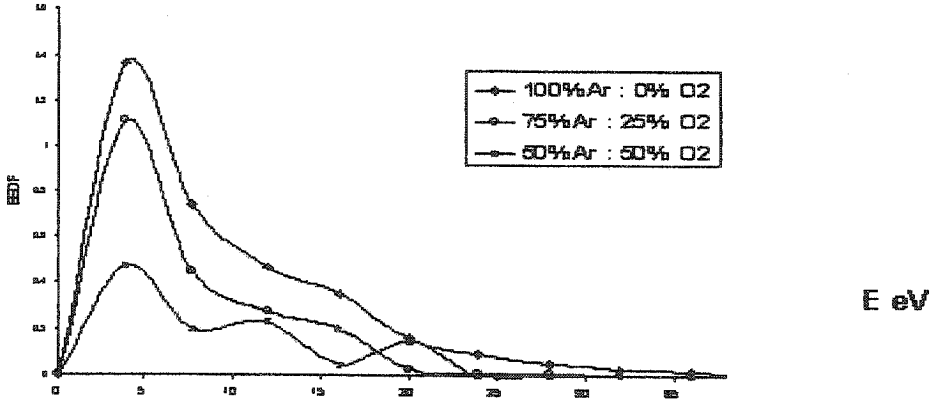


Fig.(4) Electron Energy distribution function

REFERENCES

(1) K.H. Bai, J.I. Hong, S.J. You, C.K. Choi, and H.Y. Chang; Phys. Plasma; 9, 1025 (2002).
(2) J. Asmuseen; J. Vac. Sci. Technol.; A7, 883 (1989).
(3) O.A. Popove, J. Vac. Sci. Technol.; A7, 894 (1989).
(4) R.W. Bosvell and R.K. Porteous; Appl. Phys. Lett.; 50, 1130 (1987).
(5) F.F. Chen; Plasma Phys. Contr. Fusion; 33, 339 (1991).
(6) A.W. Desilva, "Plasma Diagnostics", Lecture Notes, University of Maryland, (1991).

Surface Treatment of Polymer Material Using Argon Glow Discharge

M.A.Hassouba, N.I.Hendawy and F.F.Elakshar *
Physics Dept. Faculty of Science, Benha University, Egypt.
** Physics Dept. Faculty of Science, Azhar University, Egypt.*
hassouba@yahoo.com

ABSTRACT

Surface treatment of polymer material (Polyester sample) was performed in the DC glow discharge, using Ar gas. The effect of the experimental parameters of the glow discharge (e.g. the gas pressure p & the sample treatment time t) on the wettability of thin Polyester sample is studied. The wettability was characterized by the water repellency (water spray test).

In the present work, it was shown that at a constant gas pressure (2 or 5 mbar) , the wettability of the Polyester sample was decreased by increasing the treatment time of the sample in the glow discharge. At constant exposure time (2 , 5, 7 or 10 min.) the wettability of the Polyester sample was increased by increasing the gas pressure.

Key words: Glow Discharge/ Surface Treatment/ Wettability.

INTRODUCTION

The plasma treatment of surfaces in which plasma active species interact only very superficially with the material, i.e. with the adsorbed surface monolayers or with the first few monolayres of the surface material itself, is considered. Such interaction can significantly affect the surface energy, wettability, printability, adhesion and other commercially important properties of surface [1]. This sort of plasma treatment is called "surface activation".

Using cold plasmas for surface activation of polymers is not a new subject, it was first suggested by Beauchamp and Buttrill in 1968. It is generally difficult to adhesively bond polymers to themselves or other materials. Polymers such as fluoropolymers, which is characterized by high chemical inertness, thermal stability and electrical insulating properties, have very low surface tension, and consequently it causes negligible bonding to the other materials especially metals [2]. Plasma surface treatment allows the modification of the surface characteristics of polymers and improved their bonding to the other materials, without affecting the bulk properties. The methods employed to modify properties of polymeric surfaces include surface activation, deposition and grafting. Surface activation is especially important for polymeric materials [2].

The aim of the present work is to investigate the surface treatment of polymer material (Polyester sample) using DC glow discharge, in order to change the wettability of thin polyester layers. The experimental parameters considered are the gas pressure P and the duration time of exposure t.

EXPERIMENTAL SETUP

The experimental setup has been fully described elsewhere [3]. In the present work, a surface treatment, using Argon plasma, was performed for polyester layers in order to change their wettability. The polyester samples have circular layers, each of them has a diameter of 20 cm and thickness of 0.1 cm. The polyester sample was placed on the anode surface inside the discharge tube. The experimental parameters considered in this treatment are the gas pressure (P) and the treatment exposure time (t). The discharge current, discharge voltage and the interelectrode distance were 5 mA, 600 volt and 4 cm, respectively. The wettability of the polyester layers was determined before and after the plasma

treatment using a measurement of " the water repellency test ". This test measures the percentage of free water and the state of dampness of water-proof textiles. Through a nozzle (of diameter 0.889 cm, 19 small holes) 250 ml of water (at room temperature) was sprayed from a pot to a test specimen laid sloping at an angle of 45° (for 25—30 sec.) then the percentage of free water clinging to the specimen was measured.

In the present work, the treatment exposure time was varied in the range of 2—15 minutes and the gas pressure was varied in the range of 0.5—5 mbar.

RESULTS AND DISCUSSION

Exposure of polymers to suitable plasmas can cause chemical and physical changes to their surface or near-surface layers. These changes produce more reactive surfaces and affect wetting properties, cross-linking and molecular weight. Surfaces can thus be engineered to achieve the necessary properties, such as wettability, adhesion, barrier protection, material selectivity and even biocompatibility[4].

Figure (1) and (2) show the water repellency is jump from zero up to 70 % at 2 mbar and up to only 52 % at 5 mbar after 2 minutes exposure time in plasma. By increasing the exposure time to 15 minute, the water repellency increased up to 90 % at 2 mbar and to 70 % at 5 mbar, this means that the wettability of the polyester layers is decreased by increasing the treatment exposure time. Also these figures show that, the change in the water repellency is large at short exposure times and it becomes very small with increasing the exposure time. This is due to, in plasma surface treatments, using glow discharge the maximum treatment efficiency is reached in very short exposure time [4].

On the other hand, Figs. (3), (4), (5) and (6) show the water repellency of the polyester layers as a function of the gas pressure, at constant treatment exposure times 2, 5, 7 and 10 min., respectively. The repellency of the polyester layers decreased by increasing the gas pressure. Thus, the wettability of the polyester layers was increased by increasing the gas pressure. Since when the gas pressure has increased the number of collisions between the charged particles and the neutral atoms is increased inside the discharge tube, this leads to an increase of the electron density. These electrons lose more of their energy in the collisions, so, the electron temperature is decreased, i.e. increasing the gas pressure increases the electron density and decreases the electron temperature at the same time. The best plasma surface treatment of polymers is obtained with high plasma density and low energy of electrons or ions[1,3], so, the wettability of the polyester samples is increased by increasing the gas pressure (i.e. by decreasing the electron temperature and increasing the plasma density).

The experimental data of the polyester wettability agree with the results, obtained by Clement et. al., [5]. The latter studied the polystyrene thin films wettability using DC pulsed glow discharges in nitrogen gas. They showed that, the metastable atoms of nitrogen gas seem to play an important role for the surface treatment. It is generally admitted that the chemical and physical nature of the outer monolayers of the polymer are modified by the electronically, vibrationally and rotationally excited species produced in the plasma.

ACKNOWLEDGEMENT

The authors would like to thank Prof.Dr. M.A.Saad, head of Textile Engineering Dept., National Research Center, for his cooperation during this work.

REFERENCES

(1) J.R.Roth, "Industrial Plasma Engineering", Vol.2; Applications to Nonthermal Plasma processing, IOP (2001).
(2) A.Grill, "Cold Plasma in Material Fabrications", The Institute of Electrical and Electronics Engineers. Inc., New York (1993)
(3) M.A.Hassouba, F.F.Elakashar and A.A.Garamoon, Fizika A, 11, 81 (2002).
(4) H.K.Yasuda, "Plasma Polymerization and Plasma Interactions with Polymeric Materials", John Wiley and Sons Inc., New York (1990).
(5) F.Clement, B.Held, N.Soulem and N.Spyou, Eur.Phys.J.AP., 13, 67 (2001).

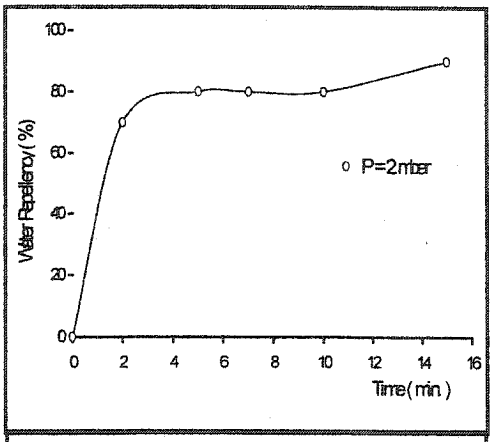


Fig. (1) The relation between the water repellency as a function of the treatment exposure time at a constant gas pressure (P = 2 mbar). The discharge current and voltage were 5 mA and 600 volt.

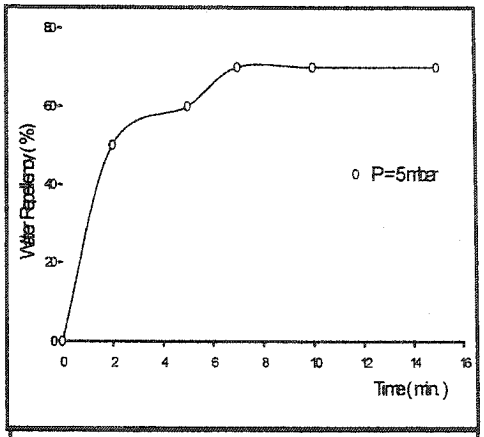


Fig.(2) The relation between the water repellency as a function of the treatment exposure time at a constant gas pressure (P = 5 mbar). The discharge current and voltage were 5 mA and 600 volt.

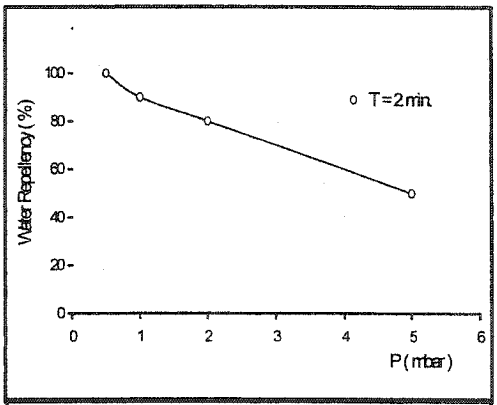


Fig. (3) The relation between the water repellency as a function of the gas pressure at a constant treatment duration time (t = 2 min.). The discharge current and voltage were 5 mA and 600 volt.

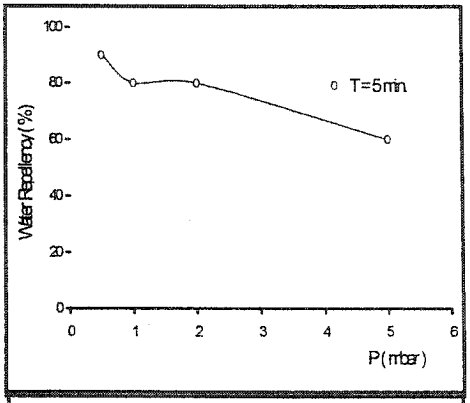


Fig. (4) The relation between the water repellency as a function of the gas pressure at a constant treatment exposure time (t = 5 min.). The discharge current and voltage were 5 mA and 600 volt.

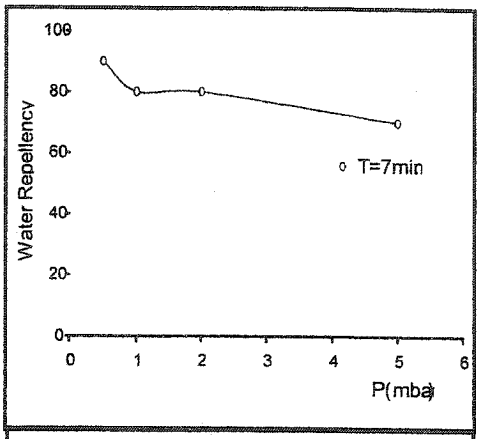


Fig. (5) The relation between the water repellency as a function of the gas pressure at a constant treatment exposure time (t = 7 min.). The discharge current and voltage were 5 mA and 600 volt.

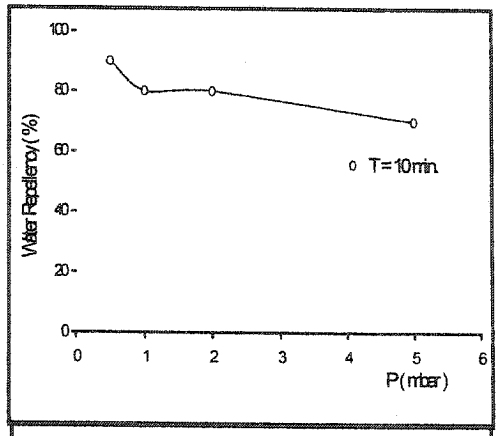


Fig. (6) The relation between the water repellency as a function of the gas pressure at a constant treatment exposure time (t = 10 min.). The discharge current and voltage were 5 mA and 600 volt.

Improvement of Stainless Steel Properties with Titanium Oxides Deposited by Pulsed Ion Implantation Using DPF

S.A. El-Badry[1], Z. Abdel Hamid[2], U.M. Rashed[1], and A.H. Saudy[1]
[1] *Phys. Department, Alazhar Univ. Faculty of Science, Cairo, Egypt.*
[2] *Metal coating & protection Lab. CMRDI, P.O. box. 87, Helwan, Cairo, Egypt.*
usamarahshed@yahoo.com

ABSTRACT

The work in this paper is focused on preparation of hard ceramic films of titanium oxide by pulsed ion implantation and on investigation of their corrosion. Ion implantation is an interesting method to control surface properties of materials.

The titanium oxide films were deposited on 316 stainless steel substrates using dense plasma focus (DPF) technique. The DPF device was operated on oxygen ambient gas at pressure of 2 mbar and 13kV charging voltage of the capacitor bank. the substrates were subjected to several DPF shots. The influence of the shots number on the properties of deposited films was investigated using various analysis methods.

X-ray diffraction (XRD), scanning electron microscope (SEM) and energy dispersive x-ray (EDX) were performed to reveal the structural properties and surface morphology. Standard adhesion tests were studied. Hardness measurements and hot corrosion were also studied.

Key Words: DPF, Ti_2O_3, XRD,SEM, and EDX

INTRODUCTION

The DPF device [1,2] is a simple device which generates high densities (10^{25}-10^{26} m^{-3}) and high temperatures (1-2keV) plasma. The DPF has been established as a source of highly energetic ions having energies in the range of 25keV to 8MeV [3,4], fusion neutrons, X-rays and relativistic electrons.

In this paper, highly energetic ion and electron beams were used to prepare a ceramic layer of titanium oxide Ti_2O_3. The properties of these films especially composition, hardness, adhesion and hot corrosion resistance were investigated.

Titanium oxide coatings are one of the best current biocompatible materials [5,6]. Titanium oxide thin film coatings reactively sputter deposited, which have a high refractive index and dielectric constant, present wide applicability in optics and microelectronics. These coatings have already been the focus of many studies [7,8]. Vanes, turbine and various components in fuel conversion units, that are subjected to thermal fluctuations under normal operation conditions need protection from high temperature degradation. This is usually performed by using a hard ceramic coating such as Ti_2O_3.

EXPERIMENTAL SETUP

The DPF device used in this paper is a Mather type plasma focus with 3.3 kJ energy which is being powered by a single 30 μF, 15 kV fast discharging Maxwell capacitor. Ti target was inserted into anode so that it covers the rim of anode and the substrate holder was incorporated in the vacuum chamber facing Ti insertion. The stainless steel (316) substrates is a typically 70 mm length and 3 mm thick. The samples were mechanically polished with SiC paper and cleaned before mounting in the holder. Figure (1) shows the details of experimental set up of DPF used in Ti_2O_3 deposition.

The coated samples were preheated at 600 °C for 30 min. to stress release of coating layer. X- ray diffraction analysis was carried out using p. w. 1051 Philips X- ray diffractometer and energy dispersive X-ray system (EDX) Model JOL/ISM- 5410 were used to obtain detailed information on elemental analysis of the coating samples. The thickness of the coating layers was measured as a function of number of shots for each sample using coating thickness gage 6000 – N4. Adhesion was measured by cross cut method according to international standards ISO 2409 (66), the coating adhesion was classified to 6 classes. The corrosion resistance of the coated and uncoated samples was measured by heated the samples in crucible furnace with NaCl at 850 °C for different time up to 15 hrs. The surface morphology for the coated before and after corrosion was studied using scanning electron microscope (SEM). Michrohardness measurements of the deposit layer were determined by an indentation technique using a diamond pyramid indenter at 100 gf load.

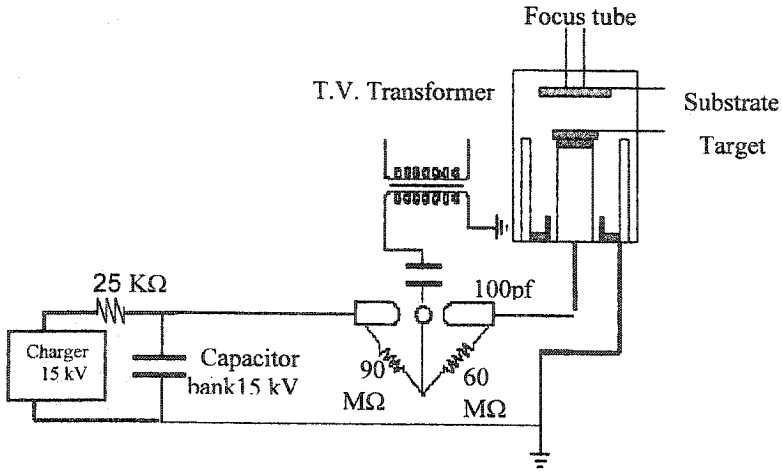


Fig. 1 The details of experimental set up of DPF used in Ti_2O_3 deposition.

RESULTS AND DISCUSSION

The used target material is a pure titanium (Ti). Fig. (2) shows EDX analysis for the target material. The variation of Ti_2O_3 coating thickness as a function of a number of DPF shots (n) is shown in figure (3). It has found that, for n<15 shots the thickness increases with increasing n. This is due to the deposition rate. While for n>15 the film thickness decreases slightly with increasing n. This decrease can be attributed to the balance between the rate of film build up and film removals due to the impact of the substrate surface by high accelerated O_2 ions. The adhesion of the coating layer is the important parameter for estimation of coating performance, which depends on the crystal size and coating structure. it was estimated in the present by a Finger nail rapid scratch test. It was found that the adhesion of titanium oxide to the stainless steel base metal has high adhesive strength and classified in class (0) according to ISO classification. This high adhesion is attributed to the structure of titanium oxide matrix. The coating analysis is examined using X- ray diffraction (Fig.4). The result clearly indicates that the diffraction lines correspond to the titanium oxide structure.

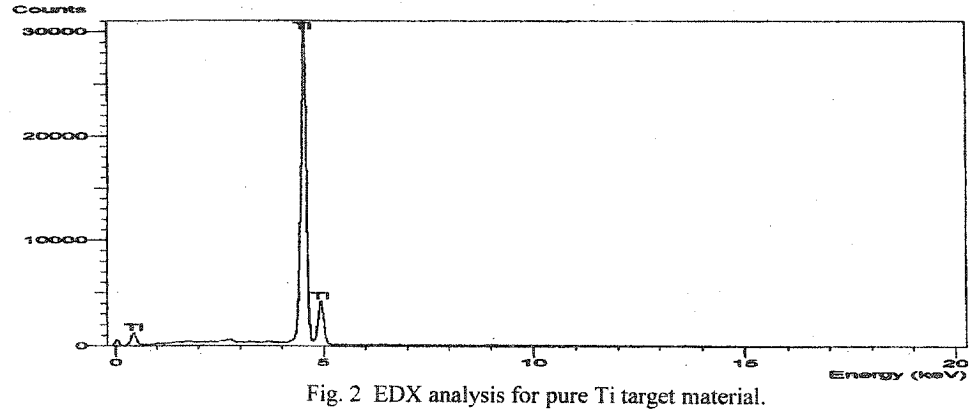


Fig. 2 EDX analysis for pure Ti target material.

Microhardness is assessed by Vickers indentation under 100gf. The microhardness of the samples have been increased from 264 Hv (uncoated) to 460 Hv (coated). This increase in hardness is attributed to a combined effect of heat treatment hardening and structure of titanium oxide matrix.

In this investigation the hot corrosion of 316 stainless steel coated and uncoated was studied under aggressive conditions of sodium chloride salt. The samples were exposed to hot air atmosphere in electric furnace maintained at 850 °C for period up to 25 hrs. Fig. 5 shows the effect of hot corrosion in sodium chloride for the uncoated (a,b and c) and coated (d,e and f) samples. An attack of the stainless steel surface is clearly noted for the surface morphology shown by Fig.5 (b and c) for attack time of (15 and 25hrs), respectively. since sodium chloride

melts at 800 ^{o}C, the surface of the sample is thus covered by a molten salt layer, which prevents atmospheric oxygen to be delivered to the metal surface, so the surface of metal reacts with the melt only and intergranular attack may start. Figure 5 (a,b and c) indicates that, the corrosion areas of uncoated sample increases rapidly with increasing attack time. Figure 5 (d, e, and f) shows a surface morphology of coated sample maintained without any attack up to 25hrs, compared with uncoated stainless steel sample. This can be attributed to the presence of Ti_2O_3 layer which prevents attack of sodium chloride melt to react with a stainless substrate. The protection is afford by titanium oxide layer and restricted inward and outward diffusion. The coated layer of titanium oxide contributes to the restricted diffusion and titanium oxide layer acts as a barrier to direct contact of the subsequent layer, with the salt. The results indicate superior hot corrosion resistance of coated layer.

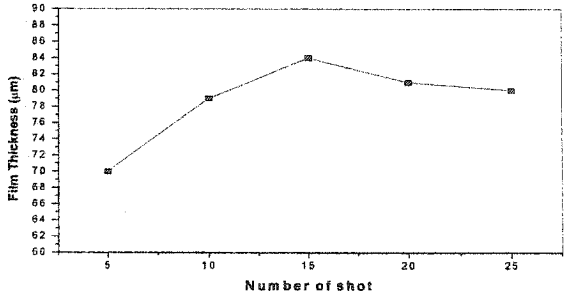


Fig. 3 The relation between film thickness and number of shots.

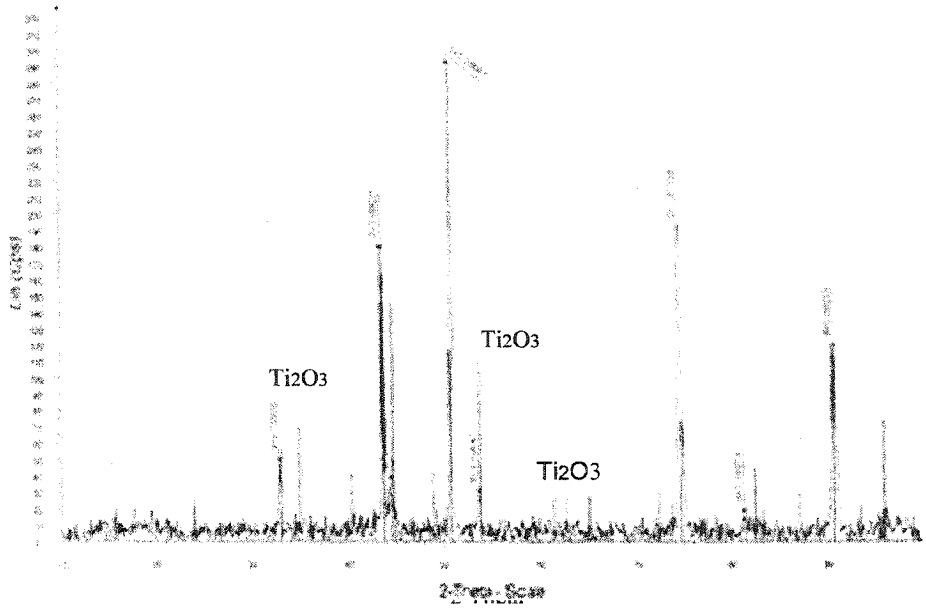
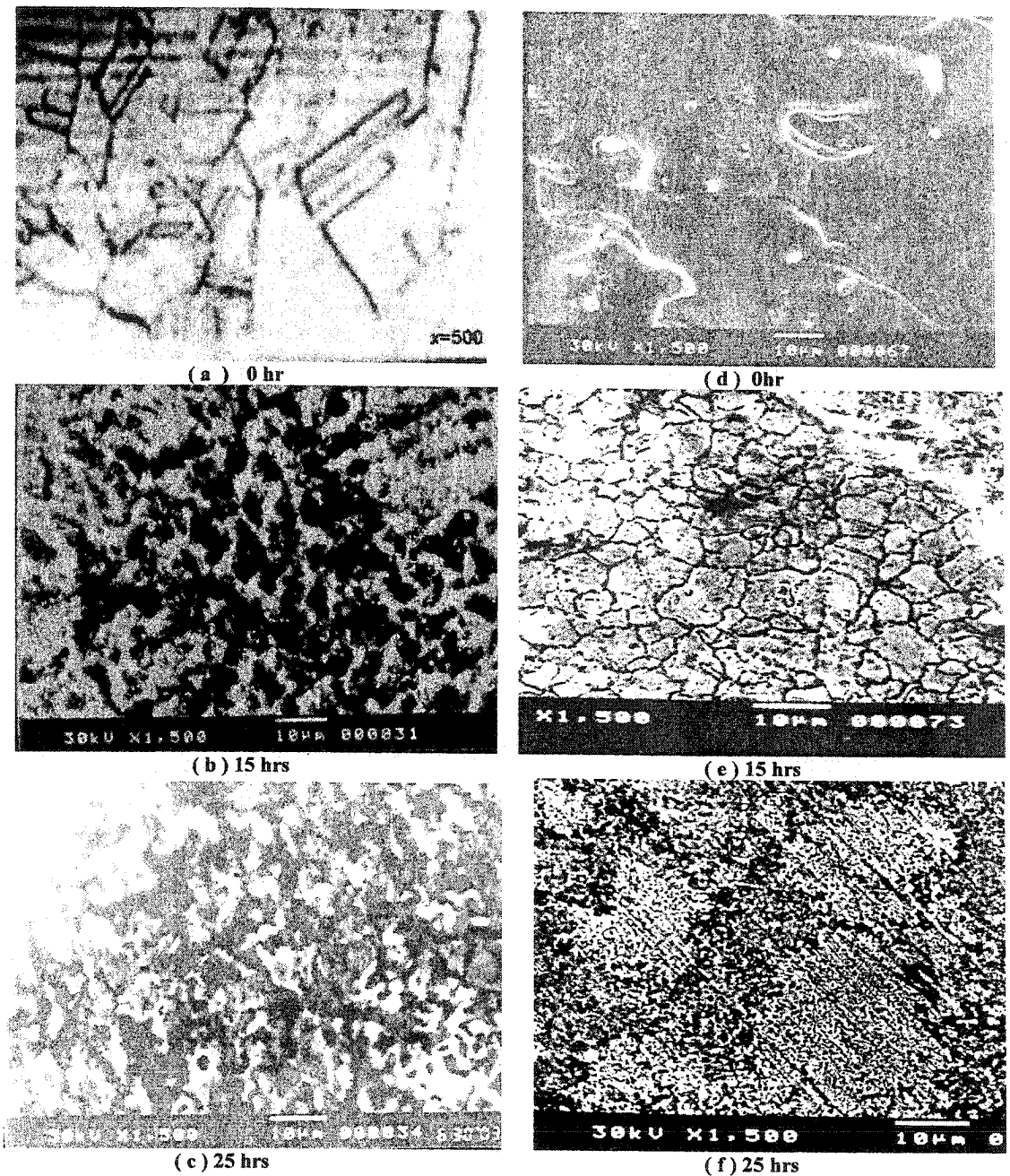


Fig.4 XRD analysis of the coated substrate by Ti_2O_3 thin film.

REFERENCES

(1) J.W. Mather, Phys. Fluids 7, 5, 1964.
(2) S. Lee, T.Y. Tou, S.P. Moo, M.A. Eissa, A.V. Gholap, K.H. Kwka, S. Mulyodrono, A.J. Smith, Suryadi, W. Usada, and M. Zakaullah, J. Phys., 56, 62, 1988.
(3) R.L. Gullickson, and H.L. Sahlinl, J. Appl. Phys., 49, 1099, 1978.
(4) G. Gerdin, W. Stygar, and F. Veenneri, J. Appl. Phys., 52, 3269, 1981.
(5) T. Hanawa, M. Ota, Appl. Surf. Sci. 55, 263, 1992.
(6) U. Moller, R. Hauert, Thin Solid Films, 290, 323, 1996.
(7) K. Okimura, A. Shibata, Jpn. J. Appl. Phys. 36, 4917-4921, 1997.
(8) K. Okimura, N. Maeda, A. Shibata, Thin Solid Films, 286, 32-34, 1996.



(a) 0 hr

(d) 0hr

(b) 15 hrs

(e) 15 hrs

(c) 25 hrs

(f) 25 hrs

Fig. 5 Surface morphology of base metal substrate (a,b,c) and coated substrate by Ti_2O_3 (d,e,f) after corrosion test for 0,15 and 25 hrs at 850°C by NaCl.

DC Plasma Ion Implantation in an Inductively Coupled RF Plasma

C.Silawatshananai[1], N.Matan[1], C.Pakpum[1], N.Pussadee[2], P.Srisantitam[2], S.Davynov[2], T.Vilaithong[2]

[1]Institute of Science, Walailak University, Nakhon Si Thammarat, Thailand, 80160.

[2]Fast Neutron Research Facility, Faculty of Science, Chiang Mai University, Chiang Mai, Thailand,50250.

Schaivit@wu.ac.th

ABSTRACT

Various modes of plasma ion implantation have been investigated in a small inductively coupled 13.6 MHz RF plasma source. Plasma ion implantation with HVDC(up to –10 kV bias) has been investigated in order to incorporate with the conventional implantation of Diamond Like Carbon. In this preliminary work, nitrogen ions are implanted into the stainless steel sample with a dose of $5.5x10^{-2}$ cm for a short implanting time of 7 minutes without target cooling. Surface properties such as microhardness, wear rate and the friction coefficient have been improved. X-RAY and SEM analyses show distinct structural changes on the surface. A combination of sheath assisted implantation and thermal diffusion may be responsible for improvement in surface properties.

Key words: Low Temperature Plasmas Applicaitons, Plasma Ion Implantation

INTRODUCTION

Various types of plasma sources may be used in conventional plasma ion implantation for surface modification of materials[(1)]. For ease in operation and low impurities, an inductively coupled 13.6 MHz RF plasma may be chosen. Our plasma is produced in a cylindrical stainless steel chamber of 31 cm in diameter and 42.5 cm in length[(2)]. The RF power at 50-250 W is applied to the two turns insulated helical antenna placed inside the chamber, an array of permanent magnet buttons is used to assist in plasma confinement. The strength of the cusp field inside the chamber is 670 gauss. Plasma parameters are characterized by a single Heiden RF compensated Langmuir probe and an Ocean Optics optical emission spectrometer. An optical pyrometer is also used to check target surface temperature. A water cooled target holder can place the sample along the line of sight directly opposite to the antenna.

Four modes of operations may be carried out, namely: (1) cw RF plasma-DC negatively biased target, (2)cw RF plasma-pulse negatively biased target[(3)], (3) pulse RF plasma-DC negatively bised target[(4)] , and (4) pulse RF plasma –pulse negatively biased [target(5)]. These modes of operation offer advantages and disadvantages as discussed by a number of authors shown, and they benefit material surface improvement with wide range of ion species and energy. In this paper, we present the work on HVDC bias technique. A combined PIII and deposition process will later be used to fabricate the diamond like carbon (DLC)coating. Stainless steel is used as a test specimen that has been prepared with standard procedures.

RESULTS

Stainless steel were implanted with nitrogen ions at –10 kV bias, RF power 250 W and gas pressure 0.5 mtorr, with or without cooling at different implanting times.

1.Tribological test results are summarized in the Tables 1 and 2

Table 1.Microhardness test of specimens before and after implantation

Specimen number	Implant time (minutes)	Dose (cm^{-2})	Unimplanted	Implanted	Change (%)
104	7.5+cooling	$5.9x10^{17}$	184.94+/-72	293.13+/-71	58.50
103	7.0	$5.5x10^{17}$	192.5+/-7.5	338.3+/-106	75.74
105	11.0	$8.2x10^{17}$	195.79+/-13.6	300+/-77	53.22

Table 2.Wear test

Specimen number	Friction coefficient	Wear Rate
unimplanted	0.71	$3.9x10^{-7}$
104	0.67	$8.29x10^{-8}$
103	0.39	$3.67x10^{-8}$
105	0.51	$1.09x10^{-7}$

2.Pin –on-disk wear test

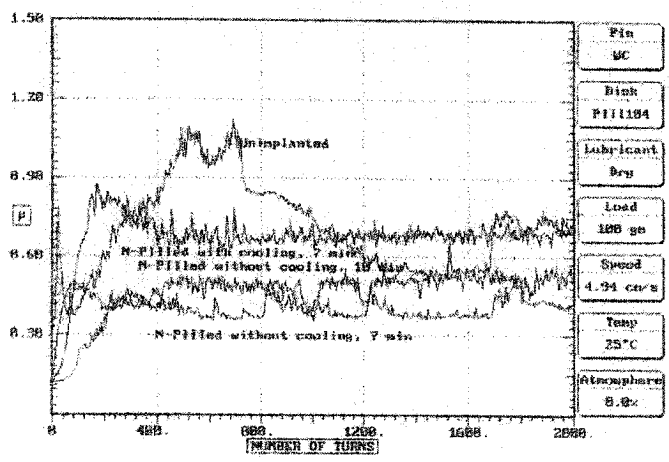


Fig.1.Graph of tribological analysis

2.Structural analysis results from X-RAY and SEM studies are shown in Figs.2 and 3

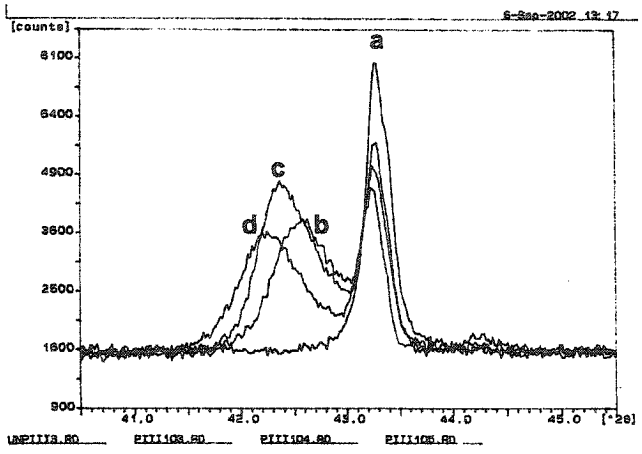


Fig. 2 X-ray diffraction profile in (111) plane a) unimplanted specimen, b) implanted specimen for 7 minutes without cooling (No.103), c) implanted specimen for 11 minutes without cooling (No.105) and d) implanted specimen for 7.5 minutes with cooling (No.104). Expanded Austenite is evident in sample b,c,d.

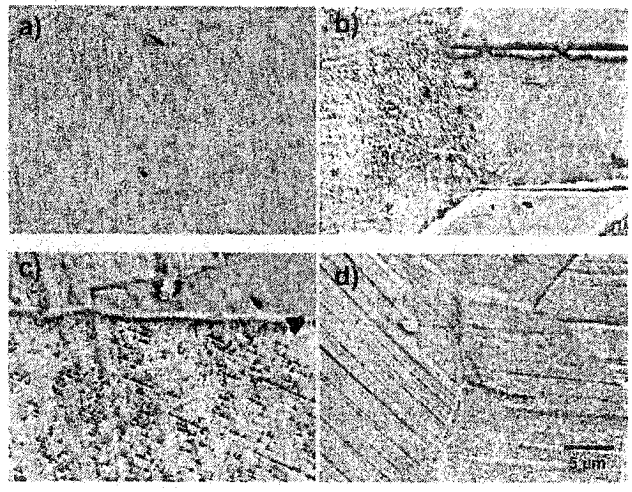


Fig.3 Scanning Electron Microscope images a) unimplanted specimen, b) implanted specimen for 7 minutes without cooling (No.103), c) implanted specimen for 11 minutes without cooling (No.105)

d)implanted specimen for 7.5 minutes with cooling (No.104). Implantation time and heating affect the grain edges and shear on the surfaces.

CONCLUSION

We have accomplished the ion implantation with HVDC (up to –10kV, limited by power supply available) in an RF discharge without the occurance of arcing. The test on stainless steel using nitrogen ions shows improvement in surface properties. The process renders some advantages over pulse ion implantation such as less stringent requirement on the HV pulse modulator. Furthermore, it can be incorporated in the so called PIII&D process which is suitable for fabrication of some material such as DLC.

ACKNOWLEDGEMENT

This work was supported by grants from the Walailak University , the National Metal and Materials Technology Center and the Thailand Research Fund.

REFERENCES

(1) A.Anders ed.; "Handbook of Plasma Immersion Ion Implantation and Deposition", John Wiley, (2000).
(2) P.Suanpoot, T.Vilaithong, M.W.Rhodes and D.Boonyawan, J.Plasma Fusion Research, Series1; 526(1998).
(3) J.R.Conrad and J.R.Radke, J.Appl.Phys.; 62, 4591 (1987).
(4) K.N.Leung; US Patent No.5558718, (1996).
(5) J.Brutcher, R.Gunzel, W.Moller; Surf.Coat.Technolo., 93 (1997).

Ion Implantation on Nickel Targets by means of Repetitive Plasma Focus Device

S. Vitulli[1,*], M.L. Apicella[2], L. Rapezzi[1], M. Samuelli[2]
[1]*ENEA Brasimone, loc. Brasimone, 40032 Camugnano, Bologna, Italy*
[2]*ENEA Frascati, via Enrico Fermi, 45 - 00044 Frascati, Roma, Italy*
silvia.vitulli@inwind.it

ABSTRACT

Some test has been done in order to assess the possible use of a Plasma Focus as an implanter. The device utilized is the repetitive Plasma Focus operating in the ENEA Brasimone Center. The implanted sample is a sheet of Nickel with a surface of 17 cm^2 inserted in a rigid sample at a variable distance from the top of the anode. After irradiation the sample is analyzed with Auger spectroscopy that provides the surface concentration of the various elements on the sample at different implantation depths. The result of the analysis shows that the Plasma Focus is an effective implantation source, even for metallurgical applications.

Key Words: Plasma Focus, Ion Implantation, Auger Spectroscopy

INTRODUCTION

The Plasma Focus (PF) is a device consisting of two coaxial electrodes in vacuum connected to a fast high voltage capacitor bank. When the HV is applied to the electrodes through a spark gap, electrical breakdown develops on the surface of the insulator and the discharge is driven by the Lorentz force to run along the gap between the electrodes at a speed of some 10^7 cm/s and when reaches the end of the inner electrode collapse on the axis of the device focusing in a hot blob of plasma (Plasma Focus). In this phase strong electric fields are generated that produce intense ion beams. The duration of each discharge is of the order of 10 μs. Normal implanters are basically made of an ion source, an acceleration stage and an extraction stage. They are expensive and require high vacuum. Normally the sample is implanted inside a large vacuum chamber. As a matter of fact most of the treatments are done on relatively small samples (tools, prostheses, catheters). In our opinion the advantage of the PF can be in the ease of the operation and in the reliability. For instance the device operates at pressures of the order of ten mbar allowing the connection to large objects to be implanted without putting them in a large vacuum chamber. The study of the characteristics of the ion beams emitted by the PF machines has been and is currently the object of a wide set of experiments that have produced a large amount of papers in the literature [1-6]. Our work is focussed not on the study of the characteristics of the beams or of optimizing at a fine level the production, but on the gross characteristics of the emission measured in terms of the effective capability of modifying the properties of the target samples. For normal applications, the order of magnitude of the implantation density required is: 10^{14}-10^{15} ions/cm^2 for semiconductor technology; 10^{16} ions/cm^2 for ion mixing technologies; 10^{17} ions/cm^2 for metallurgical applications.

EXPERIMENTAL SET-UP AND PROCEDURE

We operate our PF at 6 kJ, 21kV and with central electrode of positive polarity (anode). The discharge current is of the order of 0.5 MA. The central hollow electrode, made of tungsten, has a diameter of 34,5 mm and a length (outside the insulator) of 7,5 cm. The outer electrode is a cylinder made of stainless steel with a radius of 4,5 cm and an height equal to that of the total central electrode (electrode + insulator length). A turbo pump provides the initial vacuum and no particular care has been taken to assure the cleanliness of the vacuum. The gas to be implanted is in the vacuum chamber

---

* Now at IASF/CNR, via Gobetti, 101 – 40129 Bologna, Italy

at a pressure typically of 4 mbar. The insulator, made of quartz, is a cylinder of 8,6 cm height and the total surface exposed to the plasma is 54 cm^2. The implanted sample is a sheet of Nickel with a surface of 17 cm^2 and a thickness of 0,1 mm. The sample was inserted in a rigid sample-holder made of SS that keeps it parallel to the electrode at a distance that can be varied. The discharges are made using pure Nitrogen. The distance of the sample was initially set on the axis of the machine at a distance of 10 cm from the upper part of the central electrode. The sample was immediately destroyed evidently by the shock due to the impact of the plasma sheet. The distance sample-electrode has been then progressively increased up to a value of 20 cm where no visible damage was produced by large series of discharges. The sample was removed after 62 discharges (at 0,5 Hz) and analysed with Auger spectroscopy. It must be noted that after the series of discharges the central electrode presented just on axis a clear hole showing that material of the central electrode was removed (probably by the impact of high energy electron beams produced in the PF).
The Auger technique is perhaps the most versatile method to analyse surface atomic composition, because it has good sensitivity for a wide range of elements and can be reasonably quantitative. The depth resolution of Auger technique is only few angstroms and deeper regions of the sample are analysed by progressively removing the deposited material with an Ar ion beam.

EXPERIMENTAL RESULTS

Fig. 1 shows the results of the Auger analysis. In *Fig. 2* it is put in evidence the behaviour of N implantation from *Fig. 1*. In *Figs. 1 and 2* there are shown the measured concentrations of the various elements found on the surface progressively eroding the sample at a rate of one monoatomic layer. A measure on a monoatomic layer volume is made each 70 nm in the erosion process. It should be mentioned that some traces are present of Fe, O and C that we attribute to the preparation procedure of the sample. The Auger measurements have been performed on four zones of the sample, located relative to the PF axis at P_1 = 1 cm, P_2 = 0,75 cm, P_3 = 1 cm and P_4 = 2,25 cm in different azimuthally directions. No significant variations of the results are observed in the four zones. The results reported in *Fig. 1* and *2* refer to the zone P_1.

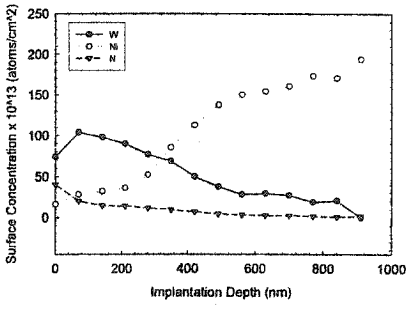


Fig. 1 Surface concentration of W, Ni and N found with Auger analysis on the Ni irradiated target.

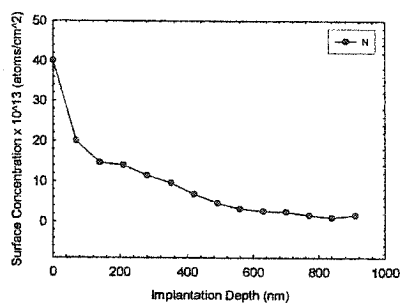


Fig. 2 Surface concentration of N on the Ni target

Looking in particular at the Nitrogen implantation, upon integration of the concentration up to the maximum penetration (about 900 nm), and being the inter-atomic distance of the Ni substrate equal to 2,2 Å, it is found that the surface content of nitrogen after implantation in the four measurement zones is N_{P1} = 4,7 10^{17} atoms/cm^2, N_{P2} = 3,6 10^{17} atoms/cm^2, N_{P3} = 4,1 10^{17} atoms/cm^2, N_{P4} = 3,7 10^{17} atoms/cm^2. The maximum variation from the average of the content is less than 17%.

DISCUSSION

The main difficulty in interpreting the experimental results is due to the presence of a large amount of W. On the surface it reaches a concentration greater than 50% and it is present on the sample up to a

depth of 850 nm with a concentration of about 10%, lower detectable limit for such element with our Auger apparatus. Two different mechanisms can produce the presence of W on the sample.
The first deals simply with the implantation of the W extracted by the electron beam generated by the PF from the centre of the anode where it is clearly visible that material has been removed by the discharges. The W ions should be accelerated toward the sample by the same electric field (and voltage) causing the relativistic electron beam. An evaluation of the W energy spectrum from the implantation range into the sample, in the hypothesis of single ionized ions, made with the same procedure that in the following is performed for the implantation of Nitrogen, indicates a spectrum extending from 1.5 to 8 MeV In the literature it is reported that the electron beams in the PF have energies of the order of 1 MeV. Moreover multiple ionized ions (up to 8) are reported reaching energies of 12-14 MeV[1,7]. The intensity of such beams is nevertheless quite low. We cannot so exclude such mechanism but we consider it unlikely.
The second mechanism deals with the melting of the sample surface hit by the splashing of the plasma sheet in the late part of his life when it is strongly doped by the material coming from the electrodes (practically a W plasma). Consequently an alloy is formed between W and the sample material. The fact that the sample was systematically macroscopically damaged when placed at a distance less than 20 cm from the electrode is an indication that the acting mechanism is the second.
It is anyway clear that the deposition of W on and inside the sample is cumulating with the number of discharges. The composition of the sample is so varying as long as the PF discharges go on. This fact is important in deducing the energy spectrum of the N ions implanted on the sample by the measure of the projected range which depends upon the sample composition. In evaluating the spectrum we use the following approximate formula [8]:

$$E_{[keV]} = \frac{R_{p[nm]} \cdot \rho_{[g/cm^3]} \cdot Z_1^{2/3} \cdot (3 \cdot M_1 + M_2)}{39 \cdot (M_1 + M_2)} \qquad (1)$$

where R_p is the projected range of the implanted ion (i.e. the projection of the range along the normal to the sample surface), E his energy, ρ the density of the target material, M_2 is the atomic weight of the target (sample) atoms, M_1 and Z_1 are the atomic weight and the atomic number of the implanting ions.
Eq. (1) is valid if the average energy loss of the ions into the target material results from elastic collisions with the target atoms (nuclear stopping or elastic energy loss). The alternative mechanism of loss is toward the electrons of the target atoms (electronic stopping or inelastic energy loss). The use of *(1)* represents well the ion energy spectra reported in the following for energies greater than about 100 keV for Nitrogen impinging ions.
Taking into account the approximations and the intrinsic range straggling, it descends that the precision of the deduced energy spectrum is quite poor. Anyway this is a general limit of the method unless very refined measurements are not performed. We evaluate that the precision of the deduced energy spectrum is of the order of 30%.
Fig. 3 reports the energy spectrum deduced with the elaboration of *Fig. 2* for the implantation of Nitrogen. As the implantation takes place on a sample having a composition varying as the series of discharges is going on, in *Fig. 3* the two different spectra are reported, corresponding to the implantation on a sample having the initial composition (i.e. pure nickel) and on a sample having the final composition, i.e. that of *Fig. 1*. The real spectrum is then laying somewhere between the two reported spectra. Anyway this result is acceptable considering the above mentioned small precision of the method. In evaluating the energy spectrum of the N ions impinging on the alloy Ni+W the following relationship for the projected range has been used [8]:

$$R_p(A_xB_y) \cong (x \cdot N_A + y \cdot N_B) \cdot \frac{\left(\frac{R_p(A)}{N_A}\right) \cdot \left(\frac{R_p(B)}{N_B}\right)}{\frac{y \cdot R_p(A)}{N_A} + \frac{x \cdot R_p(B)}{N_B}} \qquad (2)$$

Where x and y are respectively the relative number of atoms of the two components A and B normalized to 1 (x+y =1) and $R_p(A)$, $R_p(B)$, N_A and N_B are the projected ranges and the atomic densities of pure hypothetical substrates of the two elements.
The energy spectrum on Ni+W of *Fig. 3* is obtained by applying *Eq. (2)*, using the composition of *Fig.1* in steps of 70 nm.

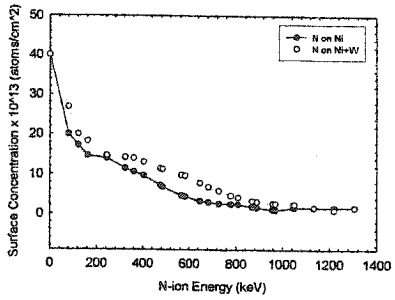


Fig. 3 N implantation on two different backgrounds

CONCLUSIONS

Taking into account the required levels of implantation reported in the Introduction for an implanter being competitive, our results show that the PF is an effective source for implantation even for metallurgical applications (i.e. about 10^{17} ions/cm^2 and depth of some 100 nm). The implantation appears uniform within 17% on an area of 16 cm^2.
The analysis of the experimental results show nevertheless that the PF beam presents a broad energy spectrum, a characteristic not compatible with semiconductor technology applications.
Besides the implantation of the filling gas ions, some macroscopic modification takes place on the sample surface due to the material of the electrode impinging on it. The mechanism is not clear but it can be due to the melting of the sample surface upon the impingement of the plasma sheet with the consequent formation of a surface alloy on which the filling gas ions are implanted. Depending on the applications the possibility of creating under controlled conditions a surface alloy on the target material can have a positive impact on the usefulness of the PF as an implanter.

REFERENCES

(1) L. Bertalot et al. "Experiments on plasma focus dynamics, neutron production and ion emission" Proc.Plasma Phys. and Controlled Nuc. Fusion Research Conf. Brussels (1980) IAEA ed. Vienna (1981) p.177
(2) J.N. Feugeas et al " Nitrogen implantation of AISI 304 SS with a coaxial plasma gun" J.Appl.Phys. 2648, 64 (1988)
(3) H.Kelly et al. " Analysis of the nitrogen ion beam generated in a low-energy plasma focus device by a Faraday cup operating in the secondary electron emission mode" IEEE Trans. Plasma Sci. 113, 26 (1998)
(4) J.N. Feugeas et al. " Thermal effect of pulsed ion implantation with a coaxial plasma gun" Industrial Applications of plasma Physics, Bonizzoni et al ed., Ed. Compositori Bologna (1993) p.551
(5) H.Kelly et al. "Coating on metallic samples produced by a small energy plasma focus" Plasma Sources Sci. Technol. 704, 5 (1996)
(6) M. Sadowsky et al. " Comparison of characteristics of pulsed ion beams emitted from different small PF devices" Nukleonica 179, 45 (2000)

(7) L. Jakubosky et al. "Measurements of charged particles beams from plasma focus discharges " Proc.Plasma Phys. and Controlled Nuc. Fusion Research Conf. Sorrento (2000), IAEA ed. Vienna Paper ICP01
(8) M.Nastasi, J.W.Mayer and J.K.Hirvonen : "Ion-solid interactions. Fundamentals and applications" Cambridge University Press ed. Cambridge (1996)

Laser Plasma Interaction

Fast Ions From Picosecond Laser-Plasma Interaction

J. Badziak[(1)], H. Hora[(2)] S. Jabłoński[(1)] J. Krása,[(3)] L. Láska[(3)], P. Parys[(1)], K. Rohlena[(3)], J. Wołowski[(1)]

[(1)]*Institute of Plasma Physics and Laser Microfusion, Hery Str. 23, 00-908 Warsaw, Poland*
badziak@ifpilm.waw.pl
[(2)]*Dept. Theoretical Physics, University of New South Wales, Sydney 2052, Australia*
[(3)]*Institute of Physics, A.S.C.R., Na Slovance 2, 182 21 Prague 8, Czech Republic*

ABSTRACT

Properties of fast ion fluxes emitted from the plasma created onto Au massive target by an 1-ps laser pulse of subrelativistic intensity ($\leq 10^{17}$W/cm^2) are investigated and compared to the ones produced by a 0.5-ns laser pulse. It is shown that characteristics and plausible mechanisms of fast ion generation are essentially different for the two considered cases. In the long-pulse case several groups of fast ions are emitted into a wide solid angle and self-focusing of the laser beam in plasma and various plasma instabilities seems to determine the ion flux properties. In the short-pulse case only a single fast ion group with a small angular divergence is generated and ions are likely to be accelerated by an axial ponderomotive force produced at the skin-layer interaction of the pulse with a preplasma layer in front of a target.

Key Words: Fast Ions, Plasma, Picosecond Laser

INTRODUCTION

Energetic ions, emitted from plasma produced by the interaction of a high-intensity laser pulse with a solid target, are currently the subject of intensive study stimulated by the prospect of their unique applications in accelerator technology [(1)], fast ignition of nuclear fusion [(2)], material science [(3)], and medicine [(4)]. In the recent years both long (ns and subns) [(5)] and short ($\leq$ 1ps) [(6)] laser pulses have been used to produce intense ion fluxes with ion energies from hundreds of keV up to tens and hundreds of MeV. However, characteristics of an ion flux emitted from plasma depend not only on the laser pulse duration and intensity but also on many other factors (e.g. laser focusing conditions, laser prepulse parameters, target features), so a detailed quantitative comparison of the ion characteristics from hitherto performed long-pulse and short-pulse experiments, where different experimental arrangements have been used, can be difficult or impossible. As a result, also possible advantages (or disadvantages) of ion fluxes produced by short-pulse lasers over the ones generated by long-pulse lasers are not fully and unambiguously determined.

In this paper, properties of fast ion fluxes emitted from the plasma created onto Au target by an 1-ps laser pulse of subrelativistic intensity ($\leq 10^{17}$W/cm^2) are investigated and compared to the ones produced, in the same experimental conditions, by a 0.5-ns laser pulse of energy similar to that of the 1-ps pulse ($\leq$ 0.7J). It is shown that both the temporal and spatial characteristics of fast ion emission as well as the dependencies of ion energies on laser intensity are essentially different for the two considered cases.

EXPERIMENTAL ARRANGEMENT

The experiment was performed with the use of terawatt Nd:glass chirped-pulse-amplification (CPA) laser, generating a 1-ps pulse of short-time scale (< 1ns) intensity contrast ratio ~ 10^4 at λ = 1.05 μm [(7-8)]. The long-time scale ($\geq$ 1 ns) intensity contrast ratio was higher than 10^8. The linearly polarized laser beam was focused by an on-axis f/2.5 parabolic mirror, with a hole in the centre, onto Au massive target at an angle of 0° with respect to the target normal. The maximum intensity of the focused laser beam was about 10^{17} W/cm^2. As results from our plasma expansion velocity measurements the

thickness of the preplasma layer, L_{pre}, produced by the laser prepulse on the target surface was $\leq 5\mu m$. By removing the compressor gratings from the optical path of the CPA system the laser delivered high-contrast 0.5-ns pulses of intensity up to $2 \times 10^{14} W/cm^2$ and with the wavelength, laser energy (up to 0.7J) and focal spot diameter ($d_{foc} \approx 20\mu m$) close to those of the ps pulses.

The measurements of the ion flux parameters were performed with the use of ion collectors (ICs) and an electrostatic ion-energy analyzer (IEA) [8]. The IEA and the ring ion collector (IC1) measured the backward-emitted ion beam passing through the hole in the parabolic mirror along the target normal and the laser beam axis. For a rough estimation of the angular distribution of ion emission two additional collectors, viewing the target at angles Θ of 26° and 34° with respect to the target normal, were applied.

RESULTS AND DISCUSSION

Fig.1 presents a typical IC1 collector signals illustrating temporal runs of backward ion emissions from Au target for the cases of 1-ps and 0.5-ns laser pulses. The rough angular distributions of fast ion emission for the ps and subns pulses are presented in Fig. 2 (the distributions for the peak ion current density are approximated by $j_p = a \cos^x \Theta + b \cos^y (\Theta - \Theta_0)$. The above figures demonstrate principal differences in properties of fast ion fluxes emitted from plasmas produced by short and long laser pulses. In the long-pulse case several groups of fast ions (index f in Fig. 1) are generated. The maximum of the fast ion current density occurs outside the target normal ($\Theta = 0°$) and the angular divergence of the fast ion expansion is high.

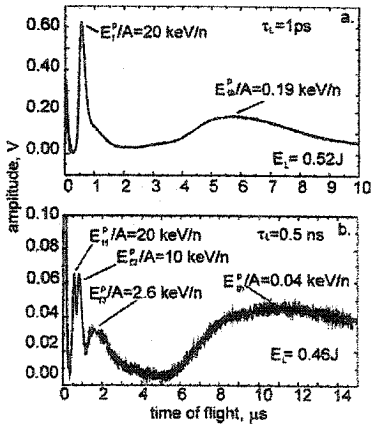


Fig.1.IC1 collector signals from Au target irradiated by 1-ps (a) and 0.5-ns (b) laser pulses. The peak ion energies per nucleon are indicated.

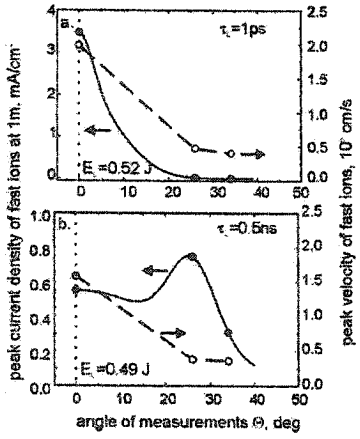


Fig.2. The rough angular distributions of peak current densities and peak velocities of backward-emitted fast ions driven by 1-ps (a) and 0.5-ns (b) laser pulses.

In the short-pulse case only a single fast ion group is generated and this group is well separated in time from a thermal ion group. The fast ions expand with small angular divergence and with a pronounced maximum along the target normal (at $\Theta \geq 26°$ only ions of the current density by more than 100 times less than those for $\Theta = 0°$ were recorded). The above features were observed independent of laser energy and of the laser focus position with respect to the target surface (within $\pm$ 0.8 mm).

Our IEA measurements showed that both for the short-pulse and long-pulse cases the fast ion groups contain highly charged ($z \sim 20 - 30$) Au ions and contaminant species (H, C and O).

The highest charge states and maximum energies of H, C, O and Au ions measured by the IEA were comparable for both the cases.

Significant differences in properties of ion fluxes produced by ps and subns laser pulses one can also observed when dependencies of the maximum and peak (≈ mean) ion energies on laser intensity I are taken into account. For the subnanosecond pulses the ion energies follow approximately the square-root dependence on the intensity, which is consistent with the hot electron temperature dependence on $I\lambda^2$ obtained by Gitomer et al. [9] by means of a compilation of the data from various laboratories. However, for the ps pulses, the ion energies increase roughly linearly with the laser intensity.

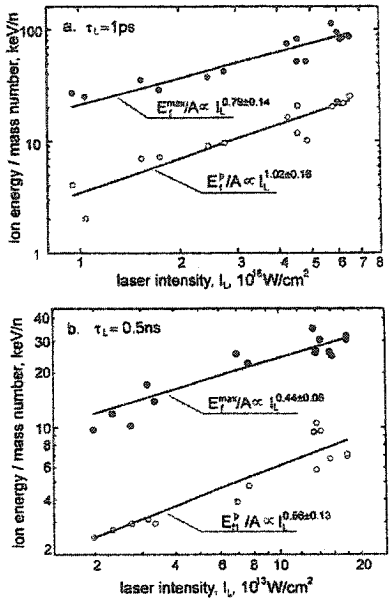


Fig.3. The maximum and the peak fast ion energies, measured in the direction normal to Au target, as a function of laser intensity for 1-ps (a) and 0.5-ns (b) laser pulses.

Contrary to the long-pulse case where self-focusing of laser beam in plasma and various plasma instabilities may contribute to the production of hot electrons and the fast ion generation [9-10] our results obtained with the ps laser pulse can be qualitatively explained when based on less complex physical picture assuming that the main role in the ion acceleration process is played by non-linear ponderomotive forces produced at the skin-layer interaction of the pulse with a thin ($L_{pre} << d_{foc}$, sec. 2) preplasma layer in front of the target [10]. In such a case, the ps laser beam interacts most intensively with the plasma in the skin layer near the surface of the critical electron density $n_{ec} = m_e\omega^2/4\pi e^2$ (ω is the laser frequency) and the geometry of the interaction is almost planar ($L_{pre} << d_{foc}$). The high plasma density gradient in the interaction region produces a non-linear ponderomotive force acting – at the laser beam incidence perpendicular to the target surface –nearly parallel to the target normal. Due to the almost one-dimensional geometry of plasma acceleration the emitted fast ion beam has a small angular divergence, as observed (Fig. 2a). The energy of ions accelerated by the ponderomotive force can be estimated from [10]: $E_i \approx (s/2)z\, m_e^{\circ} c^2[(1+ 3I/I_{rel})^{1/2} - 1]$ where $s = S - 1$, $S = 1/|n|$ is dielectric swelling factor, n is the plasma refractive index, m_e° is the electron rest mass, z is the ion charge state and $I_{rel} \approx 4.1 \times 10^{18}/\lambda^2$ [W/cm^2, μm] is the relativistic intensity.

At subrelativistic laser intensities ($I << I_{rel}$) we have $E_i \approx (3/4)sz\, m_e^{\circ} c^2 (I/I_{rel})$, in agreement with the roughly linear dependence $E_i(I)$ shown in Fig. 3a.

CONCLUSIONS

In conclusion, it has been shown that properties and plausible mechanisms of the fast ion generation are essentially different for plasmas produced by short (≤ 1ps) and long (> 0.1ns) laser pulses. In the long-pulse case several groups of fast ions are emitted into a wide solid angle and self-focusing of the laser beam in plasma and various plasma instabilities seems to determine the ion flux properties. In the short-pulse case only a single fast ion group with a small angular divergence is generated and ions are likely to be accelerated by an axial ponderomotive force produced at the skin-layer interaction of the pulse with a preplasma layer in front of a target. For applications of laser-driven ion fluxes the short-pulse laser-plasma interaction can be more favourable due to better temporal and spatial characteristics of the ion flux and a higher fast ion current.

REFERENCES

(1) H. Haseroth and C.E. Hill, Rev. Sci. Instrum., **67**, 1328 (1996).
(2) M. Roth et al., Phys. Rev. Lett. **86**, 436 (2001).
(3) F.P. Boody et al., Laser Part. Beams, **14**, 443 (1996).
(4) S.V. Bulanov et al., Phys. Lett. A **299**, 240 (2002).
(5) E. Woryna et al., Appl. Phys. Lett. **69**, 1547 (1996), L. Láska et al., Rev. Sci. Instrum. **69**, 1072 (1998), D.G. Hicks et al., Phys. Plasmas **8**, 606 (2001), J. Wołowski et al., Plasma Phys. Control. Fusion **44**, 1277 (2002), L. Láska et al, Plasma Phys. Control. Fusion **45**, 585 (2003).
(6) E.L. Clark et al., Phys. Rev. Lett. **85**, 1654 (2000), S.P. Hatchett et al., Phys. Plasmas **7**, 2076 (2000), A. Maksimchuk et al., Phys. Rev. Lett. **84**, 4108 (2000), J. Badziak et al., Phys. Rev. Lett. **87**, 215001 (2001), M. Zepf et al., Phys. Plasmas **8**, 2323 (2001), J. Badziak et al., Appl. Phys. Lett. **79**, 21 (2001), M. Hegelich et al., Phys. Rev. Lett. **89**, 085002 (2002), M. Zepf et al., Phys. Rev. Lett. **90**, 064801 (2003), J. Badziak et al., Nucl. Instrum. Meth. Phys. Res. A **498**, 503 (2003).
(7) J. Badziak et al., Opt. Commun. **134**, 495 (1997).
(8) J. Badziak et al., J. Phys. D **34**, 1885 (2001).
(9) S.J. Gitomer et al., Phys. Fluids **29**, 2679 (1986), and references therein.
(10) H. Haseroth and H. Hora, Laser Part. Beams **14**, 393 (1996), and references therein.

Detection and Evaluation of Uranium in different Minerals by Gamma Spectrometry and Laser Induced Breakdown Spectroscopy

F. M. Sergani[*], M.A. Khedr[*], Sayed A. El Mongy[**] and M. A. Harith[*].
** National Institute of Laser Enhanced Sciences (NILES), Cairo University.*
*** National Center for Nuclear Safety, Atomic Energy Authority, Nasr City, Cairo.*
sayedelmongy@hotmail.com

ABSTRACT

Analysis, detection and evaluation of source nuclear materials (e.g. uranium) in different minerals by sensitive techniques are a vital objective for uranium exploration, nuclear materials extraction, processing and verification. In this work, uranium in different geological formations was determined using gamma spectrometry and laser induced breakdown spectroscopy (LIBS). The investigated samples were collected from different regions distributed all over Egypt. The samples were then prepared for non-destructive analysis. A hyper pure germanium detector was used to measure the emitted gamma rays of uranium and its daughters in the samples. The concentrations of uranium in ppm (μg/g) in the investigated samples are given and discussed in this work. The highest uranium concentration (4354.9 ppm) was found in uranophane samples of Gattar rocks.

In Laser induced breakdown spectroscopy (LIBS) technique, plasma was formed by irradiating the rock surface with focused Q-switched Nd:Yag laser pulses of 7 ns pulse duration at the fundamental wavelength (1064 nm). Atoms and ions originating from the rock surface are excited and ionized in the laser produced hot plasma (~10 000K). The plasma emission spectral line is characteristic of the elements present in the plasma and allows identification of the uranium in the uranophane mineral. The strong atomic line at 424.2 nm is used for the qualitative identification of uranium. It can be mentioned that the elevated levels of uranium in some of the investigated uranophane samples are of great economic feasibility to be extracted.

Keywords : Gamma spectroscopy / Laser induced plasma / uranium minerals

INTRODUCTION

There are many destructive and non-destructive techniques to be used for the analysis of uranium. This work aims at using of γ-radiation and LIBS for the detection of uranium in different minerals selected from different areas in Egypt. Radio-analytical methods such as alpha spectrometry and mass spectrometry have traditionally been used for the determination of low-level natural radioisotopes. These methods are indispensable for detecting low nuclide concentrations, i.e. below 10^3 pg/g, at the cost of labor-intensive radiochemical processing of the sample[(1)]. In cases where low detection limits are not required, high-resolution gamma spectrometry provides the alternative of a non-destructive, multi-elemental, and less time consuming technique. Its feasibility has often been illustrated in the quantitative analysis of uranium, thorium and their decay products in environmental samples[(2)]. In LIBS technique, measurements can be carried out rapidly and on-line, thereby avoiding the long lag times associated with some other analytical techniques. In fact, elements can be identified in minutes once a reference database has been established and calibrations have been made. Because the laser beam is focused to a small spot (1–50μm), the technique provides spatial resolution of the sample composition for the evaluation of inhomogeneities. This method can also be adapted for remote analysis, which is particularly useful in radioactive environments[(3)]. On the other hand, most of destructive analytical procedures for the determination of uranium and thorium show difficulties with Egyptian iron rich silicate rocks[(4,5)] (e.g., hematitized granites).

DESCRIPTION OF THE INVESTIGATED SAMPLES

Seven Uranophane samples were collected in December 2002 from Gebel Gattar (height; 1965 m.), which is located in the Northern part of the Eastern desert, 35 km NW Hurghada city. The area is located between latitudes 27^0 12 30 and 27^0 21 59 and Longitudes 33^0 12 30 and 33^0 25 00 E. Gebel Gattar area has a rugged mountainous nature and is traversed by few major wadis[6].

Eleven rock samples were also collected from different areas distributed all over Egypt. All the collected samples were crushed, sieved, and packed in 100 ml containers for gamma ray analysis. The rock samples without any changes in their morphology were investigated by LIBS. The uranophane samples were palletized in the form of disc for LIBS investigation. Standard materials containing well-known concentration of uranium were used for quality control and calculation of the uranium concentration.

MATERIALS AND METHODS

1- Gamma Spectrometry

Gamma ray spectrometry is a powerful technique for determining qualitative and quantitative low-level natural and artificial radioactivity in environmental, nuclear materials and geological samples through their gamma- ray emission[7]. Gamma ray spectrometer equipped with hyper pure germanium detectors was used in this work. It consists of a hyper pure germanium detector (Tennelec Model) of a planar configuration with a high voltage power supply (negative polarity),a spectroscopy amplifier ,An analog –to-digital converter (ADC) and a 8192 multi-channel analyzer (MCA). The HPGe gamma ray spectrometer used has efficiency of 40% and a resolving power of 1.95 at 1332 keV of Co-60, a course and fine gain control of the spectroscopy amplifier; its differentiating and integrating time constants and all other parameters were adjusted before measurements. The best energy resolution and good linearity of the spectrometer were also selected.

2- Laser Induced Breakdown Spectroscopy (LIBS)

LIBS is a promising method which enables the elemental analysis of various rock samples in a small volume, based on atomic emission lines. When a powerful pulsed laser is focused on a surface, a tiny amount of the material is vaporized and through further photon absorption, it is heated until it ionizes[3]. This laser-induced plasma is a micro-source of light that can be analyzed by a spectrometer. The Nd: Yag laser is operated at the fundamental wavelength (1064nm). The target sample could be positioned and moved in all directions by micrometer screws with respect to the laser beam. The target could be rotated around an axis normal to the optical plane formed by the intersection between the laser beam and the optical axis of the spectrometer, thus allowing the laser to bombard the rock surface at variable angles[3]. The light emitted from the plasma was imaged 1:1 by a second quartz lens with focal length = 25 cm, into the entrance slit, typically a 20 μm-wide, of CM 112-cvi-sp (1/8 meter). The spectrometer has a grating with 1200 grooves per mm blazed at 250 nm, and a reciprocal linear dispersion of 0.63 nm/mm. The emission spectra were monitored by a CCD Camera Apogee (as given in figure 1). The obtained spectra consist of lines corresponding to the uranium element evaporated from the rock surface.

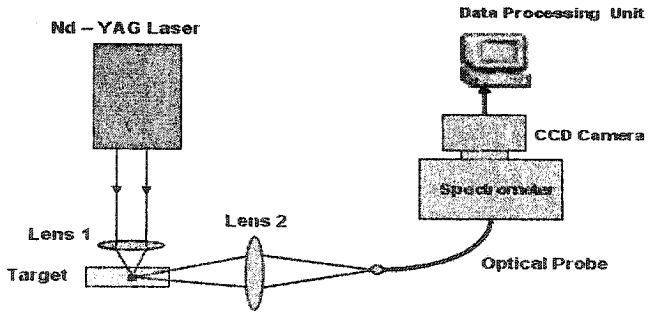


Fig.(1) LIBS Experimental Setup

RESULTS AND DISCUSSION

The results of the gamma spectrometric analysis of uranophane rock samples show that the uranium concentrations exhibited a remarkable variation (Figures 2,3 and Table 1). The uranium concentration in the analyzed rock samples ranged from 3.8 ppm to 4354.9 ppm.

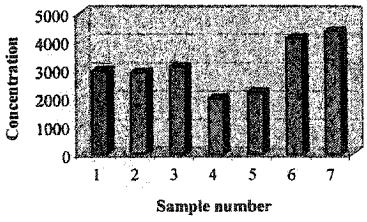


Figure (2) Variation of uranium concentration in different rocks samples (ppm)

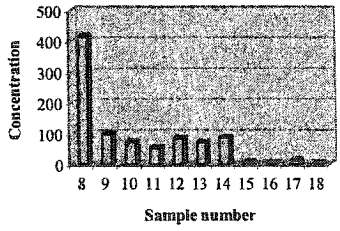


Figure (3) Variation of uranium concentration in different rocks samples (ppm)

Such remarkable variation reflects a lesser homogeneity than expected and may be indicative of a difference in the environment, which might have prevailed during the deposition. It is also possible that inhomogeneity might have been acquired post depositionally due to either water leaching or enrichment.

The possibility of oxidation of U(IV) to U(VI) to form the more mobile uranyl compound (UO_2)—followed by leaching would eventually result in lowering the initially higher U content . This situation could be also facilitated by the radioactive decay of U(VI)[8]. The post-depositional environment of uranium in the younger pink granites at Gattar II North Eastern desert, Egypt is more favor. Geological exploration in this area shows relatively high alteration products where considerable hematization resulted in an iron content ranging from 3-7%. Iron had been liberated from iron sulphide mineral whose oxidation gives sulphate iron in acid solution[9,10]. Sulphate, like carbonate (CO_2/P_2O_8), forms complex compounds with uranyl ion[9,10]. The sulphate complexes are not so stable as those with carbonate but are sufficiently stable to increase the solubility of U(VI) mark ably[9]. This indicates that the uranyl sulphate dissolved in water would have a few percent of its uranium available as uranyl ion[9,10].

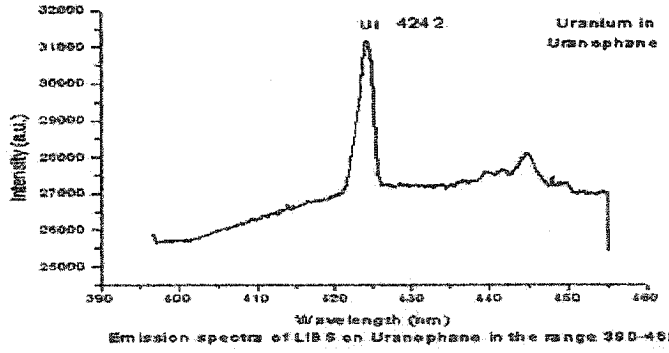


Figure (4) The Emission Spectrum of LIBS on Uranophane Rock

The spatial distribution of uranium plasma produced by applying the LIBS technique on uranophane rock surface was studied. It was found that as the distance from the target varies in mm, the spectral line intensity changes. The figure (4) shows the spectral line intensity of uranium at wavelength 424.2 nm (424.2 nm) in the range 390-460 nm.. The value between brackets is the literature value. The uranium element in all the investigated uranophane samples was also detected by LIBS at the same wavelength (424.2 nm). The high uranium content in the investigated uranophane samples shows the

economic importance of such ore. Extraction of uranium from such complexes will be of great economic feasibility. The same result has been recently published[11]. As a matter of fact, uranium concentration of 500 ppm is economically feasible to be extracted[12].

Table 1 The Gamma Spectrometry Results of the Analyzed Rock Samples

Sample Site	Serial No.	Site Description	U Concentration (ppm)
Gattar 1	1	Northern part of the Eastern desert	2958.7
Gattar 2	2	Northern part of the Eastern desert	2887.5
Gattar 3	3	Northern part of the Eastern desert	3088.8
Gattar 4	4	Northern part of the Eastern desert	4116.8
Gattar(R1)	5	Northern part of the Eastern desert	1977.1
Gattar(R2)	6	Northern part of the Eastern desert	2190.8
Uranophane	7	Northern part of the Eastern desert	4354.9
Monazite	8	Rosetta	415.8
Zircon	9	Rosetta	74.3
Zirconium	10	Rosetta	99.1
Routile	11	Rosetts	56
Phosphate	12	Assuit	85.4
Phosphate	13	Abu-Zaabal	73.2
Phosphate	14	Kafr El Zeit	87.8
Manganeese	15	Um Bogma, Sinai	7.1
Manganeese	16	South Egypt	6.1
Illiminite	17	Rsetta	14.7
Granite	18	Aswan	3.8

CONCLUSION

Based on the non-destructive Gamma and LIBS assay, it can be concluded that the investigated minerals contain uranium with wide variation and high concentration: from 3.8 ppm to 4354.9 ppm. This means that some of the analyzed samples especially Gattar granite (uranophane) are of economic concern. The economic feasibility study concerning extraction of uranium from Gattar (uranophane) rock is highly recommended. The techniques used are sensitive enough to detect uranium in different minerals with high accuracy.

REFERENCES

(1) Bickel et al.,2000. Radiochemistry: Inconvenient but Indispensable, Applied Radiation and Isotopes 53, 5-11.

(2) Bunzl et al., 1994. Transect survey of Uranium, Lead and Potassium in an agricultural soil near an exhaust-ventilating shaft of a uranium mine. The Science of the Total Environment 149, 225-232.

(3) Sergani 2001., Msc.,Elemental analysis of some minerals using LIBS., NILES, Cairo Uni, Egypt.

(4) Adams, J.A.S. and William, J., Maeck, Journal of Analytical Chemistry, 26, 1635-1639 (1954).

(5) Tesuya,Kiriyama and Rokuro Kuroda, Japan Analytical Chemica Acta., 71, 375-381 (1974).

(6) Roz., M.E.,1994: Geology and Uranium Mineralization of Gebel Gattar area, northern eastern desert, Egypt Msc. Fac.Sci.,AL Azhar Uni.,Cairo, Egypt.

(7) G.Routhomel, C.E.,"Applied Gamma-ray spectrometry", Pergamon press (1972).

(8) Hume, W.F., 1934:Geology of Egypt V.II part 1 Geol.Surv. Egypt.

(9) A. M. El Kammar, and F.Hassan, 1975.,Environmental Conditions Affecting the Distribution of Uranium and Rare Earth Elements in Egyptian Phosphorites.,Egypt. J. Geol.19, 169-178.

(10) M. A. Abdelhameed, 2002., Application of Acriflavine basic dye for Uranium and Thorium Analysis in Iron rich Siliate rock samples., Oriental J. Chemistry, V 18, 421-426.

(11) A. El-Shershaby, "Study of Radioactivity Levels in granite of Gable Gattar II in the north eastern desert of Egypt", Applied Eadiation and Isotopes vol. 57 (2002).

(12) David Bodonsky, " Nuclear Energy, Principles, Practices and Prospects", American Institute of Physics, New York, USA(1996).

Quantitative Elemental Analysis of Agricultural Drainage Water Using Laser Induced Breakdown Spectroscopy

M. Soliman, W. Tawfik and M.A. Harith
National Institute of Laser Enhanced Science (NILES), Cairo University, Cairo, Egypt

ABSTRACT

Application of laser induced breakdown spectroscopy (LIBS) to the qualitative and quantitative analysis of trace elements in agriculture drainage water has been considered. In the present work we are studying the effect of the presence of an increasing number of different salts on the limit of detection (LOD) in agriculture drainage water.

Key Words: LIBS, toxin elements, drainage water.

INTRODUCTION

An official strategy of the Ministry of Public Works and Water Resources is to use drainage water as one of the water resources for the supply of water to newly reclaimed lands. On the other hand the drainage of municipal and industrial wastes sometimes pollutes the water in certain locations. In addition, the excessive use of fertilizers may lead to water contamination by some components such as phosphate, nitrate, and ammonia.

LIBS is a well-established analytical technique[1,2]. It can briefly be described as an elemental analysis based on the emission from plasma generated by focusing a laser beam on a sample.

LIBS was applied for experiments on liquids with different types of configurations including plasma formation on the surface[3,4], on the bulk liquid[5-9], on droplets[10,11],and on liquid jets[12-17]. Experimentally there were many problems to overcome in performing LIBS in liquids generally and in water specially.

In general, it was not possible to collect atomic line spectra from breakdown plasma originating in the bulk solution. This was mainly because of in-bulk generation of the plasma carries the penalty that plasma light observation times are extremely short, usually of the order 1 μs or less, Knopp et al.[9].

The major disadvantage of in-bulk analysis is the severely reduced plasma emission intensity in comparison with results obtained at the liquid's surface[3,4].

Different geometrical arrangements have been suggested to avoid splashing and consequent opacity of the light collecting optical components in the vicinity of the produced plasma.

Generally, time-resolved LIBS has been used to avoid the intense initial continuum emission and to improve the SNR by gating off the early stages of the plasma emission. A suitable choice of the time delays in detecting the emission spectra allows selective assignment of the resolved line emission to different elements.

EXPERIMENTAL SETUP

The plasma formation was attained with the aid of a Q-switched Nd:YAG laser (Continuum Surelite I - Nd :YAG) operating at 1064 nm (pulse duration of 7 ns). The laser beam with pulse energy of 180 mJ was transported by two reflective dichroic mirrors and focused on the water surface by a 10 cm-focal length quartz lens to generate the plasma. For agriculture drainage water quantitative elemental determination, the laser direction was tilted at an angle of 30° to the water surface to avoid water splashing. This was done using the dichroic mirror at 45° with a reflection of about 100 % for the 1064 nm. To improve data reproducibility, a low laser pulse repetition rate of 0.2 Hz was used to get rid off any shockwaves produced ripples on the water surface. A one

meter length fused-silica optical fiber mounted on a micro *xyz*-translation stage is used to collect the emission light from the plasma plume and to feed it to an Echelle spectrometer (Mechelle 7500, Multichannel instruments, Sweden). The Echelle grating spectrometers designed for operation in high orders and high angles of incidence and diffraction, can provide high resolution in a more compact size and cover a much wider spectral range than conventional grating spectrometers[18]. The Mechelle 7500 provides a constant spectral resolution (CSR) of 7500 corresponding to 4 pixels FWHM over a wavelength range 200 – 1000 nm displayable in a single spectrum. A gateable, intensified CCD camera, (DiCAM-Pro 12 bit Intensified Imaging) coupled to the spectrometer was used for detection of the dispersed light. To avoid electronic interference and jitters, the intensifier high voltage was triggered optically. Echelle spectra display, control, processing and analysis were done using both Mechelle software (Multichannel instruments, Stockholm, Sweden) and GRAMS/32 version 5.1 Spectroscopic Data Analysis Software (Galactic Industries, Salem, NH, USA).

RESULTS AND DISCUSSION

1. Optimizing the Experimental Conditions.

Using a classical LIBS configuration, however, as used for LIBS on solids with the laser beam perpendicular to the surface leads to splashing in the case of liquids. Splashing results in covering the focusing optics with droplets and, therefore, prevents further use of this technique. This can easily be explained by the fact that the plasma expansion at atmospheric pressure is directed perpendicularly to the surface. Thus, a tilted configuration (as described in the experimental setup section) can minimize this phenomenon. Another important effect is the perturbation that takes place at the water surface following each laser pulse. By using a low laser frequency of 0.2 Hz, it was shown that measurements were more reproducible. Moreover, enhancement of the data reproducibility can be achieved by accumulation of consecutively measured spectra. It was previously found that the lowest value of relative standard deviation RSD of the H_α spectral line intensity does not change significantly by increasing the number of shots more than 50; accumulating fifty spectra in each case was carried out therefore in all subsequent measurements. Mechelle software (Multichannel instruments, Stockholm, Sweden), is used to acquisit, to record and to sum separately these 50 spectra; their average value then represents a point on the calibration curve for each element at a specific concentration as will be explained below.

Another important parameter in LIBS is time resolution as already shown for solids and gases analysis[19-23]. For improving the sensitivity in any LIBS experiment. In doing so, a three dimensional display of typical laser induced plasma emission spectra captured at different delay times t_d. The time delay of 1500 ns gives an optimum S/B ratio where the emission coming from the plasma continuum does not interfere with the analytical lines of the elements of interest. A shorter time delay leads to strong background emission and a longer delay does not improve the S/B ratio. This is because, as the plasma cools down, the intensity of the ionic lines decreases, due to recombination, after reaching its maximum while neutral lines show up for longer time.

2. Trace Determination in Water, Calibration Curves and Limit of Detection

The optimized experimental parameters for laser pulse energy, gate delay time, gate width, number of accumulated single shot spectra, and geometrical arrangements are fixed for all experimental data acquisition procedures. The panoramic Echelle spectra in the spectral range 200 – 1000 nm made it possible, for the first time, to normalize the whole spectral range from the UV-emission of F2- lines at 239.27 to the far visible emission of the Ca-lines at 393.36 and 396.83 nm by the emission of the strong and well resolved H_α line at 665.27 nm applying the so-called internal standardization method. This method is based on the following principle: a number of reference samples are prepared, all having a similar and known elemental composition. Usually, in such a set of samples, a suitable element dominates (internal standard) and defines the sample properties in view of the 'matrix effects'. It is, therefore, expected that plasma emission be less affected from sample to sample.

In a LIBS experiment, the ratio of the line intensity of a trace element to the emission line of the internal standard is measured and plotted as a function of the known concentration ratios in the reference samples.

.A series of measurements between 40 ppm and the detection limits of elements Ca, Fe, Cu were performed for the agriculture drainage water matrix. Figure 1 represents linear calibration curve for Fe (373.71).

Before performing the calibration curves for the above mentioned eight elements, the agriculture drainage water sample is analyzed for these trace elements using the Atomic Absorption Spectroscopy AAS technique, and their concentration values are shown in table 2. The agriculture drainage water sample is taken from a specific agriculture field located beside a steel factory in the south of Cairo delta. Then the elements concentrations given in table 2 are taken into consideration as a background when preparing the selected elemental sample solution.

Table 2: The agriculture drainage water sample is taken from a specific agriculture field located beside a steel factory in the south of Cairo delta and the analysis is done using AAS.

Element	Fe		Ca		Cu	
Concentration (ppm)	AAS	LIBS	AAS	LIBS	AAS	LIBS
	0.85	1.27	27.89	30.2	0.1	0.1
	0.53	0.34	16.58	17.5	0.09	0.03
	0.54	0.34	14.84	15.28	0.02	0.05
	0.33	0.29	19.52	17	0.15	0.016
	0.20	0.25	31.04	17.39	0.02	0.033
	2.22	2.1	34.75	22.73	0.03	0.032
	0.4	0.7	30.83	29.52	0.12	0.035

The limit of detection was calculated from the formula [24]

$$LOD = 3\,\sigma / s,$$

where σ is the standard deviation of the background and s is the calibration slope.

A comparison of the detection limits found in this work and those reported in the literature are given in table 3.

Table 3: The LOD obtained for the measured elements in agriculture drainage water.

Element	Wavelength (nm)	Detection limit (ppm) (this work)	Detection limit (ppm) (literature)
Fe	373.71	0.65	30 (23)
Ca	393.36	0.15	0.3 (23)
Cu	327.70	0.10	7 (23)

Figure 2 represents linear calibration curve for Ca (393.36 nm), and Figure 3 represents linear calibration curve for Cu (324.70nm),

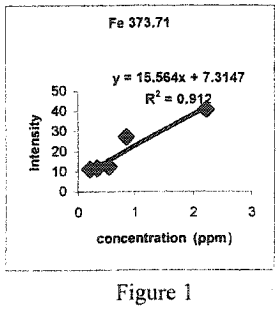


Figure 1

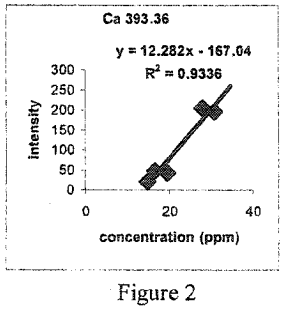


Figure 2

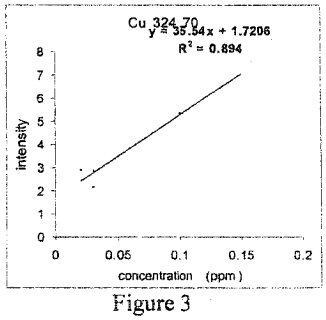


Figure 3

CONCLUSION

Exploiting the LIBS technique with an Echelle spectrometer facilitated the simultaneous multi-channel analysis in a wide spectral range, which saved time and efforts. Moreover, the use of an Echelle spectrometer coupled to an intensified CCD camera advantageously provided panoramic spectra extending over the wavelength range 200 to 1000 nm. This facilitates the normalization of the analyses line spectra by the strong and well-resolved H_α line that improves the reliability and reproducibility of the LIBS technique compared to the conventional narrow range grating spectrometer LIBS experiments. Simultaneous optimization of the experimental parameters over such wide spectral range and the use of the same delay time, gate width, laser pulse energy, number of accumulated single-shot spectra and geometrical arrangements throughout all the measurements of the selected eight elements. Elemental line intensities were monitored in the LIBS as a function of the analyte concentration to determine both the corresponding calibration curves and the detection limits. Others who performed their experiments using conventional spectrometers and re-optimizing the experimental parameters for each element compare the obtained results with previously obtained results.

REFERENCES

(1) V. Majidi. M.R. Joseph; Crit. Rev. Anal. Chem.; 23, 143 (1992).
(2) D.A. Rusak, B.C. Castle, B.W. Si-niih, J.D. Winefordner; Crit.Rev. Anal. Chem.; 27, 257 (1997).
(3) C. Area, A. Ciucci, V. Palleschi, S. Rastelli, E. Tognoni; Appl. Spectrosc.; 51, 1102 (1997).
(4) L.M. Berman, P.J. Wolf; Appl. Spectrosc.; 52, 438 (1998).
(5) J.R. Wachter. D.A. Cremers; Appl. Spectrosc.; 41, 1042 (1987).
(6) D.A. Cremers, L.J. Radziemski, T.R. Loree; Appl. Spectrosc.; 38, 721 (1984).
(7) Y. Oki, K. Furukawa, M. Maeda; Optics Comm.; 133, 123 (1997).
(8) T. Kitamori, T. Matsui, M. Sakagami, T. Sawada; Chem. Lett.; 2205 (1989).
(9) R. Knopp, F.J. Scherbaum, J.I. Kim; Fresenius J. Anal. Chem.; 355, 16 (1996).
(10) D.E. Poulain, D.R. Alexander; Appl. Spectrosc.; 49, 569 (1995).
(11) H.A. Archontaki, S.R. Crouch; Appl. Spectrosc.; 42, 741 (1988).
(12) S. Nakamura, Y. Ito, K. Sone, H. Hiraga, K.I. Kaneko; Anal. Chem.; 68, 2981 (1996).
(13) W F. Ho, C.W, Ng, N.H. Cheung; Appl. Spectrosc.; 51, 87 (1997).
(14) Y. Ito, 0. Ueki, S. Nakamura; Anal. Chim. Acta; 299, 401 (1995).
(15) N.H. Cheung, E.S. Yeung; Appl. Spectrosc.; 47, 882 (1993.).
(16) N.H. Cheung, E.S. Yeung; Anal. Chem.; 66, 929 (1994).
(17) C.W. Ng, W.F. Ho, N.H. Cheung; Appl. Spectrosc.; 51, 976 (1997).
(18) J. W. Olsen; Spectroscopy; 14, 27 (1999).
(19) M. Casini, M.A. Harith, V. Palleschi, A. Salvetti, D.P. Singh, and M. Vaselli; Laser Part. Beams; 9, 633 (1991).
(20) J.B. Simeonsson, AW. Miziolek; Appl. Opt.; 32, 939 (1993).
(21) V. Majidi, M.R. Joseph; Crit. Rev. Anal. Chem.; 23, 143 (1992).
(22) D.A. Rusak, B.C. Castle, B.W. Smith, J. D. Winefordner, Crit. Rev. Anal. Chem. 27 (1997) 257.
(23) P. Fichet, P. Mauchien, C. Moulin ; Appl. Spectrosc.; 53, 1111 (1999).
(24) J.D. Ingle Jr, S.R. Crouch; in "Spectrochemical Analysis", ed. K.M. Lafferty, Prentice Hall, New Jersey, 1988.

Laser Applications



A Comparative Study of Nd-Yag and Excimer Lasers Induced Plasma Evolution

S. Abdelli-Messaci, T. Kerdja, S. M-Aberkane, and S. Malek
Laboratoire d'Interaction Laser-Matière,
Centre de Développement des Technologies Avancées
Po. BOX 17, Baba-Hassen, Algiers, Algeria
messaci@cdta.dz

ABSTRACT

In order to have a good understanding of the link between laser ablation deposition conditions and the nature of the deposited thin film, a spatio-temporal evolution study of laser induced carbon plasma surrounded by nitrogen atmosphere is investigated. Depending on laser fluence and laser wavelength the laser ablated plasma may consist of atoms/ions, molecule or clusters. In this work, we present a comparative study of experimental results obtained using spectroscopic emission diagnostic of carbon plasma created by an excimer laser KrF (248nm,30ns) and a Néodymium-Yag laser (1.06um, 25ns).

Key Words: Pulsed Laser Deposition (PLD), Laser Ablation, Emission Spectroscopy

INTRODUCTION

In the last few years, pulsed laser deposition (PLD) has become a field of increasing importance in the growth of high-quality thin films. Pulsed laser ablation technique has been extended to deposition of several materials[1] such as superconductor, magnetic, ferroelectric and piezoelectric and mainly materiel based on carbon as nitride, diamond like carbon, fullerene and nanostructure.
The physico-chemical characteristic of deposited film depend on irradiation condition (laser energy density, laser wavelength, laser duration), the nature of ambient gas and substrate temperature.
The films obtained in vacuum present generally the same composition or close to the irradiated targets. In presence of reactif gas, the interaction process of the laser induced plasma with the ambient gas is complex. It leads to a deposited films with diverse properties. More investigations are still necessary to have a good comprehension of these phenomena.
Characterization of graphite laser ablation in nitrogen shows the presence of excited and ionized mono-atomic carbon, excited diatomic C_2 and CN molecules as well as excited and ionized nitrogen molecules and mono-atomic. The occurrence of these species and their evolution depend on laser fluence and laser wavelength[2]. The present paper studies the spatio-temporal evolution comparison of C^+, C, C_2, CN, N_2^+ and N^+ of carbon plasma induced by excimer laser and Nd-Yag laser. C, C^+, N^+ species are represented by respectively C, C^+, N^+ lines at 247.8, 426.7 and 399.5 nm respectively and C_2, CN, N_2^+ molecules by the (0, 0) band head of CN, C_2, and N_2^+ at 388.3, 516.5 and 391.4 nm respectively.

EXPERIMENTAL SETUP

A carbon plasma is induced both by a KrF excimer laser beam (λ= 248 nm, τ = 25 ns, E = 300mJ, f = 10Hz) and by a Nd-Yag laser beam (λ= 1.06 µm, τ = 25 ns, E = 100mJ, f = 0.3Hz). The laser beam is focused on a rotating graphite target at an incidence angle of 45° through a set of lenses. In the case of excimer laser, two crossed cylindrical lenses of 1 m focal length aligned with a spherical lens of 0. 5 m focal length are used. However, in the case of Nd-yag laser we have used only a spherical lens of 0.5 m focal length. The target chamber is evacuated to a pressure of 10^{-6} mbar and then is filled with nitrogen gas at a pressure of 1 mbar. The plasma emission is optically imaged on a 100 µm entrance slit of Spex spectrometer with a magnification of 1 at a right angle to the normal of the target surface. The spectral lines and molecular band emissions of different species of carbon surrounded by a nitrogen gas having a spectral resolution of 0.08 nm, are collected by a fast photomultiplier with 2.2 ns rise time. This latter is connected to a digital oscilloscope (TDS3032).

RESULTS AND DISCUSSION

In figure 1, we present the maximum emission intensity of CN and C_2 of carbon plasma induced by Nd-Yag laser at 8 and 35 J/cm^2. For both laser fluences, CN and C_2 intensity emission are involved in the same manner and the maxima of the transient maximum emission intensity of CN and C_2 are in the same region. An intensity decreasing of C_2 and CN occurs at 35 J/cm^2, and the maxima moves towards the target surface. CN emission persists up to 14mm at 8J/cm^2 and disappears at 8mm for 35 J/cm^2. This can be explained by the fact that the carbon plasma species are very energetic at 35 J/cm^2 and can lead to molecules dissociation since the band energy of CN and C_2 are respectively 7.2 and 6.2 eV. Indeed at these laser fluence the atomic carbon species are predominent and very energetic and their kinetic energy can exceed 100 eV. With 1.06 μm laser wavelength one part of laser energy creates the plasma and the second part serve to heat it. We note also that the CN and C_2 intensity emissions depend on laser fluence while those of the excimer laser induced carbon plasma do not depend on laser fluence as shown on figure 2.

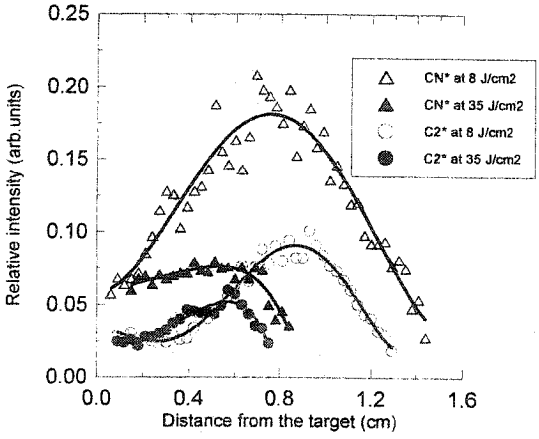


Fig. 1. C_2 and CN emission intensity as function of distance for two laser fluences of 1.06 μm radiation.

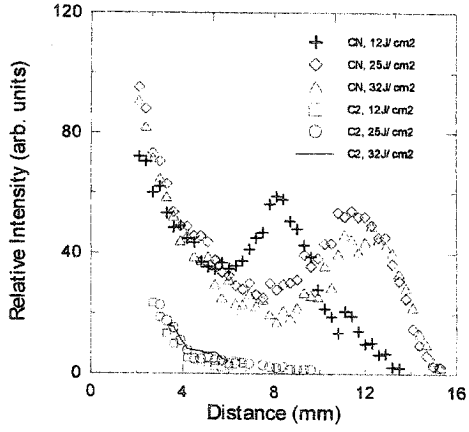


Fig. 2. C_2 and CN emission intensity as function of distance for three laser fluences of 248 nm radiation.

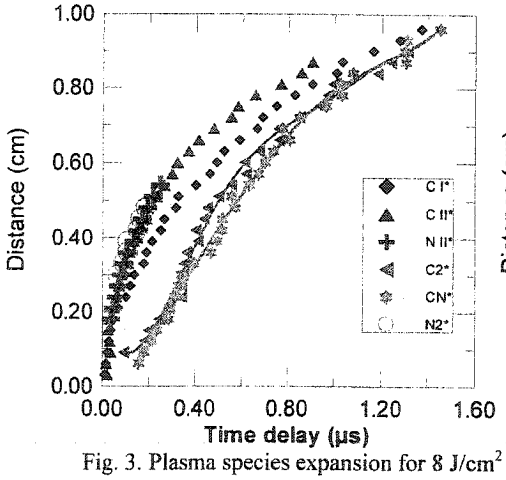


Fig. 3. Plasma species expansion for 8 J/cm^2 of laser fluence of 1.064 μm radiation.

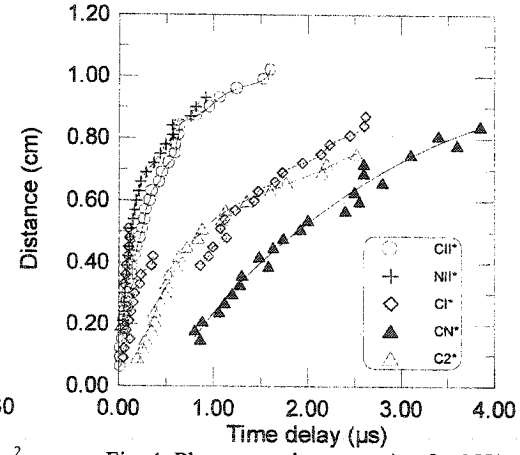


Fig. 4. Plasma species expansion for 35J/cm^2 of laser fluence of 1.064 nm radiation.

C^+, C, N^+ emissions intensity evolution are similar to that of C_2 [3] for the three laser fluences. The maximum emission intensity of CN remains constant as the fluence increases and it moves away from the target surface. The CN emission persists up to 15 mm. The localisation of the maxima of CN corresponds to the stopping distance of C^+. For 248 nm laser produced carbon plasma surrounded by 1 mbar of nitrogen pressure, C^+ and C evolution present two stage of expansion [4].The first stage is well fitted using drag force model and the second by the shock wave model.

At 8 J/cm^2, CN and C_2 emissions are strongly correlated as show on figure 3; CN and C_2 velocity are similar. At 35 J/cm^2, CN and C_2 emissions are not correlated [5] and the CN velocity is lower than that of the C_2 (figure 4).

The behaviour of CN evolution in comparison with that of C_2 evolution does not change with laser fluence for 248 nm laser induced carbon plasma. The C_2 velocity remains lower than the CN one for the three laser fluences for distances up to 4 mm (figure 5). For distances above 8 mm from the target surface the CN evolution follows the C, C^+ and N^+ evolutions.

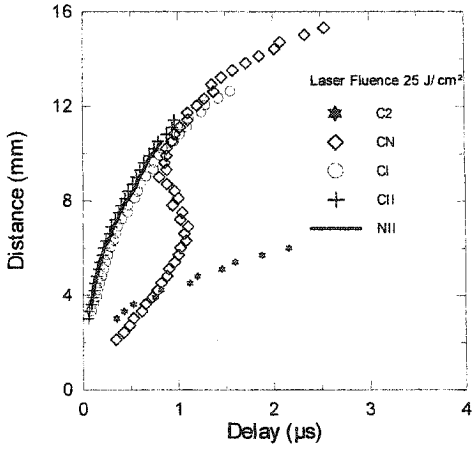


Fig. 5. Plasma species expansion for 25J/cm^2 of laser fluence of 248 nm radiation.

CONCLUSION

We have investigated the excimer and Nd-Yag laser ablated graphite target in presence of a nitrogen ambience by emission spectroscopy diagnostic. The spatio-temporal evolution of plasma species were compared between those produced by 248 nm excimer laser and those by 1.06µm Nd-Yag laser. We have found that the plasma species evolution depend on laser fluence and laser wavelength. But in the case of 1.06 µm laser induced carbon plasma we found that depend also on laser fluence.

REFERENCES

(1) D.B Chrisey and G.K. Hubler, *Pulsed Laser Deposition of Thin Films*, (Wiley and Sons, NewYork 1994)

(2) A.A. Voevodin, J.G. Jones, and J.S. Zabinski, J. Appl. Phys., **92**, 2, 2002, 724.

(3) S. Abdelli-Messaci, T. Kerdja, S.M-Aberkane, A.Bendib, S. Lafane, K.Yahiaoui and S. Malek, Proceedings ISPC 16, June 21,Taormina, Italy, 2003.

(4) S. Messaoud-Aberkane, T. Kerdja, S. Abdelli, S. Nait-Amor, S. Lafane, S. Malek and K. Yahyaoui, Proceeding IGPIGXXVI, July 15, Greifswald , Germany, 2003.

(5) S. Abdelli-Messaci, T. Kerdja, A. Bendib and S. Malek; J. Phys. D: Appl. Phys. **35**, 2772, (2002).

Modelling of Vapour Expansion in Deep Penetration Laser Welding

E.H. Amara[1], R. Fabbro[2] and A. Bendib[3]
[1]Centre for Development of Advanced Technologies, Po. Box 17, Baba Hassen, Algiers, Algeria
[2]Coopération Laser Franco-Allemande, 16 bis Av. Prieur de la Côte d'Or 94114 Arcueil, France
[3]Houari Boumedienne University of Sciences and Technologies, Bab-Ezzouar, Algiers, Algeria
amara@cdta.dz

ABSTRACT

In order to obtain the vapour parameters distribution inside a keyhole induced during laser welding , the local absorbed laser intensity on keyhole walls is firstly calculated by ray-tracing. The vapour ejection velocities on the walls are thus deduced and used as boundary conditions to solve the hydrodynamic equations describing the vapour flow. The finite volume method used to solve numerically the equations in steady state case, allows to obtain the distribution of the vapour density, pressure, temperature and velocity inside the keyhole. The role of the outside pressure on the vapour parameters distribution is investigated.

Keywords: keyhole, ray-tracing, vapour ejection, vapour flow.

INTRODUCTION

In laser welding the energy is deposited deeply inside a narrow cavity created by the incident beam. This cavity, surrounded by the melted metal, is maintained open by continuous vaporization of the material. The induced vapour pressure acts with the ablation pressure against the pressures due to the liquid flow and surface tension effect to avoid cavity collapsing. As suggested in ref.(1), the vapour pressure induced by the laser beam on the keyhole wall, might have some stabilizing effects by providing a more uniform distribution of the pressure on the wall. It is the aim of our work to obtain the distribution of the vapour parameters (density ρ , pressure p, temperature T, velocity v) inside the keyhole and especially on the walls. In this paper, a keyhole profile obtained by a self-consistent calculation[(1)] is used in our treatment. In our ray-tracing procedure, the laser beam aperture inside the cavity and the multiple reflections effects are taken into account. The ray-tracing allows to obtain the local absorbed intensities and the local surface temperature on the keyhole walls. The deduced local gas ejection velocities on the edge of Knudsen layer, constitute the boundary conditions of the finite volume problem describing the vapour hydrodynamic.

THE LOCAL ABSORBED INTENSITY

A ray-tracing technique is used to follow the rays constituting the laser beam from their entrance inside the keyhole till leaving it after they have undergoing a given number of reflections on the walls while an amount of the laser energy is locally absorbed at each reflection. A given region will be irradiated and thus will absorb the laser energy once or more time depending on its illumination by the laser beam during the multiple reflection process. The successive energies deposited after each reflection on a given area are summed and the total local absorbed intensity is deduced. The focal spot radius used in the ray-tracing procedure can be deduced from the expression[(2)]:

$$r_1=\frac{2\lambda_1 f Q}{\pi d_1} \qquad (1)$$

where Q is the beam quality factor, d_l the diameter, λ_l the wavelength, and f the focale length of the lens. To obtain the absorbed power density on a given region of the keyhole wall, a gaussian beam shape is subdivided in a given number of intervalles. The obtained impact coordinates of two close rays on the keyhole wall, allows to obtain the local laser absorbed intensity knowing the local incident intensity deduced. The energy remaining from a previous impact propagates inside the cavity while an amount of it is deposited during local absorption at each wall striking. An attenuation of the beam is expected during its travel accross the vapour. The local absorbed intensity depend on the incidence angle of the rays on the walls, the incident intensity, the absorption coefficient of the material and the vapour attenuation. The absorbed intensity eq.(2) serve to heat the liquid region and to vapourize it.

$$I_{abs} = A_o\, I_{inc} \cos(\alpha_{inc})^{q+1} \exp(-\mu\, d_p) \qquad (2)$$

THE BOUNDARY CONDITIONS

The local surface temperature[3-4] determination would allow to know some interesting quantities such as the recoil pressure, the evaporation front and ejected vapour velocities, the mass flux .... Our approach consist in the comparison of the laser absorbed intensity given by Semak's model[5] to that we obtain by using the ray-tracing procedure. Semak gives the absorbed intensities, knowing the drilling and melt ejection speeds as a function of the liquid surface temperature. Considering the mass flux conservation :

$$\rho_m v_v = \rho_g v_g \qquad (3)$$

where v_v is the evaporation front velocity inside the liquid region, v_g the vapour ejection velocity , ρ_m and ρ_g are respectively the melt and the vapour densities. And supposing that the vapour is a perfect gas we can states :

$$\rho_g = (M_a/N_a k_B) P_s/T_s \qquad (4)$$

P_s is the saturated pressure given in (5), T_s is the deduced surface temperature, M_a the atomic mass of the material, N_a Avogadro number and k_B Boltzmann constant.We can thus obtain the gas velocity at the edge of Knudsen layer by combining (3) and (4) :

$$v_g = \rho_m v_v\, (N_a k_B\, T_s / M_a P_s) \qquad (5)$$

and deduce the ablation pressure given by :

$$P_a = \rho_g\, v_g^2 /2 \qquad (6)$$

The calculated gas ejection velocities, dependent on the deduced local surface temperature which depend itself on the local absorbed intensity, are used as boundary condition for the numerical treatment of the vapour flow problem.

VAPOUR FLOW MODELING

The vapour induced by wall evaporation is considered as a compressible ideal gas. The compressibility effects are encountered in gas flows at high velocity and/or in which there are large pressure variations. When the flow velocity approaches or exceeds the speed of sound of the gas or when the pressure change in the system is large, the variation of the gas density with pressure has a significant impact on the flow velocity, pressure, and temperature. To solve our vapour compressible flow problem, we have used FLUENT softwares, composed of the pre-processor Gambit12 used for setting geometry, meshing and boundary types of our domain, and Fluent6 to perform the calculations and post-processing. An implicit scheme is used and the Spalart –Allmaras model that solves a modeled transport equation for the turbulent viscosity is suitable for solution convergence.

RESULTS AND DISCUSSIONS

Among the results given by our modeling we present the distributions of density, pressure, temperature, velocity of the flow inside a self-consistent keyhole taken from ref. (1), for different ambiant pressures.We note on figures (1),(2),(3) where (a), (b), (c) and (d) correspond respectively to ambiant pressures equal to: 0.1 atm, 1 atm, 5 atm, and 10 atm, that the distribution of the density, pressure and temperature inside the keyhole becomes more or less uniform as the outside ambiant pressure grows.

Indeed compressible flows can be characterized by the value of the Mach number M=v/c, where $c=(\gamma RT)^{1/2}$ is the local speed of sound in the gas. At Mach numbers much less than 1, compressibility effects are negligible and the variation of the gas density with pressure can safely be ignored in the flow modeling. As the Mach number approaches 1, compressibility effects become important. When the Mach number exceeds 1, the flow is termed supersonic, and may contain shocks and expansion fans. which can impact the flow pattern significantly.It is shown on figures (4) representing the velocity distribution that more the ambiant pressure is low more the flow become supersonic. At an ambiant pressure of 1 atm the flow is supersonic at the throttle of the cavity, whereas it is supersonic and reaches a value of Mach 2 at the exit of the cavity when the ambiant pressure equal 0.1 atm. For the higher ambiant pressures the flow is subsonic over all the cavity due to the quasi uniformity of the pressure distribution inside the keyhole. The occurence of some friction effects can be concluded and this fact can make evident the contribution of the vapour on stabilizing the keyhole wall by acting against the pressures that tend to obliterate the cavity. We note that this effect is important at low ambiant pressures (0.1 atm), where high values of the x-velocity and its direction toward the liquid region especially at keyhole rear side where the bulk of liquid metal is present.

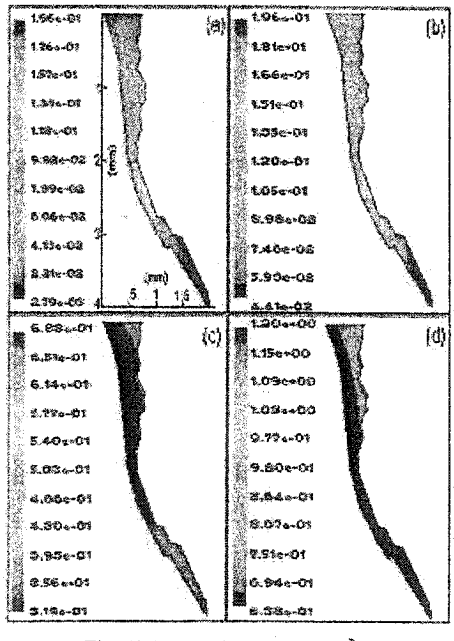


Fig.(1) vapour density (kg/cm^3)

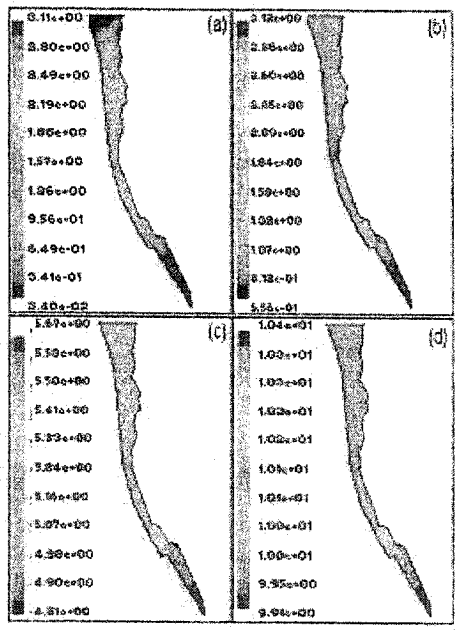


Fig.(2) vapour static pressure (atm)

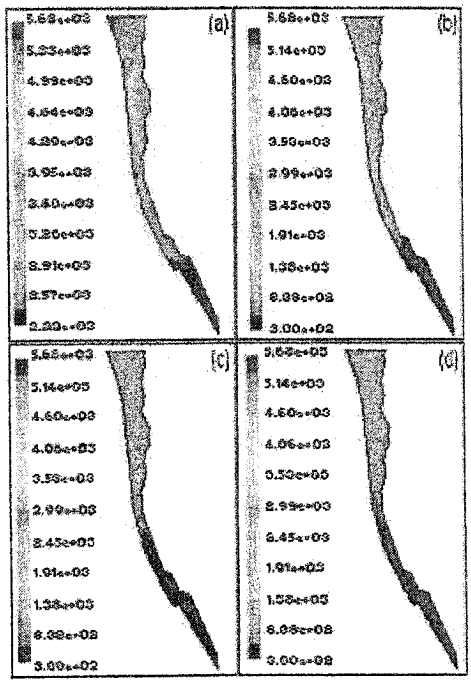


Fig.(3) static temperature (K)

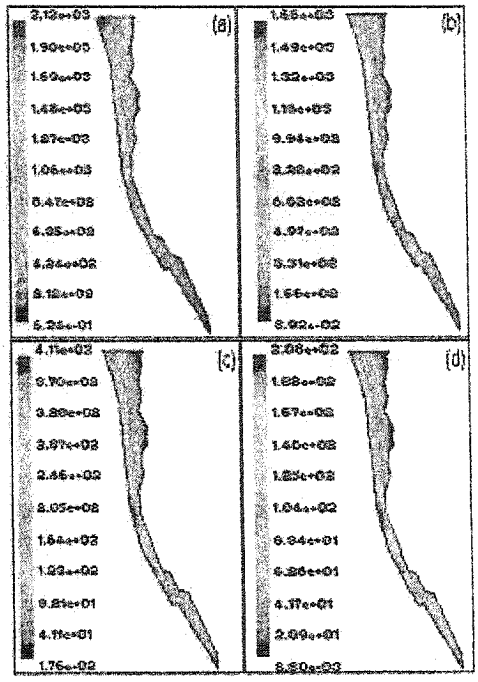


Fig.(4) velocity magnitude (m/s)

CONCLUSION

The results of ray-tracing procedure make clearly evident the importance of considering the role of the multiples reflections in the physics processes occuring inside the keyhole. Indeed, the knowledge of the local laser absorbed intensity is necessary to estimate the vapour parameters distribution[6-7] inside the keyhole and especially on the walls. The role of the vapour pressure have to be taken into account in self-consistent keyhole profile calculation.

REFERENCES

(1) R. Fabbro and K. Chouf ; J. Appl. Phys.; 87, 4075 (1999)
(2) A. Kaplan ; J.Phys.D :Appl.Phys.; 27, 1805 (1994)
(3) P. Solana and J.L. Ocana ; J.Phys.D :Appl.Phys.; 30, 1300 (1997)
(4) C.J. Knight ; AIAA Journal ; 17, 519 (1979)
(5) V. Semak and A. Matsunawa ; J.Phys.D : Appl.Phys. ; 30, 2541 (1997)
(6) E.H. Amara and A. Bendib ; J. Phys. D : Appl. Phys. ; 35, 272 (2002)
(7) E.H. Amara , R. Fabbro and A. Bendib ; J. Appl. Phys.; 93, 4289 (2003)

Experimental and Theoretical Investigations of Craters Formation in Solid Targets Under the Action of Powerful Laser Pulse

T. Pisarczyk[a], S. Gus'kov[b], Ya. Doskach[b], A. Kasperczuk[a], S. Borodziuk[a], M. Kalal[e], E. Krousky[d], J. Limpouch[d,e], K. Masek[d], P. Pisarczyk[f], K. Rohlena[d], V. Rozanov[b], J. Ullschmied[c]

[a]*Institute of Plasma Physics and Laser Microfusion, 23 Hery St., 00-908 Warsaw 49, Poland*
pisaro@ifpilm.waw.pl
[b]*P.N. Lebedev Physical Institute of RAS, 53 Leninski Ave., 119991 Moscow, Russia*
[c]*Institute of Plasma Physics of the AS CR, Za Slovankou 3, 182 21 Prague 8, Czech Republic*
[d]*Institute of Physics of the AS CR, Na Slovance 2, 182 21 Prague 8, Czech Republic*
[e]*Faculty of Nuclear Sciences and Physical Engineering, Czech Technical University in Prague, Brehova 7, 115 19 Prague 1, Czech Republic*
[f] *Institute of Computer Science, Warsaw University of Technology, 15/19 Nowowiejska St. 00-665 Warsaw, Poland*

ABSTRACT

Reported investigations of the crater formation process were carried out at the PALS (Prague Asterix Laser System) iodine laser facility. The craters produced by high intensity laser pulses ($10^{13\text{-}15}$ W/cm^2) on surfaces of massive solid targets were measured using optical microscopy and wax-replica technique. Plasma expansion out of the target was observed by means of three-frame interferometry. The results are interpreted theoretically using a simplified model of the laser target interaction. Collisional and resonance absorption of the laser radiation are included, as well as the emission of fast electrons. Also taken into account are the target ablation and the shock wave propagation.

Key Words: Laser-Produced Plasma, Crater, Absorption of Laser Radiation, Interferometry

INTRODUCTION

One of the useful approaches at investigating the physics of laser matter interaction and its technological application is based on the powerful laser pulse action on a massive thick target, accompanied by creation of a crater on the target surface. Measurements of the crater parameters in different experimental conditions give possibility to study not only the general features of the shock wave dynamics in solids and the phase transition produced but also important physical characteristics of the laser-matter interaction. As it is shown in the paper, the methods of definition of the absorbed laser energy in the target, of the fractions of laser energy absorbed in evaporated and non-evaporated parts of the targets, and of the amplitude of shock wave in the solid part of the target could be developed. The main goal of the experiments was to investigate the crater formation and to measure the depth and the radius of the craters which were produced in Al massive targets under the action of laser pulses with parameters varying within a wide range of values. One- and two dimensional theoretical models of the post-pulse crater formation by the shock wave propagating and decaying in solids after the end of the laser pulse are presented and applied for explanation of the results obtained in the experiments.

EXPERIMENTAL SETUP AND RESULTS

Plasma was generated by an iodine laser beam[1] on the surface of a planar solid target, made of aluminum. Two harmonics of laser radiation: the first one with a wavelength of $\lambda_1 \cong 1.315$ μm and

the third one with $\lambda_3 \cong 0.438$ μm were used. The essential part of investigations was carried out with laser energy of $E_L \cong 100$ J and pulse duration of 0.4 ns. Additionally, some shots were performed for the energy $E_L \cong 600$ J. The investigations were carried out at different levels of intensity of the laser radiation on the target. The maximum of the intensity occurring in the focal point corresponded to the minimum focal spot radius of 35 μm. To study the plasma expansion, a three-frame interferometric system with automated image processing was used[2]. Interferometric measurements allowed us to observe the process of the outflow of plasma from the crater. Fig. 1a and Fig. 1b illustrate the outflow of plasma from the crater for the two wavelengths used.

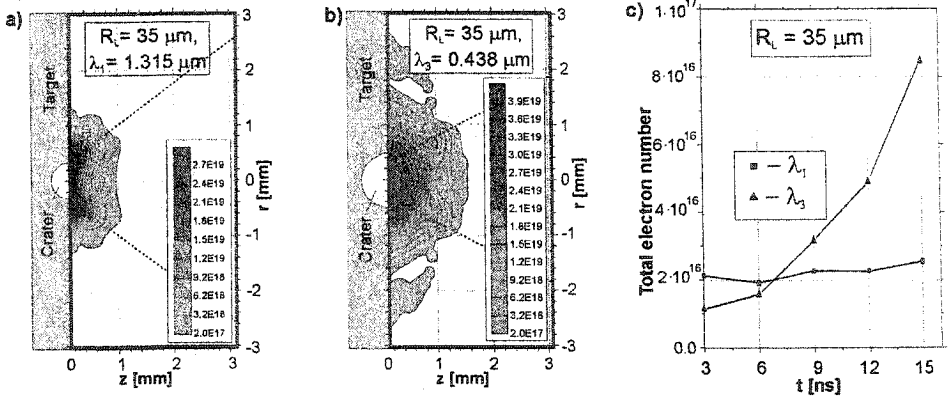


Fig. 1: Electron density in the plasma outflow from the craters at the moment $\Delta t = 15$ ns for cases: a) $\lambda_1 = 1.315$ μm, b) $\lambda_3 = 0.438$ μm, and c) variations with time of the total electron number.

With the shorter wavelength, the plasma blob has dimensions approximately twice as large as the blob generated by the longer one. The more intensive outflow of plasma results in a bigger crater. In the case of the longer wavelength, the outflow of plasma has approximately a uniform character (the total electron number is roughly conserved at the level of $2 \cdot 10^{16}$, Fig. 1c), while for the shorter wavelength the total electron number grows in time very fast, reaching a value of about $8 \cdot 10^{16}$ at the time $\Delta t = 15$ ns. Thus, such diagrams can provide information about the dynamics of the crater creation process. In other words, one may conclude that a shorter laser wavelength means deeper laser penetration (higher critical density), and more efficient collisional absorption. Consequently, the laser-induced shock wave is stronger, and the mass of the material ejected from the target and the crater volume are enhanced. The crater dimensions were obtained by means of optical microscopy measurements (Table 1). In order to obtain the shape of the craters, craters' replicas were made of wax.

DISCUSSION AND CONCLUSION

To interpret the experimental results we use the theoretical model[3] for modelling the laser radiation absorption and the crater production. In this model we include all the main physical processes taking part in the investigated phenomenon: laser energy absorption, matter evaporation and corona creation, energy transfer from the corona to the dense material of the target during the laser pulse; shock waves creation and propagation, matter melting by the shock waves and subsequent melted matter ejection from the growing crater. In the Table 1 the following values are presented:

- R_L - the laser spot radius; E_L, I and λ - energy, intensity and wavelength of the laser radiation, respectively;
- empirical values measured in the experiment: R_c and H_c - the crater radius and depth, respectively; V_c - the crater volume;

- theoretically calculated values: $\sigma = E_s / E_{ab}$ - ablation loading efficiency, E_s - energy transformed to the shock wave propagating in the condensed part of the target, E_{ab} - absorbed laser energy; $k_{ab} = E_{ab} / E_L$ - laser energy absorption coefficient.

Table 1:

	E_L=100 J, λ=0.438 μm				E_L=100 J, λ=1.315 μm			
Shot number	I_1^*	I_2	I_3	I_4	II_1^{**}	II_2^*	II_3	II_4
R_L (μm)	35	100	300	600	35	100	300	600
I (W/cm^2)	$7.1 \cdot 10^{15}$	$8.3 \cdot 10^{14}$	$8.8 \cdot 10^{13}$	$2.2 \cdot 10^{13}$	$7.1 \cdot 10^{15}$	$8.3 \cdot 10^{14}$	$8.8 \cdot 10^{13}$	$2.2 \cdot 10^{13}$
$I\lambda^2$ (W μm^2 /cm^2)	$1.3 \cdot 10^{15}$	$1.5 \cdot 10^{14}$	$1.7 \cdot 10^{13}$	$4.2 \cdot 10^{12}$	$1.2 \cdot 10^{16}$	$1.4 \cdot 10^{15}$	$1.5 \cdot 10^{14}$	$3.8 \cdot 10^{13}$
EXPERIMENT								
R_c (μm)	475	550	600	700	330	280	400	630
H_c (μm)	500	600	700	280	400	340	480	160
V_c(cm^3)	$2.1 \cdot 10^{-4}$	$3.4 \cdot 10^{-4}$	$4.9 \cdot 10^{-4}$	$3.6 \cdot 10^{-4}$	$8.8 \cdot 10^{-5}$	$5.5 \cdot 10^{-5}$	$1.4 \cdot 10^{-4}$	$1.3 \cdot 10^{-4}$
THEORY								
$\sigma = E_s / E_{ab}$	0.027	0.04	0.077	0.085	0.1	0.015	0.022	0.027
$k_{ab} = E_{ab} / E_L$	0.34	0.37	0.27	0.19	0.039	0.16	0.28	0.21

* in these cases the resonant absorption mechanism is responsible for the significant part of energy absorption, ** in this case the resonant absorption mechanism is dominant.

First of all, note the main general features of the conditions of laser-plasma interaction and the measured results. For the shots when the values of parameter $I\lambda^2$ are greater than 10^{14} W μm^2/cm^2, the resonance mechanism gives a significant contribution to the laser radiation absorption together with inverse bremsstrahlung process and one must take into account that some fraction of the absorbed laser energy (20 -30 %) transforms into the energy of fast electrons. Other shots (I_2-I_4, II_3 and II_4) have been performed in the conditions when the parameter $I\lambda^2$ was close or less than the value 10^{14} W μm^2/cm^2 and it seems reasonable to assume that the laser light was absorbed as a result of the inverse bremsstrahlung process, without generation of fast electrons. To describe the ablation pressure formation we use a self-similar solution for the isothermal expanding of the given mass of matter[4]. Taking into account the two-dimensional effect we can get the expressions for main parameters of laser-produced torch: ρ_a, c_a, p, which is the density, sound velocity and pressure of the plasma near the surface of evaporation, respectively. In addition, by taking advantage of (5) and (6) we can get formulas for σ – the efficiency of ablation loading (for both the absorption mechanism), M_c – the matter melted by the shock wave and D_s – shock wave velocity. Duration of laser pulse (τ_L = 0.4 ns) is much less than the time of crater-produced shock wave decay (several tens of nanoseconds). For this reason the matter evaporation time by laser pulse is much less than the matter emission from crater by shock wave. The velocity of laser-evaporated matter V_h is much higher than that of the shock wave-emitted matter V_c: $V_h / V_c \approx (\rho_0 / \rho_{cr})^{1/2}$ (ρ_0 is the density of solid Al, ρ_{cr} is the critical density); $V_h \approx$ (3-7) $\cdot 10^7$ cm/s, $V_h \approx$ (2-4) $\cdot 10^6$ cm/s. These features are illustrated by the data on Fig.1. The total numbers of electrons at the average ion charge Z = 5 correspond to the mass of emitted matter $7 \cdot 10^{-7}$ g (λ = 0.438 μm) and $2 \cdot 10^{-7}$ g (λ = 1.315 μm). These values are by three orders of magnitude smaller than the total crater masses ($5.7 \cdot 10^{-4}$ g for λ = 0.438 μm and $2.7 \cdot 10^{-4}$ g for λ = 1.315 μm) and mainly correspond to the masses of laser-evaporated matter. But the increase of total electron number after 6 ns for the third harmonic represents the contribution of shock wave-emitted mass. The beginning time of this contribution is the time during which the ions with the velocity $V_h \approx 4 \cdot 10^6$ cm/s fly the half of plasma torch length, approximately 500 μm. This time is about 10 ns which is in a good agreement with experimental data. The dependencies of σ and k_{ab} (the ablation loading efficiency and the laser energy absorption coefficient) on the laser spot radius are shown in Fig. 2a. One can see a dramatic

fall of k_{ab} and rise of σ for $R_L = 35$ μm at the laser wavelength $\lambda = 1.315$ μm at bigger laser spot radii. This effect is due to the change laser absorption mechanism, for the first harmonic in particular. For the bremsstrahlung absorption mechanism of the laser radiation the efficiency of ablation loading increases at the decreasing laser radiation wavelength. For the planar laser plasma expansion the efficiency of ablation loading does not depend on the laser pulse intensity and increases linearly at the decreasing laser radiation wavelength. Two-dimensional effects of the laser-produced plasma torch expansion sufficiently decrease the efficiency of ablation loading at the decreasing laser spot radius. The decrease of the absorption coefficient for the smaller radii is caused by the transition from the bremsstrahlung absorption to the resonant one. For the shorter wavelength (the third harmonic) this transition occurs at higher laser intensities (at smaller focal spot radii).

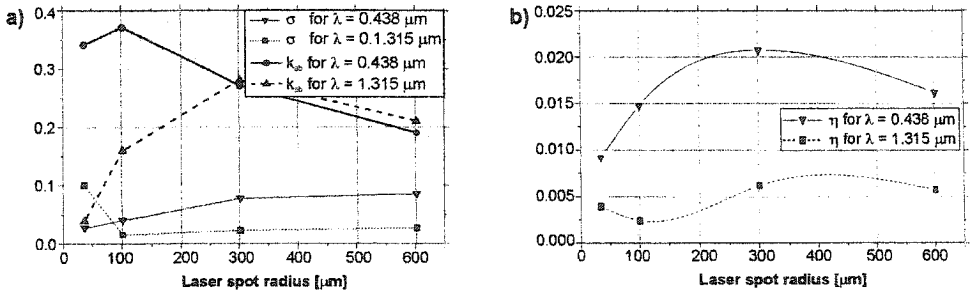


Fig. 2: Results of theoretical modeling: a) laser energy absorption coefficient and the ablation loading efficiency, and b) total laser energy transfer to the shock wave coefficient η.

In Fig. 2b the ratio of the energy transferred into the shock wave to the laser pulse energy is presented. This coefficient $\eta = \sigma k_{ab}$ shows the overall efficiency of energy transfer at the crater creation and corresponds to the mass of the ejected matter. It is obvious that η is substantially larger for the shorter wavelength. For the first harmonic a strong absorption coefficient decrease for small R_L is compensated by a sharp increase of the ablation loading. When the laser intensity increases and the wavelength decreases the average value of shock wave longitudinal velocity (along the laser pulse propagation direction) increases as $I^{1/2}\lambda^{-1/3}$. This velocity in the considered conditions falls within the range of $(1\text{-}5)\cdot 10^6$ cm/s. The transversal velocity of the shock wave near the crater hole is 1.5 - 2.5 times lower than the longitudinal one. The duration of decay of the crater-creating shock wave is in the interval (7-30) ns for different shots.

The work was partially supported by the European Committee program Transnational Access to Research Infrastructures under contract HPRI-CT-1999-0053 (PALS project 013), the Russian Foundation of Basic Research (Project # 02-02-16966) and by INTAS under the contract INTAS-01-572. Additional support was also provided by the International Atomic Energy Agency under the IFE-CRP, CZR-11655. All these financial supports are gratefully acknowledged.

REFERENCES

(1) K. Jungwirth, A. Cejnarova, L. Juha et al; Phys. Plasmas; 8, 2495 (2001).
(2) A. Kasperczuk, M. Kalal, B. Kralikova, K. Masek, M. Pfeifer, P. Pisarczyk, T. Pisarczyk, K. Rohlena, J. Skala, J. Ullschmied; Czechoslovak Journal of Physics; 51, 395 (2001).
(3) I.Ya. Doskach, T. Pisarczyk, S. Gus'kov, K. Jungwirth, M. Kalal, A. Kasperczuk, I.B. Kralikova, E. Krousky, J. Limpouch, K. Masek, M. Pfeifer, K. Rohlena, V. Rozanov, J. Skala, J. Ullschmied; ECLIM-2002 Proceedings, SPIE; vol. 5228 (2003).
(4) V.S. Imshennik; Sov. Phys. Dokl.; 5, 263 (1960).
(5) K.S. Gus'kov, S.Yu. Gus'kov; Quantum Electronics; 31, 305 (2001).
(6) S.Yu. Gus'kov, V.V. Zverev, V.B. Rozanov; Quantum Electronics; 13, 498 (1983).

Relativistic Electron Motion in Plasma During the Interaction of a Short-Intense Laser Pulse

R. Ondarza [1] and F. Gómez [2]

[1] *Instituto Nacional de Investigaciones Nucleares, A.P. 18-1027, México 11801, D.F., Mexico*

[2] *Universidad Autónoma del Estado de México, Facultad de Ciencias, Piedras Negras, A.P. 2-139, C.P. 50000, Toluca, Estado de México, Mexico*

ondarza@nuclear.inin.mx, fer@nuclear.inin.mx

ABSTRACT

The exact solution of the motion of a charged particle driven by an electromagnetic pulse shape of arbitrary polarization, propagating along the direction of an external homogeneous magnetic field is obtained from the relativistic equations. The method of solution allows to solve the trajectory of the particles driven by an electromagnetic pulse modulated by a gaussian-like envelope. The solutions reported in this work are of concern in the interaction physics of laser-produced plasmas, to study, for instance, the mechanisms of particle acceleration and plasma heating. A simple model for propagation in plasma is provided and solved from single-particle simulations.

Key Words: Relativistic motion, laser-plasma interaction.

INTRODUCTION

The interaction between charged particles and electromagnetic waves has been of fundamental importance in the study of a large number of physical phenomena, having applications, for instance, in areas related to plasma physics and particle accelerators. The motion of a charged particle in the field of a transverse electromagnetic wave propagating along a constant magnetic field was investigated by Roberts and Buchsbaum[1], who discussed the effects at cyclotron resonance of the magnetic field of the wave and the increase with energy of the relativistic mass.

The orbit solutions for the problem of a charged particle under the influence of a radiation pulse has been investigated in the past[1-3]. Krüger and Bovyn[2] integrated the force equation for a particle driven by a plane wave of arbitrary amplitude, in terms of the co-moving and inertial times. Shebalin[3] found an exact solution, as a function of the phase of the wave, for the position and velocity of a particle interacting with an electromagnetic wave. The problem of a particle embedded in an elliptically polarized wave was solved in exact form by Acharya and Saxena[4]. B.-L. Qian[5] studied the motion of a charged particle driven by a circularly polarized wave propagating along a uniform magnetic field and reported an exact solution, for certain initial conditions, and found that the particles can gain energy up to a maximum in the resonance situation for the case of a superposition of plane waves with circular polarization[6].

In Ref. 7, Ondarza solved the relativistic motion of a charged particle driven by an infinite electromagnetic wave of arbitrary amplitude and polarization propagating along the direction of an external magnetic field. The method of solution allowed to integrate in exact form the Lorentz equations yielding to analytical expressions for the electron trajectories and drift velocities of the particles. In the presence of an external magnetic field resonance effects are exhibited in the solutions.

In this paper we extend the work reported in Ref. 7 and solve the problem of a charged particle driven by an arbitrary polarized electromagnetic field. For propagation in plasma we used the model provided by Bardsley *et al.*[8] to study numerically the relativistic dynamics.

SOLUTION OF THE RELATIVISTIC EQUATION OF MOTION

The vector potential **A** associated to the radiation field can be expressed in a normalized form as $a_0 = e A / m_0 c^2$, where e, c and m_0 stand for the electron charge, the speed of light in vacuum, and the electron rest mass, respectively. The equation for a relativistic electron in plasma under the action of a laser field propagating along the x direction of an applied external homogeneous magnetic field $\boldsymbol{B}_0(x)$ is

$$\frac{d\mathbf{p}(\mathbf{r},t)}{dt} = e\,\mathbf{E}(\mathbf{r},t) + \frac{e}{c}\mathbf{v}(\mathbf{r},t)\times\left(\mathbf{B}(\mathbf{r},t)+\mathbf{B}_0\right) - m_0\omega_p^2\,\mathbf{x}\,, \qquad (1)$$

where γ is the relativistic factor given by $\gamma = (1-\beta^2)^{-1/2}$ and $\beta = |v|/c$. $\boldsymbol{E}$ and $\boldsymbol{B}$ denote the electric and magnetic fields of the wave and ω_p is the plasma frequency. The last term corresponds to the harmonic restoring force of the plasma.

The vector potential, for a monochromatic plane wave of arbitrary polarization, can be expressed as[9] $\boldsymbol{A}(r,t) = a(\eta)\,\boldsymbol{A}(\eta)$, where $\boldsymbol{A}(\eta)$ stands for $\boldsymbol{A}(\eta) = (0, (1-\delta^2)^{1/2}\sin\eta, \delta\cos\eta)$, and $a(\eta)$ gives the shape of the pulse. Here, $\eta = \omega(t - x/c)$ is the invariant phase. The parameter δ characterizes the degree of polarization $(0 \le |\delta| \le 1)$ and is given by

$$\delta = \begin{pmatrix} 0, \ \pm 1 & \text{linear polarization} \\ \pm\dfrac{1}{\sqrt{2}} & \text{circular polarization} \end{pmatrix}$$

From the expression for the vector potential and the field equations, the particle motion is given by the set of equations

$$\begin{aligned}
\frac{d(\gamma v_x)}{dt} &= -a_0\,\omega\left\{\frac{\partial a}{\partial\eta}\left((1-\delta^2)^{1/2} v_y \sin\eta + \delta v_z\cos\eta\right) + a\left((1-\delta^2)^{1/2} v_y\cos\eta - \delta v_z\sin\eta\right)\right\} \qquad (2)\\
\frac{d(\gamma v_y)}{dt} &= -a_0\,\omega\,c\,(1-\delta^2)^{1/2}\left\{\frac{\partial a}{\partial\eta}\sin\eta + a\cos\eta\right\}\left(1-\frac{v_x}{c}\right) + \alpha v_z,\\
\frac{d(\gamma v_z)}{dt} &= -a_0\,\omega\,c\,\delta\left\{\frac{\partial a}{\partial\eta}\cos\eta - a\sin\eta\right\}\left(1-\frac{v_x}{c}\right) - \alpha v_y\\
\frac{d(\gamma c)}{dt} &= -a_0\,\omega\left\{\frac{\partial a}{\partial\eta}\left((1-\delta^2)^{1/2} v_y \sin\eta + \delta v_z\cos\eta\right) + a\left((1-\delta^2)^{1/2} v_y\cos\eta - \delta v_z\sin\eta\right)\right\}
\end{aligned}$$

where $\alpha = e\lambda|\boldsymbol{B}_0| / m_0 c$ is the electron cyclotron frequency and $\lambda = \pm 1$ if $\boldsymbol{B}_0$ is along $\pm x$. The last equation is obtained from the rate of change of the kinetic energy of the particle with time.

Equating the first and the last equations of the system above we have that $1 - dx/cdt = 1/\gamma$. Integrating Eqs. (2), and choosing a pulse shape in the form $a = a(\eta) = \sin^2(N\eta)$, where N is chosen to set the number of optical cycles in the pulse. We arrive then at the differential equations

$$y''+A^2 y + B_1 N \sin\eta \sin(2N\eta) + C_1 \cos\eta \sin^2(N\eta) = 0,$$

$$z''+A^2 z + B_2 N \cos\eta \sin(2N\eta) + C_2 \sin\eta \sin^2(N\eta) = 0, \qquad (3)$$

where

$$A=\frac{\alpha}{\omega},$$

$$B_1=\frac{a_0 c}{\omega}\left(\left(1-\delta^2\right)^{1/2}+\alpha\delta\right), \qquad B_2=\frac{a_0 c\,\delta}{\omega},$$

$$C_1=\frac{a_0 c}{\omega^2}\left(\omega\left(1-\delta^2\right)^{1/2}+\alpha\delta\right), \qquad C_2=-\frac{a_0 c}{\omega^2}\left(\alpha\left(1-\delta^2\right)^{1/2}+\omega\delta\right),$$

and where we have applied the initial condition $a(\eta) = 0$. The prime denotes the derivative respect the phase η.The equation for the longitudinal displacement can be obtained from the equation for the total energy $E^2 = p^2c^2 + m_0^2c^4$ and the expression $m_0\gamma v_x = - m_0 c(1-\gamma)$. From these equations we get that the coordinates are related by

$$\left(\frac{dx}{d\eta}\right)^2=\frac{k}{2}\left\{\left(\frac{dy}{d\eta}\right)^2+\left(\frac{dz}{d\eta}\right)^2\right\} \qquad (4)$$

where we have used that $d\eta/dt = \omega/\gamma$ and $\kappa = \omega/c$. Solving the system of equations (3) and substituting in (4), we find that the solution for the coordinates is given by

$$y(\eta) = y_1 \cos\eta + y_2 \cos a\eta + y_3 \cos b\eta + y_4 \cos A\eta$$

$$z(\eta) = z_1 \sin\eta + z_2 \sin a\eta + z_3 \sin b\eta + z_4 \sin A\eta$$

$$x(\eta) = \frac{k}{4}\sum_{i=1}^{4}\beta_i\left[\beta_i\left(y_i^2+z_i^2\right)\eta+\frac{\left(z_i^2-y_i^2\right)}{2}\sin 2\beta_i\eta\right] \qquad (5)$$

$$+\frac{k}{4}\sum_{i,j=1}^{4}\frac{\beta_i\beta_j^*}{\beta_i\mp\beta_j^*}\left(z_i z_j^* \pm y_i y_j^*\right)\sin\left(\beta_i\mp\beta_j^*\right)\eta$$

where

$$y_1=\frac{C_1}{2(1-A^2)},\ z_1=\frac{C_2}{2(1-A^2)},\ y_2=-\frac{C_1+2NB_1}{4(a^2-A^2)},\ z_2=-\frac{C_2-2NB_2}{4(A^2-a^2)},$$

$$y_3=-\frac{C_1-2NB_1}{4(b^2-A^2)},\ z_3=-\frac{C_2-2NB_2}{4(b^2-A^2)},\ y_4=-(y_1+y_2+y_3),\ z_4=-\frac{1}{A}(z_1+a z_2+b z_3)$$

Here

$$a = 1 + \frac{2}{N}, \quad b = 1 - \frac{2}{N}, \quad \beta_i = (1, a, b, A), \quad \beta_j^* = (A, b, a, 1)$$

$$y_i = (y_1, y_2, y_3, z_4), \quad y_j^* = (y_4, y_3, y_2, y_1), \quad z_i = (z_1, z_2, z_3, z_4), \quad z_j^* = (z_4, z_3, z_2, z_1),$$

have been introduced for convenience.

After some cumbersome algebra, the equations above were solved in exact form to obtain the solution to the problem. We present in the poster both the complete solution to the equation of motion and its numerical integration. The case of the particle propagation through plasma was solved by means of single-particle simulations and showed a significant effect in the dynamics due to the plasma response. It is shown that residual momentum characterizes the dynamics after the action of the laser field.

CONCLUSION

We solved in exact form the equations of motion for a charged particle driven by an elliptically polarized wave of arbitrary amplitude propagating along an external and static magnetic field. The procedure followed is straight forward and allows to reduce the solutions to cases previously found by other authors. We treated the propagation through plasma using a simple model and solved the equations of motion by means of numerical simulations. We found that when the harmonic plasma response is introduced in the model, residual momentum effects characterize the dynamics of the plasma particles.

REFERENCES

(1) C. S. Roberts and S. J. Buchsbaum, *Phys. Rev.* **135**, A381 (1964).
(2) J. Krüger and M. Bovyn, *J. Phys. A: Math. Gen.* **9**, 1841 (1976).
(3) J. V. Shebalin, *IEEE Trans. Plasma Sci.* **16**, 390 (1988).
(4) S. Acharya and A. C. Saxena, *IEEE Trans. Plasma Sci.* **21**, 257 (1993).
(5) B.-L. Qian, *IEEE Trans. Plasma Sci.* **27**, 1578 (1999).
(6) B.-L.Qian, *Phys. Plasmas* **7**, 537 (2000).
(7) R. Ondarza-Rovira, *IEEE Trans. Plasma Sci.* **29**, 903 (2001).
(8) J. N. Bardsley, B. M. Penetrante and M. H. Mittleman, *Phys. Rev.* A **40**, 3823 (1989).
(9) T. J. M. Boyd and J. J. Sanderson, *The Physics of Plasmas*, Cambridge University Press (2003).

Studies of Tungsten Laser-Produced Ion Stream Expanding in Magnetic and Electric Fields.

J. Wołowski, J. Badziak, P. Parys, and E. Woryna
Institute of Plasma Physics and Laser Microfusion,
Hery St. 23, P.O. Box 49, 00-908 Warsaw, Poland
wolowski@ifpilm.waw.pl

ABSTRACT

In this paper we present a study of the influence of the magnetic and electric fields on the parameters of ion streams emitted from the plasma produced with the use of the 1-ns Nd: glass laser-pulse at the power densities 10^{10} – 10^{11} W/cm^2. These investigations were motivated mainly by the possible technical application of the laser ion sources. The observed concentration of the ion stream close to the target normal increases with the increase of the magnetic field induction and with the laser pulse energy. A transverse electric field switched on for e.g. 13 μs after laser shot was used for removing contaminant ions from the ion stream emitted from plasma.

Key words: Laser-Produced Ions

INTRODUCTION

Recent studies of the ion emission from the laser-produced plasma has been stimulated by the importance of this phenomenon for laser-driven inertial confinement fusion and by the possibility of applying laser-driven ion source (LIS) in accelerator technology and for modifying material properties through ion implantation[1-5]. External magnetic and electric fields may modify the characteristics of the laser-produced ion beams according to the specific technological demands. This work is a continuation of our previous studies[6-7] related in part to the idea of a new type of ion source introduced at the LNS-INFN in Catania (Italy). This hybrid ion source consists of the laser ion source coupled to the electron cyclotron resonance ion source[5-8]. It is believed that the magnetic and electric fields can be also employed for optimization of other applications of the laser-produced ions (e.g. for ion implantation).

ARRANGEMENT OF THE EXPERIMENT AND MEASURING METHODS

The measurements were performed with a single shot Nd:glass laser operating at the wavelength of 1.06 μm and energy up to 2 J in a1-ns pulse. The laser beam was focused at an angle of 6° with respect to the target normal by means of a lens with the focal length of a 411.6 cm onto the thick tungsten disk. The laser power density attained values from 10^{10} to 10^{11} W/cm^2. The Helmholtz coils with the inner diameter of 14 cm generating a longitudinal magnetic field with induction up to 1.2 T were located in front of the target. A cylindrical electrostatic ion-energy analyzer (IEA) was used for ion diagnostics along with 5 small ion collectors (ICs) located at different angles close to the target normal from 2.1° to 6.5 °. The IEA has a binding radius of 10 cm, the deflecting angle was 90° and the gap between the cylindrical electrodes was of 1 cm[9]. As an ion detector, a windowless electron multiplier was applied. The path of flight was 195 cm for the IEA and 74.6 cm for ICs. In front of the IC3 (at the angle of 2.3° - see Fig. 1) an ion deflecting system was located (parallel 5 cm long electrodes with a gape of 0.8 cm). This system forms the electric field perpendicular to the direction of ion expansion. The deflecting voltage of 200 V can be applied during 1-50 μs after the laser pulse.

From the signals recorded by the ICs, charge-integrated and time-resolved ion current distributions can be determined[9]. The velocity (energy) distributions as well as average and total energy carried by ions can be also delivered from the ICs signals. The IEA spectra make it possible to determine the charge states, energies and abundance of different ion species[9].

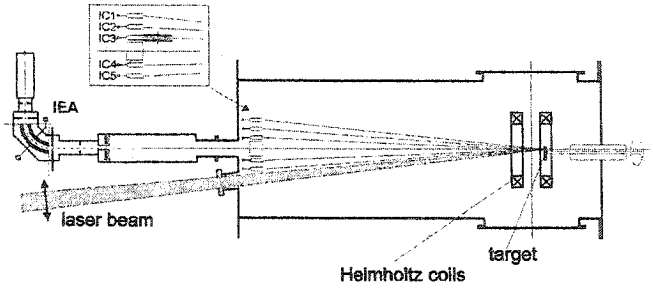


Fig. 1. Experimental arrangement.

RESULTS AND DISCUSSION

Identification of ion species on the basis of the IEA spectra shows that the target material contains some contaminants (mainly: H, C and O). The ion collector signals show the existence of two ion groups: a group of faster contaminant ions and a group of slower tungsten ions. The IEA data enable to reconstruct the IC signal as well as to determine the plasma composition as shown in Fig. 2. The valley between the faster contaminant ions and slower tungsten ions enables to estimate the maximum velocity and energy of tungsten ions: $v_{max} \approx 5.6\times10^6$ cm/s and $E_{i,max} \approx 3$ keV, respectively.

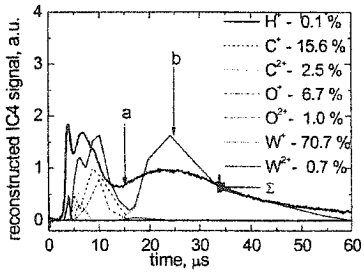


Fig. 2. IC4 signal, recorded (a) for the 2nd laser shot (E_L = 1.1 J at FP = +10 cm) and reconstructed (b) on the basis of the IEA data.

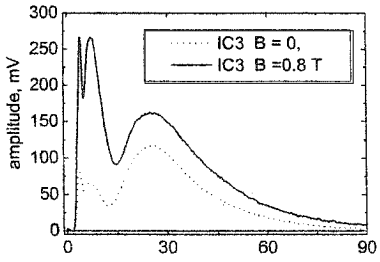


Fig. 3. IC3 signals recorded for ions expanding freely and at a presence of the magnetic field at induction of B = 0.8 T.

Typical ion collector signals recorded with the use of IC3 for plasma expanding freely and in the presence of a magnetic field of 0,4 T are shown in Fig. 3.

The angular distributions of the maximum ion current density and the peak velocity of the W ions for B = 0 and for B = 1.2 T are presented in Fig. 4. The peak ion velocity corresponds to the maximum of the ion collector signal (see Fig. 2). Both the angular distributions of the maximum ion current density are very narrow (more than 90% of the W ions were emitted at a solid angle $< 10^o$). But in the case of B = 1.2 the maximum ion current density was more than twice as large as for B = 0. The ions expanding in the directions close to the target normal attain nearly the same maximal values of the peak velocities for B = 0 and for B = 1.2 T. The peak velocity of the ions expanding in the magnetic field has a narrower angular distribution than in the case of B = 0.

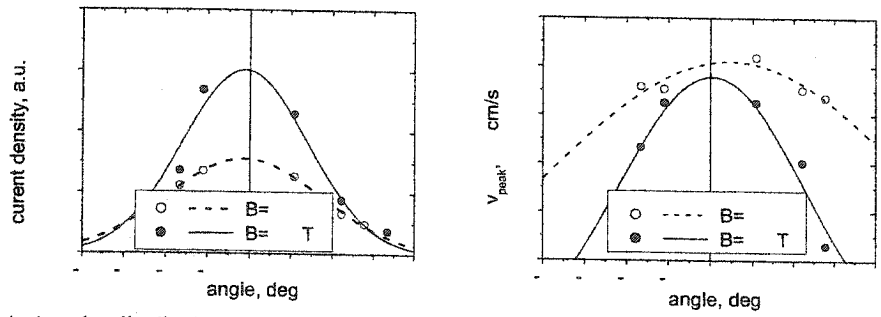


Fig. 4. Angular distributions of maximum ion current density (left) and tungsten ion velocity (right) for ions expanding freely and at a presence of the magnetic field at induction of B = 1.2 T.

The maximum of the tungsten ion current density increases with the laser pulse increase measured at B = 0, B = 0.4 T and B = 1.2 T (Fig. 5). The effect of the increasing of the ion current close to the target normal due to the magnetic field is evident.

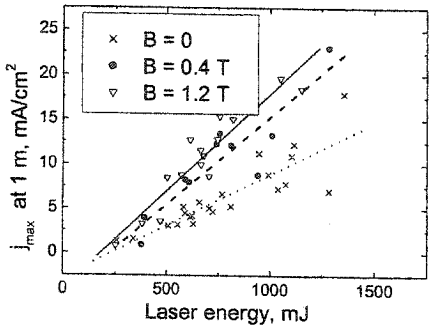


Fig. 5. The dependence of the maximum ion current density on laser pulse energy for different magnetic field inductions.

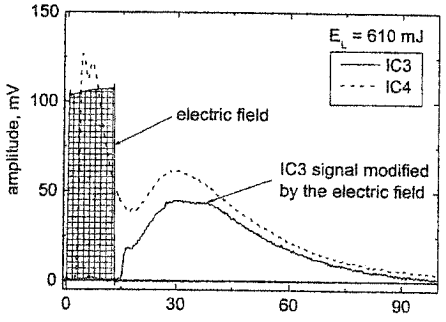


Fig. 6. Removing the light contaminant ions and the faster tungsten ions from the ion stream with the use of a transverse electric field.

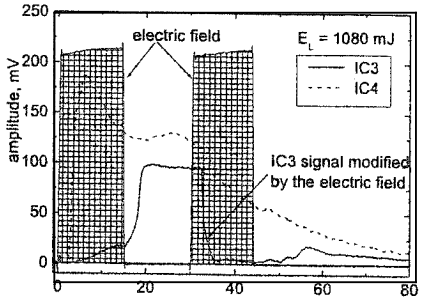


Fig. 7. Extraction of the tungsten ions with energies within the range of 0.5 –1.7 keV from the ion stream with the use of a transverse electric field.

The application of the deflecting electric field of 250 V/cm during 13 μs results in the decreasing of the contaminant ion stream reaching the IC up to values < 2% of the contaminant ion stream expanding without the electric field (Fig. 6). For extracting the tungsten ions carrying energies in a specific energy range, the deflecting electric field was applied during the first 15 μs after the laser shot and than it was switched on next time at 30 μs after laser shot also for the 15 μs. The Fig. 7 presents the IC signal modified by the electric field and (for comparison) the IC signal corresponding to the ion stream expanding without this field. The electric field extracts the tungsten ions with energies in the range of 0.5 – 1.7 keV (corresponding to ions reaching the IC collector between ~18 μs and ~33 μs). The light ions and faster tungsten ions (with energies > 1.7 keV were reduced to ~11% while the slower tungsten ions with energies in the range of 0.5 keV- 0.18 keV (arriving the collector from ~33 μs to ~54 μs) were reduced to ~12%.

SUMMARY

A longitudinal magnetic field causes the effective compression of tungsten laser-produced ions to be close to the target normal. At the highest magnetic field (B = 1.2 T) we have observed a narrowing of the angular ion velocity (energy) distribution. The maximum ion current density at angles close to the target normal increases with the increase of the magnetic field induction. However for B > 0.5 T (up to B = 1.2 T) this increase is very low. In our experimental conditions the transverse electric field, switched on for e.g. 13 μs after laser shot, influences effectively (on) the laser-produced light contaminant ions removing them from the tungsten ion stream expanding in the directions close to the target normal. Such a field, properly applied during the ion expansion time, can select the tungsten ions of energies within a particular energy range.

Acknowledgements: This work was partially supported by grant No 5 P03B 108 20 of the Polish Committee for Scientific Research.

REFERENCES

(1) H. Haseroth and H. Hora; Laser and Part. Beams **14**, 393 (1986).
(2) J. Wołowski, P. Parys, E. Woryna, L. Láska, K. Mašek, K. Rohlena, W. Mróz, and J. Farny; Proc. 12th Intern. Conf. on LIRPP, pp. 521–526, Osaka, Japan, April 1995.
(3) L. Laska, L. Láska, J. Krása, K. Mašek, M. Pfeifer, K. Rohlena, B. Králiková, J. Skála, P. Straka, E. Woryna, P. Parys, J. Wołowski, W. Mróz, H. Haseroth, A. Golubev, B. Sharkov, and G. Korschinek, Rev. Sci. Instrum.; **69**, 1072–1074 (1998).
(4) F.P. Boody, R. Höpfl and H. Hora, Laser and Part. Beams; **14**, 443 (1996).
(5) S. Gammino, G. Ciavola, L. Torrisi, L. Celona, J. Wolowski, E. Woryna, P. Parys L. Laska, J. Krasa, and G.D. Shirkov, Rev. Sci. Instrum.; **71**, 1119 (2000).
(6) J. Wołowski, L. Celona, G. Ciavola, S. Gammino, J. Krása, L. Láska, P. Parys, K. Rohlena, L. Torrisi, and E. Woryna, Laser and Part. Beams; **20**, 113 (2002).
(7) J. Wołowski, J. Badziak, P. Parys, E. Woryna, J. Krása, L. Láska, K. Rohlena, L. Ando, L. Celona, G. Ciavola, S. Gammino, L. Torrisi, High Temp. Material Processes; **6**, 521, (2002).
(8) S. Gammino, L. Torrisi, L. Andó, G. Ciavola, L. Celona, L. Láska, J. Krása, M. Pfeifer, K. Rohlena, E. Woryna, J. Wołowski, P. Parys, and G. D. Shirkov, Rev. Sci. Instrum.; **73**, 650, (2002).
(9) E. Woryna, P. Parys, J. Wolowski and W. Mroz, Laser and Part. Beams; **14**, 293 (1996).

Design and Construction of a Copper Halide CuBr Laser

K. Bourai, D. Louhibi, S. Messaoud, F. Siserir, A. Noukaz, Y. Hammoum
Centre de Développement des Technologies Avancées, Technologie des Systèmes Lasers
BP 17 Baba Hassen Algiers 16303 Algeria
kbourai@yahoo.com

ABSTRACT

In pure copper vapour lasers, the high temperature (1500°C) of operation required to generate sufficient vapour presents the main disadvantage. To overcome this inconvenience lasers were developed using copper halides for lasing in the 300 °C to 600°C range. In the present contribution we are more particularly interested in the design of a laser using a halide CuBr as lasant. The output wavelengths are 510.6 and 578.2 nm in pulsed operating mode. To dissociate the copper from its halogen and then excite it to produce the laser, a double pulse power supply is needed.

Key Words: Discharge tube, Metal vapour laser, Operating temperature, copper halide.

INTRODUCTION

Copper vapour lasers present following advantages over other visible gas lasers. The high peak power over 400 kW, the efficiency over 1% and the average power of tens of watts. Even they are available in commercial form today, these lasers are currently under research and development in our laboratory. They find application in underwater mapping, communications, high-speed photography, dermatology, dye laser pumping and entertainment. A first prototype using pure copper operating at 1500°C was developed. The laser worked for 20 hours after which technical hitches appeared due to the high temperature operating. To overcome this disappointment we are building a prototype using copper halide CuBr. Several authors[1-4] have demonstrated the use of copper halides CuCl, CuBr and CuI, to achieve sufficient copper concentration for lasing in the range of 300°C to 600°C. The CuBr laser will produce two distinct wavelengths, one at 510.6 nm and the other at 578.2 and can operate at lower temperatures. This allows the easy use of the automatic research system for power optimisation of the laser [5].

PRINCIPLE OF OPERATION

Copper vapour needed for lasing can be obtained by heating a tube discharge containing the halide CuBr. However, the copper must be first dissociated from its halogen atoms and than be excited to create the inversion of population. For this reason two electrical pulses are needed. The first pulse causes the dissociation of the copper halide molecules and the second pulse excites preferentially the upper laser levels within the recombination time of the molecule. The laser is enhanced between the $^2P_{1/2, 3/2}$ resonance levels and the lower $^2D_{5/2, 3/2}$ laser metastables levels (fig1). When the population of the metastables levels increase and terminate the inversion of population, the lasing ceases and the copper halide reforms by combination process, leading to cyclic operation and the laser medium recovers for another dissociation pulse. The dependence of laser output on tube temperature is shown in figure 2. The optimum operating temperature is 420°C[3]. This allows to avoid the use of components used for CVL's laser discharge tube such ceramic tube, ceramic fibrous insulation and vacuum jackets. The heating mode consist one of the main element in such development, but when

the self heating needs to operate at high repetition rate, the resistive heating permits to operate at low repetition rate. The discharge medium consists of copper vapour mixed to the buffer gas. This one is essential; it provides the discharge medium in the cold part of the tube and also prevents vapour from reaching and condensing on the optics. It allows the homogenisation of the active medium as well and increases by the way the life time of the laser. Best results were given using Helium at an optimum pressure of 3 to 5 torr[6].

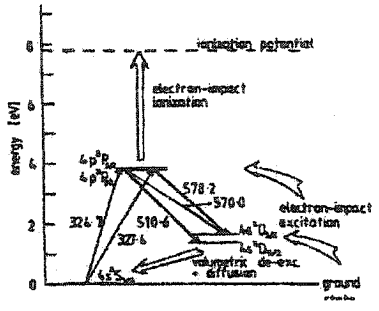


Fig 1. Partial energy -level diagram and transitions of the copper atoms[6]

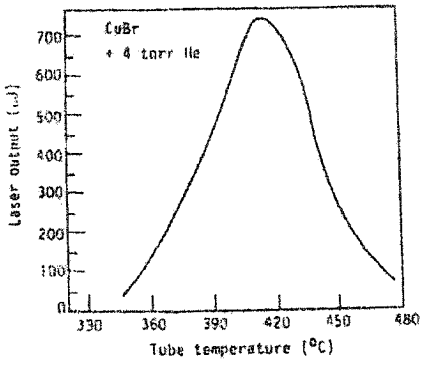


Fig 2. Dependence of laser output on tube temperature[3]. Tube length: 220 mm, Tube diameter 30mm

ELECTRICAL CIRCUIT

Considering the delay between the dissociation energy and the excitation energy and the recombination phenomena as well[2], the power supply construction became more complex. The Power supply consists of a capacitor bank C charged a given high voltage V provides needed storage energy of ½ $(CV)^2$. The molecule dissociation and laser excitation are produced respectively by double pulses generated from a trigger circuit. A typical double pulse circuit is shown in figure 3. The delay time between the two pulses will be adjusted around the optimum delay of 200 to 350µs.

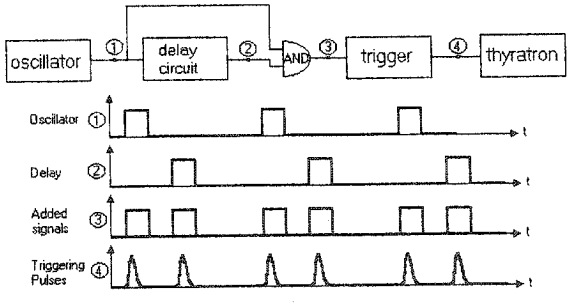


Fig. 3. Schematic diagram of the delay circuit and the timing diagram of electronics.

A classical resistive circuit is inefficient to achieve an extra energy to dissociate the molecule CuBr[8]. In addition, the charging resistance should therefore also obey the relation $Vs/R < I_h$, the thyratron hold current which is not under control of the user. To overcome this problem resonance capacitor charging circuit is usually used. A typical resonant charging circuit is shown in figure 4. The resonant charge of the capacitor Cs allows its rapid charge to a higher voltage of twice Vs which is the average of the two optima energy. The values of the inductance Lc and the storage capacitance Cs, set the time of the capacitor charging, which must be less than the thyratron recovery time. This allows the extinction of the thyratron after each excitation firing.

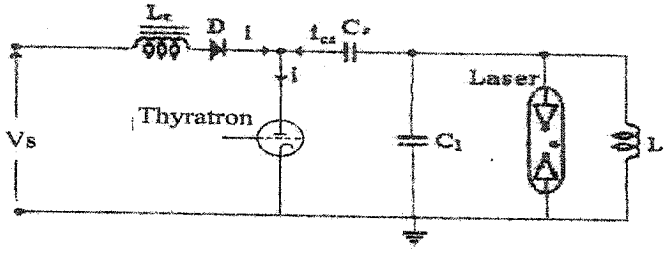


Fig. 4. Schematic diagram of the charging circuit.

THE DISCHARGE TUBE

The schematic diagram of the designed laser is given in figure 5. The laser consists of a quartz vacuum discharge tube including some pockets to contain the halide, which can be heated to the desired temperature. The inner diameter is 25 mm and its length is 650 mm, the overall tube length is 900 mm and the heated zone length is 412 mm. To operate at low repetition rate the resistive heating mode is adopted[9]. A direct coiled heating spiral is used. The heater is in direct contact with the pockets. Refractory brick can be used as thermal isolator at the heated zone. Chromel-alumel thermocouples are placed over the length of the heated zone of the discharge tube. They are related to a system, which allows the control of the temperature around the optimal required operating temperature. The ends of the heated zone are joined to a water cooled jacket at one side and a cooling pipe at the other. Both cooling water arrangements allow the cooling of these zones and the condensation of the vapour thus preventing the deterioration of the optics. The tube is joined at both ends to stainless-steel electrodes by means of O-rings. The electrodes support the windows, the gas entrance and the vacuum pump assembly. Vacuum is produced with normal vacuum pump. Sapphire windows at Brewster angle seal the ends of the tube using O-rings which allow their adjustment and their easy removal as well. A metal cylinder cover the entire active zone of the discharge tube in a coaxial structure, allowing the current return path, since the central conductor is the plasma itself. In this case the equivalent inductance of the laser is much reduced, which allows to have excitation current rising time very high. The thyratron and the very low inductance charging capacitors are mounted in a compact configuration with the discharge tube to minimise the inductance of the electrical circuit as well[10,11]. External Plano concave cavity is used. Both total reflector and output coupler with 8% reflectivity are adjustable mounted.

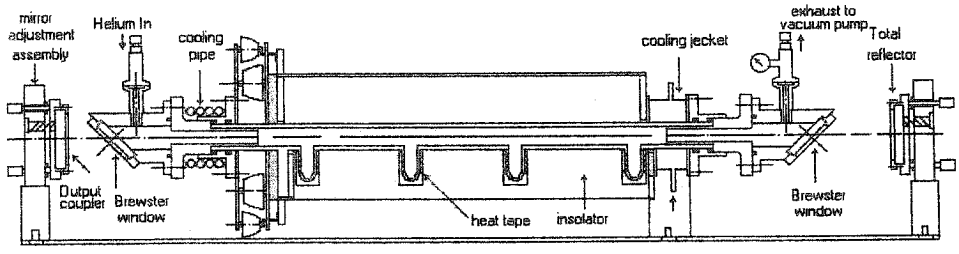


FIG. 5. Schematic diagram of the laser

CONCLUSION

Considering the physical parameters running the operation of CuBr laser and the technological specifications as well, we designed an easy assembly and easy maintenance compact system. Compared to the CVL's, the discharge tube can be straightforwardly constructed from components which are available. More considerations should be taken into account, in the design of the power supply, particularly in the optimisation of the dissociation and the excitation energies simultaneously. This device is very suitable for the experimentation of the other halides.

REFERENCES

(1) S.Gagay, I.Smilanski, L.A.Levin and G.Erez; IEEE, JQE, QE13, (1977).
(2) C.J.Chen, et al.; Applied Physics Letters, vol.23, N°9, 1 (1973).
(3) N.M.Nerheim; Journal of Applied Physics, vol. 48, N°3, (1977).
(4) N.K. Vutchkov, D.N. Astadjov, and N.V. Sabonitov; Opt. Comm., Vol. 42, (1982).
(5) D. Louhibi, M.Ghogrini, Measurement Science and Technology, 9, (1998).
(6) C.S.Liu, D.W.Feldman, J.L.Pack, L.A. Weaver; IEEE, JQE, QE13, N°9, (1977).
(7) C.E.Little, M.D. Ainsworth and J.A. Piper, Oyo Buturi, J. Japan Soc. Appl. Phys., Vol. 57, (1988)
(8) Tenenbaum, I.Smilanski, S.Gagay, G.Erez, L.A.Levin, J.Katireland S.Speiser; IEEE, JQE vol. 4; N°9, (1978).
(9) I.Smilanski, G.Erez, A.Kerman, L.A. Levin; Opt. Communication Flight 30 N°1 (1973).
(10) N.K. Vuchkov, D.N Astadjov and N.V Sabonitov; Opt. Quantum Electron, Vol. 23, (1991).
(11) N.K. Vuchkov, D.N Astadjov and N.V Sabonitov; Opt. Quantum Electron, Vol 20, (1988).

Volatilization of Tracheal Tumors by CO_2 Laser

S. Bouzid[(1)], **T. Benguedouar**[(1)], **A. Bouzid**[(1)], **Z. Daouadi**[(2)]

[(1)] *Laser Laboratories and Applications of Constantine, Faculty of Medicine, University of Constantine, Algeria*

[(2)] *University of Tunis, Tunisia*

ABSTRACT

In ENT, we often use volatilization for the treatment of the tumors. Our work consists to model volatilization by standard CO_2 laser irradiation of a tracheal tumor and to optimize the various applications in ENT. The model of calculation, that we have adopted, made it possible to describe in a realistic way the process of volatilization by taking into account the main phenomena produced during the biological laser tissue interaction. The results enable us to evaluate the distribution of the heat in the tissue and the obtained damage, and to predict the characteristics of the radiation and the exposure time necessary to have the desired effect.

Key-words: ***Volatization, laser, tracheal tumor, mathematical model***

INTRODUCTION

The tracheal tumor is observed especially in men forty years of age. It is caused by nicotinism and it is supported by associated alcoholism. The key symptom is the dysphonie, which draws the attention and allows an early diagnosis. Laser surgery uses a narrow beam of light of high energy in order to destroy the abnormal cells or the lesions, without touching nearby healthy tissues. We present a simple approach to volatilization by laser radiation by calculating the distribution of the temperature and the speed v of the ablation surface. We developed two solutions:

- one describing the transitory answer,
- the other one describes the approach to the stationary state.

RESULTS AND DISCUSSION

According to the equations of the mathematical model, our problem depends on four parameters which are: power, spot size, duration of exposure, and wavelength, which determibes the rate of absorption and dispersion in the irradiated tissue. In order to understand the laser irradiation effects in the tissue during the volatilization of a tracheal tumour, a study is being presented for a CO_2 type laser in which the power varies from 10 to 70 W, and which works in a continuous mode. The results presented in the following table allow us to determine the threshold time necessary for the surface temperature of the tissue to reach 100°C for various powers and various diameters of the spot. We notice that for in-creasing power the threshold time to reach this temperature (condition of the beginning of ablation) decreases when the spot diameter is kept constant; the absorbed energy is quickly converted to heat resulting in the creation of a local very important heat source: the biological tissue is overheated abruptly. An increasing spot diameter implies a rise of the threshold time when the power is maintained constant. With increasing spot size the irradiated zone is increased at the same time and thus the time for the tissue to accumulate the necessary energy density for the beginning of volatilization just will be longer.

The shapes of the curves in Figure 1 giving the temperature variation versus time are similar and clearly show the important three stages in order for tissular volatilization by a continuous laser with emission takes place. The temperature thus increases brutally (pre-heating or coagulation) at the beginning of the interaction due to the fact that the absorbed energy leads to heating instantaneously, then passes through a stage (stage of ablation or phase change) caused by water evaporation thus dehydrating the tissue; this loss of substance implies a change in the thermal properties, conductivity and diffusivity are reduced. After this stage of phase change the temperature rises brutally to reach very high values (more than 200°C) favourable to volatilization and carbonization of the tissue; then the temperature decreases quickly according to a quasi-exponential relief after stop of the exposure to radiation. At this stage a mechanism of cooling will be established. It should be noted that the change of the power or of the spot diameter does not influence the course of the process (Fig. 1), the events generally occur at the same temperature but only at different times. However, if the exposure time is very large, the maximum temperature reached can exceed 500°C, which makes it possible to ensure a better action of the laser on the tissue and to obtain a perfect volatilization with very high speeds and depths. By analyzing these profiles, we note that the speed of cooling is very high, the volume to be treated being relatively small. The thermal energy also does not affect neighbouring tissues, which gets an accurate check of the process.

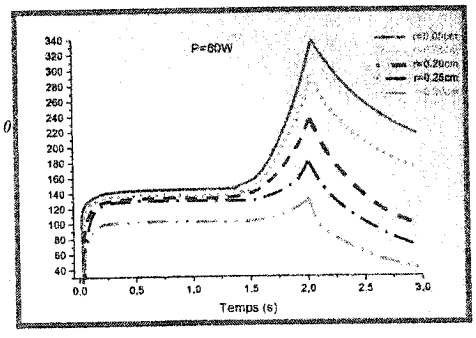


Fig. 1: Temperature versus time for different diameters

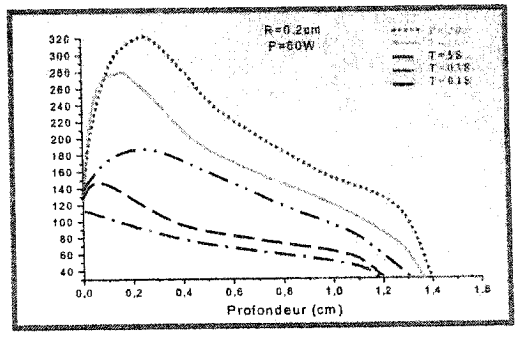


Fig. 2: Temperature versus depth

Temperature variation versus depth

The curves represented on Fig. 2 show the temperature evolution with depth for various times of irradiation, the spot diameter is taken equal to 0.2 cm and the power equal to 60 W. For T=0.1s, the temperature decreases exponentially with the depth what is due to the decrease of the intensity of the radiation in the axial direction when the laser beam penetrates the tissue: this leads to a reduction of the local heat source. If the time "T" varies from 0.2 to 0.5 s, we observe stronger heating below the surface with a temperature considerably higher than the temperature T_v of evaporation at the surface. Mathematically, for volatilization to take place it is necessary that the interaction speed $v_v = dz/dt$ is positive, thus dT/dz must also be positive, which means that the maximum temperature must occur imperatively below the surface. This is characteristic of heat sources generated by lasers. Evaporation of the surface layer produces a mechanism of convection cooling leading to an enormous increase in the temperature of layers beneath the surface; they become overheated and remain in a metastable state which after

perturbation can lead to an intense expansion of the layers and explosive removal of tissue known as Pop corn effect. In experiments the Pop corn effect is blamed on the sudden formation of vapour balls, which are formed by the evaporation of the water contained in the tissue; this is called vaporization. Once the temperature of evaporation is reached, the associated pressure connected with super-heating exceeds the internal pressure of the tissue, which will cause the explosion of the latter. Once the water is vaporized, the tissue will burn under the effect of the ongoing heating, and we will obtain complete carbonization and volatilization of the tumor.

Variation depth versus time:

For the calculation of the volitilized tissue volume, it is necessary to know the thickness of the created crater; by assuming that this volume has a cylindrical shape, we obtain the following form
$Z \times (D/2)^2 \times \pi = V$. " D " is the diameter of the spot and "Z" the depth.
The variation of the depth of volatilization versus time for various powers and for a diameter of the spot equal to 0.2 cm are presented in Fig. 3, whereas in Fig. 4 the depth is plotted for a power of 60 W and varying diameter of the spot.

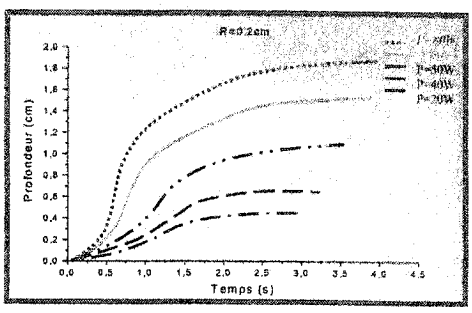


Fig.3: Depth versus time for different powers

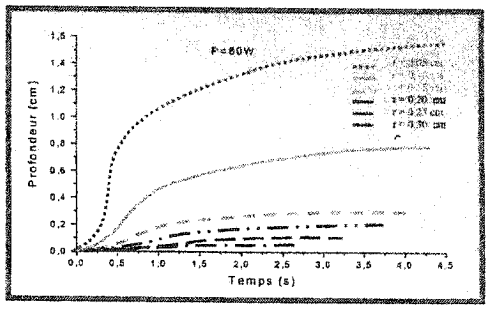


Fig.4: Depth versus time

According to these two figures, one notes that during exposure to radiations the surface of volatilization strongly progresses then turns towards tability.

Volatilization speed versus time

The evolution of the ablation speed versus time is presented in Fig. 5 and 6 for a spot diameter of 0.2 cm and various powers between 20 and 80 W, and for a fixed power of 60 W and arious spot diameters between 0.05 cm and 0.3 cm.

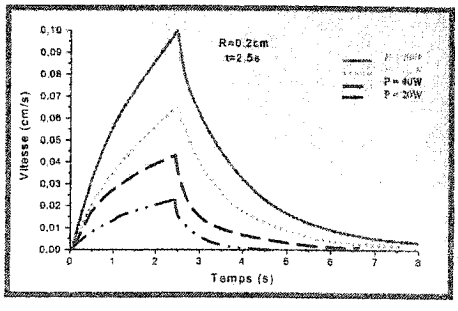


Fig.5 : volatilization speed versus time

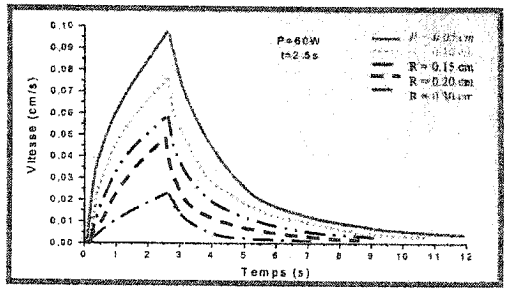


Fig.6 : volatilization speed versus time

We notice that the speed is zero at early times, then starts to increase; this growth which occurs at high temperatures (> 100°C) follows the thermal profile. After ending of the exposure to the radiation it relaxes quickly. This is due to the extension of the crater inside the tissue which minimizes the thermal energy of the structure because of water evaporation, The advance of the surface with depth as well as the speed become weak till both stop.

CONCLUSION

The estimates given by our model can be qualified preliminarily qualitative. With respect to a continuation of this study, we consider that the following points must be approached in order to improve the results:

- To conceive experimental studies completely adapted to the problem of laser interaction with biological tissue (histological study of the phenomenon)
- To improve our knowledge of thermo-ionizations parameters of studied tissue for better comprehension of the mechanisms produced during the interaction.
- To understand the thermal behaviour in its globality, it is preferable to extend the study as well by taking into account the anisotropy the blood perfusion in the tissue
- To extend the study to other wavelengths in order to compare their effect and to appreciate their effectiveness for a better ablation.
- To plan to extend modelling while following the thermal behaviour after ablation in order to quantify precisely the spreading damage near the ablated zone.

REFERENCES

(1) Bali Leila ; « thèse de magistère : modélisation de l'ablation tissulaire par laser » Laboratoire Lasers et Applications de Constantine, Algeria, février 2001.

(2) F. Bernard ; les lasers en ORL, publ. Juin 2002 - CHU Nantes – service ORL.

(3) T. Benguedouar ; 'thèse Magistère : « Volatilisation d'une tumeur trachéale par laser CO2 – Application en ORL », Laboratoire Lasers et Applications de Constantine, Algeria, Mai 2003.

Plasma Theory

Linear Landau Damping in Strongly Relativistic Quark Gluon Plasma

G. Murtaza, N. A. D. Khattak and H. A. Shah
Salam Chair in Physics, G C University, Lahore, 54000, Pakistan.
Department of Physics, G C University, Lahore, 54000, Pakistan.
schair@lhr.comsats.net.pk

ABSTRACT

On the basis of semi classical kinetic Vlasov equation for Quark-Gluon Plasma (QGP) and Yang-Mills equation in covariant gauge, linear Landau damping for electrostatic perturbations like Langmuir waves is investigated. For the extreme relativistic case, wherein the thermal speed of the particles exceeds the phase velocity of the perturbations, the linear Landau damping is absent. However, a departure from extreme relativistic case generates an imaginary component of the frequency giving rise to linear Landau damping effect. The relevant integral for the conductivity tensor has been evaluated and the dispersion relation for the longitudinal part of the oscillation obtained.

Key Words: ***Quark-Gluon Plasma, Landau damping, Conductivity tensor***

INTRODUCTION

For the last two decades, theoretical and experimental efforts are continuing to understand the characteristics of Quark-Gluon Plasma (1 - 4). In QGP, the protons and neutrons lose their identity, and the nucleus turns into a soup of strongly interacting quarks and gluons with properties different from the normal nuclear matter. The matter in the early universe was almost certainly QGP until the temperature fell below a few trillion degrees, a millionth of a second after the big bang. A similar state of matter is also supposed to exist in the core of the neutron stars. The QGP signals are being probed in the Relativistic Heavy Ion Collisions (RHIC) experiments at Brookhaven National Laboratory and the Large Hadron Collider (LHC) at CERN (5). In these experiments heavy ions like Lead (Pb) or Gold (Au) are accelerated to very high energies and are made to smash into each other, compressing the nuclear matter to extreme energy densities (greater than 1 GeV/fm^3) creating conditions akin to that of the early universe. These experiments provide unique opportunities to probe into a highly excited dense nuclear matter under controlled laboratory conditions. QGP may be regarded as the Quantum Chromodynamics (QCD) analog of the ordinary plasma phase of matter. However, unlike the ordinary plasma, the deconfined quanta of QGP are not directly observable because of the fundamental confining properties of the QCD vacuum.

In this paper we examine the linear Landau damping for electrostatic oscillations (like Langmuir waves) for extreme and strongly-relativistic velocities on the basis of semiclassical kinetic Vlasov equation for the QGP and Yang-Mills equation in covariant gauge. As it has been reported earlier that for an extreme relativistic case in which the thermal speed of the particles is fixed at the speed of light, the linear Landau damping vanishes. Evidently here the thermal speed exceeds the phase velocity of the perturbations and thus the two speeds fail to resonate. However, in the strongly-relativistic case in which the thermal speed departs from the speed of light, the imaginary part of the perturbation shows up and thus the Landau damping effect can be observed which is sensitive to the choice of wave number k and Debye Length λ_D.

LINEARIZED VLASOV THEORY OF QUARK-GLUON PLASMA

In the ultra relativistic high temperature collisionless quark-gluon plasma, the plasma species quarks, anti-quarks and gluons are supposed to be in thermal equilibrium and behave like a free gas particles obeying Fermi-Dirac and Bose-Einstien statistics respectively. In order to consider the problem of linear Landau damping for such a phase, we need to solve the Boltzmann-Vlasov kinetic equations. These equations in relativistic notation can be expressed (2,3,6,7) as:

$$\begin{aligned} p^\mu D_\mu f_{q,\bar{q}} \pm \frac{1}{2} g p^\mu \left\{ F_{\mu\nu}, \frac{\partial f_{q,\bar{q}}}{\partial p_\nu} \right\} &= 0, \\ p^\mu \tilde{D}_\mu f_g + \frac{1}{2} g p^\mu \left\{ \tilde{F}_{\mu\nu}, \frac{\partial f_g}{\partial p_\nu} \right\} &= 0, \end{aligned} \tag{1}$$

The force term $F_{\mu\nu} = (\partial_\mu A_\nu - \partial_\nu A_\mu) - ig[A_\mu, A_\nu]$ satisfies the Maxwell's equation in relativistic notation $D_\mu F^{\mu\nu}(x) - \zeta^{-1}\partial^\nu \partial^\mu A_\mu(x) = -J^\nu(x)$ where ζ is a gauge parameter and g is the coupling parameter. A_μ the field potential and D_μ and $\tilde{D}_\mu$ are the covariant derivatives respectively, which act as

$$\begin{aligned} D_\mu &= \partial_\mu - ig[A_\mu(x), .] \\ \tilde{D}_\mu &= \partial_\mu - ig\left[\tilde{A}_\mu(x), .\right] \end{aligned}$$

Here [,] denotes the commutator. The generators of the group are denoted by t^a and T^a for the fundamental and adjoint representation respectively. Thus for the fundamental representation, $A_\mu = A_u^a t^a$ and $F_{\mu\nu} = F_{\mu\nu}^a t^a$, and similarly for the adjoint representation we have, $\tilde{A}_\mu = A_u^a T^a$ and $\tilde{F}_{\mu\nu} = F_{uv}^a T^a$ with $F_{\mu\nu}^a = \partial_\mu A_\nu^a - \partial_\nu A_\mu^a + g f^{abc} A_\mu^b A_\nu^c$

The color current density J^ν is given by $J^\nu = g t^a \int d^4p\, p^\nu \left[Tr\, t^a (f_q - f_{\bar{q}}) + Tr(T^a f_g)\right]$ (2)

We also note that $Tr(t^a t^b) = \delta^{ab}$, $Tr(T^a T^b) = N_c \delta^{ab}$ and $\left[t^a, t^b\right] = i f^{abc} t^c$, where the structure constants $f^{abc} = i\left(T^a\right)^{bc}$. Here the Minkowski indices μ,ν vary from 0 to 3; and the color indices a, b, c..... run from 1 to N-1 of SU(N) gauge group with N_f flavors of quarks.

Now linearizing the equations and performing its Fourier transformation, we obtain

$$f_{q,\bar{q}}^{T(1)}(k,p) = \mp g \frac{\chi^{\nu\lambda}(k,p)}{pk + i\epsilon p_0} \frac{\partial f_{q,\bar{q}}^{(0)}}{\partial p^\lambda} A_\nu^T(k)$$

where $\chi^{\nu\lambda}(k,p) = \left((pk)\, g^{\nu\lambda} - p^\nu k^\lambda\right)$.

$$f_g^{T(1)}(k,p) = -g \frac{\chi^{\nu\lambda}(k,p)}{pk + i\epsilon p_0} \frac{\partial f_g^{(0)}}{\partial p^\lambda} \tilde{A}_\nu^T(k),$$

Using these distributions, the color current density can be expressed as

$$J^{T(1)\mu}(k) = \Pi^{\mu\nu}(k)\ A_\nu^T(k), \quad \Pi^{\mu\nu}(k) = g^2 \int d^4p \frac{p^\mu}{pk + i\epsilon p_0} (p^\nu k . \frac{\partial}{\partial p} - p . k \frac{\partial}{\partial p^\nu}) N_{eq}$$

where $N_{eq} = \frac{1}{2}\left(f_q^{(0)} + f_{\bar{q}}^{(0)}\right) + N_c f_g^{(0)}$ is the quark-gluons equilibrium number density. The above equation for the current density is the tensor analog of the generalized Ohm's Law.

To study the linear Landau damping in a quark gluon plasma (QGP), we need to calculate $\Pi^{\mu\nu}$.

For that, we define the permittivity tensor $\epsilon^{\mu\nu} = \delta^{\mu\nu} - \frac{1}{\omega^2}\Pi^{\mu\nu}$ (3)

with $\epsilon_L = 1 - \frac{1}{k^2}\Pi_{00}$ and $\epsilon_T = 1 - \frac{1}{2k^2}\Pi_{\mu\mu} + \frac{1}{2k^2}\Pi_{00}$ as longitudinal and transverse components.

The conductivity tensor Π_{00} is given by [2,3]

$$\Pi_{00} = \frac{2g^2}{(2\pi)^3}\int \frac{(\underline{k}.\underline{v})\frac{\partial f}{\partial p}}{\underline{k}.\underline{v} - \omega - i\varepsilon} d^3p$$

The wave number k and frequency ω correspond to the propagation of the oscillations in the QGP and v is the thermal speed of the plasma particles.

The treatment extended here to the problem of Landau damping in QGP is almost classical and the only place where the quantum mechanics enters is the equilibrium distribution functions for quark and gluon species of the plasma.
Since the quarks and anti-quarks are fermions, and the gluons are bosons, their equilibrium distribution functions $f_{q\bar{q}}$ and f_g are given by

$$f_{q\bar{q}} = \frac{1}{z^{\mp 1}\exp(cp/T) + 1} \qquad f_g = \frac{1}{z^{-1}\exp(cp/T) - 1}$$

where cp/T is the kinetic energy of the plasma particles for a very high temperature relativistic case, normalized over temperature (in eV). We note that in the high temperature limit, rest mass energy is ignored in the relativistic energy equation. The fugacity number $z = \exp\left(\frac{\mu}{T}\right)$ depends upon the nature and the chemical potential μ of the particles in that phase.

Extreme or Ultra-relativistic Case (i.e. v=c)

Here we discuss the extreme relativistic case when the particle thermal speed equals the velocity of light i.e., v=c. Thus for z=1 and $3\omega_p^2 = \frac{g^2T^2}{c^2}\left(\frac{1}{6}(N_f + 2N_c)\right)$, Π_{00} becomes

$$\Pi_{00} = 3\omega_p^2\left[\left(\frac{1}{3}(\frac{kc}{\omega})^2 + \frac{1}{5}(\frac{kc}{\omega})^4 + \frac{1}{7}(\frac{kc}{\omega})^6 + ...\right) - i\pi\frac{\omega}{kc}\Theta(1 - \frac{\omega}{kc})\right] \tag{4}$$

Calculating the longitudinal response function ε_L and equating it to zero, we obtain the linear dispersion relation

$$1 - \frac{3\omega_p^2}{c^2k^2}\left[\left(\frac{1}{3}(\frac{kc}{\omega})^2 + \frac{1}{5}(\frac{kc}{\omega})^4 + \frac{1}{7}(\frac{kc}{\omega})^6 + ...\right) - i\pi\frac{\omega}{kc}\Theta(1 - \frac{\omega}{kc})\right] = 0$$

The imaginary component survives only if its argument is positive i.e., $\frac{\omega}{k} < c$ (being the particle thermal speed). Therefore, Landau damping vanishes for the extreme-relativistic case.

Strongly-relativistic Case (i.e. $v \lesssim c$)

Using v=p/m, where m is the average mass of the particles and performing integration, the conductivity tensor Π_{00} becomes

$$\Pi_{00} = \frac{4g^2T^2}{c^2(2\pi)^2} \times \left(\frac{1}{45}\pi^4(\frac{c^2k^2}{\omega^2})(\frac{T}{mc^2})^2\frac{1}{3}(4N_c+7N_f)+\frac{1}{105}\pi^6\frac{c^4k^4}{\omega^4}(\frac{T}{mc^2})^4(16N_c+31N_f)\right) - \frac{1}{2}i\pi\frac{4g^2T^2}{c^2(2\pi)^2}\left(N_f\frac{\omega^2}{c^2k^2}(\frac{mc^2}{T})^2\exp(-\frac{\omega}{ck}\frac{mc^2}{T})\right) \quad (5)$$

Thus $\epsilon_l = 1 - \frac{A}{\omega^2} - \frac{Bc^2k^2}{\omega^4} + iC\frac{\omega^2}{c^4k^4}\exp(-\frac{\omega}{ck}(\frac{c^2}{v_{th^2}}))$

where $A = \frac{1}{45}\pi^2c^2k_d^2(\frac{T}{mc^2})^2(4N_c+7N_f)$, $B = \frac{\pi^4}{105}(c^2k_d^2)(\frac{T}{mc^2})^4(16N_c+31N_f)$ and $C = \frac{1}{2\pi}(c^2k_d^2)(\frac{mc^2}{T})^2N_f$ and here the Debye wave number $k_d = gT/c^2$

Defining $\omega = \omega_r + i\omega_i$ and assuming $\omega_i \ll \omega_r$, we obtain

$$\omega_r^2 = \frac{A}{2} + \frac{1}{2}\sqrt{A^2+4Bc^2k^2}$$

$$\omega_i = -\frac{\frac{c^2k_d^2}{2\pi}(\frac{mc^2}{T})^4\frac{\omega^6}{c^4k^4}\exp(-\frac{\omega_r}{ck}(\frac{mc^2}{T}))N_f}{4\omega_r^3 - 2\omega_r\left(\frac{1}{45}\pi^2c^2k_d^2(\frac{T}{mc^2})^2(4N_c+7N_f)\right)}$$

REFERENCES

(1) J.I. Kapusta, S. M. H. Wong, Phys. Rev. **D62**, 37301 (2000).
(2) *Quark-Gluon Plasma 1*, Edited by R. C. Hwa, World Scientific, 1995.
(3) *Quark-Gluon Plasma 2*, Edited by R. C. Hwa, World Scientific, 1995.
(4) *Quark-Gluon Plasma 3*, Edited by B. Sinha, S. Pal and S. Raha, Springer Verlag, 1990.
(5) "Opening of the Door to the Quark-Gluon Plasma", *CERN Courier*, www.cerncourier.com/main/articles/40/5/17; *Brookhaven Bulletin*, **54**(5), Feb. (2000); *Physics Today*, May 20(2000).
(6) U. Heinz, Phys. Rev. Lett **51**, 351(1986).
(7) U. Heinz and P. J. Siemens, Phys. Lett. **B158**, 11(1985).

Dust Acoustic Waves in a Warm Dusty Plasma with Trapped Electrons

W. F. EL-Taibany and S. K. El-Labany
Department of Physics, Faculty of Science-Damietta, Damietta El-Gedida, Egypt
eltaibany@hotmail.com

ABSTRACT

The effect of variable dust charge, dust temperature and trapped electrons on small amplitude dust acoustic waves is investigated. It is found that both compressive and rarefactive solitons as well as double layers exist depending on the nonisothermality parameter. Critical cases and cases in the vicinity of these critical cases is also discussed.

Key Words: warm dusty plasma, fluid theory, dust charge fluctuation, reductive perturbation.

INTRODUCTION

The dusty plasma has received much attention in the last few years. It exists in astrophysical bodies and space environments [1]. Normally, the low temperature plasma environment sustains a negatively charged dust formed by the attachment of the electrons to the dust grains. If one ignores the dust charge fluctuation dynamics, the dusty plasma can be regarded as a multicomponent plasma with several ionic species [2]. The dust acoustic (DA) wave was firstly interperted by Rao et al.[3]. Later, Xie et al. [4] have considered the dusty plasma with the dust charge fluctuation.

If streaming particles are injected into plasmas, we often find that they evolve towards a coherent trapped particle state. The onset of an electron trapping is also seen in the formation of double layers [5] and computer simulation [6].

The effect of adiabatic variation of dust charges on DA waves with isothermal electrons and ions [4] and solitary waves in dusty plasma with the inclusion of trapped electrons [2] have been studied. Both papers do not include the effect of dust temperature and charge fluctuation on DA waves in the presence of trapped electrons. This is the motivation of this paper. In Sec. 2, we present the relevant equation governing the dynamics of the nonlinear DA waves. In Sec. 3, the modified Korteweg de Vries (MKdV) equation has been derived. Critical cases have been discussed and the evolution equations are derived. Also, the condition under which the double layers can be formed is obtained. The last part is devoted to the discussion and conclusion.

1. Governing Equations

The basic equations describing the system in non-dimensional form [4,7] are:

$$\frac{\partial n_d}{\partial t}+\frac{\partial (n_d u_d)}{\partial x}=0, \tag{1}$$

$$\frac{\partial u_d}{\partial t}+u_d\frac{\partial u_d}{\partial x}+3\sigma_d n_d\frac{\partial n_d}{\partial x}-Z_d\frac{\partial \phi}{\partial x}=0, \tag{2}$$

$$n_i=\mu\ \exp(-s\,\phi), \tag{3}$$

$$n_e=\nu[\exp(s\beta\phi)\ \mathrm{erfc}(\sqrt{s\beta\phi})+\beta_h^{-1/2}\exp(s\beta\beta_h\phi)\ \mathrm{erf}(\sqrt{s\beta\beta_h\phi})], \tag{4}$$

$$\frac{\partial^2\phi}{\partial x^2}=Z_d n_d+n_e-n_i, \tag{5}$$

where $\sigma_d = (T_d / Z_d T_{eff}), \beta = T_i / T_e$ and $s = 1/(\mu + \beta\nu)$.
Now, the dust charge fluctuation included is determined by the charge current balance equation [8]

$$\frac{\partial Q_d}{\partial t} + u_d \frac{\partial Q_d}{\partial x} = I_e + I_i, \tag{6}$$

where Q_d is the dust charge variable. The charge currents originating from electrons and ions reach the grain surface. So, the current balance equation reads

$$I_{eo} + I_{io} \approx 0. \tag{7}$$

According to the well-known orbit-motion-limited probe model [9], the electron and ion currents for spherical dust grains with radius r, normalized by $e\pi r^2 (8T_e / \pi m_e)^{1/2}$ are given by:

$I_e = -n_e \exp(e\Phi / T_e)$ and $I_i = \alpha n_i (1 - (e\Phi / T_i))$,

where Φ denotes the dust grain surface potential relative to the plasma potential ϕ ; $\alpha = \sqrt{(\beta/\mu_i)}$ and $\mu_i = m_i / m_e \approx 1840$. Introducing $\delta = \mu / \nu$, the current balance equation becomes

$$\exp(s\beta(\psi + \phi)) - G(s\beta\phi)\exp(s\beta\psi) = \alpha\delta(1 - s\psi)\exp(-s\phi), \tag{8}$$

where $\psi = e\Phi / T_{eff}, Z_d = \psi / \psi_o$ and $\psi_o = \psi(\phi = 0)$ is the dust surface floating potential with respect to the unperturbed plasma potential at infinite place.

2. Nonlinear Dust Acoustic (DA) Waves

Employing reductive perturbation technique [10] and introducing the coordinates $\xi = \varepsilon^{1/4}(x - \lambda t)$ and $\tau = \varepsilon^{3/4} t$ where ε is a small parameter and λ is the solitary wave velocity; normalized by C_d, the dependent variables $Q = (n_d, u_d, Z_d, \phi)$ are then expanded as

$$Q = Q_o + \sum_{j=1}^{\infty} \varepsilon^{(j+1)/2} Q_j \text{ and } Q_o = (1, 0, 1, 0)$$

Substituting into Eqs. (1)-(5), and using $\Psi = \Psi_o Z_d$, in Eq. (8), the linear dispersion relation is given by $1 - \{(1+\beta)(1 - s\Psi_o)/\Psi_o(1 + \beta(1 - s\Psi_o))\} = R$, where $R = (\lambda^2 - 3\sigma_d)^{-1}$. $O(\varepsilon^{3/2})$ equations give the MKdV equation

$$\frac{\partial \phi_1}{\partial \tau} + A\sqrt{\phi_1}\frac{\partial \phi_1}{\partial \xi} + B\frac{\partial^3 \phi_1}{\partial \xi^3} = 0, \tag{9}$$

where $B = (2\lambda R^2)^{-1}$ and $A = 2B b_1 \sqrt{s\beta^3}[(\delta + \beta)^{-1} - \{(1 - s\Psi_o)/\Psi_o(1 + \beta(1 - s\Psi_o))\}]$.
Using $\eta = \xi - M\tau$ into Eq. (9) and using the boundary conditions

$$\phi_1(\eta) \to 0, (d\phi_1(\eta)/d\eta) \to 0, (d^2\phi_1(\eta)/d\eta^2) \to 0 \quad \text{as} |\eta| \to \infty, \tag{10}$$

yields the solution of (9) given by

$$\phi_1 = \phi_{1m} \text{Sech}^4(\eta / w_1), \tag{11}$$

where the amplitude ϕ_{1m} and the width w_1 are given by $(15M/8A)^2$ and $4\sqrt{B/M}$, respectively.
For some physical parameters, A= 0 and we have to use [7,10] $\xi = \varepsilon^{1/2}(x - \lambda t)$ and $\tau = \varepsilon^{3/2} t$, and following the procedure used before, $O(\varepsilon^{5/2})$, yields a system of equations that gives

$$\frac{\partial \phi_1}{\partial \tau} + A\frac{\partial \sqrt{\phi_1}\,\phi_2}{\partial \xi} + B\frac{\partial^3 \phi_1}{\partial \xi^3} + C\phi_1\frac{\partial \phi_1}{\partial \xi} = 0, \tag{12}$$

where

$$C = B[\frac{(\delta-1)}{(\delta+\beta)}\{\frac{(\delta-\beta^2)}{(\delta+\beta)} + \frac{(1+\beta)^2(1-s\Psi_o)}{\Psi_o(1+\beta(1-s\Psi_o))^2}\} + 3R(\gamma_1 - [\lambda^2 + \sigma_d]R^2)].$$

Substituting $\eta = \xi - M\tau$ into Eq. (12) and using the boundary conditions (10) yields

$$\phi_1 = \phi_{2m}\mathrm{Sech}^2(\eta / w_2), \tag{13}$$

where the amplitude ϕ_{2m} and the width w_2 are given by 3M/C and $2\sqrt{B/M} = w_1/2$, respectively. Eq.(13) indicates that only the rarefactive soliton waves exist. On the other hand, as $A \to 0$, but $A \neq 0$, Eq.(12) reduce to

$$\frac{\partial \phi_1}{\partial \tau} + D\sqrt{\phi_1}\frac{\partial \phi_1}{\partial \xi} + B\frac{\partial^3 \phi_1}{\partial \xi^3} + C\phi_1\frac{\partial \phi_1}{\partial \xi} = 0, \tag{14}$$

where we have used [11] $A\phi_2 \to 2D\phi_1/3$. Substituting $\eta = \xi - M\tau$ into Eq. (14) and integrating twice, using (10), we get

$$(d\phi_1/d\eta)^2 = M\phi_1^2/B(1 - [8D\sqrt{\phi_1}/15M] - [C\phi_1/3M]) = -V(\phi_1, M). \tag{15}$$

For the formation of double layer, we must have

$$V(\phi_m, M) = 0, (\frac{dV}{d\phi_1})_{\phi_1=\phi_m} = 0 \text{ and} (\frac{d^2V}{d\phi_1^2})^2_{\phi_1=\phi_m} < 0. \tag{16}$$

Applying these conditions, the double layer solution is given by

$$\phi_1 = (\phi_m/4)[1 - \mathrm{Tanh}(\eta/w)]^2; w = (5\sqrt{-3BC})/D \tag{17}$$

The formation of the compressive and rarefactive DA double layers depends on the sign of D.

DISCUSSION AND CONCLUSION

In this paper, we have studied the effects of adiabatic variation of charges, dust temperature and trapped electrons on DA solitary waves in dusty plasma. The dust grains variation of dust charges modifies the DA solitary waves. We have derived MKdV equation (9) and the admitted compressive DA solitary waves have been obtained. At critical values, KdV equation, Eq. (12) is derived that admits only rarefactive soliton. Also, we get the condition under which double layers can exist.

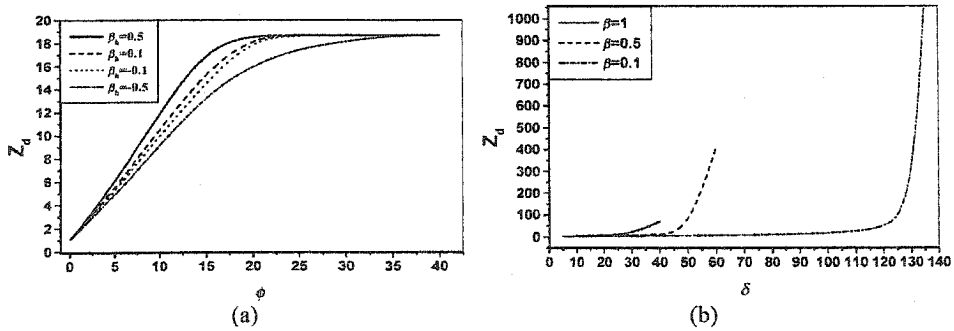


Figure 1 Z_d is plotted (a) against ϕ for different β_h values with δ =10 and β =0.5 and (b) against δ for different β values with ϕ =2 and β_h =0.9.

From numerical investigation, we can conclude that

- As ϕ increases, Z_d increases first quickly with large slope, finally it has a constant value. As β_h or β increases Z_d increases. On contrary, Z_d has a nearly fixed value for a variation in δ, except near the maximum admitted δ ; δ_{max} increases rapidly.
- λ decreases as δ or β increases. On contrary, λ increases as σ_d increases.
- For δ <3, ϕ_{1m} increases rapidly, thereafter it decreases as δ increases. Also, we conclude that, ϕ_{1m} decreases as σ_d or β_h increases. But, it increases as β increases.

ϕ_{2m} decreases slowly as δ increases, however nearest to δ_{max} , it increases rapidly. ϕ_{2m} decreases as β increases. But it increases rapidly as σ_d . This investigation would be effective for understanding the properties of grain charging and the dynamics of DA waves in the presence of trapped electrons.

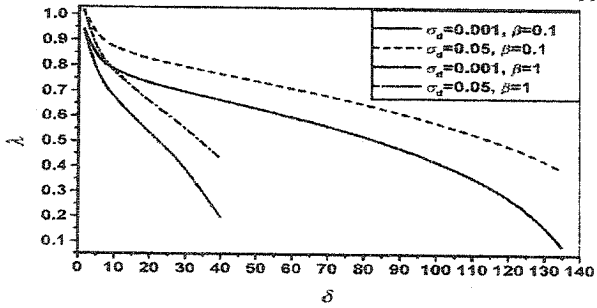
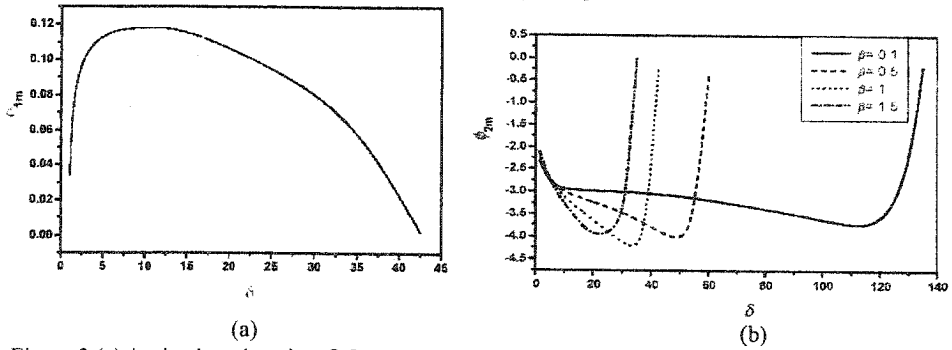


Figure 2 The variation of λ against system parameter variations



(a) (b)

Figure 3 (a) ϕ_{1m} is plotted against δ for σ_d=0.001, β=1 and β_h=-0.7. (b)) ϕ_{2m} is plotted against δ for σ_d=0.001 and different β values.

REFERENCES

(1) F. Verheest; "Waves in Dusty Plasmas", Kluwer Academic Publishers, Dordrecht (2000).
(2) G.C. Das, J. Sarma; Phys. Plasmas 5, 3918 (1998).
(3) N.N. Rao, P.K. Shukla, and M.Y. Yu; Planet. Space Sci. 38, 543 (1990).
(4) Baisong Xie, Kaifen He, and Zuqia Huang; Phys. Lett. A 247, 403 (1998).
(5) J.P. Lynov, P. Michelson, H.L. Pecseli, and J. Rasmussen; Phys.Lett. 80, 23 (1980).
(6) H. Schamel; Phys. Reports 140, 3, 161 (1986).
(7) S.K. El-Labany, and W.F. El-Taibany; Accepted for publication in J. Plasma Physics (2003).
(8) M.R. Jana, A. Sen, and P.K. Kaw; Phys. Rev. E 48, 3930 (1993).
(9) P.K. Shukla, and A.A. Mamun; "Introduction to Dusty Plasma Physics", Institute of Physics Publishing Ltd., Bristol (2002).
(10) H. Schamel; J. Plasma Phys 9, 377 (1973).
(11) S. Watanabe; J. Phys. Soc. Japan 53, 950 (1984).

MHD Plasma: Spherical Region Model-Analytical and Numerical Investigation

Ali I Mussa
Space Research Institute (SRI)
King Abdulaziz City for Science and Technology (KACST)
Riyadh 11442, P O Box 6086, Saudi Arabia
almussa@kacst.edu.sa

ABSTRACT

The effect of magnetic configurations on a MHD plasma problem is addressed. As plasma behavior is strongly affected by perturbation in the magnetic field, a great interest is to study and investigate the stability of such perturbation. Such issue shall be discussed here.

The problem of MHD plasma in a spherical geometry configuration is considered. Different schemes are considered. One of the most effective and promising solution methods, the auxiliary variational inequality methods, is used.

Thrust production due to electromagnetic body force (Lorentz force) is also of interest in this work. We intend, here, to reveal how such mechanism, using our techniques/methods, can be achieved.

Key Words: MHD Plasma, Thrust in Space, Simulation

INTRODUCTION

MHD in a spherical geometry configuration represents importance and interest via space and industrial plasma physics, geophysical and astrophysical fluid dynamics. For example, in space physics, some of the very important applications are the study of space weather, electromagnetic casting of metals, MHD power generation and MHD ion propulsion.

One of main aims of this study is to explore the general and different mathematical modeling of some real life problems that arise in the field of space plasma physics. The problem we study, which has its origin in Space Science and Earth Science, has the realistic features of, for example, spherical geometry, which has an advance over the plane layer models of many previous studies in hydrodynamics and magnetohydrodynamics stability theory. However, it is well worth (here) to mention that in order to avoid excessive mathematical difficulty, one can consider the linear problem instead rather than making a full nonlinear study. The mathematical model, we consider, is presented below.

SPHEREICAL GEOMETRY CONFIGURATION

Such configuration is very important in numerous studies. For instance, the study of the solar wind flows pasting planets and interstellar winds flows pasting stars is usually carried out in a spherical geometry configuration. Motion of satellites via the magnetospheric plasmas is another important example.

Earths magnetosphere and planetary ionospheres are best described by spherical geometry model. In laboratory plasma physics, spherical tokamaks, spherical torus and spheromaks are examples of such configuration. Practically, for stellar winds studies, spherical polar coordinates are usually assumed. The governing equations needed for the system are respectively: The continuity equation, the MHD force equation (Equation of motion), the

adiabatic pressure equation, Ohm's law, non magnetic monopoles, Ampere's law, and Faraday's law

$$\frac{\partial \rho}{\partial t}+\nabla\cdot(\rho \mathbf{v})=0\,;\rho\frac{\partial \mathbf{v}}{\partial t}+\rho(\mathbf{v}\cdot\nabla)\mathbf{v}+\nabla p-\mathbf{J}\times\mathbf{B}-\rho\mathbf{g}=0\,;\frac{\partial P}{\partial t}+\mathbf{v}\cdot\nabla P+\gamma P\nabla\cdot\mathbf{v}=0$$

$$\mathbf{E}+\mathbf{v}\times\mathbf{B}=0\,;\nabla\cdot\mathbf{B}=0\,;\nabla\times\mathbf{B}-\mu_0\mathbf{J}=0\,;\frac{\partial \mathbf{B}}{\partial t}+\nabla\times\mathbf{E}=0$$

In above equations, the electromagnetic variables are the electric field **E**, the magnetic fields **B** and the current density **J**. The fluid variables are the mass density ρ, the plasma velocity **v**, the plasma pressure P, and γ is the adiabaticity index (the ratio of specific heat). The electric and magnetic fields **E** and **B**, which appear in these expressions consist of externally applied fields and the averaged internal fields arising from long-rang inter-particle interactions.

In previous work[1], the MHD problem in rapidly rotating spherical geometry has been studied. In such a problem[1] also in Ref. (2) and to asymptotically resolve the problem, the authors considered the ansatz

$$\frac{1}{s}\frac{\partial}{\partial\phi}\sim\frac{\partial}{\partial s}\sim O(E^{-1/3}),\qquad \frac{\partial}{\partial z}\sim O(1),\qquad \frac{\partial}{\partial t}\sim O(E^{-2/3}),\qquad \text{as } E\downarrow 0$$

Lorentz force in the governing equations is presented at leading order provided that $E\downarrow 0$. At leading order, other terms can then be easily deduced. To obtain the dispersion relation, it is assumed a disturbances of the form exp[i(Ks+Mϕ - Ωt)]. After lengthy derivations, the following basic second order ordinary differential equation is obtained for appropriate boundary conditions:

$$\frac{d^2w}{dz^2}+[\frac{R(a^2-i\omega)(m^2+a^2z^2)}{a^2-iP\omega}-\frac{iRm}{a^2-iP\omega}-(a^2-i\omega)^2a^2$$

$$+\frac{Rm^2\lambda B_\phi^2(a^2z^2+m^2)}{s^2(a^2-iP\omega)(a^2-iP_m\omega)}-\frac{2a^2(a^2-i\omega)m^2\lambda B_\phi^2}{s^2(a^2-iP_m\omega)}-\frac{m^4\lambda^2B_\phi^4a^2}{s^4(a^2-iP_m\omega)^2}],$$

The dispersion relation can be then obtained by solving the two-boundary value problem for the complex eigenvalue ω. This defines ω as $\omega=\omega(s,k,m,R,\lambda)$.

The technique for obtaining the global solution is described in (1, 2).
Now, it is of interest to reconstruct and reformat the above mention problems and formulation using the double turning point theory to study the effect of imposing a homogenous or inhomogeneous axisymmetric or non-axisymmetric magnetic field into the MHD space problems (e.g., plasma thrusters).

In consequence, we start our theoretical study by considering the local asymptotic theory first. The global (complete) asymptotic results would then be implemented; on the hope that some discoveries can be greatly obtained. Extending our code, the complete spectral numerical approach, can be carried out to resolve the problem numerically in the full sphere or spherical shell geometry. The extension could benefit greatly from the variational inequality formulation. Asymptotic results and numerical results are then compared for certain regions of parameter space, to show the agreement between the leading order and the numerical results.

RESULTS AND INTERPRETATIONS

In this section we present and discus some of our main and modified magneto and non-magneto spectral code results. Runs have been carried out on a massively 32 IBM supercomputer (also on SGI Origin 2000). We present these results to prove the usefulness and the agreement between the

numerical and asymptotic results. We also present such results to motivate us to extend both techniques to the full field of plasma physics.

In figure (1) we show the magnetoconvection motions of the velocity components u_r at the equatorial plane for Prandtl numbers in the range 0.1-10 for $T=10^{12}$. The patterns of the convective flows show a spiral columnar structure. These figures make clear the concentration of the disturbance near the critical cylinder, which is a key assumption of the asymptotic theory. The drifting of the convection patterns is controlled by a phase speed $c=-\omega/m$. In consequence, the spiral columns of convection drift around in prograde, eastward, direction if $\omega< 0$ and drift westward if $\omega> 0$. In all the cases shown, the rolls drift in a prograde direction that is anticlockwise in the figures shown. Note that the figures as the Prandtl number, P, decreases the convection rolls stretch.

In figure (2) we display the patterns of magnetoconvection for the radial, b_r, and azimuthal, b_φ, components of magnetic fields in the meridional plane (r,θ) for Prandtl number, $P=10$ and $T=10^{12}$. The columnar structure is also apparent in the magnetic field perturbations. The radial field patterns show very little field escapes outer of the sphere; b_r is apparently small near the outer boundary. This is a consequence of the large wave numbers in the solution; since $\partial h_l / \partial r = -\langle (l+1)/r \rangle h$, and l is large; h is small so b_r is also small at the outer boundary.

FUTURE WORK

We are planning to study and investigate the following tasks in due course

- Construct a valid global asymptotic theory solution for a wide spectrum of MHD plasma problems at asymptotically leading order of accuracy.
- Develop robust Variational and Quasi-Variational Inequality techniques for the linear and non-linear MHD plasma problems; we could use the auxiliary Variational inequality formulation .
- Investigate the ideal MHD via the non-ideal MHD different plasma behavior adopting new techniques.
- Build Hybrid Multilevel Code (HMC), using the MHD and PIC approaches[3-5].
- Do some experimental verification.

ACKNOWLEDGEMENTS

Many thanks and appreciations are due to Dr. Turki Al-Saud, director of Space Research Institute (SRI) for his encouragement and support. Special thanks are also due to Professor Sherif Khalil for his helpful discussion, comments and kind friendship.

REFERENCES

(1) Jones, C.A., Mussa, A.I. and Worland, S.J., 2003. Magnetoconvection in a Rapidly Rotating Sphere: the weak field case, Proc. R. Soc. Lond. A **459**, No. 2031, 773-797.
(2) Jones, C.A., Soward, A.M, and Mussa, A.I., 2000. The Onset of Thermal Convection in a Rapidly Rotating Sphere, J. Fluid Mech. **405**, 157-179.
(3) Brecht, S.H., 2001. Three dimensional global hybrid particle code simulation. Proceedings of ISSS-6, Copernicus Gesellschaft.
(4) Chibbaro, S. and Zanna, L.D., 1999. A Parallel MHD Code for Origin 2000. L.go E. Fermi 5, I- 50125 Firenze, Italy.
(5) Toth, G., 1997. Numerical Simulation of Magnetohydrodynamics, Communications of the Konkoly Observatory, No. 100 (**Vol. XII, 2**), 259-270.

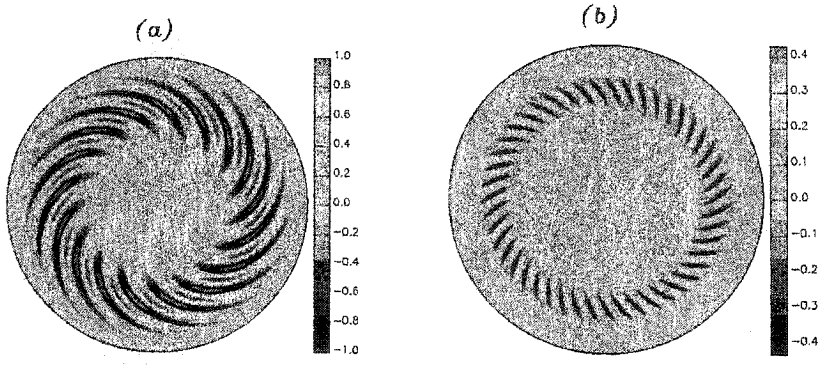


Figure 1: Contour plots of (a) velocity components u_r at the equatorial plane for P=0.1, T=10^{12}, P_m=1 and λ=1, (b) velocity components u_r at the equatorial plane for P=10, T=10^{12}, and m_c=47 and λ=0.

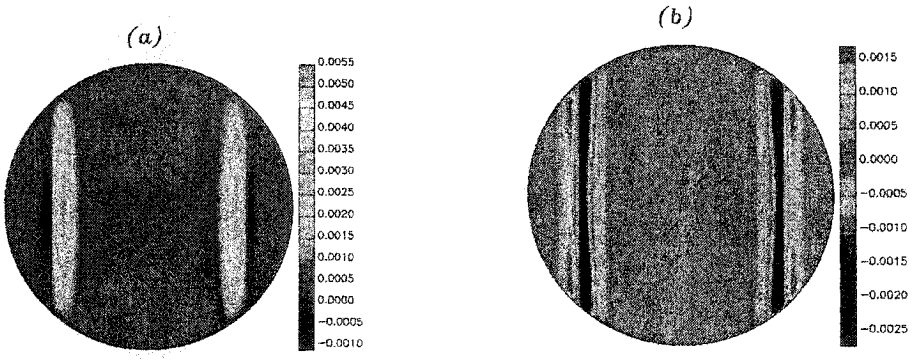


Figure 2: Contour plots of (a) magnetic components b_r in a meridional (r,θ) plane for P=10, T=10^{12}, P_m=1 and λ=1, (b) magnetic components b_ϕ in a meridional (r,θ) plane for P=10, T=10^{12}, P_m=1 and λ=1.

Field Stability by the Electron Beam in a Warm Magnetized Plasma-Filled Waveguide

Sh. M. Khalil, Y. A. Sayed, Kh. H. El-Shorbagy and A. T. El-Gendy (*)
Plasma Physics and Nuclear Fusion Dept., Nuclear Research Center, Atomic Energy Authority, Cairo – Egypt.
(*) Ain Shams University, Faculty of Science, Physics Dept., Cairo – Egypt.

ABSTRACT

We study the effect of the electron beam on the field stability and minimizing the energy losses in waveguide filled with plasma. Analytical calculations are performed to find the plasma dielectric tensor. By applying the boundary conditions at the plasma-conductor interface, we derive the dispersion equations, which describe the propagated E- and H- waves and their damping rate. The necessary condition for the field stability in the waveguide and the amplification coefficient for the E-wave are obtained. Realistic plasma conditions (i.e., its warmness and inhomogeneity under the effect of an external static magnetic field) are taken into consideration. The electron beam is found to play a crucial role in controlling the field attenuation in waveguide.

Key Words: Beam-Plasma system, Instabilities, Plasma Heating

INTRODUCTION

Efforts are paid to study the physical and geometrical parameters that cause attenuation of wave, which propagates inside waveguide filled with plasma. This subject is of currently considerable interest for plasma and fusion experiments, RF sources for the next generation of particle accelerators, plasma diagnostic techniques, optical systems and in the development of high power millimeter wave amplifiers and its application via high resolution and imaging radar, high information density communication, stability of devices based on the use of charged particle beam, and NDT (non destructive testing).

In this paper we will continue our study to include the effect of applying strong magnetic field and electron beam to minimize the energy losses in a waveguide field with warm, magnetized plasma. Also we will consider the effects of the field stability of plasma. Linearzed fluid and Maxwell's equations are used to derive the dispersion relation, the study of TE and TM modes and the power transmission, which describe different conditions of plasma filled waveguide. For example, its movability, warmness, collision, homogeneity and inhomogeneity under the effect of a strong and weak static magnetic field and the incidence of electron beam are taken into consideration [1-3].

Cartesian coordinates (X,Y,Z) rectangular waveguide are used to describe our system. In our case we consider the directions of wave propagation and the static magnetic field are in the Z-direction with non conducting media which is characterized by a permittivity tensor ε_{ij} and permeability $\mu \approx 1$. Using a rectangular waveguide with side lengths a and b related as shown to a system of Cartesian coordinates, in which the z- axis is parallel to the axis of the tube.

1. Magnetized Warm, Movable, Collisional and Homogeneous Plasma Interaction with an Electron Beam

We consider the effect of an external static magnetic interacting with an electron beam. It is shown that the plasma oscillations excited by the beam are linearly coupled to the electromagnetic modes, as we will see in our analytical calculations. It is convenient to consider that the beam density n_b be much smaller than the electron plasma density n_p $(i.e., n_b << n_p)$. This assumption enables us to continue considering small oscillations and to apply the linear approximation. We shall discuss here the case of a waveguide filled

with warm, homogeneous magnetized plasma. The summations over α include both the plasma and beam electrons. As we considered a case of high frequency waves, the oscillations of the ions are neglected [4,5].

In the present work we considered the case of interacting non relativistic electron beam and so we have got independent wave equations such that we can evaluate the TE and TM modes independently.

TE- MODE

1.1 Dispersion Relation

By applying the boundary conditions we get the dispersion relation of waves propagating inside waveguide filled with magnetized plasma, interacting with an electron beam, is describ by the refractive index.

$$n^2(\tilde{\omega}) = 1 - \frac{\omega_{cut}^2}{\tilde{\omega}^2} - \frac{\omega_{P\alpha}^2}{\tilde{\omega}^2 - \omega_{c\alpha}^2}[(1 \pm \frac{\omega_{c\alpha}}{\tilde{\omega}}) + i\mu_\alpha(1 \mp \frac{\omega_{c\alpha}}{\tilde{\omega}})] - \frac{\omega_b^2}{\tilde{\omega}_{2b}^2 - \omega_{cC\alpha}^2} \cdot [(1 \pm \frac{\omega_{c\alpha}}{\tilde{\omega}_b}) + i\mu_\alpha(1 \mp \frac{\omega_{c\alpha}}{\tilde{\omega}_b})] \quad (1)$$

where $\omega_{c\alpha} = \frac{eH_{ext}}{m_\alpha c}$, $\vec{H}_{ext} = \vec{e}_z H_0$, $\omega_{be} = (\frac{4\pi n_{ob} e^2}{m_b})^{\frac{1}{2}}$, $\omega_{P\alpha} = (\frac{4\pi n_b e^2}{m_b})^{\frac{1}{2}}$, $\tilde{\omega}_b = (\omega - k_z v_{ob})$, $\mu_\alpha = \frac{\nu_\alpha}{\tilde{\omega}}$

1) Propagation condition at

$$\frac{\omega_{cut}^2}{\tilde{\omega}^2} + \frac{\omega_{P\alpha}^2}{\tilde{\omega}^2 - \omega_{c\alpha}^2}[(1 \pm \frac{\omega_{c\alpha}}{\tilde{\omega}}) + i\mu_\alpha(1 \mp \frac{\omega_{c\alpha}}{\tilde{\omega}})] + \frac{\omega_b^2}{\tilde{\omega}_{2b}^2 - \omega_{c\alpha}^2} \cdot [(1 \pm \frac{\omega_{c\alpha}}{\tilde{\omega}_b}) + i\mu_\alpha(1 \mp \frac{\omega_{c\alpha}}{\tilde{\omega}_b})] < 1$$

2) Attenuation mode at

$$\frac{\omega_{cut}^2}{\tilde{\omega}^2} + \frac{\omega_{P\alpha}^2}{\tilde{\omega}^2 - \omega_{c\alpha}^2}[(1 \pm \frac{\omega_{c\alpha}}{\tilde{\omega}}) + i\mu_\alpha(1 \mp \frac{\omega_{c\alpha}}{\tilde{\omega}})] + \frac{\omega_b^2}{\tilde{\omega}_{2b}^2 - \omega_{c\alpha}^2} \cdot [(1 \pm \frac{\omega_{c\alpha}}{\tilde{\omega}_b}) + i\mu_\alpha(1 \mp \frac{\omega_{c\alpha}}{\tilde{\omega}_b})] \geq 1$$

3) Cyclotron resonance at $\tilde{\omega}^2 = \omega_{c\alpha}^2$

4) Electron beam resonance at $\omega^2 = \omega^2_b$

Let $H(\omega) = \sqrt{1/(0.4 + 0.0056\frac{\tilde{\omega}^2 - \omega_{c\alpha}^2}{\omega_{p\alpha}^2} + 0.0056\frac{\tilde{\omega}^2 - \omega_{c\alpha}^2}{\omega_b^2})}$

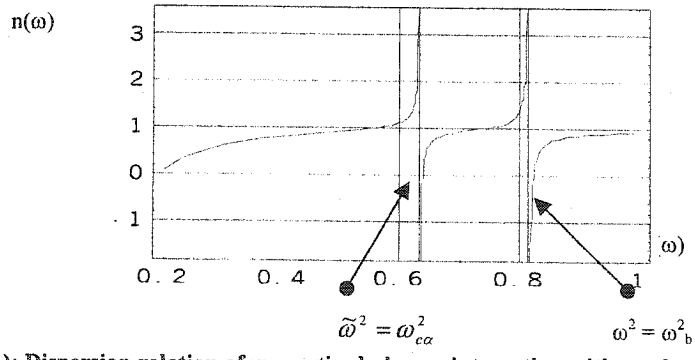


Fig. (1): Dispersion relation of magnetized plasma interacting with an electron beam with the frequency of incident wave.

As shown in fig.1 cyclotron resonance appears at $\tilde{\omega}^2 = \omega_{c\alpha}^2$ (0.56) in the absence of electron beam [5]. In present work we considered the effect of non-relativistic electron beam so, cyclotron resonance was shifted at higher frequency ($\tilde{\omega}^2 = \omega_{c\alpha}^2$ (0. 61)) in addition to the resonance that appear at $\omega^2 = \omega_b^2$ (.81). We have identified two resonances that enhance the

possibility of minimizing energy loss at higher frequencies in waveguide filled with magnetized plasma.

1.2 Power of Propagating Wave

Now we'll derive the average power flux $S_{av.}^{(P)}$ of a collisional, magnetized plasma interacting with an electron beam for the TE – mode

(i) Warm plasma

$$S_{av}^{(P)} = \frac{c}{8\pi}\sqrt{1-\frac{\omega_{cut}^2}{\tilde{\omega}^2}+\frac{\omega_{P\alpha}^2}{\omega_{c\alpha}^2-\tilde{\omega}^2}(\frac{\omega_{c\alpha}}{\tilde{\omega}})+\frac{\omega_{b\alpha}^2}{\omega_{c\alpha}^2-\tilde{\omega}_b^2}(\frac{\omega_{c\alpha}}{\tilde{\omega}_b})(\frac{c}{\tilde{\omega}\varepsilon})^2 H_0^2 \cdot \left.\begin{array}{l} \\ [(\frac{l\pi}{a})^2\sin^2(\frac{l\pi}{a}x)\cos^2(\frac{m\pi}{b}y)+(\frac{m\pi}{b})^2\cos^2(\frac{l\pi}{a}x)\sin^2(\frac{m\pi}{b}y)] \end{array}\right\} \quad (2)$$

(ii) Cold plasma

$$S_{av}^{(P)} = \frac{c}{8\pi}\sqrt{1-\frac{\omega_{cut}^2}{\tilde{\omega}^2}+\frac{\omega_{P\alpha}^2}{\omega_{c\alpha}^2-\tilde{\omega}^2}+\frac{\omega_{b\alpha}^2}{\omega_{c\alpha}^2-\tilde{\omega}_b^2}(\frac{c}{\tilde{\omega}\varepsilon})^2 H_0^2 \cdot [(\frac{l\pi}{a})^2\sin^2(\frac{l\pi}{a}x)\cdot \left.\begin{array}{l} \\ \cos^2(\frac{m\pi}{b}y)+(\frac{m\pi}{b})^2\cos^2(\frac{l\pi}{a}x)\sin^2(\frac{m\pi}{b}y)] \end{array}\right\} \quad (3)$$

1.3 Attenuation Factor

The refractive index in the complex form is:

$$n_{Real} = \sqrt{1-\frac{\omega_{cut}^2}{\tilde{\omega}^2}-\frac{\omega_{P\alpha}^2}{\tilde{\omega}^2-\omega_{c\alpha}^2}[(1\pm\frac{\omega_{c\alpha}}{\tilde{\omega}})]-\frac{\omega_{be}^2}{\tilde{\omega}_b^2-\omega_{c\alpha}^2}[(1\pm\frac{\omega_{c\alpha}}{\tilde{\omega}_b})]} \quad (4)$$

$$n_{imaj} = \frac{\mu_\alpha}{2n_{real}}[(\frac{\omega_{p\alpha}^2}{\tilde{\omega}^2-\omega_{c\alpha}^2})(1\pm\frac{\omega_{c\alpha}}{\tilde{\omega}})+(\frac{\omega_{p\alpha}^2}{\tilde{\omega}_b^2-\omega_{c\alpha}^2})(1\pm\frac{\omega_{c\alpha}}{\tilde{\omega}})] \quad (5)$$

The average rate of energy flow inside waveguide filled with magnetized plasma interacting with electron beam decreases exponentially as

$$\tilde{S}_{av} = S_0.e^{-2K_{imaj}.z}$$

$$\text{where } \exp(-2k_{imaj}.z) = \exp(-\mu_\alpha(\frac{\tilde{\omega}_\alpha}{c})[(\frac{\omega_{p\alpha}^2}{\tilde{\omega}^2-\omega_{c\alpha}^2})(1\pm\frac{\omega_{c\alpha}}{\tilde{\omega}})+(\frac{\omega_{p\alpha}^2}{\tilde{\omega}_b^2-\omega_{c\alpha}^2})(1\pm\frac{\omega_{c\alpha}}{\tilde{\omega}})\frac{1}{n_{real}}.z] \quad (6)$$

(i) Strong magnetic field

$$S_{av}^{(P)} \sim \exp(-2k_{imag}z) = \exp(-\frac{\nu_\alpha}{\omega_{c\alpha}}(\frac{\tilde{\omega}}{c})(\frac{\omega_{P\alpha}^2}{\tilde{\omega}^2}+\frac{\omega_{be}^2}{\tilde{\omega}_b^2})\frac{1}{n_{real}}.z) \quad (7)$$

$$Q_{TE} = (\frac{\nu_\alpha}{\omega_{c\alpha}}(\frac{\tilde{\omega}}{c})(\frac{\omega_{P\alpha}^2}{\tilde{\omega}^2}[1+\frac{W_{be}^2}{W_{P\alpha}^2}])\frac{1}{n_{real}}) \quad (8)$$

where $\tilde{W}_{be} = \frac{\omega_{be}}{\tilde{\omega}_b}$, $\tilde{W}_{P\alpha} = \frac{\omega_{P\alpha}}{\tilde{\omega}}$

(ii) Weak magnetic field

$$Q_{TE}\text{ (weak magnetic field)} = (\frac{\nu_\alpha}{\omega_{c\alpha}}(\frac{\tilde{\omega}}{c})(\frac{\omega_{P\alpha}^2}{\tilde{\omega}^2-\omega_{c\alpha}^2}[1+\frac{W_{be}^2}{W_{P\alpha}^2}])\frac{1}{n_{real}}) \quad (9)$$

TM- MODE

1.4 Attenuation Factor

(i) Warm plasma

The average rate of energy flow in the filled waveguide

$$S_{av}^{(P)} \sim \exp(-2k_{imag}z) = \exp(\frac{\nu}{\omega}\frac{\omega}{c}\frac{\Omega_p^2}{\omega^2}\frac{1}{n_{real}}) \quad (10)$$

$$Q_{TM} = (\frac{\tilde{\omega}}{c}\mu_\alpha \frac{\omega_{P\alpha}^2}{\omega_{c\alpha}\tilde{\omega}}[(1+\frac{\tilde{W}_{be}^2}{\tilde{W}_{P\alpha}^2}) - \frac{\tilde{\omega}}{\omega_{c\alpha}}(\frac{\tilde{W}_{cut}^2}{1-(\tilde{W}_{P\alpha}^2/1-\tilde{W}_T^2)}) - \frac{\tilde{\omega}_b}{\omega_{c\alpha}}(\frac{\tilde{W}_{cut}^2(\tilde{W}_{be}^2/\tilde{W}_{P\alpha}^2)}{1-\tilde{W}_{P\alpha}^2-\tilde{W}_T^2})]\frac{1}{n_{real}}) \quad (11)$$

where $\tilde{W}_T = \frac{\omega_T}{\tilde{\omega}}$

(ii) Cold plasma

The average rate of energy flow inside waveguide filled with magnetized plasma:

$$S_{av}^{(P)} \sim \exp(-2k_{imag.}z) = \exp(\frac{\omega}{c} n_{\text{Im}ag.}.z) \quad (12)$$

$$Q_{TM} = (\frac{\tilde{\omega}}{c}\mu_\alpha \frac{\omega_{P\alpha}^2}{\omega_{c\alpha}\tilde{\omega}}[(1+\frac{\tilde{W}_{be}^2}{\tilde{W}_{P\alpha}^2}) - \frac{\tilde{\omega}}{\omega_{c\alpha}}(\frac{\tilde{W}_{cut}^2}{1-(\tilde{W}_{P\alpha}^2)}) - \frac{\tilde{\omega}_b}{\omega_{c\alpha}}(\frac{\tilde{W}_{cut}^2(\tilde{W}_{be}^2/\tilde{W}_{P\alpha}^2)}{1-\tilde{W}_{P\alpha}^2})]\frac{1}{n_{real}}) \quad (13)$$

We conclude that warmness, negative direction of inhomogeneous plasma and small density of EB leads to good propagation and small attenuation factor.

DISCUSSIONS AND CONCLUSIONS

In this paper we have studied basic factors that considered minimizing the energy losses of electromagnetic waves propagating in waveguide filled with magnetized plasma.

Effect of magnetic field on attenuation factor in case of homogeneous plasma

(i) $$\frac{Q_{TE}(Strong\ magnetized)}{Q_{TE}(Unmagnetized)} \approx \frac{\tilde{\omega}}{\omega_{c\alpha}} < 1$$

(ii) $$\frac{Q_{TE}(Weak\ magnetized)}{Q_{TE}(Unmagnetized)} \approx \frac{\tilde{\omega}^2}{\tilde{\omega}^2 - \omega_{c\alpha}^2} \geq 1$$

(iii) $$\frac{Attenuation\ Factor\ (Strong\ magnetized)}{Attenuation\ Factor\ (Weak\ magnetized)} \approx (\frac{\tilde{\omega}}{\omega_{c\alpha}})(\frac{\tilde{\omega}^2 - \omega_{c\alpha}^2}{\tilde{\omega}}) << 1.$$

Equation (iii) indicates that the strong magnetic effect confines the energy inside the waveguide instead of escaping so it minimizes the energy losses inside waveguide better than the weak magnetic plasma and unmagnetized plasma . If we compare between the attenuation factor of two cases strong magnetic, movable and inhomogeneous plasma to homogeneous plasma $\frac{Q_{TE}(In\,\text{hom}\,ogeneous)}{Q_{TE}(Homogeneous)} \approx \delta = 1 + \frac{|k'|}{k}$.

we will get two values: 1) $|k'| = +value \rightarrow \delta > 1$ which means that the attenuation factor increases in case of inhomogeneous to homogeneous case.

2) $|k'| = -value \rightarrow \delta < 1$ which means that the attenuation factor decreases due to the negative wave number in inhomogeneous case. At magnetized plasma (for TM mode) warmness, negative direction of inhomogeneous plasma and small density of the electron beam (EB) plays an important role in reducing the attenuation factors and minimizing the energy losses inside the waveguide.

REFERENCES

(1) S.K. Ghosh and S.P. Pall, J. Plasma Phys. 29, 383 (1983).
(2) S.T. Ivanov and E.O. Alexov, J. Plasma Phys. 43, 51 (1990).
(3) J.E. Marahechi, et al., Plasma Phys. 1, 3181 (1994).
(4) Sh.M. Khalil, Kh.H. El-Shorbagy and E.N. El-Siragy, IEEE Catalog Number 99EX249 [16th National Radio Since Conference, NRSC'99, Ain Shams University, Feb. 23-25 (1999), Cairo, Egypt.]
(5) Sh.M. Khalil, Kh.H. El-Shorbagy and E.N. El-Siragy, Contribution to Plasma Physics 76 (2002).

On the Theory of Stochastic Dynamics of Magnetically Confined Plasma

R. N. El-Sharif, N. S. El-Atoy*
Plasma and Nuclear Fusion Dept., N.R.C, Atomic Energy Authority, Cairo – Egypt
**Physics Dept., Girls Colleges, KSA*
alsharifragaa@hotmail.com

ABSTRACT

This work is devoted to a study of the motion of plasma electrons in a system of two fields, a magnetic field along z-axis and wave-packet field, which propagates in the x-z plane. The strongest interaction between plasma electrons and both fields is due to their resonance with these fields. The motion of plasma electrons become stochastic when a set of resonance overlapping. Conditions for stochasticity are obtained.

Key Words: Magnetically Confined Plasma, Stochastic Dynamic

INTRODUCTION

For the last decade there has been a considerable interest in stochastic effects in many problems of importance to the magnetically confinement program[1]. Especially, work on this subject was done in connection with the stochastic instability of the magnetic field lines in Tokamaks and stellarators[2,3]. The stochasticity arises from the mixing processes of trajectories in phase space[4]. There is widescope of works devoted for the study and investigation of stochastic dynamics of magnetically confined plasma[5-9]. Destruction of magnetic surfaces by confining magnetic fields in Tokamaks has also been studied[10-13].

1. Equation of motion:

We will consider a uniform magnetic field "B_0" directed along the z-axis and an electrostatic wavepacket having components in x-z plane with a wave vector k. The Hamiltonian of a plasma electron moving in these fields has the following standard form (resonance is neglected)[14]:

$$H=\frac{1}{2m_e}\left(P-\frac{e}{c}B_o x\vec{e}_y\right)^2-e\sum_i \Phi_i\cos\left(k_z z+k_\perp x-\omega_i t\right) \qquad (1)$$

Where m_e is the plasma electron mass, e is the electron charge, P is the generalized particle momentum, and e_y the unit vector along the y-axis and Φ_i the amplitudes of the potential of the plane wave component.

Let us introduce a new coordinate:

$$\bar{x}=x-\frac{P_y}{m_e\omega_H} \quad ; \quad \frac{d\bar{x}}{dt}=V_x \qquad (2)$$

and using the polar coordinates:

$$\bar{x} = \rho \sin\varphi \quad ; \quad \bar{\dot{x}} = \rho\, \omega_H \cos\varphi \tag{3}$$

$$H = \frac{P_z^2}{2m_e} + \omega_H I - e\sum_i \Phi_i \cos\left(K_z z + k_\perp \rho \sin\phi - \omega_i t\right) \tag{4}$$

Then from (1-3) the Hamiltonian of the system is given by:

where,

$$I = \frac{1}{2} m_e \omega_H \rho^2 \quad , \quad \omega_H = \frac{eB_0}{m_e c} \text{ and } \rho \text{ is the gyration radius}$$

Using the properties of Bessel functions, equation (4) becomes:

$$H = \frac{P_z^2}{2m_e} + \omega_H I - e\sum_i \Phi_i \sum_{l=-\infty}^{l=\infty} J_l\left(k_\perp \rho\right)\cos\left(K_z z + l\phi - \omega_i t\right) \tag{5}$$

where $J_l\,(k_l\,\rho)$ is Bessel functions . For simplicity , let us introduce the notation:

$$\begin{aligned} L &= \left(L_1, L_2\right) \quad , \quad L_1 = P_Z \quad , \quad L_2 = I \\ \vartheta &= \left(\vartheta_1, \vartheta_2\right) \quad , \quad \vartheta_1 = Z \quad , \quad \vartheta_2 = \varphi \end{aligned} \tag{6}$$

Accordingly, (5) reads:

$$H = H(L, \vartheta) = H_0(L) + \mu(L, \vartheta) \tag{7}$$

where,

$$H_0(L) = \frac{1}{2m_e} L_1^2 + \omega_H L_2 \tag{8}$$

$$\mu\left(L, \vartheta\right) = \sum_i \sum_{l=-\infty}^{l=\infty} \mu_{il}(L) e^{i\left(\vartheta_1 k_z + \vartheta_2 l - \omega_i t\right)} \tag{9}$$

$$\mu_{il}(L) = -\frac{1}{2} e \Phi_i J_l(k_\perp \rho) \tag{10}$$

$$L_1 = -\frac{\partial H}{\partial \vartheta 1} = -\sum_i \sum_{l=-\infty}^{l=\infty} i\,\mu_{il}(L)\,k_z\,e^{i(k_z\vartheta_1 + l\vartheta_2 - \omega_i t)}$$

$$L_2 = -\frac{\partial H}{\partial \vartheta 2} = -\sum_i \sum_{l=-\infty}^{l=\infty} i\,\mu_{il}(L)\,l\,e^{i(k_z\vartheta_1 + l\vartheta_2 - \omega_i t)} \qquad (11)$$

$$\vartheta_1 = \frac{\partial H}{\partial L1} = \frac{L_1}{m_e} \quad , \quad \vartheta_2 = \frac{\partial H}{\partial L2} = \omega_H$$

We can obtain the following expressions from the Hamiltonion equation of motion

Taking into account the effect of resonance on the moving plasma electrons in both fields. Equation(7) will be in the form:

$$\mathrm{H}_{il} = \frac{L_1^2}{2m} + \omega_H L_2 - U_{il}\cos\psi \qquad (12)$$

Where: $U_{il} = e\Phi\ J_l(k_\perp \rho)\ , \psi\ = k_z\vartheta_1 + l\vartheta_2 + \omega_i t$ (13)

From (12) and (13) we get:

$$L_1 = -k_z U_{il}\sin\psi,\ \ L_2 = -lU_{il}\sin\psi,\ \ \psi = k_z\vartheta_1' + l\vartheta_2' - \omega_i = \omega_{il}(V_z) \qquad (14)$$

Accordingly, we can obtain the resonance condition in the form:

$$k_z V_z^{(r)} + l\omega_H - \omega_i = 0 \qquad (15)$$

Differentiating the equation for ψ in (14) with respect to time we get:

$$\frac{d^2\Psi}{dt^2} + \Omega_{il}^2 \sin\Psi = 0 \qquad (16)$$

$$\Omega_{IL} = K_Z\sqrt{\frac{U_{il}}{m_e}}$$

Equation (16) represents a differential equation which describes the phase oscillations. Using (13) the frequency of these oscillations is given by:

$$\Omega_{il} = k_z\left|\frac{e}{m_e}\Phi_i J_l(k_\perp\rho)\right|^{1/2} \qquad (17)$$

For strong fields $(k_\perp\rho\langle\langle 1)$, Ω_{il} reads:

$$\Omega_{il} = k_z\left[e\frac{|\Phi_i|(k_z\rho)^l}{2m_e}\right]^{1/2} \qquad (18)$$

If l=0 , then equation (18) reduces to the known Manley- Raw[4]:

$$\Omega_{il} = k_z \left[e \frac{|\Phi_i|}{2m_e} \right]^{1/2} \tag{19}$$

The solutions of the nonlinear resonance equation (16) are :

$$H^{(r)} = \frac{1}{2}\Psi^2 - \Omega_{il}^2 \cos\Psi = \frac{1}{2} k_z (\Delta V_z)^2 - \Omega_{il}^2 \cos\Psi \tag{20}$$

Where Ω_{il} is the frequency of the phase oscillations, : the resonance conditions of the longitudinal motion :

$$\frac{\Omega_{il}}{k_z V_z} = \left| \frac{e\Phi_i J_l(k_z \rho)}{m_e V_z^2} \right|^{\frac{1}{2}} << 1$$

$$\frac{\Omega_{il}}{\omega_H} = \frac{k_z}{\omega_H} \left| \frac{e\Phi_i J_l(k_z \rho)}{m_e} \right|^{\frac{1}{2}} << 1 \tag{21}$$

The overlapping condition of resonance of longitudinal motion may be given in terms of

$$\eta = \left(\frac{\Delta\omega}{\delta\omega} \right)^2, \Delta\omega = \frac{d\omega_{il}}{dL_l} \Delta L_l = 2\Omega_{il} \quad , \delta\omega = \left| \omega_l(V_z^l) - \omega_l(V_z^{l+1}) \right| \tag{22}$$

where "Δω" is frequency width of a nonlinear resonance and $\delta\omega$ is the distance between the resonances in the frequency . When η<1, the motion of resonance particles is very close to conditionally periodic one, while at η≥1 the motion of plasma electrons in both fields becomes stochastic. In fact, a criterion for the particle dynamics to be chaotic is:

$$\eta \geq 1 \tag{23}$$

And then η according to our calculations reads.

$$\eta = 4 \frac{k_z^2}{\omega_H^2} \frac{e|\Phi_i J_l(k_\perp \rho)|}{m_e} \geq 1 \tag{24}$$

Where η is the resonance overlap parameter [4,10].

CONCLUSIONS

In this work some aspects of the theory of stochastic dynamics of magnetically confined plasma have been studied. The first inequality from (21) shows that the seed longitudinal motion of a particle should be sufficiently strong, thus justifying the name of this type of resonance motion. The second inequality from (21) means that the uniform magnetic field should be sufficiently strong as compared with the perturbation due to the plane wave. The condition (24) implies that in the neighborhood of the zero of Bessel function J_l ($k_\perp \rho$), the inequality (24) is violated and there arises stable islands with the conditionally periodic motion of particles. The size of these islands, being of order of (l/max. η)

decreases with increasing η. This means that the system will be in a stochastic state when the condition (24) is fulfilled.

ACKNOWELGEMENT

The authors wish to thank Prof. *V V Demchemko* for fruitful collaboration, for proposing the initial scientific plan and also for many helpful discussions.

REFERENCES

(1) B.V. Chirikov, Phys. Reports 52, 264 (1979).
(2) M.N. Rosenbluth, R.Z. Sagdeev, Nuclear Fusion 6, 297 (1966).
(3) G.M.Zaslavsky, N.N. Filonenko, Nuclear Fusion 7, 253 (1967).
(4) G.M.Zaslavsky, R.Z. Sagdeev, D.A. Usikov, A.A. Chernikov "*Weak Chaos and Ouasi-Regular Patterns*", Cambridge University Press (1991).
(5) Morozov, L. Solovev, *The Geometry of the Magnetic Field Reviews of plasma physics 2* (1963).
(6) L. Solovev, V. Shafranov, *Closed Magnetic Configuration for plasma Confinement physics 5* (1965).
(7) M. Rosenbluth, Nuclear Fusion 6, 297 (1966).
(8) N. Filoneniko, Nuclear Fusion 7 253 (1967).
(9) V. Alekxin, Nuclear Fusion 11, 207 (1971).
(10) Ph. Ghendrih, H. Capes, Plasma Physics and Controlled Fusion 38, 1653 (1996).
(11) F. D'Angelo, R.Paccagnella, Plasma Physics and Controlled Fusion, 38, 313 (1996).
(12) H. Sugimoto, T. Kurasawa, Plasma Physics and Controlled Fusion 36, 383 (1994).
(13) V. Antoni, M. Bagatin, Plasma Physics and Controlled Fusion 34, 1992 (1994).
(14) R. Abraham, J.B. Marsden "*Foundations of Mechanics*" Cambridge University Press (1978).

Axisymmetric Mode Analysis for Plasma in Toroidal Devices

Bahaa F. Mohamed
Plasma Physics Dept., N.R.C., Atomic Energy Authority, Egypt
Mohamedbahf@yahoo.co.uk

ABSTRACT

The problem of electromagnetic waves in a toroidal device filled with homogeneous plasma is considered. We will restrict ourselves to the axisymmetric mode analysis with circular cross section. Due to the geometry of toroidal coordinates, which causes nonseparability of the basic equations, we solve Maxwell's equations by means of perturbation expansion in the inverse aspect ratio. Besides, we will calculate the eigenvalues and eigenmodes up to second order. .

INTRODUCTION

The radio-frequency (RF) breakdown and heating are important methods when experimenting with toroidal devices. The absorption of RF-waves is an efficient heating method[1]. Besides, plasma breakdown should occur away from the vessel wall[2]. A correct choice of the useful frequencies depends on plasma properties and their compatibility with the resonant modes of the torus. So the study of resonant modes analysis in toroidal cavities has attracted the interest of several authors who obtained the eigenmodes and related eigenfrequencies[3,4,6,7]. These theoretical studies have a complex structure due to the difficulty of calculating the resonance frequencies in the geometry of the torus by the usual analytical methods. The main mathematical difficulty is due to the nonseperability of the boundary-value problem in toroidal coordinates[5]. The resonant TE modes in toroidal resonators filled a magnetized uniform plasma has been treated by N.Schupfer[4]. In our paper, it will follow exactly the same perturbation procedure of ref. [4], but for TM modes. Besides, we will simplify the analysis by considering only an unmagnitized plasma contained in toroidal resonators with perfectly conducting walls having circular cross sections. It should be mentioned that some authors obtained exact solutions for both TE and TM modes in an empty torus (which is rather similar to our case of a uniform isotropic plasma since we are not going to solve for the eigenfrequencies explicitly and thus the frequency dependence of dielectric constant will be unimportant here)[6, 7]. We will treat the complexity of the problem by means of a perturbation expansion in the inverse aspect. Also, we will calculate the eigenvalues and eigenmodes up to the second order in that ratio.

I. Model Equations

The eigenmodes for any toroidal resonator can be determined by the study the following Maxwell's equations in a conventional coordinate system,

$$rot\ E = -c^{-1}\,\partial B/\partial t$$
$$rot\ B = \varepsilon c^{-1}\,\partial E/\partial t \qquad (1)$$

where E, B are the electric and magnetic field intensities and ε is the dielectric constant. The local coordinate system (ρ,θ,φ) is defined by[4]:

$$x = R_0 h\cos\varphi\ ,\quad y = R_0 h\sin\varphi\ ,\quad z = a\rho\sin\theta$$
$$0\le\rho\le 1\ ,\quad -\pi\le\theta\le\pi\ ,\quad 0\le\varphi\le 2\pi \qquad (2)$$

where a and R_0 are the minor and major radius, respectively, with $h = 1-\alpha\rho\cos\theta$ and $\alpha = a/R_0$ is the inverse aspect ratio.

It is well known from the previous works[5] that the general solution of Maxwell's equations in a toroidal geometry does not posses a pure TE (transverse electric) or TM (transverse magnetic) structure. Only for toroidally uniform modes (i.e., with zero mode number) a distinction between the TE and TM modes can be made. Schupfer N.[4] studied only the TE-waves. Here, we will consider symmetrical TM modes. Besides, we are going to study the axisymmetric case $(\partial/\partial\varphi = 0)$ with considering the time dependence for the fields $(e^{-i\omega t})$. Maxwell's equations read:-

$$\frac{1}{\rho}\frac{\partial}{\partial\theta}(hE_\varphi) = i\frac{\omega}{c}a\,hH_\rho \tag{3}$$

$$-\frac{\partial}{\partial\rho}(hE_\varphi) = i\frac{\omega}{c}a\,hH_\theta \tag{4}$$

$$\frac{1}{\rho}\frac{\partial}{\partial\rho}(\rho H_\theta) + \frac{1}{\rho}\frac{\partial}{\partial\theta}(H_\rho) = -i\frac{\omega}{c}a\,\varepsilon\,hE_\varphi \tag{5}$$

By substituting from equations (3–5) and by taking $E = hE_\varphi$, we obtain the wave equation :-

$$\frac{\partial^2 E}{\partial\rho^2} + \frac{1}{\rho^2}\frac{\partial^2 E}{\partial\theta^2} + \kappa^2 E + \frac{1}{\rho}\frac{\partial E}{\partial\rho} + \frac{\alpha\cos\theta}{h}\frac{\partial E}{\partial\rho} - \frac{\alpha\sin\theta}{\rho h}\frac{\partial E}{\partial\theta} = 0 \tag{6}$$

where,

$$\kappa^2 = \frac{\omega^2}{c^2}\,a^2\varepsilon \quad , \quad \varepsilon = 1-\frac{\omega_{Pe}^2}{\omega^2}-\frac{\omega_{Pi}^2}{\omega^2}$$

In order to solve equation (6), we will use the perturbation method with taking the inverse aspect ratio (α) as the expansion parameter:-

$$E = E_0 + \alpha E_1 + \alpha^2 E_2 + \ldots\ldots \tag{7}$$

II. Resonant Eigenmodes in Toroidal Resonators:

Inserting the expansion (7) into (6), we obtain the different differential equations according to the order of α. So, the zero-order equation has the form:

$$\frac{\partial^2 E_0}{\partial\rho^2} + \frac{1}{\rho^2}\frac{\partial^2 E_0}{\partial\theta^2} + \kappa_0^{\,2} E_0 + \frac{1}{\rho}\frac{\partial E_0}{\partial\rho} = 0 \quad , \quad \kappa_0^{\,2} = \frac{\omega_0^2}{c^2}\,a^2\varepsilon_0 \tag{8}$$

ω_0 *and* ε_0 denote to the zero-order frequency and permittivity associated with an eigenvalue κ_0.

The zero-order problem corresponds to the case of vanishing curvature (α=0) (i.e., the cylindrical waveguide).

Equation (8) has the following solutions:

$$E_0(\rho,\theta) = A_0\,J_n(\kappa_0\rho)\,e^{in\theta}, \quad (n = 0, \pm1, \pm2, \ldots\ldots) \tag{9}$$

where J_n is the Bessel functions.

In order to obtain the eigenfrequencies and a dispersion relation, we have to impose the electromagnetic boundary conditions that the tangential components of the electric fields should vanish on the surface of the torus and the finiteness of the solution at $\rho = 0$. Those yields (for a given n):-

$$J_n(\kappa_0) = \frac{\kappa_0}{n} J_{n-1}(\kappa_0) = 0 \tag{10}$$

We now proceed to find the first–order solution. Equation (6) becomes:-

$$L E_1 = \frac{\sin\theta}{\rho}\frac{\partial E_0}{\partial \theta} - \cos\theta \frac{\partial E_0}{\partial \rho} \tag{11}$$

where,

$$L = \frac{\partial^2}{\partial \rho^2} + \frac{1}{\rho}\frac{\partial}{\partial \rho} + \frac{1}{\rho^2}\frac{\partial^2}{\partial \theta^2} \kappa^2 \tag{12}$$

the first –order solution from equation (9), this leads E_1 in the following form:-

$$E_1 = R_1^-(\rho)\, e^{i(n-1)\theta} + R_1^+(\rho)\, e^{i(n+1)\theta} \tag{13}$$

Thus, we obtain the differential equations for R_1^- and R_1^+

$$L_{n-1} R_1^- = \frac{-A_0 \kappa_0}{2} J_{n-1}(\kappa \rho) \tag{14}$$

$$L_{n+1} R_1^+ = \frac{A_0 \kappa_0}{2} J_{n+1}(\kappa \rho) \tag{15}$$

where, $L_m = \frac{d^2}{d\rho^2} + \frac{1}{\rho}\frac{d}{d\rho} + (\kappa^2 - \frac{m^2}{\rho^2})$ (16)

To solve equation (14) and (15), we follow a generalization of the method used by Lewin [5]. So, we get:

$$R_1^+ = R_1^- = \frac{-\rho A_0}{4} J_n(\kappa \rho) \tag{17}$$

We can follow a similar procedure with the second order perturbation, so we obtain:

$$L E_2 = \frac{\sin\theta}{\rho}\frac{\partial E_1}{\partial \theta} - \cos\theta \frac{\partial E_1}{\partial \rho} + \frac{1}{2}\sin 2\theta \frac{\partial E_0}{\partial \theta} - \frac{\rho}{2}(1 + \cos 2\theta)\frac{\partial E_0}{\partial \rho} \tag{18}$$

Again by inserting E_0 and E_1, we can obtain an equation for E_2 which has a solution in the following form:-

$$E_2 = R_2^0(\rho)\, e^{in\theta} + R_2^-(\rho)\, e^{i(n-2)\theta} + R_2^+(\rho)\, e^{i(n+2)\theta} \tag{19}$$

with R_2^0, R_2^- *and* R_2^+ obey to three ordinary differential equations whose solutions can be obtained by applying the same procedure as the first-order equations:

$$R_2^+ = R_2^- = \frac{-\rho^2 A_0}{32} J_n(\kappa \rho)$$

$$R_2^0 = \frac{A_0 \rho^2}{32} \left[J_{n+2} - J_{n-2} \right]$$

RESULTS AND DISCUSSIONS

Finally, the complete solution for the equation (6) to the second order perturbation can be obtained in the following form:-

$$E = A_0 \left\{ J_n(\kappa_0 \rho) + \frac{\alpha^2 \rho^2}{32} \left[J_{n+2} - J_{n-2} \right] \right\} e^{in\theta} - \frac{\alpha \rho A_0}{4} J_n \left[e^{i(n+1)\theta} + e^{i(n-1)\theta} \right]$$
$$- \frac{\alpha^2 \rho^2 A_0}{32} J_n \left[e^{i(n+2)\theta} + e^{i(n-2)\theta} \right] \qquad (20)$$

The eigenvalues due to the toroidal effect appear as a perturbation in the following expansion $\kappa = \kappa_0 + \alpha \kappa_1 + \alpha^2 \kappa_2 + \ldots\ldots$, which are determined again from the boundary conditions. Because of the linear independence of the exponentials $e^{in\theta}, e^{i(n-1)\theta}$ *and* $e^{i(n+1)\theta}$, we can find that $\kappa_1 = 0$, and

$$\kappa_2 = \frac{\kappa_0}{16n} \frac{\left[2J_n(\kappa_0) - J_{n+2}(\kappa_0) - J_{n-2}(\kappa_0) \right]}{nJ_n(\kappa_0) - \kappa_0 J_{n+1}(\kappa_0)} \qquad (21)$$

So the toroidal electric field T_φ has been represented in (ρ , ϑ) plane (equation (20)). We notice that this field has a correction due to the toriodal effect which is different from the cylindrical case in the second and third terms as: $e^{i(n\pm1)\theta}$, $e^{i(n\pm2)\theta}$. Also the eigenvalue perturbation to the second order (equation (21)) has singularity for n modes at $J_n(\kappa_0) = \frac{\kappa_0}{n} J_{n+1}(\kappa_0)$. Numerical simulation for the structure of fields will be made in the next work to compare it with ref. (4).

REFERENCES

(1) T.H. Stix, IEEE Trans Plasma Sci., PS-12 (1984) 48.
(2) Han-Ming Wu, Rodolfo Carrera, Jiaqi Dong and Melvin E. Oakes, IEEE Trans Plasma Sci. 20 (1992) 19.
(3) F. Cap, Phys. Fluids 28 (1985) 1766.
(4) Nikolaus Schupfer, IEEE Trans Plasma Sci. 19 (1991) 906.
(5) I. Lewin, "*Theory of waveguides*", London U.K., Newness-Butterworths (1975).
(6) F. Cap and R. Duetsch, IEEE, Trans. Microwave Theory Tech, MTT-28 (1980) 700.
(7) M. Sita Janaki and B. Dasgupta, IEEE, Trans. Plasma Sci., Ps-18 (1990) 78.

Propagation of Solitary Ion Acoustic Waves In a Weakly Relativistic Warm Plasma: Isothermal Case

S.A. Elwakil*, G. Rowlands, S.K. El-labany***, A.M. El-hanbaly*, and E.K. El-shewy***

**Physics Department, Faculty of Science, Mansoura University, Mansoura, Egypt*

*** Department of Physics, University of Warwick, UK*

**** Physics Department, Faculty of Science, Mansoura University, Damietta, Egypt*

e_k_el_shewy@mans.edu.eg

ABSTRACT

The propagation of solitary ion acoustic waves in a collisionless weakly relativistic warm plasma is studied by use of the reductive perturbation method. A Korteweg-de Vries (KdV) equation is derived from the lowest order of perturbation whereas a linear inhomogeneous differential equation is obtained from the higher order of perturbation.

These two-coupled equation are combined to a single non linear partial differential equation using Lisak approach and solitary solution are found.

Key words: Ion acoustic waves , KdV equation, Solitary solution

INTRODUCTION

Washimi and Taniuti[1] were the first to use reductive perturbation method to study the propagation of ion acoustic waves in plasma. And then the attention has been focused by many authors[2-4]. The evolution of small but finite-amplitude solitary waves, studied by means of the KdV equation, is of considerable interest in plasma dynamics. The investigation of relativistic nonlinear waves has attracted interest from the point of view of investigations of laser-plasma interaction, Chian and Clemmow[5], Shukla et al[6] and space plasma phenomena, Arons[7]. However, little attention has been paid to ion-acoustic waves in weakly relativistic plasma. Recently, few articles have been published in this area[8-11]. Here we aim to study a complete description of a system by getting an equation valid to higher order of the perturbation theory using Lisak method[12]. The structure of the paper is as follows. In section two we introduce the basic equations and derive KdV and KdV-type equations. In section three the solitary solutions are presented. Finally, section three is devoted to the conclusions.

1. Basic Equations and KdV and KdV-Type Equations

Consider collisionless ionization-free unmagnetized plasma consisting of a mixture of warm ion-fluid and isothermal electrons. Assume that the ion flow velocity has a weak relativistic effect, and therefore there exist streaming ions in an equilibrium state when sufficiently small-but finite-amplitude waves propagate one-dimensionally. Such a system is governed by the following normalized equations, Nejoh[9] :

$$\frac{\partial n}{\partial t}+\frac{\partial (nu)}{\partial x}=0,$$
$$(\frac{\partial}{\partial t}+u\frac{\partial}{\partial x})(\gamma u)+\frac{\sigma}{n}\frac{\partial p}{\partial x}+\frac{\partial \phi}{\partial x}=0,$$
$$(\frac{\partial}{\partial t}+u\frac{\partial}{\partial x})p+3p\frac{\partial(\gamma u)}{\partial x}=0,$$
$$\frac{\partial^2\phi}{\partial x^2}+n-n_e=0,$$
$$n_e=\exp(\phi). \qquad (1)$$

where $\gamma \approx 1+\frac{u^2}{2c^2}$ is the relativistic factor, c is the velocity of light. In equation (1) n and n_e are the densities of ions and electrons respectively, u is the ion flow velocity, p is the ion pressure, ϕ is the electric potential and $\sigma=\frac{T_i}{T_e}$ is the ratio of the ion temperature T_i to the electron temperature T_e . All these quantities are dimensionless, being normalized as in (11). According to the general method of reductive perturbation theory, we introduce the stretched variables $\tau=\varepsilon^{3/2)}t$, $\xi=\varepsilon^{1/2}(x-\lambda t)$, where λ is the unknown phase velocity, and all the physical quantities appearing in equation (1) are expanded as power series in ε about the equilibrium values, where ε represents the relative amplitude of the perturbation. We impose the boundary conditions that as In the system of equations (1), we find that up to O (ε^2) , the system is governed by the KdV equation:

$$\frac{\partial}{\partial \tau}\phi_1+a\phi_1\frac{\partial}{\partial \xi}\phi_1+b\frac{\partial^3}{\partial \xi^3}\phi_1=0, \qquad (2)$$

Continuing to higher order in ε , we obtain the KdV-type equation

$$\frac{\partial \phi_2}{\partial \tau}+a\frac{\partial(\phi_1\phi_2)}{\partial \xi}+b\frac{\partial^3\phi_2}{\partial \xi^3}=-[A\phi_1^2\frac{\partial \phi_1}{\partial \xi}+B\frac{\partial}{\partial \xi}(\frac{\partial \phi_1}{\partial \xi})^2+C\phi_1\frac{\partial^3\phi_1}{\partial \xi^3}+E\frac{\partial^5\phi_1}{\partial \xi^5}]. \quad (3)$$

The coefficients a, b, A, B, C, and E are given in (11). Equations (2) and (3) can be combined to a single equation, using a technique used by Lisak[12]. Multiplying equation (3) by ε and adding to equation (2) , let

$$\psi=\varphi_1+\varepsilon\varphi_2$$

where φ_1, φ_2 , ψ , $\frac{\partial}{\partial \xi}$ and $\frac{\partial}{\partial \tau}$ are of order ε, ε^2, ε, $\varepsilon^{\frac{1}{2}}$, and $\varepsilon^{\frac{3}{2}}$ rspectively.

Neglecting the terms of order higher than $\varepsilon^{7/2}$, one thus obtains the following nonlinear differential equation of fifth order:

$$\frac{\partial \psi}{\partial \tau}+(a+\varepsilon A\psi)\psi\frac{\partial \psi}{\partial \xi}+(b+\varepsilon C\psi)\frac{\partial^3\psi}{\partial \xi^3}=\varepsilon B\frac{\partial}{\partial \xi}(\frac{\partial \psi}{\partial \xi})^2-\varepsilon E\frac{\partial^5\psi}{\partial \xi^5} \qquad (4)$$

Which it seems difficult to solve explicitly. We aim to simplify equation (4) by reducing its order. In order to do this we may write equation (4) in the form

$$\left(1+q_1\frac{\partial^2}{\partial \xi^2}\right)\frac{\partial \theta}{\partial \tau}+(a+\varepsilon A\theta)\theta\frac{\partial \theta}{\partial \xi}+\frac{\partial}{\partial \xi}\left[h(\theta)\frac{\partial^2\theta}{\partial \xi^2}\right]=0, \qquad (5)$$

which is called the master equation, Whitham[4]. The parameterq$_1$ and the function h(θ) in equation (5) should be determined. Via the substitution

$$\theta=\psi+q(\frac{\partial^2\psi}{\partial \xi^2}),$$

and keeping terms of order $\varepsilon^{5/2}$ and $\varepsilon^{7/2}$, (5) can be transformed into equation (4) whenever h(θ) = b + εμψ, q_1 = - ε S where μ =C -aE/b, S =E/b.
To obtain ion-acoustic solitary wave solution of equation (5), we introduce the new variables ζ= ξ-υτ , θ = Φ(ζ) and solve under boundary conditions that Φ(ζ), dΦ/d ζ and $d^2\Phi/d\zeta^2$ vanish at ζ= ± infinity, integrating and introduce the variable L =δ+ εμ Φ, multiplying by (1/L)dL/dζ one gets the energy conservation law

$$e_1\ln[L]+e_2L+e_3L^2+e_4L^3+e_5=-\frac{1}{2}\left(\frac{\partial L}{\partial \varsigma}\right)^2, \qquad (6)$$

where

$$\delta=b+\varepsilon s\vartheta,\ e_1=\vartheta\delta+\frac{a}{2\varepsilon\mu}\delta^2-\frac{A}{3\varepsilon\mu^2}\delta^3,$$

$$e_2=-\vartheta-\frac{a}{\varepsilon\mu}\delta+\frac{A}{\varepsilon^2\mu^2}\delta^2,$$

$$e_3=-\frac{a}{\varepsilon\mu}-\frac{2A}{3\varepsilon^2\mu^2}\delta,\ e_4=\frac{A}{9\varepsilon^2\mu^2}\delta^2,$$

$$e_5=-\left(e_1\ln\delta+e_2\delta+e_3\delta+e_4\delta^3\right).$$

In case of ln L<<1 and large L, equation (6) becomes:

$$e_3L^2+e_4L^3+e_5=-\frac{1}{2}\left(\frac{\partial L}{\partial \varsigma}\right)^2,$$

And admits a solitary wave solution in a form

$$L = \Phi_m \operatorname{sech}^2(D\varsigma),$$

$$\Phi_m = -\frac{e_3}{e_4},$$

$$D^{-1} = \left(0.5\left(-2[e_3]\right)^{0.5}\right)^{-1} \qquad (7)$$

Where Φ_m , D^{-1} are the soliton amplitude and the soliton width.

CONCLUSION AND REMARKS

The use of reductive perturbation method yields at the lowest order of perturbation the well known KdV equation while in the higher order , a linear inhomogeneous KdV-type equation have been derived. Using Lisak approach these two equations are combined to a single nonlinear differential equation of fifth order which is rather hard to solve.This equation is simplified by reducing its order from five to three via very tricky substitution. The solitary wave solution is obtained .

REFERENCES

(1) H. Washimi and T.Taniuti, J. Phys. Rev. Lett. 17 (1966) 996.
(2) T. Taniuti and C. Wei, J. Phys. Soc. Japan 24 (1968) 491.
(3) T. Taniuti, Supply. Prog. Theo. Phys. 55 (1974) 1.
(4) G.B. Whitham, "*Linear and Nonlinear Waves*", Wiley, New York (1974).
(5) A.C. Chian and P.C. Clemmow, J. Plasma Phys. 14 (1979) 505.
(6) P.K.Shukla, M.Y. Yu, and N.L. Tsintasze, Phys. Fluids 27 (1984) 327.
(7) Arons, J., Space Sci. Rev. 24 (1979) 417.
(8) G.C. Das and S.N. Paul, Phys. Fluids 28 (1985) 823.
(9) Y. Nejoh, J.Plasma Phys. 38 (1987b) 439.
(10) Y. Nejoh, J. Plasma Phys. 37 (1987) 487.
(11) S.K. El-Labany, J. Plasma Phys. 50 (1993) 495.
(12) M.Lisak, Physica Scripta. 17 (1978) 577.

Higher-Order Solution of an Ion Acoustic Solitary Wave in a Warm Ion Plasma: Non Isothermal case

E.K. El-shewy
Theoretical Physics Group, Physics Department, Faculty of Science, Mansoura University, Mansoura, Egypt
e_k_el_shewy@mans.edu.eg

ABSTRACT

The propagation of solitary ion acoustic waves in a collisionless plasma consisting of a warm ion fluid and hot non-isothermal electrons is studied by use of the reductive perturbation method. A modified Korteweg-de Vries (mKdV) equation that contains the lowest-order nonlinearity and dispersion is derived from the lowest order of perturbation. The higher-order dispersive effects have to be taken into account and higher-order solutions are obtained.

Key words: Ion acoustic waves, mKdV equation, Solitary solution

INTRODUCTION

An ion-acoustic solitary wave is one of the fundamental nonlinear wave phenomena appearing in plasma physics. Washimi and Taniuti[1] were the first to use reductive perturbation method to study the propagation of a slow modulation of a quasimonochromatic waves through plasma. El-Labany[2] investigated the problem of ion-acoustic solitons in a warm ion-beam-plasma system using the reductive perturbation technique. Das and Tagare[3] derive a modified KdV equation in multicomponent plasma . The perturbed KdV equation discussed by Watanabe and Jiang[4]. The higher-order equation usually includes secular terms. The elimination of secular terms in the higher-order equation gives rise to a modification of a soliton velocity.

1. Basic Equations and mKdV Equation

Let us consider a system of an unmagnetized collisionless plasma consisting of a warm ion fluid and non-isothermal electrons. In one dimension the system is given in dimensionless variables by Tiwari and Sharma[5]

$$\frac{\partial n_i}{\partial t}+\frac{\partial (n_i u_i)}{\partial x}=0,$$
$$\frac{\partial u_i}{\partial t}+u_i\frac{\partial u_i}{\partial x}+\frac{\sigma}{\beta}n_i\frac{\partial n_i}{\partial x}+\frac{1}{\beta}\frac{\partial \phi}{\partial x}=0,$$
$$\frac{\partial^2 \phi}{\partial x^2}+n_i-n_e=0,$$
$$n_e=1+\phi-\frac{4}{3}b\phi^{\frac{3}{2}}+\frac{1}{2}\phi^2+\ldots\ldots \qquad (1)$$

the electron density is given by (Schamel[6]; El-Labany [7]).

In the above equations n_i and u_i are the density and fluid velocity of plasma ions, ϕ is the electric potential. $\sigma = 3T_i / T_e$ is the ratio of the ion temperature T_i to the electron temperature T_e, and β is a parameter . All these quantities are dimensionless, being normalized as in [2] and b is a constant depending on the temperature parameters of resonant electrons (both free and trapped) and is given by $b= \pi^{(-1/2)} (1-\delta)$, $\delta = T_{ef} / T_{et}$, where T_{ef} and T_{et} are respectively the constant temperature of free electrons and the constant temperature of trapped electrons.
To derive the mKdV equation : we introduce the stretched co-ordinates, Schamel[8]: $T = \varepsilon^{3/4} t$,$\xi = \varepsilon^{1/4} (x - \lambda t)$, where ε is a small dimensionless expansion parameter and λ is the phase velocity of the ion-acoustic wave. All physical quantities appearing in equation (1) are expanded as power series in about their equilibrium values as:

$$n = 1 + \varepsilon n_1 + \varepsilon^{\frac{3}{2}} n_2 + \varepsilon^2 n_3 + ...,$$
$$u = u_0 + \varepsilon u_1 + \varepsilon^{\frac{3}{2}} u_2 + \varepsilon^2 u_3 + ...,$$
$$\phi = \varepsilon\phi_1 + \varepsilon^{\frac{3}{2}}\phi_2 + \varepsilon^2\phi_3 + ... \qquad (2)$$

We impose the boundary conditions that as ξ tends to infinity , $n_i = n_e = 1$, $u_i = \phi = 0$. The system of equations (1) up to $\varepsilon^{3/2}$ gives the mkdV equation;

$$\frac{\partial\phi_1}{\partial\tau} + \alpha_1 \frac{\partial\phi_1^{\frac{3}{2}}}{\partial\xi} + \alpha_2 \frac{\partial^3\phi_1}{\partial\xi^3} = 0,$$
$$\alpha_1 = \frac{2}{3}(b\lambda - \frac{b\sigma}{\lambda\beta}),$$
$$\alpha_2 = \frac{\lambda}{2} - \frac{\sigma}{2\lambda\beta}) \qquad (3)$$

with linear dispersion relation $\beta\lambda^2 = 1 + \sigma$. As the wave amplitude increases, the width and velocity of a soliton deviate from the prediction of the mKdV equation . To describe the ion acoustic soliton of large amplitude, the higher-order nonlinearity and dispersive effects have to be taken into account. A method of perturbation is employed to solve the following higher-order dispersion equation of the type

$$\frac{\partial\phi_1}{\partial\tau} + \alpha_1 \frac{\partial\phi_1^{\frac{3}{2}}}{\partial\xi} + \alpha_2 \frac{\partial^3\phi_1}{\partial\xi^3} + \varepsilon\alpha_3 \frac{\partial^5\phi_1}{\partial\xi^5} = 0. \qquad (4)$$

where ε is a smallness parameter, α_3 is constant. The last term of the left-hand side in equation (4) is a perturbation added to the mKdV equation as a higher-order dispersive effects. We introduce the new variables $\zeta = \xi - \theta\tau$, $\varphi_1 = \Phi(\zeta)$ and expand $\Phi(\zeta)$, θ with respect to the smallness parameter ε as ,

$$\Phi = \Phi_0 + \varepsilon\Phi_1 + \varepsilon^2\Phi_2 + \varepsilon^3\Phi_3 + ...,$$
$$\theta = \vartheta_0 + \varepsilon\vartheta_1 + \varepsilon^2\vartheta_2 + \varepsilon^3\vartheta_3. \qquad (5)$$

Substituting and collecting together the coefficient of like power in ε one obtains the following equations;

$$-\vartheta_0 \frac{d\Phi_0}{d\zeta} + \frac{3}{2}\alpha_1 \Phi_0^{\frac{1}{2}} \frac{d\Phi_0}{d\zeta} + \alpha_2 \frac{d^3\Phi_0}{d\zeta^3} = 0,$$

$$L\Phi_1 = \vartheta_1 \frac{d\Phi_0}{d\zeta} - \alpha_3 \frac{d^5\Phi_0}{d\zeta^5},$$

$$L\Phi_2 = \vartheta_1 \frac{d\Phi_1}{d\zeta} + \vartheta_2 \frac{d\Phi_0}{d\zeta} - \frac{3}{4}\alpha_1 \Phi_0^{\frac{-1}{2}} \Phi_1 \frac{d\Phi_1}{d\zeta} + \frac{3}{16}\alpha_1 \Phi_1^2 \Phi_0^{\frac{-3}{2}} \frac{d\Phi_0}{d\zeta} - \alpha_3 \frac{d^5\Phi_1}{d\zeta^5}.$$

where the operator L is represented by

$$L = -\vartheta_0 \frac{d}{d\zeta} + \frac{3}{2}\alpha_1 \Phi_0^{\frac{1}{2}} \frac{d}{d\zeta} + \alpha_2 \frac{d^3}{d\zeta^3}.$$

We solve the first Equation successively under boundary conditions that Φ_i , d Φ_i /dζ and $d^2 \Phi_i / d\zeta^2$ (i = 0,1,2,3,..) vanish at ζ = ± infinity , yields a solitary wave solution

$$\Phi_0 = \Phi_m \sec h^4(D\zeta),\ \Phi_m = \frac{25\vartheta_0^2}{16\alpha_1^2},\quad D^{-1} = 4\sqrt{\frac{\alpha_2}{\vartheta_0}}. \qquad (6)$$

where the soliton amplitude Φ_m and the soliton width D^{-1} .
In the next orders of ε, with the aid of equation (6) one gets

$$\vartheta_1 = 256\, D^4 \alpha_3,$$

$$\Phi_1 = -\frac{900\, D^4 \alpha_3 \vartheta_0}{\alpha_1^2} S^4 + \frac{1750\, D^4 \alpha_3 \vartheta_0}{\alpha_1^2} S^6,$$

$$\vartheta_2 = 0,$$

$$\Phi_2 = -\frac{2604000\, D^8 \alpha_3^2}{\alpha_1^2} S^4 + \frac{2366000\, D^8 \alpha_3^2}{\alpha_1^2} S^6 + \frac{409600\, D^8 \alpha_3^2}{\alpha_1^2} S^8$$

$$\vartheta_3 = 0,$$

$$\Phi_3 = -\frac{315392000 D^{12} \alpha_3^3}{\alpha_1^2 \vartheta_0} S^4 + \frac{2823296000 D^{12} \alpha_3^3}{\alpha_1^2 \vartheta_0} S^6 - \frac{6649664000 D^{12} \alpha_3^3}{\alpha_1^2 \vartheta_0} S^8$$

$$+ \frac{4210304000 D^{12} \alpha_3^3}{\alpha_1^2 \vartheta_0} S^{10}. \qquad (7)$$

series of the lowest-order solution and that the wave velocity depends only on the first order of ε , while the waveform of a solitary wave depends on all orders of ε.

CONCLUSION AND REMARKS

The use of reductive perturbation method yields at the lowest order of perturbation the mKdV equation. We have used a simple method to obtain the higher-order solitary wave solutions shown an expression of the solutions in the case of a perturbed mKdV equation. Then the expansion of the wave velocity with respect to a smallness parameter together with the usual expansion of wave amplitude. The velocity variation in the higher order correspond to the frequency shift in the asymptotic method of nonlinear oscillations to the renormalization constant in the reductive perturbation method. The velocity correction appears only in the first order equation. This fact suggests that the velocity of a solitary wave is mainly determined by the non linear term, but depends weakly on the dispersive effect.

REFERENCES

(1) H. Washimi and T. Taniuti, J. Phys. Rev. Lett. 17 (1966) 996.
(2) S.K. El-Labany, J. Plasma Phys. 54 (1995) 285.
(3) G.C Das and S.G.Tagare, J. Plasma Phys. 17 (1975) 1025.
(4) S. Watanabe and B. Jiang, J. Phys. Fluid B 5 (2) (1993) 409.
(5) R. S.Tiwari and S.R. Sharma, Can. J. Phys. 60 (1982) 154.
(6) H. Schamel, J. Plasma Phys. 9 (1973) 377.
(7) S.K. El-Labany, Astrophys.and Space Science 197 (1992) 289.
(8) H. Schamel, Phys. Rep. 140 (1986) 161.

Description of an Experimental Tripolar Vortex

J. Vranješ[1], A. Okamoto, S. Yoshimura, S. Poedts[1], M. Kono[2], and M. Y. Tanaka
National Institute for Fusion Science, 322-6 Oroshi-cho, Toki City 509-5292, Japan
[1]*Center for Plasma Astrophysics, Celestijnenlaan 200B, 3001 Leuven, Belgium*
[2]*Faculty of Policy Studies, Chuo University, Hachioji, Tokyo 192 0393, Japan*
E-mail: jvranjes@yahoo.com

ABSTRACT

Description of an experimentally observed triple vortex is presented. The parabolic-like, in radial direction, concentration of neutrals turns out to be of crucial importance, resulting in an effective force directed towards the axis of the system. This neutral force causes the rotation of the plasma column in the direction which is opposite to the $\vec{E} \times \vec{B}$ drift. It is shown that for a starting gaussian density distribution and a rigid body rotation of the plasma column, in the process of self-organization, stationary triple vortex can develop.

Key words: vortex, nonlinear waves, self-organization

INTRODUCTION

Recently stationary coherent structures in the form of global triple vortices were observed in a cylindrical plasma device[1,2]. The inner diameter of the chamber is about 30 cm and the axial length of about 200 cm. Density profile measurements in the axial direction reveal that the structures are very elongated along the magnetic field lines; the temperature measurements on the other hand show a flat profile across the structures, i.e., in the radial direction. The radial cross section of the structure reveals a clear triple structure in the density profile, with two explicit humps of the density, and a centrally situated trough (Fig. 1). Such a density distribution is almost uniform along the magnetic field lines, which is confirmed by measurements at different positions in the axial direction. Related to these density profiles is the vorticity distribution as well, which mainly shows a set of two clockwise rotating lateral vortices, and a central counter-clockwise rotating vortex. An interesting and important feature of the system is a spatially nonuniform distribution of the neutral gas, which could be, roughly speaking, described by a r-dependent parabolic function; though for higher pressures a small peak in the profile seem to appear in the centrum of the cross section.

THE MODEL AND DERIVATIONS

We take a cylindrical plasma with the magnetic field oriented along its axis $\vec{B}_0 = B_0\vec{e}_z$. The plasma and neutral densities are r-dependent, and the system is subject to a r-dependent mainly poloidal rotation with the velocity $\vec{v}_0(r) = v_0(r)\vec{e}_\theta$. The equation of motion for ions is given by $m_i n_i(\partial/\partial t + \vec{v}_i \cdot \nabla)\vec{v}_i = q_i n_i(-\nabla\phi + \vec{v}_i \times \vec{B}_0) - \nabla p_i - m_i n_i \nu_i \vec{v}_i + \vec{F}_{ni}$, where ν_i is the frequency of ion-neutral collisions. The force $\vec{F}_{ni}$ describes the momentum transferred in the ion-neutral charge transfer interactions which is given by $\vec{F}_{ni} = \nu_i m_i n_i \vec{v}_n$. The neutral flow $\vec{v}_n$ is determined by the diffusion flux, $\vec{v}_n = -D_n \nabla n_n / n_n$, where D_n is the diffusion constant of neutrals, and n_n is the density of neutrals, so we have $\vec{F}_{ni} = -m_i n_i \nu_i D_n \nabla \log n_n$. The radially dependent distribution of neutrals affects the dynamics of plasma ions, resulting in effective pressure directed inside, opposing the radial electric field and making an anti-$\vec{E} \times \vec{B}$ direction of rotation. From the ion continuity equation, with the help of quasineutrality condition, in the limit of low-frequency, $\omega \ll \Omega_i \ll \Omega_e$, electrostatic perturbations propagating almost

perpendicular to the magnetic field lines, $|\vec{k}_\perp| \gg |\vec{k}_{||}|$, we obtain the following equation for the potential:

$$\left[\frac{\partial}{\partial t} + \frac{1}{B_0}\vec{e}_z \times \nabla_\perp(\Phi_1 + B_0\varphi)\cdot\nabla_\perp\right]\left[(1-\rho^2\nabla_\perp^2)\times(\Phi_1 + B_0\varphi) - B_0(\varphi+\psi)\right]$$

$$+\frac{T_e}{e}\nabla_{||}\cdot\vec{v}_{||} = 0. \tag{1}$$

Here $\nabla_\perp = \vec{e}_r\partial/\partial r + \vec{e}_\theta\partial/r\partial\theta$, and an approximate effective perturbed potential is introduced in the form $\Phi_1 = \phi_1 + \phi_{n1} \approx [\phi_1 + (T_n/e)\log n_{n1}]\Omega_i^2/(\Omega_i^2+\nu_i^2)$. The electron dynamics is represented by the Boltzmann distribution, and we have introduced the notation $\vec{v}_{i0} \equiv \vec{e}_\theta d\varphi(r)/dr = \vec{e}_\theta(d\Phi_0/dr)/B_0 - [1/(r\Omega_{ef}B_0^2)](d\Phi_0/dr)^2\vec{e}_\theta$, $v_* \equiv d\psi(r)/dr = -n_0'c_s^2/n_0\Omega_{ef}$, $\rho = c_s/\Omega_{ef}$, $c_s^2 = T_e/m_i$, and $\Omega_{ef} \equiv \Omega_i/[\Omega_i^2/(\Omega_i^2+\nu_i^2)]$. Φ_0 is the effective equilibrium potential with the physical meaning similar to the above introduced perturbed potential Φ_1. The system is in principle closed by the parallel ion momentum $[\partial/\partial t + \vec{e}_z\times\nabla_\perp(\Phi_1 + B_0\varphi)\cdot\nabla_\perp/B_0]v_{||} = 0$.

According to the experimental conditions we should search for global and stationary solutions. As the structures are very elongated along the magnetic filed lines, we shall further disregard the parallel ion dynamics and search for purely two dimensional solutions for the ion motion. Eq. (1) after one integration yields $(1-\rho^2\nabla_\perp^2)(\Phi_1 + B_0\varphi) - B_0(\varphi+\psi) = \mathcal{G}(\Phi_T)$, where $\mathcal{G}$ is an arbitrary function of the argument $\Phi_T = \Phi_1 + B_0\varphi$. We can choose $\mathcal{G}(\Phi_T) = G\cdot\Phi_T + G_0$, where G, G_0 are some constants, and introduce the notation $k^2 = G-1$, $F(r) = -B_0\varphi(r) - B_0\psi(r)$. Thus we rewrite the above given equation in the form:

$$(\nabla_\perp^2 + k^2)\left(\Phi_T + \frac{G_0}{k^2}\right) = F(r). \tag{2}$$

Here $\Phi_1 \equiv \Phi_1/B_0V_0r_0$, $\varphi \equiv \varphi/V_0r_0$, $\psi \equiv \psi/V_0r_0$, $\nabla_\perp^2 \equiv \rho^2\nabla_\perp^2$, where therefore $F(r)$ is a dimensionless function, G_0, and k are the dimensionless integration constants, V_0 is some characteristic rotation velocity, and r_0 is the radius of the plasma column.

The solution will be sought in the form $\Phi_T = -G_0/k^2 + F_1(r) + \sum_{n=1}^{\infty}\zeta_n(kr)\cos n\theta$, where $F_1(r)$ and $\zeta_n(kr)$ are some r-dependent functions. It is easily seen that in this case we obtain from (2) one equation yielding solutions in the form of the Bessel harmonics $J_n(kr)$, and the second equation in the form:

$$\left(\frac{d^2}{dr^2} + \frac{1}{r}\frac{d}{dr} + k^2\right)F_1(r) - F(r) = 0. \tag{3}$$

The solution of Eq. (3) can be written in terms of the zero order Bessel functions of the first and second kind J_0, Y_0, respectively, in the form $F_1(r) = a_0J_0(kr) + \pi Y_0(kr)\int J_0(kr)F(r)rdr/2 - \pi J_0(kr)\int Y_0(kr)F(r)rdr/2$. We use the identity

$$\int r\left[g''(r) + g'(r)/r + g(r)\right]Z_0(r)dr = r\left[g'(r)Z_0(r) + g(r)Z_1(r)\right], \quad Z_{0,1} \equiv J_{0,1}, Y_{0,1}.$$

To solve the integrals $I_1 = \int J_0(kr)F(r)rdr$, and $I_2 = \int Y_0(kr)F(r)rdr$, we have to specify the function $F(r)$, i.e., the equilibrium functions $n_0(r)$ and $v_0(r)$. We choose $F(r) = b(4 + k^2r^2)$, where b is a constant, and we shall discuss the consequences of the assumption later on. Introducing $kr = r_1$, and $g(r_1) = br_1^2$, it is seen that $g''(r_1) + g'(r_1)/r_1 + g(r1) = b(4 + r_1^2)$ and we have

$$I_1 = \frac{1}{k^2}\int\left[g''(r1) + \frac{g'(r_1)}{r_1} + g(r_1)\right]J_0(r_1)r_1dr_1 = \frac{1}{k^2}r_1[g'(r1)J_0(r_1) + g(r_1)J_1(r_1)]. \tag{4}$$

Similarly we solve the second integral yielding $I_2 = r_1\left[g'(r1)Y_0(r_1) + g(r_1)Y_1(r_1)\right]/k^2$. Thus we write $F_1(r) = a_0J_0(kr) + br^2$. Consequently the solution can be written in a general form as $\Phi_T(r,\theta) =$

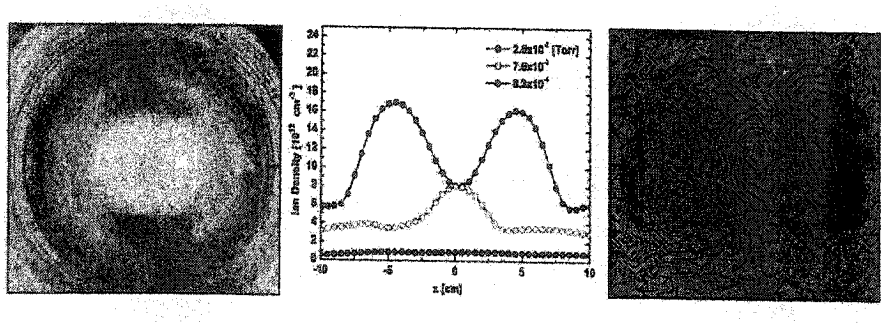


Figure 1: End-view of the tripolar vortex (left), the corresponding ion density profile (middle), and the vorticity (right).

$-G_0/k^2 + a_0 J_0(kr) + br^2 + \sum_{n=1}^{\infty} a_n J_n(kr) \cos n\theta$. In order to describe the standing triple structure which was observed in the experiment, in the above summation we keep the second harmonics only, yielding

$$\Phi_T(r,\theta) = -\frac{G_0}{k^2} + br^2 + a_0 J_0(kr) + a_2 J_2(kr) \cos 2\theta. \tag{5}$$

Physically justified boundary conditions include a not θ-dependent solution at the border $r = r_0$, yielding $kr_0 = z_m$, where z_m is the m-th zero of the Bessel function $J_2(kr)$. From this condition the constants k are G are determined. Note also that the condition of the absence of radial velocity at $r = r_0$, i.e., $\partial\Phi_T(r_0,\theta)/\partial\theta = 0$, is already satisfied. Similarly, the condition $\partial\Phi_T(0,\theta)/\partial\theta = 0$ is satisfied at $r = 0$ due to the attributes of the Bessel functions J_n, where $n \geq 1$.

The potential Φ_T includes the total (equilibrium plus perturbed) electrostatic potential $\phi_E = \phi_1 + \phi_0$, and the earlier discussed contribution of the neutrals $\phi_n = \phi_{n1} + \phi_{n0}$; at the edge of the plasma column we have the neutral contribution only. From this we calculate G_0, which results in the following final expression for the plasma potential describing the tripolar vortex:

$$\phi_E(r,\theta) = -\phi_n(r) + \phi_n(r_0) + b(r^2 - r_0^2) + a_0 \left[J_0(kr) - J_0(kr_0)\right] + a_2 J_2(kr) \cos 2\theta. \tag{6}$$

A typical measured plasma density profile in the bulk plasma before the formation of the observed triple structure is gaussian-like, close to the form $n_0(r) = n_{00} \exp(-\alpha^2 r^2)$, where n_{00}, α are some given experimental quantities. Therefore, using the definition of $\psi(r)$, and the assumption for $F(r)$ one can directly find $v_0(r) = -2r(k^2 b/B_0 + \alpha^2 c_s^2/\Omega_i)$. Thus, introducing the assumption for $F(r)$ we have restricted the model to the rigid body rotation of the bulk plasma. According to the experiment, the slope in the plasma profile (determined by α) is correlated to the slope of the neutral density gradient; the bigger α means the bigger neutral pressure gradient, i.e., the rotation velocity is proportional to the neutral pressure gradient as it should be expected. We choose $m = 2$, i.e., the first nontrivial zero of the $J_2(kr)$, which yields $kr_0 = 5.136$, and we plot the potential for some prescribed $\phi_n(r)$. Measurements reveal that the neutral profile is mainly parabolic-like, though at some higher pressures a small hump in the profile appears in center of the column. Therefore we choose it in the form $\phi_n(r) = a_n \exp(-c_n r^2) + b_n r^2$, where the constants a_n, b_n, c_n can be varied in order to describe the real situation; in accordance to the experiment the second term is the leading order one.

REFERENCES

(1) A. Okamoto *et al*; Phys. Plasmas; 10, 2211 (2003).
(2) J. Vranješ *et al*; Phys. Rev. Lett.; 89, 265002 (2002).

Nonlinear Wave Interaction in Selfgravitating Fluid

J. Vranješ, S. Poedts, and M. Kono[1]

Center for Plasma Astrophysics, Celestijnenlaan 200B, 3001 Leuven, Belgium
[1]*Faculty of Policy Studies, Chuo University, Hachioji, Tokyo 192 0393, Japan*
E-mail: jvranjes@yahoo.com

ABSTRACT

Nonlinear wave coupling is investigated in rotating self-gravitating astrophysical fluids. The precipitation of wave energy towards both longer and shorter wave lengths is demonstrated. The former should be of importance for the formation of structures in rotating astrophysical objects like proto-galaxies and galaxies.

Key words: nonlinear waves, self-gravity, direct and inverse cascade

INTRODUCTION

The direct and inverse cascading is a well established theory in the description of nonlinear drift waves. In so-called weakly nonlinear theory it predicts the precipitation of energy both towards smaller wave-lengths resulting, in principle, with the increased heating and turbulence of a plasma, and towards larger wave-lengths, i.e., formation of macroscopic structures. The predicted energy transfer towards larger scales can further be used as a fact in the theory of vortices, so that the corresponding nonlinear equations are solved searching for stationary, large scale structures which should represent a saturated, stationary state of the predicted energy precipitation. The appropriate numerical simulations, yielding formation of zonal flows or vortices[1], seem to support such a scenario. In the present work[2] we apply the nonlinear theory described above to the problem of perturbations in a large-scale, astrophysical, rotating self-gravitating fluid. The role of the Lorentz force from the drift wave theory here is played by the Coriolis force, and the nonlinearity is of the same type, i.e., in the form of a vector-product (or the Poisson bracket).

NONLINEAR WAVE INTERACTION

We use the standard set of equations describing nonlinear perturbations in a self-gravitating rotating fluid:

$$\frac{\partial \rho_1}{\partial t} + \nabla \cdot [(\rho_0 + \rho_1)\vec{v}_1) = 0, \quad \nabla^2 \varphi_1 = 4\pi G \rho_1,$$
$$\left(\frac{\partial}{\partial t} + \vec{v}_1 \cdot \nabla\right) \vec{v}_1 = 2\vec{v}_1 \times \vec{\Omega}_0 - \nabla\varphi_1 - \frac{\nabla p_1}{\rho_0}, \tag{1}$$

We study low-frequency isothermal perturbations taking $p_1 = c_s^2 \rho_1$, where c_s is the sound speed, assuming the equilibrium fluid as uniform, and subject to a uniform rotation, and keeping thermal terms to the first order. The cartesian rectangular coordinate system is used locally so that the constant angular velocity is given by $\vec{\Omega}_0 = \Omega_0 \vec{e}_z$.

Making the vector product of Eq. (1) and $\vec{e}_z$ we obtain the perpendicular velocity calculated to the second order small terms in the form:

$$\vec{v}_{\perp 1} = \frac{1}{2\Omega_0} \vec{e}_z \times \nabla \mathcal{L} \varphi_1 - \frac{1}{4\Omega_0^2} \left(\frac{\partial}{\partial t} + \frac{1}{2\Omega_0} \vec{e}_z \times \nabla \mathcal{L} \varphi_1 \cdot \nabla\right) \nabla \mathcal{L} \varphi_1, \quad \mathcal{L} = 1 + \frac{c_s^2 \nabla^2}{\omega_0^2}. \tag{2}$$

The indices 0 and 1 here denote the equilibrium and perturbed quantities, respectively, and $\omega_0^2 = 4\pi G\rho_0$. Assuming perturbations propagating perpendicular to the rotation vector, the subscript $\perp$ will be omitted in the further text. The first term in Eq. (2) is the leading order one. Using Eq. (2), the continuity equation yields the following equation describing local nonlinear perturbation of the gravity potential in the rotating fluid:

$$\left(\frac{\partial}{\partial t} + \frac{1}{2\Omega_0}\vec{e}_z \times \nabla\mathcal{L}\varphi_1 \cdot \nabla\right)\left(\frac{1}{\omega_0^2} - \frac{\mathcal{L}}{4\Omega_0^2}\right)\nabla^2\varphi_1 = 0. \tag{3}$$

Eq. (3) comprises the nonlinear term which is of the vector-product type. That kind of nonlinearity is known to be responsible for some specific, vortex-type, solutions. In the linear limit Eq. (3) does not describe the standard Jeans' gravitational instability. In order to obtain the Jeans' instability the velocity is to be calculated up to the small terms of the third order, i.e., to the order of $\partial^3/\Omega_0^3\partial t^3$. In that case, for perturbations of the form $\sim \exp[i(\vec{k}\cdot\vec{r} - \omega t)]$ we obtain the standard criterion for instability in the presence of rotation

$$k^2c_s^2 - 4\pi G\rho_0 + 4\Omega_0^2 < 0. \tag{4}$$

The fact that the modes can be linearly unstable at much longer time scales will be kept in mind in the further analysis.

Suppose now that Eq. (3) describes the nonlinear interaction of three waves, and we shall write the perturbed potential as a sum

$$\varphi = \sum_{j=0}^{2}\phi_j \exp[i(\vec{k}_j\vec{r} - \omega_j t)] + \sum_{j=0}^{2}\phi_j^* \exp[-i(\vec{k}_j\vec{r} - \omega_j t)], \tag{5}$$

where $*$ denotes the complex-conjugate quantity, and ϕ_j are the complex amplitudes. Further, without loss of generality we use the following resonant conditions for the wave-vectors and frequencies $\vec{k}_0 = \vec{k}_2 - \vec{k}_1$, $\omega_0 = \omega_2 - \omega_1$. Setting (5) into Eq. (3), after some straightforward algebra we obtain the following set of equations describing the time dependence of the amplitudes of three waves that interact nonlinearly:

$$\frac{\partial\phi_0}{\partial t} = c_0\phi_1^*\phi_2, \quad \frac{\partial\phi_1}{\partial t} = c_1\phi_0^*\phi_2, \quad \frac{\partial\phi_2}{\partial t} = c_2\phi_0\phi_1. \tag{6}$$

Here the coupling constants c_j, $(j = 0, 1, 2)$ are given by

$$c_0 = -\frac{\vec{e}_z(\vec{k}_1 \times \vec{k}_2)}{2\Omega_0 k_0^2\left[\frac{1}{\omega_0^2} - \frac{1}{4\Omega_0^2}\left(1 - \frac{c_s^2k_0^2}{\omega_0^2}\right)\right]}\left\{k_2^2\left(1 - \frac{c_s^2k_1^2}{\omega_0^2}\right)\left[\frac{1}{\omega_0^2} - \frac{1}{4\Omega_0^2}\left(1 - \frac{c_s^2k_2^2}{\omega_0^2}\right)\right]\right.$$
$$\left. -k_1^2\left(1 - \frac{c_s^2k_2^2}{\omega_0^2}\right)\left[\frac{1}{\omega_0^2} - \frac{1}{4\Omega_0^2}\left(1 - \frac{c_s^2k_1^2}{\omega_0^2}\right)\right]\right\}, \tag{7}$$

$$c_1 = \frac{\vec{e}_z(\vec{k}_0 \times \vec{k}_2)}{2\Omega_0 k_1^2\left[\frac{1}{\omega_0^2} - \frac{1}{4\Omega_0^2}\left(1 - \frac{c_s^2k_1^2}{\omega_0^2}\right)\right]}\left\{k_0^2\left(1 - \frac{c_s^2k_2^2}{\omega_0^2}\right)\left[\frac{1}{\omega_0^2} - \frac{1}{4\Omega_0^2}\left(1 - \frac{c_s^2k_0^2}{\omega_0^2}\right)\right]\right.$$
$$\left. -k_2^2\left(1 - \frac{c_s^2k_0^2}{\omega_0^2}\right)\left[\frac{1}{\omega_0^2} - \frac{1}{4\Omega_0^2}\left(1 - \frac{c_s^2k_2^2}{\omega_0^2}\right)\right]\right\}, \tag{8}$$

$$c_2 = \frac{\vec{e}_z(\vec{k}_0 \times \vec{k}_1)}{2\Omega_0 k_2^2\left[\frac{1}{\omega_0^2} - \frac{1}{4\Omega_0^2}\left(1 - \frac{c_s^2k_2^2}{\omega_0^2}\right)\right]}\left\{k_1^2\left(1 - \frac{c_s^2k_0^2}{\omega_0^2}\right)\left[\frac{1}{\omega_0^2} - \frac{1}{4\Omega_0^2}\left(1 - \frac{c_s^2k_1^2}{\omega_0^2}\right)\right]\right.$$

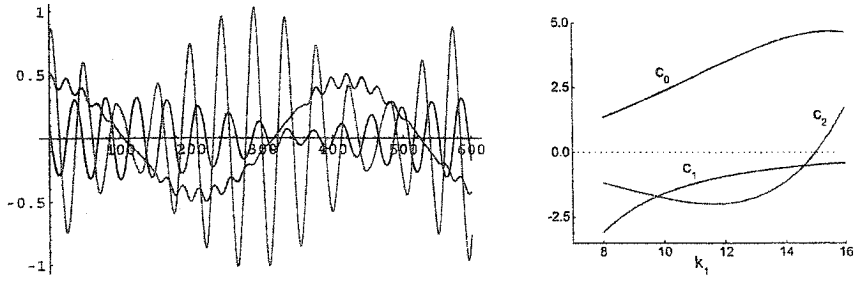


Figure 1: A typical time dependence of the amplitudes of three nonlinearly interaction modes (left). Coupling coefficients vs. k_1 (right).

$$-k_0^2\left(1-\frac{c_s^2k_1^2}{\omega_0^2}\right)\left[\frac{1}{\omega_0^2}-\frac{1}{4\Omega_0^2}\left(1-\frac{c_s^2k_0^2}{\omega_0^2}\right)\right]\Bigg\}. \tag{9}$$

Combining Eqs. (6) and after one integration one can write the following expression for the time evolution of the mode ϕ_0:

$$\frac{\partial|\phi_0|^2}{\partial t}=\pm2\sqrt{F(|\phi_0|^2)},\quad F(|\phi_0|^2)=c_1c_2|\phi_0|^6+c_0(c_1A_2+c_2A_1)|\phi_0|^4+c_0^2A_1A_2|\phi_0|^2+A_0, \tag{10}$$

$$A_1=|\phi_1(t=0)|^2-\frac{c_1}{c_0}|\phi_0(t=0)|^2,\quad A_2=|\phi_2(t=0)|^2-\frac{c_2}{c_0}|\phi_0(t=0)|^2,$$

$$A_0=\frac{1}{4}\left[\frac{\partial|\phi_0(t=0)|^2}{\partial t}\right]-\left[c_1c_2|\phi_0(0)|^6+c_0(c_1A_2+c_2A_1)|\phi_1(0)|^4+c_0^2A_1A_2|\phi_0(0)|^2\right].$$

An equation similar to Eq. (3) can be written for electrostatic perturbations in a rotating inhomogeneous dusty plasma[3] in the form

$$\left(\frac{\partial}{\partial t}-\vec{e}_z\times\nabla_\perp\phi_1\cdot\nabla_\perp\right)\left[\ln n_{d0}-(1-\nabla_\perp^2)\phi_1\right]=0, \tag{11}$$

where the following normalization is introduced

$$\frac{\partial}{\partial t}\equiv\frac{1}{2\Omega_0}\frac{\partial}{\partial t},\quad \nabla\equiv\rho_d\nabla,\quad \phi_1\equiv\frac{e\phi_1}{\kappa T_{ef}},\quad T_{ef}=\frac{Z_dn_{d0}T_iT_e}{n_{i0}T_e+n_{e0}T_i},\quad \rho_d^2=\frac{Z_d\kappa T_{ef}}{4\Omega_0^2m_d}.$$

Here Ω_0 is the angular rotation frequency of a dusty plasma with the equilibrium density gradient in the direction perpendicular to the axis of rotation, and electrons and ions are Boltzmann distributed. Assuming perturbations proportional to $\exp(-i\omega t+i\vec{k}\cdot\vec{r})$, from Eq. (11) one obtains the dimensionless dispersion equation for the mode propagating perpendicular both to the density gradient and the axis of rotation $\omega=(\vec{e}_z\times\vec{k})\cdot\nabla\ln n_{d0}/(1+k_\perp^2)$. From Eq. (11) one readily obtains a set of equations for the time dependence of the amplitudes of waves that interact nonlinearly, in the form (6). Consequently the physical picture of the nonlinear interaction of waves in such different systems is the same.

A typical time behavior of the interacting modes for a certain set of parameters is presented in Fig. 1 (left), showing a periodic exchange of energy. Further we discuss some physically distinct cases which can be studied analytically. The signs of the coupling constants are discussed in the various limits of the wave numbers. An example is presented in Fig. 1 (right). Here for fixed k_0, k_2 we vary k_1 and calculate the coupling constants $c_{0,1,2}$. The intermediate and growing mode is k_0 as long as $k_1<k_{0,2}$. When

k_1 becomes larger than k_0, the intermediate and decreasing becomes k_1, while k_2 becomes increasing. Here, for illustration we take numerical values typical for our Galaxy $\omega_g = 9.15 \cdot 10^{-16}$ s^{-1}, $\Omega_0 = 10^{-15}$ s^{-1}.

REFERENCES

(1) M. Kono and E. Miyashita; Phys. Fluids; 31, 326 (1988).
(2) J. Vranješ and S. Poedts; Phys. Rev. Lett.; 89, 131102 (2002).
(3) J. Vranješ and P. K. Shukla; Phys. Lett. A; 316, 91 (2003).

Dust Charge Fluctuations in a Magnetized Dusty Plasma

M. Salimullah[a)], I. Sandberg[b)], and P. K. Shukla[b)]
[a)] *Department of Physics, Jahangirnagar University, Savar, Dhaka-1342, Bangladesh*
[b)] *Institut für Theoretische Physik IV, Fakultät für Physik und Astronomie, Ruhr-Universität Bochum, D-44780 Bochum, Germany*
msu@juniv.edu

ABSTRACT

Charging currents of electrons and ions to a spherical dust grain in a uniform magnetized dusty plasma have been examined. It is found that the external magnetic field reduces the charging currents, thereby decreasing the dust charge fluctuation damping of a low-frequency electrostatic wave in a dusty plasma.

***Key Word:** Dust Charging, Charge-Fluctuation Damping, Dust-Lower-Hybrid Wave*

It is well known[1] that dust charge fluctuations induce a damping of the dust-acoustic and dust ion-acoustic waves in an unmagnetized dusty plasma. There has been a significant progress in the study of unmagnetized dusty plasma physics, which is summarized by Mendis[2]. However, space and laboratory dusty plasmas are usually confined in external magnetic fields. To the best of our knowledge, there does not exist a theory for the dust charge fluctuations and the consequent effect of the dust charge fluctuation damping of the low-frequency waves in the presence of an external magnetic field in a dusty plasma.

The charging of a spherical probe in a magnetic field has been investigated in connection with the charging of satellites and rockets in the Earth's ionosphere and magnetosphere[3], by assuming that the electron Debye radius, λ_{De} is usually much larger than the probe size, a ($a \ll \lambda_{De}$) in space conditions. In the collisionless limit, strong magnetic field effect has been considered in the limits $\lambda_{mfp} \gg a$ and $\rho_e \ll a$, where λ_{mfp}, a and ρ_e are the mean-free-path, the probe radius, and the electron gyroradius[4], respectively.

We consider a dusty plasma in the presence of an external magnetic field $\hat{\mathbf{z}}B_0$, where $\hat{\mathbf{z}}$ is the unit vector along the z axis and B_0 is the magnitude of the external magnetic field. The plasma constituents are electrons, ions, and negatively charged micron-sized spherical dust grains. Following Tsytovich *et al.*[5], we first discuss the effects of an external magnetic field on equilibrium charging currents. In a weak magnetic field, the electron gyroradius (ρ_e) is much smaller than the dust size and the change of dust charges is relatively small. Here, electrons rapidly approach the dust grain surface along the external magnetic field direction, so that fast electrons charging a grain may have a Boltzmann distribution. Accordingly, the Orbital Motion Limited (OLM) electron current remains in tact and we have[3]

$$I_{e0} = -n_{e0} A_e u_e \exp(eV_d/T_e), \tag{1}$$

where n_{e0} is the unperturbed electron number density, A_e is the average dust charging cross section which is somewhat smaller than the geometrical cross section πa^2 of a dust particle, $u_e = \sqrt{8/\pi} v_{te}$, $v_{te} = (T_e/m_e)^{1/2}$ is the electron thermal speed, T_e is the electron temperature, m_e is the electron mass, e is the magnitude of the electron charge, and $V_d (= \phi_d - \phi_p \sim Z_d e/a)$ is the potential of the dust grain relative to the plasma potential. On the other hand, ions are

attracted by dust and their effective cross section A_i is larger than the geometrical cross section. The OLM ion current then reads

$$I_{i0} = n_{i0} A_i u_i (1 + eV_d/K), \tag{2}$$

where n_{i0} is the unperturbed ion number density, $u_i = \sqrt{8/\pi} v_{ti}$, $v_{ti} = (T_i/m_i)^{1/2}$ is the ion thermal speed, T_i is the ion temperature, m_i is the ion mass, and $K = m_i v_i^2/2$ is the kinetic energy of ions before encountering the grain potential. The bracketed term is the focusing factor. At equilibrium, we have

$$n_{i0} = n_{e0} + Z_{d0} n_{d0}, \tag{3}$$

where Z_{d0} is number of electrons residing on the dust grain surface, and n_{d0} is the unperturbed dust number density. It turns out that for weak magnetic fields the dust charge remains the same.

For stronger magnetic fields (viz. $B_0 \geq (c/ea)\sqrt{m_i T_i}$) in a plasma, the ion gyroradius becomes smaller or comparable to the dust size. Here, both the electron and ion currents are modified due to the strong magnetization of the plasma particles. Tsytovich *et al.*[5] treated this problem numerically and reported the dependence of dust charge on the external magnetic field strength as well as on the parameter $\mu = \sqrt{m_i T_i / m_e T_e}$, where $m_i/m_e(T_i/T_e)$ is the ion to electron mass (temperature) ratio. They found that the dust charge in a strong magnetic field can be substantially larger (up to 12 times) than in the absence of the magnetic field (or in a weak magnetic field).

Next, we consider electrostatic perturbations $(\omega, \mathbf{k})$ accounting for dust charge fluctuations. The charging equation for dust particles in a dusty plasma is

$$d_t Q_{d1} = I_{e1} + I_{i1}, \tag{4}$$

where Q_{d1} is the perturbation of the dust charge in the presence of the perturbed electron and ion currents $I_{e1,i1}$ associated with the perturbed plasma particle distribution functions in the electrostatic field. Here, ω and $\mathbf{k}$ are the frequency and the wavevector, respectively.

To calculate the perturbed currents of the magnetized electrons and ions, we assume $\rho_{e,i} \geq a$, where ρ_j is the Larmor radius of the species j (j equals e for electrons, i for ions and d for dust grains). We employ the guiding-center coordinates[6] and obtain the perturbed distribution function in the presence of the electrostatic potential $\Phi(\mathbf{x}.t)$ as

$$f_{j1}(\mathbf{x}, \mathbf{v}, t) = -\frac{q_j \Phi(\mathbf{x}, t)}{T_j} \sum_l \sum_n J_l \left(\frac{k_\perp v_\perp}{\omega_{cj}} \right) J_n \left(\frac{k_\perp v_\perp}{\omega_{cj}} \right)$$

$$\times \exp\left[i(n-l)(\theta - \delta) \right] \left(1 - \frac{\omega}{\omega - k_\parallel v_\parallel - n\omega_{cj}} \right) f_{j0}, \tag{5}$$

where $\Phi(\mathbf{x}, t) = \Phi_0 \exp\left[i(\mathbf{k} \cdot \mathbf{x} - \omega t) \right]$, Φ_0 being the amplitude of the electrostatic perturbation, θ is the angle between $v_\perp$ and the x-axis, δ is the angle between $k_\perp$ and the x-axis, J_l is the $l-$th order Bessel function of the first kind, and $\parallel$ ($\perp$) denotes a quantity parallel (perpendicular) to $\hat{\mathbf{z}}$.

Thus, in the presence of a low-frequency electrostatic field, the charging current perturbations are

$$I_{j1}(\mathbf{x}, t) \equiv \oint \mathbf{J}_j \cdot d\mathbf{S} = 2\pi a^2 q_j \int (v_\perp \cos\theta + v_\perp \sin\theta + v_\parallel) f_{j1} d\mathbf{v}, \tag{6}$$

where f_{j1} is given by Eq. (5). After a straightforward calculation, we then obtain from Eq. (6)

$$I_{j1}(\mathbf{x},t) = -4\pi a^2 q_j n_{j0} \frac{q_j \Phi(\mathbf{x},t)}{T_j} \exp\left(-\frac{q_j \Phi_G}{T_j}\right) \left(\frac{T_j}{2\pi m_j}\right)^{1/2} F_j, \tag{7}$$

where $F_j = F_{j1} + F_{j2} + F_{j3}$, with

$$F_{j1} = \sqrt{\frac{\pi}{2}} \sum_n \frac{n\omega_{cj}}{k_\perp v_{tj}} I_n \exp(-b_j) \left[1 + \frac{\omega}{\sqrt{2}k_\parallel v_{tj}} Z(\xi_n)\right], \tag{8}$$

$$F_{j2} = -i\sqrt{\frac{\pi}{2}} \frac{k_\perp v_{tj}}{\omega_{cj}} \sum_n \left[1 + \frac{\omega}{\sqrt{2}k_\parallel v_{tj}} Z(\xi_n)\right] \frac{d}{db_j} \left[I_n \exp(-b_j)\right], \tag{9}$$

$$F_{j3} = \sqrt{\frac{\pi}{2}} \frac{\omega}{k_\parallel v_{tj}} \sum_n I_n \exp(-b_j)[1 + \xi_n Z(\xi_n)], \tag{10}$$

and $\xi_n = (\omega - n\omega_{cj})/\sqrt{2}k_\parallel v_{tj}$.

For $\omega \ll \omega_{cj}$, $k_\perp v_{tj} \ll \omega_{cj}$, and $k_\parallel v_{tj} \ll |\omega|, |\omega - n\omega_{cj}|$, the modification factor F_j reduces to

$$F_j \simeq \sqrt{\frac{\pi}{2}}(1 - b_j) \left[\frac{k_\perp v_{tj}}{\omega_{cj}} \left(\frac{\omega}{\omega_{cj}} - i\frac{k_\parallel^2 v_{tj}^2}{\omega^2}\right) - \frac{k_\parallel v_{tj}}{\omega}\right]. \tag{11}$$

When $k_\parallel/k_\perp \ll \omega^2/\omega_{cj}^2$ and if we neglect the small imaginary term in Eq. (9), the modification factor is found to be

$$F_j \simeq \sqrt{\frac{\pi}{2}} \frac{k_\perp v_{tj}}{\omega_{cj}} \frac{\omega}{\omega_{cj}} (1 - b_j), \tag{12}$$

which is less than unity.

We note from Eq. (7) that for $b_j \ll 1$ and $k_\parallel v_{tj} \ll \omega$, the perturbed currents in a uniform magnetized dusty plasma is reduced by a factor F_j from the unperturbed currents to the grains.

For $|\omega| \ll \omega_{cj}$, $k_\perp v_{tj} \ll \omega_{cj}$ and $k_\parallel v_{tj} \gg |\omega|$, $|\omega - n\omega_{cj}|$, we obtain from Eqs. (8)–(10)

$$F_j \simeq \sqrt{\frac{\pi}{2}}(1 - b_j) \left(\frac{\omega}{k_\parallel v_{tj}} + i\frac{k_\perp v_{tj}}{\omega_{cj}}\right). \tag{13}$$

For $|\omega|/k_\parallel v_{tj} \gg k_\perp v_{tj}/\omega_{cj}$ we can neglect the imaginary part in Eq. (13), and F_j again becomes less than unity. Equations (12) and (13) reveal that F_j is less than unity for both high- and low-parallel phase velocity waves.

Taking $n_j = n_{j0} + n_{j1}$ and $Q_d = Q_{d0} + Q_{d1}$, we obtain from Eq. (4)

$$Q_{d1} = -i\beta(\omega)\Phi/\omega, \tag{14}$$

where

$$\beta(\omega) = \frac{a^2}{\sqrt{2\pi}} \left[\frac{\omega_{pe}}{\lambda_{De}} \exp\left(\frac{e\Phi_G}{T_e}\right) F_e(\omega) + \frac{\omega_{pi}}{\lambda_{Di}} \left(1 - \frac{e\Phi_G}{T_i}\right) F_i(\omega)\right]. \tag{15}$$

Here, $\lambda_{Dj} = v_{tj}/\omega_{pj}$, $\omega_{pj} = \left(4\pi n_{j0} q_j^2/m_j\right)^{1/2}$, and $F_{e,i}(\omega)$ are given by Eq. (10) or Eq. (11) depending on the conditions of the wave perturbation and the plasma parameters.

To demonstrate how the external magnetic field affects the damping of a low-frequency electrostatic mode propagating nearly perpendicular to the magnetic field direction, we consider a magnetized dusty plasma with finite electron and ion temperatures. For $\omega_{cd}, kv_{td}, k_\parallel v_{ti}, k_\parallel v_{te} \ll$

$|\omega| \ll \omega_{ci}$, ω_{ce} and $b_{e,i} \ll 1$, the electrons and ions are strongly magnetized, while cold dust grains are unmagnetized.

Poisson's equation in the presence of a low-frequency mode and dust charge fluctuations is

$$k^2\Phi + 4\pi(n_{e1}e - n_{i1}e - n_{d1}Q_{d0} - n_{d0}Q_{d1}) = 0, \tag{16}$$

where Q_{d1} is given by Eq. (16) for F_j given by Eq. (11). Inserting $n_{j1} = -(k^2\chi_j/4\pi q_j)\Phi$, where $\chi_e \simeq (\omega_{pe}/\omega_{ce})^2(k_\perp/k)^2 - (\omega_{pe}/\omega)^2(k_\parallel/k)^2$, $\chi_i \simeq (\omega_{pi}/\omega_{ci})^2(k_\perp/k)^2 - (\omega_{pi}/\omega)^2(k_\parallel/k)^2$ and $\chi_d \simeq -(\omega_{pd}/\omega)^2$ in Eq. (17), we obtain $\epsilon(\omega, \mathbf{k})\Phi = 0$, where the dielectric constant of a magnetized dusty plasma is

$$\epsilon(\omega, \mathbf{k}) = 1 + \frac{k_\perp^2}{k^2}\frac{\omega_{pi}^2}{\omega_{ci}^2}\left(1 + \frac{n_{e0}m_e}{n_{i0}m_i}\right) - \frac{k_\parallel^2}{k^2}\frac{\omega_{pe}^2}{\omega^2}\left(1 + \frac{n_{i0}m_e}{n_{e0}m_i}\right) - \frac{\omega_{pd}^2}{\omega^2} + i\frac{4\pi n_{d0}\beta(\omega)}{k^2\omega}. \tag{17}$$

Neglecting the dust charge fluctuations, one readily obtains from $\epsilon(\omega, \mathbf{k}) = 0$ the dust-lower-hybrid (DLH) wave frequency[7]

$$\omega = \frac{k}{k_\perp}\frac{\omega_{pd}\omega_{ci}}{\omega_{pi}}\left(1 + \frac{k_\parallel^2}{k^2}\frac{\omega_{pe}^2}{\omega_{pd}^2}\right)^{1/2} \equiv \omega_r, \tag{18}$$

where $n_{i0}m_e \ll n_{e0}m_i$ has been assumed. However, dust charge fluctuations introduce a damping of the DLH waves with a damping rate

$$\gamma_L = -4\pi\, n_{d0}\, \beta(\omega_r)/k^2, \tag{19}$$

which is obtained from Eq. (17) by letting $\omega = \omega_r + i\gamma_L$, with $\gamma_L^2 \ll \omega_r^2$. Here, $\beta(\omega_r)$ is modified from the unmagnetized value[1] by the factors F_e and F_i, given by Eq. (12).

To summarize, we have investigated the influence of an external magnetic field on dust charge perturbations in a dusty plasma. It is found that the external magnetic field reduces the charging currents on the dust grains, thereby decreasing the dust charge fluctuation damping of a low-frequency electrostatic wave through the reduction of $\beta(\omega_r)$ by the factors F_e and F_i, which are given by Eq. (12) or Eq. (13). In order to have some appreciation of our results, we estimate the frequency and the damping rate by taking the plasma and wave parameters which are relevant for laboratory discharges. Accordingly, we take $n_{i0} \sim 10^9$ cm^{-3}, $n_{d0} \sim 10^4$ cm^{-3}, $Z_{d0} \sim 5 \times 10^3$, $T_e \sim 1$ eV, $T_i \sim 0.1$ eV, $B_0 \sim 400$ G, and $a = 10$ μm. For $k_\perp \sim 1$ cm^{-1} and $k_\parallel^2/k_\perp^2 \ll Z_{d0}^2 n_{d0}m_e/n_{e0}m_d$, the frequency and the damping rate of the dust lower-hybrid are 10 s^{-1} and 2 s^{-1}, respectively. In conclusion, we state that knowledge of dust charge fluctuation induced damping of waves is required in calculating the thermal wave spectrum by using a fluctuation dissipation theorem.

REFERENCES

(1) R. K. Varma, P. K. Shukla, and V. Krishan, Phys. Rev. **E 47**, 3612 (1993).
(2) D. A. Mendis, Plasma Sources Sc. Technol. **11**, A219 (2002).
(3) E. C. Whipple, Rep. Prog. Phys. **44**, 1197 (1981).
(4) L. Parker and B. L. Murphy, J. Geophys. Res. **72**, 1631 (1967).
(5) V. N. Tsytovich, N. Sato, and G. E. Morfill, New J. Phys. **5**, 43 (2003).
(6) C. S. Liu and V. K. Tripathi, Phys. Reports **130**, 143 (1986).
(7) M. Salimullah, Phys. Lett. **A 215**, 296 (1996); M. Salimullah, M. R. Amin, M. Salahuddin, and A. Roy Chowdhury, Phys. Scripta **58**, 76 (1998).

PIC-Monte Carlo Simulation of Electronic Avalanches Leading to the Formation of Discharges

H. Ghalila, M. Chrigui, Z. Ben Lakhdar
Laboratoire de Spectroscopie Atomique et Moleculaire et Applications
Univesite Tunis ElManar, Faculte des Sciences de Tunis, Tunis, Tunisie
Corresponding author. E-mail : ghalila.sevestre@planet.tn

ABSTRACT

We present here a new PIC Monte Carlo code designed for the study of the microscopic process involved during the first steps of the formation of the electrical discharges. We focus our attention on the collisional mechanisms leading to the formation of the electronic avalanches, which are responsible of apparition of space charge. The photoionize process is taken into account by using Penney and Hummerts relation who related the number of ionized collisions to the number of photoionized ones. The simulations presented follow electron beam evolved in nitrogen gas with different pressures and for different values of the external electric field.

Keywords: PIC-Monte Carlo simulation; Gas discharge; Electronic avalanche; Streamer

INTRODUCTION

Representation of elementary process occurring in electrical breakdown of a neutral gas make easier the understanding of the formation and the evolution of the plasma state and the property of the gas discharges. Unfortunately the large number of those elementary process associated to the large kind of process don't allow to model exactly the evolution of the system as a whole. To circumvent this problem we use mathematical theories or numerical simulation to approach more precisely the experimental observations. Among the different models of numerical simulation, the PIC (Particle In Cell) Monte Carlo method reproduces the corpuscular evolution of the matter. These kinds of investigation have been carried out for a number of years and we based our development on the works realized by Kline and Siambis[1]. They study specially the growth of the ionization of a nitrogen gas under uniform electrical field produced by plane electrodes. They focus their investigations on the transition of electronic avalanche into a streamer, which appear when the size of electronic avalanche becomes great enough that their space charge produce a field, which reach the value of the external electric field.

In PIC technique, particles are followed one by one through a spatial and temporal mesh. The strength responsible of their motion is the sum of the external field with the self-consistent field. The principal disadvantage of this kind of simulation is the limitation of the number of the numerical particles we can really use to simulate the huge number of real particles. To approach the reality, the numerical particles, which also called macro-particles, represent in fact a large number of elementary particles. Furthermore the size of these macro-particles can be modified to speed up the calculation for example or when carrying a mapping of the particles as we will see later. The spatial dimension of the code is 2D1/2 (2D in space and 3D in space velocity) which allows us to simulate discharges evolved in cylindrical geometry. The Monte Carlo technique is based on stochastic description of the gas. During their travel, particles interact with others through several kinds of collisions so that their motion became unpredictable. Furthermore each collision is described with cross section which is a probabilistic term. For that reason the stochastic approach is well adapted to simulate these events. In theoretical point of view, the topic we are interested in also motivate the use of PIC Monte Carlo simulations because the transitory nature of its evolution. During the first step of the growth of the ionization there is no suitable equilibrium approximation can be made. Then the fluid model based on

$$\frac{d\gamma v}{dt} = \frac{e}{m}\left[\left(\vec{E} + \vec{E}_{ext}\right) + \vec{v}\times\left(\vec{B} + \vec{B}_{ext}\right)\right] \quad (4)$$

Collisional processes are based on experimental data that gives collision frequencies versus electron energy for nitrogen at pressure of 1 Torr. The smallest delay between two collisions evaluate with these data is about 10^{-11} *sec*. Then the time step Δt is small enough to take into account all the collisions. The probability of a collision during Δt is given by $P(t) = 1 - e^{(-\nu\, \nu(t)\, \Delta t)}$. To carry out a collision, this probability is compared with random number from a uniform distribution. If the random number is less than P(t) then we induce collision. Another uniform random number decides which type of collision the electron undergoes. For all cases the new direction of the incident electron and of the secondary electron produce by ionization is decide by another random number from uniform distribution included in $[-\pi , \pi]$. In the case of inelastic collision, we assume that the electron with energy below 20 eV lose all its energy during the collision. For electron with energy above 20 eV exciting collision takes 14°eV and ionizing collision take 15,5°eV. In the case of ionization, the remain energy is shared between the incident and the secondary electron.

The photoionization is based on the experimental results obtained by Penney and Hummert[7] which gives relation between the number of photoionization produced in a region of the space to the number of ionization produced in another region. The photoionization occur every *nsec*. In this problem we expect that the number of photoionization decrease exponentially with the distance to the axe then we also fixed the maximum value of the radius R_M°=°5 mm where photoionization can occur to limit the number of needless calculations.

The number of charge particles growth quickly do to the ionization and photoionization. So we need to proceed at mapping to reduce this number without changing the distribution function. This mapping is applied simultaneously to the electrons and to the ions. Furthermore we distinguish particles resulted from ionization of the initial electrons injected from the cathode and which are designed as primary particles, with particles resulted from the photoionization and which are designed as secondary particles. For each species we proceed as follow. To keep the spatial distribution the mapping is carry out in the cells where the number of charge particles overtake 200. And to keep the velocity distribution, we split it in a 5 parts after reordering the particles in ascending energy. Every part contains the same number of particles, which is reduced to the tenth in each part. All the parameters dedicated for the mapping are introduced as input data and can be changed easily to speed up the calculations with retaining a good accuracy.

SIMULATIONS AND RESULTS

We present in this paper two series of simulations. For all the simulations, we follow a small beam of electrons with 1mm radius initiated around the axe.

- In the first series, we calculate the drift velocity and the Townsend coefficient for different value of the reduced electric field (E/P). These two parameters are determined experimentally so we can validate the algorithms. We expect to find the classical behavior of electronic avalanche which is described with

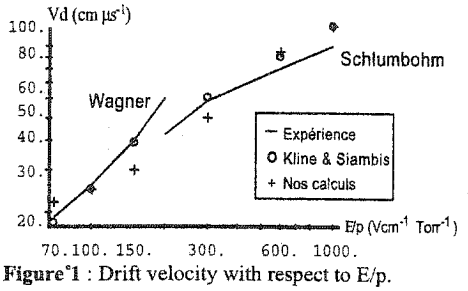
$$N(t) = N(t_0)\exp^{\alpha v_d (t - t_0)} \quad (5)$$

where v_d is the drift velocity calculated with v_d°=°"vf(v)dv andα is the Townsend coefficient obtained from (5) : α°= Ln(N/N$_0$)/ v_d(t - t_0).

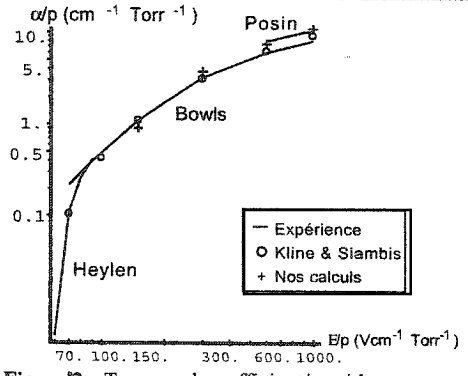
We simulate several cases corresponding to different values of E and of the pressure P. We gives here the results obtained for six values of reduced electric field (E/P). These results are the same as those presented in°[1] which are put again (points) in the figures 1 and 2 for the comparison. Experimental results[8-11] are also shown as smooth curves.

As we can see, we have a good agreement between experimental and the simulation results which indicates that the collision calculations accurately predict the growth of pulsed electron into the avalanche.

- The second series of simulation is dedicated to the study of the streamers and to their formation into the gas. We follow here the evolution of a single avalanche initiated with a pulse of 500 electrons injected at the initial time only. This avalanche evolve in a nitrogen gas at 1 Torr with electric field E = 100 kV/m. To highlight the role of the photoionization we compare two kinds of simulation for the same case, one with the photoionization and the other without the photoionization.
In order to show the state of the plasma and to reproduce the brightness of the luminous front, we have built a diagnostic which calculate the number of excitation produced during 0,5 ns. After this delay the number of excitation is reset to zero. In fact we fixed a delay for all desexcitation. We localize in that way the hot region of the plasma.



Figure°1 : Drift velocity with respect to E/p.



Figure°2 : Townsend coefficient/p with respect to E/p.

CONCLUSION

As we can see, the great advantage of these simulations is the knowledge of the electron distribution function, which allow us to determine the entire transport coefficient (drift velocity, diffusion coefficient). The introduction of collisional effect through the binary collision between electron and gas molecule gives the ionization coefficient, which show the mechanism of the electronic avalanche. The effect of the photoionization is clearly shown with the formation of the cathode and anode directed streamer. The good agreement between simulation and experiment[a(12)] encourage us to applied this code to more realistic case like the study of the electrical discharge with very general electric field.

REFERENCES

(1) L.E. Kline, J.G. Siambis, Phys. Rev. A, 5(2) (1972) 794.
(2) A. Poinsignon, These, Universite Paul-Sabatier, Toulouse, Fevrier 1994.
(3) D. Djermoune, These, Universite Paris VI, Decembre 1996.
(4) E.E. Kunhard, T.Y. Tzeng, Phys. Rev. A, 38(A) (1987) 1410.
(5) H. Raether, Butterworths, London, 1964.
(6) H. Ghalila, These, Universite Paris-Sud, Orsay, Janvier 1994.
(7) G.W. Penney, G.T. Hummert, J. Appl. Phys. 41 (2) (1970) 572.
(8) H. Schlumbohm, Z. Physik 182 (1965) 317.
(9) Masch, Ayres, Posin. Phys. Rev. 50 (1936) 650.
(10) W.E. Bowls, Phys. Rev. 53 (1938) 293.
(11) A.E.D Heylen, Nature 183 (1959) 1545.
(12) K.H. Wagner, Z. Physik A, 189 (1966) 465.

Dielectric Permittivity of Dusty Plasma with Account of Dipole Moments of Granules

V.N. Mal'nev, Eu.V. Martysh
Taras Shevchenko Kyiv National University, Vladimirska str. 60, 01033, Kiyv-33, Ukraine
emart@mail.univ.kiev.ua

ABSTRACT

We evaluated a contribution of the electric dipole moment of elongated granules in the tensor of dielectric permittivity of dusty plasmas. It is shown that it can be of the same order as the contribution of charged granules. The interaction of rotating dipole moments with plasma waves result in the Landau damping that does not depend on a wave vector. Availability of the electric dipole moments of granules results in mostly cases in a decay of plasma waves that could exist in ordinary electron-ion plasmas.

Key Words: Dusty Plasma, Elongated granules, Dipole Moment, Dielectric Permittivity

INTRODUCTION

The low frequency dispersion properties of the dusty plasma associated with translation degrees of freedom of charged granules have been studied intensively in numerous papers[1-2]. In the dusty plasma with elongated granules, a typical frequency ω_T appears that is the frequency of heat rotation of the granules. Charged elongated granules have electrical dipole moments that may interact with the plasma self-consistent field and contribute to the low frequency dispersion properties of the dusty plasma.

The tensor of dielectric permittivity of the electron-ion plasma with neutral molecules possessing constant electric dipole moments have been considered within the framework of the simplest model of spherical particles with installed point dipoles[3]. The main result of this study was a conclusion that dipole molecules provide the additional Landau damping with a decrement $\gamma \sim \exp(-\omega^2/\omega_T^2)$ that does not depend on a wave vector. This means that the eigen vibrations that weakly decay in a conventional electron-ion plasma may be suppressed in the plasma with an impurity of polar molecules if the frequencies of these vibrations are close to $\omega_T = \sqrt{T/J}$, (J is a moment inertia of the rotator).

RESULTS & DISCUSSIONS

In this paper, we consider the dusty plasma with identical elongated granules possessing a constant electric charge q and dipole moment p. To describe a contribution of rotating electrical dipole moments to the tensor of dielectric permittivity, we consider the polarizability of a gas of rigid dipoles in the field of electromagnetic wave. Further, it would be convenient to use some results obtained in quantum mechanics. Particularly, the average dipole moment p of a quantum system in a state n, induced by the external electromagnetic field $\tilde{\vec{E}} = \vec{E}_0 \cos\omega t$ is given be the relation[3]

$$\vec{p}_n = -\sum_k \frac{2\omega_{nk}\left\langle n\left|\hat{\vec{p}}\right|k\right\rangle\left(\left\langle k\left|\hat{\vec{p}}\right|n\right\rangle\cdot\tilde{\vec{E}}\right.}{\hbar(\omega_{nk}^2-\omega^2)}. \qquad (1)$$

Here n and k are set of quantum numbers that characterize the quantum system, summation in (1) is taken over all quantum states of the system, $\omega_{nk} = (E_n - E_k)/\hbar$, E_n are energy levels of the system. This relation is obtained in the first order of the quantum mechanic perturbation theory in the long wave approximation when a wavelength of the electromagnetic field is much larger than a typical size of the system. In this case, the operator of perturbation is $\hat{W} = -\hat{\vec{p}}\cdot\vec{E}$. The matrix elements of the operator of dipole moment $\left\langle n\left|\hat{\vec{p}}\right|k\right\rangle$ are taken on the wave functions of the unperturbed system.

In our case, the quantum system is an isolated rigid rotator possessing a dipole moment p. The unperturbed wave functions are the spherical functions $Y_{lm}(\vartheta,\varphi)$, where l and m are the orbital and azimuth quantum numbers respectively, ϑ and φ are the polar and azimuth angles of the vector of dipole moment $\vec{p}$. According to the well-known selection rules, the nonzero matrix elements are given by the relations[4]

$$\langle l+1,m|\hat{p}_z|l,m\rangle = p\sqrt{\frac{(l+1)^2-m^2}{(2l+3)(2l+1)}},\ \langle l-1,m|\hat{p}_z|l,m\rangle = p\sqrt{\frac{l^2-m^2}{(2l+1)(2l-1)}}, \tag{2}$$

$$\langle l+1,m+1|x+iy|l,m\rangle = p\sqrt{\frac{(l+m+2)(l+m+1)}{(2l+3)(2l+1)}},\langle l-1,m+1|x+iy|l,m\rangle = -p\sqrt{\frac{(l-m)(l-m-1)}{(2l+1)(2l-1)}} \tag{3}$$

$$\langle l+1,m-1|x-iy|l,m\rangle = -p\sqrt{\frac{(l-m+2)(l+m+1)}{(2l+3)(2l+1)}},\langle l-1,m-1|x-iy|l,m\rangle = p\sqrt{\frac{(l+m)(l+m-1)}{(2l+1)(2l-1)}}. \tag{4}$$

First of all we consider the z-projection of the induced dipole moment p_z in the quantum state $|n,m\rangle$. Inserting the expressions of matrix element (2) in (1) and taking into account the expression of energy levels of the rotator

$$E_l = \hbar^2 l(l+1)/2J, \tag{5}$$

and carrying out summation in (1) over m from $-l$ to $+l$, we obtain

$$d_l^z = \frac{d^2}{3J}\left\{\frac{(l+1)^2}{\frac{\hbar^2(l+1)^2}{J^2}-\omega^2}-\frac{l^2}{\frac{\hbar^2 l^2}{J^2}-\omega^2}\right\}\widetilde{E}_z. \tag{6}$$

This relation allows us to obtain the polarizability tensor α_{ij} of the individual rotator in a weak varying electric field by using a relation: $d_l^z = \alpha_{zz}^l(\omega)\widetilde{E}_z$. It is easy to show that $\alpha_{xx}^l(\omega) = \alpha_{yy}^l(\omega) = \alpha_{zz}^l(\omega) \equiv \alpha^l(\omega)$. Combining three last formulas we get

$$\alpha^l(\omega) = \frac{d^2}{3J}\left\{\frac{(l+1)^2}{\frac{\hbar^2(l+1)^2}{J^2}-\omega^2}-\frac{l^2}{\frac{\hbar^2 l^2}{J^2}-\omega^2}\right\} \tag{7}$$

This expression must be averaged over all quantum states with the help of the Boltzmann distribution

$$\alpha(\omega) = \frac{1}{Z}\frac{d^2}{3J}\sum_{l=0}^{\infty}\exp\left\{-\frac{\hbar^2 l(l+1)}{JT}\right\}\left\{\frac{(l+1)^2}{\frac{\hbar^2(l+1)^2}{J^2}-\omega^2}-\frac{l^2}{\frac{\hbar^2 l^2}{J^2}-\omega^2}\right\},\ Z = \sum_{l=0}^{\infty}(2l+1)\exp\left\{-\frac{\hbar^2 l(l+1)}{JT}\right\}$$

Here T is the temperature of rotational degrees of freedom. After carrying out summation in the last formula with respect to l, we obtain the polarizability of an individual dipole.

Further we consider the classical limit when the distance between energy levels of the rotator[5] is very small compared to with the temperature

$$\Delta E/T = \hbar^2 l/JT << 1. \tag{8}$$

This inequality holds true always with the exception of extremely low temperatures. It allows us to pass from summation over l into integration. In this limit, the main contribution in $\alpha(\omega)$ are given by large values of $l>>1$. Keeping this in mind, we could rewrite the corresponding expression as follows

$$\alpha(\omega)=\frac{1}{Z}\frac{d^2}{3J}\int_0^\infty 2l\exp\left\{-\frac{\hbar^2 l^2}{2JT}\right\}\frac{dl}{\frac{\hbar^2 l^2}{J^2}-\omega^2},\quad Z=\int_0^\infty 2l\exp\left\{-\frac{\hbar^2 l^2}{2JT}\right\}dl=\frac{2JT}{\hbar^2}. \tag{9}$$

It is convenient to introduce a new variable of integration $x=\hbar l/\sqrt{2JT}$ and rewrite (9)

$$\alpha(\omega)=\frac{d^2}{3T}\int_0^\infty\frac{x\exp(-x^2)dx}{x^2-y^2},\quad y=\frac{1}{\sqrt{2}}\frac{\omega}{\omega_T}. \tag{10}$$

Here $\omega_T=\sqrt{T/J}$ is a quantity proportional to the angular velocity of the rotator. The integrand of (10) has a singularity on the real axis at a point $x=y$. According to the Landau rule[5] of rounding the singularity the integral (10) may be presented in the form

$$f(y)=P\int_0^\infty\frac{x\exp(-x^2)}{x^2-y^2}dx+i\frac{\pi}{2}\exp(-y^2). \tag{11}$$

Here P means the principal value of the integral. At arbitrary y the integral in (11) may be evaluated numerically. A result of numerical calculations is presented in Fig.1.

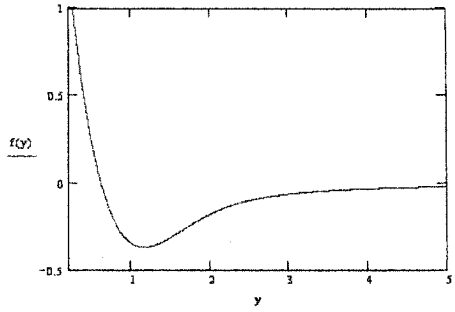


Fig. 1. A graphic representation of the function $f(y)$.

For the "high" frequencies $\omega>>\omega_T$, integration could be performed after expansion of the denominator into the power series with respect to $x^2/y^2<<1$. The result is

$$\mathrm{Re}\,\alpha(\omega)\approx-\frac{d^2}{3J\omega^2}\left[1+2\frac{\omega_T^2}{\omega^2}\right]. \tag{12}$$

A comparison (15) with the numeric calculation (see Fig. 1) shows good agreement starting with $y=2$. Formula (12) does not work in the limit of the "low" frequencies $\omega<<\omega_T$, when time-depended perturbation theory is invalid. In this case, one could expect that dipoles have time to reach the thermal equilibrium that corresponds to the Boltzmann distribution of dipoles in a constant electric field. Therefore, we could accept that α does not depend on frequency ω and equals to the static Langevin polarizability

$$\alpha(\omega)\approx d^2/3T. \tag{13}$$

Now we consider the longitudinal dielectric permittivity of the dipole plasma ε. It could be presented as a sum of terms corresponding to a contribution of the charged components electrons ε_e, ions ε_i, charged granules ε_g, and dipole moments of the granules

$$\varepsilon_l=\varepsilon_e+\varepsilon_i+\varepsilon_g+4\pi N_g\alpha(\omega), \tag{14}$$

where N_g is a density number of granules, $\alpha(\omega)$ is given by (12). Analytic expressions of dielectric functions of electrons, ions, and charged granules are well known[1]. Below we consider low frequency vibrations of the dusty plasma associated with rotational motion of the dipole moments of granules. Let these degrees of freedom be in the thermal equilibrium with the same temperature T. Displacements of the rotators that move with the heat velocity v_T for the time of the order of a period of revolution is of the order of its typical size $v_T/\omega_T \sim a$. At higher frequencies, the positions of the mass centers practically do not change for this time. Therefore, at these frequencies, the granules have no time to change their coordinates. In other words, the granules are being at rest. Using the well-known condition $\varepsilon(\omega,k)=0$, one could analyze the low frequencies vibrations of the dusty plasma with account of the dipole moments of granules. The dipole moments of granules could give small shifts to the frequencies of eigen vibrations of the conventional electron-ion plasma. The dipole moments of the granules could play more important role in the collisionless damping of the plasma vibrations. The point is that the Landau damping in the electron ion plasma is exponentially small for the long-wave vibrations (in comparison with the Debye length. The collisionless damping due to the rotation of dipoles does not depend on the wave vector at all. Therefore, the eigen vibrations of the electron-ion plasma could be suppressed at a proper concentration of granules provided that the corresponding frequency is close to the frequency of thermal rotation of granules ω_T.

CONCLUSIONS

In conclusion we point to the special type of weakly damping eigen vibrations that could exist in the dusty plasmas with granules that posses electrical dipole moments. Let us consider a frequency range $\omega_T << \omega << kv_{Ti}$ (k is a wave vector, v_{Ti} is the thermal velocity of ions. In this low frequency range, the dispersion equation of the longitudinal waves may by written in the form [2]. Separating the real part, we obtain a dispersion of the low frequency longitudinal vibrations of dusty plasma with account of the granule dipole moments. In a general case it has a rather cumbersome form. It could be simplified in particular cases. For example, in the case when all electrons are "sitting" on the granules and in the long wave approximation $ka_i << 1$, we obtain:

$$\omega = k\sqrt{\left[1+\frac{m_g d^2}{3Je^2Z^2}\right]\frac{Z^2T_i}{m_g}} \quad . \tag{15}$$

The second term in the brackets corresponds to a contribution of the granule dipole moments. For granules that could be treated as charged needles we may set $d \sim eZL$ and $J = m_g/12$. Therefore, the frequency of the so-called dusty acoustic waves with account of the dipole moments of granules is $\sqrt{5}$ times higher comparatively with the dusty plasma with spherically symmetric granules. In conclusion we would like to underline that the low frequency waves (21) are weakly damping only if $\omega >> \omega_T$ (frequency of the dipole heat rotation). Otherwise, these waves will be suppressed by the Landau damping associated with the interaction wave-rotating dipoles.

ACKNOWLEDGMENT

This work was supported by Science and Technology Center in Ukraine, grant NN37.

REFERENCES

(1) D.D. Tskhakaya, P.K. Shukla, N.L. Tsintsadze, Zhur. Exper. Teor. Fiz. **120**, 340 (2001).
(2) P.K. Shukla, A.A. Mamun, "*Introduction to Dusty Plasma Physics*", IoP Publishing, Bristol, (2002).
(3) Solomon.Mulugeta and V. Mal'nev, J. Plasma Phys. **39**, 475 (1988).
(4) H.A. Bethe and Ed.E. Salpeter, "*Quantum Mechanics of One-and Two-Electron Atoms*", Springer (1957).
(5) E.M. Lifshitz and L.P. Pitaevskii, "*Physical Kinetics, Course of Theor. Physics*", v.10, Oxford (1997).

Magnetic Susceptibility of Complex Plasma with Ferromagnetic Granules

V.N. Mal'nev, Eu.V. Martysh
Taras Shevchenko Kyiv National University, Vladimirska str. 60, 01033, Kiyv-33, Ukraine
emart@mail.univ.kiev.ua

ABSTRACT

We obtained analytic expressions of the permeability tensor of the dusty plasma consisting of granules with magnetic moments. In the case of the plasma with ferromagnetic granules in the external constant field this magnetic dipoles could be arranged along the field. The waves of magnetic polarization are predicted in this type of plasma. A possibility of realization of a negative permittivity and permeability in this plasma is discussed.

Key Words: Complex Plasma, Granules with Magnetic Moments, Permeability Tensor

INTRODUCTION

In this report we consider the low frequency dispersion properties of the dusty plasma with ferromagnetic negatively charged granules. We assume that typical sizes of the granules are small enough to treat them as one-domain ferromagnetic particles. All granules possess the same constant magnetic dipole moment d_m and the moment of inertia J. Such a system may be created in laboratory by imposing the constant magnetic field that provide a saturation of the granule magnetization to the dusty plasma. A notation about an experimental study of this type of dusty plasma is given in[1]. The collective properties of the electron-ion plasma with the neutral component consisting of paramagnetic atoms were considered in[2].

The magnetization of the dusty plasma, associated with orientation individual magnetic moments of granules in the field of external electromagnetic wave, may be obtained in the same manner as the polarization of granules with electrical dipole moments[3]. There are two limiting cases: "low" frequency processes when a frequency of the external electromagnetic wave is much smaller than a frequency of the thermal rotation $\omega << \omega_T$ and "high" frequency processes when the inverse inequality $\omega_T << \omega$ holds true ($\omega_T^2 = T/J$, T is an absolute temperature).

In the low frequency domain, the magnetic permeability is a constant and given by the Langevin formula

$$\mu(\omega) = 1 + \frac{4\pi N_g d_m^2}{3T}, \qquad (1)$$

where N_g is a density number of the granules, d_m is a magnetic moment of an individual granule.

In the high frequency domain $\mu(\omega)$ has a real and an imaginary parts;

$$\mathrm{Re}\,\mu(\omega) = 1 - \frac{4\pi N_g d_m^2}{3J\omega^2}, \qquad (2)$$

$$\mathrm{Im}\,\mu(\omega) \sim \exp(-\omega^2/\omega_T^2). \qquad (2a)$$

The imaginary part (2a) relates to a special type of the Landau damping[3] that appears due to the interaction of plasma waves with the so called resonant dipoles whose angular velocities is close to the wave frequency. The main peculiarity of this damping is that it does not depend on a wave vector unlike the conventional Landau damping[4]. This means that the plasma waves with the frequencies ω close to ω_T will be suppressed.

RESULTS & DISCUSSIONS

The dispersion properties of the dusty plasma with ferromagnetic granules in the external constant homogeneous magnetic field are considerably more interesting. To simplify the problem, we consider the case when the energy of magnetic dipole in the constant homogeneous magnetic field H_0 is much larger than their thermal energy T. It means that $d_m H_0/T >> 1$. Therefore, we may consider the magnetic moments "cold" and oriented practically along the magnetic field. In the field of the external electromagnetic wave with a magnetic component $\vec{H}(\vec{r},t) = \vec{H}\exp[i\vec{k}\vec{r} - i\omega t]$ the dipoles slightly change orientation with respect to z-axis. In a general case, the Lagrange function of an individual magnetic dipole may be written in the form

$$L = \frac{m_g v^2}{2} + \frac{J}{2}(\dot{\theta}^2 + \dot{\varphi}^2) + d_m H_0 \cos\theta + \vec{d}_m \cdot \vec{H}(\vec{r},t)\ , \qquad (3)$$

where m_g is the mass of granule, $\vec{v}$ is a velocity of the translation motion of the mass center of magnetic dipole, spherical polar θ and azimuth φ angels describe an orientation of the vector of magnetic moment, H_0 is the external magnetic field directed along z-axis, $\vec{H}(\vec{r},t)$ is the varying magnetic component of the self-consistent electromagnetic field that is the first order of smallness in comparison with H_0. The equations of motion that follows from (3), we present in the form

$$\begin{aligned} & m_g \dot{\vec{v}} = -\frac{\partial U}{\partial \vec{r}}, \quad U = -\vec{d}_m \cdot \vec{H}(\vec{r},t); \\ & J\ddot{\theta} + d_m H_0 \sin\theta = -\frac{\partial U}{\partial \theta}, \\ & \ddot{\varphi} = -\frac{\partial U}{\partial \varphi}. \end{aligned} \qquad (4)$$

In the long wave approach, when a wavelength of the field λ is large in comparison with a typical size of the magnetic dipole l, $\frac{\partial U}{\partial r} \sim \frac{l}{\lambda} << 1$. This means that we may ignore the first equation of the system (4) and take into account only the rotation degrees of freedom of the magnetic moment. Keeping in mind that in the spherical system of coordinate $\theta << 1$, we rewrite the potential energy U of the dipole introducing the amplitudes of varying magnetic field

$$U \approx -d_m\{\theta\cos\varphi H_x + \theta\sin\varphi H_y + H_z\}\exp(-i\omega t)\,, \qquad (5)$$

Here we ignore the dependence of the magnetic field on r in accordance with the long wave approximation.

The second equation of (4) taking into account of the inequality $\theta << 1$ is the equation of motion of driven harmonic oscillator with the natural frequency $\omega_0 = \sqrt{d_m H_0 / J}$. In the zero-order approximation from the third equation of system (4), we have that varying field is zero and the azimuth angle is $\varphi = \Omega t$. The angular frequency Ω obviously coincides with the thermal frequency $\omega_T = \sqrt{T/J}$. Comparing these frequencies, we get $\omega_T / \omega_0 = \sqrt{d_m H_0 / T} >> 1$ that requires the model of the cold ferromagnetic granules. This means that in our model the rotation of dipoles around z-axis is slow in comparison with oscillations of θ. In another words, we could set φ to be a constant and solve the equation of $\theta(t)$

$$\ddot{\theta} + \omega_0^2\theta = \frac{d_m}{J}[H_x\cos\varphi + H_y\sin\varphi]\exp(-i\omega t)\,. \qquad (6)$$

The partial solution of this equation that describes forced vibrations could be written as

$$\theta(t) = \frac{d_m}{J}\frac{H_x\cos\varphi + H_y\sin\varphi}{\omega_0^2 - \omega^2}\exp(-i\omega t)\,. \qquad (7)$$

Now we can find the magnetization of a unit volume of the ferromagnetic component by comparing the expression

$$M_i = N_g d_{mi} \tag{8}$$

with the phenomenological expression

$$M_i = \chi_{ij} H_j \tag{8a}$$

In these formulas $i,j = x,y,z$. Recalling that in our model

$$d_{mx} = d_m \theta \cos\varphi,\ d_{my} = d_m \theta \sin\varphi,\ d_{mz} \cong d_m, \tag{9}$$

with the help (7), we find that the tensor of magnetic susceptibility has the following nonzero components

$$\chi_{xx}(\omega) = \frac{d_m^2 N_g}{2J} \frac{1}{\omega_0^2 - \omega^2},\ \chi_{yy}(\omega) = \frac{d_m^2 N_g}{2J} \frac{1}{\omega_0^2 - \omega^2}. \tag{10}$$

The rest components of this tensor are zeros. A factor ½ in the denominators is a result of averaging $\cos^2\varphi$ and $\sin^2\varphi$. Now we could write down the permeability tensor that emerges in the dusty plasma due to availability of the granules with magnetic dipole moments. It has diagonal form with the components

$$\mu_{xx} = \mu_{yy} \equiv \mu = 1 + \frac{\Omega_m^2}{\omega_0^2 - \omega^2},\ \mu_{zz} = 1;\ \ \Omega_m = \sqrt{\frac{2\pi N_g d_m^2}{J}}. \tag{11}$$

The rest components are equal to zero.

In conclusion, we consider the additional waves that may exist in the dusty plasma with ferromagnetic granules. The dispersion law for monochromatic waves propagating in a medium with arbitrary permittivity $\varepsilon(\vec{k},\omega)$ and permeability $\mu(\vec{\kappa},\omega)$ tensors can be obtained from Maxwell's equations. For electromagnetic fields depending on space-time co-ordinates according to exp $(i\vec{\kappa}\cdot\vec{r} - i\omega t)$, these equations are:

$$\begin{aligned} &\vec{\kappa}\times\vec{E} = \frac{\omega}{c}\vec{B},\quad \vec{\kappa}\times\vec{H} = \frac{\omega}{c}\vec{D}, \\ &\vec{k}\cdot\vec{B} = 0,\qquad \vec{k}\cdot D = 0, \\ &\vec{D} = \varepsilon\left(\vec{k},\omega\right)\cdot\vec{E},\ \ \vec{B} = \vec{H} + 4\pi\vec{M} = \mu\left(\vec{k},\omega\right)\cdot\vec{H}. \end{aligned} \tag{12}$$

Here $\vec{E}(\vec{k},\omega)$ and $\vec{H}(\vec{k},\omega)$ are the Fourier transforms of the electromagnetic field. The permeability tensor of our media are given by (11). The permittivity tensor of the dusty plasma in the coordinate system with z-axis along the constant magnetic field H_0 could be presented in the following form[5]

$$\begin{aligned} &\varepsilon_1 = \varepsilon_{xx}(\omega) = \varepsilon_{yy}(\omega) = 1 - \sum_\sigma \frac{\Omega_\sigma^2}{\omega^2 - \omega_{H\sigma}^2},\ \ \varepsilon_3 = \varepsilon_{zz}(\omega) = 1 - \sum_\sigma \frac{\Omega_\sigma^2}{\omega^2}, \\ &\varepsilon_{xy}(\omega) = \varepsilon^*{}_{yx}(\omega) = -i\varepsilon_2 = -i\sum_\sigma \frac{\omega_{H\sigma}}{\omega} \frac{\Omega_\sigma^2}{\omega^2 - \omega_{H\sigma}^2}, \end{aligned} \tag{13}$$

$\Omega_\sigma = \sqrt{\dfrac{4\pi e_\sigma^2 N_\sigma}{m_\sigma}}$ is the plasma frequency, $\omega_{H\sigma} = \dfrac{e_\sigma H_0}{m_\sigma c}$ is the cyclotron frequency, σ numerates the kinds of charged particles: *e*(electrons), *i* (ions), and *g* (granules).

It will be convenient to introduce the inverse tensor permeability μ_{ij}^{-1} with the help of a relation $\mu_{ik}^{-1}\mu_{kj} = \delta_{ij}$. It follows from (11) that

$$\mu_{xx}^{-1} = \mu_{yy}^{-1} = \frac{1}{\mu},\ \mu_{zz}^{-1} = 1. \tag{14}$$

Eliminating the vector of magnetic induction *B* from the Maxwell equations (12), we obtain the system of linear algebraic equations with respect to the components of the electric field vector

$$[\mu\varepsilon_1 - \eta^2\cos^2\theta]E_x - i\varepsilon_2 E_y + \eta^2\sin\theta\cos\theta E_z = 0,$$
$$i\varepsilon_2 E_x + [\mu\varepsilon_1 - \eta^2(\cos^2\theta + \mu\sin^2\theta]E_y = 0, \qquad (15)$$
$$\eta^2\sin\theta\cos\theta E_x + [\mu\varepsilon_3 - \eta^2\sin^2\theta]E_z = 0,$$

$\eta=kc/\omega$ is the refraction index, θ is the angle between the wave vector $\vec{k}$ and the magnetic field $\vec{H}_0$. Equating to zero the determinant of the system (15), we get the equation

$$\mu(\omega)\{a\eta^4 + b\eta^2 + c\} = 0, \qquad (16)$$

$a = (\varepsilon_1\sin^2\theta + \varepsilon_3\cos^2\theta)[1 + (\mu - 1)\sin^2\theta]$,

$b = \mu(\omega)(\varepsilon_2^2 - \varepsilon_1^2)\sin^2\theta - \varepsilon_1\varepsilon_3[1 + \cos^2\theta + (\mu - 1)\sin^2\theta]$,

$c = \mu^2(\omega)[\varepsilon_1^2 - \varepsilon_2^2]\varepsilon_3$.

If granules have no magnetic moments $\mu(\omega)\to 0$, equation (16) coincides with the corresponding result for the magneto active plasma[5].

CONCLUSIONS

Equation (16) splits into two equations $\mu(\omega)=0$ and $a\eta^4+b\eta^2+c=0$. The first one relates to collective vibration of magnetic dipoles in the plane perpendicular to the constant magnetic field H_0. We will call them the waves magnetization. The dispersion law of these waves is given by the following expression

$$\omega = \sqrt{\frac{d_m H_0}{J}\left(1 + \frac{2\pi N_g d_m}{H_0}\right)}. \qquad (17)$$

The second equation describes the dispersion of waves in the dusty plasma with participation of magnetic dipoles. In the case of ferromagnetic granules with anomalous magnitude of magnetic moments their contribution to the dispersion properties of the dusty plasma could be important. However, this problem requires a special study.

Here we would like to note that the components of the permeability tensor (11) in a frequency range $\omega > \sqrt{\omega_0^2 + \Omega_m^2}$ are negative. We may hope that for special set of parameters of the dusty plasma with ferromagnetic granules it is possible to meet conditions for realization of negative dielectric and magnetic permittivity ($\varepsilon<0$ and $\mu<0$) simultaneously.

ACKNOWLEDGMENT

This work was supported by Science and Technology Center in Ukraine, grant NN37.

REFERENCES

(1) V.I. Molotkov, M.Yu. Pustyl'nik, V.M. Torchinskii, and V.E. Fortov, Proceedings of the Conference on Plasma Chemistry, Moscow, pp. 51-54 (2002).
(2) W. Bantikassegn and V.N. Mal'nev, J. Plasma Phys **45**, 125 (1991).
(3) Solomon Mulugeta and V. Mal'nev, J. Plasma Phys **39**, 475 (1988).
(4) E.M. Lifshitz and L.P. Pitaevskii, "*Physical Kinetics, Course of Theoretical Physics*", **v.10**, Oxford (1997).
(5) A.Sitenko and V.Mal'nev, "*Plasma Physics Theory*", Chapman & Hall, London (1995).

MISCELLANEOUS

FTIR Spectroscopic Study of the Low-Temperature Dependent Structural Changes in Isotactic Polypropylene

Rasha M. Khafagy [1] and Y. A. Badr [2]

[1] *Faculty of Women for Art, Science and Education, Physics Department, Ain Shams University, Cairo, Egypt*

[2] *National Institute of Laser Enhanced Sciences (NILES), Cairo University, Cairo, Egypt*

rashakhafagy@hotmail.com

ABSTRACT

The in situ FTIR spectroscopic study of isotactic polypropylene (iPP) showed that structural changes are induced at liquid nitrogen temperature, and start to show up in the FTIR spectra with heating from -196°C to +120°C. This structural change leads to the detection of an abnormal behavior in the MIR absorption spectra of the investigated sample. Lowering the temperature brought the chains closer together and so increased the inter-chain interaction. At -196°C, splitting of some regularity bands assigned to helical chains within the *crystalline region* was observed, showing that the regularity of the chains increases due to cooling. Heating from -196°C caused an opposite configurational/conformational disordering, which resulted in the appearance of new broad bands (600-700), (1614-1640) and (3050-3550) cm^{-1}. These structural changes might be due to both twisting and folding of the chains which gave rise to bands assigned to the various bending modes of the CH_2 molecules, in addition to the rotational isomers (conformers), resulting from rotation of the vinyl and alkyne end groups. Moreover, our experimental study of the behavior of several regularity bands suggests that at temperatures in the vicinity of +120°C, another high temperature structural changes resulting from the disordering of helical sequences in the non-crystalline region takes place. DSC study of the thermally treated and untreated sample confirmed the obtained results.

Keywords: FTIR Spectroscopy, DSC, Isotactic Polypropylene, Structural changes

INTRODUCTION

The microstructure of a semicrystalline polymer is heterogeneous, consisting of crystalline and non-crystalline regions. The heterogeneity of the microstructure comes from the different molecular structure of the amorphous and crystalline regions [(1)]. In the amorphous regions, chains are randomly coiled whereas in the crystals they are arranged in a three-dimensional lattice. Due to this heterogeneity, ultimate properties of the material are found to depend on microstructural factors, and must be highly influenced by the degree of crystallinity [(1, 2)], the size and type of spherulites formed, the lamellar thickness and the crystalline orientation [(2)]. Thus in the polymer processing technology it is relevant to consider means of characterizing the microstructure in order to evaluate the effect of various processing parameters.

In the infrared spectra of crystalline polymers, some absorption bands are very sensitive to the physical state of the sample. According to different origins, these sensitive bands can be classified into two categories [(3)], one of which is caused by intermolecular forces in the crystal lattice where the polymer molecules pack together in a regular three-dimensional arrangement, and this kind of band is often termed as *crystallinity band*. The other is connected with the intramolecular vibration coupling within a single chain, and this kind of band is defined as a *regularity band*. For iPP, most of the bands

appearing below 1400 cm^{-1} belong to the regularity bands [3]. Thus differences in the vibrational spectrum of chains in crystals with a unique regular helical conformation, compared with chains in non-crystalline regions with irregularities or non-helical conformation must be expected [1]. In the present work, it is aimed to account for the variations observed in the FTIR spectra measured at different temperatures that could be associated with different environments in which the polymer chains are found, and with the packing geometries and the unit cell parameters. We obtained a thermally treated iPP characterized with the heterogeneous microstructure, which might fit different technological applications of iPP especially concerning transparency and modulus.

EXPERIMENTAL

Commercial grade of ELTEX iPP resin pellets manufactured by "Solvay", Belgium, were used in the present study. 1 mm thick samples were prepared using a hot-press, by melting at 210°C for 5 min at pressure 100 bar. Samples have a medium melt flow index 11g/10min, density 900 kg/m^3, melting point 160°C and crystallization temperature 114°C. FTIR spectra were collected at different temperatures by using "BRUKER-IFS 66/S" spectrometer, "Specac" variable temperature cell (P/N 21525) and temperature controller measuring from -196°C to +250°C, with cooling rate ±5°C/min.

RESULTS

Fig.1 shows the FTIR spectra of iPP at Room temperature, -196°C and +120°C. Cooling iPP down to -196°C resulted in sharpening of the peaks. Some of the bands showed a reduction in their intensities due to cooling, such as: 808, 814, 1219, 1256, 1640, 1694 and 3143 cm^{-1}, while others showed an intensity increase such as: 940, 1044, 1103, 3206, 3348, 3410 cm^{-1}. In addition, obvious splittings in the continuous regions of the spectrum were observed (Fig.1a, b). Also, new bands appeared due to cooling, such as: 1039, 1084, 1194, 1512 and 1712 cm^{-1}.

After reaching -196°C, the sample was heated up gradually to +120°C, which leads to the detection of an anomalous behavior in the FTIR absorption spectra as shown in Fig.2a:

1. Heating up didn't show any variations until -80°C was reached where the intensity of all the bands in the ranges 2000-2500 and 3050-3550 cm^{-1} were found to increase. Further heating caused the intensities of both ranges to continuously increase, associated with broadening in the second range until they become a continuous and broad band at -30°C.

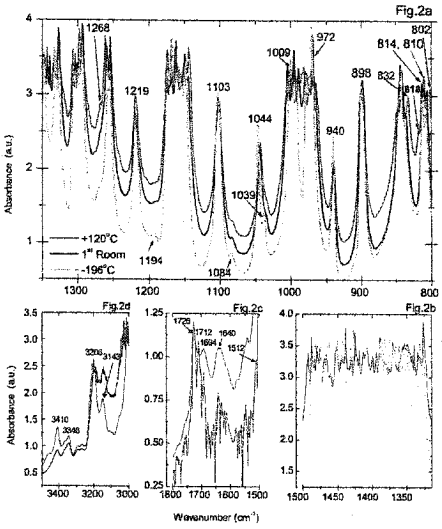
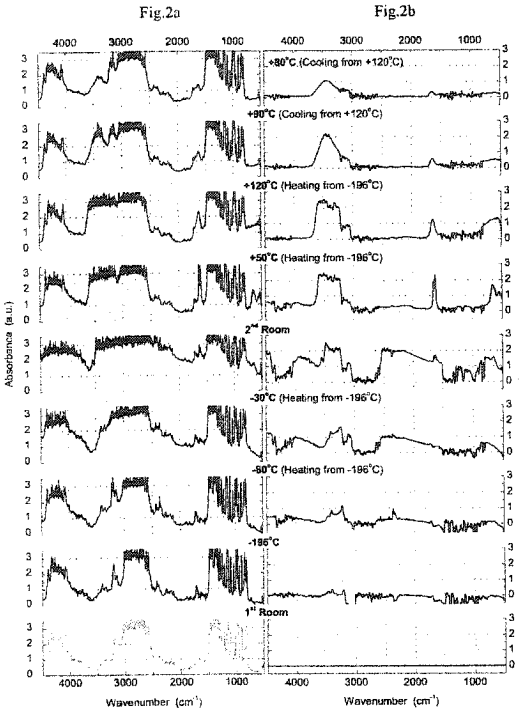


Figure 1: FTIR spectra for iPP at different temperatures & spectral ranges.

2. When the room temperature is reached again, the broadening was extended in the range 2300-3500 cm^{-1}, in addition to the appearance of new band at 3555 cm^{-1}, accompanied by an increase in the background of the spectrum in the range 500-800 cm^{-1} and the creation of the doublet 1614-1640 cm^{-1}.
3. At +50°C, the broad band in the range 2300-3600 cm^{-1} started to split again. This splitting was accompanied by a remarkable increase in the intensity of the doublet 1614, 1640 cm^{-1} in addition to the creation of a strong broad band in the range 600-700 cm^{-1} showing that this temperature is very critical for controlling the mechanism of structural changes occurring in iPP due to thermal treatment.



4. Up to +120°C all the new bands were decreasing, but they didn't disappear. The original spectrum of iPP was accomplished again at +70°C after cooling from +120°C. For clarity, all the FTIR spectra were subtracted from the spectrum measured at room temperature (Fig.2b), resulting in the so-called difference spectra. Spectra resulting from this subtraction illustrate the variations resulting from thermal treatment only, where any unaffected bands were found to be absent since the subtraction in this case = 0.

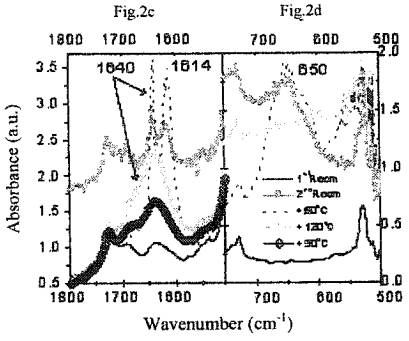


Figure 2: FTIR spectra for iPP at different temperatures, **2a:** Normal FTIR spectra, **2b:** Difference spectra showing the structural changes only, **2c:** Spectra in the range 1500-1800, **2d:** Spectra in the range 500-750cm^{-1}.

DISCUSSION

The macromolecular chain of semi-crystalline iPP has 3_1 helix structure, and the regularity bands located at 806, 840, 843, 898 and 1103 cm^{-1} are characteristic for the helical structure. Cooling the sample caused sharpening and splitting of most of the peaks as illustrated in Fig.1, because cooling leads to a thermal contraction of the crystal lattice, bringing the chains closer together and so increasing the inter-chain interaction. This causes an increase in the regularity of the chains. Crystal splitting due to inter-chain interactions in the unit cell has been observed below -196 °C [4] for the 806 cm^{-1} band. In our case, in addition to the splitting detected at the 806 cm^{-1} band, the range 965-1007 cm^{-1}, which contains peaks assigned to the helical structure was split into 2 broad bands at 972 (assigned to the symmetry of the 3_1 helical structure) and 1009 cm^{-1}. Although these splittings are very weak, they do indicate that these particular regularity bands are related to helical chains within the *crystalline region*. On the contrary, the band at 840 cm^{-1}, which is assigned to helical chains where the *trans–gauche* (*tg*) conformation has been disrupted [5], tends to be one sharp band, supporting the conclusion that the 840 cm^{-1} band is due to helical chains with isomeric defects. The small bands appearing due to cooling at -196°C: 1039, 1083, 1194 & 1512.7 cm^{-1} are due to configurational order, some of which differ in position from the peaks belonging to iPP, and could be related to structural defects. They are modes involving mixtures of two or more vibrations: C-C chain stretching, C-CH_3 stretching, CH_2 rocking, C-C-C bending, C-H bending and CH_3 bending.

Heating the sample from -196°C resulted in relaxation process leading to the opposite configurational/conformational disordering effect. This configurational disordering might be resulting in the appearance of the new broad band at 600-700 cm^{-1}, in addition to other changes, which might be due to the appearance of other structures rather than the isotactic one such as the appearance of irregularities due to such a configurational order-disorder transition occurring at +50°C. Such loss of regularities might also cause the peaks due to skeletal vibrations to be smeared out over a range of frequencies, i.e. a decrease in the intensities associated with a shift in ν in both sides, leading to merging of bands and flattening of almost the whole pattern could take place, as is observed in the 2nd room temperature spectrum and up in the region 2500-4500 cm^{-1}.

The new band: 3050-3550 cm^{-1} and the doublet: 1614-1640 cm^{-1}, are assigned to the C-H stretching mode of the alkyne end group (C≡C–H) [5], and to the out of plane deformation mode of trans–CH=CH– [ν(C=C)] of the vinyl end groups respectively. Frequencies of the vinyl group are altered with oxygen dissolved in the sample, the most notable of which is a doubling and intensifying of the strong C=C stretching frequency vibrating at 1614 and 1640 cm^{-1} [6]. These bands are temperature dependent [6] as they increase in intensity with increasing temperature. This shows that the doubling is caused by rotational isomers (conformers), resulting from rotation of the vinyl C-O bond.

This anomalous behavior could be related to the configurational/conformational isomerism either due to the chain folding and twisting or due to the rotation of isomerisms as a result of the thermal contraction and expansion of the chains. This is proven with the existence of the various bending modes of the CH_2 molecule, which is known to twist within the range 630-700 cm^{-1} [6]. The lowest hydrogen wag of the vinyl group in hydrocarbons is at 630 cm^{-1} while the maximum is at 700 cm^{-1} including in-phase and out of plane cis wag, and CH_2 twisting vibrations. When +120°C is reached some new bands appeared such as: 802, 810, 814 and 832 cm^{-1} assigned to chains in non-helical conformation [7], thus giving evidence on the configurational transformation occurring at high temperature since the band at 832 cm^{-1} is related to the melt like amorphous phase [1].

The interpretation given here on the appearance of the new bands: 650, 1614 and 1640 cm^{-1} at +50°C was confirmed with DSC thermograms shown in Fig.3, which illustrate endothermic peaks at -2°C, +50°C, 0°C and +110°C. Melting occurred at +158.1°C requiring energy -72.4 mJ for the untreated sample while it occurred at +157.7°C with less energy (-45.6 mJ) for the thermally treated one. On the other hand, solidification occurred at +114°C with energy +6.26 mJ for the fresh sample and at +102.63°C (12°C less) with energy +0.94 mJ (5 times less) for the thermally treated sample.

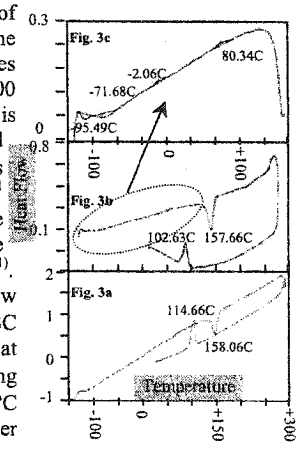


Figure 3: DSC thermograms for iPP, **3a:** untreated sample, **3b:** thermally treated sample.

REFERENCES

(1) A. S. Nielsen, D. N. Batchelder and R. Pyrz; Polymer; **43,** (9) 2671 (2002).
(2) F.J. Wortmann and K.V. Schulz; Polymer; **37,** 819 (1996).
(3) X.Y. Zhu, D.Y. Yan, and Y.P. Fang; J. Phys. Chem. B; **105**, 12461 (2001).
(4) J.M. Chalmers, H.G.M. Edwards, J.S. Lees, D.A. Long, M.W. Mackenzie and H.A. Willis; J. Raman. Spectrosc.; **22,** 613 (1991).
(5) N.B. Colthup, L.H. Daly, S.E. Wiberley; Infrared and Raman Spectroscopy, Academic Press: New York (1990).
(6) N.B. Colthup, L.H. Daly, S.E. Wiberley, Introduction to Infrared and Raman Spectroscopy, Academic Press: New York (1964).
(7) D.I. Bower and W.F. Maddams; The vibrational spectroscopy of polymers, Cambridge University Press, Cambridge: Great Britain (1992).

Computer Controlled Atom-Trapping Atomic Absorption Spectrophotometer with Water Cooled Stainless Steel Collector Tubes.

A.N. Abdel Rahman , A.M. Abdel-Daiem and M.A. Ebraheim
Faculty of Science - Zagazig University.

ABSTRACT

To enhance the efficiency of air acetylene flame atomic absorption spectrophotometer (ACFAAS), a water cooled atom-trap spectrometer (WCATS) has been developed. A stainless steel tube precoated by NaCl with 4 mm outer diameter and 2 mm inner diameter is used as trapping collector. It was adjusted using a home made computer controlling system. The effect of the trap position, the flame conditions, the coolant flow rates, the pre-coating time and the collection time were studied. The sensitivity of Pb indicates a noticeable enhancement of sixty times after a collection time of 3 min.

Key Words*: *Lead, Atom-Trapping, Atomic Absorption

INTRODUCTION

The atom-trapping atomic absorption technique (ATAAT) was first introduced by *Lau et al in 1976,* then extensively studied by *West and co-workers*[1-7]. (ATAAT) achieves greater sensitivity than conventional atomic absorption measurements by pre-concentrating the analyte atoms within the flame before measurement. When the water–cooled tube is located in the flame, the analyte atoms are trapped on the cold surface and subsequent release provides a much bigger signal than that obtained by the normal technique. This phenomenon of atom collection has been described[1], and further investigations have been made on the mechanism governing trapping and release of analyte species[2]. The possibility of using metal instead of silica tubes has also been examined and the technique has been applied to various elements.

The determination of heavy metals, especially of some toxic elements, which play important roles in biological mechanisms, has been receiving much attention[8]. Even very low concentrations of some toxic metals can cause serious biological disorders that can lead to serious diseases.

There are several methods to en-rich the analyte concentration by chemical precipitation or coupled HPLC FAAS. Such methods may introduce impurities to the natural sample while ATAAT is free of such effects. Lead is an element that has received considerable attention in recent years because of its high toxicity. The prolonged intake of even low concentrations of lead in drink water can cause serious toxic effects [9].

The FAAS has a lower sensitivity for the determination of lead at the characteristic concentration of about 1 ppm. Accordingly direct determination of trace amounts of lead at ppb level is necessary. Applying the ATAAT, 2.7, 1.6, 18.2 and 10.5- fold improvement in sensitivity for lead was obtained as compared with conventional FAAS when dual silica tube coated by Fe_3O_4,V_2O_3,Al_2O_3 and $La(OH)_3$ respectively was used at a collection time of 2 min [9].

The aim of this work is to develop a practical and sensitive method for direct determination of trace amounts of lead in nature and various water samples by (ATAAT) using a stainless steel tube.

EXPERIMENTAL

Reagents

A lead stock standard solution, containing 1000 ppm of lead, was prepared by dissolving 0.5 g of lead acetate in 273 ml of di-ionized water while adding droplets of nitric acid. Working standard solutions were prepared daily by serial dilution of the stock solution with di-ionized water.

Apparatus

A RANK HILGER Atomspek H1580 atomic absorption spectrometer equipped with a Pb hollow-cathode lamp was employed for the measurement of absorbance. A slit width of 0.2 mm was used to isolate the 228.8 nm resonance line. The improved atom trapping equipped with a water-cooled stainless-steel trap tube, air compressor, water pump, computer controlling system and the measuring system were made in our laboratory as shown schematically in Fig. 1.

A movable stainless-steel trap tube (4 mm outer diameter and 2 mm inner diameter) was positioned 8 mm above the burner and 1 mm below the light pass. Cooled tap water of constant flow rate 4.8 l/min was passed through the tube during the collection cycle. Lead solution was aspirated normally into the air–acetylene flame for an appropriate collection time up to 3 min. An appreciable proportion of the analyte condensed on the cold surface of the tube. After the collection cycle, the tap water was shut off and the coolant water was flushed out of the tube automatically by the compressed air causing rapidly heating of the tube. Accordingly, lead was released into the flame and an improved signal was recorded Fig. 2.

The home made water/air control system C consists of a computer interface via the computer parallel port Fig.3a. Two outputs of the data-bus from the parallel port of a personal computer have been used to control two solenoid valves, one for a water stream D0 and the other for air stream D1. The period of controlled cycles Fig. 3b was done by a basic program constructed especially for this experiment. Heating and cooling cycles were fully automatic controlled using this system.

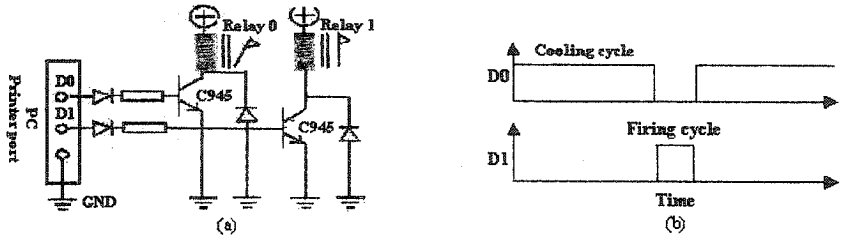


Fig. 3a) Computer interface b) Heating and cooling cycles.

RESULTS AND DISCUSSION

The atomic absorption spectrophotometer was first put to work after adjusting its analytical conditions; burner height, HCL feeding current and flow rates of both fuel and air using a standard solution of Pb. Consequently, the working curve of Pb was obtained as shown in Fig. 6b.

The atom -trapping collector was then mounted to the system and the proper conditions for getting the highest sensitivity was investigated as follows:

Effect of trap position

The position of the tube was first taken at 8 mm above the burner slot. Using this height as priminary position, the distance between the collector and the light pass was studied as shown in Fig. 4a. This was done by measuring the absorbance of 10 ppm Pb at each height using collection time of 1.5 min, firing time of 20 s and a water flow rate 4.8 l/min .

It is clear that the smaller the distance between the tube and the light beam, the higher the absorbance. The proper distance between trap tube and the burner slot was examined also using the same previously conditions as shown in Fig. 4b.

The results given in Fig. 4 indicated that, in order to obtain better sensitivity and precision, the trap tube must be positioned 8 mm above the burner slot and 1 mm below the light pass.

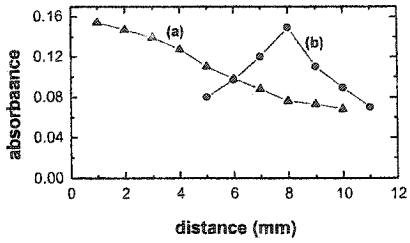


Fig. 4a) Relationship between absorbance and distance between trap tube and the light pass.
b) Relationship between absorbance and distance between trap tube and burner slot.

Effect of water flow rates

The effect of the coolant water flow rate on the absorbance was examined at the optimum conditions found in the previous section, and the results are given in table (1). They indicatelthat the flow rate of 4.8 L/min is the most suitable one where the temperature of the inlet water was 28 ^{0}C and 32 ^{0}C after passing through the tube.

Table (1)

Water flow rate l/min	4.8	4.1	3.12	2.64
Inlet water / ^{0}C	28	28	28	28
Outlet water / ^{0}C	32	34	35	39
Absorbance	0.15	0.11	0.07	0.02

Effect of stainless-steel tube without coating

The increasing in sensitivity in case of atom-trapping is indicated by drawing the relationship between the relative absorbance with and without trapping and the concentration. The results measured at the above conditions are given as illustrated in Fig. 5. The slope of the obtained line is 2.0416 and indicates an increase in sensitivity by a factor of two when a stainless–steel tube without coating was used.

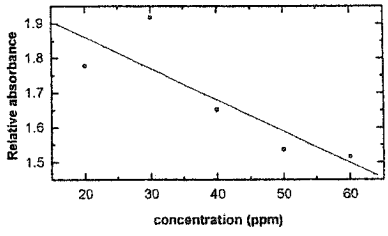


Fig. 5) Relation between relative absorbance and concentration

Effect of surface coating of the tube

The sensitivity of atomic trapping technique is known to be affected by the nature of the collector. In order to overcome the need of using different collectors, coating the trap with some elements can provides a similar effect.

The relation between the concentration at constant time of 30 s and the absorbance is shown in table (2).The relation between the collection time at constant concentration of 4000 ppm and the absorbance has been shown in table (3). It is noticed that the absorbance increases with increasing of both concentration and collection time.

Table (2)

Concentration of coating for 30 sec (ppm)	1000	2000	3000	4000
Absorbance	0.05	0.09	0.14	0.15

Table (3)

Time of coating using 4000 ppm (second)	10	20	30	40
Absorbance	0.075	0.109	0.15	0.16

Effect of collection time

The effect of sample collection time on the sensitivity of the used technique has been investigated by measuring the absorbance of 10 ppm lead solutions at different collection times as shown in fig (6a).

The obtained straight line provides us with different information. First, the intersection of the line with the absorbance scale at 0.02 points to a concentration of 10 ppm without collection which proves the reliability of the method. Second, the absorbance after 3 min collection time was found to be about 0.3. Using the calibration curve of lead measured by normal (AAS), Fig. 6b, this absorbance is corresponding to 700 ppm. Accordingly, the observed increase in sensitivity is about 70 times which is nearly the 60-times increase measured from Fig. 6a.

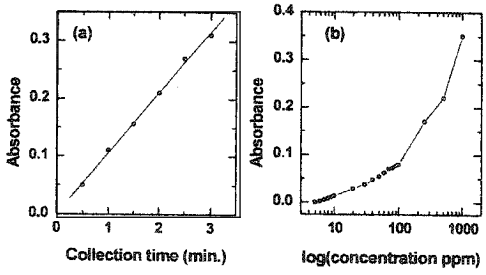


Fig. 6 a) the relation between absorbance and collection time.
b) The calibration curve of Pb without collection.

CONCLUSION

Using the ATAAT has increased the sensitivity of detecting trace amounts of lead. This technique enables the analyst to determine lead at its natural abundance without any further pre-concentration.

REFERENCES

(1) J. Khalighie, A.M. Ure and T.S. West; Anal. Chim. Acta 107,191 (1979).
(2) J. Khalighie, A.M. Ure and T.S. West; Anal. Chim. Acta 117, 257 (1980).
(3) J. Khalighie, A.M. Ure and T.S. West; Anal. Chim. Acta 131, 131 (1981).
(4) J. Khalighie, A.M. Ure and T.S. West; Anal. Chim. Acta 134, 271 (1982).
(5) J. Khalighie, A.M. Ure and T.S. West; Anal. Chim. Acta 141, 213 (1982).
(6) J. Khalighie, A.M. Ure and T.S. West; Anal. Chim. Acta 146, 171 (1983).
(7) J. Khalighie, A.M. Ure and T.S. West, Anal. Proc 20, 114 (1983).
(8) D.Q. Zhang, C.M. Li, L.L. Yang, H.W. Sun; J. Anal. At. Spectrom. 13, 1155 (1998).
(9) S.H. Wen, L.L. Yang and Z.D. Ciang, J. Anal. At. Spectrom. 11, 265 (1996).

List of Participants

List of Participants

1. Algeria

S. ABDELLI-MESSACI
Centre de Développement des Technologies Avancées (CDTA)
BP 17, Baba Hassen
16303 Algiers
Algeria
Tel: 00213-021-351018
Fax: 00213-21-351039
messaci@cdta.dz

S. BOUZID
Faculté des Medicine
Br 31, No. 1, Custantine
Algeria
Tel: 00213-31-633043
Fax: 00213-31-633043
samiabouzid@hotmail.com

E. AMARA
Centre de Développement des Technologies Avancées (CDTA)
P.O. 17, Baba Hassen
16303 Algiers
Algeria
Tel: 00213-021-351018
Fax: 00213-21-351039
amara@cdta.dz
e.amara@caramail.com

Z. BEDRANE
Theoretical Physics Laboratory
Faculty of Sciences
Abou-Bekr Belkaid University
B.P. 119, 13000 Tlemcen
Algeria
Tel: 00213-43- 204330
zeyneb.bedrane@hotmail.com

R. BENSAID
Laboratoire de Physique Théorique
Dèpartement de Physique
Faculté des Sciences
Université de Aboubekr Belkad B.P. 119
Tlemcen 13000
Algeria
Tel: 00213-43-204330
Fax: 00213-43-204330
rahma.ben@wissal.dz

K. BOURAI
CDTA Lasers & Applications Laboratory
Cité 20 Août 1965
BP 17 Baba Hassan
Algies
Algeria
Tel: 00213-21-351018-4
Fax: 00213-21-351039
kbourai@yahoo.com

S. W. RACHEDI
Laboratoire de Physique Théorique
Département de Physique
Faculté des Sciences
Université de Aboubekr Belkad B.P. 119
Tlemcen 13000
Algeria
Tel: 00213-43-204330
Fax: 00213-43-204330
rachedi.w@wissal.dz
rachedi.w@yahoo.fr

2. Australia

S. LEE
32 Oakpark Drive
Gladstone
VIC 3148
Australia
Tel: 0061-3-98882883
Fax: 0061-3-98882883
leesing@optusnet.com.au

3. Belgium

G. VAN OOST
Dept. of Applied Physics
Ghent University
Rozier 44 B-9000 Gent
Belgium
Tel: +32-9-2643834
Fax: +32-9-2644198
guido.vanoost@ugent[illegible]

J. VRANJES
Center for Plasma Astrophysics
Celestijnenlaan 200 B
3001 Leuven
Belgium
Tel: +32-32-7021
Fax: +32-32 -7998
jvranjes@yahoo.com

4. Canada

M. SHOUCRI
Institut de Researche
Hydro-Quebec (IREQ)
1804 BLVD Lionel Boulet,
Varennes, Qc,
Canada
Tel: 00450-6528723
Fax: 00450-6528625
shoucri.magdi@ireq.ca

5. Chile

L. SOTO
Commsion Chilene
de Energia Nuclear
Casi 188-D, Santiago
Chile
Tel: 0056-2-2731827
Fax: 0056-2-2738723
lsoto@cchen.cl

6. China

N. JIANG
Institute of Physics
Chinese Academy of Sciences,
P.O.Box 603,
Beijing 100080
China
Tel: 0086-10-82649131
Fax: 0086-10-82649131
jiangnan@aphy.iphy.ac.cn

7. Czech

K. KOLACEK
Institute of Plasma Physics
Academy of Sciences of
the Czech Republic
Za Slovankou 3, P.O. Box 17,
CZ 182 21 Prague 8
Czech Republic
Tel: 00420-26605 3224
Fax: 00420-28659 2644
kolacek@ipp.cas.cz

J. SCHMIDT
Institute of Plasma Physics
Academy of Sciences of
the Czech Republic
Za Slovankou 3, P.O. Box 17,
CZ 182 21 Prague 8
Czech Republic
Tel: 00420-26605 3247
Fax: 00420-28659 2644
schmidt@ipp.cas.cz

J. STOCKEL
Institute of Plasma Physics
Academy of Sciences of
the Czech Republic
Za Slovankou 3, P.O. Box 17,
CZ 182 21 Prague 8
Czech Republic
Tel: 00420-286 890-450
Fax: 00420-286-586 389
stockel@ipp.cas.cz

8. France

J. P. GUNN
DRFC Bat. 508, CEA Cadarache,
13108 Saint Paul
Lez Durance
France
Tel: 0033-442-257902
Fax: 0033-442-257902
jamie.gunn@cea.fr

9. Georgia

T. KALADZE
Vekua Institute of Applied
Mathematics
Tbilisi State University
2 University Str., 380043 Tbilisi
Georgia
Tel: 00995-32-305995
Fax: 00995-32-001153
kaladze@viam.hepi.edu.ge

10. Germany

W. DEMTROEDER
Dept. of Physics
University of Kaiserslautern
D67663 Kaiserslautern
Germany
Tel: 0049-631-2052344
Fax: 0049-631-3114914
demtroed@physik.uni-kl.de

K.-H. FINKEN
Institut für Plasmaphysik
Forschungszentrum Jülich GmbH
P.O. Box 1913, D-52425 Jülich
Germany
Tel: 0049-2461-61-5646
Fax: 0049-2461-61-5452
k.h.finken@fz-juelich.de

E. HINTZ
Institut für Plasmaphysik
Forschungszentrum Jülich GmbH
P.O. Box 1913, D-52425 Jülich
Germany
ehintz@t-online.de

H.-J. KUNZE
Ruhr Universität Bochum
Institut für ExperimentalphysikV
44780 Bochum
Germany
Tel: 0049-234-32-25785
Fax: 0049-234-32-14175
hans-joachim.kunze@ruhr-uni-bochum.de

A. NICOLAI
Institut für Plasmaphysik
Forschungszentrum Jülich GmbH
P.O. Box 1913, D-52425 Jülich
Germany
Tel: 0049-2461-61-5752
a.nicolai@fz-juelich.de

11. Egypt

A. M. ABDEL-LATIF
Nuclear Research Centre
Atomic Energy Authority
13759 Cairo
Egypt

S. A. Shalaby
Plasma Phys. & Nuclear Fusion Dept.
Nuclear Research Centre
Atomic Energy Authority
13759 Cairo
Egypt
saffa.shalaby@yahoo.com

M. A. EISSA
Physics. Dept.
Faculty of Science
Al-Azhar University
Cairo
Egypt
Tel: 002-02-6900141

T. ALLAM
Plasma Phys. & Nuclear Fusion Dept.
Nuclear Research Centre
Atomic Energy Authority
13759 Cairo
Egypt
Tel: 002-02-2750825
tarekmya1@hotmail.com

M. ALSHERSHABY
9 Sedi Abdl-Aal St.
Kaliob EL-Balad, Kaliobia
Egypt
Tel: 002-02-2150918
002-012-3543319
falhosadarsh2002@yahoo.com

E. AMER
Faculty of Engineering
Zagazig University
Zagazig
Egypt
melshaer@link.net

A. M. ATIYA
Nuclear Research Centre
Atomic Energy Authority
13759 Cairo
Egypt

N. BASSEL
Accelerator and Ions Sources Dept.
Nuclear Research Centre
Atomic Energy Authority
13759 Cairo
Egypt
Tel: 002-02-4824384

A. B. BESHARA
Plasma Phys. & Nuclear Fusion Dept.
Nuclear Research Centre
Atomic Energy Authority
13759 Cairo
Egypt
Tel: 002-02-4025542

F. EBRAHIM
Plasma Phys. & Nuclear Fusion Dept.
Nuclear Research Centre
Atomic Energy Authority
13759 Cairo
Egypt
Tel: 002-02 -6398296

G. EL-ARAGI
Plasma Phys. & Nuclear Fusion Dept.
Nuclear Research Centre
Atomic Energy Authority
13759 Cairo
Egypt
Tel: 002-02-4682315
Fax: 002-02-4691749
elaragi@yahoo.com

A. EL-BENDARY
Physics Dept., Faculty of Science
Tanta University, Tanta, Egypt
Tel-002-040-2216942
Fax: 002-040-3350804
abendary15@hotmail.com

A. B. EL-BIALY
3 Ahmed El-Sawy St.
Nasr City, Cairo
Egypt
Tel: 002-02-2750825
aidabialy@hotmail.com

H. EL-GAMAL
Plasma Phys. & Nuclear Fusion Dept.
Nuclear Research Centre
Atomic Energy Authority
13759 Cairo
Egypt

S. EL-HOUT
Metallurgy Dept.
Nuclear Research Centre
Atomic Energy Authority
13759 Cairo
Egypt
samiahoot@yahoo.com

G. EL-KASHEF
Plasma Phys. & Nuclear Fusion Dept.
Nuclear Research Centre
Atomic Energy Authority
13759 Cairo
Egypt
Tel: 002-02-4682315
Fax: 002-02-4691749

T. EL-KHALAFAWY
Plasma Phys. & Nuclear Fusion Dept.
Nuclear Research Centre
Atomic Energy Authority
13759 Cairo
Egypt
Tel: 002-010-5175012
002-02-2600079
Fax 002-02-2876031
elkhalafawy_tom@yahoo.com

A. M. EL-NADI
Laser Institute and
Faculty of Engineering
Cairo University
Giza
Egypt
Tel: 002-010-1023275
002-02-5675242
Fax: 002-02-5723486
aelnadi@hotmail.com

M. EL-SAYED ALI
Metallurgy Dept.
Nuclear Research Centre
Atomic Energy Authority
13759 Cairo
Egypt
mmes25@hotmail.com

R. EL-SHARIF
Plasma Phys. & Nuclear Fusion Dept.
Nuclear Research Centre
Atomic Energy Authority
13759 Cairo
Egypt
Tel: 002-02-4144093
Fax: 002-02-4144093

E. El-SHEWY
Physics Dept.
Faculty of Science
Mansoura University.
Mansoura
Egypt
Tel: 002-010-5231769
e.k.el.shewy@mans.edu.eg

K. EL-SHORBAGY
Plasma Phys. & Nuclear Fusion Dept.
Nuclear Research Centre
Atomic Energy Authority
13759 Cairo
Egypt
Tel: 002-02-4682315
Fax: 002-02-4691749
shorbagy4@hotmail.com

A. B. EL-SISI
Plasma Phys. & Nuclear Fusion Dept.
Nuclear Research Centre
Atomic Energy Authority
13759 Cairo
Egypt
Fax: 002 02 2876031
ashrafelsisi@hotmail.com

W. EL-TAIBANY
Theoretical Plasma Physics Group
Department of Physics
Faculty of Science-Damietta
Damietta El-Gedida
P.O. Box 34517
Egypt
Tel: 002-057-365270
Fax: 002-057-403 866
eltaibany@hotmail.com

H. EL-TAYEB
Plasma Phys. & Nuclear Fusion Dept.
Nuclear Research Centre
Atomic Energy Authority
13759 Cairo
Egypt
Tel: 002-02-5701772
hoda.eltayeb@hotmail.com

W. GABER
Plasma Phys. & Nuclear Fusion Dept.
Nuclear Research Centre
Atomic Energy Authority
13759 Cairo
Egypt
wgaber2@yahoo.com

A. GARAMOON
Plasma Technology Center
Faculty of Science
Al-Azhar University, Cairo
Egypt
Tel: 002-02-6249139
Fax: 002-02-2629256
abdougaramoon@hotmail.com

M. GHONEIM
Fuel Manufacture Pilot Plant
Nuclear Research Centre
Atomic Energy Authority
13759 Cairo
Egypt
Tel: 002-02-4691756
Fax: 002-02-4691756

A. HASSAN
Accelerators & Ions Sources Dept.
Nuclear Research Centre
Atomic Energy Authority
13759 Cairo
Egypt
Tel: 002 02 3508247
amein.hassan @yahoo.com

M. HASSAOUBA
Faculty of Science
Benha Univ.
Benha
Egypt
Tel: 002-012-2743885
Fax: 002 013 222578

H. HEGAZY
Plasma Phys. & Nuclear Fusion Dept.
Nuclear Research Centre
Atomic Energy Authority
13759 Cairo
Egypt
Tel: 002-02-4620812
Fax: 002 02 2876031
hos_heg@yahoo.com

M. A. EBRAHEIM
Department of Physics
Faculty of Science
Zagazig University
Zagazig
Egypt
abdeldaiem@hotmail.com

R. M. KHAFAGY
Faculty of Women for Art, Science and Education
Physics Dept.
Ain Shams University
Cairo
Egypt
rashakhafagy@htomail.com

A. A. I. KHALIL
National Institute of Laser Science
Cairo University
Cairo
Egypt
Tel: 002-02-3655681
002-0106178587
ahmedassad@hotmail.com

M. KHEDR
Laser System Dept.
National Institute of Laser Science
Cairo University, Giza
Egypt
Tel: 002-02-5675224
Fax: 002-02-5729499
makdr@yahoo.com

A. MOHMOUD
Physics Dept.
Faculty of Science
Alazhar Univ. Assiut Branch
Assiut
Egypt

R. A. MOHAMMED
Nuclear Research Centre
Atomic Energy Authority
13759 Cairo
Egypt

A. MAHDY
Plasma Phys. & Nuclear Fusion Dept.
Nuclear Research Centre
Atomic Energy Authority
13759 Cairo
Egypt
aimahdy@yahoo.com

A. MASHALL
52 Toman Bai St,
Saria El-Koba, Cairo
Egypt
Tel: 002-02-4524350
daby2003@yahoo.com

M. M. MASSOUD
Plasma Phys. & Nuclear Fusion Dept.
Nuclear Research Centre
Atomic Energy Authority
13759 Cairo
Egypt
Tel: 002-02-2734510
mmmasoud@mailer.eun.eg

B. MOHAMED
Plasma Phys. & Nuclear Fusion Dept.
Nuclear Research Centre
Atomic Energy Authority
13759 Cairo
Egypt
Tel: 002-02-4682315
Fax: 002-02-4691749
mohamedbahf@yahoo.com

H. T. MOHASSEN
Nuclear Research Centre
Atomic Energy Authority
13759 Cairo
Egypt

S. OTHMAN
Fuel Manufacture Pilot Plant
Nuclear Research Centre
Atomic Energy Authority
13759 Cairo
Egypt
Tel: 002-02-4691756
Fax: 002-02-4691756

A. M. RACHED
Nuclear Research Centre
Atomic Energy Authority
13759 Cairo
Egypt

Y. A. SAYED
Plasma Phys. & Nuclear Fusion Dept.
Nuclear Research Centre
Atomic Energy Authority
13759 Cairo
Egypt
Tel: 002-02-4682315
Fax: 002-02-4691749
yousryelagamy@yahoo.com

F. SERGANI
National Institute of Laser Science
Environmental Laser Application Dept.
Cairo University, Giza
Egypt
Tel: 002-02-5675276
Fax: 002-02-5729499

M. K. SHAAT
Reactor Division
Nuclear Research Centre
Atomic Energy Authority
13759 Cairo
Egypt
Tel: 002-02-4620787
Fax: 002-02-4691754
m. shaat30@hotmail.com

W. SHRKAWY
Physics. Dept.
Faculty of Science
Al-Azhar University
Cairo
Egypt
Tel: 002-02-2733268
Fax: 002-02-2733268

H. SOLIMAN
Plasma Phys. & Nuclear Fusion Dept. Tel: 002-02-2717596 soliman.hanaa@hotmail.com
Nuclear Research Centre
Atomic Energy Authority
13759 Cairo
Egypt

S. E. SOLIMAN
Nuclear Fuel Tech. Dept. Tel: 002-02-3451795
Hot. Lab. Centre
Atomic Energy Aurthority
13759 Cairo
Egypt

A. H. SOUADI
Physics. Dept. Tel: 002-02-4697768
Faculty of Science
Al-Azhar University
Cairo
Egypt

W. Tawfik
National Institute of Laser Science Tel: 002-02-5675276
Environmental Laser Application Dept. Fax: 002-02-5729499
Cairo University, Giza
Egypt

S.WALLY
Fuel Manufacture Pilot Plant Tel: 002-02-4691756
Nuclear Research Centre Fax: 002-02-4691756
Atomic Energy Authority
13759 Cairo
Egypt

A. A. YOUSSEF
Nuclear Physics Dept. joseph@hotmail.com
Nuclear Research Centre Fax: 002-02-4620790
Atomic Energy Authority
13759 Cairo
Egypt

A. M. YOUSSEF
Department of Physics Tel: 002-02-3384365 Ahmed.yousseef@yahoo.com
Faculty of Science 002-057-403083
Mansoura University Fax: 002-57-403868
Damietta
Egypt

N. F. ZAHRAN
Basics Nuclear Science Division nfzahran@yahoo.com
Nuclear Research Centre Fax: 002-02-4620790
Atomic Energy Authority
13759 Cairo
Egypt

S. ZAKHARY
Accelerator Dept. Tel: 002-02-6393558 zakharysafwat@yahoo.com
Nuclear Research Centre
Atomic Energy Authority
13759 Cairo
Egypt

12. India

M. P. SIRVASTAVA
Dept. of Physics and Astrophysics
University of Delhi, Delhi
Delhi-11000, India
mps@himalaya.du.ac.in

13. Italy

B. STEWART
Office of External Activities
Abdus Salam ICTP
Strada Costiera 11,
34100 Trieste
Italy
Tel: +39-040-2240 536
Fax : +39-040-2240 558
stewart@ictp.trieste.it

S. VITULLI
IASF/CNR
via Gobetti,
101-40129 Bologna
Italy
Tel+39-051-6398662
Fax: +39-051-6398723
vitulli@bo.iasf.cnr.it

14. Libya

A. ALABYAD
Tajoura Nuclear Research Centre
Plasma Dept., Fax: 00218 21 3614143
Tajoura
Libya
Tel: 00218 21 3614133
alabyad@yahoo.com

B. ESMAIL
Tajoura Nuclear Research Centre
Plasma Dept.,
Tajoura
Libya
Tel: 00218 21 3614133
Fax: 00218 21 3614143
esmail@yahoo.com

M. Mansour
Tajoura Nuclear Research Centre
Plasma Dept.,
Tajoura
Libya
Tel: 00218 21 3614133
Fax: 00218 21 3614143

15. Mexico

R. ONDARZA-ROVIZA
Ins Nacional de Investigcionnes Nucleares
Addo Postal 10-1027,
Col Escandon, Mexico 11801, D.F.
Mexico
Tel: 0055-53-297200
Fax: 0055-53-297332
oadarza@nuclear.inin.mx

16. Pakistan

G. MURTAZA
G. C. University,
Lahore-54000
Pakistan
Tel: 0092-42-9212245
Fax: 0092-42-7243198
murtaza.qau@yahoo.com
schair@ihr.comsats.net.pk

17. Poland

J. BADZIAK
Institute of Plasma Physics and Laser Microfusion, Hery St. 23
P.O. Box 49, 00-908 Warsaw
Poland
Tel: 0048-22-683 9878
Fax: 0048-22-666 8372
badziak@if.pilm.waw.pl

T. PISARCZYK
Institute of Plasma Physics and
Laser Microfusion, Hery St. 23
P.O. Box 49, 00-908 Warsaw
Poland
Tel: 0048-22-683-7096
Fax: 0048-22-666-8372
pisaro@ifpilm.waw.pl

J. WOLOWSKI
Institute of Plasma Physics and
Laser Microfusion, Hery St. 23
P.O. Box 49, 00-908 Warsaw
Poland
Tel:0048-22-683-9605
Fax: 0048-22-666-8372
wolowski@ifpilm.waw.pl

18. Russia

A. KOSTROV
Institute of Applied Physics
Russian Academy of Science
Dept. of Plasma Physics &
High Power Electronics
603950,
Ulyanov str. 46,
Nizhny Novgorod
Russia
Tel: 007-8312-367821
Fax: 007-8312-362061
kstr@appl.sci-nnov.ru

G. SERGEY
Institute of Applied Physics
Russian Academy of Science
46 Ulyanov str.
Nizhny Novgorod 603950
Russia
Tel: 007-8312-364068
Fax: 007-8312-366086
gol@appl.sci-nnov.ru

19. Saudi Arabia

A. HALA
Space Research Institute-KACST
Riyadh
Saudi Arabia
amhala@hotmail.com

A. MUSSA
Riyadh 11442
P.O. Box 6086
Saudi Arabia
Tel: 00966 14 813560
Fax: 00966 14 813845
almuss@kacst.edu.sa

20. Singapore

R. S. RAWAT
National Institute of Education
Nanyang Technological University
1 Kanyang Walk,
Singapore-637618
Tel: 0065-67903826
Fax: 0065-58969432

21. Syria

S. AL-HAWAT
Physics Dept.
Atomic Energy Commission of Syria
P.O. Box 6091 Damascus
Syria
Tel: 00963-11-5410968
Fax: 00963-11-6112289
shhawatt@aec.org.sy

T. ALISSA
Higher Institute of Applied
Sciences and Technology
Damascus, P.O. Box 31983
Syria
Tel: 00963-11-512-4639
Fax 0963-11--223-7710

M. NADDAF
Research Dept. of Physics
Atomic Energy Commission of Syria
P.O. Box 6091 Damascus
Syria
Tel: 00963-11-2132580
Fax: 00963-11-6112289

S. SALOUM
Physics Dept.
Atomic Energy Commission of Syria
P.O. Box 6091 Damascus
Syria
Tel: 00963-11-2132580
Fax: 00963-11-6112289
ssaloum@aec.org.sy

S. SOULAYMAN
Higher Institute of Applied
Science and Technology
Damascus, P.O. Box 31983
Syria
Tel: 963(11)-512-4639
Fax: 963(11)-512-2237710
ssoulayman@netcourier.com

22. Sudan

A SIR EILKHATIM
Sudan Institute for Natural Sciences
Khartoum
P.O. Box 3045
Sudan
Tel: 00249-12-206816
Fax: 00249-11-771336
amnasirelkhatim@yahoo.co.uk

23. Thailand

C. SILAWATSHANANAI
Institute of Science
Walailak University
222 Thaiburi,Tasala, NakornSiThammarat
Thailand 80160
Tel: 0066-2-075-672055
Fax: 0066-2-075-672004

24. Tunisia

H. GHALILA
Laboratoire de Spectroscopie
Atomique et Moléculaire et Application
Faculté des Sciences Campus El Manar
Tunis
Tunisia
Tel: 00216-71-872600
ghalila.sevestre@planet.tn

25. Ukraine

Y. MARTYSH
Taras Shevchenko National Kyiv Univ.
Volodimirska Str. 64,
Kyiv-33, 01033
Ukraine
Tel. 0038-044-558-1263
emart@mail.univ.kiev.ua

I. ONISHCHENKO
National Science Centre
"Kkarkov Inst of Physics
and Technology"
Academic Str.1, Kharkov 61108
Ukraine
Tel: 00038-0572-356611
Fax: 0038-0572-353564
onish@kipt.kharkov.ua

previously published in this series

Joint German-Indonesian Seminar on R&D Activities using the MPR-30
Jakarta, August 19-21,1985
GERMAN-INDONESIAN COOPERATION
ISBN 3-89336-011-5

Joint German-Indonesian Seminar on Public Acceptance, Waste-Management, and Nuclear Safety
Jakarta, October 7-9,1986
GERMAN-INDONESIAN COOPERATION
ISBN 3-89336-012-3

VIIIth German-Yugoslav Meeting on Materials Science and Development Ceramics and Metals
edited by Drago Kolar, Marija Kosec and Johanna Krawczynski
Brdo pri Kranju, May 18-21,1987
GERMAN-YUGOSLAV COOPERATION
ISBN 3-89336-001-8

Proceedings of the Fourth Workshop on Two-Phase Flow Predictions
edited by M. Sommerfeld and H. Zeisel
Erlangen, October 21-23,1987
GERMAN-YUGOSLAV COOPERATION
ISBN 3-89336-002-6

IInd Workshop on Process Automation
Darmstadt, November 2-6, 1987
GERMAN-YUGOSLAV COOPERATION
ISBN 3-89336-003-4

Ist German-Yugoslav Meeting in the Framework of the Bilateral Project Development of Innovation Structures in Yugoslavia
edited by G. Bräunling and V. Mateji
Innovation Consultancy Centers
Plitvice, September 5-7,1988
GERMAN-YUGOSLAV COOPERATION
ISBN 3-89336-024-7

Proceedings of the 8th Winter School on Proteinases and their Inhibitors: Recent Developments
edited by E. Auerswald, H. Fritz and V. Turk
Tiers, March 8-12, 1980
GERMAN-YUGOSLAV COOPERATION
ISBN 3-89336-020-4

Second German-Greek Workshop on Materials Research for Information Technology
edited by G. Kaiser and H. Wenzel
Jülich, May 22-23,1989
GERMAN-GREEK COOPERATION
ISBN 3-89336-018-2

Seminar Fertigungsplanung und -steuerung
zusammengestellt von
Burghild Wienecke-Toutaoui,
Rolf Albrecht
Split, 7. und 8. Juni 1989
GERMAN-YUGOSLAV COOPERATION
ISBN 3-89336-025-5

IXth German-Yugoslav Meeting on Materials Science and Development Emerging Materials by Advanced Processing
edited by Wolfgang A. Kaysser, Jutta Weber-Bock
Hirsau/Stuttgart, April 16-19, 1989
GERMAN-YUGOSLAV COOPERATION
ISBN 3-89336-026-3

Bilateral Seminars of the International Bureau

1 IInd German-Yugoslav Meeting in the Framework of the Bilateral Project
Development of Innovation Structures in Yugoslavia
Innovation Management
Plitvice, October 18-20,1989
edited by Vlastimir Mateji
GERMAN-YUGOSLAV COOPERATION

2 IInd Workshop on Plasma and Laser Technology
Cairo, February 21-28, 1990
edited by E. Hintz
GERMAN-EGYPTIAN COOPERATION

3 Seminar on Emissions and Air Quality
Thessaloniki, October 9, 1990
edited by N. Moussiopoulos, D. Kaiser
GERMAN-GREEK COOPERATION

4 5th Workshop on Two-Phase Flow Predictions
Erlangen, March 19-22, 1990
edited by M. Sommerfeld, D. Wennerberg (1991)

5 IInd Workshop on Plasma and Laser Technology, Volume 2
Cairo, February 21-28, 1990
edited by Ph. Mertens, B. Schweer (1991)
GERMAN-EGYPTIAN COOPERATION

6 2. Brasilianisch-Deutsches Symposium für Naturstoffchemie
2. Simposio Brasileiro-Alemao de Produtos Naturais
Hannover, 28. Juli - 10. August 1991
herausgegeben von G. Habermehl (1991)
DEUTSCH-BRASILIANISCHE ZUSAMMENARBEIT

7 3rd German-Greek Workshop on
Materials Research for Information Technology
Thessaloniki, September 26-27, 1991
edited by G. Kaiser, N. Constantopoulos (1992)
GERMAN-GREEK COOPERATION

8 Egyptian-German Springschool and Conference
Particle and Nuclear Physics
Cairo, April 11-19, 1992
GERMAN-EGYPTIAN COOPERATION

9 Seminar on Monitoring and Modelling in the Mesoscale
Thessaloniki, September 27, 1991
edited by N. Moussiopoulos, G. Kaiser (1992)
GERMAN-GREEK COOPERATION

10 3rd Workshop on Process Automation
Ljubljana, May 22-24, 1991 (1992)
GERMAN-SLOVENIAN COOPERATION

11 Course on Medical Aspects of Nuclear and Radiation Accidents
Cairo, April 11-16, 1992
edited by A.M. El-Naggar, D. Nentwich (1992)
GERMAN-EGYPTIAN COOPERATION

12 Egyptian-German Springschool and Conference
Particle and Nuclear Physics, Volume 2: Contributed Papers
Cairo, April 11-19, 1992
GERMAN-EGYPTIAN COOPERATION

13 Indo-German Workshop on
High Pressure Technology-Engineering
Pune, January 3-4, 1992
edited by R.V. Chaudhari, H. Hofmann (1993)
GERMAN-INDIAN COOPERATION

14 6th Workshop on Two-Phase Flow Predictions
Erlangen, March 30 - April 2,1992
edited by M. Sommerfeld (1993)

15 3rd Workshop on Plasma and Laser Physics
Ismailia, October 3-7,1993
edited by Ph. Mertens (1994)
GERMAN-EGYPTIAN COOPERATION

16 Utilization of the Low Active Waste Incinerator
Facility (LAWI) for Research and Development Work
Cairo, December 11-12, 1993 (1994)
GERMAN-EGYPTIAN COOPERATION

17 8th SIMCER International Symposium on Ceramics
Biomaterials - Special Meeting of the Project EUREKA 294
Rimini, November 10-12, 1992
edited by I. Stamenkovi, J. Krawczynski (1994)
GERMAN COOPERATION with the University "Sv. Kiril i Metodij", Skopje

18 Conceptual Approaches to the Support of Industrial
Research and Development in Slovenia
Ljubljana, November 10, 1993
edited by M. Komac, J. Krawczynski (1994)
GERMAN-SLOVENIAN COOPERATION

19 German-Egyptian Seminar on Environmental Research
Cairo, March 21-23, 1994
edited by H.F. Aly, D. Nentwich (1994)
GERMAN-EGYPTIAN COOPERATION

20 1st Slovene-German Seminar on Joint Projects in Materials Science and Technolgy
Portoro, Oct. 2-4, 1994
edited by D. Kolar, D. Suvorov (1995)
GERMAN-SLOVENIAN COOPERATION

21 Conceptual approaches for an industry-related promotion of research
and development in Croatia
Workshop Proceedings, Zagreb June 28-29, 1994
edited by S. Lange, J.Švarc (1995)
GERMAN-CROATIAN COOPERATION

22 German-Egyptian Seminar on Science Policy and Management
Cairo, April 8-9, 1995
edited by A. A. El Sayed, D. Nentwich (1995)
GERMAN-EGYPTIAN COOPERATION

23 Indo-German Workshop on
Antiinflammatory Drugs from Natural Sources
Jammu Tawi, 10-11th April 1995
edited by H.T.P. Ammon, R.S. Kapil (1995)
GERMAN-INDIAN COOPERATION

24 German - West Sumatra Seminar on
R & D Management and its Role for Industrial Development
Bukittinggi, West Sumatra, Indonesia, November 28-30, 1994
edited by D. Nentwich (1996)
GERMAN-INDONESIAN COOPERATION

25 Indo-German Workshop on
Technology Development and Transfer
New Delhi, February, 7th-10th, 1995
edited by R. J. Peters, H. R. Bhojwani (1996)
GERMAN-INDIAN COOPERATION

26 Proceedings of the 3rd Workshop on Information Technology
Berlin, December 14th-15th, 1995
edited by St. Jähnichen, C. J. P. de Lucena (1996)
GERMAN-BRAZILIAN COOPERATION

27 Fourth Workshop on
Plasma and Laser Physics
Cairo - Egypt, February 26-29, 1996
edited by H.-A. Claaßen, H.-B. Schweer (1997)
GERMAN-EGYPTIAN COOPERATION

28 2nd Indo-German Workshop on Microelectronics
Suraj Kund, New Delhi, December, 7th-8th, 1995
edited by R. N. Biswas, H. L. Hartnagel
GERMAN-INDIAN COOPERATION

29 Trends in Radiation and Cancer Biology
edited by R. N. Sharan (1998)
INDO-GERMAN COOPERATION

30 Recent Aspects of Cellular and applied Radiobiology
edited by F. H. A. Schneeweiss, R. N. Sharan (1999)
INDO-GERMAN COOPERATION

31 Fourth Bar-Ilan-Ulm-Workshop in Mathematics
Workshop Proceedings
Ulm, June 29 - July 1, 1998
edited by H. Lanzinger, U. Stadtmüller (1999)
GERMAN-ISRAELIAN COOPERATION

32 Aspects of Pan-African Tectonics
edited by H. de Wall, R.O. Greiling (1999)
GERMAN-EGYPTIAN / GERMAN-MOROCCAN COOPERATION

33 Egyptian - German Workshop on
Materials and Processes for Advanced Technology:
Materials for Energy Systems
edited by D. Stöver, M. Bram (2003)
GERMAN-EGYPTIAN COOPERATION

34 First Cairo Conference on Plasma Physics & Applications
CCPPA2003
Cairo, 11 – 15 October 2003
edited by H.-J. Kunze, T. El-Khalafawy, H. Hegazy (2004)
GERMAN-EGYPTIAN COOPERATION



Forschungszentrum Jülich
in der Helmholtz-Gemeinschaft

ISBN 3-89336-374-2

Boltzmann's moments can't lead to accurate solution of this problem. The electronic distribution function is being built and PIC Monte Carlo calculations give it to us as a result. Then we have the evolution of all the kinetic parameters so we can also calculate all the coefficient transport. When the steady state is reach, all those results can be used for fluid simulation as initial parameters.

The physical point we focus our investigations on concern the study of the mechanisms responsible of the apparition of the streamers which are observed in the vicinity of the avalanche and which appear like a very fast luminous front. This critical point was the subject of several works and it's steeled relevant today[2,3]. Numbers of mechanisms have been proposed to explain the transition of an avalanche into streamer. Among this explanations the role of the distribution velocity distribution and also the role of the photoionization are shown with the use of Monte Carlo[1,4]. Experimental conditions (pressure, gas, electric field, and geometry) decide of the relative importance of the different mechanisms and we aim here to find again these experimental behaviors.

PHYSICAL PROBLEM AND ITS NUMERICAL FORMULATION

The physical problem we are interested in corresponds to a cylindrical nitrogen gas embedded in a uniform electrical field produced by plane parallel electrodes. The different cases we simulate describe a single avalanche evolve in low pressure gas of about 1 Torr and high overvoltage (20%). We expect in this condition a very fast growth of ionization with streamer development. Rather[5] shows that an overvoltage of about 20% is enough to observe streamers development. Electronic avalanche starts with some electrons, which are put simply on the cathode. The growth can begin with a single stationary electron injected only at the initial time or more electrons which released from small area with initial energy of about 1 eV during a very short time (about 1 picosec) to simulate a small beam like those produced by cathodic spot or pulse of electrons like those produced by laser pulse.

We took the same parameters as Kline and Siambis[1] to compare our results with there. The electrodes are 4 cm apart and the voltage is 40 kV. The nitrogen gas is at 1 Torr. The initial distribution of particles correspond to a few electrons injected at the initial time with initial energy comprise between 0 and 1 eV. This emission is located in a small area located in the vicinity of the axis. Because of the one dimensional of their simulations we add high magnetic field (5 Tesla) to obtain one-dimensional motion. We study the evolution of the system during 20 nsec.

We use the central difference scheme to formulate numerically the analytical expression. This scheme is based on a spatial and temporal regular mesh which must allow us to observe collective effects of plasma like electron plasma frequency ω_{pe} and electron Debye length λ_D and also to enable us to reproduce the collision frequency. An estimation of ω_{pe} and λ_D can be done with using the maximum number of electrons[1] which is stabilize to 5.10^{10} after 20 nsec of simulation. If we take this value as the maximum of the density, we can estimate the maximum value of $\omega_{pe} = (n_e^2/m\varepsilon_0)^{1/2}$ = 12.6 GHz and of $\lambda_D = (v^2/\omega_{pe}^2)^{1/2}$ = 0.1 mm. The spatial cell size $\Delta z = \Delta r$ = 1 mm and the temporal cell size Δt = 2 picoses are then small enough to give accurate results. In fact the spatial cells are larger than the value of λ_D but this estimation is also very wide because the ω_{pe} is in fact smaller.

Resolution of charge conservation law couple with the Ampere and Faraday law[6] give us the self electric and magnetic field produced by the evolution of the charge particles. External fields are uniform and constant during the calculations. The self electromagnetic field is added to the external field in the Lorentz movement equation to solve the system self-consistently.

$$\vec{\nabla}\,\vec{J} = -\frac{\partial \rho}{\partial t} \tag{1}$$

$$\frac{\partial \vec{E}}{\partial t} = \frac{1}{\mu_0 \varepsilon_0}\left(\vec{\nabla} \times \vec{B} - \mu_0 \vec{J}\right) \tag{2}$$

$$\frac{\partial \vec{B}}{\partial t} = -\vec{\nabla} \times \vec{E} \tag{3}$$